PROCEEDINGS

SEVENTEENTH WORKSHOP
GEOTHERMAL RESERVOIR ENGINEERING

January 29-31, 1992

Henry J. Ramey, Jr., Roland N. Horne,
Paul Kruger, Frank G. Miller,
William E. Brigham, Jean W. Cook
Stanford Geothermal Program
Workshop Report SGP-TR-141

Library of Congress Catalog Card No. 86-643338
ISSN 1058-2525

TABLE OF CONTENTS

MODELLING - III

RESERVOIR MECHANICS

CONCLUDING DISCUSSION

PAPERS NOT PRESENTED

PREFACE

The Seventeenth Workshop on Geothermal Reservoir Engineering was held at Stanford University on January 29-31, 1992. There were one hundred sixteen registered participants which equaled the attendance last year. Participants were from seven foreign countries: Italy, Japan, United Kingdom, France, Belgium, Mexico and New Zealand. Performance of many geothermal fields outside the United States was described in the papers.

The Workshop Banquet Speaker was Dr. Raffaele Cataldi. Dr. Cataldi gave a talk on the highlights of his geothermal career. The Stanford Geothermal Program Reservoir Engineering Award for Excellence in Development of Geothermal Energy was awarded to Dr. Cataldi. Dr. Frank Miller presented the award at the banquet.

Thirty-eight papers were presented at the Workshop with two papers submitted for publication only. Dr. Roland Horne opened the meeting and the key note speaker was J.E. "Ted" Mock who discussed the DOE Geothermal R. & D. Program. The talk focused on aiding long-term, cost effective private resource development.

Technical papers were organized in twelve sessions concerning: geochemistry, hot dry rock, injection, geysers, modelling, and reservoir mechanics. Session chairmen were major contributors to the program and we thank: Sabodh Garg, Jim Lovekin, Jim Combs, Ben Barker, Marcelo Lippmann, Glenn Horton, Steve Enedy, and John Counsil.

The Workshop was organized by the Stanford Geothermal Program faculty, staff, and graduate students. We wish to thank Pat Ota, Ted Sumida, and Terri A. Ramey who also produces the Proceedings Volumes for publication. We owe a great deal of thanks to our students who operate audiovisual equipment and to Francois Groff who coordinated the meeting arrangements for the Workshop.

Henry J. Ramey, Jr.
Roland N. Horne
Frank G. Miller
Paul Kruger
William E. Brigham
Jean W. Cook

PROCEEDINGS, Seventeenth Workshop on Geothermal Reservoir Engineering
Stanford University, Stanford, California, January 29-31, 1992
SGP-TR-141

DOE GEOTHERMAL R&D PROGRAM FOCUSED ON FACILITATING LONG-TERM, COST-EFFECTIVE PRIVATE RESOURCE DEVELOPMENT

John E. Mock, Director

Geothermal Division
U.S. Department of Energy

ABSTRACT

Analyses conducted in support of the National Energy Strategy projected that as much as 22,000 megawatts of cost-effective, moderate-temperature geothermal energy are available to the U.S. over the long-term, or to the year 2030. Thus, the primary hydrothermal technology research goal of the Department's Geothermal Division is to facilitate the ability of the private sector to exploit competitively this large source of energy up to that capacity level or greater. The primary mechanism for implementing this goal is an R&D core program cost-shared with industry focused on major cost-sensitive technology areas: exploration technology, reservoir engineering and management, and drilling.

The NES analyses also indicated that electricity generated with energy derived from hot dry rock could be a geographically dispersed, logical follow-on to hydrothermal electricity in the longer term. In order to demonstrate whether energy at useful temperatures can be extracted over extended periods at competitive energy prices, a long-term flow test of an experimental HDR system will be conducted.

This paper describes DOE's current participation in R&D activities leading to the development of "cutting edge" technology that will serve the geothermal industry's interest well into the next century.

INTRODUCTION

National market-analysis models developed in support of the National Energy Strategy show that when reasonable assumptions are made about the characteristics of U.S. geothermal resources and technology, continued markets for, and economic benefits from, can be projected for geothermal energy. In a scenario which assumes continuation of today's national energy policy, the NES projects that 22,100 (net summer capacity) of hydrothermal electric capacity will be in use in 2030. To derive this projection, my staff and the Meridian Corporation developed special simulators using existing resource and cost data, including projected mid- and long-term effects of research on technology cost-effectiveness. The quantitative research objectives of the DOE geothermal R&D program were used as a basis for technology improvement up to 2010, after which a more optimistic "breakthroughs" scenario for technology improvement was applied. The resulting cost-supply curves for hydrothermal electricity were then used in the primary NES economics model, FOSSIL-2, which competes most energy supply technologies against incremental demands to the year 2030.

For hot dry rock, the DOE/Meridian economic supply model indicated that if 10 percent of the moderate-to-high thermal gradient area of the U.S. could be used for HDR applications, the technically feasible potential would be about 19,000 GWe for 20 years with about 3,800 GWe occurring at economically attractive sites. In 1990, the 3,800 GWe could have had an average break-even price of just over 8¢/kWh in 1990 dollars. By 2010, the price could drop to about 5.3¢/kWh, and the long-run cost could be as low as 4¢/kWh if all the postulated technology developments occur.

The NES provides for a climate in which geothermal energy can reach reasonable expectations of growth through its commitment to substantial diversification of U.S. sources of energy. Specifically, it is stated, the Strategy "will spur more...competition throughout the energy sector, expand the fuel and technology choices available to the Nation, [and] improve U.S. research and development...." What is needed in renewable energy, including geothermal, the Strategy concludes, "is the opportunity to translate R&D progress to practice, removal of market barriers, and continued *focused* R&D to realize the full potential of these technologies."

This, then, is the goal of the DOE R&D program -- to focus on activities that will facilitate long-term, cost-effective private geothermal development. If successful, the program will enhance the ability of the geothermal industry to compete within the NES policy framework of market reliance -- i.e., "wherever possible, markets should be allowed to determine prices, quantities, and technology choices."

HYDROTHERMAL PROGRAM IMPLEMENTATION

The primary mechanism for achieving the hydrothermal objectives of this goal is an R&D core program cost-shared with industry focused on major cost-sensitive technology areas: exploration technology, reservoir engineering and management, and drilling, the costs of which impact both exploration and reservoir engineering and management.

Exploration Technology

A number of the U.S. hydrothermal reservoirs that were explored by industry beginning in the late 1960's and through a cooperative government/industry exploratory drilling program are in commercial production today. However, further near-term development will be limited by the availability of proven reservoirs. William P. Short III of Kidder, Peabody, & Co. predicts that "if there is insufficient evidence to classify a geothermal field's resource as proven, that geothermal field will probably not be developed in the 1990's." He bases his prediction on several factors, not the least of which is the lack of risk capital to commit to geothermal exploration and development programs.

And with today's technology limitations which require the drilling and testing of at least one expensive deep well to determine the producibility of a reservoir -- at costs of $1.5 to $3.5 million each -- the up-front risk capital needed by an industry described by Dr. Jim Combs as one of "cash-short entrepreneurs" is very large. In calling for continued cost-shared geothermal exploration and reserves confirmation R&D by DOE, industry, and academia, Dr. Combs of Geo Hills Associates said this effort is needed to resolve the "Catch-22" situation in which the industry finds itself. That is, he said, "industry needs to prove a viable geothermal reservoir without spending much money in order to acquire a long-term power sales contract with a utility which can be used to finance the project in order to drill and test the wells that are needed to prove the efficacy of the power generation project."

In response to this critical industry need, our R&D program is undertaking to select the most innovative methods to locate and characterize undiscovered resources. We are investigating the range of optical, electromagnetic, geochemical, gravitational, and biological methods that may offer promise as exploration techniques. Industry is actively involved with us in technology development to produce the new generation of instruments necessary to discover hidden geothermal systems, and we are planning to conduct a cooperative venture designed to confirm the existence of a suspected hydrothermal system. An RFP will be issued asking industry to propose a favorable exploration target based on its information up to that point. An area will be selected for completing exploratory work that has not been done, and finally a deep hole will be drilled to confirm the findings of the less expensive technologies or to determine where those methods failed.

Our current planning anticipates that this innovative research into improved exploration techniques will be continued and expanded as future resources permit to meet industry's needs for this function during the next decade and beyond.

Reservoir Engineering and Management

The need for improved methods, equipment, and materials for geothermal reservoir engineering and management is demonstrated conclusively by the current problems at The Geysers. And the need can only become more critical as hot water fields begin to mature and new reservoirs are identified bringing their own sets of characteristics and complexities to be delineated and managed in developing and implementing exploitation strategies.

The successful performance of geothermal reservoirs in terms of meeting contractual requirements for production quantity, quality, and longevity have implications far beyond the economics of the particular producer and user in each case. Successful performance is vital to the survival of geothermal energy as a reliable and accepted alternative fuel within regulatory and energy planning communities -- as well as the investment community. Successful performance in terms of environmental quality is vital to the acceptance of this resource by every level of government and the public. Less than successful performance invites our critics, doubters, and competitors to challenge the validity of this resource in the marketplace.

Thus, a very high priority continues to be given to the development of new techniques for locating and characterizing fractures and reservoir boundaries, to assess fluid recharge, and to understand complex reservoirs. Many in this workshop audience are long time participants in this R&D program element and will be reporting on their activities in detail, so I will confine my remarks to a brief summary of our Fiscal Year 1992 approach.

Research related to a better understanding of The Geysers system is continuing to be emphasized to aid the industry in managing the field for sustained production. Geophysical and geochemical studies related to fractured geothermal systems are investigating phenomena unique to vapor-dominated systems and the generic need for injection of water into all fractured geothermal systems to efficiently recover the resource. The benefits of this effort will extend beyond The Geysers and provide field management guidance for other major U.S. producing fields which depend on fracture permeability.

The research will include studies for the identification of fracture systems early in the exploration and drilling stages, the development and refinement of methods to model flow of reservoir fluids and injected fluids in fractured reservoirs, and the development of tracers which can be used in high-temperature hydrothermal reservoirs.

Drilling

The successful accomplishment of a major objective of the FY 1992 drilling R&D will advance both exploratory drilling and field management techniques. This objective is the development of downhole memory instrumentation to improve logging of geothermal wells.

The drilling experts at Sandia National Laboratory report that downhole measurements are not commonly used in the geothermal industry even though they possess a demonstrated capability of providing data important to development and maintenance of geothermal fields. Log data, for example, can provide the basis for engineering and permitting decisions involving corrosion control and the design/evaluation of cement bonding operations. In addition, log data on parameters such as fracture density, size, and orientation can guide well placement.

The use of logs in geothermal fields has been inhibited by the lack of high-temperature tools as well as uncertainty as to their value. However, a Sandia review of the logging literature indicates that similar uncertainties initially existed with respect to hydrocarbon applications, but as the ability developed to make downhole measurements, the interpretation of the data often produced unexpected beneficial results. A similar experience is expected in regard to geothermal applications.

The Sandia approach to instrumentation for high-temperature wells is to use a downhole memory unit that stores the data in a computer system. This technique is potentially inexpensive and does not require extensive uphole equipment or an expert crew, attributes which may lead to applications beyond use in geothermal wells.

DOE is funding, in conjunction with industry, the design and construction of a high-temperature spectral gamma tool based on the downhole memory concept. It will be designed for 400°C operation and will be compatible with small diameter coreholes in response to industry's needs for reduced exploration costs. New higher temperature tools being developed for deep gas wells will be evaluated by a cooperative arrangement among Sandia, geothermal operators, and a logging company.

Another element in the FY 1992 drilling R&D directed toward reducing exploration costs is the consideration of advanced coring concepts utilizing high-speed coring rigs to drill small, less expensive holes. It will be determined whether an industry cost-shared field test can be developed to compare directly productivity from the same formation in large and small wells. The field test would include injectivity/productivity correlations and use downhole instrumentation to supplement the wellhead measurements for better definition of the flow conditions in the wellbore.

HOT DRY ROCK PROGRAM IMPLEMENTATION

As most of you know, the Geothermal Research, Development, and Demonstration Act of 1974 mandated that the production and use of all forms of geothermal energy be investigated. At about the same time, a patent was issued to researchers at the Los Alamos Laboratory for the HDR extraction concept, and work began on the first HDR reservoir at Fenton Hill, New Mexico. Experimental work has continued from that time, and now we are examining the commercial prospects of this technology.

The first reservoir was tested successfully for about one year and demonstrated that the concept "works" -- i.e., it demonstrated that heat could be extracted from rock at reasonable rates without insurmountable technical problems or serious environmental effects. A deeper, hotter reservoir was constructed, and, after corrections to connect the two well bores, tested for 30 days in 1986. The production flow rate, fluid temperature, and, consequently, the thermal power increased throughout the test. The flow impedance continually declined as did the rate of water loss. By the end of the test, about 70 percent of the injected water was being produced at a temperature of 190°C. The power level reached about 10MW$_t$.

More recently, preparations have been made to conduct a long-term flow test, which, if successful, will provide an example of the potential of the HDR concept over long periods of time and a benchmark for the development of commercial HDR systems. The objectives of the long-term flow test fall into three categories:

- Technical goals
  - Evaluating the useful lifetime of the reservoir, quantifying water consumption rates, measuring production fluid flow and temperatures, and determining the power production of the reservoir.
- Operational goals
  - Understanding the important operating parameters of the system including maintenance requirements, ongoing costs, and other relevant information.

- Scientific goals

  Increasing the levels of understanding in seismology, tracer technology, and underground reservoir engineering.

In a preliminary system checkout in December prior to actual start-up in January 1992, all major components of the plant performed adequately with a production temperature of 154.3°C.

This initial stage was observed by representatives attending a renewable energy conference conceived by former U.S. Secretary of the Interior Stewart Udall, and co-sponsored by the Center for Resource Management, Los Alamos National Laboratory, the Electric Power Research Institute, Southern California Edison, and Bechtel. The meeting heard reports on international HDR projects by representatives from Japan, the European Community, and the United Kingdom. Dr. Paul Kruger of Stanford University presented a summary of the Russian HDR effort. A panel was then convened to discuss the economics of HDR and the factors necessary for commercialization of the technology. The meeting concluded with the reading of a statement urging increased support for HDR development and proposing a series of concrete steps to move the technology forward. As has traditionally been the case with respect to the recommendations of industry and other sectors of the geothermal community regarding the conduct of hydrothermal R&D, the views of these distinguished individuals will be considered in planning for future research program activities.

CONCLUSION

While legislation needed to implement certain aspects of the National Energy Strategy is still under consideration by Congress, we do not really need new legislation to continue our effort to meet the NES goal of more competition in the energy sector and expansion of the available fuel and technology choices. We also do not need legislation to *use* the NES goals in support of geothermal energy. We should never waste an opportunity to remind decision-makers that this resource is "made-to-order" for implementing the strategy developed at the highest levels of government.

I believe that the geothermal R&D program I have highlighted here supports the recent call of the President for "an energy future that opens the door to new and diverse energy sources" and provides "the responsible leadership of industry and government."

PROCEEDINGS, Seventeenth Workshop on Geothermal Reservoir Engineering
Stanford University, Stanford, California, January 29-31, 1992
SGP-TR-141

THE UK GEOTHERMAL HOT DRY ROCK R&D PROGRAMME

Paul MacDonald, Ann Stedman and Geoff Symons

Energy Technology Support Unit
Harwell, Oxfordshire OX11 0RA
United Kingdom

ABSTRACT

The UK hot dry rock research and development programme is funded by the Department of Energy and aims to demonstrate the feasibility of commercial exploitation of HDR in the UK. The philosophy of the UK programme has been to proceed to a full-scale prototype HDR power station via a number of stages:

- *Phase 1*
  Experiments at shallow depth (300 m) to assess the feasibility of enhancing the permeability of the rock.
- *Phase 2*
  Studies at intermediate depth (2500 m) to determine the feasibility of creating a viable HDR subsurface heat exchanger.
- *Phase 3*
  Establishment of an HDR prototype at commercial depth.

The programme has run over a 15 year period, and has been formally reviewed at stages throughout its progress. The 1987 review towards the end of Phase 2 identified a number of technical objectives for continuing research and proposed that the initial design stage of the deep HDR prototype should start.

Phase 3A is now complete. It addressed:

- the feasibility of creating an underground HDR heat exchanger suitable for commercial operation
- techniques for improving hydraulic performance and correcting short circuits in HDR systems
- modelling of the performance, resource size and economic aspects of HDR systems.

The work has been conducted by a number of contractors, including Camborne School of Mines, Sunderland and Sheffield City Polytechnics and RTZ Consultants Limited.

This paper focuses upon the experimental work at Rosemanowes in Cornwall and the recently completed conceptual design of a prototype HDR power station. The economics of HDR-generated electricity are also discussed and the conclusions of a 1990 programme review are presented. Details of the HDR programme to 1994, as announced by the UK Department of Energy in February 1991, are included.

INTRODUCTION

For nearly 20 years there has been interest in research and development aimed at extracting the heat from hot dry rock (HDR). The technology for extracting the heat involves pumping water down a borehole drilled from the surface, circulating it through artificially enlarged fissures in the hot rock and bringing it back to the surface via a second borehole[1]. See Figure 1.

The UK programme has proceeded in 3 phases. The programme chronology and cumulative expenditure to April 1991 are shown in Figure 2.

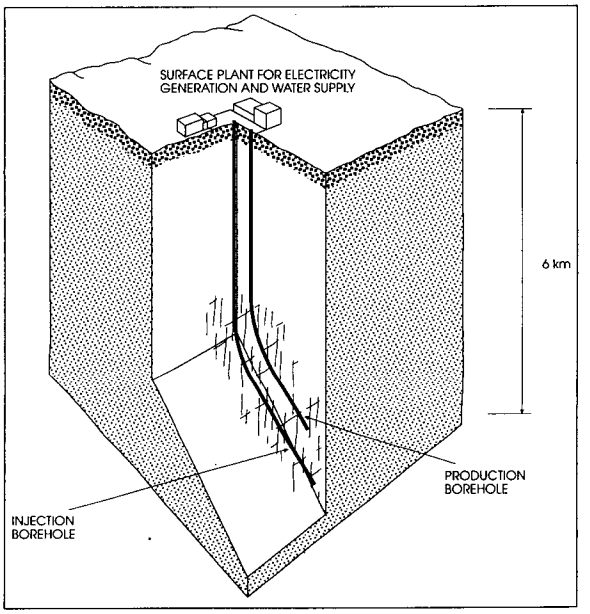

Figure 1 *Schematic representation of an HDR system in the UK*

1977–1980 PHASE 1

The major work under Phase 1 was a small-scale field trial at Rosemanowes, aimed at linking four 300 m deep boreholes over a horizontal distance of 40 m. Earlier work at Los Alamos in the United States had already shown that water could be circulated between two boreholes after hydraulic stimulation (at 3000 m), but the resistance to flow had been unacceptably high and it was

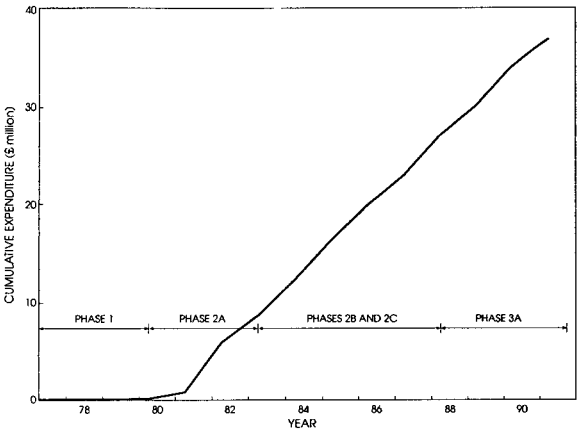

Figure 2 *Chronology of Phases 1 to 3A at Rosemanowes, and the cumulative expenditure by the UK Department of Energy to April 1991*

believed that much of the impedance was concentrated in the zones immediately surrounding the boreholes. One objective of Phase 1 of the CSM work was to show that the use of controlled explosions within the boreholes could improve the permeability of the rock adjacent to the wellbore and initiate new fractures, which might themselves be stimulated hydraulically to provide a low impedance path between the boreholes by way of the natural joint system.

During Phase 1, the combination of explosives and hydraulic fracturing followed by water circulation reduced the impedance of the system by a factor of 50 relative to that achieved previously (at Rosemanowes and at Los Alamos) by hydraulic fracturing alone. The lowest impedance achieved was close to 0.1 MPa per l/s, a value which was considered to be necessary for a commercial prototype.

In several senses, however, the conditions of this experiment were unrepresentative of those expected in a deeper system. At 300 m, the direction of minimum principal stress in the rock at Rosemanowes is vertical; consequently, the fractures that were opened were essentially in the horizontal plane. At depths greater than 400–500 m, the minimum principal stress will normally be horizontal and hence fractures will open preferentially in a vertical plane. It is now recognised that many aspects of the behaviour of shallow fractures (mode of opening, consequent water loss, etc) are different from those at depth. Nevertheless, at the time, the results of Phase 1 gave sufficient confidence in the experimental procedures to justify a second phase of investigation.

1980–1983 PHASE 2A

Phase 2 was an eight-year project in total, aimed at engineering a commercial-scale HDR heat exchanger. However, instead of drilling to the commercial depth of 6 km, it was decided to drill two boreholes to a depth of about 2 km. This reduced the drilling costs and meant that rocks at a temperature of about 80°C would be reached. Phase 2 aimed at engineering a subsurface system with the hope that, if successful, it might have relevance to conditions at 6 km. However, many of the temperature-dependent aspects of reservoir performance at 6 km, such as geochemical and thermal drawdown effects, could not be evaluated directly at 2 km. The rock jointing and stress régime at 6 km depth would eventually have to be determined.

The first part of Phase 2 (ie Phase 2A) lasted from 1980 to 1983 and was funded in part by the Commission of the European Communities. During this period, two boreholes deviated from the vertical by 30° were drilled, in the same plane and spaced 300 m apart at depth, to a depth of 2 km. Figure 3 shows the wellheads at Rosemanowes. Hydraulic fracturing was carried out with water from the lower borehole to try to open up the near-vertical joints rising to and intersecting the upper borehole. When circulation started, the system did not behave as predicted: water losses were excessive and the pumping pressures required for circulation were too high. It was not possible to get within a factor of ten of the target production flow rate of 75 l/s. Examination of the microseismic evidence during stimulation and circulation showed a large 'cloud' beneath each borehole but the pumping and tracer tests showed that inter-connection between the boreholes was poor. To try to improve this connection by further hydraulic stimulation could have risked even greater water losses.

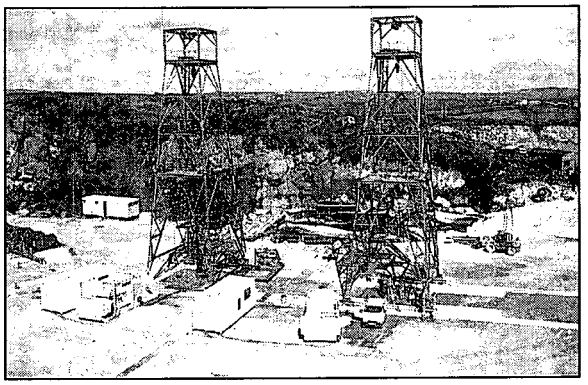

Figure 3 *Towers above production and injection boreholes at Rosemanowes Quarry, Cornwall, UK*
(Photo courtesy Camborne School of Mines)

The technical status of the work at Rosemanowes was reviewed early in 1984 by a group of outside consultants working with CSM staff. They concluded that a number of important technical issues were unresolved:

- how the geological structure (particularly the permeability and variability of rock joints) affects the development of a subsurface heat exchanger
- how the shear stresses affect the permeability of joints at depth
- the role of ambient reservoir pressure in hydraulic fracturing, and how it affects flow rates and water losses.

1983–1988 PHASES 2B AND 2C

Measurements made after the two boreholes (RH11 and RH12) had been drilled at Rosemanowes Quarry showed that the direction of the maximum principal stress in the ground was aligned almost exactly with the borehole deviation – the worst possible alignment for maximising the intersection of the boreholes with the most easily opened joints. Therefore a new borehole (RH15) was drilled at Rosemanowes at the end of 1984 to a depth of 2600 m and along a helical path crossing the microseismic 'cloud' at right angles to the vertical plane of the first two boreholes, to try to get the maximum number of intersections. The Phase 2B programme was started by using a medium-viscosity gel to try to open up the volume between this new borehole and the deeper of the original boreholes.

The circulation programme with the new arrangement at Rosemanowes represents the longest continuous circulation of any HDR system to date. The injection and production flow rates between 1985 and 1989 are illustrated in Figure 4. The results show that Phase 2B was dominated by a gradual increase in the injection flow rate. Measurements in Phase 2C established that impedance fell as the injection pressure and flow rate increased. The upper limit of injection pressure, above which the size of the envelope of microseismicity and water losses increased unsatisfactorily, was demonstrated to be 10 MPa above hydrostatic pressure. This suggested an optimum hydraulic performance at Rosemanowes of:

- injection flow rate 24 l/s
- impedance 0.6 MPa per l/s
- water loss 21%.

This hydraulic performance fell well short of the targets established in 1987 for a deep 'commercial' prototype. However, it was suggested[2] that a prototype might be engineered by combining a number of underground modules in parallel; in this way the system could have the required impedance without being limited to the volume of one module.

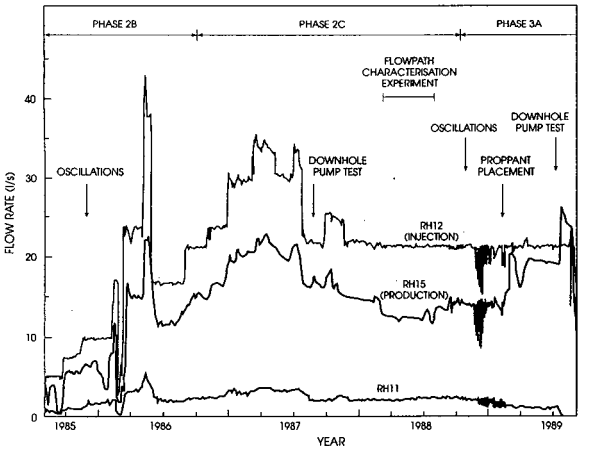

Figure 4 *Injection and production flow rates measured in the Rosemanowes system during 1985–89*

The circulation experiments showed that the new system at Rosemanowes had substantially lower impedance and lower water losses than its predecessor, but its better hydraulic performance had been achieved at the expense of thermal performance[3]. The temperature of water at the top of the production borehole dropped from 80°C to 55°C over a three year period from 1985 to 1988. Thermal modelling following a flow path characterisation experiment (using pulses of injected tracers) indicated the presence of a 'short circuit' between the boreholes. This short circuit through the system significantly reduced its effectiveness as a heat exchanger. The rock surrounding the short circuit had cooled more rapidly than the rest of the reservoir and had introduced colder water to the production borehole.

A review[2, 4] of the HDR R&D programme was started during 1987, towards the end of Phase 2. Its purpose was to consider the current status of the technology and to examine the case for proceeding further. The review was carried out for the Department of Energy by the Energy Technology Support Unit at Harwell and involved all the main contractors in the programme plus members of the Geothermal Energy Steering Committee. It concluded that significant uncertainties remained with the HDR concept, which should be viewed as being still at the experimental stage. A number of specific problems with HDR technology were identified:

- the effective size of the subsurface heat exchanger then available was almost two orders of magnitude smaller than required for a commercial system
- the thermal behaviour of the heat exchanger was unsatisfactory (because of excessive temperature drawdown and short circuiting) and water losses were too large
- the concept of engineering an underground HDR heat exchanger had not been validated
- a commercial system was likely to require the creation of several 'modules' in a multi-stimulation operation. This concept needed validation.

1988–1991 PHASE 3A

The experimental work was continued[5] in Phase 3A with further circulation and other tests at Rosemanowes Quarry. Phase 3 involved no further drilling.

In a downhole pump test in Phase 2C, lowering the pressure in the production well was thought to have closed the joint apertures close to the borehole and increased impedance. An experiment in Phase 3A to place a proppant material in the joints near the production borehole was designed to demonstrate that this effect might be remedied in a deep system. The sand used as proppant was carried into the reservoir as part of a secondary stimulation using a high viscosity (700 cP) gel. This stimulation significantly reduced the water losses and impedance but it also worsened the short

circuiting and lowered the flow temperature into the production borehole still further. It was concluded that the proppant technique would need to be used with caution in any attempt to manipulate HDR systems.

An experiment was also carried out in Phase 3A to shut off the section of the production borehole that had been shown by the flow path characterisation experiment of Phase 2C to contain the exit from the short circuit. A temporary packer assembly was installed close to the bottom of the borehole to seal off all the upper parts of the wellbore and a production flow test carried out to measure the flow rate from the low flow zone at the bottom of the borehole under these conditions. The short circuit was sealed off but a very low flow rate was obtained, and a further stimulation carried out from the bottom of the borehole gave no significant increase in flow.

A subsequent interpretation of these results by CSM suggested[6] that the most recently stimulated zone was parallel to, but largely unconnected with, the previously stimulated zone alongside. It was suggested that this result could have a significant influence on HDR design, requiring as many as twenty parallel stimulations (or cells) rather than the five that had been proposed earlier.

Two other important studies were included in Phase 3A:

- RTZ Consultants Limited, assisted by CSM, carried out a conceptual design for a 6 km deep, commercial, HDR prototype power station.
- Sunderland Polytechnic, in association with Sheffield City Polytechnic, developed[7] an integrated spreadsheet model describing the costs and performance of an HDR power station.

The RTZC study and the conclusions from the cost modelling are discussed in the next sections.

CONCEPTUAL DESIGN OF AN HDR POWER STATION

RTZ Consultants Limited (RTZC) were commissioned in April 1989 to perform a conceptual design study for the construction of a deep HDR prototype and associated power generation station in the UK. The work included an assessment of the feasibility of creating an underground HDR heat exchanger suitable for commercial operation and the definition of a programme plan for the development of a deep HDR prototype. Early in this study it was concluded that it was not practical to design a system for a depth greater than 6 km, due mainly to drilling constraints. The RTZC final report[8] was published in 1991.

Geological conditions

RTZC examined the available data and CSM's predictions for the geological, geothermal and geomechanical conditions likely to be encountered at the 6 km depth of an HDR prototype. They concluded that:

- The geological environment at 6 km depth, particularly the characteristics of existing joints and fractures, was highly conjectural and would not be known until drilling to these depths was carried out.
- If technical viability were to be established, it could only be as a result of an extended research programme relevant to a deep HDR system. This would require exploration to, and experimental work at, 6 km depth.
- Even if the technology were demonstrated to be viable, each and every HDR system would, due to geological variations, individually carry significant risk of technical failure as distinct from the certain repeatability of successive units of a conventional generation programme.

Design of the underground heat exchanger

RTZC studied the various experiments carried out by CSM in their attempts to create a working HDR subsurface heat exchanger. They concluded that, even at this advanced stage in the UK's HDR investigations, there was an inadequate understanding of the principles governing underground stimulation and of the engineering techniques required to construct a working heat exchanger:

- Experiments in the granite in Cornwall at 2.5 km depth had shown that it was possible to increase the permeability of a rock mass containing joints and fractures by high pressure hydraulic injection – one form of stimulation. However, the increases so far achieved had not been sufficient to permit flow through the rock with an acceptable level of impedance and, consequently, pumping effort.
- There was a general assumption, implicit behind the use of microseismicity as a predictive tool, that hydraulic connections existed between the injection borehole and recorded seismic events, and consequently that clusters of events represented flow paths. This assumption was unproven and had not been confirmed by flow measurements.
- Flow through the underground system at Rosemanowes had been dominated by the effects of short circuits. These effects were an inevitable consequence of geological heterogeneity and therefore would be a feature of any stimulated rock mass. Successful operation of an HDR system would depend on exploitation and management of these short circuits.
- CSM had argued that the most promising way forward for reservoir creation was by smaller more numerous stimulations than previously proposed. RTZC acknowledged the logic of this but, in the absence of any demonstrable proof by circulation, had based their conceptual design of a deep prototype on five modules.

RTZC conclusions

The main conclusion of the RTZC study[8] was that generation of electrical power from hot dry rock was unlikely to be technically or commercially viable in Cornwall, or elsewhere in the UK, in the short or medium term.

Any expectation of private capital investment in the commercial development of HDR technology in the UK was unrealistic in the foreseeable future.

Plans to construct a deep prototype HDR system in the UK should be shelved indefinitely.

Short and medium term commercial development of HDR technology should be abandoned.

Any meaningful continuation of the UK HDR R&D programme would be costly, uncertain in outcome and therefore difficult to justify but should be directed towards the basic geotechnical aspects of HDR.

ECONOMICS, COSTS AND THE RESOURCE

Resource estimates

Several estimates of the geothermal HDR resource in the UK have been made since 1976, as illustrated in Figure 5. The early estimates were very optimistic and assumed that any technical difficulties would be solved in time. The 1976 calculations[9] predicted that south-west England could yield a total output of medium-grade heat from HDR (at about 200°C), equivalent to 8000 million tonnes of coal (ie about 60,000 TWh). Converted into electricity with an efficiency of 10%, this represented a resource of about 5000 TWh(e).

A strategic review undertaken by ETSU in 1982 indicated[10] that the HDR electricity resource might be between 2500 and 60,000 TWh for depths down to 8 or 9 km in the UK. (Annual electricity generation in the UK is about 250 TWh.)

In 1985, Newton estimated[11] that the UK geothermal HDR resource could provide 20,000 to 130,000 TWh, with a 'credible contribution' to electricity generation of up to 25 TWh/y (10% of present UK electricity demand) for about 800 years. Drilling to a depth of 9 km was then envisaged.

The latest estimate of accessible resource (ie the resource located within the practical limit of borehole drilling – currently set at 6 km) was prepared for the 1990 HDR programme review and is shown in Figure 6. The

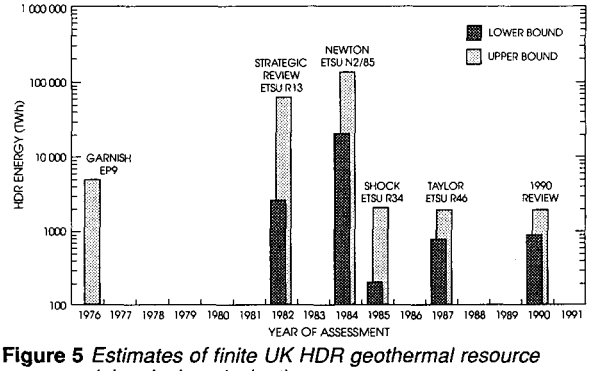

Figure 5 *Estimates of finite UK HDR geothermal resource (electrical equivalent)*

accessible resource is shown as a cumulative function of cost. The data were calculated from temperature distributions provided by CSM and the British Geological Survey and based on extraction using the Sunderland cost model with an 8% discount rate. From this evidence, the geothermal HDR accessible resource in the UK ranges from 900 TWh (for Cornwall alone) to 1880 TWh (for the whole of the UK).

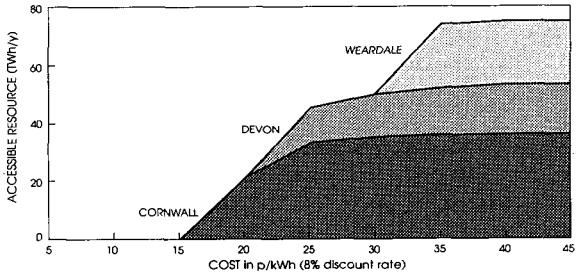

Figure 6 *The UK geothermal HDR accessible resource as a function of cost (1990 values)*

1990 cost estimates

The capital cost of an early post-prototype commercial HDR station was estimated by RTZC to be about £45 million. This is to be compared with the estimate of £35 million from the Sunderland cost model. The RTZC costs are greater due to differences in contingencies (15% rather than Sunderland's 5%), management (7.5% rather than 5%) and other special circumstances. RTZC assumed levels of cost consistent with normal industrial projects and appropriate to an early post-prototype system; Sunderland were more optimistic in this regard.

Sunderland estimated that the cheapest HDR-generated electricity in the UK (ie from south-west England) would cost between 12p/kWh and 19p/kWh (at 1990 prices and for discount rates of 2% and 10% respectively) assuming a plant lifetime of 18 years and a maximum drilling depth of 6 km. The Sunderland design produced 4.5 MW of output power, of which 0.8 MW was needed to pump the circulating water through the boreholes and underground heat exchanger.

The RTZC design produced 3.3 MW of output power and, for an 'optimistic' case, required 0.5 MW of this power for water circulation. For this optimistic case, the equivalent costs for generating electricity in the RTZC design are 19p/kWh and 34p/kWh. (Their lifetime of 20 years included 2.5 years for construction, making it almost equivalent to the 18 year operating lifetime of the Sunderland case.)

RTZC also considered a 'realistic' case, which assumed 1.5 MW to pump the circulating water and a higher impedance in the HDR system. In this case, the power costs became 25p/kWh and 53p/kWh for the 2% and 10% discount rates.

Part of the differences in costs between Sunderland and RTZC resulted from the differences in output power:

RTZC's proposal used currently available 'Ormat' type turbines, whereas Sunderland assumed that higher performance binary cycles would be developed and be available in the long term. Hence, RTZC's cost estimates are appropriate to the short term and Sunderland's results are based upon longer-term developments.

International comparison of costs

A recent study by Tester and Herzog[12] reviewed seven HDR cost studies and developed a generalised HDR economic model to calculate the break-even electricity price as a function of the thermal gradient. Their predictions for the case of today's technology (ie current drilling and completion costs) and for a reservoir performance which would be required for commercial operation are shown in Figure 7. These predictions have been converted to 1990 UK costs assuming a US inflation of 5% from 1989 to 1990 and an exchange rate of US$1.6 to the pound sterling. For comparison, the latest cost estimates by RTZC (their 'optimistic' case) and Sunderland for 10% discount rate and a lifetime of 18 years are included in this figure.

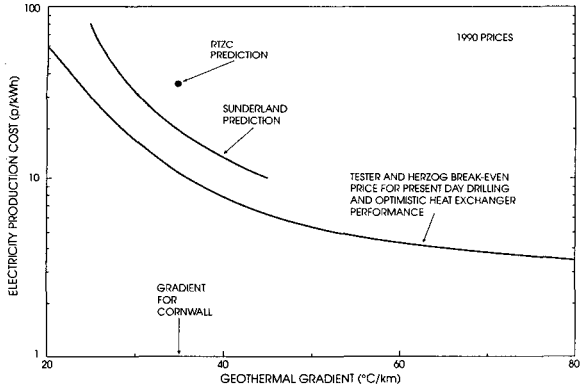

Figure 7 *Electricity production cost as a function of geothermal gradient (after Tester and Herzog)*
The costs predicted by Sunderland and RTZC (optimistic case) are also indicated for 10% discount rate and 18 year life span.

Figure 7 indicates that current forecasts of the costs of HDR electricity production are significantly higher than those made previously. Given the low thermal gradients which exist in the UK, it is now unlikely that HDR will provide an energy source with a wide application. Unless there is a significant technological break-through in an area that cannot currently be foreseen, the costs of generating electricity from HDR in the UK are likely to remain uncompetitive with conventional methods by a large margin.

THE FUTURE OF HDR IN THE UK

Review conclusions

The 1990 UK review of HDR reached the following conclusions:

- A satisfactory procedure for creating an underground HDR heat exchanger has not been demonstrated.
- A satisfactory method for sealing short circuits, other than by mechanical sealing of the production wellbore, has not yet been demonstrated.
- There is no reliable information available about the rock joints and stresses likely to be encountered at the 6 km depths needed in the UK for a commercial HDR system.
- Electricity from commercial HDR power stations is unlikely to be competitive with conventional means of generation in the short to medium term.
- Despite the early promise of the technology, HDR is still at an early stage of development. It is unlikely to attract private sector funding in the foreseeable future.
- Participation in a joint European programme offers the opportunity of resolving some of the technical uncertainties.

Future programme

In 1987 it was thought that, despite the considerable technical uncertainties facing HDR, it might still be possible to construct a 6 km deep prototype in Cornwall in the 1990s. The results of the 1990 HDR review indicate that this option is no longer a feasible proposition. Even assuming that there were successful technical developments in the long term, it is likely that the HDR resource will be much more expensive than other renewables, such as landfill gas, hydro and wind.

So far no country in the world, including the UK, has engineered an underground HDR heat exchanger which has operated successfully, with minimal temperature drawdown over a significant time period. Research into HDR technology requires complicated experimentation and is very expensive. It is therefore considered that a collaborative programme with Europe might be the best way of investigating this difficult problem over the next few years.

A decision was therefore announced by the UK Department of Energy on 1 February 1991 to direct future UK HDR work towards a collaborative research and development programme in a European partnership involving France, Germany and the European Commission. The Department of Energy is providing £3.3 million of further funding over the period 1 January 1992 to 31 March 1994 for the current phase of the UK HDR programme. Any decision on further major investment in an experimental prototype will be taken towards the end of this time, when feasibility studies of various possible sites in Europe have been completed.

The new UK R&D programme will have the following objectives:

- to improve the understanding of HDR technology in a collaborative European programme
- to further understand the costs, performance and resource size of HDR

- to carry out a programme of technology transfer
- to provide independent monitoring of seismic activity in south-west England.

An industrial consortium, which includes RTZC and French and German companies, has been formed to help co-ordinate the European programme. One of their first tasks is to evaluate the feasibility studies of the various European sites prior to any investment in a European HDR prototype.

REFERENCES

1. A review of the UK geothermal hot dry rock R&D programme. *G D Symons and J H Clarke.* Proceedings of the Sixteenth Annual Workshop on Geothermal Reservoir Engineering, Stanford CA, 22–24 January 1991.

2. Current status of hot dry rock technology with reference to South West England. *Camborne School of Mines.* ETSU Report G 137-P11, 1988.

3. Camborne geothermal energy project: Final report of Phase 2C (1986-1988). *Camborne School of Mines.* ETSU Report G 137-F, 1989.

4. The 1987-88 geothermal HDR programme review. *R J Taylor.* ETSU Report R-46, 1988.

5. Progress in hot dry rock geothermal energy technology for application in South West England (1987-1989): Summary report. *Camborne School of Mines.* ETSU Report G 151-S, 1990; Main report. *Camborne School of Mines.* ETSU Report G 151-P1, 1990.

6. Problems in the development of artificial geothermal energy exploitation in Cornwall. *R H Parker.* Proceedings of the Ussher Society, Volume 7, Part 4, 1991.

7. Cost modelling of hot dry rock systems: Volume 1 – Main report. *R Harrison and P Doherty.* Sunderland Polytechnic. ETSU Report G 138F-1, 1991; Volume 2 – Drilling costs. *N Mortimer and S Minett.* Sheffield City Polytechnic. ETSU Report G 138F-2, 1991.

8. Conceptual design study for a hot dry rock geothermal energy project: Summary report. *RTZ Consultants Limited.* ETSU Report G 153S, 1991; Main report. RTZ Consultants Limited. ETSU Report G 153, 1991.

9. Geothermal energy: The case for research in the United Kingdom. *J D Garnish.* Department of Energy, Energy Paper No 9, 1976. [HMSO, ISBN 0 11 410283 X].

10. Strategic review of the renewable energy technologies – An economic assessment. ETSU Report R13, 1982.

11. Resource size estimates for geothermal hot dry rock technology in the UK. *K Newton.* ETSU Report N2/85, 1985.

12. The economics of heat mining: An analysis of design options and performance requirements of hot dry rock (HDR) geothermal power systems. *J W Tester and H J Herzog.* Proceedings of the Sixteenth Annual Workshop on Geothermal Reservoir Engineering, Stanford CA, 22–24 January 1991.

PROCEEDINGS, Seventeenth Workshop on Geothermal Reservoir Engineering
Stanford University, Stanford, California, January 29-31, 1992
SGP-TR-141

FINE-GRAINED CLAY FRACTION (<0.2 μm) : AN INTERESTING TOOL TO APPROACH THE PRESENT THERMAL AND PERMEABILITY STATE IN ACTIVE GEOTHERMAL SYSTEMS .

Patrier, P.*, Papapanagiotou, P.**, Beaufort, D.**, Traineau, H.*** and Bril, H****

* ERM - BP 25 - 86320 Civaux - France
** Lab. Pétrologie des Altérations Hydrothermales,
URA 721 du CNRS - Univ. Poitiers
40 av. du Recteur Pineau - 86022 Poitiers cédex - France
*** IMRG-BRGM - BP 6009 - 45060 Orléans cédex 2 - France
**** Lab. Géologie - Univ. Limoges - 123 Av. A. Thomas - 87060 Limoges -France

ABSTRACT

We have investigated by X-ray diffraction the very fine grained secondary minerals (< 0.2 μm) developped in geothermal systems, in relation with their present thermal and permeability state. Because the smallest particles are the most reactive part of a rock, they are the youngest mineral phases of the geothermal fields.
This study has been performed on two active geothermal fields: Milos field, Greece (130<T<320°C) and Chipilapa field, Salvador (90<T<215°C).
In the Milos field, the mineralogical composition of the <0.2μm clay fraction observed in the reservoir strongly differs from the overlying altered metamorphic schists in the presence of abundant quantities of saponite and talc/saponite interstratified minerals at unusually high temperature. These phases are considered to be kinetically control-led "metastable" minerals which rapidly evolve towards actinolite and talc for present temperatures higher than 300 °C. Their occurrence is a good indicator of discharge in highly permeable zones.
In the geothermal field of Chipilapa, the mineralogical composition of the <0.2μm clay fractions fairly agrees with the temperatures presently measured in the wells, whereas several discrepancies may be pointed out from the compositions of coarser clay fractions (<5μm) which contain minerals inherited from higher temperature stages. Permeable zones may be evidenced from an increase of expandable components in the interstratified minerals and a decrease of the coherent domain of the unexpandable clay particles (chlorite).

INTRODUCTION

Alteration assemblages in hydrothermal systems have received a considerable attention (Lonker et al., 1990; Reyes, 1990). Many authors have shown how temperature, fluid composition and permeability could influence the compositional and structural variations displayed by secondary minerals. However the use of alteration minerals (especially clay minerals) as condition indicators in geothermal environments seems rather complicated by the previous history of these systems. Overprinting during cooling stages or kinetics during heating stages often lead to incompatible assemblages.
An interesting tool to approach the recent thermal and permeability state of a system (and to predict its evolution) may be searched in the mineralogical composition of the very fine-grained fraction of secondary minerals because it contains the youngest cristalline phases of the altered rocks. So, in our ongoing research we have investigated by X. R. D. the mineral fraction less than 0.2 μm in several drill holes of two active geothermal systems:
- the active system of Milos, Greece (drill holes MI1, MI2, MI3).
- the active geothermal system of Chipilapa, Salvador (drill holes CH9, CH7b).

GEOLOGICAL CONSIDERATIONS

1- Milos geothermal area

Milos is one of the main volcanic centres of the Aegean volcanic arc. This volcanic arc is of Pliocene age.
The very strong thermal gradient measured in the exploratory wells indicates that at the present time, the thermal activity is in a prograde stage. The reservoir (below 900m depth) is hosted in fractured metamorphic formations. The drill hole MI1 crossed alluvial deposits (0-20 m depth), polygenic formations (calcareous and volcanic rocks) and the metamorphic basement (60-1180 m depth) which belongs to greenschist and locally blueschist facies. Measured temperatures range from 130 to 320 °C. According to Liakopoulos (1987) the hydrothermal fluid in the reservoir consists of boiling sea water near 250-350 °C.

2- Chipilapa geothermal area

The area of Chipilapa, close to the Ahuachapan

geothermal field, is located in the Western part of Salvador. The stratigraphy includes pyroclastic rocks and lavas of andesitic composition, of Pliocene and Pleistocene age. Temperatures up to 215 °C (1791 m depth) have been measured in exploratory wells. However, data of fluid inclusions and the presence of relicts of epidote at shallow depth indicate that the system was subjected to higher temperatures during a previous stage. High permeable levels (total circulation loss) have been identified below approximately 1000 m depth.

METHODOLOGY

The determination of the clay fraction associated to recent hydrothermal activity needs a specific methodology which consists in extracting the fine-grained fraction of the altered rocks to minimize the "obscuring effect" of inherited minerals.

According to the available sampling, 5 to 25 g of rock were ground to obtain a powder. This fraction was dispersed in distilled water by ultrasonic treatment. The fine fraction ($<0.2\mu m$) was extracted from the $<5\mu m$ suspension by continuous ultracentrifugation (BECKMAN J2 21). The bulk suspension was introduced in the rotor with a 152 ml/mn flow rate. The rotor speed was 5000 rpm. The fine clay suspension was drawn through a millipore filter. Oriented preparations were realized by putting the filter on glass slide.

Because it strongly minimizes the influence of the non platy minerals, this method highly improves the recorded X.R.D. signals.

X-ray diffraction was carried out on air dried and ethylene glycol solvated preparations using a Philips PW1730 diffractometer (Co Kα radiation, 40 mA, 40 kV) monitored by a DACO MP numerical system. Spectra were recorded between 2 and 35 °2θ with a step size of 0.025 °2θ and a counting time of 6s. Distinction between dioctahedral and trioctahedral minerals has been made on the basis of the (060) reflection of randomly oriented powders.

Experimental diffractograms were smoothed to remove major statistical counting errors and complex spectra were decomposed in Lorentzian bands according to the method of Lanson (1990).

RESULTS

1- Mineralogy of the <0.2 μm clay fraction identified in both geothermal fields

Clay minerals have been identified according to the works of Brindley and Brown (1980) and Reynolds (1980, 1985).

- The trioctahedral clay sequence

Saponite shows typical diffractograms with basal spacings at about 17, 8.5 and 5.6 Å after ethylene glycol solvatation.

Irregular chlorite/smectite mixed-layers with high smectite content are characterized by a shift of basal spacings towards higher 2θ angle. The 001 reflection ranges between 16 and 17 Å according to their percentage of smectite component (Fig. 1).

Corrensite is a regular chlorite/smectite mixed-layer (50/50). The diffraction pattern shows peaks at about 31, 15.5, 7.8, 5.19, 4.46 and 3.45 Å.

Chlorite is a non swelling mineral characterized by basal spacings about 14, 7, 4.7 and 3.5 Å (Fig. 1).

The following minerals are observed only in Milos samples.

Talc is a non swelling mineral characterized by peaks at 9.34 and 4.6 Å.

Saponite/talc mixed-layers are characterized by a second order reflection at intermediate spacing values between the (002) reflection of smectite and the (001) reflection of talc. In the studied samples, saponite component predominates over talc component. Considering the important width of the (002) reflection, several types of randomly

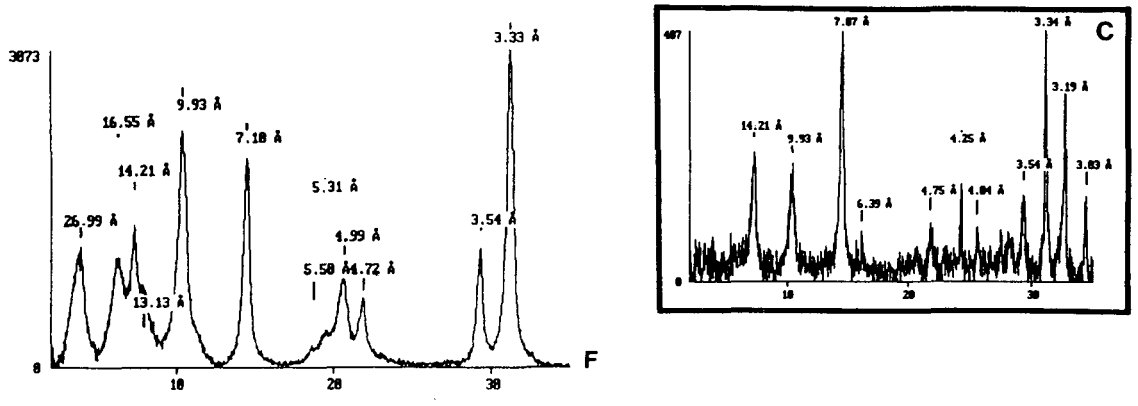

Fig. 1. X-ray diffraction patterns of the $<0.2\mu m$ clay fraction and of the coarser fraction "C" ($<5\mu m$). Sample CH7b 1066 m.

interlayered minerals probably coexist.
A mixed-layer phase characterized by a broad reflection at about 12 Å, that does not shift after ethylene glycol solvatation is locally identified. It may be an interstratification of non swelling minerals such as talc/chlorite (9.3, 14 Å).

- The dioctahedral clay sequence

Montmorillonite: diffractograms show basal spacings similar to saponite ones. The distinction of these smectites is possible by studying the position of their (060) reflection: this reflection ranges between 1.49 and 1.50 Å instead of 1.52-1.54 Å for saponite.
Regular illite/smectite mixed-layers (R1), observed in Chipilapa, show diffraction peaks at about 27-28, 13, 9-9.3, 6.7, 5.3, 4.5 and 3.3 Å (Fig. 1).
Illite and illite rich I/S mixed-layers (R3) show strong reflections near 10, 5 and 3.33 Å (Fig. 1). Minor quantities of mixed-layers generate the enlargement of the (001) reflection toward lower 2θ angle after ethylene glycol treatment.

2- Clay minerals distribution

In Milos, the following trioctahedral clay sequence has been established (Fig. 2):
Saponite (100-250m ; 130<T<170°C)
Saponite + corrensite (250-350m ; 180<T<220°C)
"12 Å interlayered mineral" + chlorite + saponite (400-600m ; 220<T<280°C)
Chlorite (650-850m ; 280<T<300°C)
Saponite ± talc + saponite/talc mixed layers are associated with actinolite below 903m depth (300<T<320°C).
The dioctahedral clay sequence is poorly developped in this field.

In Chipilapa

The alteration sequence recorded in CH9 well can be considered as a conventional pattern. The trioctahedral phyllosilicate sequence includes the successive appearance of smectite, chlorite/smectite mixed-layers and chlorite. In the same way, the dioctahedral sequence shows the development of montmorillonite, R1 and R3 mixed-layers and finally illite. However overprinting of different events is demonstrated by the crystallization of epidote and chlorite in shallow levels for lower temperatures compared to litterature data.
In CH9 well, the clay phases appear successively in a narrow range of temperature, from 185 to 214 °C.
In CH7bis well, the dioctahedral clay sequence is characterized by the successive occurrence of montmorillonite at shallow depth, R1 and R3 mixed-layers for depths which respectively exceed 306 and 748 m (T>155 °C and T>195 °C). The concentration of R1 and the disappearance of R3 mixed-layers at 898 m depth do not agree with a classical scheme of montmorillonite to illite conversion. The trioctahedral clay sequence comprises smectite in the whole well

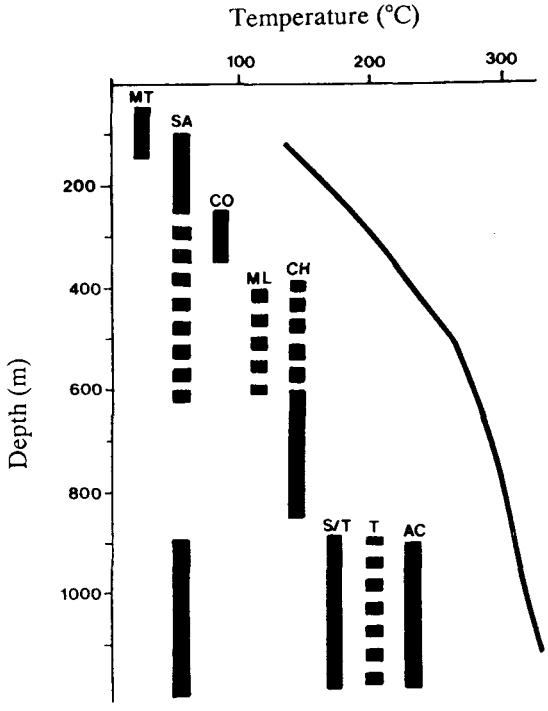

Fig. 2. Fine-grained clay minerals (<0.2μm) and present temperatures versus depth in Milos drill hole MI1. MT: montmorillonite, SA: saponite, CO: corrensite, ML: "12 Å phase", CH: chlorite, S/T: saponite/talc, T: talc, AC: actinolite.

(110<T<204°C), corrensite between 408 and 556 m depth (174<T<197°C), chlorite from 652 m depth (T>195°C).
Measurements on diffraction spectra of the fine fraction can be realized considering their good resolution. The thickness of chlorite particles (coherent domain) and the variation in percentage of expandable layers in chlorite/smectite have been investigated.

3- Coherent domain of chlorite particles

The coherent domain of a particle is the thickness (number of layers) which diffracts coherently. (001) peak width at half height is inversely proportional to the average thickness of the phyllosilicate population. In order to obtain the chlorite size all along the well, we have decomposed the (002) reflection in one or two lorentzian bands, considering or not the existence of associated mixed-layers chlorite/smectite. Such an investigation has been realized on samples from CH9 well, because of the great occurrence of chlorite in this well. Peak width at half height deduced from the whole reflection ranges from 0.42 to 0.71 °2θ and from 0.31 to 0.49 °2θ for the chlorite component of the decomposed reflection (Fig. 3). For comparison, the

same values deduced from the coarser fraction (<5μm) have also been calculated: they range from approximately 0.33 to 0.16 °2θ.

4- Distribution of smectite and chlorite/smectite with low chlorite content

These phyllosilicates are of great interest because they are sensitive to thermal conditions (Bettison and Schiffman, 1988). According to Reynolds (1980), the (001) reflection of these minerals shifts towards high 2θ angles with increasing chlorite content. These minerals have been investigated in samples collected from CH7b well.

The position of their (001) reflection ranges between 16.9 and 16.5 Å (Fig. 4). It decreases with depth up to 1006 m, if we except the level 808m. For depth higher than 1006 m, an opposite trend is evidenced.

INTERPRETATION

1- Mineralogy of Milos geothermal area

The mineralogy of the <0.2μm clay fraction points out several interesting results. The trioctahedral sequence recognized in the formations which overly the reservoir (weak fracture permeability) obeys a classical alteration scheme largely described in geothermal systems and in diagenetic environment (Bettison and Schiffman, 1988; Inoue, 1987). However, the paragenesis observed in the reservoir (high permeable zone) consists of non common minerals for such thermal conditions (T>300°C). Saponite, talc/saponite mixed-layers, actinolite and talc are incompatible phases according to litterature and therefore cannot be interpreted in term of thermodynamical equilibrium.

Saponite has been hydrothermally synthetized by Iyama and Roy (1963) for temperature as high as 850 °C. However the reactivity of this mineral is high for such an elevated temperature and it evolves towards more stable phases such as anthophyllite + talc. According to Whitney (1983), for temperature close to 400 °C, after 200 days, saponite is transformed into saponite/talc mixed-layers.

The association described in Milos includes therefore all the minerals produced in synthesis experiments. They probably belong to the same sequence of mineral transformation, in which saponite and talc/saponite mixed-layers are metastable and so the youngest phases. Indeed the precipitation of smectite must be very recent with

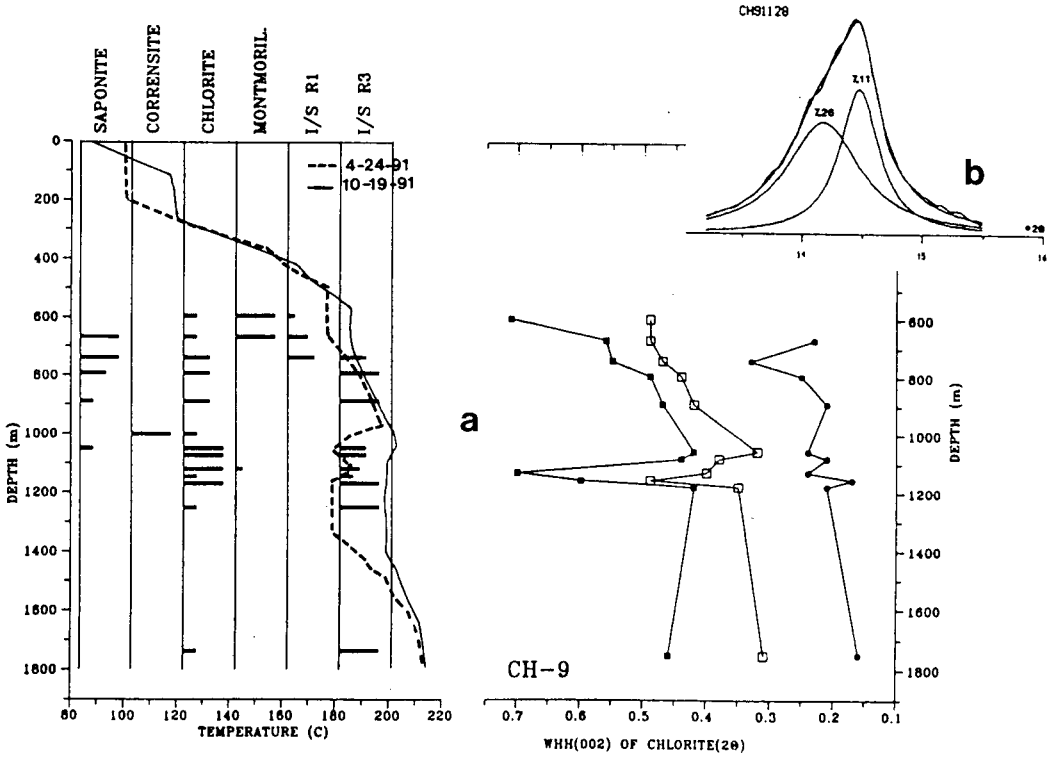

Fig. 3a. Distribution of temperatures and of <0.2μm clay minerals in CH9 well. Width at half height of (002) peak of chlorite (°2θ) is a plotted as a function of depth and measured temperatures.
■: (002) peak attributed entirely to chlorite
□: chloritic component of the decomposed signal (example Fig. 3b.)
●: " " for a <5μm clay fraction.

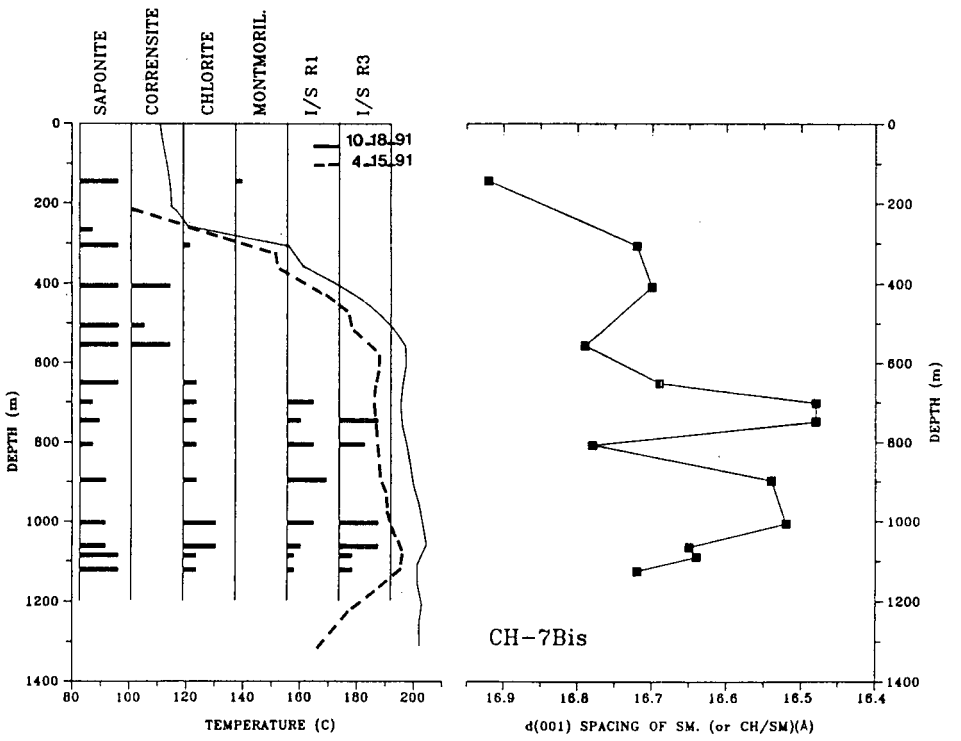

Fig. 4. Distribution of temperatures and of <0.2μm clay minerals in CH7b well. d(001) spacing of smectite or chlorite/smectite mixed-layers with high smectite content is plotted as a function of depth and temperature.

regard to its instability for such conditions.
The kinetic control of this association explains the discrepancy which appears between the <0.2μm clay mineralogy and the phases predicted by thermodynamic modelizations, based on equilibrium statement (Liakopoulos, 1987). The abundance of smectite is explained by discharge processes of oversaturated liquid in response to the boiling of the incoming sea water (Papapanagiotou et al., 1992).
In conclusion, the mineralogy of the fine-grained fraction clearly evidences the limitation of geothermometers based on chemical equilibrium and reveals close relations between metastable clays and highly permeable levels. The mineralogy of the fine fraction could therefore be a useful tool to evidence zones of high permeability and so productive zones in high enthalpy geothermal systems.

2- Mineralogy of Chipilapa geothermal field

The <0.2μm clay fraction minimizes the contribution of paleohydrothermal minerals. The alteration sequence so determined in CH9 well is a typical clay sequence. Informations deduced from it are in good agreement with the measured present temperatures. They do not evidence a strong physico-chemical disequilibrium like in Milos.
Below 1050 m depth, chlorite is the only trioctahedral phase, for temperature in agreement with those reported in litterature (about 200°C). The "coherent domain" of chlorite particles (X.R.D. peak width at half height) has been reported as a function of depth and temperature (CH9 well)(Fig. 3). The evolution of X.R.D. peak width and the temperature profile are very similar. The increase of peak width (lower particles thickness) recognized around 1100 m depth corresponds to highly permeable level as it is suggested by the response of the temperature profile to the absorption of drilling muds. This permeable level could give way to cold water circulations. The parallel between the temperature and chlorite grain size profile recorded by the < 0.2 μm clay fraction is not perceptible for chlorites of coarser clay fractions (<5μm). Such chlorites which appeared during previous higher temperature stages totally obscur the contribution of the most recent chloritic material.
The alteration zoning recognized in CH7b differs from the previous well in the sense that smectite and chlorite/smectite mixed-layers with high smectite content crystallize up to the bottom of the well. Because lithology and temperature in CH7b are the same as in the previous well, the crystallization of smectite could be attributed to different physico-chemical characteristics of hydrothermal fluids (colder meteoric water contamination). The d(001) of smectite and mixed-layers has been reported as a function of depth and temperature (Fig. 4). The

variation of the percentage of smectite interstratified with chlorite is parallel to the temperature profile. The thermal gradient, directly dependent on rock permeability, could expressed the degree of contamination by colder fluids. It seems particularly interesting to note that the occurrence of nearly pure smectite (saponite) at about 800 m depth coincides with an inversion of the vertical thermal gradient.

CONCLUSION

X-ray diffraction on $<0.2\mu m$ mineralogical fraction extracted from cuttings (or cores) of two distinctive geothermal fields provides new informations on the very recent alteration processes and hence allows to access to their present physical state. Among these informations, the most interesting one concerns the variation of the expandable components in the interstratified clay minerals (illite/smectite or chlorite/smectite) and the crystal size (coherent domain) of the unexpandable clays (chlorite) as a function of temperature and permeability data recorded in exploration wells.

In systems subjected to a prograde alteration stage, as in Milos, the presence of high enthalpy reservoir (highly permeable levels) is clearly evidenced by metastable mixed-layered minerals whose present mineralogical state is inferred to be essentially controlled by kinetic factors (t*T).

In systems subjected to a retrograde alteration stage, as in Chipilapa, the $<0.2\mu m$ clay fraction strongly minimizes the "obscuring" effect of the paleohydrothermal clay phases (chlorite). The mineralogical composition of this clay fraction fairly agrees with the present thermal conditions in most of the investigated wells. However the presence of high permeable levels is identifiable through the lower coherent domain of chlorite particles in the reservoir.

Now, it would be interesting to test the response of the $<0.2\mu m$ clay fraction to variations of hydrothermal conditions (discharge and recharge zones).

REFERENCES

Bettison, L.A. and Schiffman, P. (1988), "Compositional and structural variations of phyllosilicates from the Point Sal ophiolite, California", American Mineralogist, 79, 671-695.

Brindley, G.W. and Brown, G. (1980), "Crystal structures of clay minerals and their X-ray identification", G.W. Brindley and G. Brown eds., Mineralogical Society, London, 495 p.

Inoue, A. (1987), "Conversion of smectite to chlorite by hydrothermal and diagenetic alterations, Hokuroku kuroko mineralization area, Northeast Japan", Proceed. Intern. Clay Conf. Denver 1985, 158-164.

Iiyama, J.T. and Roy, R. (1963), "Unusually stable saponite in the system Na_2O-MgO-Al_2O_3-SiO_2", Clay Minerals Bulletin, 5, 29, 161-171.

Lanson, B. (1990), "Mise en évidence des mécanismes réactionnels des interstratifiés illite/smectite au cours de la diagenèse", Thesis, University Paris 6, France, 366 p.

Liakopoulos, A. (1987), "Hydrothermalisme et minéralisations métallifères de l'île de Milos, Cyclades, Grèce", Thesis, University Paris 6, 279 p.

Lonker, S.W., Fitzgerald, J.D., Hedenquist, J.W. and Walshe, J.L. (1990), "Mineral-fluid interactions in the Broadlands-Ohaaki geothermal system, New Zealand", American Journal of Science, 290, 995-1068.

Papapanagiotou, P., Beaufort, D., Patrier, P. and Traineau, H. (1992), "Clay mineralogy of the $<0.2\mu m$ rock fraction in the MI-1 drill hole of the geothermal field of Milos". 6th congress of the Geological Society of Greece, May 25-27, Athens.

Reyes, A.G. (1990), "Petrology of Philippine geothermal systems and the application of alteration mineralogy to their assessment", Journal of Volcanology and Geothermal Research, 43, 279-309.

Reynolds, R.C. (1985), "Newmod computer program for the calculation of one dimensional diffraction pattern of mixed layered clays", Publ. by author, 8 Brook road, Hanover, New Hampshire.

Reynolds, R.C. (1980), "Interstratified minerals", in Crystal structures and X-ray identification of clay minerals, GW Brindley and G. Brown eds., Mineralogical Society, London, 249-274.

Whitney, G. (1983), "Hydrothermal reactivity of saponite", Clays and clay minerals, 31, 1, 1-8.

ACKNOWLEDGEMENTS

We are grateful to the Compagnie Française de Géothermie and the Comission Ejecutiva Hidroelectrica del Rio Lempa for providing well data and samples.

PROCEEDINGS, Seventeenth Workshop on Geothermal Reservoir Engineering
Stanford University, Stanford, California, January 29-31, 1992
SGP-TR-141

HYDROGEOLOGIC AND HYDROGEOCHEMICAL ASSESSMENT OF GEOTHERMAL FLUIDS IN THE PYRAMID LAKE AREA, WASHOE COUNTRY, NEVADA

S. Bwire Ojiambo*

University of Neva, Reno
Mackay School of Mines
Hydrology/Hydrogeology Program, Reno, NV.89557

ABSTRACT

This paper evaluates the hydrogeological and hydrogeochemical characteristics of the geothermal fluids in the Pyramid Lake area using data from existing published and unpublished reports on springs, challow and deep wells in the area. Four geochemical provinces, namely, chloride, bicarbonate, suphate and mixed chloride-bicarbonate have been identified. Chloride waters are found in known geothermal areas. Two subsurface water recharge zones which feed the shallow and deep geothermal systems are proposed. These are the Virginia Mountains and their Northern extension and the Fox and Lake Ranges. Tertiary and Quaternary faulting systems in these mountains and Ranges act as heat conduits for geothermal fluids. The Needle Rocks geothermal system is postulated to be deeper than the San Emidio system. A connection between the Needle Rocks system and the Pyramid and Anaho islands warm springs is not clear from this study because of lack of chemical data from these islands. More systematic measurements of static water levels, temperatures, well lithology, water chemistry and isotopes data are recommended to enable better understanding of the geothermal systems in the area.

INTRODUCTION

This study was carried out in summer 1991 as part of graduate study in regional groundwater flow system in the Pyramid Lake area. The area, north of Reno, Nevada was selected because of its naturally occurring hot springs, drilled geothermal areas at Empire/San Emidio and the Needle Rocks area and because of continued interest by the local community and private investors to develop geothermal power stations in the area. The study included a review of the existing literature on Geothermal and groundwater flow systems of the area with special emphasis on the hydrogeochemistry of the waters, temperatures and study of hydrogeological parameters of the wells and reinterpretations of the data to develop a conceptual model. No computer modelling was done due to limited available time. Drs. W. Berry Lyons and E. (Britt) Jacobson acted as advisors to the author during the study.

*Permanent Address
Kenya Power & Lighting Co. Ltd
P.O. Box 30099
Nairobi, Kenya.

PREVIOUS WORK

The majority of the literature on this area is on the paleoclimatology and geomorphology of the Quaternary Lake Lahontan. Reports by Glancy and Rush (1968) and by Van Denburgh, Lamke and Hughes (1973) cover surface and shallow groundwater resources of the northern and southern parts of the study area. Previous work on geothermal occurrences in the area is covered under the Northern Basin and Range Province reports by several researchers. Garside (1974) and Olmstead, et. al. (1975) have written on the hydrothermal systems in Nevada with some examples from the study area.

Garside and Schilling (1979) provide comprehensive data and map on thermal waters in Nevada which was updated by Purkey in 1990. Trexler, Flynn, Koenig and Ghusn, Jr. (1983) updated their earlier map on Geothermal Resources of Nevada showing locations of the thermal areas. Trexler, 1990 (unpublished report) gives chemistry of the San Emidio geothermal area and has also worked on the detailed geology and faulting system of the same area (pers. comm.).

The geology of the area is well covered by Bonham, (1969).

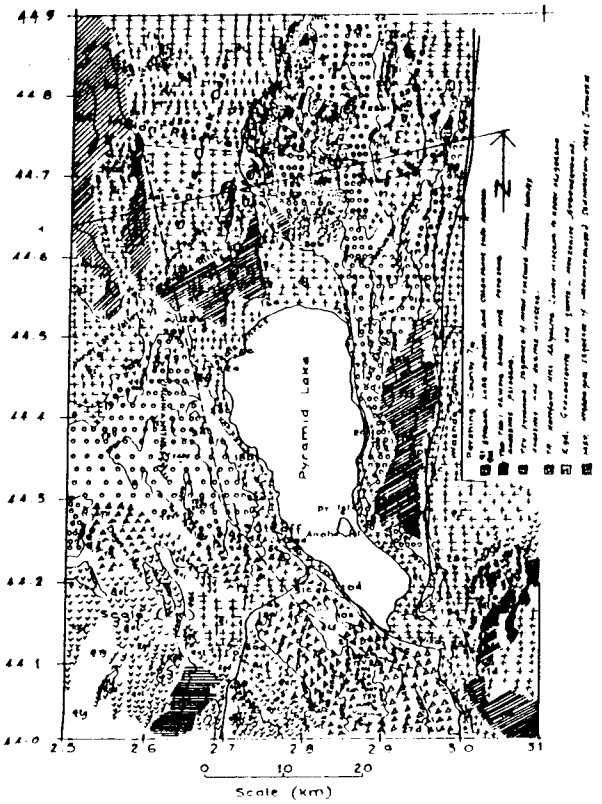

Fig.1 Generalized geology of the Pyramid Lake area.

GEOLOGICAL SETTING

Figure 1 shows the generalized geology of the study area adapted from Bonham, (1969). The oldest rocks are the basement Jurassic meta-sedimentary Nightingale Sequence (Msr) found in Fox Range and Northern Lake Range at elevations about 1200 meters above Pyramid Lake. Medium to coarse-grained granodiorite and quartz monzonite plutonic rocks of Cretaceous age intrude the Nightingale Sequence and also occur to the extreme southwestern part of the study area.

The oldest of the Tertiary formations are the Oligocene/Miocene Hartford Hill Rhyolite (Th) to the southwest of Pyramid Lake. Miocene basalt, andesite and dacite flows called the Pyramid Lake sequence are found on the Virginia Mountains to the west and in the Lake Range to the east extending northwards to Fox Range. During the Pliocene Epoch extensive basalt flows associated with intrusive dikes derived from fissures occurred in the Terraced hills, Black Mountain, and Red Rock Hills northwest of Pyramid Lake (Tba). On the eastern slopes of the Lake Range, these basalts are found in association with pyroxene andesites (Tab).

The Smoke Creek Desert, San Emidio Desert, Honey Lake Valley, Truckee Valley, the area between Terrace hills and Pyramid Lake, and around the shores of the lake are largely covered by Pleistocene lake deposits (Ql) of silt, clay gravels and calcareous tuffa. Stream valleys and some hill slopes are covered by young recent stream and eolian deposits (Qal) (Bonham, 1969). Most of the wells drilled in the area discharge water from these two Quaternary aquifer formations.

HYDROGEOLOGIC CONDITIONS

Hydrogeological data from 61 shallow and deep wells in the area were examined. Most of the wells (50) are less than 100 meters deep and about 67% of them have some record of static water levels.

A mean specific capacity of 3.8 lps/m was calculated from twelve wells around San Emidio Desert and the town of Nixon. These wells produce water from recent lake and stream deposits. Lack of proper data for computation of aquifer parameters such as hydraulic conductivity, transmissivity and storativity greatly limited more meaningful model conceptualization.

A composite piezometric surfaces map from available water levels data mainly from the drillers' reports was constructed (Fig 2).

Two possible recharge areas occur to the southwest along the Virginia Mountains, and to the north in the Fox Range area.

The contours indicate subsurface flows towards the Pyramid Lake from the two recharge zones and towards the San Emidio/Empire geothermal areas.

Static water levels around Nixon town show haphazard spatial variations which made it difficult to draw potentiometric contours. The static water levels seem to parallel the NE-SW Nightingale Mountains faulting system to the southeast of the study area. More water level measurements are required to facilitate the interpretation of ground water behaviour in the area.

Data on the well lithology and aquifer formation is limited. Glancy, et. al (1967) and Van Denburgh, et. al. (1973)

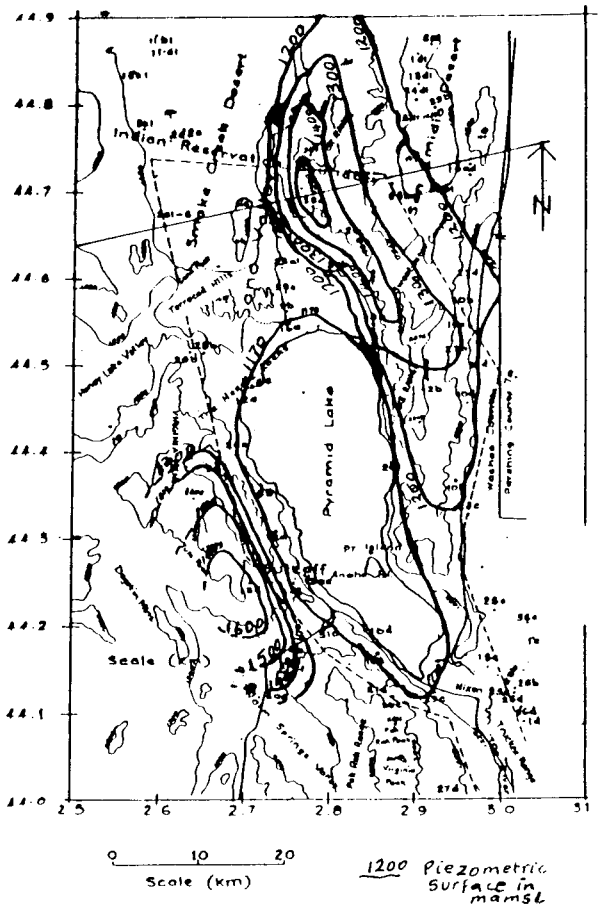

Fig.2 Composit piezometric surfaces map of the Pyramid Lake.

recognized three major aquifers in the area. These are:

(1) Younger alluvium made of unconsolidated sedimentary deposits with variable permeability found around lake shores and valleys.

(2) Older alluvium made of unconsolidated and semi-consolidated sedimentary deposits of high to low permeability found mainly on flat plains and valleys. The majority of the wells are located in this aquifer type.

(3) Consolidated rocks largely having little or no interstitial permeability. These are mainly intrusive igneous and metamorphic rocks. Less wells are located in this formation than in the older alluvium formation.

GEOCHEMICAL CHARACTERISTICS OF THE FLUIDS

Chemical Provinces

The chemical composition of waters from 30 shallow groundwater and deep geothermal wells and from warm and cold springs was evaluated and HCO3+CO3-Cl-SO4 and Ca-Na+K-Mg trilinear diagrams drawn to examine the possibility of classifying the fluids. Most of the spring fluids and all those from wells plotted above 50% of Na+K rendering no good classification from the cation plot. The anion plot gives four possible fluid chemical provinces as shown in Figure 3.

(a) Chloride-rich waters mostly from hot wells and springs and Pyramid Lake.

(b) Bicarbonate rich waters mostly from springs and some cold wells.

(c) Mixed waters, from wells and one spring.

(d) Sulfate-rich waters, from one well, spring and Truckee River.

General geographical distribution of the above water provinces are shown in Figure 4. Bicarbonate waters are the least mineralized using the specific conductance, Na+K and Ca+Mg concentrations as a measure. All the waters have pH between 7 and 10 with the mean at 7.8.

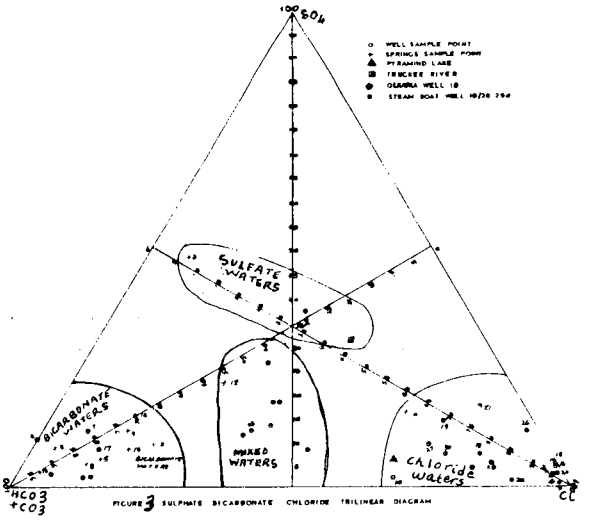

Fig.3 Sulphate bicarbonate chloride trilinear diagram

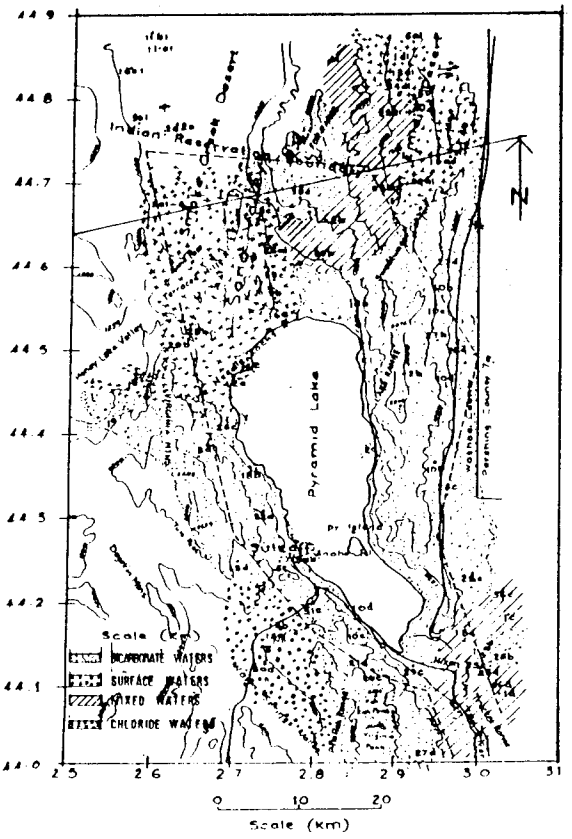

Fig.4 Geochemical classification of the Pyramid Lake areasubsurface waters

Chemical Geothermometers

A large number of water chemistry analyses obtained from the area give no SiO2 concentrations. Most of the early analyses do not separate Na and K concentrations. This is a major drawback in attempting to compute chemical geothermometers where concentrations of Na, K, Ca, Mg and SiO2 are required.

However, there is correlation between high aquifer temperatures with chloride-rich fluids especially around San Emidio.

The three geothermal wells of the Needle Rocks have measured downhole temperatures although they had not equilibrated and are all below the indicated average subsurface geochemical temperatures of 140 C even from the deepest well #1 which is 1807 meters deep. In the San Emidio area, the maximum down-hole temperature measured at 590 meters is 148 C in the Philips Petroleum Co. Well # 29/13-16ad giving a temperature gradient of over 200 C per km. If this temperature is extrapolated downward, the indicated 190 C geochemical reservoir temperature would be reached around 750 meters.

The subsurface temperatures as indicated by geochemical geothermometry show that the two known geothermal areas in the study area, namely, the Needle Rocks and San Emidio have moderate reservoir temperatures sufficient for binary system power generation. Furthermore, it can be inferred that the Needle Rocks system has lower temperatures and deeper reservoir than the San Emidio one. Wells may have to be drilled deeper than 1500 meters at the Needle Rocks while at San Emidio, the deeper reservoir should be within 750 meters depth. Geochemical temperatures from wells 24d1 and 25d1 north of San Emidio show a northward drop in temperatures indicating possible northward flow of water and cooling of geothermal fluids.

Stable Isotopes Data

Five isotope data was available from the areas shown hereunder:-

Name	d 0	dD
Needle Rocks Well #1	-6.33	-106.5
M.K. Steward Prod. Well #1. 21(1)	-11.99	-107.4
Ditto, Irrg. Well	-14.86	-115.5
San Emidio Hot Springs (29/23-9/16)	-11.73	-106.6
San Emidio	-14.24	-110.2

Flynn and Buchanan (1990) found that the best fit meteoric line for the Great Basin is:

$$dD = 7.55d\ 0 - 0.5$$

which they took to be the same as the global meteoric water line for practical purposes.

The five data points were plotted on the meteoric water line graph (Fig. 5). They all show oxygen-18 shift. The hot Needle Rocks geysering well has the largest shift (+8%) while the San Emidio geothermal well and hot spring have a + 2% oxygen-18 shift. The San Emidio cold springs and irrigation well show negligible shift. The higher oxygen-18 concentrations at the Needle Rocks corroborate the earlier stated

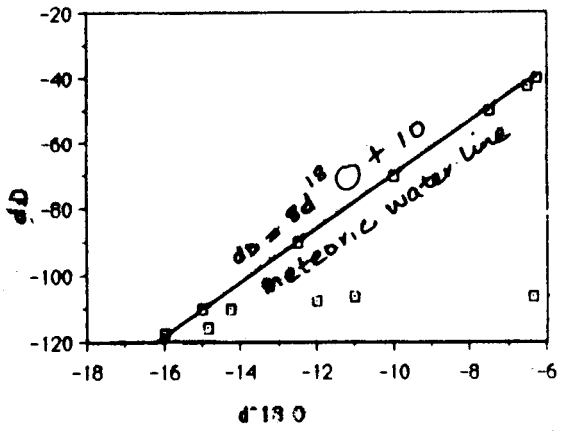

Fig.5 Deuterium vs. oxygen-18 isotope diagram

fact that it is deeper seated and most likely undergone more water-rock reactions and longer residence time than the San Emidio system. With such limited data, it may not be prudent to draw many conclusions. More isotope data are required to be able to relate the isotope values to the recharge and hydrothermal reactions of the fluids in this area. Furthermore, there are no data at all on isotopes in the study area south of the Needle Rocks to enable overall interpretation of isotope variations in the area.

MIXING MODEL

Figures 3 and 4 show the four water provinces in the study area. Mixed waters are found to the North and South Eastern. The mixed waters in the Nixon town area may be derived from mixing of bicarbonate and deeper waters or due to evolution of bicarbonate waters via evaporation and water-rock reactions.

The mixed water north of San Emidio may be due to mixing between hot chloride richer waters with bicarbonate regional waters. Trexler (1990) has proposed 3:1 mixing between shallow waters and geothermal waters using TDS concentrations. Very few TDS data are available from the area and it is difficult to extend this conclusion further, but does not appear a plausible mixing model.

The Pyramid Lake has a specific conductance of 8400 micro-mhos/cm. Mixing 70% of the lake water with 30% of the shallow groundwater yields fluids of similar conductance as that of the Needle Rocks geothermal fluids. This may be the likely source of the fluids until more data is available.

CONCEPTUAL MODEL

Figure 6 shows the proposed hydrothermal conceptual model for the San Emidio and Needle Rocks geothermal systems. The cross section line is shown on Figures 2 and 4.

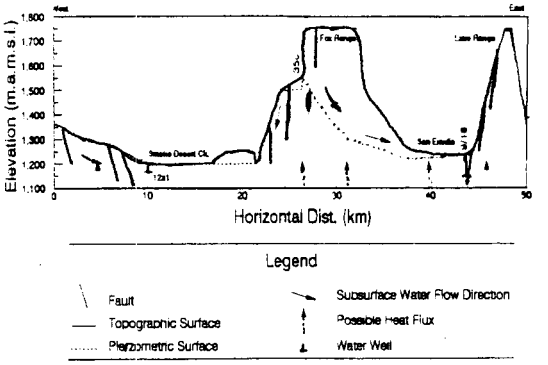

Fig.6 Proposed conceptual flow model of the Smoke Creek/San Emidio area

The study area lies within the transitional zone between the Basin and Range Provinces and the Sierra Nevada where regional structural control is by the Walker Lane faulting system. The youngest volcanic activity recorded from rocks in the area is at least 2 million years (Bonham, 1969).

This was mainly intrusive dike basalt flows derived from fissures and some andesites (Bonham, 1969). Any heat generated by this activity may not be waning away. Faulting activity has, however, continued into the Pleistocene and perhaps Holocene (Bonham, 1969). Regional high heat flow in the Basin and Range Province combined with these locally intense activities may cause the heat anomaly in the area. Most of the faulting is in Virginia Mountains and their northern extension, Terraced Hills, Fox Range and Lake Range (Bonham, 1969) and most likely act as conduits for deep, hot geothermal fluids.

The piezometric surface map (Fig. 2) shows two possible recharge zones in the Fox Range to the northeast and the Virginia Mountains and their northward extension on the west. The general subsurface water flow is from the western divide eastward towards Pyramid Lake and Smoke Creek Desert. Flows from the Fox Range are westward into the Smoke Creek Desert and east and north-eastward towards San Emidio. A westerly flow component from Northern Lake Range into San Emidio is also possible but data to support this may need to be collected further east of the study area.

It is postulated that the Needle Rocks geothermal area could be obtaining its recharge water from the northwestern mountains, Sano Valley and downward percolating water from Pyramid Lake. San Emidio geothermal fluids flow northwards from the geothermometry evidence. This is supported by the general groundwater flow from Fox Range towards San Emidio (Figure 2) assuming that the deep geothermal fluids rise through faults and laterally mix with shallow waters flowing in the same direction.

The heat source from the Needle Rocks and San Emidio Desert geothermal areas may be associated with the Walker Lane faulting system and the regional high heat flow, but localized to higher gradients in these areas. Strong fault system to the northwest and intercrossing of NW-SW, N-S and NW-SE faulting systems over Sand Pass and Terraced Hills may have caused localized high heat gradients and increased hydrothermal reactions resulting in hot chloride fluids seen in the northwest. Similarly, faulting in the Fox and Northern Lake Range is proposed as forming the flow paths for the hot fluids and the development of chloride fluids in the San Emidio area.

The NW-SE trending faults from Terraced Hills most likely continue under Pyramid Lake to Pyramid and Anaho Islands causing the warm springs reported on these islands.

DISCUSSION AND CONCLUSIONS

Hydrogeochemistry shows four chemical water provinces with the chloride waters associated with waters of the Needle Rocks and San Emidio geothermal systems. Statistical correlation of the ionic concentrations against conservative chloride ion is poor maybe due to poor sampling and analysis or both. The high oxygen-18 shift at the Needle Rocks may be due to evaporation and longer residence time of the fluids in this area. More evenly distributed isotope data from the area are necessary before detailed interpretation can be made.

Figure 6 gives the preliminary conceptual model of the geothermal systems in the area. More temperature measurements and chemical data plus a closer look at the local tectonic setting of the geothermal systems are necessary to further develop this model. The heat sources may be either below the Ranges themselves or more shifted and localized below or near the two known hot fluid areas at San Emidio and Needle Rocks.

Elaborate modelling was not done due to time limitations and quality of the available data. This work should hopefully encourage more detailed work on these interesting geothermal systems and the flow model of the groundwater by other researchers.

Geochemical geothermometry interpretation is also limited by the availability and distribution of the data.

REFERENCES

BLACKWELL, D.D., 1983, Heat Flow in the Northern Basin and Range Province: GRC Spec. Report No. 13, pp.81-92.

GARSIDE, L.J., 1974, Geothermal exploration and development in Nevada through 1973: Nev. Bureau of Mines and Geol.

GARSIDE, L.J. and SCHILLING, J.H., 1979, Thermal Waters of Nevada: Nev. Bureau of Mines and Geol., Bull 91, p.163.

GLANCY, P.A. and RUSH, F.E., 1968, Water - Resources Appraisal of Smoke Creek - San Emidio Desert area, Nevada and California; Nev. Dept. Conserv. of Nat. Resources, Water - Resource. - Reconn. Series Report 44, p.57.

PURKEY, B.W., 1990, Geothermal wells drilled in Nevada since 1979: Nev Bureau of Mines and Geol. LISTL-5.

TREXLER, D.T., 1988, Geothermal Assessment of the Pyramid Lake Indian Reservation, Washoe County, Nevada: Report prepared for ORMAT Energy Systems, Inc., Unpubl., P.23.

TREXLER D.T., 1990, Chemical analysis of thermal and non-thermal water in the vicinity of the San Emidio Desert, Washoe County, Nevada: Unpubl. Report prepared for Mr. M.B. Stewart, San Emidio Resources, Yerington, NV.

TREXLER, D.T., FLYNN, T., KOENIG, B.A. and GHUSN, Jr, A., 1983, Geothermal Resources of Nevada Map: UNLV, Environ. Research Center, Div. of Earth Sciences.

VAN DENBURGH, A.S., LAMKE, R.D. and HUGHES, J.L., 1973, A Brief Water-Resources Appraisal of the Truckee River Basin, Western Nevada: Nev. Dept. Conserv & Nat. Resources, Water Resources-Reconn. Ser. Rept. 57, p.122.

PROCEEDINGS, Seventeenth Workshop on Geothermal Reservoir Engineering
Stanford University, Stanford, California, January 29-31, 1992
SGP-TR-141

MODELLING $CaCO_3$ DEPOSITION IN GEOTHERMAL WELLBORES

Donald E. Michels

Don Michels Associates
P.O. Box 8652
Missoula, Montana 59807
406/728-2576

INTRODUCTION

The capacity of a geothermal liquid to carry calcium varies mainly with the concentrations of CO_2 and HCO_3, temperature and ionic strength, of which the CO_2 concentration (pressure) changes most in the wellbore. Wellbore models that carry accurate computations for CO_2 and other gas pressures might be adapted to compute profile thicknesses of $CaCO_3$ scale.

A general model for carbonate scale deposition in a wellbore must make a simultaneous accounting for pressures of H_2O, CO_2, and two or three other gases plus salt effects on those pressures. In addition, the elevation of flash initiation must be accurately identified and combined with profiles of temperature, etc., in the 2-phase zone. Such a model has been developed and its principle features are described here, including calibration of some factors with measured scale deposits.

The model provides insight about the scale deposition processes through parametric studies. Tactics and strategies for confronting the effects of $CaCO_3$ deposition in wells and wellfields can be explored with the model. Modelling of specific wellbores/wellfluids can help quantify risks and benefits concerning scale inhibition, wellfluid monitoring, timing of consequences relating to failure of scale inhibiting apparatus, urgency of remedial actions, and other aspects.

BASIS OF THE MODEL

The main features are a computed solubility of calcite, identification of where flash initiation begins, temperature profile above the bubble point, and incremental deposition of calcite through the temperature (elevation) interval.

Calcite Solubility

The solubility of $CaCO_3$ (calcite or aragonite) in geothermal waters commonly is represented by a solubility product, K_s, that varies with temperature; $K_s = [Ca^{++}][CO_3^{=}]$. K-values are thermodynamically defined stability coefficients varying only with temperature.

The molar solubilities of calcite and aragonite differ trivially and the numerical distinction is not relevant for modelling. However, aragonite scales tend to be softer and less adherent than calcite, so, an indicator of which polymorph actually forms has operational merit. A predictor can be based on contrasts of mechanisms for crystal growth and this model includes such an indicator.

Since neither the original calcium concentration nor the carbonate ($CO_3^{=}$) concentration can be directly measured in a geothermal context, additional equilibrium constants must be introduced, which lead to components that can be measured, specifically CO_2 and HCO_3^{-}.

$$K_0 = [H_2CO_3]/P_{CO2}$$
$$K_1 = [H^+][HCO_3^-]/[H_2CO_3]$$
$$K_2 = [H^+][CO_3^=]/[HCO_3^-]$$

Here, it is useful to express $CaCO_3$ solubility as a liquid's "carrying capacity" for calcium, as in Eq. 1.

$$(Ca) = K_0K_1K_2P_{CO2}A/K_2(HCO_3^-)^2a_{+2}a_{-1}^2 = mol/l \qquad (1)$$

Parentheses denote concentrations which are related to activities (brackets, []) through activity coefficients, $a_i = [i]/(i)$, that represent a chemical effectiveness. a-values vary with temperature, ionic strength, and properties of specific ions; a_{-1} and a_{+2} refer to bicarbonate and calcium respectively. Their numerical values range from less than 0.2 through 0.9 in the overall spectrum of geothermal resources and must be computed specifically for each temperature step in a wellbore model.

CO_2 pressure and concentration of bicarbonate vary within the wellbore profile and may be considered as chemical determinants for the liquid's capacity to carry dissolved calcium. They are the dominant forms of carbon in geothermal systems and may be accurately sampled and measured in surface fluids

Most geothermal wellbores penetrate rocks which contain calcite, hence produced liquids are saturated (equilibrated) at the local static conditions. Typically, there is an imperfect match between the apparent, or measured, field solubility of calcite and the theoretical solubility calculated with activity and stability coefficients and measured bicarbonate. Thus, factor A in Eq. 1 represents a local, well-specific constant that makes the computation of Eq. 1 correspond to the initial field saturation of calcium.

Elevation of the Bubble Point

A lowest elevation in a well that involves vapor phase corresponds to the initiation of boiling and the loss of CO_2 from the liquid. This begins the activation of scale-forming reactions. Elevation of this bubble point (BPE) can be accurately computed without reference to any factors of the two-phase zone or of the wellhead conditions. Essentially, overpressured fluid below the BPE rises to the location where the fluid's total vapor pressure (TVP) equals the local hydraulic pressure; equation 2 applies. Scaling initiated in the wellbore requires that $BPE > Z_{inflow}$, but scaling initiated in reservoir rocks can be accomodated by the model.

$$TVP_{BPE} = P_{res} - pg(BPE-Z_{res}) - F(BPE-Z_{inflow}) - R/PI \quad (2)$$

P_{res} represents a static reservoir pressure at some reference elevation, (Z_{res}) a hydraulic head ($pg\delta Z$) appears between the elevations of the reservoir reference and BPE, a friction effect (F) exists between the elevation of fluid inflow to the wellbore and BPE, and a drawdown is represented as the ratio of discharge rate (R) to productivity index (PI). Z_{BPE} may be computed explicitly by rearranging (2).

TVP is the sum of H_2O vapor pressure of the liquid (due to its temperature) and the Henry's law pressures (HLP) for all other "gas" species dissolved in the liquid.

$$TVP_{BPE} = \{P_{H2O} + HLP_{CO2} + HLP_{CH4} + HLP_{N2} + HLP_{H2} + \ldots.\}_{BPE}$$

All these vary markedly with temperature and HLPs are much more sensitive to salt effects than is P_{H2O}. Wellbore heat losses between the inflow elevation and BPE should be accounted for when computing TVP_{BPE}, which is different from TVP_{res}. Without accurate handling of HLP sum, BPE will be mis-identified and the pressure gradient wrongly computed in the early stages of steam development, where scale deposition is most significant.

Temperature Profile in the Wellbore

Temperature profile above the bubble point is computed according to principles described earlier (Michels 1985). Unlike most other wellbore simulators, in this, total pressure is treated as a dependent variable (joint function of temperature and multiple fluid components and gases). The CO_2 pressure component is applied in equations (1) and (2), providing for accurate coordination of the temperature profile with local calcite solubility.

Friction effects in this temperature-drop model conform to von Karmen principles in the region of 1-phase liquid, extended, with modification, to modest elevations above the BPE. At higher elevations, two-phase fluid friction may be computed without reference to a mechanical roughness of the casing. Instead, concepts and procedure have been developed to compute the interaction between the liquid layer on the casing and the moving two-phase fluid in the bore. The concept incorporates liquid surface tension in a way that drag (friction) becomes a property of the fluid, which varies with temperature, and not a property of the casing metal (which is obscurred by the liquid layer in any case).

Incremental Deposition of $CaCO_3$

Within the well profile, local solubility of calcite is computed in terms of the residual liquid's capacity to carry calcium (Eq. 1). Incremental deposition is computed as the difference between the carrying capacities at the ends of temperature-defined intervals. If the two-phase zone is long enough, a minimum calcite solubility occurs within the wellbore, marking the upper limit of scale deposition.

PRESSURES OF CO_2 AND OTHER GASES

Three concepts of gas pressures are required to make a proper accounting; Henry's Law pressure of the gas species in liquid, distribution of gas species between liquid and vapor, and effect of salt content on the solubility and distribution.

The Henry's law pressure (HLP) commonly is considered as a solubility, but is more accurately considered as an escaping tendency of gas species from the liquid. It was originally defined as the concentration of a gas species in liquid under a vapor phase pressure, but the presence of a vapor phase is not essential. HLP (of a gas species) may be visualized similarly to the H_2O vapor pressure in an overpressured context. HLPs for each gas species are additive to the H_2O vapor pressure when computing TVP. The correlations between HLPs and temperature are unique for each gas species and dissolved salts in the liquid increase their escaping tendency -- a salting-out effect.

For CO_2 in geothermal engineering circumstances the data from Ellis and Golding (1963) is most useful because it provides for simultaneous accounting of temperature and salt effects. A functional equation for the HLP_{CO2} based on their data for temperature, salt content and CO_2 pressure, is given by Eq. 3, which applies from 100-350°C and 0 to >70,000 mg/kg chloride. Chloride is useful as a convenient indicator of overall salt content in the liquid.

$$HLP_{CO2} = 0.281 - 0.000232\,|\,T-175\,|^{1.3} + (9.98\times10^{-7} + 5.4\times10^{-9}T)Cl_{eq} = MPaa/(g/kg) \qquad (3)$$

Equation (3) shows a minimum solubility at 175°C, a prominent (+) salt effect, and a strong (+) salt-temperature interaction. Commonly, chloride is the dominant anion and an equivalent chloride concentration can be constructed from measured concentrations (adjusted for steam loss);
$Cl_{eq} = Cl^- + 0.58HCO_3^- + 0.74SO_4^= = mg/kg.$

For non-CO_2 gases, HLPs can be computed conveniently using equations with the form of (4). Factor S is a salting-out coefficient described later.

$$HLP_g = S\{a + b/(T+273)\} \qquad (4)$$

Values for a and b given below are based on Himmelblau (1960) and apply only at temperatures higher than the solubility minima, T in Celsius.

	a	b	$T_{lower\ limit}$
CH_4	-12.2	7860	116
N_2	-11.5	7440	111
H_2	-82.1	53100	84

Although CO_2 generally is the dominant gas component in terms of mole fraction, its pressure effects may be less dominant. This is due to the lower molecular solubilities of methane, nitrogen, and hydrogen. Nominally, if CO_2 comprises 90 (mole) percent of the non-condensible gases, it contributes only 50 percent of the overall sum of HLPs. Thus, disregarding non-CO_2 gases can yield a serious underestimate of overall gas effects on BPE.

Hydrogen sulfide (H_2S) has important safety and environmental aspects, but is generally insignificant in its contribution to TVP. HLP_{H2S} may be disregarded in other than exceptional circumstances; some Hawaiian wells are exceptional. Sulfide mineral scales are sometimes important and profiles of their deposition potentials can be appended to this basic model. They are not considered further at this time.

Distribution of gas species between liquid and vapor becomes important after a vapor phase develops. The distribution is most conveniently described by the form of equation 5,

$$\log(n_v/n_l) = \log B = d+eT \quad (5)$$

where n=mole fraction of a gas in the vapor (v) and liquid (l) phases, T in Celsius. Values of d and e listed below are from Giggenbach (1980) and refer to salt-free water.

	(d)	(e)
CO_2	4.7593	-0.01092
CH_4	6.0783	-0.01383
N_2	6.4426	-0.01416
H_2	6.2283	-0.01403

Salting-out effects are similar for all gas species because salts operate more strongly on H_2O molecules than on the dissolved gas molecules. Equation (3) evaluated with and without a chloride concentration (Equation 6) yields a multiplier (S) for the salt effect on Henry's law pressures. Although S is based on CO_2 it can be directly applied to the other gases.

$$S = (HLP_{CO2})_{salty}/(HLP_{CO2})_{no-salt} \quad (6)$$

Salt effects on properties of H_2O are computed with correlation equations based on Haas, (1976).

CALIBRATION OF THE MODEL

Defects in the Equilibrium Assumption

A straight forward application of the model is a presumption of equlibrium. This implies that change in calcite solubility and the physical deposition of scale on the wellbore keep pace with the rate of temperature drop and exhalation of CO_2 from liquid. Equilibrium for the ionic aspects of the overall reaction mechanism is reasonable. Specifically, chemical steps represented by $2HCO_3^- \rightarrow CO_3^= + H_2O$ and $Ca^{++} + CO_3^= \rightarrow CaCO_3$ have been observed to operate in 2 to 5 milliseconds in the context of pressure jumps in mist flow circumstances. These times include delays for transport of liquid droplets to pipeline walls (Michels, 1984 and unpublished research). When parcels of activated liquid (eventually) reach the casing wall, diffusion of scale components to growth sites occurs in the boundary layer and scale deposition reaction reactions proceed quickly.

Two factors in the wellbore near BPE are important. (i) Degassing of liquid requires nucleation of bubbles, which can be slow or incomplete (soda-pop effect) at a defined temperature. Thus, a real residual liquid is less activated to deposit scale than an equilibrium liquid. (ii) The ionic reactions of scale formation do not occur isolated in the liquid phase but require a physical surface for crystal nucleation and growth and dissipation of energy released during bond formation. Crystal growth (which is scale deposition) occurs on the casing walls where it is found. [*A common perception holds that scale forms in the liquid and deposits on casing due to physical effects. This is definitely incorrect for calcite and probably incorrect for aragonite.*] Thus, fluid in the interior of the wellbore that becomes saturated in calcite just above the BPE does not de-saturate until fluid eddies carry it to the casing wall. This is a mixing-length effect, a process involving several meters of elevation (with subsequent additional activation due to decreased pressure, etc. along the pathway). These non-equilibrium features require empirical calibration of the model.

The equilibrium assumption results in maximum scale thickness at the BPE (abrupt step from zero thickness) with subsequent deposition decreasing upwardly at a decreasing rate. That is, topography of the scale surface predicted by the equilibrium assumption is everywhere concave toward the wellbore interior, which is not observed.

Measured Scales in Wellbores

Scale thickness profiles were carefully measured *in situ* (multifinger caliper) in seven geothermal wells at Dixie Valley, Nevada (Benoit 1987). Only two wells (84-7 and 73-7) had relatively stable production rates prior to scale measurements, so, presumably, their BPEs were stable. Well 73-7 had the smallest measured scale thickness and other events compromised the measurement details, thus, 84-7 is the strongest reference well for calibrating the model. Other wells had decreasing production rates that indicated falling BPEs. Lengths of deposition zones ranged from 300 to more than 500 meters, but the longer zones belonged to wells with falling BPEs. Additional data included recalculated reservoir brine compositions, CO_2 contents, estimates of total scale masses deposited in wells, and total liquid volumes.

All measured surface profiles (Benoit, 1987) showed deposition maxima, variously 30 to 100 meters above the lowest elevation of scale. Lowest maxima, 35 and 45 meters were for wells 73-7 and 84-7 which had stable BPEs. These wells also had profiles that were concave toward the well interior at elevations above the maximum thickness. Other wells had profiles that were variously concave, linear, or convex, plausible consequences of unstable BPEs and indicators of unsuitability for calibration.

Modelling indicates that the first 50 meters or so above the BPE are involved with bubble flow; adiabatic temperature decreases there are 0 to >2 degrees, fluid speeds are 0.5 to 4 m/s and vapor volume fractions of 0 to 0.25.

Objectives in Calibration

Three components of the model require empirical calibration; delayed degassing of the liquid, mixing length effect, and A-factor for initial saturation of calcium. Degassing effects and the A-factor may be cast as multipliers of the brine's local carrying capacity for calcium, yielding a local "net effectve" carrying capacity. Deposition within a temperature step is computed as the difference between "net effective" capacities at the ends of the step. A mixing length effect applies to this difference.

Using an A-factor in Eq. 1 accepts the theoretic calcite solubility as having the correct shape and approximate magnitude for a geothermal context. Thus, magnitude of the A-factor essentially addresses a local calibration. It may be chosen so the model wellhead concentration of calcium matches the measured concentration of residual calcium. [This empirical step merely collects overall errors and imprecisions involved with the calcite solubility calculation, of which there are several. For example, two activity coefficients (one of them squarred) are uncertain due to extension of the DeBye-Hückel calculation method beyond its concentration range of applicability. The four separate K-values involved are based on experiments of contrasting characteristics and precision. Furthermore, those experimental matrices had undefined relevance to geothermal conditions. Error in reported bicarbonate concentration also finds compensation in A.]

Degassing is promoted by increased surface/volume ratio for residual liquid. Thus, the approach toward equilibrium may be expected to improve exponentially as the vapor volume fraction increases. A suitable term has the form [exp(-a/f)] which approaches unity as f-->0.2+ if a≈0.00X, (f = vapor volume fraction). Calibration for delayed degassing involves selecting a value for (a) and using [exp(-a/f)] as a multiplier to the carrying capacity of equation (1).

Mixing length involves an increment of scale deposition that is activated in a narrow elevation range but spread over a wider interval that includes the activation interval plus additional elevation above that interval. The mixing length effect is most apparent in the first few increments of elevation above the BPE. Elsewhere, deposition activated at lower elevations deposits in zones from which newly activated deposition escapes, providing a kind of compensation to the equilibrium deposition computed for higher elevation zones.

Higher fluid speeds increase turbulent shear and smaller bore diameters decrease the eddy diffusion distances to casing walls (scale deposition sites). Both factors would appear to favor shorter mixing lengths. Thus it seems puzzling that well 73-7, with larger bore than 84-7 (.255 vs .224 m ID) and smaller 1-phase liquid velocity (0.5 vs 2.6 m/s) would show maximum scale deposition closer to the BPE (35 vs 45 m). Perhaps damage to the scale deposit in 73-7 (Benoit, 1987) resulted in under-measurement of maximum deposition in 73-7. Although defining a mixing length to incorporate bore diameter and fluid speed is appealing, calibration is not feasible with only one reliable scale profile, so these aspects will not be considered further in this report. Instead, only a height correlation will be used.

At the upward limit of scale deposition the mixing length effect becomes suppressed. Elevation of the upper limit of scale deposition is defined in the model by a minimum in the brine's carrying capacity for calcium. Above that elevation, the carrying capacity increases all the way to steam separator. Consequently, activated scale potential that is unspent below the upper elevation limit may be partly resorbed by the liquid. Since scale deposition in this tail region will be small in any case, the mixing length effect is considered inconsequential.

Only a fraction of the scale deposition potential activated within the first increment of elevation (Z_1) above the BPE is deposited within that increment. Yet, the net deposition within subsequent Z_i include activation from lower increments. Thus, the apparent fraction of available (equilibrium) activation that actually deposits in Z_i approaches unity as the fluid moves away from the BPE. The value of that "apparent" fraction is estimated here by $\exp\{-Z_i/(m\Sigma Z)\}$, when ΣZ is the sum of elevation increments between the BPE and lower bound of Z_i and m is chosen to make an empirical fit to the short interval involved with measured zero-to-peak scale thickness.

Calibration values are those that yield the match (Figure 1) between model and measured scale profiles for wells 84-7 and 73-7. For the calibration, $A_{84-7} = 8.97$, $A_{73-7} = 6.23$, a = .001, and m = 0.8.

Figure 1 should be construed as a test for only the shape of the scale topography. A mass balance (exact thickness match) was not feasible due to uncertainties in (i) amount of liquid involved with the measured scale, (ii) porosity of the measured scale, and (iii) whether a softer form of scale (aragonite ?) in the upper deposition zone was under-measured by the caliper fingers.

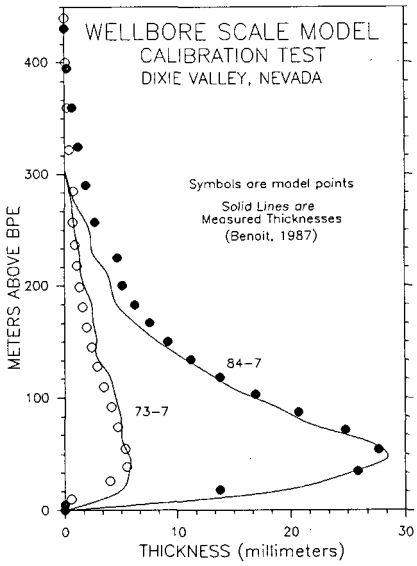

Figure 1: CALIBRATION RESULTS

A non-model multiplier for the model thickness was found which gave a good match with the peak thickness and then uniformly applied over the entire interval. This provides a fair test for model shape of the deposit.

A mass balance is best indicated by the match of calcium concentrations with, versus without scale inhibitor, determined from surface sampling (Benoit, 1991). For the case of 84-7, the "no-inhibitor" residual calcium concentration of 1.29 mg/kg was used to derive A = 8.97. This yields a model concentration of pre-flash calcium = 3.60 mg/kg, which compares to the "with inhibitor" calcium measurement of 3.6 ppm. This result suggests that chemical aspects of modelling are satisfactory.

For the modelling, data for chloride, bicarbonate, and sulfate conformed to wellfluid compositions in Benoit (1987) and model wellbore dimensions to actuals. Reservoir and well productivity data were not provided so model values were chosen to yield a BPE that matched the lower limit of scale deposition. A match to wellhead conditions was achieved by adjusting wellbore heat losses.

PARAMETRIC STUDIES

Two important factors in wellbore scale are how fast does it accumulate and where is it located. Both are related to the liquid's local carrying capacity for calcium, which varies with elevation in the wellbore largely due to decreases in temperature and P_{CO2}. Other major factors affecting calcium carrying capacity are (initial) bicarbonate and CO_2 concentration. Physical factors for the model wellbore were set at nominal values, uniform among most figures. Wellbore heat losses were set at zero.

CO_2 Effect on Temperature and Pressure Profiles

Figures 2A and 2B do not depict scale, but show profiles of wellbore temperature and pressure for a variety of initial CO_2 contents at a single model reservoir temperature and fluid composition. Greater CO_2 concentrations cause significant lowering of the BPE and modest increases in wellhead pressure without changing the essential shape of the pressure profile.

Contrastingly, the CO_2 effect on temperature profiles changes the shape so strongly that the order of curves in the family inverts between the BPE and wellhead. Without CO_2, the temperature profile near the BPE is concave up whereas with higher CO_2 concentrations it is concave down. All lowerings of BPE in Figures 2 are assignable to CO_2.

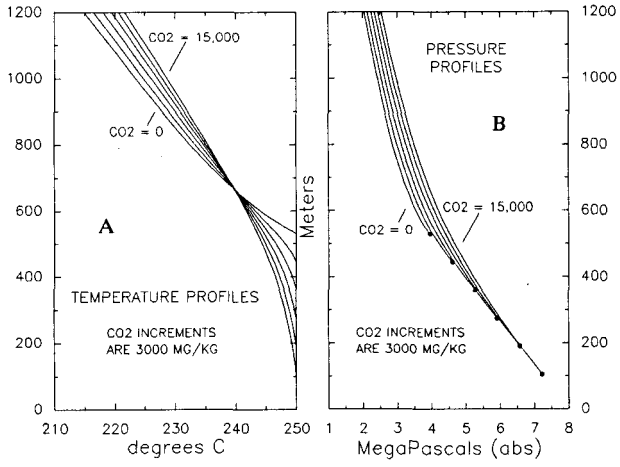

Figure 2: CO_2 EFFECT ON P-T PROFILES

Temperature Effect on Scale Profiles

Figures 3A and 3B show the calcium carrying capacity and scale build-up rate for a range of initial fluid temperatures. Other factors, CO_2, overall salt content, etc., were held constant and the same as for Figures 2. Lower BPE in Figures 3 are due to the higher pressure(s) of H_2O which is consequent of the higher temperature(s) [CO_2 effect on TVP decreases with increasing temperature above 175°C]. At higher initial temperatures, the calcite saturation is smaller, reflecting a general knowledge that carbonate scales tend to be less severe in hotter wells.

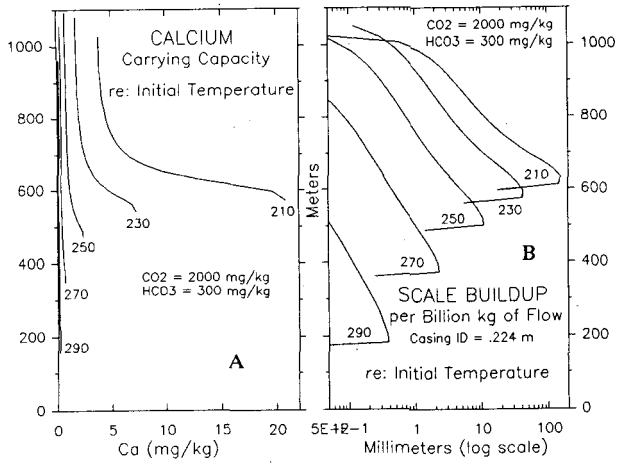

Figure 3: INITIAL TEMPERATURE EFFECTS

CO_2 Effect on Scale Profiles

Figures 4A and 4B also show calcium carrying capacity and scale build-up rates at one initial temperature with variable initial CO_2 content. Other factors are the same as for Figures 2. For 4A and 4B the initial ratio of $Ca/HCO_3^- << 1$ and the initial calcium concentrations vary in nearly direct proportion to the CO_2 contents. The thickness of scale and length of the scale deposition zone also increase in nearly direct proportion to the initial CO_2 content. [Irregularities in the peak shapes are artefacts from the plotting program.]

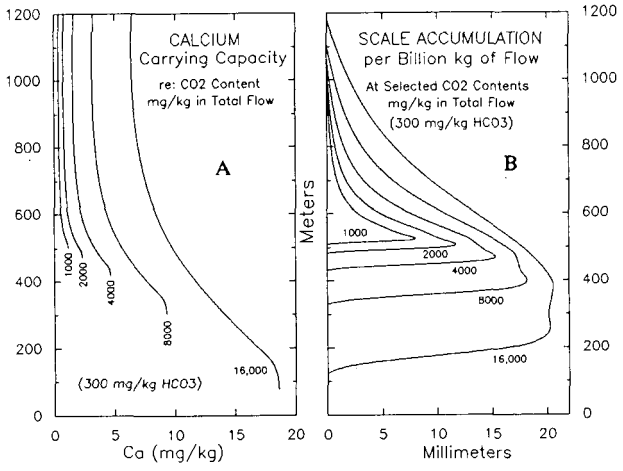

Figure 4: INITIAL CO_2 EFFECTS

HCO_3^- Effect on Scale Profiles

Figures 5A and 5B show calcium carrying capacity and scale buildup rate for various HCO_3^- concentrations with other factors similar to those for Figures 4. For Figures 5, $Ca << HCO_3^-$ and scale deposition *decreases* strongly with increasing HCO_3^-. This contrasts with Figures 6A and 6B, wherein $Ca > HCO_3^-$ and scale deposition *increases* with increasing HCO_3^-.

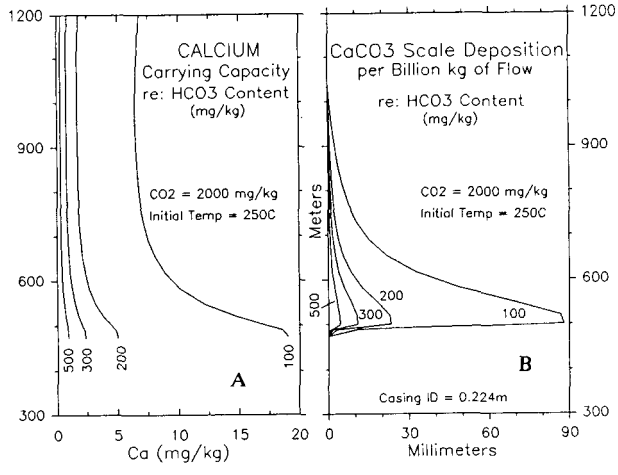

Figure 5: BICARBONATE EFFECTS with HCO_3^->Ca

Figure 6: BICARBONATE EFFECTS
with HCO_3^-<Ca

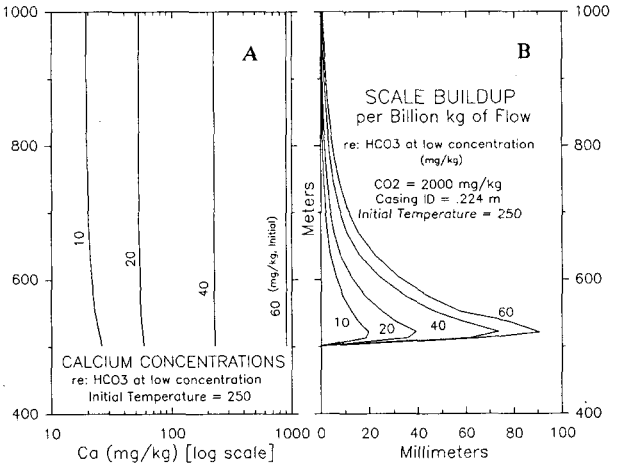

Effect of a non-CO_2 Gas

Non-CO_2 gasses do not affect the chemical solubility of calcite (scale components) but they do affect the distribution of scale in the earliest stages, through their effect on the two-phase pressure profile. Figures 7A and 7B show the effect of variable methane (CH_4) concentrations on temperature profile and scale thickness profile, with uniform initial temperature and CO_2 content. Since the non-CO_2 gas effect operates over the zone of maximum scale deposition the matter could be critical to issues of near-closure of a bore by scale buildup.

Figure 7: EFFECT OF non-CO_2 GAS
(Methane)

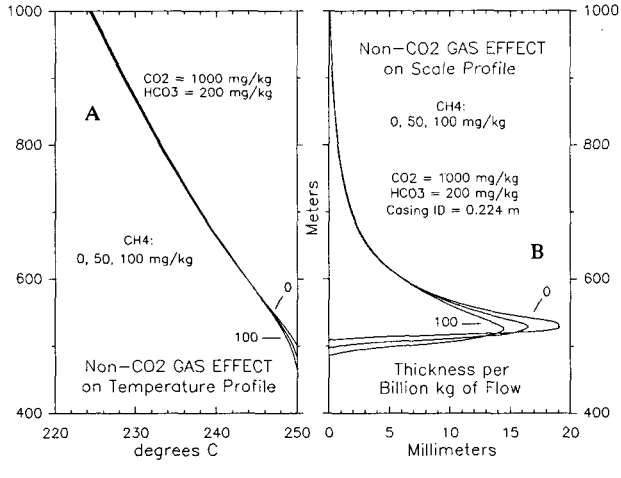

APPLICATIONS

Parametric studies show the multi-dimensional phenomenon of $CaCO_3$ scale deposition is too complicated for practical "rules of thumb". Modelling can accurately account for multi-dimensionality and there are several practical applications.

Monitoring Scale Inhibition Systems

Chemical methods of inhibiting carbonate scale are well-developed in regard to chemicals available and modestly developed in regard to hardware which places chemicals below the BPE. Importantly, wells equipped with scale inhibition systems must be monitored to show that the complete system continues to function as intended.

Monitoring scale inhibitor systems may require frequent surface samples of liquid for direct analysis of some scale components. Frequency of sampling should be matched to a well's severity of scaling so that failure of the inhibition system is discovered before costly scale-up of the well occurs. Some wells may permit two weeks or more of uninhibited production, but a few can yield expensive problems in two or three days. Modelling studies can help balance the risks and costs of monitoring by identifying a most practical sampling frequency.

In addition to frequency of sampling, the chemical analysis method must be sensitive enough to give a clear signal of status. Calcium analysis is easy and practical for low-calcium waters, but greater sensitivity and reproducibility are needed for waters with intermediate calcium concentrations. Calcium analysis is not practical for monitoring high-calcium waters. Modelling can help define the analytical requirements and evaluate sampling for alternative components, such as HCO_3^- or pH, etc.

Coping With Emergency Conditions

When a scale inhibition system fails there may remain a motive to keep the well in production a while longer for any of several practical reasons, e.g., overall steam requirements, inadequate availability in other well capacities, scheduled maintenance, etc. Modelling can show how much time may be "bought" with temporary uninhibited production and identify the wellbore consequences. This greatly aids emergency decisions that affect operating costs versus revenues. Modelling can also explore the advantages of running the defective well at non-routine rates, possibly to shift the location of maximum scale buildup as a device to moderate the consequences.

Wellfield Development

Wellfields present a range of chemical and production conditions and this range may cross the boundary between problematic and no-problem wellbore scaling. The pattern of scaling across the field can be sharpened by modelling studies, thereby aiding in site selection for fill-in wells.

The decision of whether to budget for scale inhibition equipment on wells to be drilled near the boundary can be greatly aided by modelling which explores the consequences of not inhibiting.

Wellfield Operations

Some wells are only marginally in need of a scale inhibition system in the sense that costs of dealing with (forecast) uninhibited scale deposits might be similar to, or less than, the (forecast) costs of installing, maintaining, and monitoring an inhibition system. Decision-making in these near-border cases can be strongly supported by scale modelling studies.

Among the no-inhibition options are arcane alternatives, such as programmed decreases in production which raise BPE to avert a critical narrowing of the wellbore

by scale. This can extend the time before cleanout, reduce the number of rig setups over the well life, and reduce annual wear on the wellbore. Modelling can show the border of practicality for such tactics including specifications for when and to where the BPE might be shifted from time to time, and how to establish the desired shift.

SUMMARY

Modelling $CaCO_3$ *scale buildup in geothermal wells* requires coordination of a wellbore simulator function with an accurate accounting for CO_2 pressure which fits with a chemical solubility calculation. A general model must include *effects of salts and non-*CO_2 gases. Some non-ideal and non-equilibrium factors can be calibrated with data from wellbore measurements. Such a model has been developed and partly calibrated.

Parametric model studies enable comprehension of how the many important factors of scale deposition inter-relate. One example concerned the effect of various initial bicarbonate concentrations on the consequent thickness of scale which developes. The sense of effect, increased versus decreased thickness, inverts with HCO_3^->>Ca or HCO_3^- << Ca.

Uninhibited scale deposition may, or may not, cause specific wells to be uneconomical. Modelling studies can address such economic issues and provide refined guidance for operating marginal wells, whether or not scale inhibitors are used.

Modelling can also be applied to strategies of wellfield development, especially when the field involves a gradient of scale-forming tendencies among its wells.

REFERENCES

Benoit, W.R., 1987, Early stage carbonate scaling characteristics in Dixie Valley wellbores: Geoth. Res. Counc. Trans., p 495-502.

_____, 1991, personal communication.

Ellis, A.J. and R.M. Golding, 1963, The solubility of carbon dioxide above 100°C in water and in sodium chloride solutions: Amer. J. Sci., v 261, p 47-61.

Giggenbach, W.F., 1980, Geothermal gas equilibria: Geochim. et Cosmochim. Acta, v 44, p 2021-2031.

Haas, J.L., 1976, Thermodynamic properties of the coexisting phases and thermochemical properties of the NaCl component in boiling NaCl solutions: U.S. Geol. Surv. Bul. 1421-B Revised, 71 pp.

Michels, D.E., 1985, A temperature-drop model for two-phase flow in geothermal wellbores: Tenth Workshop on Geothermal Reservoir Engineering, Stanford Univ., Jan. 22-24.

_____, 1984, Calcium carbonate deposition -- contrasts in mechanisms among boilers, desalinators, and geothermals: Amer. Inst. Chem. Engrs., Symposition, San Francisco, Nov 27.

ACKNOWLEDGEMENTS

I appreciate Dick Benoit, of Oxbow Geothermal, Inc., for his help regarding wellbore scale data and interpretation.

PROCEEDINGS, Seventeenth Workshop on Geothermal Reservoir Engineering
Stanford University, Stanford, California, January 29-31, 1992
SGP-TR-141

HYDROTHERMALLY ALTERED AND FRACTURED GRANITE AS AN HDR RESERVOIR IN THE EPS-1 BOREHOLE, ALSACE, FRANCE

A. Genter and H. Traineau

BRGM/IMRG, BP 6009, 45060 Orléans Cedex 2, France

ABSTRACT

As part of the European Hot Dry Rocks Project, a second exploration borehole, EPS-1, has been cored to a depth of 2227 m at Soultz-sous-Forêts (France). The target was a granite beginning at 1417 m depth, overlain by post-Paleozoic sedimentary cover.
Structural analysis and petrographic examination of the 800-m porphyritic granite core, have shown that this rock has undergone several periods of hydrothermal alteration and fracturing. More than 3000 natural structures were recorded, whose distribution pattern shows clusters where low-density fracture zones (less than 1 per meter) alternate with zones of high fracture density (more than 20 per meter).
Vein alteration, ascribed to paleohydrothermal systems, developed within the hydrothermally altered and highly fractured zones, transforming primary biotite and plagioclase into clay minerals. One of these zones at 2.2 km depth produced a hot-water outflow during coring, indicating the existence of a hydrothermal reservoir. Its permeability is provided by the fracture network and by secondary porosity of the granitic matrix resulting from vein alteration.
This dual porosity in the HDR granite reservoir must be taken into account in the design of the heat exchanger, both for modelling the water-rock interactions and for hydraulic testing.

INTRODUCTION

The objective of this European Hot Dry Rock (HDR) geothermal project is to develop an artificial heat exchanger within a granite covered by 1400 m of sedimentary cover. The site is located in the Upper Rhine Graben, on a marked thermal anomaly, giving a temperature of 140°C at 2 km depth in the former borehole GPK-1 drilled in 1987 (Kappelmeyer et al., 1991). Close to it a second exploration borehole, EPS-1, has been fully cored to a depth of 2227 m, providing 810 m of granite core.

Geologic investigations in HDR experiments are mainly concerned with describing the natural joint network that will be used to develop the artificial heat exchanger, and with gaining good understanding of the chemical and mineralogical features of the crystalline medium that will interact with the injected fluids. Continuous coring of the granite borehole EPS-1 provides an exceptional opportunity to achieve these aims.

FRACTURE STUDIES

About 3700 structures were recorded along the 810 m of granite-core sections (Fig. 1, 2). They were classified, according to their origin, into natural brittle fractures and artificial discontinuities induced by stress-release in the core. In this paper, only natural fractures are considered. These were created during the successive tectonic stages that affected this late-Hercynian granite.

Subhorizontal joints

These are mainly natural fractures without any indicator of movement, such as striation. They represent 4.5% of all natural fractures, are concentrated at the top of the granite, and their density decreases regularly with depth until 1700-1800 m (Fig. 2). Their average width is less than 0.5 mm. These joints seem to be related to isostatic unloading of the emerging granite during the Permian, under oxiditing conditions. They are sealed by iron oxides, but quartz, accessory calcite and clay minerals are also present as fillings.

Minor fractures

This is the most abundant type of structure recorded from the core sections, forming 69% of the total number of natural fractures. Their average width is about 0.5 mm, they dip steeply and are sealed by hydrothermal deposits of calcite, chlorite, quartz, sulfides, epidote and accessory hematite. Generally, the wall rocks in the area surrounding these minor fractures are not affected by alteration and show no evidence of movement. They are organized in clusters with zones of high fracture concentration where the maximum fracture density may exceed 20 per metre (Fig. 2).

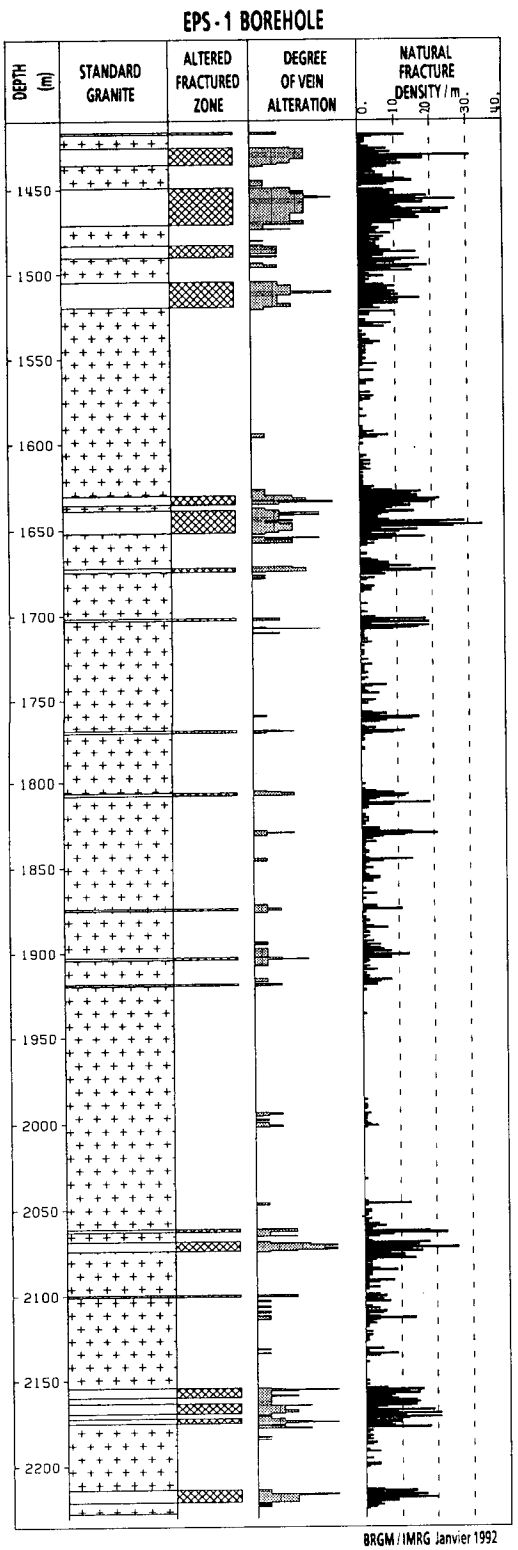

Fig. 1 : Composite petrographic log of borehole EPS-1 showing the relationship between petrography, vein alteration and density of natural fractures

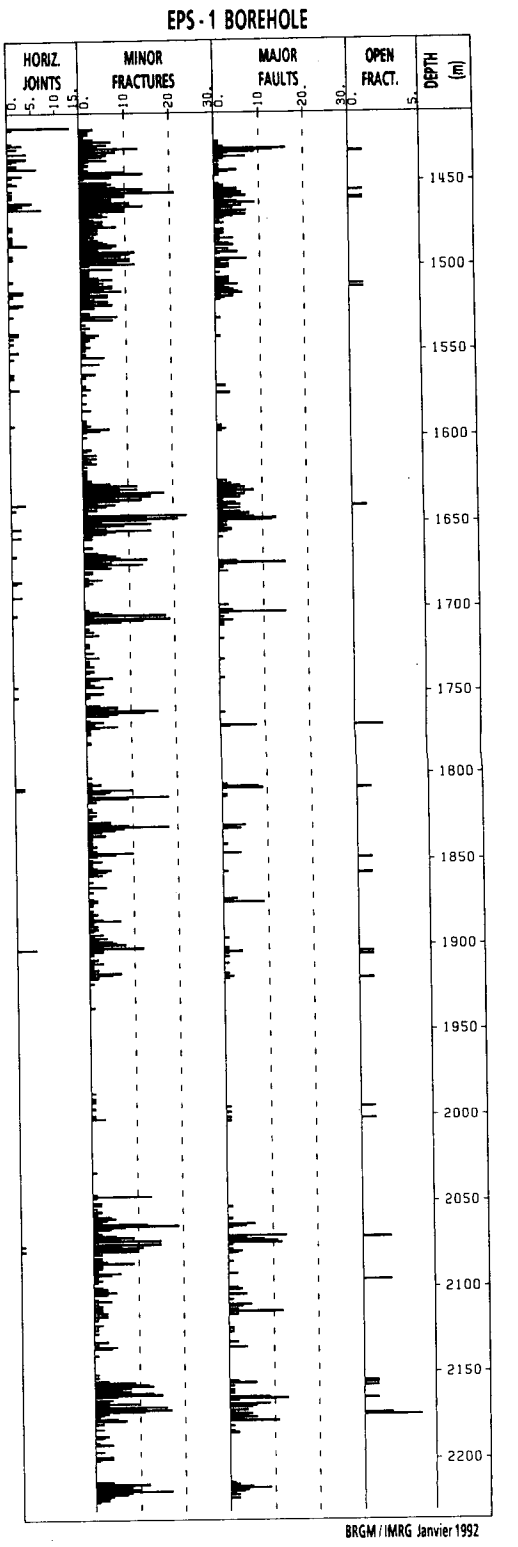

Fig. 2 : Density of different types of natural structures recorded in borehole EPS-1

Major faults
These are natural fractures showing presumed movement indicators and filled with mineral deposits. They represent 25% of the total number of fractures. Normal, reverse and shear faults were all observed. Although they were not formed during the same tectonic episode, these different types of major faults occur in the same depth intervals. Major fractures have an average width of 2.4 mm and typically have been filled by several successive hydrothermal deposits (quartz, clay minerals, carbonates, barite, sulfides). Their density distribution is virtually identical to that of the minor fractures (Fig. 2), so that together they form the main fracture zones in the granite, where they are associated with breccia, cataclastite and protomylonite.

Open fractures
About thirty natural discontinuities can be classified as open fractures, representing only 1% of the natural fractures identified on the core sections. These fractures show a moderate free aperture of 1.5 mm, but they have an average sealed width of 25 mm. The most common mineral fillings are quartz, calcite, clay minerals, barite and hematite. The thickest is a 250 mm-thick quartz-vein at 2175 m depth in the highly fractured zone that produced hot water during coring. The open fractures are mainly located within zones of high fracture density (Fig. 2), and their maximum density was recorded in the outflow zone.

Orientation of fractures
The core sections were not oriented during drilling; instead, we drew an arbitrary reference line. The core pieces in which structural features were present were photocopied using an unrolled photocopy machine which produces flatcore copies. The fracture traces were analysed and recorded by digitizer using BRGM software. Fracture-orientation data were then deduced from the comparison between cores and borehole imagery (Tenzer et al., 1991).

A stereonet of an oriented zone is presented in Fig. 3. The main vertical fracture sets strike N110° with a dip of 75°N and N165° with a dip of 80°E. Several secondary directional fracture sets exist locally. The set striking N165° is related to a paleostress field that probably was reactivated during the Oligocene E-W rifting activity of the Rhine Graben. As emphasized by Genter et al. (1991) in GPK-1 borehole, this structural set is also roughly parallel to the direction of present maximum horizontal stress measured in GPK1 borehole, which is N155° to N176° (Rummel and Baumgärtner, 1991).

PETROGRAPHY OF THE GRANITE AND HYDROTHERMAL ALTERATION

EPS-1 borehole intersected the same granite as GPK-1 borehole about 500 m away. This massif is fairly homogeneous and composed of a porphyritic granite with K-feldspar megacrysts, quartz, plagioclase, biotite, hornblende, and accessory titanite and magnetite.
Two main types of hydrothermal alteration were observed macroscopically in the cores: an early stage of pervasive alteration and subsequent vein alteration, as in borehole GPK-1 (Genter, 1989).

Pervasive alteration
This alteration took place on a large scale within the granite without visible modification of the rock texture. Low-grade transformation of biotite and plagioclase lead to the formation of chlorite, corrensite, calcite, epidote and white mica. In Fig. 1, zones affected by pervasive alteration and zones of massive unaltered granite are both included in the same "standard granite". Some of the joints sealed by calcite, chlorite, sulfides or epidote are related to this early stage of alteration.

Subsequent vein alteration
Vein alteration was closely related to fracturing along "fractured and hydrothermally altered zones" (Fig. 1), which are 1-15 m thick and represent about 10% of the total section. The intense fracturing created cataclastic granite, breccia, microbreccia and protomylonite; the primary texture of the granite may be destroyed in the most strongly fractured rocks, creating a fracture porosity partly sealed by hydrothermal products (quartz, calcite, illite, chlorite, sulfides, barite, hematite). Wall-rock alteration is intense in many places. Pre-existing biotite, hornblende and plagioclase have been partly dissolved and then transformed to dioctahedral mica inducing secondary matrix porosity.

An example of a "fractured and hydrothermally altered zone" observed between 2069 and 2075 m depth is given on Fig. 4, showing the relationship between cataclastic facies, degree of vein alteration (expressed as grade of transformation of primary minerals) and natural fracture density.

As illustrated on Fig. 4, the dip of such zones which concentrate steeply dipping fractures, is expected to be high.

EPS-1 BOREHOLE

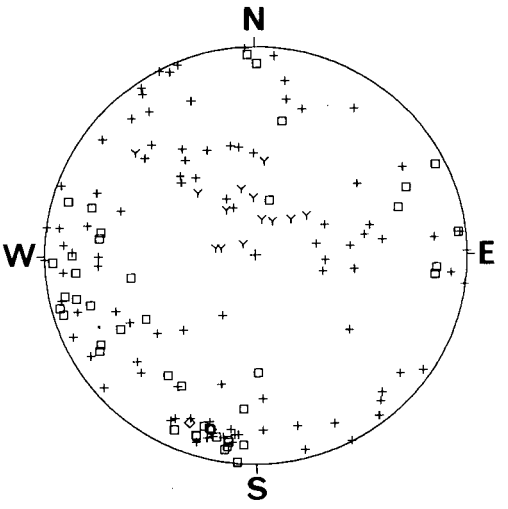

Schmidt stereographic net lower hemisphere

Legend :

Y subhorizontal joint □ major fault

◇ open fracture + minor fracture

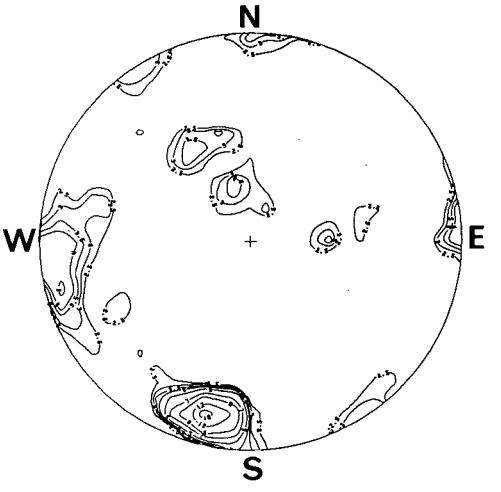

Density diagram. 152 data

Fig. 3 : Poles of natural fractures from 1507 m to 1530 m depth

EPS-1 BOREHOLE

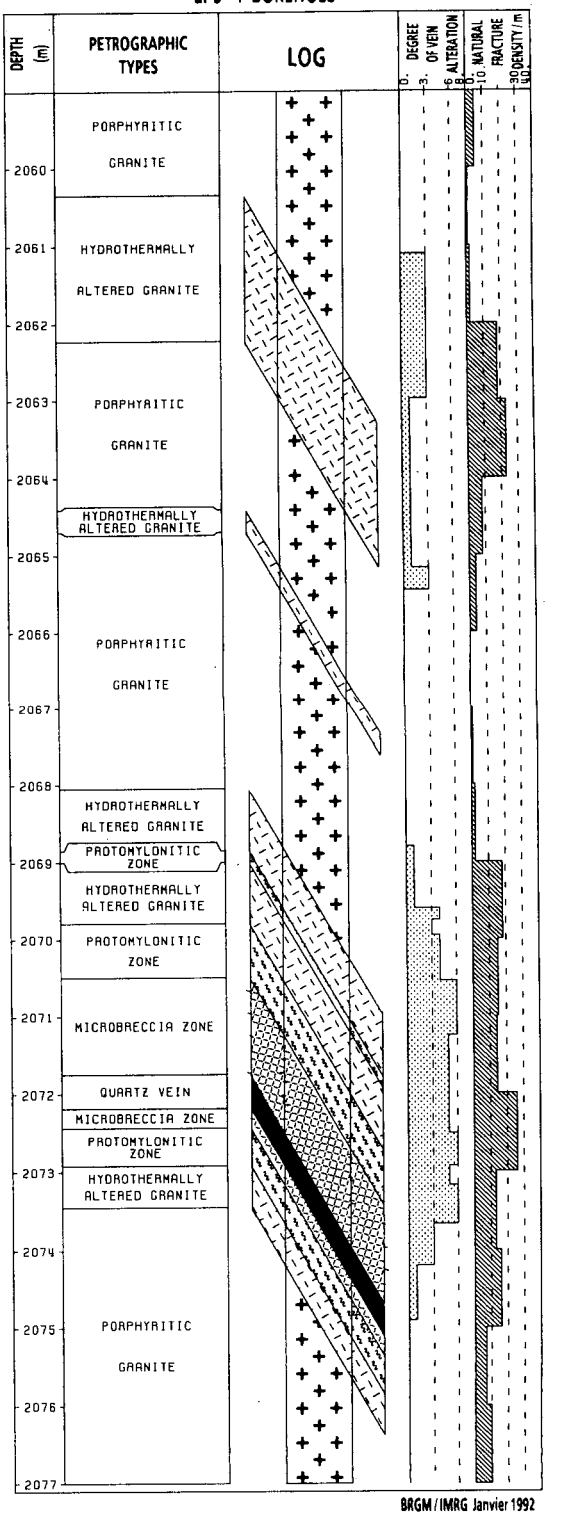

Fig. 4 : Detail of a fractured and hydrothermally altered zone developed within the Soultz granite as revealed by the examination of the EPS-1 core sections

The survey of all altered and fractured zones encountered on the core sections allows to define a general pattern for them, with from the centre to edge:

1) An inner zone of intense fracturing, with the formation of breccia zones and in places protomylonitic textures. Biotite and plagioclase are readily altered, K-feldspar megacrysts are intensely fragmented, and primary texture of the granite disappears. Fractures are commonly sealed by vuggy quartz veins up to 20 cm thick.

2) An intermediate zone where fracturing is less intense, with minor or major fractures, leading to the formation of cataclastic granite. Alteration is uniformly strong, and biotite and plagioclase have been transformed into clay minerals.

3) An outer zone where fracture density is close to zero, but alteration is intense. Biotite and plagioclase are readily transformed into clay minerals. This zone represents the proximal wall rock effect of a major fault zone, and the rock within it has been classified as hydrothermally altered granite.

These altered and fractured zones could be ascribed to paleohydrothermal systems developed within the granite. A hot-water outflow during coring showed that some of these fractured and hydrothermally altered zones are still active and related to a present-day hydrothermal system.
Their permeability seems to be provided both by the fracture network and by secondary porosity in the granite, as a result of vein alteration that partly dissolved pre-existing minerals (biotite, hornblende, plagioclase) and precipitated newly formed white mica.

IMPLICATIONS FOR HDR RESERVOIR DEVELOPMENT

The geologic characteristics of the HDR Soultz site are mainly controlled by its location within the Rhine Graben. Most of the natural fracture sets observed on the cores have been generated or reactivated by an E-W extensional regime during the Oligocene. The present stress field indicates extensional regime typical of a graben system with the present-day maximum horizontal compressional stress field (Sigma H), oriented N155° to N176° (Rummel and Baumgärtner, 1991). The natural subvertical structures, parallel to Sigma H, will have tendency to be open like tension gashes.

From the viewpoint of developing an HDR reservoir at the Soultz site, the granite environment can be classified into three main types: a) "standard granite" with a low natural fracture density, which corresponds to the standard model of the Hot Dry Rock reservoir; b) fractured and hydrothermally altered zones related to paleohydrothermal systems, similar to self-sealed fracture reservoirs observed in natural geothermal systems; and c) fractured and altered zones that are still active and related to a present-day hydrothermal system.
A relation between zones of vein alteration and fracture systems had already been identified in the investigations on cuttings from GPK-1 borehole (Traineau et al., 1991), but the examination of the EPS-1 cores greatly increased our understanding of these zones. They show a general pattern in which fracture density decreases from the centre to the margins. Intensity of vein alteration depends on this structural framework. The permeability of fractured and hydrothermally altered zones can be ascribed to a dual-porosity model, involving the fracture network and the dissolution-precipitation processes of vein alteration. This appears very important for modelling the fluid circulation and water-rock interactions during development of the future HDR reservoir. Furthermore, the orientation of fracture zones obtained from borehole imagery will enable us to predict the extent and geometry of the flow path within the granite.
As the main fracture sets within these zones are roughly parallel to the maximum horizontal stress, they constitute the most attractive target for development of a future Hot Dry Rock reservoir.

ACKNOWLEDGEMENTS

This research was carried out in the framework of the European Hot Dry Rock Project funded by the Commission of the European Communities (DG XII). Geologic investigations were supported in part by the Bureau de Recherches Géologiques et Minières and in part by the Agence Française pour la Maîtrise de l'Energie.

REFERENCES

Genter, A.; (1989), "Géothermie Roches Chaudes Sèches: le granite de Soultz-sous-Forêts (Bas Rhin, France). Fracturation naturelle, altérations hydrothermales et interaction eau-roche", Ph.D. thesis, University of Orléans, France, 201p.

Genter, A.; Martin, P.; and Montaggioni, P. (1991), "Application of FMS and BHTV tools for evaluation of natural fractures in the Soultz geothermal borehole GPK1", Geotherm. Sci. & Tech. Vol.3 (1-4), pp. 69-82.

Genter, A.; and Traineau, H. (1991), "Geological survey of the HDR borehole EPS1, Soultz-sous-Forêts, France", BRGM report no. 32433 IRG SGN 91, 25 pp.

Kappelmeyer, O.; Gérard, A.; Schloemer, W.; Ferrandes, R.; Rummel, F.; Benderitter, Y. (1991), "European HDR project at Soultz-sous-Forêts: general presentation", Geotherm. Sci. Tech., vol. 2 (4), pp. 263-289.

Rummel, F.; and Baumgärtner, J. (1991), "Hydraulic fracturing stress measurements in the GPK1 borehole, Soults-sous-Forêts", Geotherm. Sci. & Tech., Vol. 3 (1-4), pp. 119-148.

Tenzer, H.; Mastin, L.; and Heinemann, B. (1991), "Determination of planar discontinuities and borehole geometry in the crystalline rock of borehole GPK1 at Soultz-sous-Forêts", Geotherm. Sci. & Tech., Vol. 3, (1-4), pp. 31-67.

Traineau, H.; Genter, A.; Cautru, J.P.; Fabriol, H. and Chevremont, P. (1991), "Petrography of the granite massif from drill-cutting analysis and well-log interpretation in the HDR borehole GPK1 (Soultz, Alsace, France)", Geotherm. Sci. & Tech., Vol. 3 (1-4), pp. 1-29.

PROCEEDINGS, Seventeenth Workshop on Geothermal Reservoir Engineering
Stanford University, Stanford, California, January 29-31, 1992
SGP-TR-141

NEW PROJECT FOR HOT WET ROCK GEOTHERMAL RESERVOIR DESIGN CONCEPT

Hideaki Takahashi and Toshiyuki Hashida

Research Institute for Fracture Technology
Tohoku University
Sendai/980, Japan

ABSTRACT

This paper presents the outlines of a new Hot Wet Rock (HWR) geothermal project. The goal of the project is to develop a design methodology for combined artificial and natural crack geothermal reservoir systems with the objective of enhancing the thermal output of existing geothermal power plants. The proposed concept of HWR and the research tasks of the project are described.

INTRODUCTION

It is well known that the productivity of geothermal wells is strongly dependent on the existence of cracks in rock masses. The concept of Hot Dry Rock (HDR) has been proposed in an attempt to create an artificial heat exchanging circulation system by means of well stimulation techniques such as hydraulic fracturing. This idea has attracted considerable interests and resulted in large-scale research projects in the U.S., Europe and Japan. The majority of currently operating geothermal power plants in Japan heavily rely on natural geothermal fluid stored in the existing subsurface crack network. However, the potential thermal energy from the surrounding areas is typically not fully utilized and remains unexploited. The thermal power output is therefore limited, unfortunately. Thus, there is a strong need for enhancing the thermal power of the existing geothermal reservoirs and for extending their operation life.

In response to the need, a new academic research project has been launched at Tohoku University, Japan. This research project is directed towards establishing an engineering design methodology for the further development of existing natural geothermal reservoirs. We have adopted the basic idea of HDR, and combined the existing available geothermal reservoir in the developments. As a result, the new concept of Hot Wet Rock (HWR) is created. The schematic of the concept is illustrated in Fig. 1. The HWR system refers to the combined natural and artificial crack network.

In this paper, the outlines of the new research project for HWR are presented, and the research tasks of working groups formed in the project are briefly described.

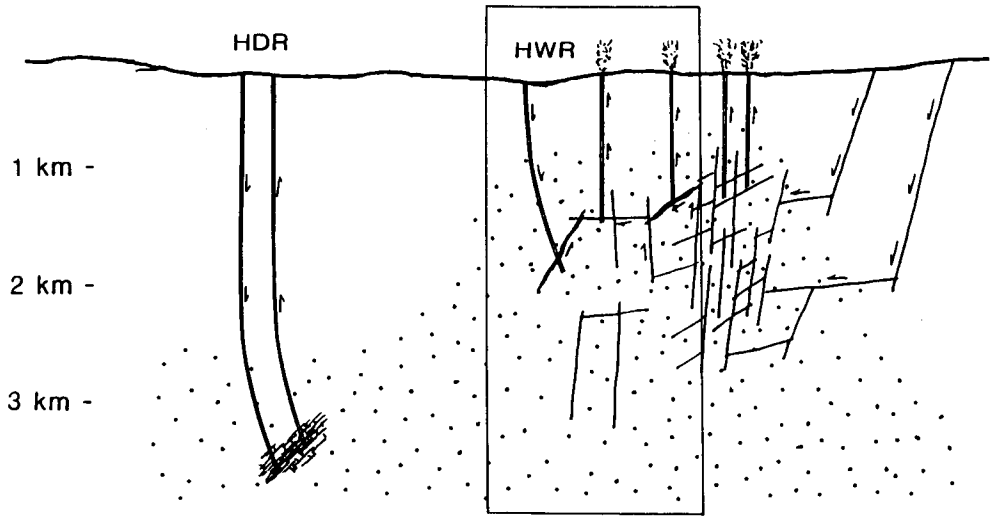

Fig. 1. The concept of Hot Wet Rock (HWR) geothermal reservoir

OUTLINES OF HWR PROJECT

The HWR project is being carried out in close cooperation with the MITI-NEDO geothermal energy development program (1989-1993). Fig. 2 shows the project organization structure. A research group of geothermal energy extraction engineering (GEEE) has been formed at Tohoku University. This research group is composed of several interdisciplinary teams, and plays a technical leading role in the project. As indicated in Fig. 2, a number of private companies and national research laboratories are also participating in the project.

The HWR concept specifically aims to connect a designed artificial crack with a preexisting geothermal reservoir in order to take full advantage of the surrounding area which is full of potential thermal energy. The establishment of the combined methodology for HWR systems calls for several element technologies. The following investigations form the major research tasks of the project:

(1) Monitoring and modelling of natural crack networks
(2) Design methodology of artificial heat exchange surfaces: optimization of the location and size of artificial cracks
(3) Heat extraction simulation from the combined geothermal reservoir
(4) Methods for predicting long-term reservoir performance

The methods listed above are being developed through working group activities in GEEE as shown in Table 1. The table also shows key personnels and their contributions. The GEEE team has carried out a research project on the design methodology of artificial crack-like reservoir for HDR geothermal energy extraction, which was a grant-in-aid for special distinguished research supported by the Government of Japan, Ministry of Education, Science and Culture (Abé , H. and Takahashi, H., 1983, Takahashi, H. and Abé , H., 1987, Niitsuma, H., 1989). The former project is called Γ-project. A crustal rock fracture mechanics approach has been proposed for HDR systems, and verified through field experiments. In the research task (2) of the HWR project, the fracture mechanics methodology is employed and further extended to the combined geothermal reservoir system.

The methodology is scheduled to be applied in the Yunomori geothermal field of the MITI-NEDO program. The temperature in the field is estimated to be about 200 °C at a depth of 1500 m. The time schedule of well drilling and experimentation is shown in Table 2. The HWR project provides academic supports for designing a geothermal reservoir in the model field along the time schedule.

RESEARCH ACTIVITIES IN GEEE

In this section a brief description of the individual research task is presented together with some results obtained to date. Given the importance of the natural crack characterization on the proposed combined geothermal reservoir performance, various crack monitoring techniques and modeling methods are being developed within the WG research activities. Fig. 3 illustrates a process for the development of design methodology for HWR systems. The WG researches are also designed to establish a data base of subsurface structures.

(1) Subsurface Structure Evaluation WG

Development of methods for monitoring subsurface cracks is a key issue for the design and performance evaluation of HWR systems. In this project extensive

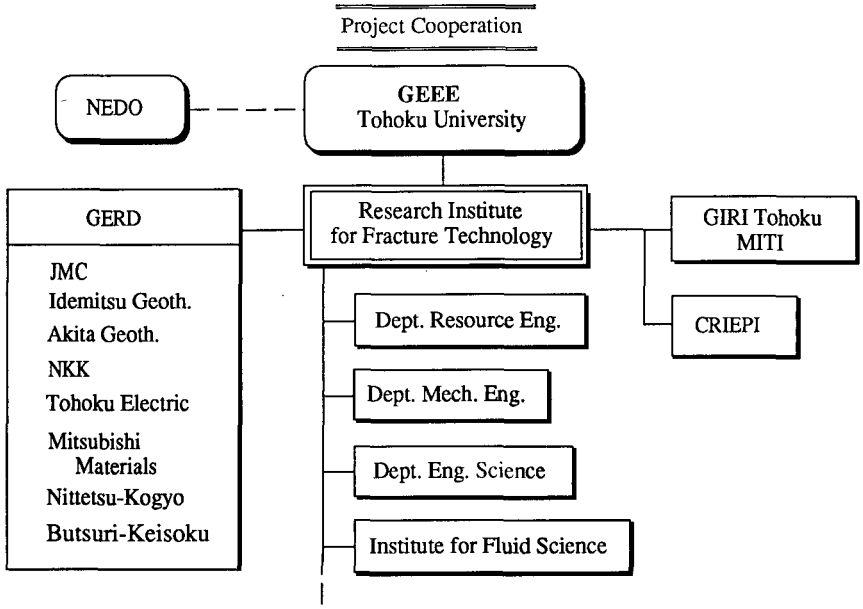

Fig. 2. Research organization structure of HWR project and project cooperation

Table 1. Research group of geothermal energy extraction engineering (GEEE), Tohoku University

Project Chairman	Prof. H. Takahashi (Research Inst. for Fracture Technology)
Project Vice-Chairman	Prof. K. Nakatsuka (Dept. of Resource Eng.)

Working Group	Personnels and Organization	
	WG Leader	WG Subleader
Subsurface Structure Evaluation WG	Prof. H. Niitsuma (Dept. of Resource Eng.)	Ass. Prof. M. Sato (Dept. of Resource Eng.)
Subsurface Crack Design WG	Prof. K. Hayashi (Inst. for Fluid Science)	Ass. Prof. T. Hashida (RIFT*)
Rock Mass Property Evaluation WG	Ass. Prof. K. Matsuki (Dept. of Resource Eng.)	Ass. Prof. T. Hashida (RIFT)
Thermal Design and Evaluation WG	Prof. T. Shoji (RIFT*)	Prof. K. Hayashi (Inst. for Fluid Science)

* RIFT: Research Institute for Fracture Technology

Table 2. Time schedule of MITI-NEDO project: Yunomori field experiments

Year	Schedule
1989	Selection of model field: Yunomori field
1990	Test drilling
1991	Drilling of production well
1992	Hydraulic fracturing (#1)
	Drilling of reinjection well
1993	Hydraulic fracturing (#2)
1994	Circulation test

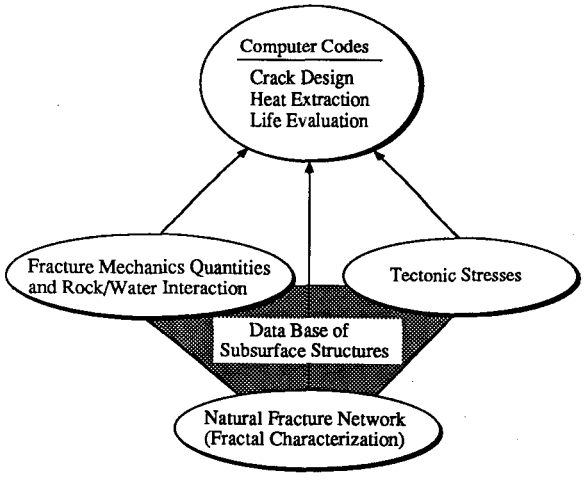

Fig. 3. Flow of research and data base

experimental and theoretical investigations are programmed in order to develop reliable methods for evaluating preexisting fracture networks and for detecting artificial cracks induced by hydraulic fracturing technique. The methods being developed are listed in the following:

(a) Monitoring of Preexisting Fractures
- ○ Triaxial shear shadow
- ○ Shear wave splitting
- ○ Acoustic emission monitoring of drilling
- ○ Borehole radar
- ○ Magnetic tracer test

(b) Monitoring of Artificial Fractures
- ○ Downhole acoustic imaging (triaxial hodogram AE source location); Theoretical study on AE source mechanism is also supporting the development of the method.

For each method, suitable signal detectors and signal processing techniques are being developed. For example, a wideband and high sensitive triaxial seismic detector has been developed for downhole AE source location. In conjunction with the sensor development a new calibration technique for detectors has been devised, which utilizes the spectral matrix analysis to improve the accuracy of the detection of P-wave direction in the triaxial hodogram analysis. The usefulness of the new detector and analyzing technique has been verified through experiments in the GEEE Higashihachimantai model field (Moriya et al., 1990, Niitsuma et al., 1991). In the tests seismic sources were simulated using an air gun in a borehole, and signals from the artificial source were monitored by the triaxial AE sensor set in an another borehole. Fig. 4 compares the results of source location evaluated by the spectral matrix analysis with those obtained by the conventional method in time domain. The points along the vertical axis indicates the actual location of the artificial seismic sources. It is seen that the new signal processing technique reduces significantly the error in the source location. Furthermore, a triaxial shear shadow technique has been applied to delineate the single crack created by hydraulic fracturing in the Higashihachimantai model field in the

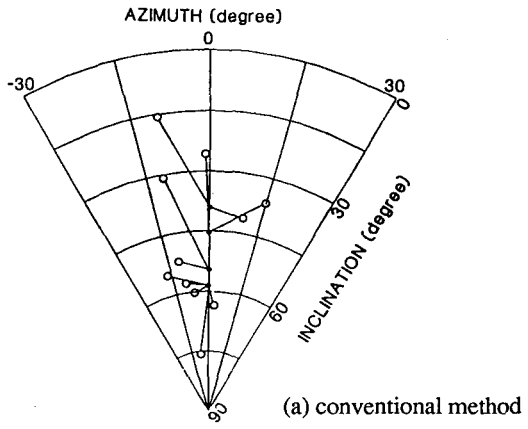

(a) conventional method

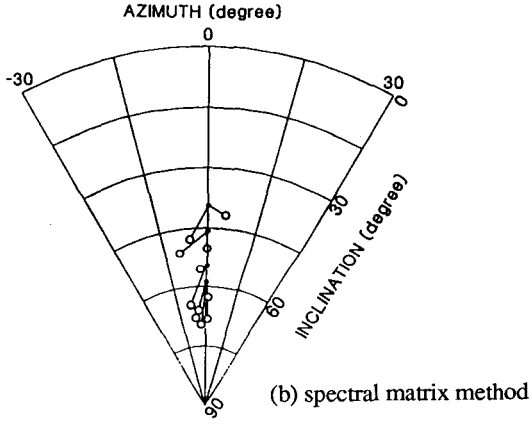

(b) spectral matrix method

Fig. 4. Results of AE source location in calibration tests

course of Γ-project (Niitsuma, H. and Saito, H., 1991). It has been demonstrated that the crack orientation determined by this technique was consistent with that predicted by tectonic stress measurements and core sample observation. The technique is currently being extended to cover more complex fracture networks.

(2) Subsurface Crack Design WG

The research items are outlined below.

(a) Tectonic stress determination; There has been no analyzing method applicable to determine in-situ stresses under the influence of thermal stresses in hydraulic fracturing method. Such a method is now under investigation.

(b) Subsurface crack evaluation based on pressure-flow rate-time records; Computer codes are under development to simulate the crack growth induced by hydraulic fracturing in HWR systems on the basis of the fracture mechanics approach. In order to support the development experimentally, a downhole devise for measuring the crack opening displacement has been fabricated.

(c) Percolation modeling for predicting reservoir performances; Percolation theory is employed to characterize fracture type reservoir and to predict reservoir performance (Usui, T. et al., 1991). Fig. 5 shows a model to examine the effect of an artificial crack on the reservoir permeability. The rectangular inspection area around the injection well is divided into 60×60 grids and the artificial crack is envisioned to extend horizontally towards existing reservoir from the injection well. Natural cracks within the inspection area were generated by using the percolation theory. Namely, the existence or absence of natural crack at the grid point was determined on the basis of the probability density, p. The value of p corresponds to the natural crack density. One segment of grid line whose both ends are assigned under a given value of p is taken as an unit of natural crack. Fig. 6 gives an example of result predicted by the model, where L_{path} represents the minimum length of connected paths between injection well and existing reservoir in terms of grid numbers. Higher value of L_{path} can be taken as reflecting higher flow impedance. It is seen that the L_{path} drops rapidly as the artificial crack length reaches 18 grid length. As exemplified in the above example, the percolation model enables an quantitative prediction of an improvement of reservoir permeability by artificial cracks.

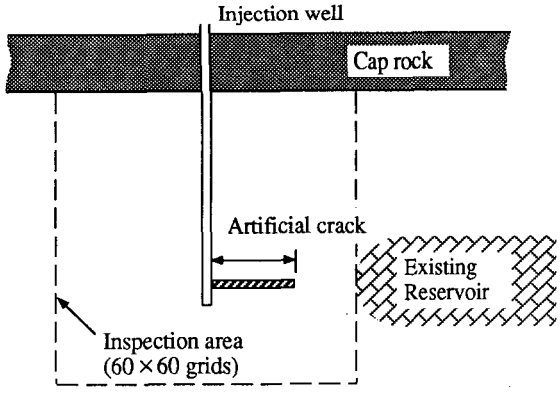

Fig. 5. Reservoir model for examining the effect of an artificial crack on the flow impedance

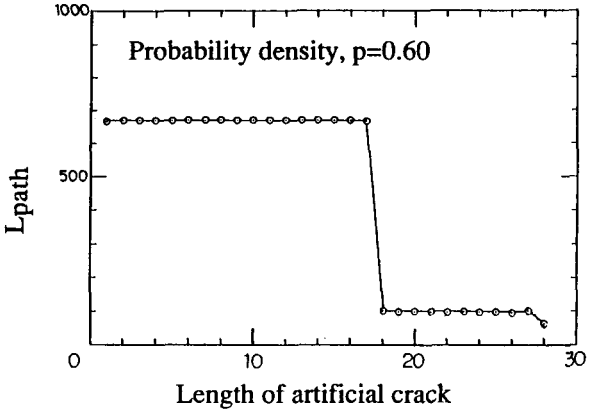

Fig. 6. Example of numerical results based on percolation theory

(3) Rock Mass Property WG

In order to provide rock mass property and rock/interaction data necessary for the subsurface crack design and thermal extraction analysis, the following investigations are being carried out:

(a) Development of fracture toughness testing method; Core-based test methods are being developed to determine the fracture toughness K_{Ic} under confining pressures. In addition to ISRM suggested core specimens, i.e. short rod and chevron bend, round compact tension specimens are used to evaluate the K_{Ic} in the mutually orthogonal orientations from one piece of core sample.

(b) Determination of tectonic stresses by use of rock core; Various methods including ASR, AE, DSA and DRA will be utilized to finally develop an integrated technique for determining accurate tectonic stresses in addition to the hydraulic fracturing method mentioned above.

(c) Water-rock interaction; Autoclave experiments are performed to determine the kinetics of dissolution and scaling. Investigation of the effect of dissolution on the permeability and the slip resistance along preexisting fractures is also included.

(d) Fractal geometry characterization of geothermal reservoir fracture network: Recent geophysical investigations have revealed that subsurface fracture network could be described by a fractal geometry. In the following a fractal geometry based approach is briefly presented (Watanabe, K. and Takahashi, H., 1991). The fractal relation between fracture length r and the number of fractures N whose length is equal to or larger than r may be expressed by

$$N = Cr^{-D} \qquad (1)$$

where D is fractal dimension and C is a constant which depends on the fracture density of rock mass. Fig. 7 shows an example of fracture network generated by the developed method on the basis of the fractal relation. Based on the recent observation (Meredith, P.G., 1990), the D is assumed to be 1.0 in the computation. The parameter C may be related to the number of fractures measured along a scan-line (as illustrated in Fig. 7) by the following equation

$$C = m / \left\{ \overline{\cos\theta_i} (1 - \ln r_{min}) \right\} \qquad (2)$$

where m is the number of fracture per unit length of the scan-line and $\overline{\cos\theta_i}$ represents an average of $\cos\theta_i$ with θ_i being fracture angle. r_{min} is the smallest observable length of fracture and depends on the resolution of measurement. The equation allows the parameter C to be determined from the observation of core samples. The above method for characterizing the fracture network has been applied to Kakkonda geothermal field in Japan. The result is shown in Fig. 8 in terms of a comparison between the computed fracture density parameter and the fluid loss observed during well drilling in the field. The general correspondence suggests that the modeling procedure provides a reasonable means for characterizing geothermal subsurface fracture networks.

Fig. 7. Fracture network simulated by means of fractal relation

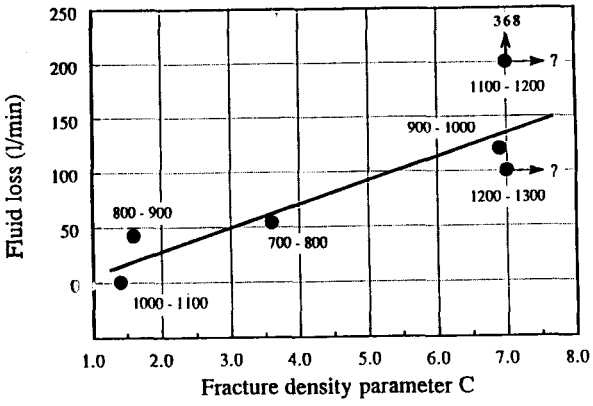

Fig. 8. Comparison between computed fracture density and fluid loss observed during well drilling

(4) Thermal Design and Evaluation WG

It is well accepted that the primary fluid flows occur not through homogeneous rock formation, but through fracture networks in fracture type geothermal reservoirs. Considering the complex geometry of fracture networks, it is essential to develop an efficient numerical method for analyzing the heat and fluid flows in HWR reservoirs. LINK (Line-Source and/or Sink Implanted Networks for Fractured Continua) method based on a double porosity and double permeability model has been developed (Kimura, S. et al, 1991, Masuda, Y.et al, 1991). The concept of the numerical method is shown in Fig. 9. In the method the heat and fluid flows in the fracture, and those in the less permeable rock are calculated separately. As schematically illustrated in Fig. 9, the transport between the rock and fracture network is modelled through one dimensional links. Specifically, the interaction between the fractures and the rock formation is taken into account through sink and source terms in a set of governing equations, describing the transport in the respective system. The present method has been proven to be ten times more efficient than a conventional algorithm by carrying out FEM

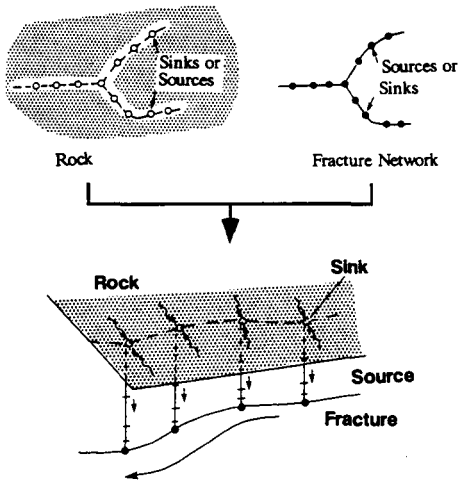

Fig. 9. Concept of proposed LINK method

computations on a simple two-dimensional model. The method is currently being extended to three-dimensional and complex fracture networks. Furthermore, experimental results of dissolution and scaling kinetics are incorporated into the simulator to develop a method for predicting the long-term reservoir behavior based on the rock-water interactions.

Preceding the massive hydraulic fracturing in the Yunomori field, some element technologies above mentioned are being tested in the GEEE Higashihachimantai geothermal model field and Kamaishi test field. Ultimately, the outputs of each individual groups will be integrated to form the foundation of the design methodology for HWR systems.

CONCLUDING REMARKS

The HWR research project outlined in this paper focuses on the development of an engineering methodology for combined fracture type geothermal reservoirs. The technology is expected to enable the further development and enhancement of the thermal power of existing geothermal reservoirs, and then to extend their operation life time. The interdisciplinary approach of the project would facilitate to establish a useful data base of geothermal subsurface structure, which is needed to determine the optimal artificial crack and to design the well stimulation procedure. A comprehensive HWR design methodology, coupled with a subsurface structure data base should be evolved and verified through the field experiment in the course of this project.

ACKNOWLEDGEMENTS

The authors would like to acknowledge New Energy and Industrial Technology Development Organization (NEDO), and Geothermal Energy Research & Development Co., Ltd. (GERD) for their close collaborations with the GEEE group. TH wishes to thank Dr. H.C. Wu for useful discussions.

REFERENCES

Abé, H. and Takahashi, H. (1983), "Crustal Rock Fracture Mechanics for Design and Control of Artificial Subsurface Cracks if Geothermal Energy Extraction Engineering (Γ-Project)," Proc. 9th Workshop on Geothermal Reservoir Engineering, Stanford University, pp. 403-408.

Kimura, S., Masuda, Y. and Hayashi, K. (1991), "An Efficient Numerical Method Based on Double Porosity Model to Analyze Heat and Fluid Flows in Fractured Rock Formation," Transactions of the Japan Society of Mechanical Engineers (B), 57-538, pp. 2083-2087 (in Japanese).

Masuda, Y., Kimura, S. and Hayashi, K. (1991), "Heat Extraction Simulation from Fractured Rock by a Double Porosity and Double Permeability Model," Journal of the Geothermal Research Society of Japan, 13-3, pp. 179-190 (in Japanese).

Meredith, P.G., "Cracking, Damage and Fracture in Stressed Rock: A Holistic Approach," Proc. of Nato Advanced Research Workshop on Toughening Mechanisms in Quasi-Brittle Materials, Northwestern University, July 16-20, 1990, pp. 73-104.

Moriya, H., Nagano, K. and Niitsuma, H. (1990),"Precise Estimation of AE Source Direction by Spectral Matrix Analysis," Progress in Acoustic Emission V, Proc. the 10th Int. Acoustic Emission Symposium, Sendai, Japan, Oct. 22-25, 1990, The Japanese Society for Non-Destructive Inspection, pp. 244-251.

Niitsuma, H. (1989),"Fracture Mechanics Design and Development of HDR Reservoirs -Concept and Results of the Γ-Project, Tohoku University, Japan," Int. J. Rock Mech. Min. Sci. & Geomech. Abstr., 26-3/4, pp. 169-175.

Niitsuma, H., Moriya, H. and Nagano, K. (1991), "Calibration Method Using the Spectral Matrix for Downhole Triaxial Seismic Detectors," in Preprint of 5th Conf. on AE/MA in Geological Structures and Materials, June, 1991.

Niitsuma, H. and Saito, H. (1991),"Evaluation of the Three dimensional Configuration of a Subsurface Artificial Fracture by the Triaxial Shear Shadow Method," Geophysics, in press.

Takahashi, H. and Abé, H. (1987), "Fracture Mechanic Applied to Hot Dry Rock Geothermal Energy," in Fracture Mechanics of Rock, pp. 241-276, B.K. Atkinson ed, Academic Press London, 1987.

Usui, T., Shoji, T. and Hayashi, K. (1991), "Percolation Modeling of a Fracture Type Reservoir - Prediction of an Improvement of Reservoir Productivity by an Artificial Crack," in Preparation.

Watanabe, K. and Takahashi, H. (1991),"Fractal Geometry Characterization of Geothermal Reservoir Fracture Network," Submitted to Journal of Geophysical Research.

PROCEEDINGS, Seventeenth Workshop on Geothermal Reservoir Engineering
Stanford University, Stanford, California, January 29-31, 1992
SGP-TR-141

THE LONG TERM OBSERVED EFFECT OF AIR AND WATER INJECTION INTO A FRACTURED HYDROTHERMAL SYSTEM

**Mario César Suárez Arriaga, Mirna Tello López,
Luis del Río and Héctor Gutiérrez Puente**

COMISION FEDERAL DE ELECTRICIDAD

**A.P. 31-C, Morelia, Michoacán, 58290 MEXICO.
Tel. (451) 43970; Fax. (451) 44735**

ABSTRACT

Injection of atmospheric air mixed with waste reinjection liquid, has been occurring since 1982 at the Los Azufres, México volcanic hydrothermal system. Several chemical and thermodynamical evidences show that air injection into this fractured geothermal field, could be considered as a long term natural tracer test. Nitrogen and Argon separated from the air mixture migrate from reinjection wells to production zones following preferential paths closely related to high permeability conduits. These paths can be detected, looking into the N_2 solubility evolution of production wells.

The anisotropic natûre of the fractured volcanic rock, would demand considerably amounts of artificial tracer in order to be detected at the producing wells, specially when fluid extraction is low. This explains the unsuccessful recovery of the artificial tracer tests performed in past years at Tejamaniles, the southern field's sector. On the other hand, chloride concentrations and other salts, are increasing in the liquid produced by the oldest wells of the sector.

INTRODUCTION

Los Azufres reservoir is a fractured volcanic hydrothermal system, located at the western portion of the Mexican Neo-Volcanic Axis. Descriptions of this field have been previously published: Gutiérrez et al,1982; Dobson,1984; Cathelineau et al, 1985; Suárez et al, 1990. Los Azufres generates 90 MW_e and during the next two years, 53 additional MW_e are going to be installed. For nine years Tejamaniles, the field's southern sector (Fig. 1), has been in continuos increasing exploitation; today, 630 T/h of steam are extracted and 600 T/h of waste liquid are, by gravity, injected back into the formation. This is the only alternative to avoid the environmental impact of liquid waste disposal. Simultaneously with geothermal water reinjection, an important amount of air has been continuously inflowing to the reservoir through the open injection wellheads. There are evidences that this incidental injection of air provokes the separation of Nitrogen and Argon from the original gaseous mixture within the formation, and the migration of both gases from the reinjection zones to the production zones following high permeability preferential paths.

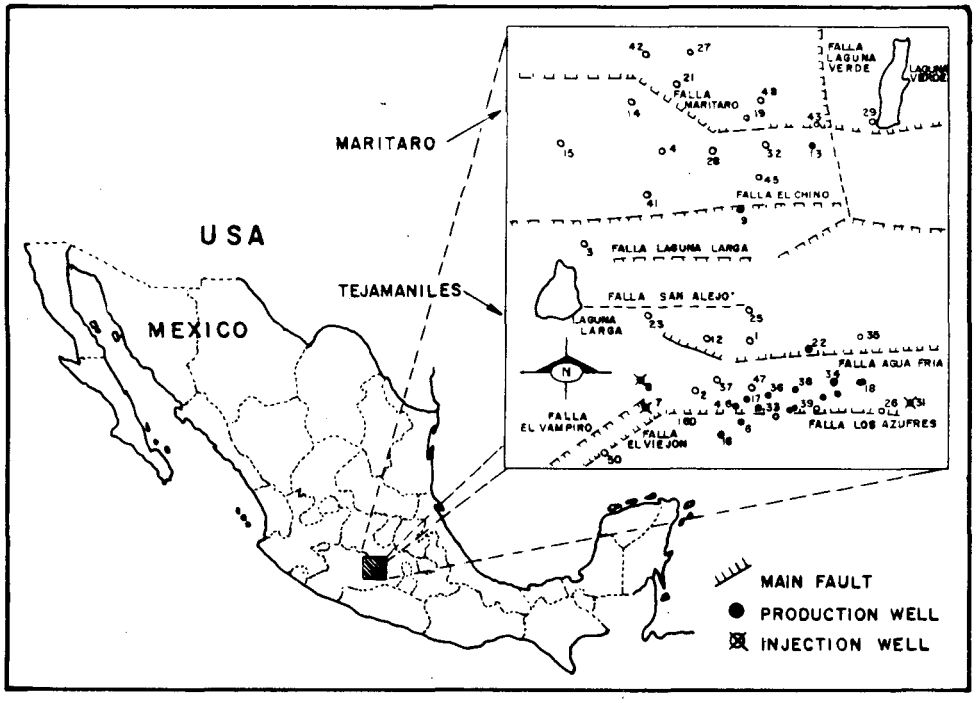

FIG. I.- LOCATION OF THE LOS AZUFRES GEOTHERMAL FIELD

TABLE 1.- OLDER WELLS AT TEJAMANILES AND THEIR INTERSECTIONS WITH MAIN FAULTS.

WELL	TYPE	z (masl)	Qmax (T/h)	LINER (m/depth)	FAULT	INTERSECTION (m/depth)	INTERSECTION (masl)
Az-6	prod.	2826	- 40	648-861	Los Azufres	900	1926
Az-7	inj.	2759	+325	1665-1706	El Viejón	1700	1059
Az-8	inj.	2808	+300	1991-2299	Tejamaniles	2020	788
Az-16D	prod.	2833	- 40	851-1039	(deviated)	?	?
Az-17	prod.	2820	- 50	561-622	Puentecillas	627	2193

Qmax represents a typical rate of mass extraction for producing wells, and a maximum value of injected liquid accepted by the well.

TRACER STUDIES AT LOS AZUFRES

Between August 1983 and July 1987 six tracer tests were performed at Los Azufres. In 3 of these tests some amount of artificial tracer (Potassium Iodide and Iridium-192) was injected into wells Az-7 and Az-8. Those investigations had very low effectiveness in the understanding of the real phenomena because no return of the tracer was detected at the two closest wells Az-2 and Az-16D; as has been reported by Horne and Puente in 1989. These authors concluded either: the tracer was retained within the reservoir by some mechanism, or the return occurred after the monitoring was terminated, or was at such low concentration as to escape detection. The general conclusion was that tracer return times could be longer than expected at this portion of the reservoir. At that time, the effect of global production could not be taken into account. Roland Horne (*ibidem*) was one of the first investigators to notice that N_2 concentration at well Az-16D was higher than the normal N_2 solubility of the reservoir's fluid, suggesting that the intake of atmospheric air was so important that this gas could be detected at the production region.

THE REINJECTION/PRODUCTION ZONE

The Tejamaniles' reservoir is formed by rhyolites in the upper levels, between 2300 and 2950 masl; below, by fractured andesites. The most important production zone is a two-phase portion located between 1600 and 2300 masl; wells Az-6, Az-16D and Az-17 that we have analyzed, are completed here. At these levels, the effective porosity ranges between 0.10 to 0.15 and the average reservoir permeability is high (≥ 100 → 1000 md; Suárez et al, 1990). A deeper liquid compressed zone has been found between 400 and 1200 masl. Several important faults exist in this sector, intersected by the wells at different depths (López, 1991); some intersections are shown in table 1. Between the Agua Fría and Los Azufres faults (Fig. 1), there is an intensely fractured region known as Puentecillas Fault, that could be a main responsible conduit of fluid through East-West direction.

SOME PRODUCTION AND INJECTION DATA

Since August 1982, two wellhead non-condensing units, generating 5 MW_e each, were installed at Tejamaniles: Unit 1 connected to wells Az-6 and Az-16D and Unit 2 connected to well Az-17. In September 1987 Unit 6 has been connected to well Az-18 in order to generate 5 additional MW_e. In November 1988 a 50 MW_e unit was installed at Tejamaniles (the steam is coming from wells Az-22, Az-33, Az-35, Az-36, Az-37, Az-38 y Az-46; Fig.1). These plants have been in continuous operation with a total mass extraction of about 630 T/h.

The injected liquid mass evolution at each well is difficult to evaluate because the normal operation of the electrical plants requires, very often, to change the amount and direction of the waste liquid from one well to another (the current reinjection wells are Az-3, Az-7, Az-8 and Az-31 for the southern sector). The injection rate at well Az-7 has varied from 20 T/h to 260 T/h and for well Az-8 the same parameter has varied from 15 T/h to 300 T/h. The maximum amount of fluid accepted by each well is about 300 T/h. The temperature of injection varies between 40 to 50 °C at atmospheric pressure (0.73 bar).

The horizontal distances of the reinjection wells from the nearest production wells ranges from 1000 to 2000 m.; the injection wells being 500 to 1000 m. deeper. The total vectorial distance between production and injection zones is a critical parameter because reinjection too close to the producing zone would sooner or later provoke a drop on the temperature of the produced fluid. Enthalpy data at Tejamaniles, with the only exception of well Az-33, show that the liquid is reinjected at adequate depth and distance from the production zones, (Suárez et al.,1990). Up to this moment, the thermodynamical effect of reinjection has been beneficial for the energy production and longevity of this geothermal field.

THE INJECTION OF AIR AND WATER

The exploitation of Tejamaniles occurs parallel to the injection of "cold" liquid and air. Simultaneously with the extraction/injection of geothermal fluid, an important amount of air has been continuously flowing into the reservoir through the open injection wellheads; some amount of atmospheric air is also'dragged' from the open surface of the collection boxes. Figure 1 shows the areal disposition of the reinjection/production system; figure 2 exhibits the details of the injection system at well Az-8 and the device used to measure the amount of air injected. We have measured at well Az-8: 274 Kg/h of air in 231 T/h of water. Using a similar method, some careful measures have been done at well Az-3: in 120 T/h of liquid, 350 kg/h of air are injected. These values are just two indicative points of an unknown air injection history. For technical reasons it was not possible to perform the same experiment at well Az-7.

Data coming from two-phase wells, show that concentration of chlorides and other salts (calcium, cesium, potassium, rubidium, sodium, etc.) dissolved in the separated liquid, have been growing since June 1986, (Fig. 7). This effect extends to wells Az-16D, Az-33, Az-37 and Az-46 and could have a close relation with the injection of liquid into the reservoir by inducing successive concentration of the same injected water within the production zones.

FIG. 2.- DETERMINATION OF THE RATE OF AIR INJECTED IN WELL Az-8

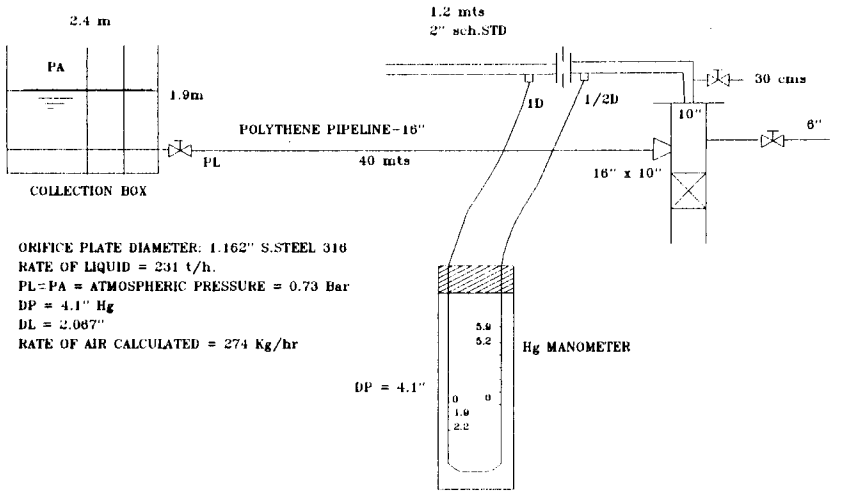

THE AIR INJECTION EFFECT

Reinjection of nearly 18 million tons of water since 1982 up until December 1991, has been accomplished mainly through wells Az-7 and Az-8. The injection of liquid has been accompanied by some amount of air. The rich geochemical history of wells Az-6, Az-17 (both, producing superheated steam) and Az-16D (two-phase), shows that Nitrogen in steam, has been increasing remarkably since 1986, but in different amounts at each well. Well Az-6 has the lower trend on its N_2 evolution, while well Az-16D has the highest.

The natural N_2 solubility in the fluid at Los Azufres reservoir represents about 0.2 % in weight. Figures 4, 5 and 6 show the behavior of N_2 and Ar as a function of time; the vertical axis has a different scale for every figure, but the effect is the same: the amount of Nitrogen has been continuously growing since 1986 until the first semester of 1989. After that date, the value is descending until the first semester of 1990 when it grows again, until the beginning of 1991, when N_2 decreases one more time.

This behavior is closely related to the injection evolution and the air inflow to the reservoir. This history is very irregular because of the practical field's operation (Fig. 3). At the same time, molar ratio N_2/Ar has been decreasing with time reaching, in some cases, an atmospheric value equal to 83.6.

Oxygen coming together with Nitrogen into the reservoir is not taken into account beacause it does not appear in any production well; it must be "consumed" by chemical reducing agents present in the reservoir, probably within the neighborhood of the injection wells. The influence of all the other gases forming the air mixture is neglected.

Fig. 3.- RATE OF FLUID INJECTION AT WELL Az-7.

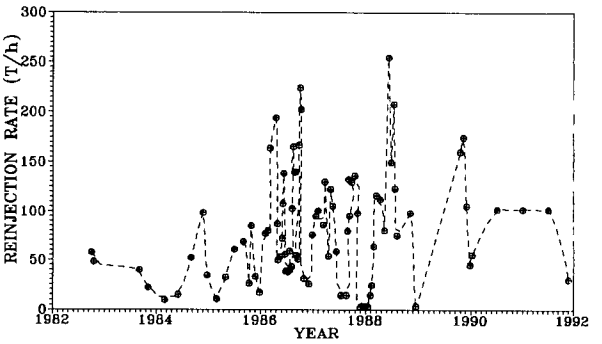

INTERPRETATION AND DISCUSSION OF FACTS

With those evidences, the injection of air into this intensely fractured system could be considered as a long term natural tracer test. Nitrogen separated from the air mixture is transported by extraction/injection gradients, to the production zones. At reservoir thermodynamical conditions, N_2 mobility is superior to the mobility of steam; therefore, Nitrogen must arrive first to the extraction zones through higher permeability conduits. It is enough to look into the field's wells with the highest N_2 content, in order to know where are the preferential paths of the reservoir. This is the case for wells Az-16D and Az-17. The first one has been deviated 66° NW at an inclination of 56°; thus it could intersect El Viejón Fault establishing a good communication with the injector Az-7. Well Az-17 intersects Puentecillas System, communicating with both injectors through El Viejón and Puentecillas crossing. Well Az-6, shows a lower N_2 influence thus, average permeability decreases in this section.

Fig. 4.- NITROGEN AND ARGON EVOLUTION AT WELL Az-6

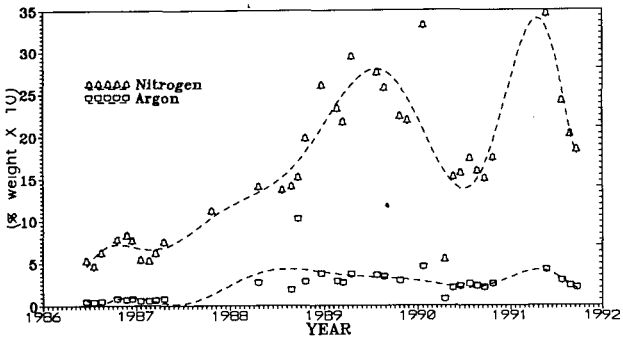

Fig. 5.- NITROGEN AND ARGON EVOLUTION AT WELL Az-17.

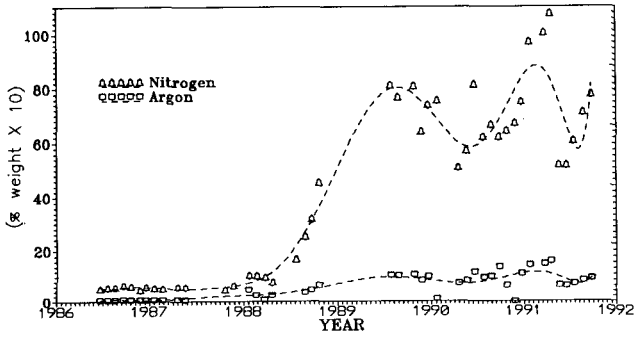

Fig. 6.- NITROGEN AND ARGON EVOLUTION AT WELL Az-16D.

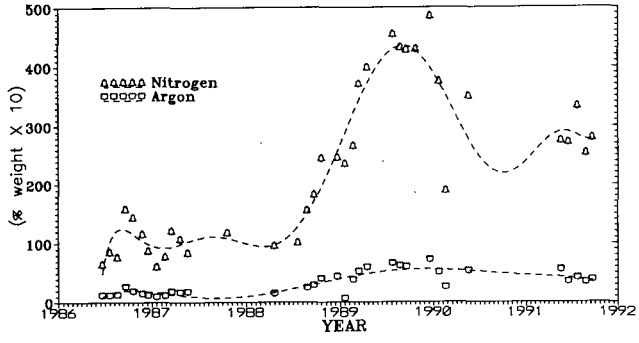

Fig. 7.- EVOLUTION OF CHLORIDES AT WELL Az-16D.

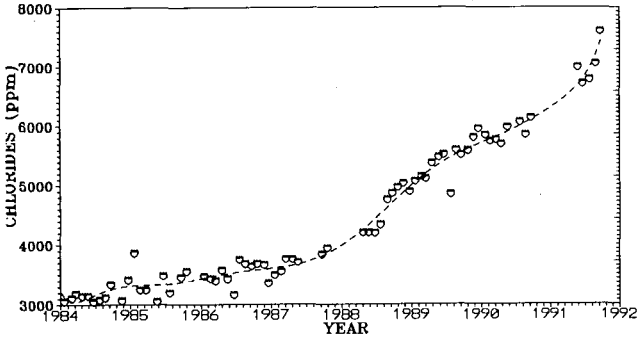

Well Az-37 and Az-46, younger steam productors, present the same trend as well Az-17. For well Az-2, closest to the reinjection section, there is no data. Well Az-33, with some higher N_2 content, behave similar to well Az-6; its distance to the injection area (1500 m.) seems to be a limit for Nitrogen transport and detection: no N_2 effects are noticed in any other well located after this sector.

The undesirable aspects of reinjection such as serious interference of the lower enthalpy water with the energy outflow of the producing wells, or decreasing formation permeability by chemical deposition, or contamination of groundwater have never been noticed either at this field.

CONCLUSIONS

- Reinjection of liquid and air at Los Azufres geothermal field, could be considered as a long term injection test using the Nitrogen of the air as a natural tracer.

- Air mixed with the liquid, breaks up into its primary components; Nitrogen propagates very fast through the fractures and faults network finally arriving to the production zones by means of a hydrodynamic dispersion mechanism with negligible thermal interference.

- It suffices a very simple analysis of Nitrogen production data, in order to detect preferential fluid paths into the reservoir.

- The use of numerical multicomponent reservoir simulators, together with the preceding analysis, could permit realistical estimation of the permeability tensor acting in the zone.

- Air is a good and cheap natural tracer.

REFERENCES.

CATHELINEAU,M.,OLIVER,R.,NIEVA,D.,GARFIAS, A. (1985). 'Mineralogy and distribution of Hydrothermal Mineral Zones in Los Azufres (Mexico) Geothermal Field'. Geothermics, Vol. 14 No.1, pp. 49-57.

DOBSON,P. (1984). "Volcanic Stratigraphy and geochemistry of Los Azufres geothermal center, Mexico". MS Thesis, Stanford University.

GUTIERREZ N.,AUMENTO,F. (1982).'The Los Azufres (Mich.,Mexico) Geothermal Field'. 26th Inter. Geological Congress,J. Hydrology 56,pp.137-162.

LOPEZ, Aída. (1991). Personal Communication.

HORNE,R.N. and H.G.PUENTE, (1989). 'Tracer Testing at Los Azufres'. Proceedings, 14th Workshop on Geothermal Reservoir Engineering, pp.197-199. Stanford University, Stanford,Ca.

SUAREZ,C.,NARANJO,S.,MORENO,J.,ESTRADA,R., (1990). 'Los Azufres: The Initial Response of a Fractured Hydrothermal System to Exploitation'. Proceedings 15th Workshop on Geoth. Reservoir Engineering, pp.29-38, Stanford University, Ca.

PROCEEDINGS, Seventeenth Workshop on Geothermal Reservoir Engineering
Stanford University, Stanford, California, January 29-31, 1992
SGP-TR-141

Vapour Generation in Hot Permeable Rock Through Injection of Water

Shaun D. Fitzgerald and Andrew W. Woods

Institute of Theoretical Geophysics,
Department of Applied Mathematics and Theoretical Physics
Cambridge University, England, CB3 9EW

Abstract

We present a non-linear model to describe vapour generation in a hot, permeable rock through injection of water. We develop similarity solutions describing the steady injection of fluid from a line source. A systematic parameter study has shown that, with other parameters fixed, as (i) the reservoir pressure increases, the mass fraction vaporised decreases; (ii) the reservoir temperature increases, the mass fraction vaporised increases; (iii) as the mass injection rate increases, the mass fraction vaporised decreases; and (iv) as the porosity increases, the mass fraction vaporised decreases.

We then present similarity solutions which describe injection from (i) a point source, with the mass flux injected proportional to $t^{1/2}$; and (ii) a planar source, with the mass flux injected proportional to $t^{-1/2}$, where t is the time of injection. These results suggest that for steady injection, the vapour production gradually increases for injection from a point source, and gradually decreases for planar injection. We confirm this prediction with numerical calculations describing the vapour production resulting from steady injection from line, point and planar sources.

Introduction

Vapour dominated geothermal reservoirs have great economic potential as an energy source. For example, the Geysers in California has the potential of producing 2000MW and the Larderallo field in Italy also produces much energy. However, a major problem with such a resource is the replacement of fluid, which is extracted through turbines, in order to tap the energy. In the Geysers reservoir, fluid levels have diminished drastically following massive exploitation of this energy resource; today, the reservoir can only provide 1500MW of power, although the turbines were designed to generate 2000MW (Kerr, 1991).

One practical means of recharging reservoirs is through the injection of water, at high pressure, into the reservoir. As the water migrates through the rock, it is heated up and a fraction vaporises. Fundamental understanding of the controls acting upon this vaporisation process is crucial in order to optimise the efficiency of any recharge program. In an important, recent contribution, Pruess *et al* (1987) analysed the injection of fluid from a line source, and presented a linearised similarity solution. We have built upon this study in several fundamental ways; we have (i) retained the full-nonlinear model; (ii) identified and explained the physical controls upon vapour production; (iii) carried out a systematic parameter study; (iv) calculated similarity solutions for point, line and planar source injection geometries and (v) analysed the full time-dependent process. Our suite of theoretical models identifies some of the most important controls upon vapour production.

A model of re-injection of water

Our model of the injection of water into a geothermal reservoir is based upon a number of simplifications and incorporates many of the features of the model of Pruess *et al.* (1987). Perhaps the most important simplification is the approximation that the reservoir is a permeable rock; on a sufficiently large scale, this assumption will capture many of the basic dynamical controls, even for a fracture dominated reservoir (Bodvarsson, 1972; Pruess *et al.* 1987). We also assume that the fluid supplied to the interface with the vapour has attained the interface temperature; this follows from the result that in the liquid saturated region, the isotherms lag behind the advancing and vaporising fluid front (Woods and Fitzger

ald, 1992).

We also assume that the rate of diffusion of heat in the alongflow direction in the vapour region is much more rapid than the rate of migration of vapour; this implies that to leading order, the vapour-saturated region is isothermal.

Finally, we assume that gravity has a secondary role upon the motion of the injected water, and that it is primarily driven by pressure gradients; this approximation is valid if the pressure gradient across the vapour, ahead of the interface exceeds the gravitational force acting upon the fluid, as is the case for sufficiently rapid injection. The geometry of injection we model is shown in figure 1. Further details of the model, and a fuller discussion of the assumptions, are given in Woods and Fitzgerald (1992).

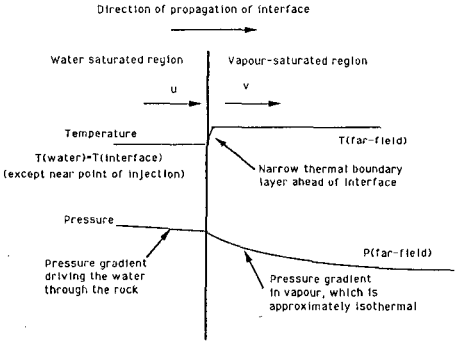

Figure 1 - Schematic of Interface

The motion of the vapour is governed by the conservation of mass

$$\frac{\partial \rho_v}{\partial t} + \nabla(u_v.\nabla\rho_v) = 0 \qquad (1)$$

together with the momentum equation, modelled by Darcys Law (Rubin and Schweitzer, 1971, Dagan, 1989)

$$\mu u_v = -k\nabla P \qquad (2)$$

and the equation of state (Young, 1988)

$$P = \rho_v R_g T Z \qquad (3)$$

where ρ_v is the vapour density, u_v the vapour velocity, k is the permeability of the host rock, μ the dynamic viscosity of the vapour, R_g the gas constant, T the temperature and Z is the compressibility, which is approximately constant over the range of pressures and temperatures which arise in a geothermal reservoir.

These equations are coupled with the conservation equations across the water-vapour interface. The conservation of mass across the interface has the form

$$\rho_v u_v = (1-R)\rho_w u_w \qquad (4)$$

where u_w is the fluid velocity, ρ_w the fluid density, and $1-R$ is the mass fraction vaporised. The conservation of energy has the form

$$\phi(1-R)\rho_w(h_{v\infty} - C_p T_i) = R(1-\phi)\rho_r C_{pr}(T_\infty - T_i) \qquad (5)$$

where C_p is the specific heat at constant pressure, $h_{v\infty}$ is the enthalpy of the vapour ahead of the thermal boundary layer in the vapour-saturated region, and subscripts w, v denote the water and vapour. Finally, the interface temperature and pressure are related by the Clausius-Clapyron relation, as specified by the international steam tables. A simple empirical relationship which applies for $150 < T < 250°C$ is

$$P = 6.7T^{0.23} \qquad (6)$$

It may be shown that by combining the above equations, the rate of migration of pressure ahead of the interface satisfies the nonlinear diffusion equation

$$\frac{\partial P}{\partial t} = \frac{k}{\mu}\nabla.(P\nabla P) \qquad (7)$$

This equation suggests that pressure perturbations diffuse ahead of the interface at a rate $(k\hat{P}/\mu)^{1/2}$, where $\hat{P}$ represents a typical value of the pressure.

Non-linear Similarity Solutions

If we specify that the water-vapour interface has position

$$r = 2\lambda t^{1/2} \qquad (8)$$

then a similarity solution exists, in terms of a similarity variable $\eta = r/t^{1/2}$, in which a constant fraction, $1-R$, of the injected water vaporises per unit time. This is because the diffusion equation admits similarity solutions which propagate at a rate proportional to $t^{1/2}$. In these solutions, a constant fraction of the fluid injected vaporises, and the remainder invades the rock, thereby increasing the volume that is water-saturated. The fluid interface advances at a rate, proportional to $t^{1/2}$, and therefore depends upon the rate of injection in a simple manner; it is readily shown that (i) for planar injection, fluid must be injected at a rate proportional to $t^{-1/2}$; (ii) for line source injection, fluid must be injected at a constant rate; and (iii) for point source injection, fluid must be injected at a rate proportional to $t^{1/2}$. Pruess *et al.* analysed the injection from a line source, case (ii); in order to obtain an analytical solution, they linearised the non-linear diffusion coefficient in equation (6).

In contrast, we retain the full non-linear diffusion equation, in order to include effects resulting from variations in the pressure as the vapour migrates ahead of the interface. Further details of the derivation of our new solutions are given in Woods and Fitzgerald (1992).

Numerical solutions of the full non-linear similarity equation, together with the boundary conditions described above, allow simple determination of the effect of different reservoir properties and injection rates. In figure 2, we present four figures, modelling steady injection at a line source, which illustrate how the mass fraction vaporised changes with (i) the rate of injection of fluid; (ii) the reservoir pressure; (iii) the reservoir superheat; and (iv) the reservoir porosity.

In figure 2(i), we show the difference between the linearised and the full non-linear similarity solutions; the full solution predicts more vapour production at low injection rates and less vapour production at high injection rates. This results from the changing pressure, and hence effective diffusion coefficient, with distance from the interface, which is not included in the linearised model.

As the rate of injection of fluid increases, the total mass of vapour produced increases; this requires a greater pressure gradient to drive the vapour from the interface and so the interface pressure increases. As a result, the interface temperature increases, according to the Clapyron relation, and so less heat is available for vaporisation. This causes a decrease in the mass fraction vaporised and hence efficiency of injection.

As the reservoir pressure decreases, the difference in the maximum pressure at the interface and the far-field pressure increases; therefore, the maximum change in temeprature of the host rock, and associated heat release increases. Thus the fraction vaporised increases. Similarly, for larger reservoir temperatures, with other properties fixed, the mass fraction vaporised is greater.

If the effective porosity of the host rock increases, the heat released per unit volume of rock invaded by water decreases, and this heat released is distributed to a larger mass of water; therefore with other properties fixed, the mass fraction vaporising decreases.

Time-Dependent Numerical Solutions

The similarity solutions for injection from a point (planar) source require the mass injection rate to increase (decrease) with time, whereas the line source requires a constant injection rate (figure 3).

As mentioned above, these results suggest that for a constant injection rate, injection at a point source leads to an ever increasing mass fraction vaporised, whereas injection from a planar source implies an ever decreasing mass fraction vaporised.

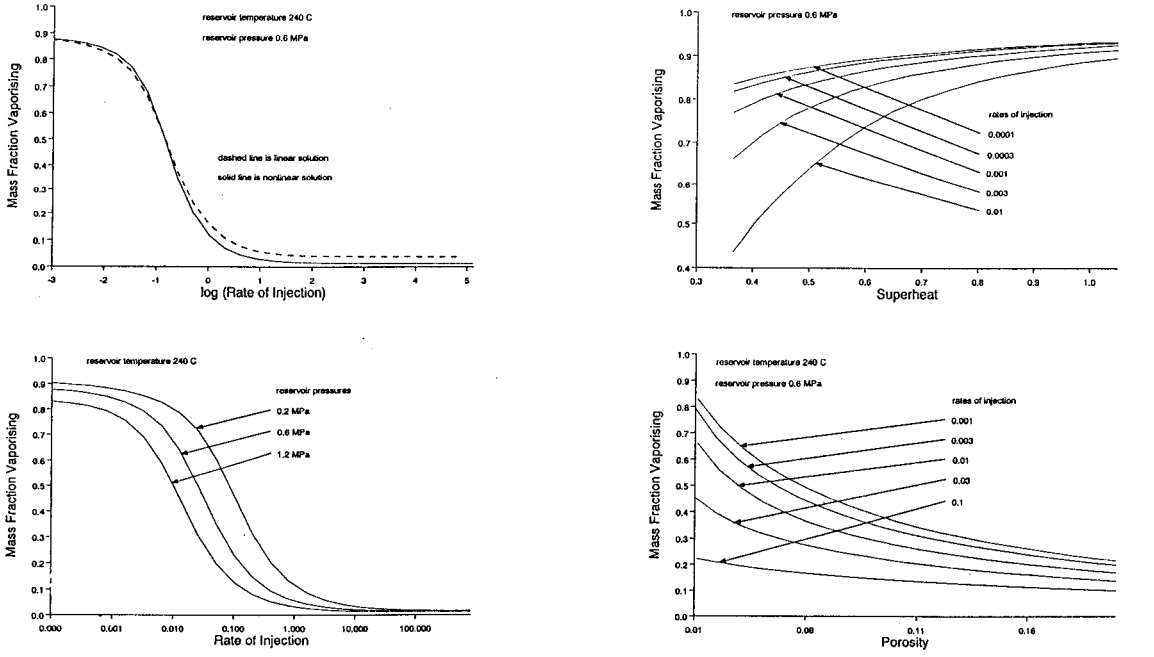

Figure 2: Parameter study of mass fraction vaporised

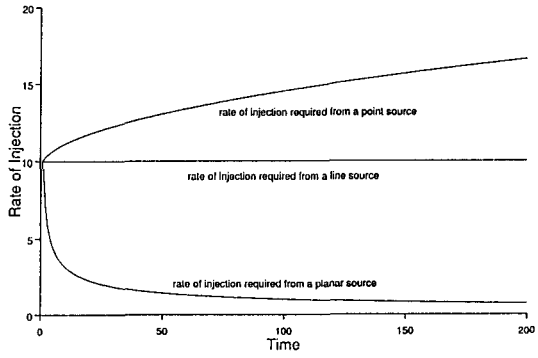

Figure 3: Mass flux injected for similarity solution

In order to test this hypothesis, we have solved numerically the time-dependent equations, given above, for injection from a point, line and planar source, with a constant rate of injection. Details of our numerical scheme are given in Woods and Fitzgerald (1992).

In figure 4(i), we present the results of our calculations. It may be seen that, as expected, the mass fraction vaporised from one dimensional injection progressively decreases, whereas, after an initial transient, the mass fraction vaporised from a point source injection, progressively increases. In figure 4(ii), we present calculation of the total mass of vapour produced as a function of time; for the case of point source injection, the total mass of vapour produced is the greatest, whereas the planar source produces the least. Essentially, this occurs because the vapour diffuses from the interface and so if the fluid front advances at a rate faster (slower) than $t^{1/2}$ then with time, less (more) vapour is able to migrate ahead of the interface, and the fraction vaporising decreases (increases).

Discussion

We note that other considerations such as the work exerted in injection, the maximum pressure which an injection pump can generate and the time available for injection need consideration.

We define the cumulative pump work, W, to be the time integral of the mass flow rate of water, Q, into the reservoir times the pressure, P, which must be applied at the well-bore to drive this flow rate

$$W = \int PQdt \tag{9}$$

In figure 5(i), we show that for three dimensional steady injection, the total pump work, per unit mass of vapour produced, is much less than that associated with steady one dimensional injection; this is because the interface pressure builds up in one-dimensional injection, and therefore requires an ever increasing well-bore pressure to continue the steady injection process,

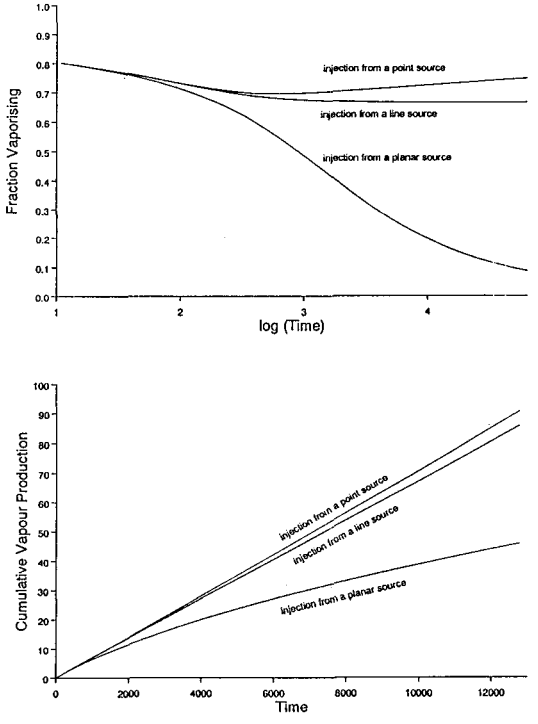

Figure 4: Steady injection in different geometries

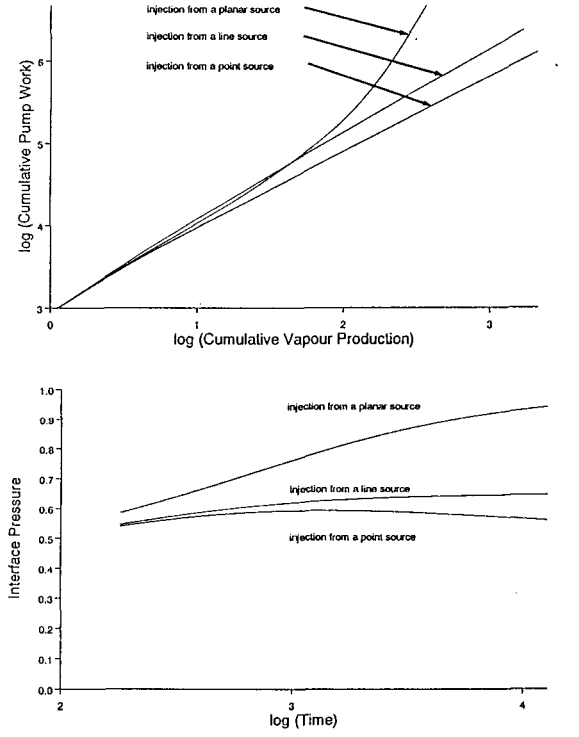

Figure 5: Pump work and interfacial pressure

figure 5(ii). In three dimensional injection, the interface pressure decreases, and therefore the wellbore pressure necessary to continue the injection decreases with time; as a result, less work is required per unit of fluid vaporised.

This is a crucial result which must be accommodated into any vapour regeneration strategy; injection from a point source ulitimately produces a greater mass of vapour per unit mass of fluid injected, and also requires much less pump work in order to produce that vapour.

However, we note that the optimal conditions in the reservoir for extraction of power through turbines may be incompatable with the optimal conditions for vapour generation through injection; this leads to a more complex problem of operating efficiency. In addition, the initial cost of installing drill holes to cause point and line sources of fluid needs consideration. We plan to address some of these issues through further development of our model.

Conclusions

Our results have important implications for the optimal strategy one should adopt in any scheme for vapour regeneration. From our study, it is clear that (i) the larger the volume of rock into which the injection occurs, the greater the mass fraction that will be vaporised - injection from a point source is the most efficient injection technique, requiring the minimum pump work and resulting in the maximum mass of vapour per unit mass of water input to the reservoir; (ii) the more rapidly the fluid is injected, the less efficient the vapour production, since the interface pressure increases, and so less thermal energy can be extracted from the rock for vaporisation; and (iii) the lower the reservoir pressure on injection, the greater the efficiency of injection, since, with optimal three-dimensional injection, the host rock can cool to the saturation temperature associated with the reservoir pressure (except at very long times, when thermal diffusion becomes important, Woods and Fitzgerald, 1992).

We are developing our model to include other effects, for example, a geothermal temperature gradient, inhomogeneities in the reservoir structure, and gravity.

References.

Bodvarsson, G., 1972, Thermal problems n the siting of reinjection wells, Geothermics, 1(2), 63-66.

Kerr, R.A., 1991, Geothermal tragedy of the commons, Science, 253, 134-135.

Pruess *et al.*, 1987, An analytical solution for heat transfer at a boiling front moving through a porous medium, Int. J. Heat Mass Transfer, 30(12) 2595-2602.

Rubin, A. and Schweitzer, S., 1972, Heat transfer in porous media with phase change, Int. J. Heat and Mass Transfer, 15, 43-60.

Woods, A.W. and Fitzgerald, S.D., 1992, The generation of vapour through injection of cold water into a hot, permeable rock, sub-judice.

Young, J.B., 1988, An equation of state for steam for turbomachinery and other flow calculations, J. Eng. Gas Turbines Power, 110, 1-7.

PROCEEDINGS, Seventeenth Workshop on Geothermal Reservoir Engineering
Stanford University, Stanford, California, January 29-31, 1992
SGP-TR-141

A CUBIC MATRIX-FRACTURE GEOMETRY MODEL FOR RADIAL TRACER FLOW IN NATURALLY FRACTURED RESERVOIRS

Jetzabeth Ramírez-Sabag[1] and Fernando Samaniego V.[2]

Universidad Nacional Autónoma de México
Facultad de Ingeniería, UNAM
04510 México, D.F.

ABSTRACT

This study presents a general solution for the radial flow of tracers in naturally fractured reservoirs, with cubic blocks matrix-fracture geometry. Continuous and finite step injection of chemical and radioactive tracers are considered. The reservoir is treated as being composed of two regions: a mobile where dispersion and convection take place and a stagnant where only diffusion and adsorption are allowed. Radioactive decay is considered in both regions. The model of this study is thoroughly compared under proper simplified conditions to those previously presented in the literature. The coupled matrix to fracture solution in the Laplace space is numerically inverted by means of the Crump algorithm. A detailed validation of the model with respect to solutions previously presented and/or simplified physical conditions solutions (i.e., homogeneous case) or limit solutions (i.e., naturally fractured nearly homogeneous) was carried out. The influence of the three of the main dimensionless parameters that enter into the solution was carefully investigated. A comparison of results for three different naturally fractured systems, vertical fractures (linear flow), horizontal fractures (radial flow) and the cubic geometry model of this study, is presented.

INTRODUCTION

It is well known that an important fraction of worldwide reservoirs (geothermal and petroleum) are found in naturally fractured reservoirs (Aguilera,1980; van Golft-Rach, 1982; Saidi, 1987). Fluid and heat flow in these systems are more complex than in conventional non-fractured formations for which the theory of fluid and heat flow is at a more advanced level. Determination of an optimal exploitation scheme for a fractured reservoir rest on the ability to adequately characterize this heterogeneous system, that will be extremely important for performance predictions and for enhanced heat recovery studies. The effort needed to accomplish this task is bigger than that required for conventional reservoirs, since two parts compose the porous medium, and are to be properly studied, the fractured and the matrix system. A very important contribution toward accomplishing the characterization of these reservoirs is provided by the interpretation of tracer flow tests.

There are several papers that deal with the flow of tracers in naturally fractured reservoirs, for a review see the papers by Ramírez et al.(1990 and 1991), These papers are concerned with vertical (linear flow) and horizontal (radial flow) fractures. A more realistic visualization of naturally fractured systems has been that of Barenblatt (1960), further discussed by Warren and Root (1963), which presents the naturally fractured reservoir as an idealized system formed by identical cubes, separated by an orthogonal network of fractures. The flow is considered to take place in the fractured network, while the matrix continuously feeds the system of fractures. Assuming transient fluid flow from the matrix to the fractures and cubic geometry of the matrix blocks, Lai et al. (1983) presented a flow model and its correspondent solution for the previously mentioned flow problem. A review of the literature does not show a solution for the radial flow of tracers considering the cubic matrix-fracture geometry model used in the pressure transient analysis theory of Lai et al.

1 UNAM
2 UNAM and PEMEX

The purpose of this study is to present a general solution for the radial flow of tracers in naturally fractured reservoirs, considering cubic matrix-fracture geometry. Continuous and finite step injection of chemical and radioactive tracers are considered. This solution takes into account all the important mechanisms that affect tracer flow: diffusion, convection, adsorption and radioactive decay.

MATHEMATICAL MODEL

The model considered in this study is shown in Fig. 1. The naturally fractured medium is represented by means of a system of identical cubic blocks separated by and orthogonal network of fractures. The system shown in this figure consists of two flow regions: 1) a mobile region constituted by the network of fractures and 2) a stagnant or immobile region. Both regions are interconnected by means of a thin fluid layer contained within the immobile region, which controls the fluid and mass transfer between the regions. This type of visualization of the problem has been used previously by other authors (Deans, 1963; Walkup and Horne, 1985; Maloszewski and Zuber, 1985; Chen, 1986; Rivera et al., 1987; Ramírez et al., 1988 and 1991).

In the mobile region 1, the following effects are considered:

a) Longitudinal dispersion that includes molecular diffusion:

$$D_r = \alpha v + D_m \qquad (1)$$

The perpendicular z or r directions, depending on the faces of the cubic block considered, horizontal or verticals (Fig. 1), is not dealt with because it is assumed that fracture width 2w is small and, consequently there is no concentration gradient in this direction.

b) Convection, Based upon the discussion presented in a), flow velocity in the perpendicular directions is assumed to be uniform and only its variation is considered along the r direction. For the case of this study of radial flow under constant rate injection, velocity is defined as

$$v = \frac{a}{r} \qquad (2)$$

where

$$a = \frac{Q}{2\,\pi\,H\,\phi_1} \qquad (3)$$

c) Decay, This condition is considered for the case of a radioactive tracer of decay time less than the transit (travel) time.

For the immobile region the following effects are studied:

a) Diffusion. This effect is only considered in the perpendicular directions because the longitudinal component is assumed to be negligible

b) Adsorption
c) Decay

Based upon the above mentioned assumptions, considering an incompressible fluid, the governing equations for tracer concentrations in the fracture and in the porous matrix can be stated in dimensionless form as follows (Fig. 2):

a) Fractures:

$$\frac{1}{r_D}\frac{\partial^2 C_{D21}}{\partial r_D^{\,2}} \frac{1}{r_D}\frac{\partial C_{Dr1}}{\partial r_D} - \gamma\, C_{Dr_1} + \frac{6}{d_D}\frac{\phi_2}{\phi_1}.$$

$$D_{D2}\left(\frac{\partial C_{Dr2}}{\partial z_D}\right)_{z_{Do}} = \frac{\partial C_{Dr1}}{\partial t_D} \qquad (4)$$

b) Matrix:

$$D_{D2}\,R\,\frac{\partial^2 C_{Dr2}}{\partial z_D^{\,2}} + \frac{2}{z_D}\,D_{D2}\;R\,\frac{\partial C_{Dr2}}{\partial z_D}$$

$$-\gamma\, C_{Dr2} = \frac{\partial C_{Dr2}}{\partial t_D} \qquad (5)$$

where the definitions of the dimensionless groups used in Eqs. 4 and 5 are

$$t_D = \frac{Qt}{2\pi\, H\phi_1\alpha^2} = \frac{at}{\alpha^2} \qquad (6)$$

$$C_{Dr1} = \frac{C_{r1} - C_i}{C_o - C_i} \qquad (7)$$

$$C_{Dr2} = \frac{C_{r2} - C_i}{C_o - C_i} \qquad (8)$$

$$r_D = \frac{r}{\alpha} \quad (9)$$

$$z_D = \frac{z}{\alpha} \quad (10)$$

$$d_D = \frac{d}{\alpha} \quad (11)$$

$$z_{Do} = \frac{d}{2\alpha} + \frac{\delta}{\alpha} \quad (12)$$

$$D_{D2} = \frac{D}{a} \quad (13)$$

$$\gamma = \frac{\lambda\alpha^2}{a} \quad (14)$$

$$R = \frac{\phi_2}{\phi_2 + \rho k(1-\phi_2)} \quad (15)$$

The last term of the left hand side of Eq. 4 considers the interaction between the fractured and the matrix systems, representing a diffusion mass transfer from the fractures to the matrix at z_{Do}, Eq. 12.

Tha equations that complete the continuons injection tracer flow problem are given by Eqs. 16-21:

Boundary conditions

$$C_{Dr1}\ (r_{Do}\ ,\ t_D) = 1 \quad (16)$$

$$C_{Dr1}\ (\infty\ ,\ t_D) = 0 \quad (17)$$

$$C_{Dr2}\ (r_D,\ z_{Do}, t_D) = C_{Dr1}(r_D, t_D) \quad (18)$$

$$\left(\frac{\partial C_{Dr2}}{\partial z_D}\right)_{(r_D,\ 0,\ t_D)} = 0 \quad (19)$$

Initial conditions

$$C_{Dr1}\ (r_{Do}\ ,0) = 0 \quad (20)$$

$$C_{Dr2}\ (r_D,\ z_D\ ,0) = 0 \quad (21)$$

To find a solution to this problem the Laplace transformation method was used. The resulting equation after the application of this method to Eqs. 4 and 5, and 16-21, coupling the differential equations yields:

$$\frac{d^2\bar{C}_{Dr1}}{dr_D^2} - \frac{d\bar{C}_{Dr1}}{dr_D} - r_D\ \xi_{r2}\ \bar{C}_{Dr1} = 0 \quad (22)$$

where

$$\xi_{rc} = s + \gamma + \varepsilon \left\{ \beta_{rc}\coth(\beta z_{Do}) - 1/z_{Do} \right\} \quad (23)$$

$$\varepsilon = \frac{6}{d_D}\ \frac{\phi_2}{\phi_1}\ D_{D2} \quad (24)$$

$$\beta_{rc} = \sqrt{\frac{s + \gamma}{RD_{D2}}} \quad (25)$$

with the following boundary conditions:

$$\bar{C}_{Dr1}\ (\ r_{Do}\ ,s) = \frac{1}{s} \quad (26)$$

$$\bar{C}_{Dr1}\ (\infty,\ s) = 0 \quad (27)$$

Eq. 22 with boundary conditions given by Eqs. 26 and 27, define the mathematical model in Laplace space, for the radial continuous flow of tracers in naturally fractured reservoirs, with cubic blocks matrix-fracture geometry. It can be observed that it is similar to the stratified naturally fractured model of Ramírez et al. (1991). Thus, following the results of these authors, substituting the definitions for the Airy functions given in their paper (Abramowitz and Stegun, 1970, p. 448 Eq. 10.4.59), we get the following Laplace space continuous solution:

$$\bar{C}_{Dr1} = \frac{1}{s} exp\left(\frac{Y - Y_o}{2}\right)\left\{\frac{A_i(\xi_{rc}^{1/3}Y)}{A_i(\xi^{1/3}Y_o)}\right\} \quad (28)$$

A solution for the finite step injection case may be obtained through the use of Eq. 28 and the principle of superposition.

In some field operations, the tracer is injected for a short period and are referred to as "spike" injection tests (Walkup, 1984). It has been stated (Walkup, 1984; Walkup and Horne, 1985; Ramírez et al.,1991) that the solution for a spike injection test can be derived through

the time derivative of the finite step solution.

VALIDATION OF THE MODEL

The solution to the continuous tracer injection given by Eq. 28 can be simplified to particular cases, such as a naturally fractured system with horizontal fractures and a homogeneous system.

First, we will deal with the homogeneous simplification. If matrix porosity ϕ_2 and the matrix diffusion coefficient D_2 be small, the matrix (immobile) region will behave as it were impermeable and tracer flow will occur only through the fractures, resulting in negligible values of the third term of the right hand side of Eq. 23, $\varepsilon\ (\beta_{rc} \cdot \coth(\beta_{rc} z_{Do}) - 1/z_{Do}) \cong o$. For this case the model given by Eqs.22-27 is identical to the simplified model, for the above mentioned conditions, for horizontal fractures presented by Ramírez et al. (1991), and their discussion in relation to the comparison with respect to previous works (Moench and Ogata, 1981; Hsieh, 1986) holds.

With regard to the naturally fractured case, the model of this study can also be compared to the horizontal fractures model of Ramírez et al. (1991). It can be concluded that the differential coupled equations that describes these two tracer flow problems differ only in the definitions of the ξ_i,s parameters, essentially in relation to the third term that represents the matrix-fracture interaction, due to the differences in matrix-fracture geometry involved. A particular solution (at least theoretically) can be presented for the case of cubic blocks size d equal to the reservoir thickness H, which allows a direct comparison between the models. Before doing this, the influence of the hyperbolic functions that enter into both models, $\tanh\ (\sqrt{\beta_{rh}}\ (E/\alpha - 2z_{Do}))$ for the horizontal fracture model and $\coth\ (\beta_{rc}\ z_{Do})$ for this cubic matrix-fracture model, was thoroughly investigated for practical ranges of the parameters involved, concluding that essentially the results of their evaluation give unit values. Thus the ξ_i,s parameters are expressed by the following equations:

$$\xi_{rh} = s + \frac{D_{D2}\ \phi_2}{z_{Do}}\ \sqrt{\beta_{rh}} \qquad (29)$$

for the horizontal fractures model, and

$$\xi_{rc} = s + \varepsilon \left\{ \beta_{rc} - \frac{1}{z_{Do}} \right\} \qquad (30)$$

for the cubic matrix-fracture model. Substituting the definitions of the dimensionless parameters that enter into these equation, given by Eqs. 12, 13, 24 and 25, considering that $\delta/\alpha <<< 1$, and that d=H:

$$\xi_{rh} = s + 2\phi_2\alpha \sqrt{\frac{\pi D_2 s}{(w - s)Q}} \qquad (31)$$

$$\xi_{rc} = s + 6\phi_2\alpha \left\{ \sqrt{\frac{\pi D_2 s}{3(w - s)\,Q}} - \frac{4\pi D_{2\alpha}}{Q\ H} \right\} \qquad (32)$$

The second term in the brackets of this last expression for ξ_{rc} was evaluated similarly to the hyperbolic functions previously discussed, concluding that it is at its biggest value three orders of magnitude smaller than the first term. Thus, it can be neglected. With this result in mind, a further look at Eqs. 31 and 32 indicates that they are very similar, and as expecteddue to the fact that the cubic matrix-fracture model presents a contact area three times that of the horizontal fractures model, the numerical constant of the second right hand side term changes from 2 to 6. Again, under these conditions all the previous validation for the horizontal fractures model of Ramírez et al. (1991), holds for the subject cubic matrix-fracture geometry model

DISCUSSION OF RESULTS

The results of this discussion were generated using whenever possible the data of Chen (1986).

First, a comparison of results for the radial horizontal fractures model of Ramírez et al. (1991) and results of the radial cubic matrix-fracture geometry model of this study is shown in Fig. 3. The function $F(t_D)$ of the horizontal axis stands for the different definitions of the dimensionless time. For the results of this work, $F(t_D)$ is given by Eq. 6 and for the previous work, is given

by Eq. 6 of that paper. Also shown is the curve corresponding to the homogeneous case. We observe that, as expected due to our validation discussion related to the bigger contact area, that results for the cubic model, fall below the results for the horizontal fractures model. Unfortunately, for characterization purposes, the shape of the curves is similar, concluding that a uniqueness problem may arise if a test interpretation were to be conducted without additional information coming from other sources (i.e., geological, core analysis, well logs, etc.).

It is of interest to compare results of the two radial models already discussed to the vertical fractures model of Ramírez et al. (1990). For simplification purposes, we follow the discussion of the model validation section, that considered a cubic block size equal to the thickness H. Similar simplifications were made for the other two models. The tracer continuous injection concentration results are shown in Fig. 4. Once again, as we expect based on the physical principles of these problems, the vertical fractures model tracer response is the biggest of three (see also Fig. 3). Fig. 5 shows similar results for a finite step injection $t_D = 2.01$. Essentially the conclusions reached in relation to the results of Fig. 4 holds for this case. Additionally, we notice from results of these Figs. 4 and 5 that our main conclusion with regard to the characterization problem in naturally fractured reservoirs through tracer test is confirmed.

Next, the influence of the matrix system on continuous tracer injection results, represented by the product $\phi_2\sqrt{D_{D2}}$ that enter into Eqs. 29 and 30 (best seen in their simplifications given by Eqs. 31 and 32), is shown in Fig. 6. The maximum values of this group used, for the horizontal and cubic block models, were $1.13\text{x}10^{-4}$ and $7.2\text{x}10^{-4}$, respectively. We can observe from these results that for values of $\phi_2\sqrt{D_{D2}} < 1\text{x}10^{-6}$, the matrix system behaves as it were impermeable.

The influence of the cubic block size in the continuous injection tracer response is shown in Fig. 7. The upper most curve correspond to the homogeneous case, continuing downward with curves for different block numbers, up to a maximum value of 100. These results quite logically indicate that as the area of contact increases, the tracer concentration decreases.

Last, we wanted to quantify the effects of fracture aperture in tracer response. The results obtained for the horizontal and cubic block models, are shown in Fig. 8, for an aperture range of 1.0E-04 to 1.0E-02 m. The effect of this parameter is quite important, showing an increasing tracer response as fracture aperture w increases.

CONCLUSIONS

The main aim of this study has been to present a solution for the radial flow of a tracer in a cubic matrix-fracture geometry naturally fractured reservoir.

The main conclusions of this investigation are as follows:

1. A model is presented for the radial flow of a tracer in a cubic matrix-fracture geometry naturally fractured reservoir. It considers all the important mechanisms that affect tracer flow: diffusion, convection, adsorption and radioactive decay.

2. The Crump numerical Laplace inversion algorithm was found again to be highly reliable.

3. A thorough validation of the present model against simplified and particular solutions published in the literature was carried out published in the literature was carried out.

4. Solutions are presented for the continuous and finite step injection cases.

5. A comparison of the horizontal and cubic block radial solutions with the vertical fracture solution, for continuous and finite step injection, indicates that a uniqueness problem may arise in the interpretation of a test, especially to distinguish between the radial flow cases.

6. It was found that for the radial flow cases discussed in this study, the matrix system be haves as it were impermeable for values of the group $\phi_2\sqrt{D_{D2}}$ less that $1x10^{-6}$

NOMENCLATURE

a = advection parameter, Eq. 3 L^2/T
$A_1(x)$ = Airy function
C = tracer concentration
C_D = dimensionless tracer concentration, Eqs. 7 and 8
$\overline{C}_D$ = Laplace space dimensionless tracer concentration
D_{D2} = dimensionless matrix diffusion coefficient, Eq. 13
D_m = molecular diffusion coefficient, L^2/T
D_r = longitudinal dispersion coefficient, Eq. 1, L^2/T
d = matrix block size, L
d_D = dimensionless matrix block size, Eq. 11
$F(t_D)$ = dimensionless time for a specific flow geometry (linear flow or radial flow)
H = reservoir thickness, L
k = adsorption constant, L^3/M
N = number of cubic blocks in reservoir thickness H
Q = constant injection rate, L^3/T
r = radial distance, L
r_D = dimensionless radial distance
R = dimensionless parameter, Eq. 15
s = Laplace space parameter
t = time, T
v = fluid velocity, Eq. 2, L/T
w = fracture half width, L
Y = variable transformation, $r_D + 1/4\xi_{rc}$
z = vertical coordinate, L
z_{Do} = dimensionless vertical distance of the fluid film exterior boundary, Eq. 12 (Fig. 2)

Greek symbols

α = longitudinal fracture dispersivity, L
β_{rc} = parameter, Eq. 25
γ = dimensionless parameter, Eq. 14
δ = stagnant fluid film thickness, L
ε = dimensionless parameter, Eq. 24
ξ_{rc} = dimensionless parameter, Eq. 23
λ = radioactive decay constant, T^{-1}
ρ = fluid density, M/L^3

Subscripts

c = cubic
D = dimensionless
h = horizontal
i = initial
o = origin or related to tracer injection concentration
r = radial
1 = mobile or fractured region
2 = immobile (fluid layer and porous matrix) region

REFERENCES

Abramowitz, M. and Stegun,I.A., 1970. Handbook of Mathematical Functions with Formulas, Graphs, and Mathematical Tables. National Bureau of Standards, Washington, D.C.

Aguilera, R., 1980. Naturally Fractured Reservoirs. PennWell Books, Tulsa Oklahoma.

Barenblatt, G.I., Zheltov, Iv. P., and Kochina, I.N., 1960. Basic Concepts in the Theory of Seepage of Homogeneous Liquids in Fissured Rocks. J. Appl. Math. Mech.,24 (5) 1286-1303.

Chen, C-S., 1986. Solutions for Radionuclide Transport from an Injection Well into a Single Fracture in a Porous Medium. Water Resour. Res., Vol. 22 No. 4 (April) 508-518.

Chen, C-S, 1987. Analytical Solutions for Radial Dispersion with Cauchy Boundary at Injection Well. Water Resour. Res., Vol. 23, No. 7 (August) 1217-1224).

Deans, H.A., 1963. A Mathematical Model for Dispersion in the Direction of Flow in Porous Media Soc. Pet. Eng. Jour. 3(1):49-52.

Hsieh, P.A., 1986. A New Formula for the Analytical Solution of the Radial Dispersion Problem. Water Resour. Res., Vol. 22, No. 11 (Oct.) 1597-1605.

Lai, C.H., Bodvarsson, G.S., Tsang, C.F. and Witherspoon, P.A., 1983. A New Model for Well Test Data Analysis for Naturally Fractured Reservoirs. Paper SPE 11688, presented at SPE California Regional Meeting, Ventura, Ca., March 23-25.

Maloszewski, P. and Zuber, A., 1985. On the Theory of Tracer Experiments in Fissured Rock with Porous Matrix. J. Hydrol. 79, 333-358.

Moench, A.F. and Ogata, A., 1981. A Numerical Inversion of the Laplace Transform Solution to Radial Dispersion in a Porous Medium. Water Resour. Res., Vol. 17 No. 1 (Feb.) 250-252.

Ramírez, J., Rivera, J., and Rodríguez F., 1988. Tracer Flow Model for Naturally Fractured Geothermal Reservoirs. Proceedings,Thirteenth Workshop on Geothermal Reservoir Engineering, Stanford U., Stanford, Ca., January 19-21, SGP-TR-113.

Ramírez, S.J., Rivera, R.J., Samaniego, V.F., and Rodríguez, F., 1990. A Semianalytical Solution for Tracer Flow in Naturally Fractured Reservoirs. Proceedings, Fifteenth Workshop on Geothermal Reservoir Engineering, Stanford U.,Stanford, Ca.,January 23-25, 1990.

Ramírez, S.J., Samaniego V.F., Rivera R.J. and Rodríguez F., 1991. An Investigation of Radial Tracer Flow in Naturally Fractured Reservoirs. Proceedings, Sixteenth Workshop on Geothermal Reservoir. Engineering, Stanford U., Stanford, Ca., January 23-25

Rivera, R.J., Ramírez, J., and Rodríguez, F., 1987. Parallel Fractures Model for Tracer Flow Through Geothermal Reservoirs-Preliminary Results. Proceedings, Twelfth Workshop on Geothermal Reservoir Engineering, Stanford U., Stanford, C.A., January 20-22, SGP-TR-109.

Saidi, A.M., 1987. Reservoir Engineering of Fractured Reservoirs. Total Edition Presse, Paris.

Van Golf-Racht, T.D., 1982. Fundamentals of Fractured Reservoir Engineering. Elsevier, Amsterdam.

Walkup, G.W.,Jr., 1984 Characterization of Retention Processes and Their Effect on the Analysis of Tracer Tests in Fractured Reservoirs. Stanford Geothermal Program, SGP-TR-77, Stanford Ca.

Walkup, G.W. and Horne, R.N., 1985. Characterization of Tracer Retention Processes and Their Effect on Tracer Transport in Fractured Geothermal Reservoirs Paper SPE 13610, presented at California Regional Meeting, Bakersfield, Ca., March 27-29.

Warren, J.E. and Root, P.J., 1963. The Behavior of Naturally Fractured Reservoirs. Soc. Pet. Eng. J. (sept. 1963) 245-255; Trans., AIME, VOL. 228.

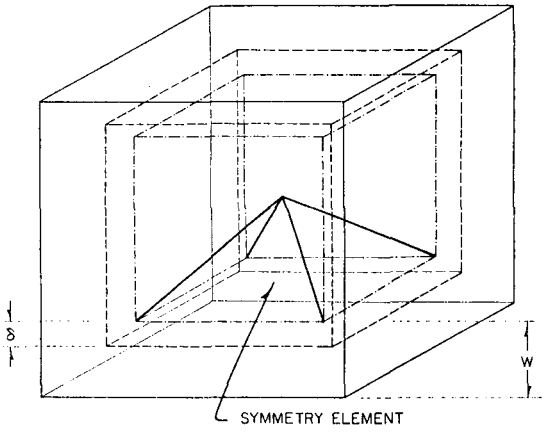

Fig 2 Proposed model for representation of the flow of a tracer in a naturally fractured medium. One dimensional fluid flow approximation

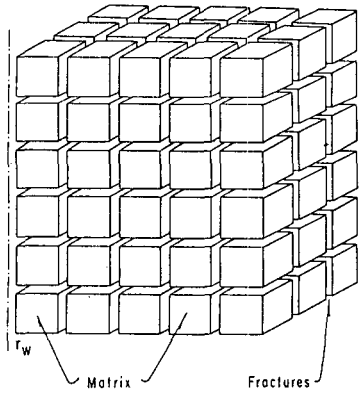

Fig 1 Idealized proposed model of naturally fractured reservoirs

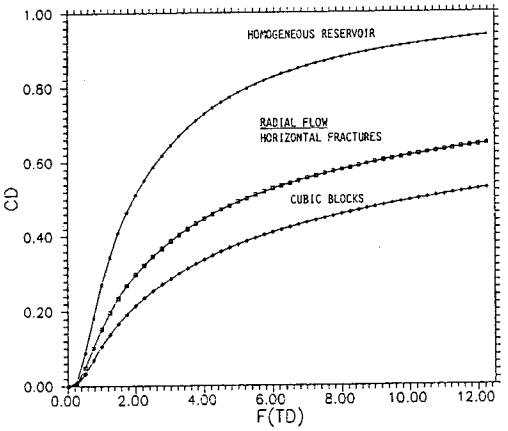

FIG. 3 COMPARISON OF HORIZONTAL AND CUBIC BLOCKS CONTINUOUS TRACER CONCENTRATION SOLUTIONS.

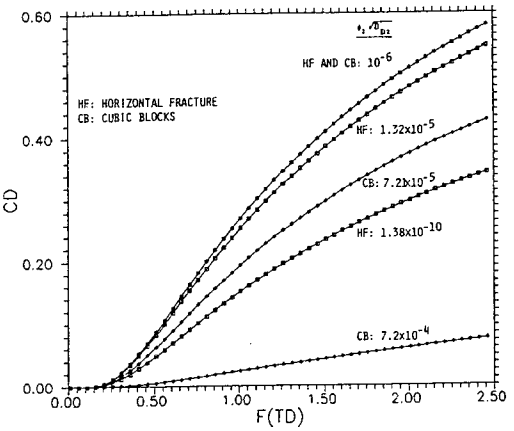

FIG. 6 INFLUENCE OF THE MATRIX CHARACTERISTICS ON THE HORIZONTAL AND CUBIC BLOCKS CONTINUOUS TRACER CONCENTRATION RESULTS.

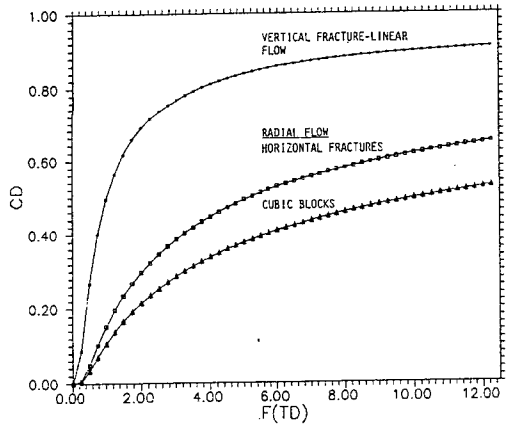

FIG. 4 COMPARISON OF THE VERTICAL FRACTURES (LINEAR) AND RADIALS CONTINUOUS TRACER CONCENTRATION SOLUTIONS.

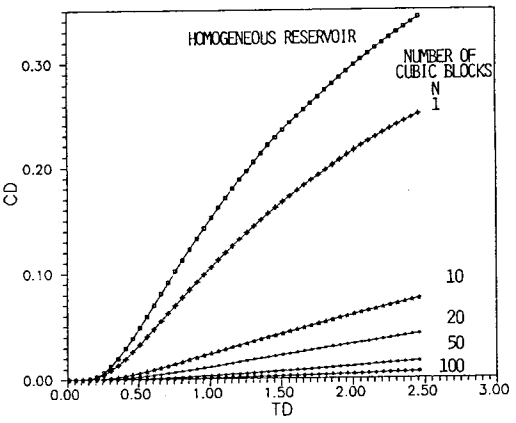

FIG. 7 INFLUENCE OF THE CUBIC BLOCK SIZE ON THE CONTINUOUS TRACER CONCENTRATION RESULTS.

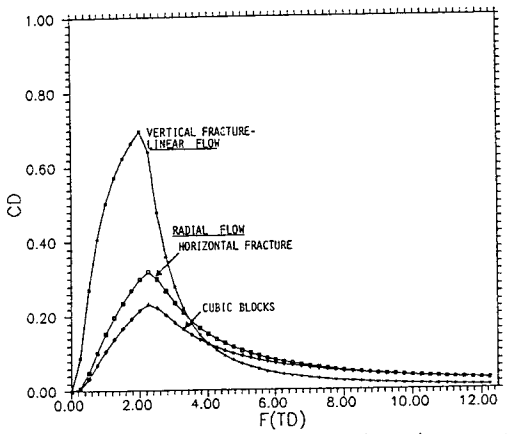

FIG. 5 COMPARISON OF THE VERTICAL FRACTURES (LINEAR) AND RADIALS FINITE STEP TRACER CONCENTRATION SOLUTIONS.

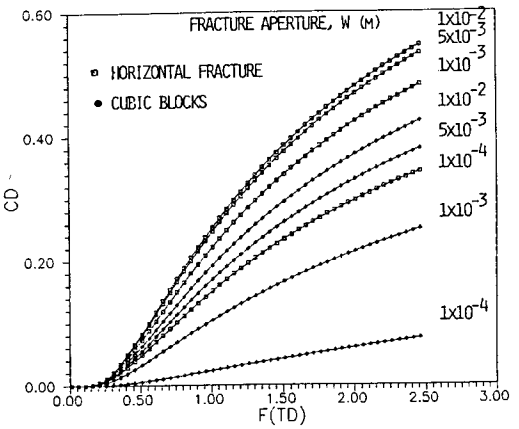

FIG. 8 INFLUENCE OF FRACTURE APERTURE ON THE HORIZONTAL AND CUBIC BLOCKS CONTINUOUS TRACER CONCENTRATION RESULTS.

PROCEEDINGS, Seventeenth Workshop on Geothermal Reservoir Engineering
Stanford University, Stanford, California, January 29-31, 1992
SGP-TR-141

Parametric Study of Reservoir Properties and Their Effect on Energy Recovery

Mike Shook

Idaho National Engineering Laboratory, Idaho Falls, ID 83415-2107

INTRODUCTION

Geothermal energy constitutes an important energy resource worldwide. Effective management of such a resource requires an understanding of a complex set of physical phenomena, including interphase mass transfer, convective transport of mass, and conduction and convection of energy. The coupled nature of these processes frequently requires that numerical simulation be used to investigate reservoir response to different management strategies.

The first stage of designing a simulation study of a particular reservoir involves defining the boundaries of the reservoir itself. We must determine the reservoir structure, the "edges" of the field, select the appropriate boundary conditions to be used, *ie*, whether pressure support from an adjacent aquifer is present, values of heat flux, etc. Having determined the three-dimensional extent and shape of the reservoir, we must identify the relevant fluid and petrophysical properties to be used in the simulation. In fractured geothermal systems, this data includes absolute and relative permeabilities for the fractures and rock matrix, fracture spacing and orientation, capillary pressure-saturation relationships, thermal conductivities, and others.

While it is fairly straightforward to identify the data required for accurate simulation of a geothermal reservoir, data acquisition is a different matter. Reservoir engineering is unique in the engineering disciplines in that much of the data is inferred by indirect means rather than being collected or measured. The data that can be measured (relative permeability, for example) can be of questionable reliability, in that the rock is removed from its native state, and conditions altered. Much of the data is also fit to empirical relationships; some is even estimated from these relationships. Due to the inherent uncertainties is this data, results of simulation studies using these data must be used with caution.

Of course, each of the variables noted above do not impact simulation results in the same way. In fact, errors in some of the data may exert little or no effect on our results. If that is the case, little effort need be expended by the geothermal operator to obtain this data. The problem is knowing which data exerts the most influence on simulation results, and therefore which should receive highest priority in acquisition efforts. The study presented in this paper seeks to answer this question by quantifying the effect changes in various parameters have on reservoir response to injection in a vapor-dominated reservoir. From a base case reservoir dataset we will examine differences in injectate recovery and steam energy produced as input data is varied. Parameters that are examined include relative permeability and capillary pressure relationships, fracture spacing, initial liquid saturations, and geologic structure.

DESCRIPTION OF THE BASE CASE

The base case selected for this study is an inverted 5-spot well pattern on 820 acre spacing. This well pattern exhibits symmetry in all four producers in homogeneous, isotropic media. Reservoir dimensions are 6000′ x 6000′ x 3600′. Structure has been neglected; the reservoir is a parallelepiped. Petrophysical properties, including permeabilities, porosities, and fracture spacing, are consistent with published Geysers data, and are summarized in Table 1. Relative permeability curves are also those typically encountered in Geysers simulations: Corey curves are used for matrix curves and straight line curves for the fractures. These are shown graphically in Figures 1-2. Capillary pressure has been neglected from the base case.

The mesh used in this simulation study is 11 x 11 areally, and 7 layers. Mesh refinement with depth is used, consistent with the findings of Lai and Bodvarsson (1991). The four producing wells are completed in the middle five layers, and injection occurs in the second layer (from the top).

Work supported by the U.S. Department of Energy under
DOE Contract No. DE-AC07-76ID01570.

The simulator used in this study is TETRAD[1], a fully implicit, multi-phase, multi-component finite difference simulator. Details and validation of TETRAD are found elsewhere (Vinsome, 1991; Shook and Faulder, 1991).

The exploitation scenario for this study is as follows. Following a period of equilibration, the wells are produced on a surface flowing pressure constraint of 150 psia. At t=10 years injection begins, and 30% of the mass produced is reinjected. This is continued until t=30 years.

Selected results from this base case simulation are given in Figures 3-4. Figure 3 shows steam production history and steam quality for any one well (recall the symmetry). After an initially high rate, the wells decline harmonically at a rate of about 10%/yr. The steam is initially saturated, and a small amount of liquid is also produced. At t=10 years injection begins, and shortly thereafter the production history changes dramatically. The liquid production rate increases beginning 4 years after injection commences, and increases rapidly. Furthermore, from Figure 4 we see that most of the injectate is recovered as liquid; injection has quenched the reservoir bottom. In fact, at t=17.5 years the steam quality of produced fluids falls below 85%. This is the lower limit of allowable quality used in this study. For the purposes of this study, a well producing in excess of 15% liquid is assumed to be a "problem well", and any additional energy, mass, etc. from that well is excluded from further consideration.

An obvious comparison that can be made here concerns what impact injection had under these conditions. In order to make this comparison we have made another simulation of the base case model, but without any reinjection of the produced mass. Cumulative steam energy recovery histories for these two cases are given in Figure 5. As can be seen from this figure, injection in this particular case was not beneficial with respect to energy recovery. In fact, average pressures and temperatures are lower in the base case than in the no-injection case, due to the quenching of the bottom of the reservoir. Furthermore, since much of the injectate was recovered as liquid, there is not an appreciable difference in final mass in place between the two runs. Of course, different well completions could have offset the unfavorable breakthrough of liquid; however, such changes were not investigated. The point to note here is that injection does not necessarily improve reservoir behavior in vapor-dominated geothermal reservoirs.

A PARAMETRIC STUDY

The Effect of Reservoir Structure

The first reservoir parameter that was varied was the reservoir structure. Two perturbations were made to the base case reservoir shape. The first change was to incorporate actual geologic structure to our reservoir description; we next included an accurate description of the top of the reservoir but used a flat reservoir bottom. These two cases are shown in Figures 6-7.

The reservoir structure shown in Figure 6 is an actual portion of southeast Geysers, as mapped by a cooperative industry effort (Thompson and Gunderson, 1989; Thompson, 1989). This case uses top of steam as the reservoir top, and top of felsite as the bottom. While the felsite is not, in general, the reservoir bottom, it is believed to be a good approximation in this portion of the field. Figure 7 uses the same structure map at the top of the reservoir and a flat bottom. In both cases the average reservoir thicknesses are the same as in the base case.

When we include structure to the base case reservoir description, the reservoir response to injection changes significantly. In Figure 8 we show cumulative, field-wide steam energy recovery histories for the three cases. The solid line in this figure is the base case; recall that all producers watered out at t=17.5 years. As can be seen from this figure, failure to include correct reservoir structure can drastically alter predicted results. This is true not only of rate of energy recovery, but also ultimate energy recovery and liquid breakthrough in wells. Top of structure tends to alter ultimate energy recovery, but has much less effect on rate of energy recovery. Therefore, while top of reservoir is an important piece of information in a simulation study, the reservoir bottom is the single most important piece of structural information.

Relative Permeabilities and Residual Saturations

Relative permeability expresses the ability of a fluid to move as a function of that fluids' saturation. Typical relative permeability curves used in geothermal simulations are given in Figures 1-2. Corey relative permeability curves are often used for the matrix, while straight line relative permeabilities are assumed for the fractures. Two important differences exist between the curves shown in these figures. First, note that the use of Corey curves results in a large "total mobility hole" at intermediate liquid saturations. This means that, for a given pressure drop, both phases are less able to flow and therefore a lower total flow rate occurs. Second, note the differences in residual saturations between the two curves. It is frequently assumed that negligible phase trapping occurs in the fractures, whereas in the matrix fairly large residual saturations have been assumed. It should be noted that

direct measurements of relative permeabilities and residual saturations have not been made on Geysers rock.

Three sensitivity studies were made to the base case relative permeability curves. Two of the runs involved changes to the relative permeability curves in the fractures. The straight line curves were replaced by Corey curves, once using the same residual saturations as in the matrix, and the other using the Corey curves but no residuals in the fractures. A third run was made to look at variations in liquid mobility in the matrix. For this run, the liquid exponent in the matrix was changed to 2.5, approximately the largest liquid mobility in the matrix that would still flash to steam upon entering the fractures (Pruess and Narasimhan, 1982). Results from this study are given in Figure 9. As can be seen from this figure, steam energy recovery appears fairly sensitive to fracture relative permeability functions. Also, note that the use of Corey curves with and without residual saturations in the fractures resulted in virtually identical energy recovery histories. It follows,then, that reservoir response varied because of the shape of the relative permeability curves used. Thus, the "mobility hole" noted above accounted for the delay in liquid production, and the related increase in energy recovery.

Capillary Pressure and Initial Matrix Saturations

Two additional petrophysical properties and conditions that are difficult to measure are capillary pressures and initial matrix liquid saturations. Capillary pressures have historically been neglected in geothermal simulations, probably due to the lack of measurements. Values used for initial matrix saturations have varied from 50% to over 80%. Recent studies have suggested that a fairly large initial liquid saturation existed at The Geysers, based in part on Pruess' study of the evolution of a vapor-dominated reservoir from a liquid-dominated one (1985), and a field-wide history match study by Williamson (1990). Of course, there are now areas of The Geysers that are experiencing superheat conditions, so liquid saturations can vary from a large, virgin value to zero.

The capillary pressure curve used in this study is based on a fairly conservative scaling of Leverett J-function (Leverett, 1941), and is given in Figure 10. No attempt was made to account for possible hysteresis due to imbibition or drainage. Two different initial liquid saturations were also considered; the base case value of 0.8, and a second case of 0.4. Each of these cases was run with and without capillary pressure.

Intuitively, one would expect incorporation of capillary pressures at a large liquid saturation to have little effect. This is borne out in this study, as shown in Figure 11. Given the relatively small capillary pressure at a liquid saturation of 0.8, the injectate imbibes only slightly. This results in a moderate (1.5 year) delay in liquid breakthrough, and a small increase in energy production.

Both a lower liquid saturation, and also capillary pressures at this lower saturation play a more important role in reservoir response. Figure 12 shows energy recovery histories for the base case, the base case with lower initial liquid, and the case of lower liquid saturation and capillary pressure. The case of lower liquid saturation results in less pressure support from the matrix, and therefore a reduction in both energy recovery rate and cumulative energy recovered. When capillary pressure is included in this run, however, response to injection changes appreciably. The injectate imbibes strongly into the matrix, resulting in a drastic (over 10 year) increase in liquid breakthrough time. This in turn results in nearly a 40% increase in energy recovery over the lower liquid saturation case. Thus, capillary pressures can have a dramatic effect on simulation results, but are much more important at low liquid saturations for the capillary pressure curves used here.

Fracture Spacing and Shape Factors

The final studies presented here concern dual porosity parameters. In simulating this fractured reservoir, we have using the Warren and Root dual porosity formulation (Warren and Root, 1963), with fracture spacing of 150' and the shape factor as defined by Gilman and Kazemi (1983). The shape factor for square matrix blocks is given as:

$$\sigma = 12/L^2$$

where L is the fracture spacing. Defining the correct shape factor has been an ongoing concern in the petroleum literature since the original Warren and Root work. Shape factors as large as $60/L^2$ have been used. Rossen and Shen (1989) point out that the shape factor depends on the process being modelled, and therefore one is unable to determine in advance what shape factor should be used.

In this study we have varied both fracture spacing and shape factors. Fracture spacing was varied from 150' to 300', with the attendant reduction in shape factor. The shape factor was then changed in another run from $12/300^2$ to $48/300^2$, which corresponds to the shape factor used in the base case run.

Results from this study are given in Figure 13. Clearly, both fracture spacing and shape factor both impact simulation results. Errors associated with either of these input parameters can drastically alter our predictive ability. There has been to date virtually no research on shape factors for

geothermal simulations; this study points out the need for such research to be done.

SUMMARY AND CONCLUSIONS

This paper has examined the influence of several reservoir parameters and conditions on steam energy recovery in the presence of injection. On the basis of this work, we draw the following conclusions:

Reservoir structure plays an extremely important role in correctly modelling injectate movement and energy recovery. Knowing the location and shape of the reservoir bottom is the single most important piece of structural information.

Fracture relative permeability curves affect reservoir response in injection, primarily because of the presence - or lack thereof - of a "mobility hole" seen in the Corey curves. Residual saturations in the fractures do not have much affect on reservoir behavior.

Capillary pressures can have an important affect on energy recovery, but primarily at low liquid saturations.

Parameters used in the dual-porosity approach of simulating fractured media are extremely important, and cause large variations in simulation results.

Much additional work is required to improve our simulation abilities. Research topics of interest include measurements of relative permeability- and capillary pressure-saturation relationships, improved estimates of reservoir bottom, and the development of the correct shape factor for use in geothermal simulations.

ACKNOWLEGEMENTS

I gratefully acknowledge Dave Faulder's help in reviewing the manuscript, Mike Carpenter's assistance in final preparation, and thank the management of EG&G for permission to publish this work.

REFERENCES

Gilman J.R., and H. Kazemi, "Improvements in Simulation of Naturally Fractured Reservoirs", *Society of Petroleum Engin. J.*, August 1983.

Lai, C.H., and G.S. Bodvarsson, "Numerical Studies of Cold Water Injection into Vapor-Dominated Geothermal Systems", SPE # 21788, Presented at the Western Regional Meeting, Long Beach, CA., Mar 20-22, 1991.

Leverett, M.C., "Capillary Behavior in Porous Solids," *Trans.* AIME (1941) **142**, 152-169.

Pruess, K., "A Quantitative Model of Vapor Dominated Geothermal Reservoirs as Heat Pipes in Fractured Porous Rock", *Trans*, Geothermal Resources Council, **13**, August, 1985.

Pruess, K. and T.N. Narasimhan, "On Fluid Reserves and the Production of Superheated Steam From Fractured, Vapor-Dominated Geothermal Reservoirs", *J. Geophy. Res.*, **87(B11)**, November 10, 1982.

Rosen, R.H., and E.I.C. Shen, "Simulation of Gas/Oil Drainage and Water/Oil Imbibition in Naturally Fractured Reservoirs", *SPE Reservoir Engin*, Nov. 1989.

Thompson, R.C., "Structural Stratigraphy and Intrusive Rocks at The Geysers Geothermal Field", *Trans.* Geothermal Resources Council, **13**, August, 1989.

Thompson, R.C., and R.P. Gunderson, "The Orientation of Steam-Bearing Fractures at The Geysers Geothermal Field", *Trans.* Geothermal Resources Council, **13**, August, 1989.

Shook, G.M., and D.D. Faulder, "Validation of a Geothermal Simulator", EG&G Report # EGG-EP-9851, Oct. 1991.

Vinsome, P.K.W., "TETRAD Users Manual, Version 9.4", Dyad Engineering, Calgary Canada, 1991.

Warren, J.E., and P.J. Root, "The Behavior of Naturally Fractured Reservoirs", *Society of Petroleum Engin. J.*, Sept. 1963.

Williamson, K.H., "Reservoir Simulation of The Geysers Geothermal Field", *Proceedings*, 15th Workshop on Geothermal Reservoir Engineering, Stanford, CA, Jan. 1990.

Table 1. Summary of Properties and Initial Conditions Used

Reservoir Properties and Initial Conditions	Matrix	Fractures
Porosity	0.045	0.02
Permeability (md)	0.01	10.
Relative Permeability:		
Liquid	$k_{rl}=S^4$	$k_{rl} = S_l$
Steam	$k_{rg}=(1-S)^{2.5}$	$k_{rg} = (1-S_l)$
	where $S = (S_l - S_{lr})/(1-S_{lr}-S_{gr})$	
Residual Saturations:		
Liquid	0.3	0
Steam	0.05	0
Initial Saturations	$S_l = 0.8$	$S_l = 0.0008$

Initial Pressure = 500 psig @ Top of Reservoir (1000 ' SS)

Initial Temperature = 470° F @ Top of Reservoir

Rock Heat Capacity = 0.238 BTU/lb

Rock Density = 165 lb/ft3

Rock Thermal Conductivity = 40 BTU/lb° F D

Fracture Spacing = 150'

Grid Data

NX = 11 NY = 11 NZ = 7

Δx = 545.5' Δy = 545.5' 1250' > Δz > 66'

Figure 1. Corey Relative Permeability Curves

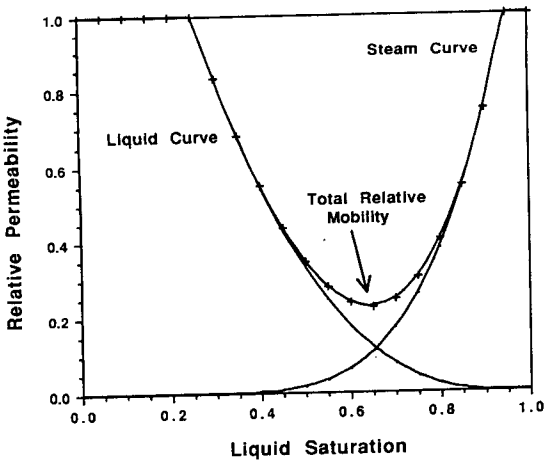

Figure 2. Straight Line Relative Permeabilities

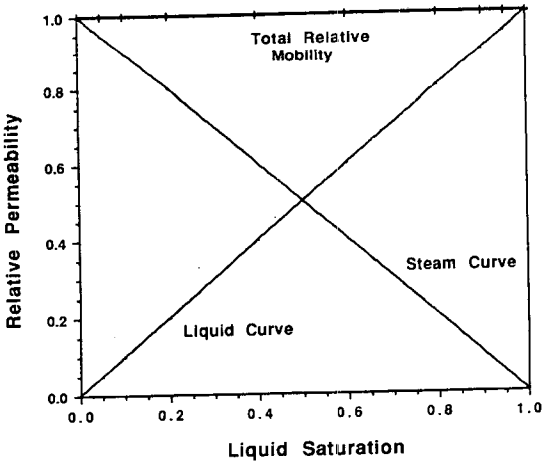

Figure 3. Steam Rate and Quality vs Time for Base Case.

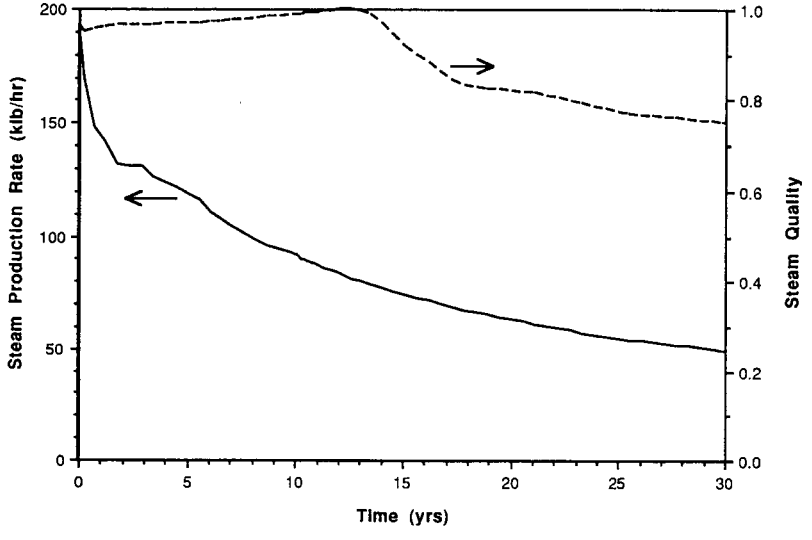

Figure 4. Tracer Recovery Histories for the Base Case.

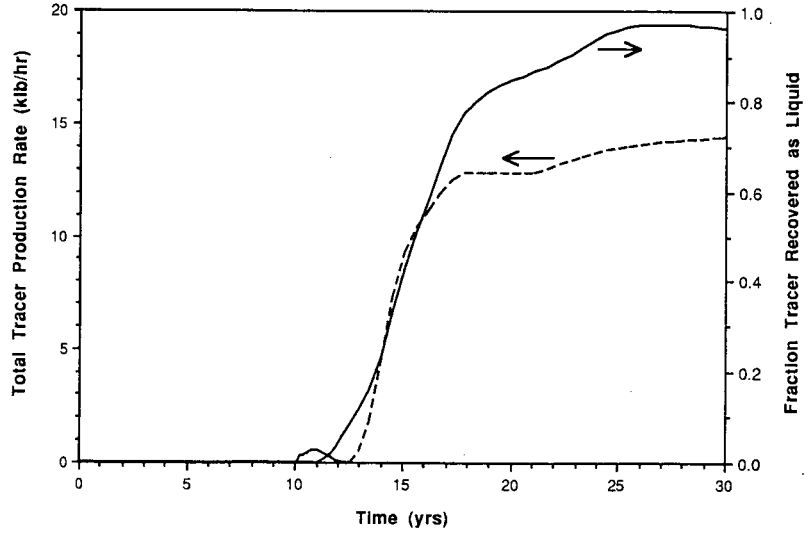

Figure 5. Comparison in Steam Energy Recovery for 30 % Reinjection vs No Injection Case

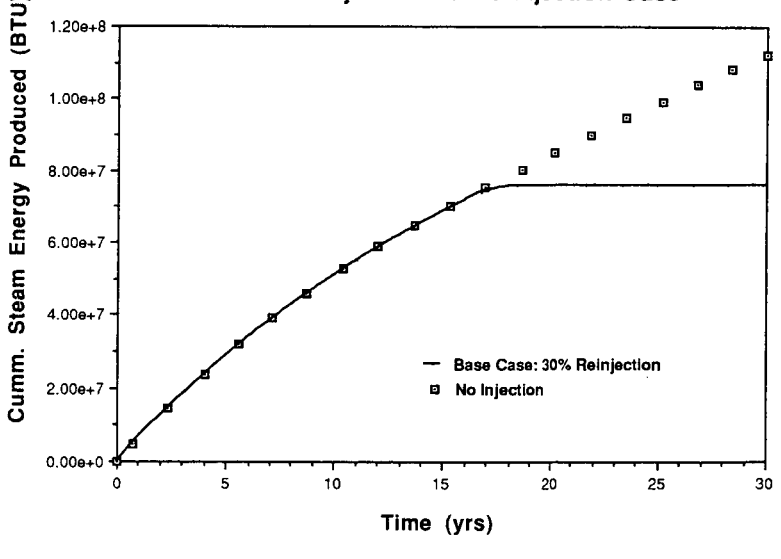

Figure 6. Reservoir Structure Case 1, Actual Portion of SE Geysers

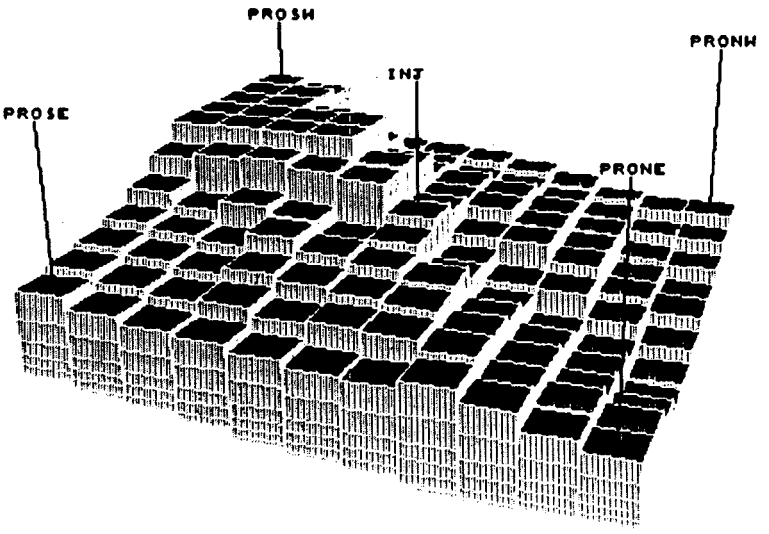

Figure 7. Reservoir Structure Case 2, Structure at Top, Flat Bottom

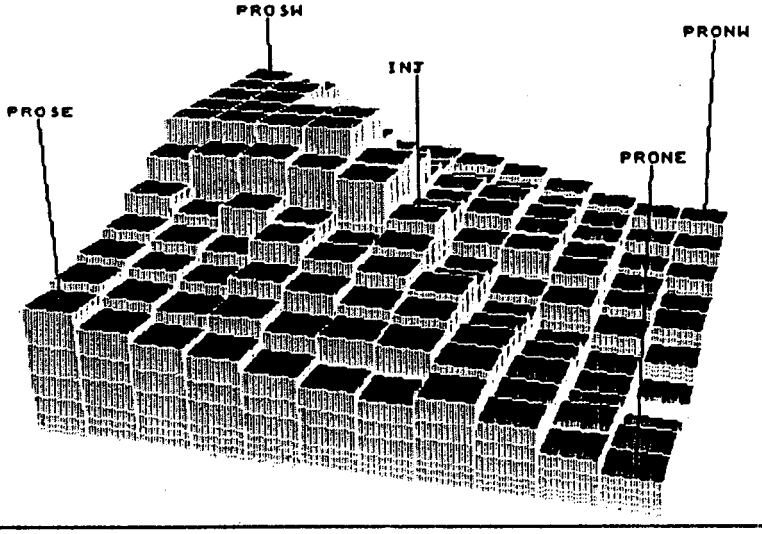

Figure 8. Energy Recovery as a Function of Reservoir Structure

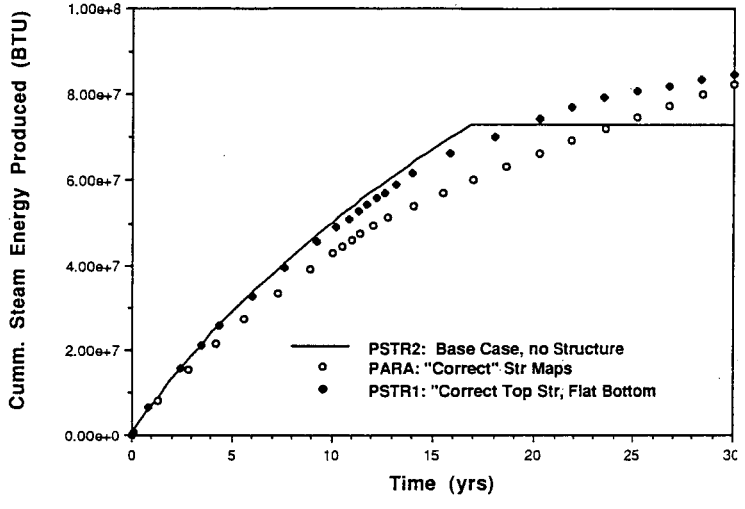

Figure 9. Energy Recovery as a Function of Relative Permeability Curves and Residual Saturations

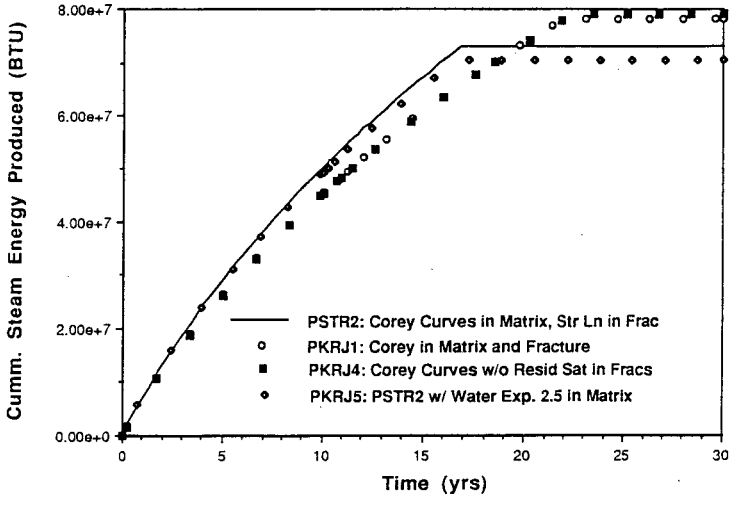

Figure 10. Capillary Pressure Curves Used.

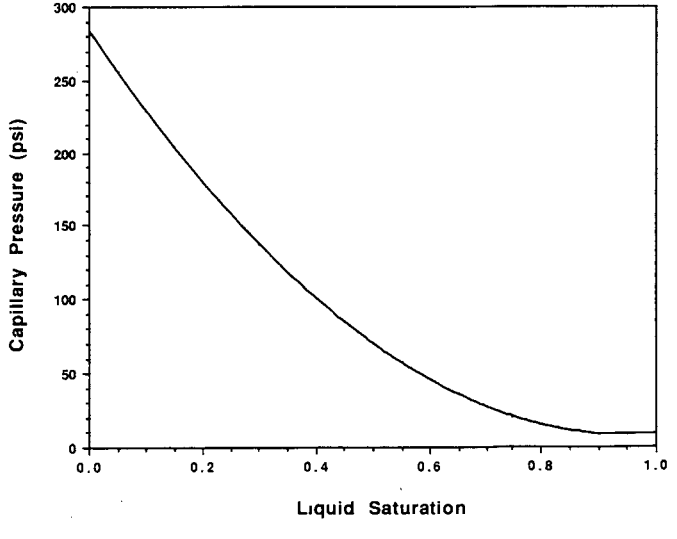

Figure 11. Energy Recovery as a Function of Capillary Pressure and Initial Saturations

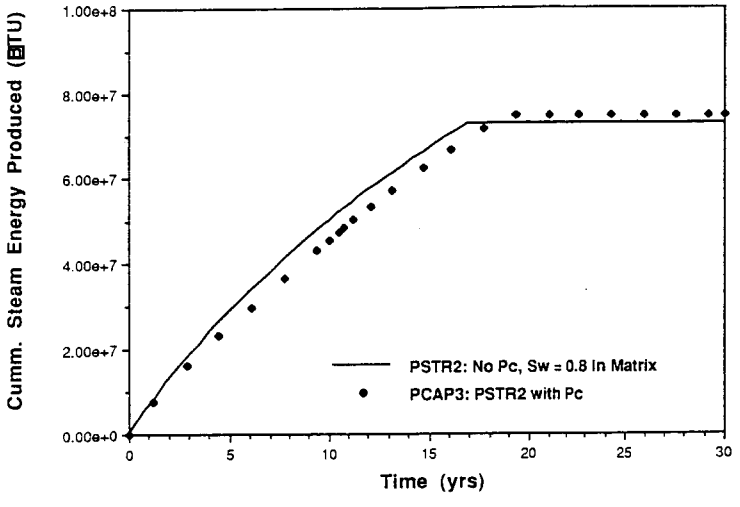

Figure 12. The Effect of Capillary Pressure on Energy Recovery at Lower Initial Water Saturation

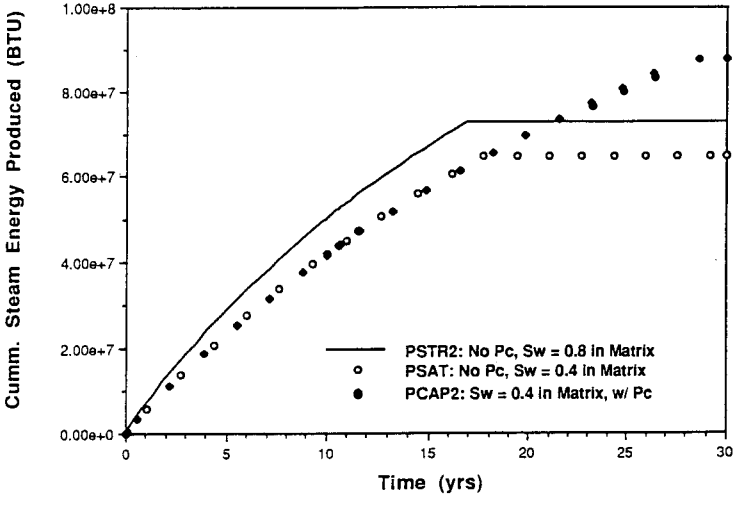

Figure 13. Energy Recovery as a Function of Fracture Spacing and Shape Factors Used

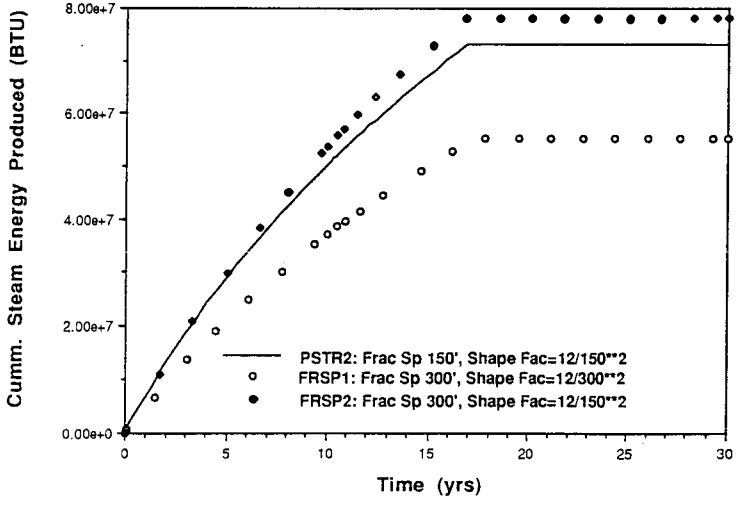

PROCEEDINGS, Seventeenth Workshop on Geothermal Reservoir Engineering
Stanford University, Stanford, California, January 29-31, 1992
SGP-TR-141

PRELIMINARY RESULTS AND STATUS REPORT OF THE HAWAIIAN SCIENTIFIC OBSERVATION HOLE PROGRAM

Harry J. Olson
Hawaii Natural Energy Institute, University of Hawaii at Manoa
811 Olomehani Street
Honolulu, Hawaii 96813

John E. Deymonaz
Geothermal Drilling Consultant
Route 3, Box 3783D
Hermiston, Oregon 97838

ABSTRACT

The Hawaii Natural Energy Institute (HNEI), an institute within the School of Ocean and Earth Science and Technology, at the University of Hawaii at Manoa has drilled three Scientific Observation Holes (SOH) in the Kilauea East Rift Zone to assess the geothermal potential of the Big Island of Hawaii, and to stimulate private development of the resource. The first hole drilled, SOH-4, reached a depth of 2,000 meters and recorded a bottom hole temperature of 306°C. Although evidence of fossil reservoir conditions were encountered, no zones with obvious reservoir potential were found. The second hole, SOH-1, was drilled to a depth of 1,684 meters, recorded a bottom hole temperature of 206.1°C and effectively defined the northern limit of the Hawaii Geothermal Project-Abbott - Puna Geothermal Venture (HGP-A/PGV) reservoir. The final hole, SOH-2, was drilled to a depth of 2,073 meters, recorded a bottom hole temperature of 350.5°C and has sufficient indicated permeability to be designated as a potential "discovery". The SOH program was also highly successful in developing slim hole drilling techniques and establishing subsurface geological conditions.

INTRODUCTION

The Hawaiian Islands are located above a geologic "hot spot" in the earth's mantle that has been volcanically active over the past 70 million years. The Big Island of Hawaii has an obvious, large potential for geothermal energy resources, both for electrical generation and direct utilization. Since the drilling of the HGP-A well in 1976 and the discovery of the HGP-A/PGV geothermal reservoir along the eastern portion of the Kilauea East Rift Zone, geothermal power potential on the Big Island has been estimated to be in the range of 500 to 700 megawatts (Thomas 1987).

The Hawaii Deep Water Cable Program, which was initiated in 1981 by the Hawaiian and Federal Governments to explore the technical, environmental and financial dimensions of a cable system to transmit geothermally generated electricity from the Big Island to the load center on Oahu, was based on the assumption that the estimated reservoir size was realistic. However, at the time the estimate was made, no wells had been drilled outside the area adjacent to the HGP-A well, and the reservoir potential of the Kilauea East Rift Zone was essentially unknown, and certainly not proven. Further exploration and definition of the HGP-A/PGV reservoir area by subsequent developers did little to indicate reservoir potential beyond the immediate area. Although several production wells have been drilled recently on Puna Geothermal Venture (PGV) property, approximately one quarter mile to the north of the HGP-A well, these wells have not had extensive flow testing, and currently, the only reservoir with a "known" or "proven" production capability is that tapped by the HGP-A well. Similarly, the discovery that has been reported by the True/Mid-Pacific Geothermal Venture on property owned by the Estate of James Campbell approximately seven miles to the west of the HGP-A well, has not had sufficient drilling or flow testing to classify the discovery as "proven".

The Scientific Observation Hole (SOH) program was planned and implemented in 1988 by the Hawaii Natural Energy Institute, an institute within the School of Ocean and Earth Science and Technology, at the University of Hawaii at Manoa. The SOH program was initially funded to drill four SOHs to a nominal depth of 1,200 meters (4,000 feet), to test the geological condition and the geothermal potential within Geothermal Resource Subzones (GRZ) along the Kilauea East Rift Zone, and to drill two holes in the Haleakala Southwest Rift Zone on the island of Maui. These holes were designed to assess the geothermal potential of these two areas by providing a general knowledge of rock types, alteration, and structures within the rift zones, the depth to potential geothermal reservoirs, the depth and composition of ground water, and the temperature of rock and fluids at depth. Although the SOHs are for scientific observation and monitoring purposes only and are prohibited by the terms of their permits from flow testing or production, flow capability of production sized wells can be estimated using injection techniques.

Initial attempts to permit the two SOHs on the island of Maui met with such intense local opposition, that the two holes scheduled to be drilled in the Haleakala Southwest Rift Zone were withdrawn from further consideration during the initial phase of the program. Experience during the drilling of the first hole in the Kilauea East Rift Zone caused further extensive modification of the drilling plan by increasing the targeted drilling depth from 1,200 meters (4,000 feet) to 2,000 meters (6,500 feet). Because of this and difficult drilling conditions resulting in increased drilling costs, the scope of the program was consequently modified to provide fewer, but deeper holes.

The SOH program specifically meets the University of Hawaii's stated mission of providing scientific and technology transfer to the private sector for utilization and commercialization and has provided a stimulus for private development of Hawaii's geothermal resources. To date, after the completion of three holes, effective

techniques have been devised to drill slim, rotary and core holes to depth in excess of 2,070 meters (6,800 feet), and has:

- established subsurface thermal continuity along the Kilauea East Rift Zone,
- defined the shallow limits of the northern boundary of the HGP-A/PGV reservoir, and
- discovered a potential geothermal reservoir in a previously untested area.

Present plans call for the permitting and drilling of additional SOHs in Phase II of the program in other areas of geothermal potential, not only on the Big Island and Maui, but also on Lanai and Oahu if sufficient interest and funds are available. Areas of geothermal potential on the Big Island and Maui are shown on Figure 1. If the SOHs are successful in locating or indicating additional geothermal reservoirs, the program will expand Hawaii's geothermal resource base not only for electrical generation potential, but also for direct utilization in such fields as food and materials processing, brine handling and utilization, agriculture, aquaculture, geothermal spas, and other uses involving the heat of the earth.

The SOH program has been described in more detail by Olson (1988), Olson, et al. (1990a) and Olson, et al. (1990b).

STATUS OF DEVELOPER ACTIVITY AND THE SOH PROGRAM

As of this date, PGV has drilled three geothermal wells in fallow sugar cane fields and papaya orchards on agricultural land near a residential development in the Kapoho GRZ. The first well drilled (KS-3) intersected a steam zone, which probably will not be produced due to chemical problems. The second well (KS-7) unexpectedly intersected a very shallow production zone and had to be abandoned. The third well (KS-8) also intersected the shallow production zone and will probably become an important producer. As of the end of 1991, PGV essentially had completed construction of its 25 megawatt (net) power plant, and was planning an operational test of the plant utilizing steam generated in boilers using county water. However, as of the writing of this paper the County of Hawaii had imposed a geothermal drilling moratorium which is currently in effect at the PGV project due to an accidental, uncontrolled venting of steam from the KS-8 well. Nevertheless, if the moratorium is lifted shortly, as expected, the power plant could be producing power for the Big Island as soon as PGV can complete the number of wells necessary to supply steam to the power plant.

True/Mid Pacific Geothermal Venture (T/MPGV) has drilled a well with three kick-offs in forested, conservation land within the Kilauea Middle East Rift GRZ. On the last kick off, True intersected a steam zone and, after a short flow test, announced a discovery. However, no details of the producibility of the well are currently known. The T/MPGV group is currently planning to drill a second well, but as of the writing of this paper had not prepared the site for drilling.

The objectives of the SOH program as stated in the enabling legislation are to stimulate geothermal development and to confirm the geothermal resources of Hawaii. The first goal of stimulating geothermal development has been met, as two developers, PGV and T/MPGV are currently involved in exploration and development along the Kilauea East Rift Zone.

In spite of the unfavorable permitting, regulatory and business environment, and intense local opposition to geothermal development, the second goal of the SOH program has been partially met in that the SOH program has assessed a portion of the Kilauea East Rift Zone in which the active geothermal developers are operating. The program has been an outstanding success to date in developing effective drilling techniques, reducing drilling expenses, providing deep geologic sections along the area of interest, establishing thermal continuity within the KERZ, defining limits to the HGP-A/PGV reservoir, and discovering a potential reservoir in an untested area.

To date three of the four permitted SOHs have been drilled. The location of the SOHs, the GRZs, and the production wells drilled by PGV and T/MPGV are shown on Figure 2. Although all the necessary permits have been approved for SOH-3, the State of Hawaii has decided to defer the drilling of SOH-3 until additional SOHs are permitted with provisions to allow pumping or flow testing of the holes to obtain fluid groundwater and reservoir samples.

SOH-4

The first hole drilled, SOH-4, was drilled to a total depth of 2,000 meters (6,562 feet), and recorded a bottom hole temperature of 306.1°C (583°F). Although evidence of fossil reservoir conditions were found, no zones with obvious reservoir permeability were encountered. No problems were encountered in core drilling the upper section of subaerial basalt flows and dikes. However, severe rotary drilling problems with lost circulation and reaming were encountered in the upper 610 meters (2,000 feet) of the hole, resulting in large overruns in drilling costs. These problems were solved by slowly and carefully drilling blind for 50 to 100 meters (150 to 300 feet) through lost circulation zones instead of cementing whenever circulation was lost, by using thin cement mixtures to regain circulation, and opening the core hole with rotary tools to the final hole size in one pass instead of two. After casing was set and cemented, core drilling proceeded with only minor problems to the bottom of the hole in a heated section of submarine basalts. At a depth of approximately 1,200 meters (4,000 feet) State officials decided to deepen the hole to a depth of approximately 2,000 meters (6,500 feet) because temperatures of 200°C (400°F) or higher had not been recorded during drilling. At this time, the other scheduled SOHs also were targeted to depths of approximately 1,825 to 2,000 meters (6,000 to 6,500 feet). Total direct drilling costs for SOH-4 were $1,404,805, or $702.40 per meter ($214.08 per foot). Drilling performance is shown graphically for depth versus cost for all the SOHs in Figure 3, and for depth versus time for all the SOHs in Figure 4. The temperature gradient of SOH-4 and the other SOHs are shown in Figure 5. Interestingly enough, SOH-4 was initially considered to be a "failure" by State officials because the bottom hole temperature was not as high as the 358°C (676°F) encountered in the HGP-A well, because of the large cost overrun, as compared to the cost estimated for the original 1,200 meter (4,000 foot) depth planned for the hole, and because the hole did not

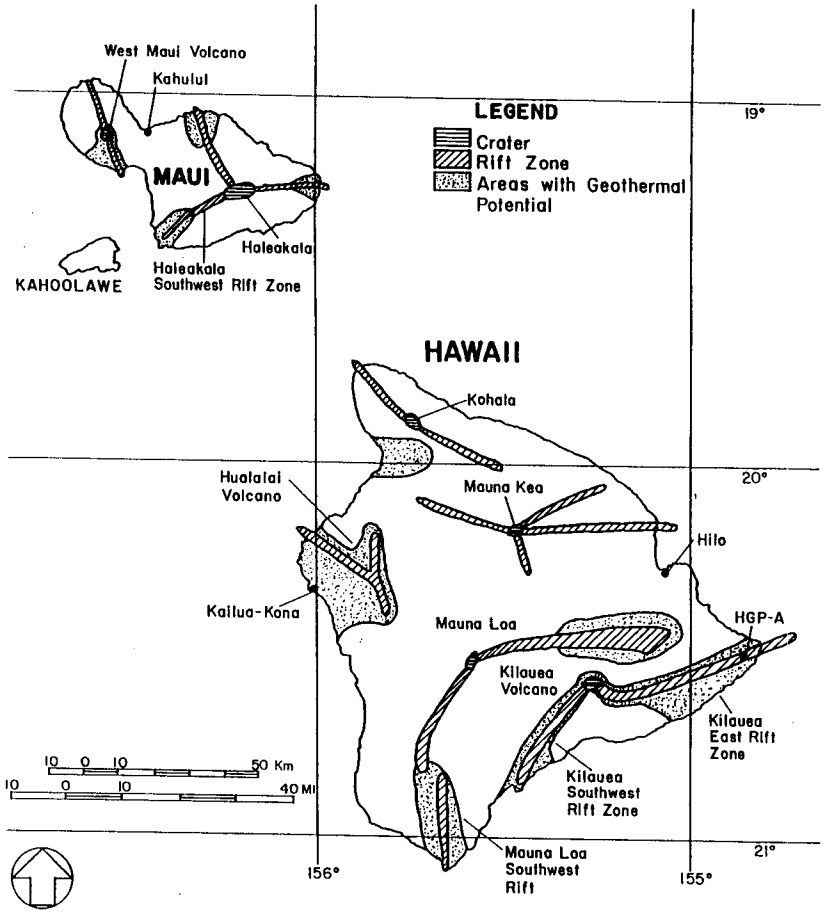

Fig. 1 Volcanic features and areas with geothermal potential on Maui and Hawaii (Source: Geothermal Resources of Hawaii, 1983)

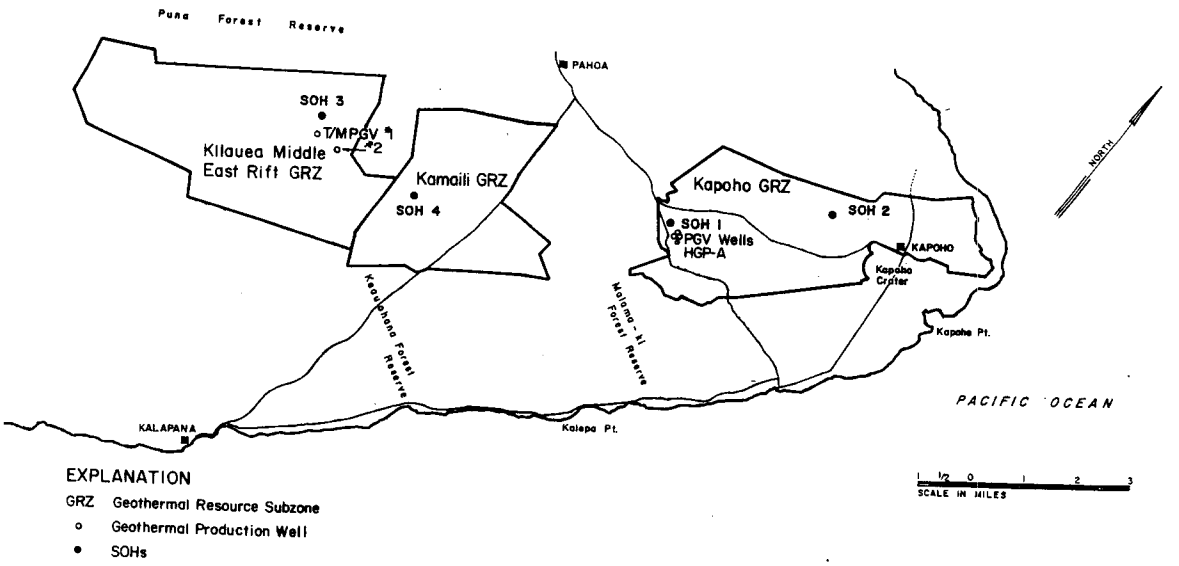

Fig. 2 Location of SOHs on the Big Island

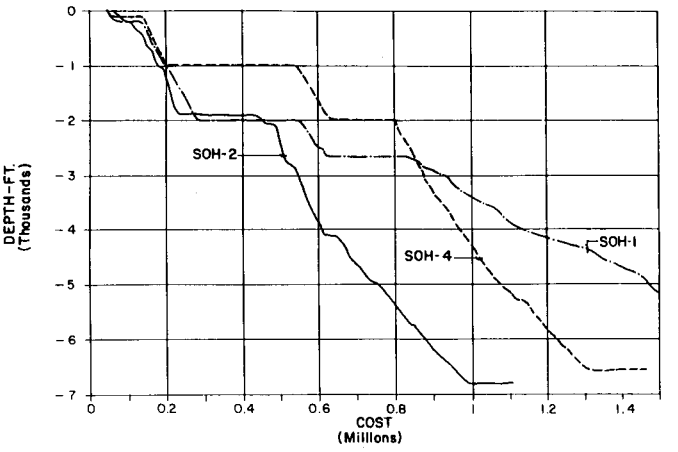

Fig. 3 SOH drilling performance depth vs. cost

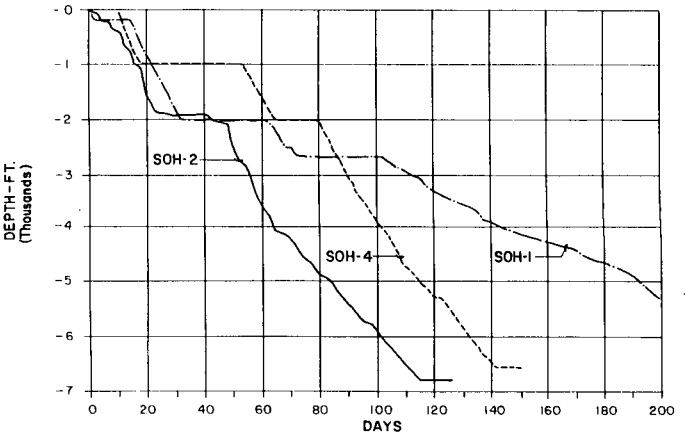

Fig. 4 SOH drilling performance depth vs. time

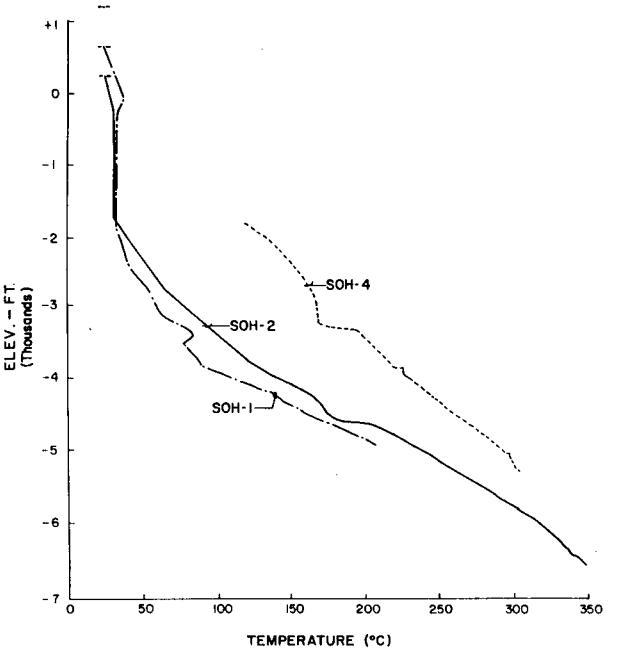

Fig. 5 SOH temperature vs. elevation

encounter a reservoir. This resulted in renewed efforts to educate the officials to the realities of drilling economics, programmatic goals, and expected results.

SOH-1

The second hole, SOH-1, was drilled to a total depth of 1,684 meters (5,526 feet) and recorded a bottom hole temperature of 206.1°C (403°F). The drilling and casing plan for the upper 610 meters (2,000 feet) was modified, utilizing the experience gained in the drilling of SOH-4, by omitting the initial 305 meters of 9-5/8 inch casing and using 7 inch casing from the surface to a depth of 610 meters (2,000 feet). This resulted in rapid progress with essentially no drilling problems and cost savings of approximately $240,000 as compared to SOH-4 at a similar depth. When coring resumed below the casing, however, very severe drilling problems were encountered due to highly fractured, cool (<38°C or <100°F), submarine basalt, sands, and dikes, in the interval between 610 and 1,370 meters (2,000 to 4,500 feet), resulting in short bit life, short (15 to 45 centimeters or 6 to 18 inches) core runs, stuck drill rods and massive cost overruns. The fractured submarine basalt and dikes broke off in small fragments around and in front of the bit and rolled about the drilling surfaces, wearing the bit face matrix and gouging out the diamonds. The exterior gauge of the bits was reduced and the interior gauge enlarged resulting in short core runs which stuck in the core barrel, and resulted in the necessity of redrilling the hole to reach bottom. Core life averaged between 3 and 6 meters (10 to 20 feet), resulting in constant tripping of the rods to replace bits and causing the driller to "affectionately" refer to this interval as the "hole from hell". Below 1,370 meters (4,500 feet) the temperature increased rapidly, resulting in normal drilling runs, core recovery of nearly 100%, and long bit life, due to fracture filling or bonding of the fractures by thermal metamorphism. Total drilling costs were $1,562,647 or $927.76 per meter ($282.78 per foot), causing the hole to be stopped approximately 300 meters (975 feet) short of the its targeted depth.

SOH-2

The third hole, SOH-2, was drilled to a total depth of 2,073 meters (6,802 feet) and recorded a bottom hole temperature of 350.5°C (663°F). The drilling and casing plan was again modified to incorporate the lessons learned in the drilling of the first two holes. To reduce drilling costs, the upper 580 meters (1,900 feet) of the SOH was rotary drilled with no coring. Casing was set approximately 30 meters (100 Feet) higher in SOH-2 than in the other two SOHs because of a sudden 4° deviation in the hole in an 8.2 meter (27 foot) interval between a depth of 567 to 575 meters (1,860 to 1,887 feet), which resulted in several drill collar twist offs and fishing jobs. After the casing was set, coring was attempted with unsatisfactory results similar to those encountered in SOH-1. At that time a decision was made not to attempt to fight the hole down by coring, and the hole, subsequently, was rotary drilled to approximately 1,250 meters (4,100 feet). As circulation was lost at the surface, only a few scattered rock samples were collected in the upper rotary portion of the hole. However, the dogleg caused by the sudden hole deviation, persisted through the casing and drilling continued to be plagued by repeated twist offs to the bottom of the hole. Luckily all the twist offs occurred inside the casing and fishing, although time consuming and costly, did not result in major delays or loss of the hole. Temperature at a depth of 1,250 meters (4,100 feet) was 132.7°C (270.9°F) which was sufficient to bond the fractured submarine basalts (or the section previously had been subjected to higher temperatures with the same results), and coring proceeded rapidly and smoothly to the bottom of the hole. Subsequent injection testing indicated that a permeable interval between 1,488.3 and 1,505.7 meters (4,883 to 4,940 feet) with a temperature of 210.3°C (410.5°F) can be designated as a possible "discovery" Additional drilling in the vicinity of SOH-2 should intersect fracture permeability below a depth of 1,825 meters (6,000 feet) with fluid temperatures in excess of 300°C (572°F). Total drilling costs were $1,098,760 or $530.03 per meter ($161.53 per foot), which represented a savings of greater than $300,000 while drilling 73 meters (240 feet) deeper than SOH-4, and greater than $460,000 while drilling 389 meters (1,276 feet) deeper than SOH-1.

Analysis of the drilling results indicates that the key to reducing costs involves more than drilling faster. Over the long run, staying out of trouble usually results in faster penetration rates and lower drilling costs. Consequently, after the experience with the twist offs in SOH-2, a decision was made to core drill the subaerial basalts and then open the hole by rotary drilling, which results in a straight hole and more data, rather than to attempt to reduce costs by not coring and running the risk of twist offs and possible loss of the hole.

PRELIMINARY SOH PROGRAM RESULTS

Very preliminary results from SOH program indicate that:

- Core (slim) holes can be successfully drilled to depths in excess of 2,070 meters (6,800 feet) and can be used to assess geothermal resource potential at substantial savings in drilling and permitting costs and environmental impact. Initial drilling results indicate that SOHs can be most efficiently drilled by a combination of rotary and core drilling techniques.

- It has not been possible to collect uncontaminated groundwater or reservoir fluids in the SOHs in a cost effective manner by bailing. To obtain reliable samples the holes must either be pumped or flowed. As groundwater and reservoir fluid chemistry is vital to the assessment of the geothermal potential of an area, future SOHs will be permitted to allow the sampling of downhole fluids by pumping or flowing.

- The geothermal potential of the Kilauea East Rift Zone has not been proven and additional production and assessment drilling must be completed before an accurate estimate of the size of the resource can be made.

- A single large geothermal reservoir (or several large reservoirs) probably does not exist along the KERZ. The geology of the geothermal reservoirs that do exists is probably highly complex and the reservoirs may be relatively small and discontinuous. SOH-1 essentially defined the northern boundary of the HGP-A/PGV reservoir, which has produced between 2 and 3 megawatts of electrical power with a plant factor of greater that 90% for over 7-1/2

years. Utilizing published data from HGP-A, the KS wells drilled by Thermal Power in the early 1980s, and SOH-1, reservoir conditions at a depth of 1,250 meters (4,100 feet) and a cutoff boundary of 200°C (392°F) indicate a narrow, easterly dipping resource approximately 800 meters (2,600 feet) wide that is open to the west, as shown in Figure 6. This isotherm map does not reflect the shallow reservoir intersected by PGV's KS-7 and KS-8 wells. Sufficient published data are not available to predict the vertical size and extent of the reservoir.

ACKNOWLEDGMENTS

This is School of Ocean and Earth Science and Technology contribution number 2716.

REFERENCES

Olson, H.J., 1988, Hawaii Program for the Confirmation and Stimulation of Geothermal Resources Development; Geothermal Resources Council Transactions, v. 12, p. 193-196.

Olson, H.J., Seki, A.S., Deymonaz, J.E., and Thomas, D.M., 1990a, The Scientific Observation Hole (SOH) Program; Geothermal Resources Council Transactions, v. 14, p. 791-798.

Olson, H.J., Seki, A.S., Deymonaz, J.E., and Thomas, D.M., 1990b, The Hawaiian Scientific Observation Hole Program: A Case History and Status Report; Proc, 12th New Zealand Geothermal Workshop 1990, p. 303-307.

Thomas, D.M., Cox, M.E., Helsley, C.E., Kauahikaua, J.P., Lienert, B.R., Mattice, M.D., and Thomas, T.L., 1983, Geothermal Resources Map of Hawaii, Hawaiian Institute of Geophysics, University of Hawaii, compiled by National Geophysical Data Center, National Oceanic and Atmospheric Administration for the Geothermal and Hydropower Technology Division, United States Department of Energy.

Thomas, D.M., 1987, A Geochemical Model of the Kilauea East Rift Zone, U.S. Geological Survey Prof. Paper 1350, Volcanism in Hawaii, v. 2, Chap. 56, p. 1507-1525.

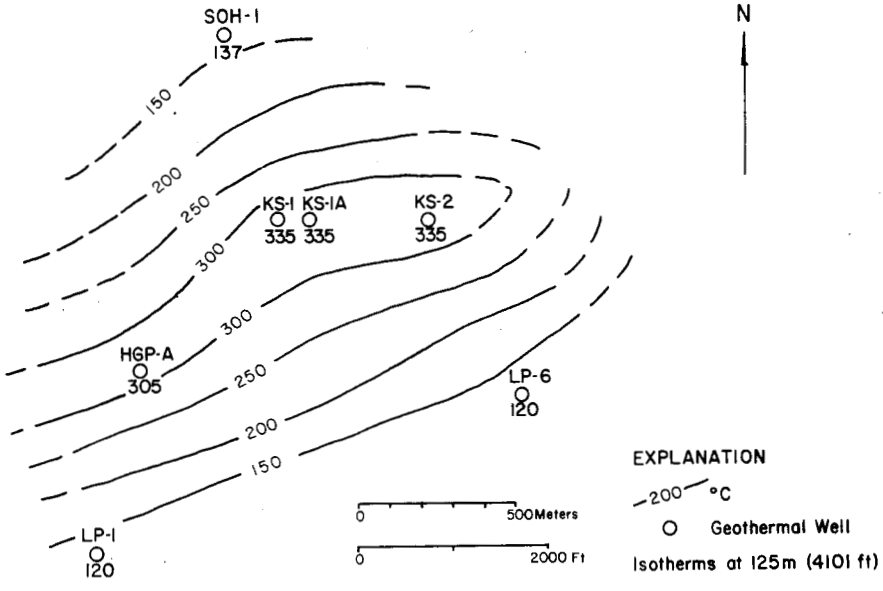

Fig. 6 HGP-A-PGV geothermal reservoir

PROCEEDINGS, Seventeenth Workshop on Geothermal Reservoir Engineering
Stanford University, Stanford, California, January 29-31, 1992
SGP-TR-141

Determining the 3-D Fracture Structure in the Geysers Geothermal Reservoir

Charles G. Sammis, Linji An, and Iraj Ershaghi

University of Southern California

Introduction

The bulk of the steam at the Geysers geothermal field is produced from fractures in a relatively impermeable graywacke massif which has been heated by an underlying felsite intrusion. The largest of these fractures are steeply dipping right lateral strike-slip faults which are subparallel to the NW striking Collayomi and Mercuryville faults which form the NE and SW boundaries of the known reservoir. Where the graywacke source rock outcrops at the surface it is highly sheared and fractured over a wide range of scale lengths. Boreholes drilled into the reservoir rock encounter distinct "steam entries" at which the well head pressure jumps from a few to more than one hundred psi. This observation that steam is produced from a relatively small number of major fractures has persuaded some analysts to use the Warren and Root (1963) dual porosity model for reservoir simulation purposes. The largest fractures in this model are arranged in a regular 3-D array which partitions the reservoir into cubic "matrix" blocks. The net storage and transport contribution of all the smaller fractures in the reservoir are lumped into average values for the porosity and permeability of these matrix blocks which then feed the large fractures. Recent improvements of this model largely focus on a more accurate representation of the transport from matrix to fractures (e.g. Pruess et al., 1983; Zimmerman et al., 1992), but the basic geometry is rarely questioned. However, it has long been recognized that steam entries often occur in clusters separated by large intervals of unproductive rock (Thomas et al., 1981). Such clustering of fractures at all scale lengths is one characteristic of self-similar distributions in which the fracture distribution is scale-independent. Recent studies of the geometry of fracture networks both in the laboratory and in the field are finding that such patterns are self-similar and can be best described using fractal geometry. Theoretical simulations of fracture development in heterogeneous media also produce fractal patterns. However, a physical interpretation of the mechanics which produce the observed fractal geometry remains an active area of current research. Two hypotheses for the physical cause of self-similarity are the Laplacian growth of fractures in a self-organized critical stress field, and the evolution of percolation clusters in a random medium. Each predicts a different fractal dimension. The more important questions from a reservoir engineering point of view are: 1) is the network of fractures in the Geysers reservoir fractal and if so over what range of fracture sizes is the self-similarity observed and what is its fractal dimension, and 2) do the conventional dual porosity numerical simulation schemes provide an adequate description of flow and heat mining at the Geysers? Other papers in this volume by Acuna, Ershaghi, and Yortsos (1992) and Mukhopodhyoy and Sahimi (1992) address the second question. The primary objective of this paper is to try to answer the first. Toward this goal we have mapped fracture patterns in surface exposures of the graywacke source rock at the outcrop scale (meters), at the road-cut scale (tens of meters) and at the regional scale (kilometers). We have also examined cores collected at depth from the graywacke reservoir rocks, and analyzed drilling logs making use of the pattern of steam entries as well as the fluctuations in drilling rate.

Mapping fracture patterns at The Geysers field

The graywacke reservoir source rock outcrops at several locations in the Geysers geothermal field. One particularly good location is at well site GDC-21 where the drilling pad has been cut from the hillside revealing a near vertical wall of graywacke which is about 100 feet long and 40 feet high. The graywacke at this location has a cataclastic texture where the largest clasts are on the order of 10 feet in diameter. Although the outcrop appears to have a fluction structure suggesting a component of ductile deformation, close inspection of the folds shows that they are composed of multiply fractured graywacke layers in which virtually all the strain appears to have been accommodated by brittle fracture. The largest clasts contain complex fracture patterns which are easily visible due to the infilling with minerals of a contrasting color. In fact, at this outcrop virtually all of the fractures have been filled. The fracture patterns in three such clasts were mapped from photo mosaics and one example is shown as Fig 1. A sec-

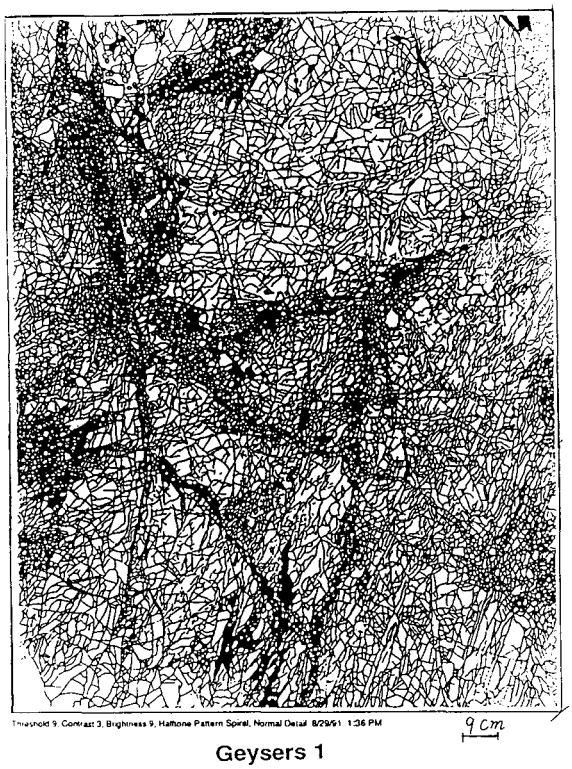

Figure 1: Fracture patterns of the Graywacke outcrop.

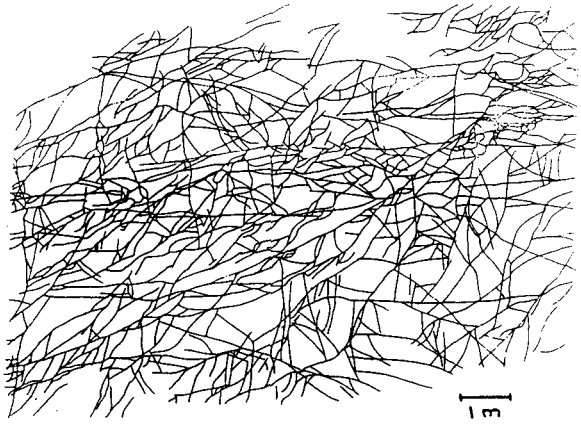

Figure 2: Fracture pattern from the road cut outcrop.

ond outcrop occurs in a road cut. The graywacke at this site is also highly fractured but more uniform in texture so that one continuous fracture pattern covers the entire roadcut. A map was prepared from a photo mosaic and is shown in Fig 2. The fractures at this outcrop were also mineralized. Finally, a fault map for the entire field was prepared using fault maps in the literature. Hebein (1986) mapped the regional fracture pattern under the assumption that local drainage patterns are fault controlled. He showed that the drainage pattern is consistent with the hierarchical pattern of conjugate shears expected in the regional stress field. In Fig. 3 we show the fault map plus the regional drainage pattern.

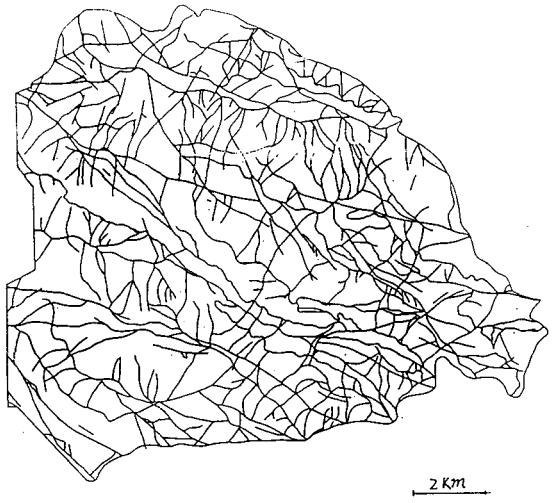

Figure 3: Fault and drainage pattern in The Geysers geothermal area.

Testing the fracture patterns for self similarity and measuring the fractal dimension

The fracture patterns in Figures 1, 2 and 3 were tested for self-similarity using the box counting method used by Barton and co-workers to characterize fracture patterns at a site under consideration for nuclear waste disposal at Yucca Mountain, Nevada (Barton and Hsieh, 1989; Barton, 1992). In this method the minimum number of square tiles which are required to completely cover the fracture pattern, N_r, is determined as a function of the edge length, r, of a tile. If the pattern is self-similar, then $N_r \propto r^{-D_f}$ where D_f is the fractal capacity dimension of the pattern. In essence, one is measuring how the open area between fractures changes with scale. Hence this may also be viewed as a measure of the clustering of the fractures. If the fracture pattern is very homogeneous with little clustering, then D_f approaches 2. Such a pattern, if it extended over all scale lengths, would fill the plane with fractures. At the other extreme, as the fractures become increasingly clustered, D_f approaches 1. In this limit, all fractures lie on a line (and hence have dimension one). A schematic illustration of the box counting method is given in Fig. 4.

For any physical system, the self-similarity can only extend over a limited range of scale-lengths. The largest scale length to which self-similarity extends we call the upper fractal limit, while the shortest we call the lower fractal limit. These limits may be set by the physical limits of the system or, possibly, by the degree of evolution of the physical process

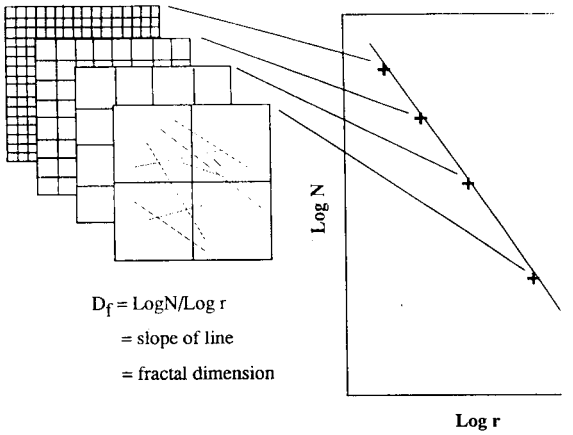

Figure 4: Schematic representation of box counting method for measuring fractal dimension.

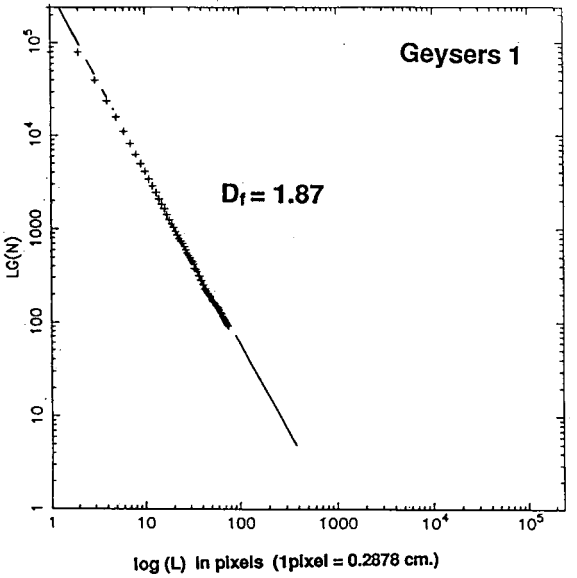

Figure 5: Fractal analysis of the fracture pattern in the Graywacke outcrop.

which is producing the self-similarity. The fractal limits are determined by the box counting algorithm as the limits between which the log(Nr) vs. log r plot is linear. A computer program has been developed which covers the digital image of a fracture pattern with a square grid and finds the minimum number of occupied squares with respect to rotation and translation of the grid. The procedure begins with a fine grid at the smallest resolved scale of the data. The grid size is then systematically increased until all the squares are occupied. The program was tested by measuring geometrical fractal gaskets and random fractals of known dimension. When applied to the outcrop scale fracture pattern in Fig. 1 it yielded Fig. 5. The other two small-scale outcrop patterns were similar. All were self-similar over a range of scales from about 0.5 to 20 centimeters and had fractal dimensions between 1.8 and 1.9. The road cut pattern in Fig. 2 is analyzed in Fig. 6 where it has a fractal dimension of 1.9 between scale lengths of about 0.3 and 4 meters. The regional fault

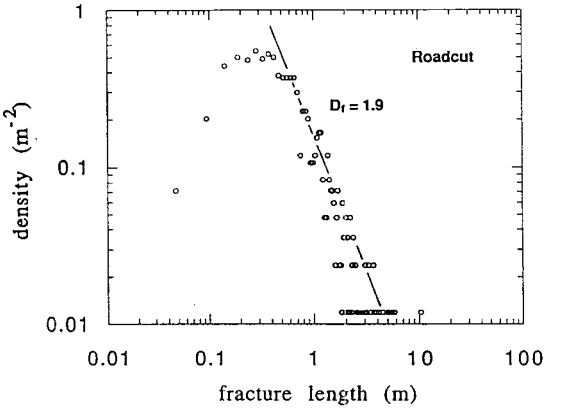

Figure 6: Fractal analysis of road cut fracture pattern in the Graywacke.

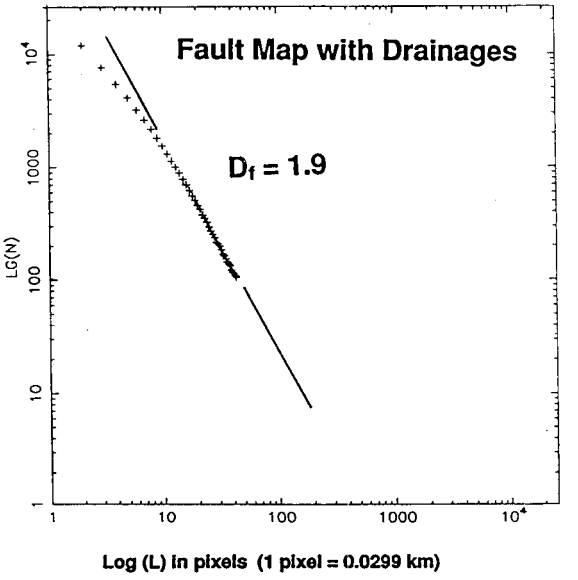

Figure 7: Fractal analysis of the pattern of faults and drainages.

pattern including the drainage pattern in Fig. 3 is analyzed in Fig. 7. It has a fractal dimension of about 1.9.

Each pattern is thus self-similar with a fractal dimensions between 1.8 and 2.0. This implies only moderate clustering. It is, in fact, possible to show that all three fracture patterns are mutually self-similar across the entire range from outcrop to regional scale. To demonstrate this global self-similarity, the number of fractures per unit area was determined as a function of fracture length for each pattern. When the log of the area density is plotted

as a function of the log of the fracture length in Fig. 8, all three distributions lie on a line with slope 2. This is precisely the requirement for self-similarity. Because the number of fractures per unit area scales as their length squared, then the number of fractures in an area scaled to the fracture length will be a con-

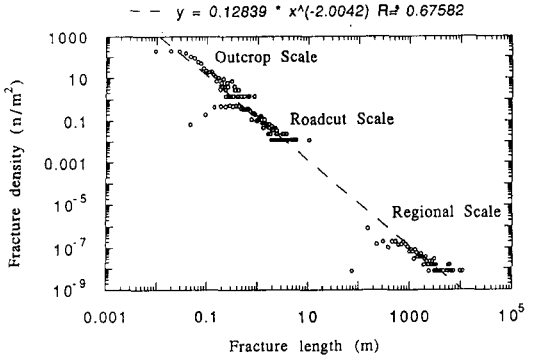

Figure 8: Self similarity of fracture density over a wide range of scales.

stant. Stated another way, it is impossible to tell at what scale a given fracture diagram was mapped.

Examination of cores from the reservoir

Examination of cores from the graywacke reservoir rock led to two significant observations. First, many cores contained numerous fractures at the same scale as those observed in outcrop. Like the outcrop fractures, the core fractures were sealed by mineralization. Other sections of the recovered core were completely granulated. The surfaces of the rock fragments showed mineral deposition and alteration suggesting that the rock had been fragmented in the reservoir and not as a result of drilling induced fractures. Our tentative conclusion from these core observations is that many of the smaller fractures in the reservoir are sealed and that most of the storage and transport may occur through larger shear fractures which are multiply fractured cataclastic zones of finite width. It should be emphasized that this is only a tentative conclusion. Thin open fractures which cut the borehole are difficult to distinguish from breaks in the core caused by drilling stresses. Even if the distinction could be made, the core recovery is rarely complete enough to allow a meaningful analysis of the intervals between such breaks. Having said this, the presence of sealed fractures throughout the reservoir, and the common occurrence of cataclastic zones several feet in width are unambiguous.

Analysis of steam entries

Borehole deviation and steam entry data for about 200 wells were analyzed. We observed that wells which deviate in the NE and SW directions tend to intersect more steam entries. This is consistent with the hypothesis that steam entries correspond to near vertical NW striking fractures which are parallel

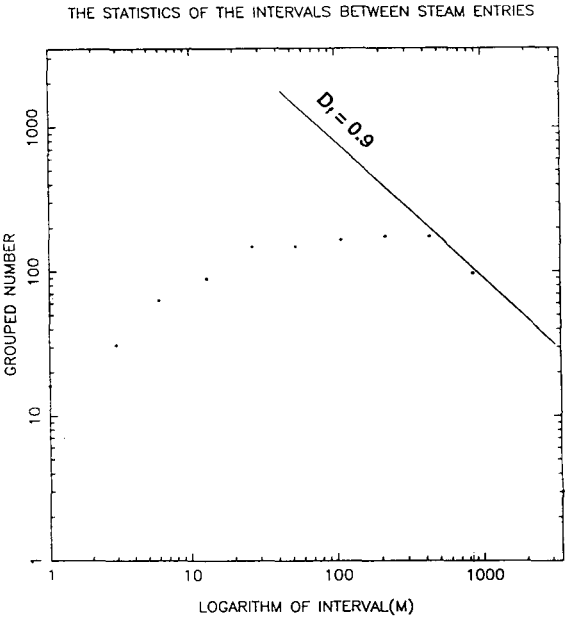

Figure 9: Statistical distribution of spacing between steam entries as sampled by boreholes.

to the regional shear fabric. However, the weakness of the anisotropy suggests that the pattern is more complex - a conclusion which is supported by the complexity of the regional faulting pattern in Fig. 3. If the pattern of fractures in the Geysers reservoir is self-similar and isotropic, then this geometry should be reflected in the spatial pattern of steam entries. For example, the intervals between steam entries should follow a power law distribution. Also, if the pressure jump associated with a fracture is proportional to its size, then number of steam entries should also vary as a power of their size. To test the intervals between steam entries for a power law distribution, the log of the number of intervals is plotted as a function of the log of the interval length in Fig. 9. If the fracture distribution in the reservoir were self-similar and isotropic with dimension comparable to that observed in outcrop (D_f = 1.8 - 1.9), then the intervals should be distributed according to a power law with slope 1-D_f = 0.8 - 0.9. The line in Fig. 9 has slope 0.9. Note that it only fits the data for intervals between about 300 and 900 meters. One possible interpretation is that many of the smaller fractures spaced more closely that 300 meters are either sealed by mineralization or yield too small a steam entry pressure jump to be reliably recorded. The observation that too few larger intervals are recorded may be a sampling error because few of the wells intersect more than 1000 meters of reservoir rock. In Fig. 10 the log of the number of steam entries is plotted as a function of the log of the pressure jump. The distribution is not power law over any range. This may be due in part to

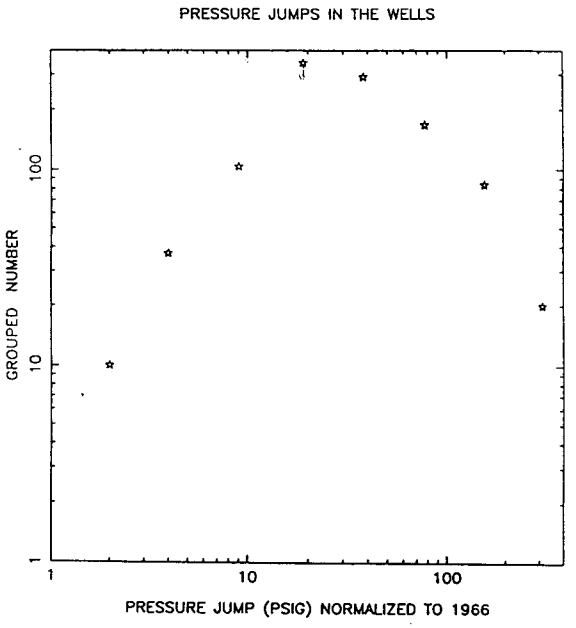

Figure 10: Statistical distribution of pressure jumps from steam entries.

the mineralization and sampling problems discussed above, but may also imply that the pressure jump does not scale with the fracture size. As a final analysis of the steam entries, the well head locations and deviation data were used to find the latitude, longitude and true depth (with respect to sea level) of all the steam entries. A 3-D box counting algorithm was used to test the pattern for self-similarity. The 3-D box counting is directly analogous to the 2-D technique discussed above except that the minimum number of cubes required to contain all the points is determined as a function of the length of the cube edge. The resultant log-log plot is shown in Fig. 11 where the pattern is seen to be self-similar for length scales between 1,000 and 10,000 feet with a fractal

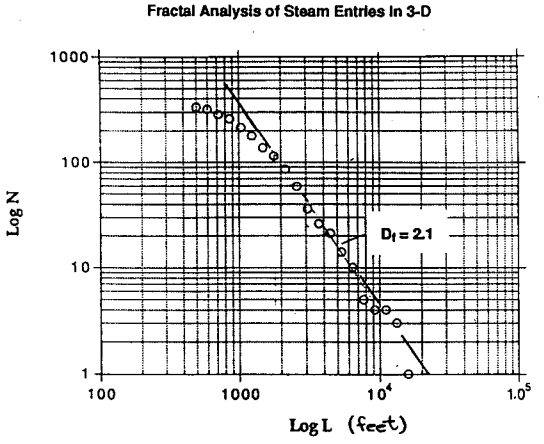

Figure 11: Three-dimensional fractal analysis of steam entries.

dimension of $D_f = 2.1$. This dimension is significantly lower than $D_f = 2.8$ which would be expected if the patterns observed in outcrop were typical of the 3-D patterns in the reservoir. However, Sahimi (1992) predicts that the fractal dimension of fracture networks which develop in 3-D can not simply be found by adding one to the dimension measured in 2-D section. Numerical simulations of the nucleation and growth of fractures in random media predict $D_f = 2.5$. The slightly lower observation of $D_f = 2.1$ is consistent with the hypothesis that the wells under sample the fracture network which produces the steam entries (Robertson et al., 1991).

Analysis of drilling records

The drilling records or "mud logs" contain more information than simply the location and size of steam entries. They also contain a continuous record of the drilling rate of penetration, as well as a record of the rotation rate and weight on the bit. The lithology is also recorded. Because the lithology does not change significantly for large distances within the reservoir, it is reasonable to associate changes in the penetration rate with changes in the fracture density in the graywacke. The basic assumption is that penetration is more rapid in highly sheared rock than it is in unfractured rock. The raw penetration rates were corrected for changes in rotation rate and weight on bit by calculating a drilling factor dexp defined by Jorden and Shirley (1966). The drilling exponent is plotted as a function of depth in Fig. 12.

Fluctuations in the drilling factor as a function of depth were analyzed using the fractal analysis technique discussed by Hewett (1986) and used by Leary (1992) to characterize sonic and electrical resistivity logs from the 3.5 km deep well near the San Andreas fault at Cajon Pass, southern California. In this method, the drilling parameter data are rescaled to have a zero mean and a unit variance and a cumulative sum is computed as a function of depth. This cumulative sum is then partitioned into segments of length L, and for each segment the range of variation R and the standard deviation S of the data

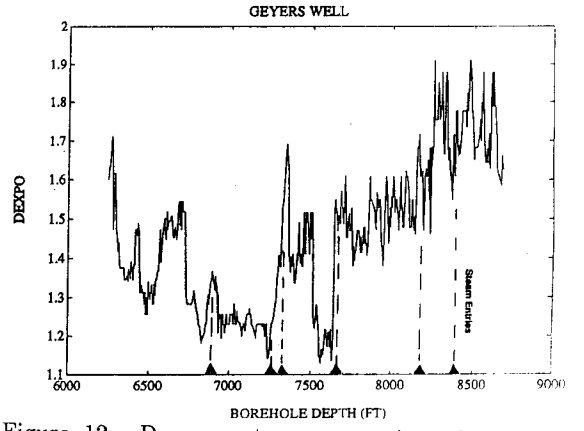

Figure 12: D-exponent representation of drilling rate.

within that segment are computed. This procedure is repeated for a number of different values of L ranging from the shortest resolved length of the data to the entire length of the mud log. For scale invariant fluctuations, the ratio R/S scales with the interval length L as L^H where H is called the Hurst exponent. If the observed Hurst exponent is $H = 0.5$, then the data fluctuations are uncorrelated. This is the case for Brownian motion. If $H > 0.5$ then the fluctuations are positively correlated (i.e. they have persistence). In our case this would imply that zones of fractured rock are spatially clustered. If $H < 0.5$ then the data fluctuations are negatively correlated (they have anti persistence). Note that many values of R/S are obtained for each value of L - more for short values of L, less for long values, decreasing to one value when L equals the length of the data set. In Fig. 13 the average value of log (R/S) is plotted as a function of log L for the drilling data in Fig. 12. The linear trend indicates scale independence over the entire range while the slope $H = 0.56$ indicates weak clustering. How do the drilling rate fluctuations correlate with the steam entries? Figure 12 shows that there is not a one-to-one correlation between increases in the drilling rate and the location of the steam entries. Rather, the steam entries tend to cluster in the broad bands of rapid drilling. The rough structure in Fig. 12 shows two fractured zones approximately 300 feet wide which have their centers separated by about 1000 feet. In analyzing

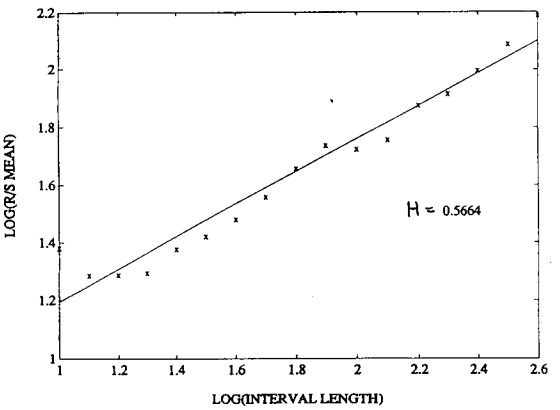

Figure 13: Estimation of H-exponent for R/S analysis of D-exponent data.

steam entries from six other wells, we find that they are also generally clustered in bands a few hundred feet thick with a spacing of about 1000 feet.

Summary and Discussion

The study of the fracture patterns at the Geysers geothermal field has led to the following general conclusions:

1. The fractures mapped in surface exposures of the Graywacke reservoir rock are fractal with dimension $D_f = 1.9$ in 2-D planar section. This is true at the outcrop, roadcut, and regional scales.

2. When the logarithm of the fracture densities measured at the three scales above are plotted as a function of the logarithm of the fracture length, all three measurements lie on the same line with slope 2. This implies that the fracture distribution is scale independent over a range of scales from centimeters to kilometers.

3. Most fractures mapped at the outcrop and roadcut scale are sealed by mineralization.

4. Cores recovered from the reservoir also show that many of the smaller fractures are filled by mineralization. However, many sections of the core are totally fragmented. Mineral deposits on the fragments imply that the break up was not due to drilling damage, but that such cores probably represent cataclastic zones associated with larger shear fractures (faults).

5. Steam entries are highly clustered in the reservoir. They appear to be fractal with a capacity dimension of $D_f = 2.1$.

6. Drilling records show that the steam entries in each well are clustered in bands a few hundred feet wide spaced at about 1000 foot intervals.

7. Drilling rate records also show a fractal clustered structure having a Hurst exponent of 0.56. We make the assumption that drilling rate is correlated with fracture density since it does not appear to be sensitive to variations in graywacke lithology. However no direct correlation was observed between increases in drilling rate and steam entries. Rather, steam entries tend to cluster in broad zones of rapid drilling which are several hundred feet wide.

The picture of the reservoir which emerges is one in which the steam is stored and transported the multiply fractured conduits several hundred feet wide and spaced roughly one thousand feet apart. This scale is on the order of the regional faulting pattern in Fig. 3 which suggests that the steam conduits are the major shear fractures in the reservoir. Smaller fractures (many of which are tensile) appear to be sealed both in surface exposures of the reservoir rock and in cores take directly from the reservoir.

References:

Acuna, J.A., Ershaghi, I. and Yortsos, Y.C., "Fractal Analysis of Pressure Transients in the Geysers Geothermal Field," paper presented at the 1992 Stanford Geothermal Workshop.

Barton, C.C., and Hsieh, P.A., A Field Guide for the 1989 International Geologic Congress, A.G.U. (1989).

Barton, C.C., "Fractal Analysis of the Sealing and

Spatial Clustering of Fracture Fractals and Their Use in the Earth Science" 1992. (C.C. Barton, P.R. La Pointe, ed. GSA Memoir, 1992).

Hebein, J.J., Geothermal Resources Council Bulletin **14**, #6, 13-16, (1985).

Hewett, T., paper SPE 15386 presented at the 61st Annual Fall meeting of SPE, New Orleans, LA, October 5-8, 1986.

Leary, P., "Deep Borehole Log Evidence for Fractal Distribution of Crystalline Rock Fractures Over 1 M to 1000 M Scale Length" Geo. J. Int. (in press 1992).

Mukhopadhyay, S. and Sahimi, M., "Computer Simulation of Heat Transfer and Two-Phase Flwo in a Fractal Fracture Network" paper presented at 1992 Stanford Geothermal Workshop.

Thomas, R.P., Chapman, R.H. and Dykstra, H., "A Reservoir Assessment of The Geyers Geothermal Field" California Division of Oil and Gas, Publication No. TR27, 1981.

Warren, J.E. and Root, P.J., J. Geophys. Res., **91**, 1921-1926 (1986).

Zimmerman, R., Chen, G. and Bodvarsson, G., "A Dual-Porosity Reservoir Model with an Improved Coupling Term" paper presented at 1992 Stanford Geothermal Workshop.

PROCEEDINGS, Seventeenth Workshop on Geothermal Reservoir Engineering
Stanford University, Stanford, California, January 29-31, 1992
SGP-TR-141

FRACTAL ANALYSIS OF PRESSURE TRANSIENTS IN THE GEYSERS GEOTHERMAL FIELD

J. A. Acuna, I. Ershaghi and Y. C. Yortsos

Petroleum Engineering Program
Chemical Engineering Department
University of Southern California
Los Angeles, CA 90089-1211

ABSTRACT

The conventionally accepted models for the interpretation of pressure transient tests in naturally fractured reservoirs usually involve simplistic assumptions regarding the geometry and transport properties of the fractured medium. Many single well tests in this type of reservoirs fail to show the predicted behavior for dual or triple porosity or permeability systems and cannot be explained by these models. This paper describes the application of a new model based on a fractal interpretation of the fractured medium. The approach, discussed elsewhere [2], [6], is applied to field data from The Geysers Geothermal Field. The objective is to present an alternative interpretation to well tests that characterizes the fractured medium in a manner more consistent with other field evidence. The novel insight gained from fractal geometry allows the identification of important characteristics of the fracture structure that feeds a particular well. Some simple models are also presented that match the field transient results.

INTRODUCTION

Pressure transient responses predicted by the dual or triple porosity models [1], [18], [19] are sometimes not observed in actual transient tests in naturally fractured reservoirs. In some cases the observed behavior is similar to that of a single fracture cutting the wellbore. The well response is characterized by parallel linear plots of pressure and pressure derivative vs time on a log-log scale with a slope m between 0 and 0.5 and a separation equal to $\log(\frac{1}{m})$ as shown in Figure 1. Such behavior is ordinarily explained by assuming the existence of a single fracture of finite conductivity intersecting the well, [3], [8]. This type of response has also been explained as a transition between single infinite conductivity fracture flow ($\frac{1}{2}$ log-log slope) and radial flow (semilog straight line) in the parallelepiped reservoir model [9], [11]. Another case often observed involves pressure derivative plot with a negative slope not large enough to be interpreted by a spherical flow regime. In systems where individual wells are connected to networks of fractures, alternative conceptual models need to be proposed. The purpose of this investigation was to examine the feasibility of using fractal geometry

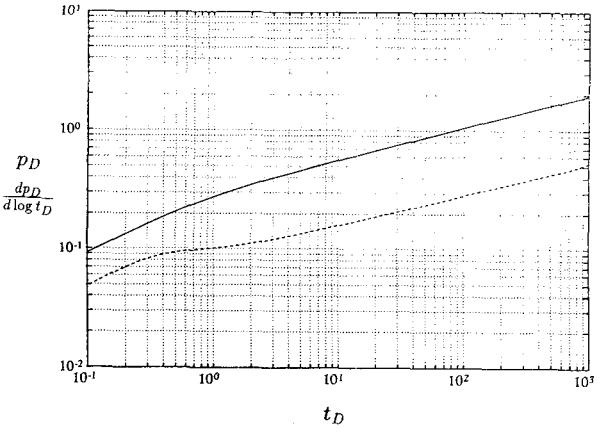

Figure 1: Pressure (solid) and pressure derivative (dashed) for a fractal fracture network $m = 0.27$ ($\delta = 0.73$)

to interpret the above responses in a manner consistent with the expectation that networks of fractures dominate the flow behavior.

The application of fractal geometry to the analysis of pressure transient tests resulted from a direct extension of novel discoveries in diffusion in disordered media and fractal objects [13], [15]. It has been found that the diffusion process, which also governs pressure transient tests, occurs in a unexpected fashion when the medium is highly disordered or fractal. Such phenomena, classified in general as "anomalous diffusion" [13], have helped in explaining many slow diffusion processes poorly understood only a few years ago.

The application of these concepts to pressure transient testing in fractal fractured systems was proposed by Chang and Yortsos [6], who described the general theoretical formalism. The theory was tested using numerical models of fractured networks in the recent work of Acuna and Yortsos [2]. A key feature of a fractal transient response is that the log-log plot of pressure derivative versus time is linear. The observed slope depends on the dimensionality and ranges between -0.5 and 0.5. Where -0.5, 0 and 0.5 correspond to spherical, radial and linear flow respectively. When the slope is between 0 and 0.5, the pressure curve is parallel to the pressure derivative curve, making the identification easier. Regardless of dimensionality, all responses can

be considered as particular cases of a general solution.

Although theory and numerical examples have been presented elsewhere [2], [6], [10], practical applications to real well tests have been limited [5]. The Geysers Geothermal Field, whose characterization is still elusive, represents an excellent test case to explore the feasibility of a fractal structure. In particular, the nature of drilling fluid, air, used in the bulk of the fractured system helps in examining fractures relatively free of near-wellbore damage.

THEORETICAL BACKGROUND

The finite conductivity single fracture model [3], [8] predicts that at early times the pressure behavior can be approximated by the expression

$$p \approx At^m \tag{1}$$

where A is a constant. From (1) follows that the log-log plots of pressure and pressure derivative vs time will be parallel with slope m and separated by a distance equal to $\log(\frac{1}{m})$ (or $\frac{p}{t\frac{\partial p}{\partial t}} = \frac{1}{m}$). Many wells in naturally fractured reservoirs behave in this fashion although the existence of only a single fracture as cause of that behavior is not supported by other wellbore or reservoir measurements. The fractal model discussed below shows how a particular fracture network can also be responsible for that behavior.

When a fractured medium is highly disordered and fractal, the single-phase pressure transient of individual wells differ significantly from the homogeneous radial flow case [6]. The theoretical, ideal response would be described as follows: In a perfect fractal object of infinitely many generations of fractures, the mass density of any arbitrary cluster of radius r around an arbitrary point decreases in a power law fashion with respect to the distance r. The exponent of the power law is $D-d$ where D is the mass fractal dimension of the object and d the embedding dimension (2 for two-dimensional case). However, when the object has finite size, deviations with respect to this behavior are expected and will occur, although the average over many origins is expected to give the same power law [12], [14], [15]. Consider a fractal network of fractures. The "mass density" at any given radius corresponds to the average porosity at that radius r, defined as the total void volume divided by the total volume at radius r. This porosity will therefore change in a power law fashion with respect to r.

$$\phi(r) = \phi_0(\frac{r}{r_0})^{D-d} \tag{2}$$

where ϕ_0 is a constant.

Using the same reasoning, we could expect the sample permeability to also vary with r. For example, if steady-state flow across a sphere of radius r occurs, the corresponding single-phase permeability can be expressed as

$$K(r) = K_0(\frac{r}{r_0})^{D-d-\theta} \tag{3}$$

where D and θ are fractal parameters, r_0 is the minimum size considered in the network (smallest fracture) and K_0 is a constant.

These values of porosity and permeability are not point values, as traditionally interpreted, but sample (macroscopic) values over that radius r. For instance, the point value for porosity is either 0 or 1 depending on the point being on the matrix or the fracture. Here, we are concerned with the macroscopic values of these properties. The conductivity and storativity terms KA and ϕA are obtained by multiplying equations (2) and (3) by Br^{d-1}, where B is a constant. As can be observed, conductivity and storativity are power law functions of radius with different exponents. The diffusivity η is, therefore, dependent on the radius as $\eta \propto r^{-\theta}$. This variation of diffusivity with radius gives rise to several phenomena referred in general as "anomalous diffusion" [13], [15]. Diffusion over fractal objects is "anomalous" in that the standard diffusivity equation may not be used. The most rigorous alternative is to consider a Green's function approach, based on which solutions can be readily constructed [7]. A simplification of that approach at late times is a diffusivity equation, but with properties that vary spatially according to (2) and (3). Then, as shown in [6] (see also [7]), one obtains

$$\frac{\partial^2 p}{\partial r^2} + \frac{D-\theta-1}{r}\frac{\partial p}{\partial r} - r^{\theta}\frac{\partial p}{\partial t} = 0 \tag{1}$$

with boundary conditions that p vanishes as $r \to \infty$, and that constant flow rate applies at the wellbore

$$\lim_{r\to 0}(r^{D-\theta-1}\frac{\partial p}{\partial r}) = -1 \tag{2}$$

For this problem a similarity solution was obtained [6], based on which the pressure at the well p_w, after a short time, obeys the power law behavior

$$p_w(t) = C + \frac{(2+\theta)^{2(1-\delta)}}{\Gamma(\delta)(2+\theta-D)}t^{1-\delta} \tag{3}$$

where $C = \frac{\Gamma(\delta-1)}{\Gamma(\delta)(2+\theta)}$ is constant with respect to time and $\delta = \frac{D}{2+\theta}$. The constant term C becomes negligible with respect to the time dependent term when $\delta < 1$. The log-log plots of pressure and pressure derivative versus time appear as two straight parallel lines after sufficient time. When $\delta > 1$ (dimensionality greater than 2), however, the constant term becomes the asymptotic value of the pressure. In such cases only the derivative plot will show the log-log linear behavior with the pressure curve approaching asymptotically a constant value at late times. Equation (3) is valid for a single well test and it cannot be used for multiple well tests, where recourse to the Green's function formalism must be made [7]. For $\delta = 1$ the traditional exponential integral solution arises.

An alternative derivation for a similar problem was presented by Barker [4]. In his derivation conductivity

and storativity were assumed to be power law-dependent on the radius with the same exponent. Theoretically, this may only result if we assume that the area perpendicular to flow changes in a power law fashion. Doe [10] attempted to rationalize such a variation in flow area by proposing drainage volumes with unusual shapes. In the Chang and Yortsos [6] notation, this assumption is equivalent to setting the parameter $\theta = 0$, a value characteristic of perfectly connected networks. The diffusivity η is therefore constant and normal diffusion should be expected. According to Barker's solution, the slope of the log-log plot of pressure versus time must approach a constant value equal to $1 - \frac{D}{2}$. This was not observed in our numerical simulations, neither in the simulations by Polek et al. [16], instead, the value obtained from flow simulations is consistently lower than the geometric fractal dimension. The results are, however, entirely consistent with Chang and Yortsos derivation. Although Barker's theory may be appropriate for certain objects (yet to be precisely described), it is certain that it cannot be applied to describe flow in fractals.

According to Chang and Yortsos, for a two-dimensional embedding medium, the slope m of both the pressure and the pressure derivative in log-log plots is given by $m = 1 - \delta = 1 - \frac{D}{2+\theta}$. The two parameters D and θ suffice to formulate the power-law variation. A type of system that gives rise to the above variation is a network of fractures with fractal properties. Indeed, it was shown numerically [2] that in such a fractal network of fractures, the two parameters D and θ have real physical meaning and that parameters, such as permeability and fracture porosity are power-law dependent on the radius.

Parameter D is the mass fractal dimension of the network, a strictly geometric property. It is measured by plotting the cumulative "mass" or length of fractures (for fractures of the same width) contained inside a circle of radius r versus r. A linear log-log plot of mass versus radius indicates the existence of a fractal structure with an exponent identical to D. Parameter θ, on the other hand, is a property depending on both the geometry and the transport properties of the medium. In a given network, it can be measured by taking a large number of random walks of t steps each and by calculating the average square distance of the walker from the origin. Contrary to the normal situation of Euclidean geometry networks, where $< r^2 > \propto t$, fractal systems exhibit slowdown, $< r^2 > \propto t^{\frac{2}{2+\theta}}$ [13], [15], a key feature in the process of anomalous diffusion.

When dealing with transient tests from a single well only, the information at the producing well can only determine the ratio $\delta = \frac{D}{2+\theta}$. In other words, any combination of D and θ that results in the same value of δ, will produce the same slope in the pressure derivative curve. To complete the reservoir characterization, therefore, additional information is needed.

APPLICATION TO THE GEYSERS DATA

To demonstrate the feasibility of such a model we ideally need a naturally fractured reservoir, where drilling circulation losses and fracture damage are minimal. The Geysers Geothermal Field with its air drilled wells fit those requirements quite adequately.

According to [6], given sufficient time in a fractal reservoir with dimensionality D less than 2, the log-log plots of pressure and pressure derivative versus time should appear as two straight, parallel lines. Equation (6) as well as our experience with synthetic numerical networks [2] has shown that the linearity sets in earlier in the pressure derivative curve (In a way, the same is true for a homogeneous radial system ($D = 2$ and $\theta = 0$) where the asymptotic slope of $1 - \delta = 0$ is achieved faster by the pressure derivative curve). When dealing with real systems, however, finite size effects are always important. These effects are of course absent from the theoretical analysis. Thus, at early times, a real system would respond only to a few fractures of a certain finite size around the test well. The effect is mathematically equivalent to a skin factor in the pressure curve. This skin factor together with any constant contribution to the pressure response would be filtered out by the process of differentiation, thus, rendering the slope of the derivative curve much more useful than that of the pressure curve. The noise in the derivative curve is however a problem. The separation $\log(\frac{1}{m}) = \log(\frac{1}{1-\delta})$ of the two lines is invaluable in helping to identify the correct value of the slope m for dimensionality less than 2. At late times, however, boundary conditions begin to influence the data and the curves deviate from the asymptotic trend. If enough time is available in the "infinite acting" period, the pressure curve reaches a slope equal to that of the pressure derivative. For dimensionality greater than 2, the parallel slope behavior is observed only if the pressure is replaced by the term $C - p_w(t)$ where C is the asymptotic constant value of the pressure at very long time.

If additional information suggest that a network of fractures is connected to the well, the approaching of the asymptotic straight lines should be good evidence to consider power-law variation in porosity and permeability

These concepts are illustrated in Figure 2 which shows a buildup test for well A at The Geysers. Both pressure and pressure derivative plots are linear and parallel for a certain period of time, before boundary effects become significant. The slope measured from the derivative curve is $1 - \delta = 0.40$, suggesting a ratio $\delta = \frac{D}{2+\theta} = 0.60$. From our experience with synthetic fractal fracture networks, we found that the parameter θ ranges between 0 and 0.5 for various networks. If we accept that the real fracture network above behaves similarly to our artificial networks [2], possible values of D predicted are in the range $1.20 < D < 1.50$, indicating a sparse network of fractures with radial fractal dimension D in the specified range. A network with

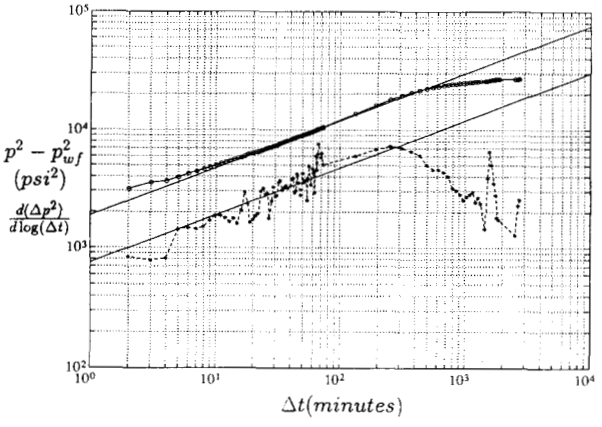

Figure 2: Pressure (o-solid), pressure derivative (*-dashed) and best fit power law ($\delta = 0.60$) at Well A.

such characteristics will be presented below.

Figure 3 shows build-up test data for another field test at location B. Pressure and pressure derivative curves are shown, the associated best fit value of δ being equal to 0.84 for the early part and it changes slightly to 0.87 for the later data. This change may be due to variations in the fractal structure or to boundary effects. Again using the previous estimates, the expected values for the mass fractal dimension D lie in the interval $1.68 < D < 2.0$. Although Figures 2 and 3 could be explained by the response of a single finite conductivity fracture model, all other available evidence such as steam entries, outcrops mapping [17], mud logs, etc, points out to the existence of a network of fractures,

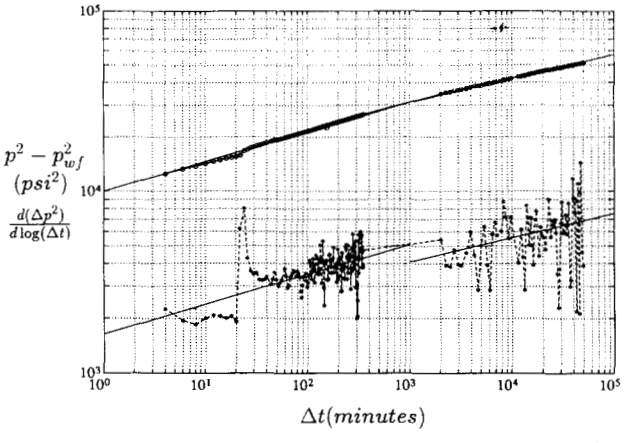

Figure 3: Pressure (o-solid) and pressure derivative (*-dashed) and best fit power law ($\delta = 0.84$ and 0.87) at Well B.

rather than one single fracture feeding the well. The fractal model proposed above gives the most plausible explanation of why a pressure transient response of wells in The Geysers resemble those of hydraulically fractured wells. We should point out that the significance of the need for a proper value of D cannot be overemphasized. For example, the resulting fracture porosity volume in a drainage volume of a disk of radius r_e and constant thickness would scale as $\phi_0 r_e^D$ which is a factor r_e^{D-2} smaller than if estimated at constant porosity.

Values $\delta = 1$ are indicative of a homogeneous radial system, as in the case of well C presented in Figure 4. Of course, there is always the possibility of D being different than 2, implying a power-law varying porosity. For example this may happen when $D = 2+\theta$ as can be corroborated from equation (3). Because the value of θ is always positive, the "homogeneous response" would

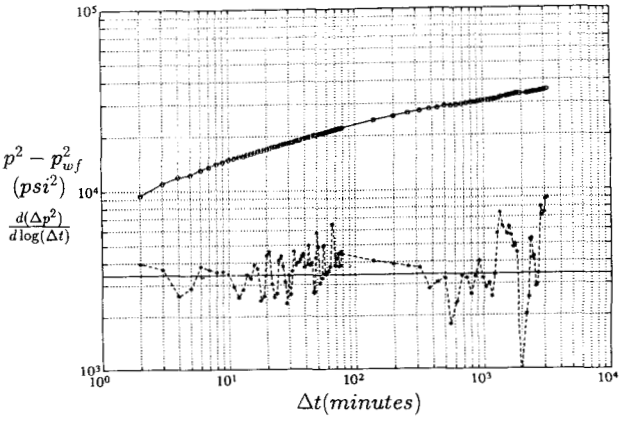

Figure 4: Pressure(o-solid), pressure derivative (*-dashed) and best fit power law ($\delta = 1.0$) at Well C.

require $D > 2$. This is not possible for a fractal embedded in a two-dimensional space, but it is for a finite size network as explained below.

The case $\delta > 1$ (negative pressure derivative slope) such as shown for well D in Figure 5 deserves particular attention. Because $\theta > 0$, values of $\delta > 1$ imply $D > 2$, namely the fracture structure is much more dense, the system features being intermediate between two and three-dimensional structure. The parallel plots will not be observed but the slope of the pressure derivative equals $1 - \delta$. The pressure curve itself equals a constant C minus a power-law term with the same exponent than the derivative curve. To improve the estimation of the slope m we draw a straight line $(C - p_w(t))$ parallel to the derivative plot separated a distance equal to $\log(\frac{-1}{m})$ $(m < 0)$, as shown in Figure 5. The value of C can be calculated as twice the value of the pressure at the intersection between the pressure curve and this parallel line. This simple geometric construction can be verified using equation (6). A trial an error approach may be necessary. In this case, the flow can be interpreted as intermediate between radial and spherical types.

We should point out that a value of the mass exponent $D > 2$ implies that the fracture mass increases with the radius with an exponent greater than 2. A network with dimensionality greater than 2 has this kind of variation. A finite 2-D network, however, can also give this type of response if the porosity increases with

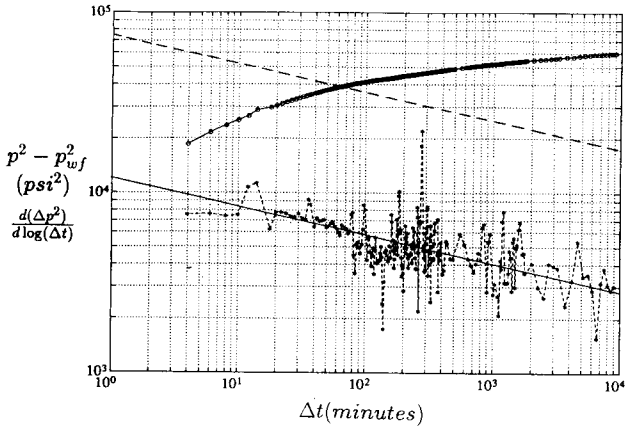

Figure 5: Pressure (o-solid), pressure derivative (∗-dashed) , best fit power law for derivative (solid) and $C - p_w(t)$ (dashed) at Well D. ($\delta = 1.16$)

radius. Although this is not possible for infinite fractal objects, it is, nonetheless, conceivable for finite size networks.

For the separate estimation of D and θ, additional information is needed. This information could be the response at observation wells located at the Euclidean distance r. The parameters could be estimated using the results of [6] and [7]. An important practical problem, however, is that a given point at a distance r is usually not representative of the behavior of every point at that same distance. The fractal parameters reflect an overall behavior, therefore, for a good estimate in a particular well, finite size effects must be minimal.

As in every inverse problem of this type, including problems in Euclidean homogeneous media, there is an inherent non-uniqueness associated with single point measurements. Thus, even though the values of D and θ may be available, the precise structure of the reservoir is unavailable, different relations giving rise to the same single-well result. Nevertheless, by applying the numerical techniques developed in [2], we may get a qualitative understanding of the structure of the network that can give rise to the responses shown above (e.g. for wells A and B).

Although we have the capability of creating more natural-looking networks, such as the ones presented in [2], there is no particular reason to include additional geometric characteristics. In the absence of other information, therefore, these models have a regular, somewhat unrealistic appearance. The networks presented do not contain many generations of fractures, therefore, the fractal mass variation with respect to radius is not expected to be observed in every point. To overcome this problem, these network are constructed in such a way that those power law variations hold for the point where the well is. This type of behavior would appear for any point of the network if the number of generations is substantially increased, something we are not able to do due to computer limitations.

Figure 6 shows a realization corresponding to a radial fractal dimension equal to 1.26. This is one of infinitely many networks that can be generated with the same radial fractal dimension. It is the presence of gaps of a given size at a given distance that controls the value of D. Because we do not have very good control on the

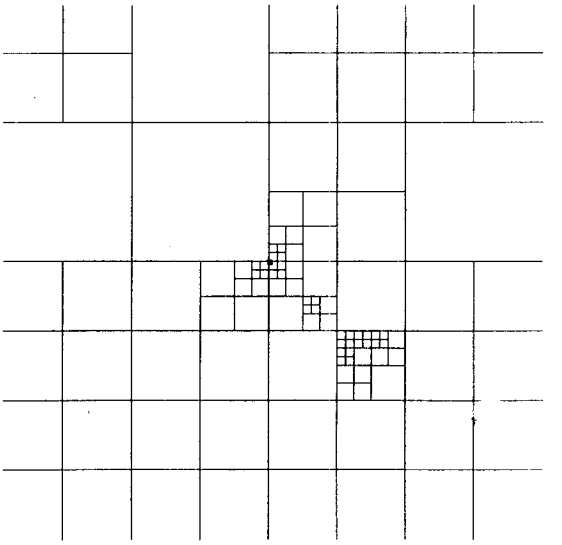

Figure 6: Synthetic network with the pressure transient response similar to that of Well A ($D = 1.26$).

value of θ, except for the fact that its range is fairly limited, a trial and error approach is necessary in order to obtain the desired value of δ (here equal to 0.60). Likewise, Figure 7 is a synthetic network whose transient response is similar to Well B. Again, this one of many possible realizations

Acceptance of a fractal model in the particular drainage area of a well implies a porosity distribution that is power-law dependent on the distance from the well, as well as within any other test volume where the fractal description applies. In such systems, significant consequences on the estimation of the pore volume associated with the well and on the expected behavior of heat recovery by cold water injection can be expected.

CONCLUDING REMARKS

We have presented an interpretation of pressure transient tests of certain wells in The Geysers Geothermal Field that behave similarly to a single fracture of finite conductivity or that tend to resemble spherical flow. Our fractal model shows how a network of fractures with some special characteristics can explain such response. This explanation appears more consistent with other field evidence [17] as well as with the concept of fracturing in naturally fractured systems.

Several wells analyzed in The Geysers Field show characteristics of fractal behavior, although the power-

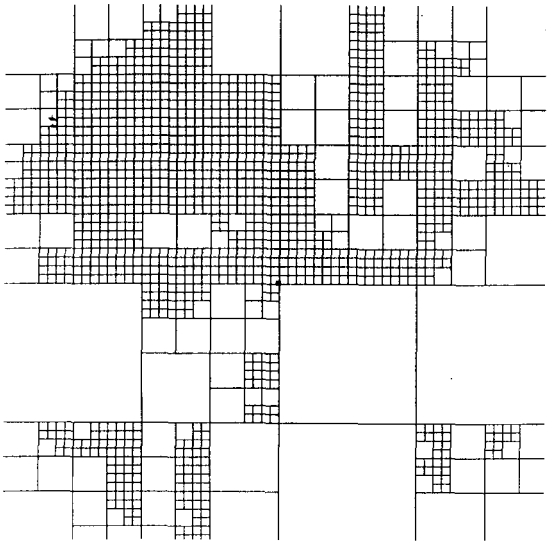

Figure 7: Synthetic network with the pressure transient response similar to that of Well B ($D = 1.84$).

law exponents are different at different locations. It was found in our previous sensitivity studies [2], and it is also evident by a casual inspection of Figures 6 and 7 that the position of the well may affect substantially the characteristics of the transient response, provided that finite size effects are important. Such would not have been the case if the upper and lower cutoffs (which correspond to the largest and smallest sizes for Figures 6 and 7, for instance),were greatly separated. Real systems, however, involve cutoffs of finite values, thus making the pressure response site specific.

This explanation can be offered to interpret why every well in The Geysers Geothermal Field does not respond in the same way. Another distinct possibility is that the true fractal parameters do vary in space as a result of different structure. Having different fractal parameters for individual wells does not invalidate the approach. On the contrary, it allows the determination of the individual parameters for each well. A true fractal reservoir would be one of infinite size in which well defined power laws for the permeability and porosity would be asymptotically approached, once the local variations at small radii have dissipated. From the limited pressure transient tests available to us we do not observe a tendency towards a single set of fractal parameters for The Geysers Field. Therefore, a single model cannot be proposed in which the entire reservoir is a single fractal object. On the other hand, the local fractal information derived from each well can be used to improve the global description of the reservoir. Future progress of this research is aimed at extracting the appropriate power-law variations for each well and to arrive at a unified model.

NOMENCLATURE

d = Euclidean dimension of medium in which fractal object is embedded
D = mass fractal dimension
K = permeability at radius r, $[L^2]$
m = slope in a log-log plot
p = pressure, $[ML^{-1}T^{-2}]$
r = radial distance, $[L]$
t = time, $[T]$
η = hydraulic diffusivity $[L^2T^{-1}]$
$\Gamma(x)$ = Gamma function
ϕ = porosity
θ = fractal exponent

ACKNOWLEDGMENTS

Support for this study was provided by the Geothermal Division of the U.S. Department of Energy through the Lawrence Berkeley Laboratory and the Center for Study of Fractured Reservoirs at the University of Southern California. The authors thank Marshall Reed from DOE for his encouragement. The first author also acknowledges the support of the Instituto Costarricense de Electricidad during his graduate work at the University of Southern California.

References

[1] D. Abdassah and I. Ershaghi. Triple-porosity systems for representing naturally fractured reservoirs. *SPE Transactions Formation Evaluation*, **281**:113, 1986.

[2] J. A. Acuna and Y.C. Yortsos. Numerical construction and flow simulation in networks of fractures using fractal geometry. *SPE paper 22703 presented at the 66th SPE Technical Conference and Exhibition,October 6-9, Dallas TX*, 1991.

[3] R. G. Agarwal, R.D. Carter, and C.B. Pollock. Evaluation and performance prediction of low-permeability gas wells stimulated by massive hydraulic fracturing. *SPE Reprint Series*, **14**:172, 1980.

[4] J. A. Barker. A generalized radial flow model for hydraulic tests in fractured rock. *Water Resources Research*, **24**:1796, 1988.

[5] R.A. Beier. Pressure transient field data showing fractal reservoir structure. *SPE Paper 20582 presented at the 65th Annual SPE Fall Meeting, New Orleans, LA, Sept. 23-26*, 1990.

[6] J. Chang and Y. C. Yortsos. Pressure transient analysis of fractal reservoirs. *SPEFE*, **289**:31, 1990.

[7] J. Chang and Y. C. Yortsos. Comments on pressure transient analysis of fractal reservoirs. *Submitted SPEFE*, 1992.

[8] H. Cinco, F. Samaniego, and N. Dominguez. Transient pressure behavior for a well with a finite-conductivity vertical fracture. *SPE Journal*, **18**:253, 1978.

[9] H. Cinco-Ley, M. Economides, and F. Miller. A parallelepiped model to analyze the pressure behavior of geothermal steam wells penetrating vertical fractures. *SPE paper 8231, presented at the 54th Annual SPE Technical Conference and Exhibition, September 23-26, Las Vegas NV*, 1979.

[10] T. Doe. Fractional dimension analysis of constant pressure well tests. *SPE paper 22702, presented at the 66th Annual SPE Technical Conference and Exhibition, October 6-9, Dallas TX*, 1991.

[11] M. Economides, D. Ogbe, F. Miller, and H. Ramey. Geothermal steam well testing: State of the art. *SPE paper 9272, presented at the 55th Annual SPE Technical Conference and Exhibition, September 21-24, Dallas TX*, 1980.

[12] J. Feder. *Fractals.* Plenum Press, New York, 1988.

[13] S. Havlin and D. Ben-Avraham. Diffusion in disordered media. *Advances in Physics*, **36**(6):695, 1987.

[14] B.B. Mandelbrot. *The Fractal Geometry of Nature.* W.H. Freeman, New York, 1983.

[15] R. Orbach. Dynamics of fractal networks. *Science*, **231**:814, 1986.

[16] J. Polek, K. Karasaki, J.C.S. Long, and J. Barker. Flow to wells in fractured rock with fractal structure. *Earth Sciences Division Annual Report 1989 Lawrence Berkeley Laboratory*, page 74, 1990.

[17] C.G. Sammis, Lin-Ji An, and I. Ershaghi. Three dimensional characterization of the fracture network at the Geysers Geothermal Field. *Paper presented at the 17th Annual Workshop Geothermal Reservoir Engineering, January 29-31, Stanford, CA*, 1992.

[18] T. Streltsova. Well pressure behavior of a naturally fractured reservoir. *SPE Transactions*, **275**:769, 1983.

[19] J.E. Warren and P.P. Root. The behavior of naturally fractured reservoirs. *SPEJ*, 3:245, 1963.

PROCEEDINGS, Seventeenth Workshop on Geothermal Reservoir Engineering
Stanford University, Stanford, California, January 29-31, 1992
SGP-TR-141

VAPOR-LIQUID COUNTERFLOW IN HETEROGENEOUS POROUS MEDIA

A.K. Stubos, C. Satik and Y.C. Yortsos

Department of Chemical Engineering
Petroleum Engineering Program
University of Southern California
Los Angeles, California 90089-1211

ABSTRACT

Based on a continuum description, the effects of permeability heterogeneity on steady state, countercurrent, vapor-liquid flow in porous media are analyzed. It is shown that the capillary heterogeneity induced acts as a body force, that enhances or diminishes gravity effects on heat pipes. Selection rules that determine the particular steady states reached in homogeneous, gravity-driven heat pipes are formulated. It is shown that the "infinite" two-phase zone terminates only if a substantial change in permeability occurs somewhere in the medium. The two possible sequences that result, namely liquid - liquid dominated - dry or liquid - vapor dominated - dry find applications in geothermal systems. Finally, it is shown that weak heterogeneity affects only gravity-driven flows, but stronger variations in permeability give rise to significant capillary effects.

INTRODUCTION

Countercurrent vapor-liquid flows in porous media have been the subject of many recent studies due to their relevance in geothermal processes, boiling, thermal methods for oil recovery and nuclear waste disposal [1-5]. Of particular interest are steady state heat pipes driven by gravity. In theory, when the system is homogeneous, an infinitely long two-phase zone of nearly constant saturation develops if the heating rate is low enough (below a critical value). Two such states are predicted, one coresponding to low liquid saturation (vapor-dominated, VD) and one corresponding to high liquid saturation (liquid-dominated, LD). In a recent note [6], using the detailed analysis described in a previous paper [7], we have proposed that the selection of the particular solution only depends on the past history of the system. For instance, in boiling applications which involve bottom heating, it is the LD branch that is followed.While, in the case of condensation of a superheated vapor (top cooling), it is the VD branch that is selected. In either of the two cases, capillarity is necessary to connect the constant saturation profiles to the subcooled or dry regions, respectively.

In practice, because of finite size, the two-phase zone must terminate at a finite location, thus, the "infinite" extent predictions of the heat pipe formalism cannot hold indefinitely. Termination of the two-phase zone must be obtained by smoothly merging the two-phase region with a subcooled liquid or a dry region, in the LD or VD cases, respectively (otherwise, non-zero vapor and liquid fluxes would exist at the impermeable boundary of the medium [6]). Analogous problems arise in the gravitational stability of counterflow vapor-liquid systems, when a vapor-rich region underlies a subcooled liquid layer. Even if we accept the suitability of the various base states used in the analysis [8,9] (the validity of which is questionable), the present consensus is that unconditional stability is possible only if a heterogeneity is present somewhere in the two-phase region.

Heat pipe instability, but in the different context of the sensitivity of steady, 1D profiles to the boundary conditions, was considered in a recent study [10]. It was suggested that, under certain conditions, a VD solution is unconditionally "unstable" and must revert to a "stable" LD configuration, or vice versa, if the boundary conditions are reversed. While not immediately apparent, this problem is really related to heterogeneity, as shown below. One should recall that boundary end effects in immiscible displacement can be considered as special cases of heterogeneity, when the change in permeability is abrupt and very large [11].

Effects of heterogeneity on vapor-liquid concurrent flow were studied in [12] where previous works on the steady state, two-phase flow of non-condensing fluids [11] were generalized. With the exception of a rather incomplete study [13], however, heterogeneity effects on countercurrent vapor-liquid flows have not been addressed in much detail and they are currently poorly understood. Cases in point are the previously mentioned questions on the termination of the theoretically "infinite" two-phase zone, on the gravitational instability and on the sensitivity to boundary conditions. This paper aims at resolving some of these issues. We investigate effects of heterogeneity under various configurations. We find that permeability (capillary) heterogeneity acts in reality as a body force (e.g. gravity), with the

important additional property that it is also spatially varying. Heterogeneity may thus enhance or counterbalance gravity effects, depending on magnitude, form and direction of change.

This paper is a brief summary of results contained in [14]. It is organized as follows: We first study the simpler, but quite useful, horizontal case. Then, we apply the results obtained to interpret effects of gravity when the heat flux is below critical. Next, we address problems involving both heterogeneity and gravity at conditions of slow and fast permeability variation. Throughout the paper, the formalism of [7] is followed.

FORMULATION

We proceed with the assumption that the main heterogeneous variable is permeability [11,12]. An important parameter which is affected in the present case of 1D counterflow is capillary pressure. This is a result of the Leverett J-function representation:

$$P_c = \frac{\sigma J(S)}{\sqrt{k}}$$

The function J (as well as the relative permeabilities) may also be taken as weakly varying, although it is the dimensional $\sqrt{k}$-dependence that basically controls the capillary variation (see also [11] for a more detailed discussion).

In the absence of heat conduction, we can formulate the problem in a straightforward fashion, because saturation and temperature are decoupled from each other and the solution is obtained by simple means. Following [7], a straightforward manipulation of mass, momentum and energy balances yields the simple equation:

$$\tau\, J'\frac{dS}{d\xi} - J\frac{d\tau}{d\xi} = \omega\frac{(k_{r\ell} + \beta k_{rv})}{k_{r\ell}k_{rv}} + sin\theta\ \tau^2 \qquad (1)$$

Here $\tau \equiv \sqrt{k/k^*}$ is the heterogeneity variable which is spatially varying, k^* denotes a constant reference permeability and superscript $'$ indicates derivatives with respect to S. The notation is identical to [7] except for τ, which here does not denote temperature. The coordinate ξ increases in the direction from the liquid to the vapor, such that the liquid velocity is positive, while the dimensionless heat flux $\omega = q\mu_v/k^* L_v g\Delta\rho\rho_v$ is normalized with a reference permeability. In this notation, therefore, different permeability regions have the same value of ω, but not the same critical values (see also below). Equation (1) must be generally solved numerically. Preliminary insight can be obtained by an analytical solution, which is possible for a special case in horizontal counterflow.

A. Horizontal Counterflow

In a horizontal system ($\theta = 0$) counterflow is driven by capillarity only [5]. It is shown in [14] that useful results are obtained in the special case when τ is piecewise linear

$$\tau = \begin{cases} 1 \ ; & \xi < 0 \\ a\xi + 1 \ ; & 0 < \xi < d \\ \tau_+ \ ; & d < \xi \end{cases} \qquad (2)$$

where $\tau_+ \equiv ad + 1$. Two different cases are considered:

1. $a > 0$ (*Figure 1a*)

Here, the permeability is increasing, and we obtain:

$$\int_{S_o}^{S} \frac{k_{r\ell}k_{rv}J'dS}{\omega(k_{r\ell} + \beta k_{rv}) + k_{r\ell}k_{rv}a\ J} = \frac{1}{a}ln(a\xi + 1) \qquad (3)$$

where S_o is the saturation at 0 (presently unknown). Because of $a > 0$, the saturation decreases steadily also within the region of heterogeneity (Figure 1). The particular saturation profile depends on the conditions imposed away from the heterogeneity. If the location of the subcooled liquid boundary on the left is known, then integration occurs from left to right, and S_o, S_1 etc. can be determined sequentially (see [14]). The reverse applies if it is the location of the dry region on the right which is known.

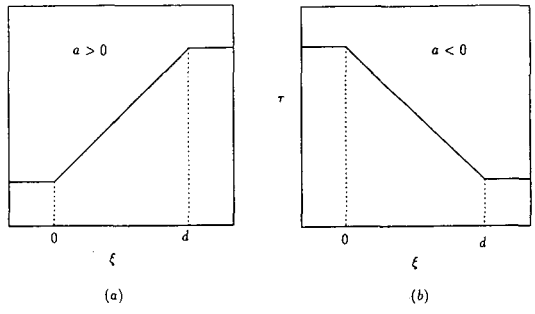

Fig. 1. Schematic of a special heterogeneity profile: (a) Permeability increase: (b) Permeability decrease.

Of special interest is the case of a sharp discontinuity ($a \gg 1$). Then (3) yields

$$\frac{J(S_1)}{J(S_o)} = \tau_+ = \sqrt{\frac{k_1}{k_o}} \qquad (4)$$

which is nothing else but the condition of constant capillary pressure, implying a saturation jump across the discontinuity. This is the static (no flow) condition, which differs from the case $a < 0$, as shown below, as well as from the case of concurrent flow [11]. In the latter, a build-up of the wetting phase saturation is necessary before a high permeability region is entered.

2. $a < 0$ (*Figure 1b*)

While the previous are straightforward, non-trivial effects arise in the case of a permeability decrease. When $a < 0$, the denominator in (3) may vanish, if ω is small enough. For this to occur, the following equation must

admit a real solution:

$$\omega = -a\ J\frac{k_{r\ell}k_{rv}}{k_{r\ell}+\beta k_{rv}} \tag{5}$$

The RHS of (5) is schematically plotted in Figure 2. We note that there exists a critical value

$$\omega_{cr,H} = (-a)\max_{S}\left(\frac{Jk_{r\ell}k_{rv}}{k_{r\ell}+\beta k_{rv}}\right) \tag{6}$$

above which a real solution to (5) does not exist. In dimensional notation we obtain:

$$q_h \propto \frac{\sigma L_v \rho_v}{\mu_v}\left(-\frac{d\sqrt{k}}{dx}\right) \tag{7}$$

Thus, sharper changes in permeability result into larger critical flux values. The system response depends on the relative value of ω:
(i) For $\omega > \omega_{cr,H}$, equation (5) has no solution. Then, the effect of heterogeneity is identical to the previous ($a > 0$), as schematically plotted in Figure 2.
(ii) For $\omega < \omega_{cr,H}$, on the other hand, equation (5) has two roots, denoted by S_{VH} and S_{LH} ($0 < S_{VH} < S_{LH} < 1$), in very close analogy with the vapor-dominated and liquid-dominated regimes, respectively, of gravity-driven heat pipes. The similarity with the latter is very interesting. Indeed, as in heat pipes, the saturation integral diverges at the two saturations, thus nearly flat saturation profiles (either VD or LD) develop to span the region of heterogeneity. Here, however, it is capillary heterogeneity, with the permeability decreasing in the direction of liquid flow, and not gravity, that sustains the constant saturation profiles.

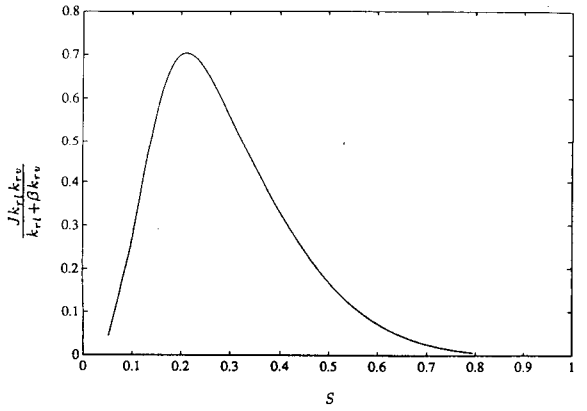

Fig. 2. The capillary heterogeneity function ω(S).

Consider, integration from the vapor side (Figure 3). This requires that superheated vapor exists somewhere on the right so that we may start integrating from the location $S = 0$ in the negative ξ direction. The saturation, S_1, reached when the heterogeneity is entered, $\xi = d$, dictates how the solution behaves inside the heterogeneity:

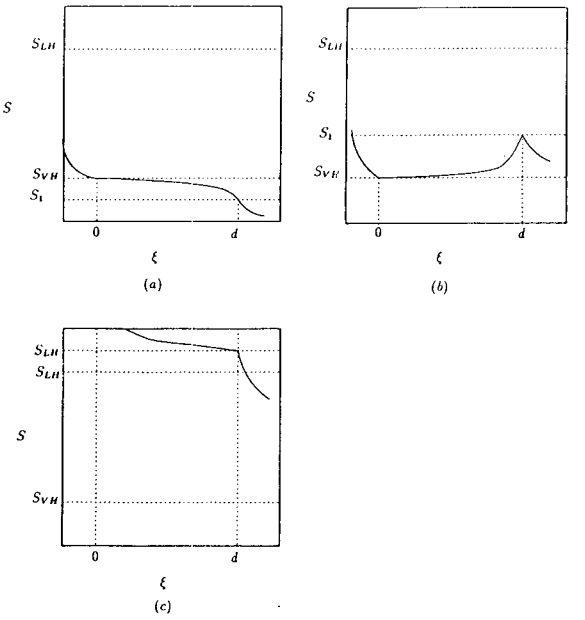

Fig. 3. Saturation profiles for integration from right-to-left: (a) $S_1<S_{VH}$; (b) $S_{VH}<S_1<S_{LH}$; (c) $S_{LH}<S_1$

- If $S_1 < S_{VH}$, then $dS/d\xi < 0$, and the solution is rapidly attracted to the asymptotic value S_{VH} as shown in Figure 3a. This is a vapor-dominated regime as in gravity-driven heat pipes. Outside the heterogeneity, $\xi < 0$, the integration is straightforward:

$$\int_{S_{VH}}^{S}\frac{k_{r\ell}k_{rv}J'dS}{(k_{r\ell}+\beta k_{rv})} = \omega\xi \tag{8}$$

This solution applies until conditions of subcooled liquid are reached ($S = 1$).
- If $S_{VH} < S_1 < S_{LH}$, then $dS/d\xi > 0$, and the solution is again asymptotic to S_{VH}, except that the saturation is now decreasing in the short region before the asymptote is reached (Figure 3b).
- Finally, if $S_{LH} < S_1$, then $dS/d\xi < 0$, but the solution cannot be now attracted to a flat profile. The latter does not develop, instead the saturation is described with the previous equations, much like the case A.1 (Figure 3c).

Consider, next, integration from the liquid side. We assume that subcooled liquid exists somewhere on the left, such that we can proceed integrating from the location $S = 1$ in the positive direction. If we denote by S_o the saturation at $\xi = 0$, the following options are possible:
- If $S_{LH} < S_o$, then $dS/d\xi < 0$, and the solution is attracted to the liquid-dominated regime with value S_{LH} (Figure 4a). After exiting the heterogeneity, further integration proceeds normally, until superheated vapor conditions are eventually reached ($S = 0$).
- If $S_{VH} < S_o < S_{LH}$, then $dS/d\xi > 0$, and the solution is attracted to the same liquid-dominated asymptote,

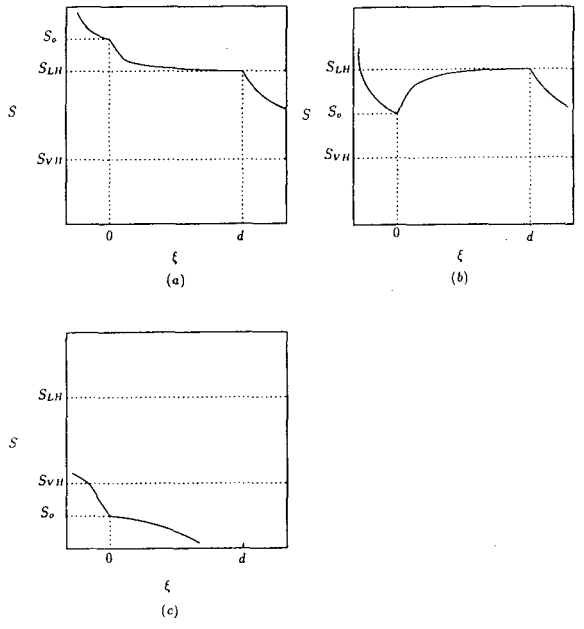

Fig. 4. Saturation profiles for integration from left-to-right: (a) $S_{LH}<S_o$; (b) $S_{VH}<S_o<S_{LH}$; (c) $S_o<S_{VH}$

except that now the saturation increases in the short region before this asymptote is reached (Figure 4b).
- Finally, if $S_o < S_{VH}$, then $dS/d\xi < 0$, but the solution is not attracted to a flat profile. Instead, it decreases relatively fast, much like in the homogeneous case (Figure 4c).

Thus, depending on the direction of integration, two different solutions (a VD and an LD) are found to satisfy the system. This feature is particular to vapor-liquid steady state counterflow. The selection of the particular paths (for example, whether it is the profiles in Figure 3 or those in Figure 4) is strictly determined from the past history of the system, which therefore attributes a hysteresis effect, albeit on a large scale [6]. The VD solutions of Figure 3 correspond to steady states reached by a system which is initially vapor-occupied and subsequently cooled from the left, while superheated conditions are maintained somewhere on the right. This is a condensation process (akin to imbibition). The LD solutions of Figure 4, on the other hand, correspond to steady states reached by an initially liquid-occupied system which is subsequently heated from the right, while subcooled conditions are maintained somewhere on the left. This corresponds to a boiling process (akin to drainage).

B. Vertical Counterflow

The above pertained to counterflow in the absence of gravity. We consider, next, the case of vertical counterflow (Figure 5). Here, two generic configurations are possible, heating from the top ($\theta = \pi/2,\ sin\theta > 0$), and heating from the bottom ($\theta = 3\pi/2,\ sin\theta < 0$).

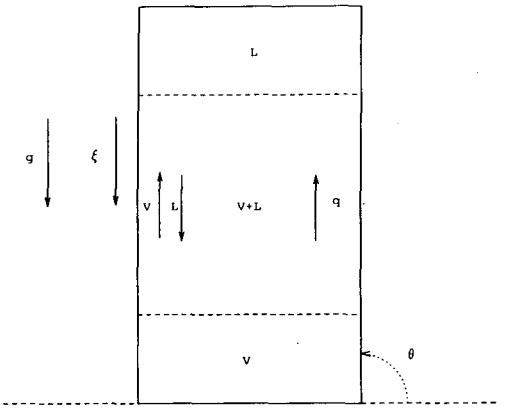

Fig. 5. Schematic of vertical counterflow.

We refer to [14] for the general case. In the first case, equation (1) yields:

$$\tau\ J'\frac{dS}{d\xi} = \omega\frac{(k_{r\ell} + \beta k_{rv})}{k_{r\ell}k_{rv}} - (\tau^2 - Ja) \qquad (9)$$

where $a(\xi)$ is the heterogeneity gradient, $a \equiv d\tau/d\xi$. In the homogeneous case ($\tau \equiv const.,\ a \equiv 0$), the RHS above vanishes for the two saturation values S_{VG} and S_{LG} that solve the equation:

$$\omega = \frac{\tau^2 k_{r\ell}k_{rv}}{k_{r\ell} + \beta k_{rv}} \qquad (10)$$

provided that $\omega < \omega_{cr,G}$. The critical value $\omega_{cr,G}$ is constant for a homogeneous system of a given permeability (e.g. equal to 0.3063 for $\tau = 1$, [3]). The two steady states of gravity-driven homogeneous heat pipes were investigated in [10], where a theory of heat pipe instability was developed. We recall that an identical multiplicity was also encountered in heterogeneous, horizontal counterflow. Because of this similarity, we contend below that, in a strict sense, instability is not really relevant and that the selection mechanisms of the horizontal case are much more appropriate.

(i) Homogeneous Systems: Steady State Selection

When the integration proceeds from the bottom (the "vapor side") upwards, it is the VD branch S_{VG} which is selected, if the starting saturation S_1 lies to the left of S_{LG}, $S_1 < S_{LG}$ (Figure 6a). This would be the case if superheated vapor existed somewhere below, as in the bottom curve of Figure 6a. In the interpretation of [6] this case could result from an initially superheated system that partly condenses due to top cooling. If $S_1 > S_{LG}$, on the other hand, a flat profile does not develop and the saturation rapidly converges to $S = 1$ (Figure 6b).

By contrast, when the integration proceeds from the top (the "liquid side") downwards, it is the LD branch, S_{LG}, which is selected, if the starting saturation S_o lies

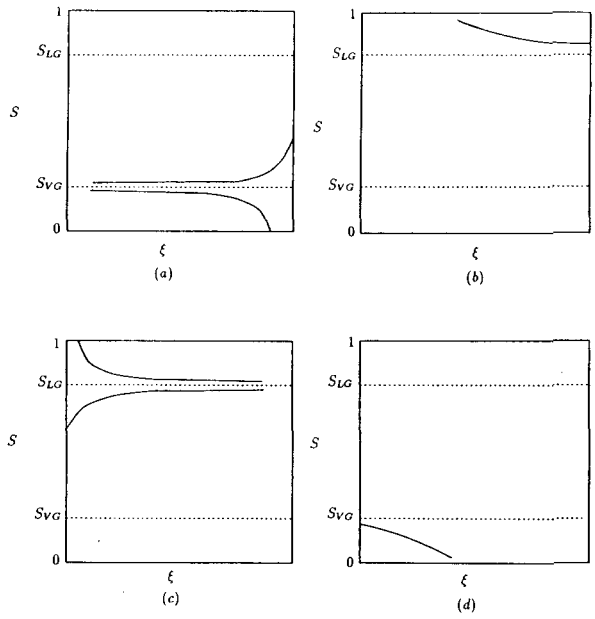

Fig. 6. Steady-state selection in homogeneous heat pipes: (a) Integration upwards, $S_1<S_{LG}$, (b) Integration upwards, $S_1<S_{LG}$, (c) Integration downwards, $S_o<S_{VG}$, (d) Integration downwards, $S_o<S_{VG}$.

to the right of S_{VG}, $S_o > S_{VG}$ (Figure 6c). This is the case of subcooled liquid somewhere at the top, a typical application being boiling [6]. If $S_o < S_{VG}$, a flat profile does not develop, the saturation rapidly approaching the dry regime, $S = 0$ (Figure 6d). We readily conclude that it is the past history of the system that determines the steady state solution. Evidently, all such saturation profiles are intrinsically stable.

(ii) Sharp Discontinuity: Termination of an "Infinite" Two-Phase Zone

Next, we consider the special case of an abrupt discontinuity ($|a| \gg 1$). This analysis is necessary to explain how VD or LD saturation profiles can merge with subcooled liquid or superheated vapor, respectively, thus how an "infinite" two-phase zone can terminate for $\theta = 3\pi/2$. In the case of large $|a|$, heterogeneity is much stronger than gravity and controls the saturation profile much like the horizontal counterflow of section A.

Consider, first, integration from the bottom within a constant permeability region (where $\omega < \omega_{cr,G}$). Then, a VD regime is rapidly reached. In a homogeneous medium this regime is predicted to continue indefinitely (although see [6] and [7]). Can this profile merge with another LD regime or with a region of subcooled liquid? The answer is negative to the first part, but not to the second. In either case, for a change in the saturation state, a region of low permeability k_t must exist somewhere at the top. Then, because a is positive and large, the response is much like in the horizontal case and capillary pressure continuity applies. If k_t is such that ω remains below critical in the top (recall that $\omega_{cr,G}$ is proportional to τ^2 or k), the previous scenario (pertaining to Figures 6a-6b) is in effect and the solution is either another VD region or a rapid approach to subcooled liquid, depending on the particular conditions. On the other hand, if $\omega > \omega_{cr,G}$ at the top, only a finite two-phase zone develops that rapidly ends by merging with a subcooled liquid region.

If integration proceeds from the top (where $\omega < \omega_{cr,G}$), an LD region is rapidly approached. Again, for this flat profile to eventually change, and for a dry region to be eventually encountered, the bottom must be at a higher permeability. Since for this case we also have $a > 0$, we can employ the same reasoning as before to reach the conclusion that it is the scenario of Figures 6c-6d that is followed, namely there will be either an attraction to another LD solution or a relatively fast approach to superheated (dry) conditions. However, in the present case, the approach to superheated conditions can also be accomplished if the bottom is at a (much) lower permeability.

A somewhat different way of stating the above is that in order to terminate a steady state vertical counterflow with $\theta = 3\pi/2$, when a VD region exists at the bottom. it is necessary that the permeability increases somewhere in the downwards direction. Subcooled liquid dominates the top. If an LD region lies at the top, the two phase zone terminates if a sharp change in permeability occurs. Superheated vapor must exist at the bottom. Significantly, LD and VD branches never merge with each other, regardless of the position or form of heterogeneity. This contrasts some of the arguments of [10] in which an "unstable" VD regime becomes connected to a "stable" LD regime, and vice versa.

(iii) General Heterogeneity Effects

Consider, next, the more general case of heterogeneity, with normal variations in τ. Equation (9) suggests that heterogeneity enhances (makes more vapor-rich or liquid-rich) the respective VD or LD regimes when $a < 0$, and acts to diminish them in the opposite case.

For a numerical example we used the profile of Figure 7a. Because here the combination $\tau^2 - aJ$ is always positive, it is possible for the RHS of (9) to vanish for all τ provided that ω is low enough ($\omega < \omega_{cr,min}$, where $\omega_{cr,min}$ must be obtained numerically). According to [14], the solution must follow closely the variation of τ^2, resulting into either an LD or a VD branch, depending on the direction of integration. Numerical results shown in Figures 7b and 7c for the respective regimes verify the theoretical predictions. After a short interval, the profiles are attracted to this asymptotic state and, with

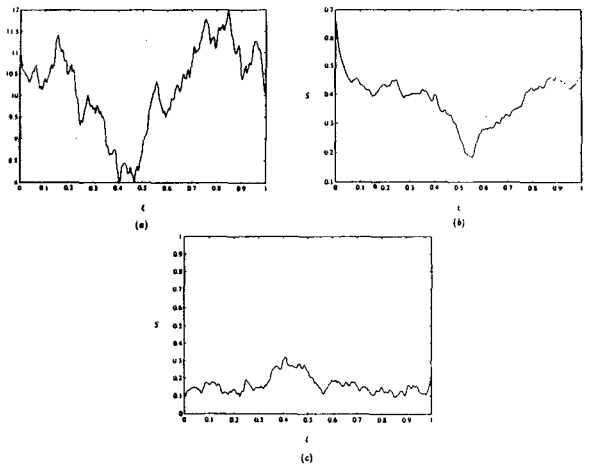

Fig. 7. Weak heterogeneity (a) τ profile, (b) *LD* regime, $\omega = 23.0$, (c) *VD* regime, $\omega = 25.0$.

a small spatial delay of about 0.05, mimic the variation of τ^2. The VD solution shows a weaker sensitivity due to the relatively narrower range of saturation values allowed. As predicted theoretically, saturations in the LD regime increase or decrease as τ increases or decreases, respectively, while the saturations in the VD regime follow opposite trends. Capillary effects are significant only near the initial boundary.

When the heat flux acquires larger values ($\omega > \omega_{cr,min}$), there are spatial locations where the local critical values may be exceeded ($\omega > \omega_{cr}(\xi)$). Then, the saturation departs from the corresponding regimes and becomes rapidly attracted to a single phase region (dry-out in the case of an LD state, as in Figure 8a, or subcooled liquid in the case of a VD state, as in Figure 8b). On the opposite side, for very low values of ω, as is typical in geothermal reservoirs, all saturation values in the VD regime are very low, hence the profile is very nearly flat, (Figure 9), despite the variation in permeability. It is clear that the existence of a flat profile should not be taken to imply a homogeneous medium.

The second case investigated corresponds to a normal variation of τ (Figure 10a). Here, the combination $\tau^2 - aJ$ changes sign often within the interval. The solution displays hysteresis again, depending on the direction of integration. However, now capillary effects are quite significant. For an LD state this is contrary to the gravity effect noted in the previous. Consider, for instance, integration from the left, where an LD regime is obtained provided that ω is low enough (Figure 10b). As long as the τ variations are not too great, the saturation values are relatively constant (early part of Figure 10b). The saturation variation is mild even though regions of relative large increase in τ are traversed. This behavior is similar to the horizontal counterflow for a negative and large. At the point where a sharp increase

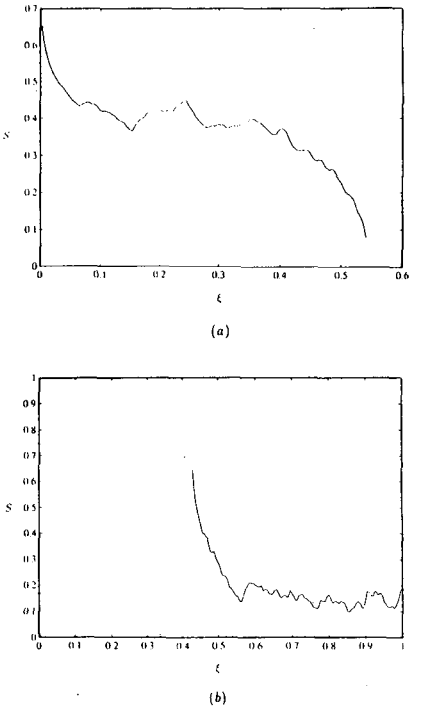

Fig. 8. Weak heterogeneity for larger heat fluxes: (a) *LD* regime, $\omega = 24.0$, (b) *VD* regime, $\omega = 28.0$.

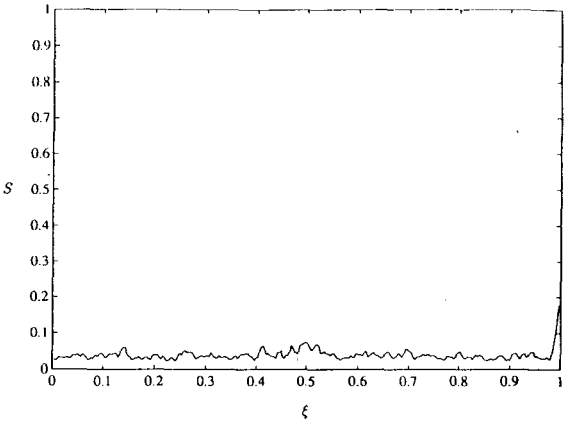

Fig. 9. The *VD* regime corresponding to Figure 7a for $\omega = 0.6$.

is encountered and a becomes large (around the midpoint of Figure 10a), capillarity dominates, capillary pressure continuity is enforced and the saturation falls significantly. If the drop is not too high, a lower saturation state, still of the VD type, will be followed in the remaining part.

Under the same conditions in ω, a VD regime arises, when the integration is from the right (Figure 10c). The first part of the profile (for ξ roughly between 0.5 and 1) corresponds to heterogeneity with generally positive slope ($a > 0$), thus capillary pressure continuity applies,

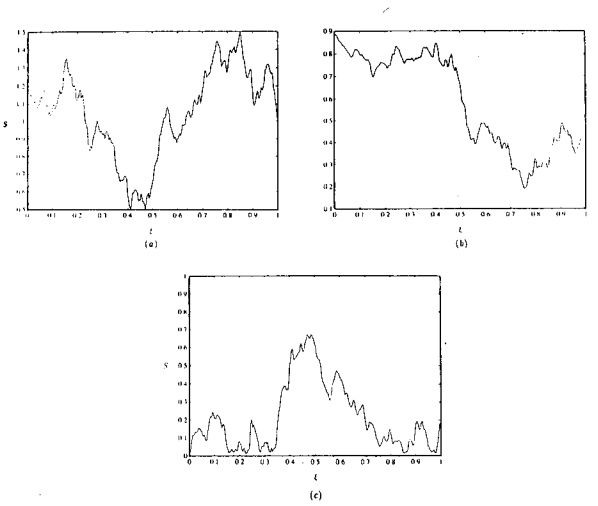

Fig. 10. Normal heterogeneity: (a) τ profile, (b) *LD* regime, $\omega = 0.02$, (c) *VD* regime, $\omega = 0.02$

the saturation rising as lower permeabilities are encountered. The second part of the heterogeneity, however, involves a rather steep negative slope (between 0.15 and 0.4). As pointed out previously, the saturation response may not be given by capillary pressure continuity alone. Indeed, after the saturation falls rapidly (for ξ between 0.3 and 0.4), further large changes in permeability do not induce significant saturation response. For further details see [14].

CONCLUSIONS

Within the framework of a continuum description, effects of permeability heterogeneity on steady state, vapor-liquid counterflow in porous media were examined. Permeability variations affect mainly two processes, gravity-driven flow and capillarity. The variations of the latter can be significant. It was shown that, as in similar previous flows [11], capillary heterogeneity acts like an external body force (such as gravity), with the additional property that it also varies spatially. For example, a multiplicity of steady states similar to gravity-driven heat pipes was found for decreasing permeabilities in horizontal counterflow and for heat fluxes lower than a critical value. Vapor-dominated and liquid-dominated regimes were obtained using selection rules that were postulated to depend on the past history (transient state) of the system. The analysis was aided by an exact solution obtained for a special heterogeneity profile [14].

The selection rules were next applied to determine the steady state regimes in gravity-driven heat pipes in homogeneous systems. It was shown that VD regimes originate from underlying dry regions, while LD regimes are extensions of overlying subcooled liquid regions. Significantly, the different regimes may never connect with each other, thus retaining their identity as long as the system remains in a two-phase state. The issue of the termination of the infinite two-phase zone was next analyzed. It was determined that termination requires that a sharp change in the permeability occurs somewhere in the medium. Across this discontinuity it was shown that, depending on past history, either the overlying LD state rapidly connects with a dry region below, or the underlying VD state rapidly converts to a subcooled liquid above. The emerging picture (from top-to-bottom) is thus, subcooled liquid - LD - (discontinuity) - dry region, or subcooled liquid - (discontinuity) - VD - dry region, in the respective cases. This ordering may be helpful in the interpretation of the nature and origin of geothermal systems. Unfortunately, this argument cannot apply for homogeneous systems, the termination of an "infinite" two-phase zone within which remains an unresolved question.

Acknowledgement: This work was partly supported by DOE Contract DE-FG22-90BC14600, the contribution of which is gratefully acknowledged.

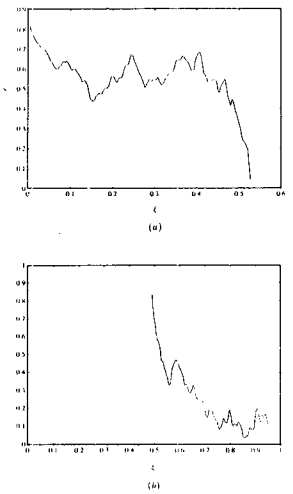

Fig. 11. Normal heterogeneity for larger heat fluxes: (a). *LD* regime, $\omega = 0.2$, (b) *VD* regime, $\omega = 0.2$.

REFERENCES

[1] Straus, J.M. and Schubert, G., One dimensional model of vapor dominated geothermal systems, J. Geophys. Res., 86, B10, 9433, 1981.

[2] Stubos, A.K. and Buchlin, J-M., Boiling and dryout in unconsolidated porous media, in "Convective Heat and Mass Transfer in Porous Media", S. Kakac, B. Kilkis, F.A. Kulacki & F. Arinc Eds., NATO ASI Series, Series E, Applied Sciences, Vol. 196, Kluwer Academic Publishers, 1991.

[3] Udell, K.S., Heat transfer in porous media considering phase change and capillarity - the heat pipe effect, Int. J. Heat Mass Transfer, 28, 485, 1985.

[4] Prats, M., Thermal recovery, SPE Monograph, Vol. 7, Dallas, Texas, 1982.

[5] Doughty, C. and Pruess, K., A similarity solution for two-phase fluid and heat flow near high-level nuclear waste packages emplaced in porous media, Int. J. Heat Mass Transfer, 33, 1205-1222, 1990.

[6] Stubos, A.K., Satik, C. and Yortsos, Y.C., Critical Heat Flux Hysteresis in Vapor-Liquid Counterflow in Porous Media, Int. J. Heat Mass Transfer, in press, 1992.

[7] Satik, C., Parlar, M. and Yortsos, Y.C., A study of steady state steam-water counterflow in porous media, Int. J. Heat Mass Transfer, 34.1755,1991.

[8] Schubert, G. and Straus, J.M., Gravitational stability of water over steam in vapor-dominated geothermal systems, J. Geophysical Res., 85, B11, 6505-6512, 1980.

[9] Ramesh, P.S. and Torrance, K.E., Stability of boiling in porous media, Int. J. Heat Mass Transfer, 33, 1895-1908, 1990.

[10] McGuinness, M.J., Blakeley, M., Pruess, K. and O'Sullivan, M.J., Geothermal heat pipe stability, Submitted to the Int. J. Heat Mass Transfer, Oct. 1990.

[11] Yortsos, Y.C. and Chang, J., Capillary effects on steady state flow in heterogeneous cores, Transport in Porous Media, 5, 399-420, 1990.

[12] Parlar, M., Zeybek, M. and Yortsos, Y.C., Steady state vapor-liquid concurrent flow: relative permeabilities and end effects, Paper SPE 20054, SPE California Regional Meeting, Ventura, CA, April 4-6, 1990.

[13] Chuah, Y.K. and Carey, V.P., Analysis of boiling heat transfer and two phase flow in porous media with non-uniform porosity, Int. J. Heat Mass Transfer, 28, 147-154, 1985.

[14] Stubos, A.K., Satik, C., and Yortsos, Y.C., Int. J. Heat Mass Transfer, submitted, July 1991.

PROCEEDINGS, Seventeenth Workshop on Geothermal Reservoir Engineering
Stanford University, Stanford, California, January 29-31, 1992
SGP-TR-141

INJECTION RECOVERY BASED ON PRODUCTION DATA IN UNIT 13 AND UNIT 16 AREAS OF THE GEYSERS FIELD

K.P. Goyal and W.T. Box, Jr.

Calpine Corporation
Santa Rosa, California

ABSTRACT

Steam production data from 13 wells including and surrounding Unit 13 injection well I-3 and 15 production wells including and surrounding Unit 16 injection well I-5 are analyzed to estimate steam decline rates with and without water injection (Figure 2). Such information is then utilized to estimate the first year recovery factor due to water injection in the southwest area of Unit 13 and the Unit 16 wellfields.

INTRODUCTION

At The Geysers geothermal field, about 20% to 30% of the steam condensate is available for disposal after evaporation in the cooling towers. Initially in 1960, the liquid effluent in The Geysers was allowed to run into Big Sulphur Creek as this was simple and inexpensive (Glenn Horton-personal communication, 1991). However, since 1969 the steam condensate has been injected back into the reservoir.

Several steam field operators have found that water injection into the Geysers' reservoir can be very useful if performed properly (Adams et al, 1991; Enedy et al, 1991: Gambill, 1990). At present, additional fresh water from Big Sulphur Creek and surface collection facilities is also being used to augment injection at The Geysers. There is even discussion of bringing treated waste water to The East Geysers from the city of Clearlake (Geothermal Report, August 1991; Goddard and Goddard 1991). Other means of collecting water such as building an impoundment facility on the Big Sulphur Creek are also being discussed by some operators in The Geysers.

Water injection into the Geysers's reservoir can be beneficial in some areas and detrimental in the other areas depending upon the fracture distribution, reservoir pressure, temperature, liquid saturation and the rock type. The positive contributions of water injection include providing reservoir pressure support, maintaining steam production rate, reducing makeup well requirements, increasing reserves and the life of the field by recovering a portion of the approximate 90% heat stored in the rocks (Dykstra, 1981). On the other hand, injection can reduce well productivity or even drown a production well completely by breakthrough of the injected cold water to a production well through some high permeability fractures. It can also create obstructions in the wellbore and reduce steam flow rate by scale buildup associated with mineral precipitation. Workovers, sometimes costly, may be needed to clean such wells to bring them back to their original productivity.

In this paper, we present the results of injection in two wellfields: Unit 13 and Unit 16 and try to quantify steam recovery due to injection in each wellfield by calculating recovery factors from the production data. A "recovery factor" is defined as the ratio of additional steam provided by injection and the amount of water injected in a given time period. Additional steam is the steam produced at the new decline rate or improvement rate established due to injection minus the steam production calculated at the previous decline rate without injection. The improvement rate is defined as the annual exponential increase in the steam flow rate. This definition is similar to the annual exponential decline rate but it represents an increase in flow rate rather than a decrease.

The recovery factor defined on the basis of production data may be different than that defined on the basis of geochemical data. Beall et al., (1989) and Gambill (1990) have used stable isotope data to estimate the recovery of injected water in the various parts of the Geysers geothermal field. Units 13 and 16 are located in The Southeast Geysers as shown in Figure 1. These units are rated at 140 GMW (gross MW) and 120 GMW respectively. Presently 32 production and 3 injection wells are located in the Unit 13 area and 17 production wells and 2 injection wells in the Unit 16 area. The outline of Unit 13 and 16 wellfields and the location of various production and injection wells used in this study are shown in Figure 2.

RECOVERY FACTOR DUE TO WATER INJECTION INTO UNIT 13 WELLFIELD:

The Unit 13 wellfield has three injection wells designated as I-1, I-2 and I-3 (Figure 2). Well I-1 has been in operation since the plant start up in May 1980 and had accepted the total

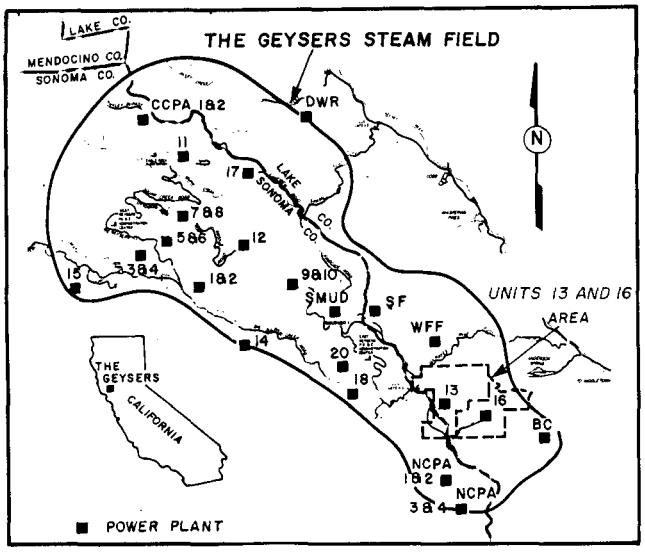

FIGURE 1: The Location Map.

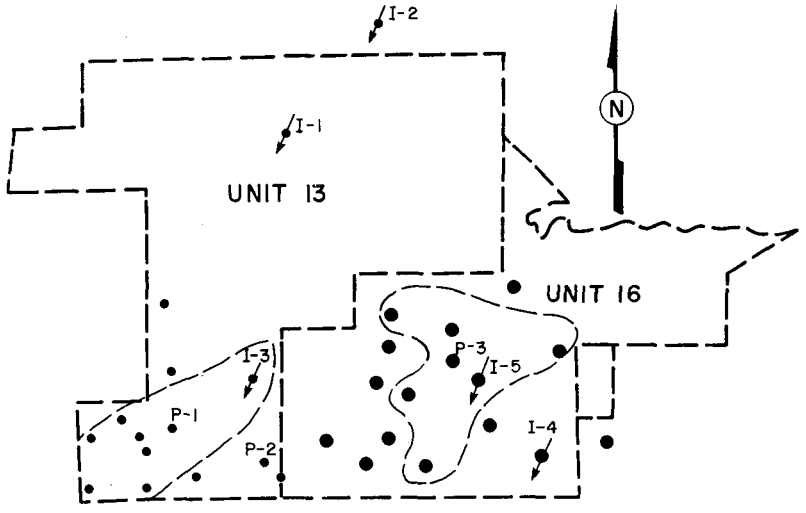

FIGURE 2: Study Area in Units 13 and 16.

plant steam condensate flow which annually averaged to about 1100 gpm until November 1984 when the second injection well I-2 became operational. Well I-2 was necessary to mitigate severe water breakthrough in the production wells offsetting I-1 during 1983-84. Between November 1984 and October 1989, the condensate was divided between these two injection wells. Originally a steam producer, well I-3 was converted to an injection well on October 30, 1989. Since then the water is primarily being split between wells I-3 and an NCPA/Calpine joint injection well (Enedy et al, 1991) with a small amount continuing to be injected into I-2. The third well I-1 is being kept as a standby Unit 13 injection well. The majority of the injected water is believed to exit these wells in fractures which originally produced steam. Perforated liners were used in I-1 and I-2 to allow deep injection below 6100' and 6800' respectively. The injected water in I-3 exits below 4000' depth and no perforated liner is installed in this well.

Thirteen wells surrounding and including the injection well I-3 and shown by solid circles in Figure 2 are monitored for their flow rate and decline rate changes. Most wells displayed a reduction in decline rate but the wells, located within the dashed outline, even exhibited an increase in their flow rate. For example, well P-1 was declining at an annual exponential rate of 18% before the injection. However, after the start of injection into I-3, its flow rate started increasing at an annual exponential rate of 55% (Figure 3). The steam flow rate of this well increased by about 20 klbm/hr after 4 months of injection. Presently, P-1 exhibits a decline rate of 13% which is 5% lower than the pre-injection value of 18%. On the other hand, the flow rate of the nearby well P-2 continues to decline at an annual exponential decline rate of 13% even after the start of injection in I-3 (Figure 4). The productivity changes observed in wells in this area suggests that most of the injected water into I-3 took a southwestern route and

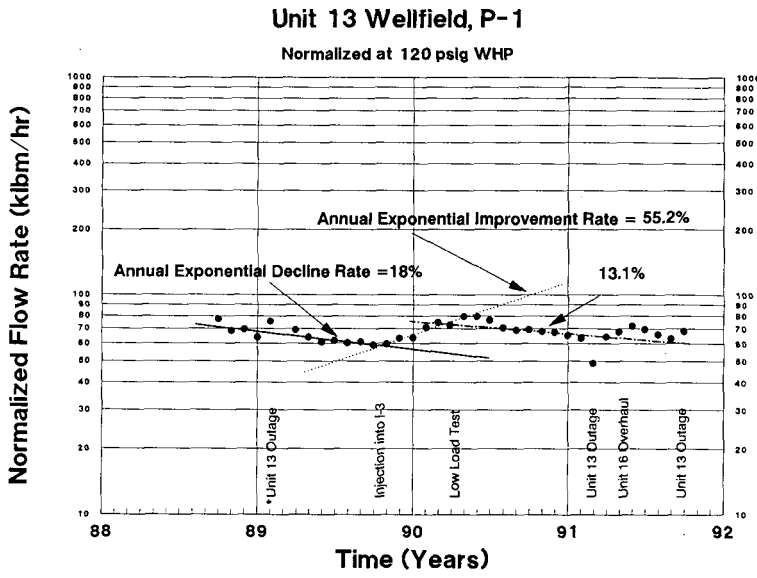

FIGURE 3: Changes in decline rates of P-1 due to injection into I-3.

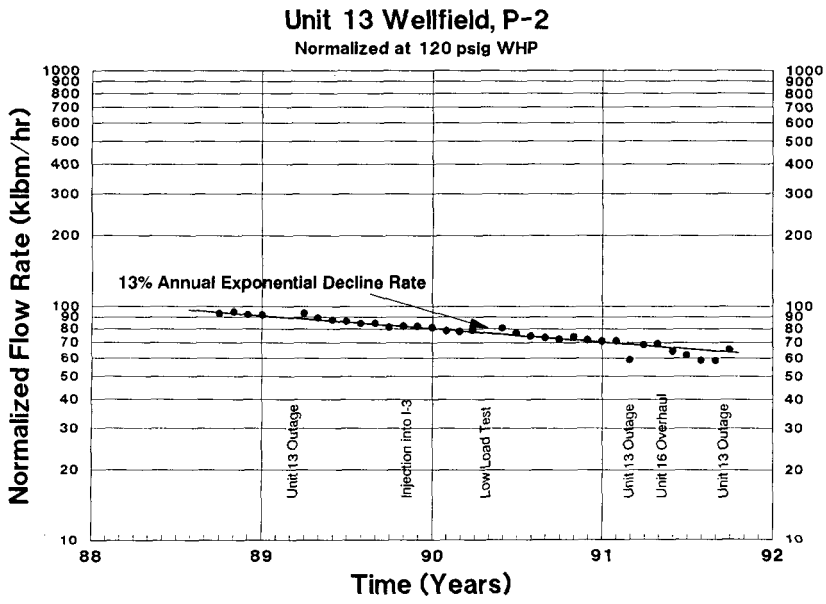

FIGURE 4: Decline rate trends of the production well P-2.

appeared as steam in wells located within the dashed outline (Figure 2).

In this study, a total of 13 wells are evaluated; 8 wells located within the dashed outline showing maximum injection benefit and the 5 nearby wells located outside the dashed outline showing some injection benefit (Figure 2). The combined normalized flow rate of all the 13 wells at 120 psig wellhead pressure (WHP) is presented in Figure 5 from January 1988 to September 1991. Due to the conversion of one production well into injection well I-3, the flow rate of only 12 wells is plotted after October 1989. Various operational activities such as plant outages and reservoir testing are also indicated in this figure.

Decline rates, shown in Figure 5, are estimated by excluding the data points affected by plant outages and testing. The 13 production wells, including I-3, exhibit an annual exponential decline of 20% before injection into I-3. During the next five months, the flow rate increased at an annual exponential rate of 25.5%. In 1990, the flow rate declined but at a slower rate of 13% as shown in Figure 5. Injection into I-3 has provided help in two forms: one in reducing decline rates and the other in providing a step increase in the flow rate. These effects are clearly shown in Figure 6 which is drawn on the linear scale. The injection rate (gpm) averaged over a month since start up in October 1989 is also shown in this figure which ranges from 300 gpm to 800 gpm. Two straight

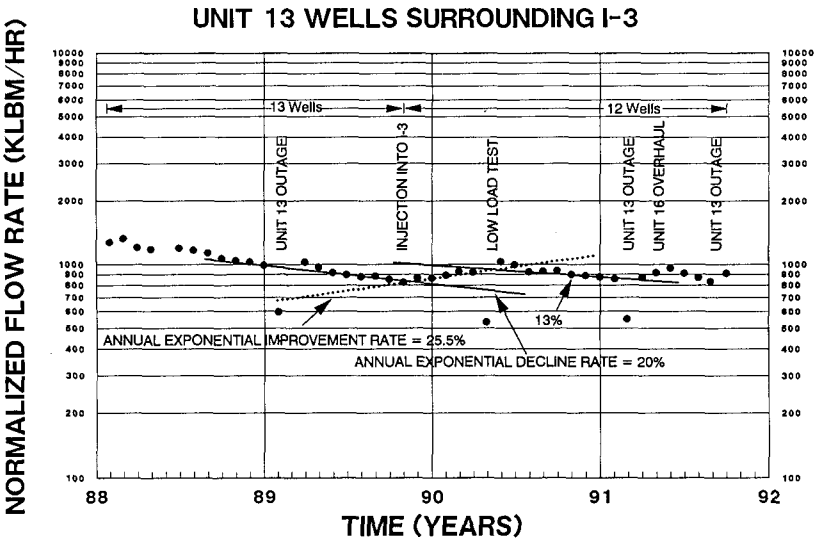

FIGURE 5: Reduction of decline rate due to injection into I-3.

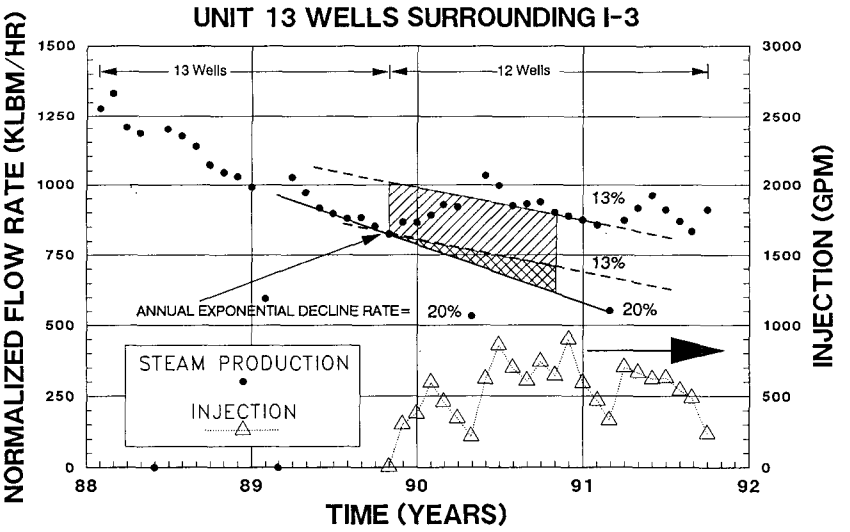

FIGURE 6: Effect of injection into I-3 on some surrounding production wells.

lines indicating annual exponential decline rates of 20% and 13% are also represented in this figure.

Figure 6 suggests a 7% reduction in decline rate and a step flow rate increase of about 190 klbm/hr. This increase was experienced by the 12 wells (13 wells minus I-3) over and above the flow rate of the original 13 wells. Annual steam production of 6.59 and 6.82 billion lbm can be estimated on the basis of 20% and 13% exponential decline rates since October 1989. This suggests a first year steam recovery of about 0.23 billion lbm from the injected water. This is shown by a hatched triangular area in Figure 6. Water injection into I-3 during the first 12 months was about 2.12 billion lbm. The ratio of steam recovery and annual water injection suggest a recovery factor of about 11%.

The step increase of about 190 klbm/hr in steam flow rate and the associated increase in steam recovery is shown by a parallelogram in Figure 6. Assuming an actual recovery equalling 2/3rd the area of the parallelogram, additional steam production of 1.11 billion lbm can be estimated in the first year (Figure 6). This step increase enhances the recovery factor to 63%. Thus the first year recovery factor in the Unit 13 area varies from about 11% to 63%. The former recovery factor is solely based on the change in the decline rate while the latter also includes the step increase in the flow rate.

A tracer test, conducted in the joint NCPA/ Calpine well, indicated a recovery of an order of magnitude lower in Unit 13 wells compared to NCPA wells (Adams et al., 1991). This suggests a minor contribution in the Unit 13 area due to

water injection into the joint injection well. Therefore the calculated recovery factors in the Unit 13 area may be slightly on the high side as they include the effect of water injection into the joint injection well.

In summary, water injection into the southwest area of Unit 13 suggests a recovery factor of 11% due to the reduction in the decline rates only. However, it enhances to 63% if the effect of the step increase in the flow rate is also considered. These recovery factors are believed to be slightly on the high side due to the pressure support provided by the water injection into the joint NCPA/Calpine well. To date, no adverse injection effects such as cooling or water breakthrough have been noted in wells in this area.

RECOVERY FACTOR DUE TO WATER INJECTION INTO UNIT 16 WELLFIELD:

The Unit 16 wellfield has two injection wells I-4 and I-5 as shown in Figure 2. Well I-4 has been in operation since the plant start up in October 1985 and had accepted the total steam condensate of about 1000 gpm until October 1, 1990, when the second injection well I-5, became operational. This change was necessary due to water breakthrough in the production wells offsetting I-4. Since then 70% to 90% of the condensate has been injected into I-5 and the rest into I-4. A perforated liner used in I-4 allows water to exit at 5600'. The injected water in I-5 exits below 4200' and no perforated liner is installed in this well.

Fifteen production wells including and surrounding injection well I-5 and shown by solid circles in Figure 2 are monitored for their flow rate and decline rate changes due to injection into I-5. Most wells displayed a reduction in decline rate and some wells, located within the dashed outline, even displayed a modest increase in their flow rate. For example, well P-3 was declining at an annual exponential rate of 11.5% before the injection into I-5 (Figure 7). Subsequent to injection its flow rate started increasing at an annual exponential rate of 13.5%. Within 4 months, its flow rate increased by 15 klbm/hr. A few other wells located within the dashed outline exhibited smaller gains than displayed by P-3. The combined normalized flow rate at 120 psig wellhead pressure of all the 15 wells shown in Figure 2 is presented in Figure 8 from March 1989 to September 1991. Due to the conversion of one production well into I-5, the flow rate of only 14 wells is plotted after September 1990. Various operational activities are also indicated in this figure.

All 15 wells display a combined annual exponential decline rate of 13.5% before the start of injection into I-5. The shift of most of Unit 16 injection to I-5 since October 1, 1990 has reduced the decline rate to 5.2% as shown in Figure 8. However, a step increase in flow rate, similar to that seen in the Unit 13 area (Figures 5 and 6), is not present in the Unit 16 area as shown in Figure 8.

The injection related effects and decline trends for Unit 16 wells are clearly represented in Figure 9 which is drawn on a linear scale. The total injection rate (gpm) into I-4 and I-5 averaged over a month since March 1989 to September 1991 is also shown in this figure. The injection rate into these two wells ranges from about 600 gpm to about 1200 gpm (Figure 9). The first year steam production of 11.47 and 11.95 billion lbm can be estimated for annual exponential decline rates of 13.5% and 5.2% respectively. This suggests an injection related increase of 0.48 billion lbm in the first year as shown by the triangular area in Figure 9. Water injection into I-4 and I-5 during the first 12 months (October 1990 to September 1991) was 3.60 billion lbm. These steam recovery and injection data can be used to calculate a first year recovery factor of 13% for the Unit 16 wellfield.

The actual recovery factor may be higher if either the injection into I-4 is not considered or steam recovery due to injection into I-4 is also considered. Such analysis was not possible since injection into I-4 commenced with the plant start up in 1985.

In summary, water injection into the southwest portion of Unit 16 suggests a recovery factor of 13% which is believed to be on the low side as the steam recovery due to injection into I-4 is not considered. Water production in certain producing wells offsetting I-5 has recently been noticed when the injection rate in I-5 exceeds 900 gpm. In an attempt to reduce this water breakthrough problem, the injection rate into I-5 has been reduced to about 600 gpm.

CONCLUSIONS:

First year recovery factors of 11% and 13% are estimated for the southwest west areas of Unit 13 and Unit 16 respectively. These estimates are based on the reduction in the decline rates due to the effect of water injection into Unit 13 well I-3 and Unit 16 well I-5. A step flow rate increase of 190 klbm/hr, observed in Unit 13 wells surrounding I-3, enhances the first year recovery factor to 63% in the southwest portion of Unit 13. A step increase in flow rate, similar to Unit 13 wells, is not observed in the Unit 16 wells.

Unit 13 recovery factors are believed to be on the high side due to the pressure support provided by the water injection into the joint NCPA/Calpine well. On the other hand the recovery factor in the Unit 16 area is believed to be on the low side since the steam recovery due to injection into I-4 is not considered.

To date no adverse effects to injection such as cooling or water breakthrough have been noted in the southwest area of Unit 13. However, water production in certain producing wells in

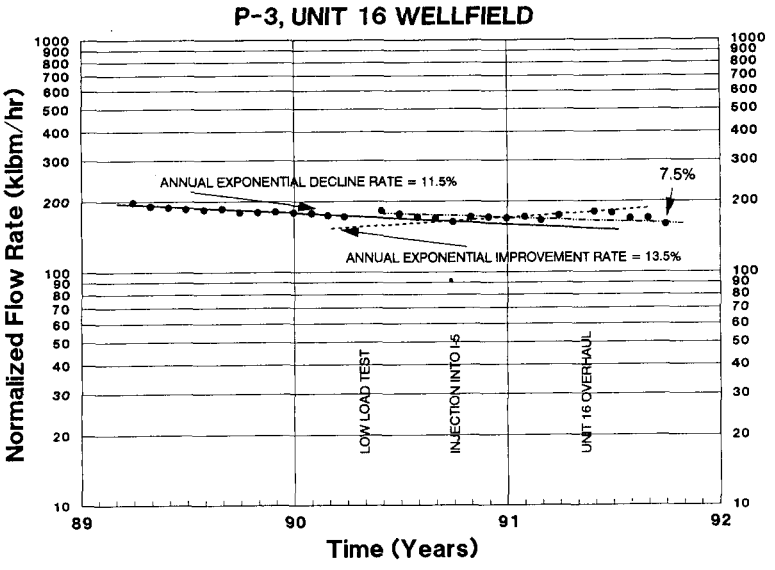

FIGURE 7: Decline rate trends of Unit 16 Well P-3.

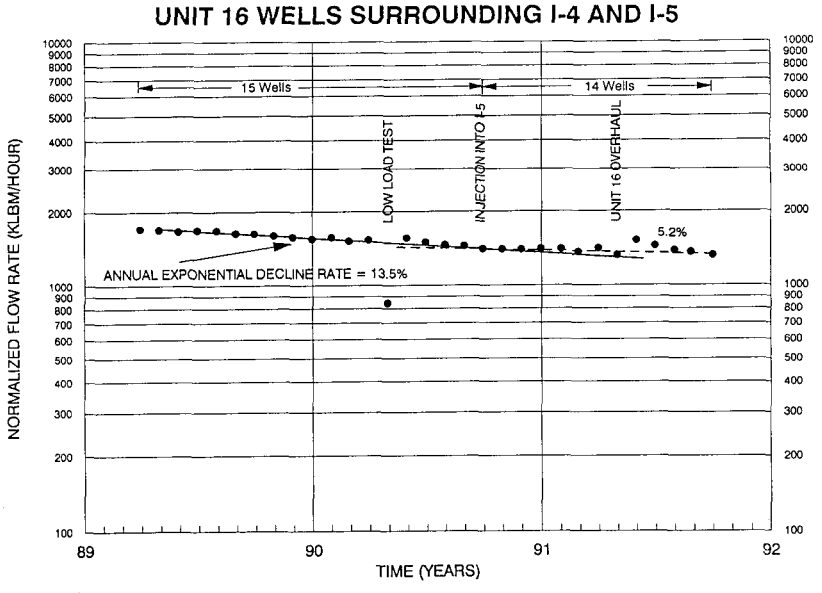

FIGURE 8: Reduction in decline rate due to inject- into I-5.

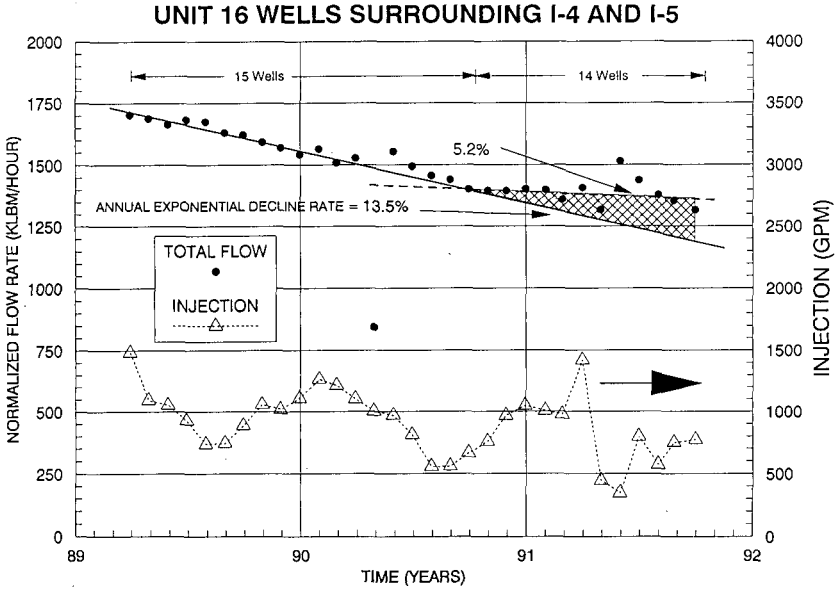

FIGURE 9: Gain in steam production due to injection into I-5.

the southwest area of Unit 16 has been noticed when the injection rate into I-5 exceeds a certain value.

The annual recovery factors are expected to continue or perhaps increase as reduced decline rates are maintained. The ultimate recovery factors in these areas are not known and depend upon reservoir hete-rogeneity, fracturing, heat transfer efficiency from rocks to water, and reservoir temperature, pressure and liquid saturation conditions.

ACKNOWLEDGEMENTS:

The authors would like to thank C. L. Wardlow and J.J. Beall for reviewing the manuscript and Calpine Corporation and Santa Fe Geothermal for permission to publish the paper.

REFERENCES:

Adams, M.C., Beall, J.J., Enedy, S.L., and Hirtz, P. (1991), "The Application of Halogenated Alkanes as Vapor-Phase Tracers: A Field Test in the Southeast Geysers," Geothermal Resources Council Transactions, Vol. 15, October 1991, pp. 457-463.

Beall, J.J., Enedy, S. L., and Box, W. T. Jr. (1989), "Recovery of injected condensate as steam in the south Geysers field," Geothermal Resources Counsil, Transactions, v. 13, pp. 351-358.

Dykstra, H. (1981), "A Reservoir Assessment of The Geysers Field, Reservoir Engineering Report," Publication Number TR-27, California Div. of Oil and Gas, Sacramento, April 1981, pp.35-49.

Enedy S., Enedy K.,and Maney J. (1991), "Reservoir Response to Injection in the Southeast Geysers," in Pre-prints 16th workshop on Geothermal Reservoir Engineering, Stanford University, Stanford California, January 23-25, 1991.

Gambill, D. T. (1990), "The Recovery of Injected Water as Steam at The Geysers," Geothermal Resources Council Transactions, Vol 14, Part II, August 1990, pp. 1655-1660.

Geothermal Report (1991), "The Geysers Hot Potato is still bobbling in hands of California Energy Commission," Vol. XX, No. 15, ISSN 0733-9100, August 1, 1991.

Goddard, C. B. and Goddard W. B. (1991), "Use of Lake County Municipal Wastewater for Geothermal Resource Replenishment," Geothermal Resources Council Transactions, vol. 15, October 1991, pp. 141-147.

PROCEEDINGS, Seventeenth Workshop on Geothermal Reservoir Engineering
Stanford University, Stanford, California, January 29-31, 1992
SGP-TR-141

Model Study of Historical Injection in the Southeast Geysers

D. D. Faulder

Idaho National Engineering Laboratory
P.O. Box 1625
Idaho Falls, ID 83402-2107

ABSTRACT

A three component model study of the historical injection of two wells in the Unit 13 area demonstrates that the recovery of injection derived steam is influenced by the geologic structure of the bottom of the reservoir and the relative location of injection wells. The migration of injectate from the first injection well, located up structure from the second, quenched the area around the second injector before it started operation. While both wells had similar cumulative mass injected, nearly five times more injection derived steam is recovered from the first injector than the second. Sensitivity runs were made to three cases of increasing matrix capillary pressure. The recovery of injection derived steam increases with higher values of capillarity. The interaction of structure at the bottom of the reservoir, injection well locations, and matrix capillarity all influence the recovery efficiency of injectate as steam. The model developed in this study will be used to evaluate injection strategies at The Geysers.

INTRODUCTION

The recent productivity and pressure declines at The Geysers are classic symptoms of reservoir fluid resource depletion. However, even if all the fluid initially in place is produced, over 90% of the usable heat remains in place. Thus, the question of how to extract more of the heat in place arises. One answer is to replace the depleted fluid with increased water injection thereby replenishing the reservoir's working fluid.

If an expanded injection program is to be undertaken it is important to understand how injected fluid behaves. We must be able to confidently model and predict the process of injection, re-vaporization, and production of injection derived steam. Additional insight into this process can be gained by studying historical injection at The Geysers. Water injection began in 1969, originally as a cooling tower waste water disposal and has gradually evolved to an accepted method of replenishing water in depleted portions of the reservoir.

A reservoir model study of the Unit 13 area was conducted with the objectives of modeling historical injection and transport of the injectate, to use the deuterium isotopic shift as a naturally occurring tracer, and to understand the importance of matrix capillary forces in the recovery of injection derived steam. The study goal was to determine how to confidently model injection into a vapor-dominated reservoir.

The Unit 13 study area was chosen for several reasons. It has over 11 years of injection history using two injection wells in the study area, exploitation started at essentially undisturbed conditions, and the reservoir performance is well represented in the literature. The study area is shown in Figure 1.

REVIEW OF APPLICABLE LITERATURE

A review of the geologic literature was conducted to develop a working conceptual geologic model. The top of the reservoir is represented by the top of the steam and the bottom of the reservoir by the top of the felsite. It is recognized the top of felsite is not the bottom of the reservoir for most of The Geysers, however several pieces of evidence suggest this is a good approximation for the Unit 13 area. Micro-seismic data for the C-11 injection area, south of the study area indicates the majority of the liquid injected into the greywacke does not appear to migrate deeply into the felsite (Enedy et al., 1991). Very few wells in the study area have productive steam bearing fractures in the felsite.

Beall (1989) noted the steam bearing fractures in the greywacke show no preferential orientation. However, there are areas of north-northeast enhanced permeability due to southeast-west northwest regional extension, resulting in high angle fractures deep in the reservoir and near the

Work supported by the U.S. Department of Energy, Assistant Secretary of Conservation and Renewable Energy, Office of Utility Technology, under DOE Contract No. DE-AC07-76ID01570.

margins (Beall et al., 1989). Thus, the greywacke can be envisioned to be pervasively fractured with areas of north-south enhanced permeability. Gunderson (1990) noted the matrix porosity was related to two factors; vertical depth and distance above the felsite. The algorithm presented by Williamson (1990) is used to implement this observation.

Past reservoir model studies of The Geysers have typically consisted of field-wide studies with the purpose of predicting overall production rates (Williamson, 1990) or of parametric studies. Parametric studies have been performed to examine sensitivities to initial matrix water saturation and heat flow (Pruess and Narasimhan, 1982), the permeability of the matrix and fractures, grid refinement with depth (Lai and Bodvarsson, 1991), and grid orientation (Pruess, 1991). Petrophysical properties for the study were selected from the above literature. The matrix steam-water relative permeability and capillary pressure behavior have not been measured and reported in the literature to date.

The initial water saturation in the matrix has not been directly measured, however a field-wide study by Williamson (1990) used a value of 82%. This high initial matrix water saturation is consistent with the studies of Pruess and Narasimham (1982) and Pruess (1985). Observed chemical and isotopic gradients of the produced steam in the Southeast Geysers are believed to be due to meteoric recharge entering the reservoir from the southeast (Truesdell et al., 1987). The calculated vapor fraction for the Southeast Geysers from Truesdell et al. indicated that the initial produced steam originated almost entirely from vaporized liquid.

DEUTERIUM TRACER DATA

Two steam condensate injection wells were used in the study area. Injector I1 was the sole injection well at the start operations in May 1980, injecting at an average rate of approximately 350 Klbm/hr through 1984. At that time a second injection well (I2) was used and the total injection volume was split. The injection histories for the two well are shown in Figure 2. The injected condensate is enriched in deuterium relative to the reservoir steam and has been used as a tracer (Beall et al., 1989; Gambil, 1990). The operator has conducted a periodic analysis of deuterium in the producing steam wells to track the movement of injection derived steam in the reservoir. This data set is used as a tracer for the model study. Figure 3 presents an example from Beall et al. (1989) of the contoured deuterium isotopic shift in the study area. Six key production wells were significantly affected by the deuterium shift from these two injectors and are labeled P1 - P6 in Figure 3. Injection derived steam was calculated using the equation presented by Beall et al. (1989).

MODEL FEATURES

A reservoir model of the study area was developed using TETRAD, a simulator which was validated with the Stanford geothermal problem set (Shook and Faulder, 1991). The dual porosity reservoir model uses three water components; 1) initial fluid in place, 2) injectate from I1, and 3) injectate from I2. Separate water components for the two injection wells allows detailed tracking of the injectate and a relative determination of the contribution of each injection well to produced injection derived steam (IDS). The model contains 1650 grid blocks, five vertical layers, and decreasing thickness with depth. The bottom layer is uniformly 75 feet thick. The actual well deviated courses are used, based on the open file records of the California Division of Oil and Gas. Fifteen percent of the matrix rock energy was assigned to the fracture domain. This value is conservative compared to the thirty percent used by Williamson (1990). Conceptually, this could be envisioned as zones of fractured rock or a pervasive micro-fracture network. Petrophysical properties were taken from the literature and are summarized in Table 1. The water-steam fracture and matrix relative permeability are presented in Figure 4. Initially, no capillary pressure was used in the matrix.

The reservoir structure was accounted for by using the top of steam and top of felsite maps presented by Thompson and Gunderson (1989) and by Thompson (1989). These maps were digitized and directly entered into the model. Figure 5 shows north-south and east-west cross-sections through the reservoir model. A key feature to note is the large amount of structural relief on the top and bottom of the reservoir model. The reservoir top has approximately 5000 feet of vertical relief over a distance of 10,000 feet, while the reservoir bottom has approximately 3,000 feet of relief over the same distance.

The study area boundary conditions were initially no-flow, however as the study progressed it became necessary to relax this condition, as explained below. The production and injection wells were placed on rate constraint in order to produce the historical rates from the study area. The production wells were set to produce to a 180 psia wellhead pressure, uncorrected for wellbore friction. Heat flow was set at a uniform vertical flux of 500 mW/m^2, consistent with published data.

MODEL CALIBRATION PROCESS

The model was allowed to equilibrate for 20 years prior to the start of exploitation, allowing steam and water saturations to adjust to a stable heat pipe and establishing a vapor-static pressure gradient. The stabilized model was then run for all exploitation cases. Completion intervals of the wells were adjusted to match the observed drilling steam entries. In the case of multiple steam entries, the dominant entry was chosen on the basis of observed compressor pressure increase during drilling. The well productivity indices (PI) were adjusted to allow the wells to produce the observed rates with the 180 psia wellhead pressure constraint. For those cases with initial rig test data, the indicated PI was used as a starting point. The initial rig test data was found to be very reliable indictor of productivity index.

Constant pressure boundaries declining with time were used on the south and west sides of the model to mimic the effect of offset production due to Unit 16, and Units 18 and 20, respectively. Published pressure histories for adjacent areas were used, (Barker et al., 1990 and Enedy et al., 1990). It was observed the injected fluid would quickly migrate to the bottom of the reservoir and flow to the north and then "puddle". A constant pressure boundary is used on the north boundary to relax the no-flow condition and pressures set to the stabilized pre-exploitation conditions. This northward flow of injectate is not surprising, considering the large amount of structural relief present at the bottom of the reservoir. This structural aspect dominates injectate flow for all cases studied.

Several exploitation runs of 1980 to 1991 production data were made with a uniform permeability structure. Additional data from well testing was used to adjust this case to a fracture permeability from 10 mD to 100 mD, generally increasing to the southeast, (Enedy, 1989b). Evidence for directional permeability was noticed on the isotope shift maps of Beall et al., (1989). Based on the ratio of length to width of the isotope shift contours, directional permeability was set as 3X=Y=Z and is consistent with the geologic model. With these changes, a reasonable pressure match was achieved with this base case. However, the modeled tracer data and implied IDS was low compared to historical conditions.

A sensitivity run was made to an initial matrix water saturation of 42%. The lower initial water saturation results in a similar pressure history as the above case; however, the producing enthalpy achieves superheat with in a few months after the start of exploitation. Enedy (1989a) indicates the wells historically did not begin producing an appreciable degree of superheat until after approximately eight years of production. Thus, the lower saturation case does match the observed production data. Again, for this case the modeled tracer recovery and implied IDS was low.

Finally, a series of sensitivity runs was made to study the effect of capillary pressure. It should be noted actual measurements of the capillary pressure have not been reported in the literature for The Geysers. Thus, a family of generic capillary pressure curves were generated as shown in Figure 6. The capillary pressure at residual water saturation varies by two order of magnitude. A scaling calculation using the Leverett J function and realistic values of permeability and porosity for Geysers reservoir matrix rock indicates capillarity could easily be as high as the upper values presented.

The modeled results for no capillarity (base case) and the three capillarity cases are plotted with the observed deuterium tracer data for well P5 in Figure 7. Well P5 is the nearest producer to the injection plume and is probably least effected by reservoir heterogeneity. As can be noted, the higher values better match the observed trends and magnitude of deuterium tracer recovery. Well P5, nearest to injection well I1 is best matched by the moderate to strong capillary pressure function. Figures 8 and 9 present the modeled injection derived steam rate history for the key production wells and the total study area. It can be noted that with increasing capillarity, the injection derived steam increases. This suggests that detailed injection modeling at The Geysers must include matrix capillarity to accurately predict the recovery of injection derived steam.

DISCUSSION OF RESULTS

The simulation results demonstrate that the recovery of injection derived steam is primarily influenced by two factors. First, the structure of the bottom of the reservoir greatly influences injectate movement. This is apparent by the migration of the injectate down the structure. It should be noted that I2 is located lower structurally from I1. When I2 began injection operations, injectate from I1 had already moved down structure, quenching this area. This resulted in low injection derived steam recovery from I2 relative to I1. Secondly, the presence of capillarity increases the recovery of injection derived steam for both wells. Table 2 presents the percent recovery of injection derived steam from each injection well. While each injection well has similar cumulative mass injected, nearly 5 times more injection derived steam is recovered from I1 compared to I2, with injection derived steam

recovery increasing with capillarity. The interaction between structure at the bottom of the reservoir, injection well location, and capillarity all influence the recovery of injection derived steam. Given the geologic structure of the bottom of the reservoir and the ability to select injection well locations, it should be possible to design and model an effective injection program.

The model developed in this study will be used to evaluate injection strategies at The Geysers. Several strategies that will be evaluated include injectate recovery sensitivity to injection rate, a more distributed injection approach, the injectate recovery efficiency of a horizontal injection well, and the selection of injection well locations to allow for reservoir structure.

CONCLUSIONS

The recovery of injection derived steam in the Unit I3 study area has had mixed results. The location of injection well I2 was less than optimally located to maximize the injectate recovery. The strong capillarity case had a total recovery of approximately 30% of cumulative mass injected.

The structure of the bottom of the reservoir can exert a great deal of influence of the direction the injectate travels. It would seem prudent to locate injection wells with this structural aspect in mind.

Modeled injection derived steam recovery is greatly influenced by matrix capillary pressure. Higher values of capillarity result in increased recovery of injection derived steam. Predictive injection modeling at The Geysers will need to consider capillary pressure effects.

The interaction between structure at the bottom of the reservoir, well locations, and capillarity all influence the recovery of injection derived steam.

The measurement of Geysers core and the determination of the actual shape of the capillary pressure curve would enhance our ability to model and predict reservoir response to injection at The Geysers. There is a need to measure the capillary pressure of actual Geysers core to determine the character and magnitude of this effect.

ACKNOWLEDGEMENTS

I would like to thank Dr. Keshav Goyal and Tom Box of Calpine Corporation for providing study data. Their assistance and cooperation are greatly appreciated.

NOMENCLATURE

k_{rg} = relative permeability of gas

k_{rl} = relative permeability of liquid

P_c = capillary pressure

P_c = capillary pressure curve parameter

P_{entry} = capillary entry pressure

S = dimensionless liquid saturation

S_{gc} = critical gas saturation

S_{ir} = irreducible liquid saturation

S_l = liquid saturation

REFERENCES

Barker, B. J., M. S. Gulati, M. A. Bryan, and K. L. Riedel; 1989; Geysers Reservoir Performance; **Trans.** Geothermal Resources Council, Vol. 13.

Beall, Joseph J., Steve Enedy, and W. T. Box, Jr.; 1989; Recovery of Condensate as Steam in the South Geysers Field; **Trans.** Geothermal Resources Council, Vol. 13, p. 351-357.

Beall, Joseph J. and W. T. Box, Jr.; 1989; The Nature of Steam Bearing Fractures in the South Geysers Reservoir; **Trans.** Geothermal Resources Council, Vol. 13, p. 441-448.

Enedy, Steve, Murray Grande, and J. L. Bill Smith; 1990; A Case History of Steamfield Development, Reservoir Evaluation, and Power Generation in the Southeast Geysers; Geothermal Resources Council *Bulletin*, Oct., p. 232-248.

Enedy, Kathleen L., 1989a; Downhole Enthalpy and Superheat Evolution of Geysers Steam Wells; **Trans.** Geothermal Resources Council, Vol. 13, p. 377-382.

Enedy, Kathleen L., 1989b; The Role of Decline Curve Analysis at The Geysers; **Trans.** Geothermal Resources Council, Vol. 13, p. 383-391.

Enedy, Steven, Kathy Enedy, and John Maney, 1991; Reservoir Response to Injection in the Southeast Geysers, **Proc.** 16th Workshop on Geothermal Reservoir Engineering, Stanford Univ., in press.

Gambil, David T.; 1990; The Recovery of Injected Water as Steam at The Geysers; Trans. Geothermal Resources Council, Vol. 14, Part II, p. 1655-1660.

Gunderson, Richard P.; 1990; Reservoir Matrix Porosity at The Geysers From Core Measurements; **Trans.** Geothermal Resources Council, Vol. 14, Part II, p. 1661-1665.

Lai, C. H. and G. S. Bodvarsson; 1991; Numerical Studies of Cold Water Injection into Vapor-Dominated Geothermal Systems, LBL-30173, 26 p.

Pruess, Karsten; 1985; A Quantitative Model of Vapor Dominated Geothermal Reservoirs as Heat Pipes in Fractured Porous Rock; **Trans.** Geothermal Resources Council, Vol. 9, Part II, p. 353-361.

Pruess, K. and T. N. Narasimhan; 1982; On Fluid Reserves and the Production of Superheated Steam From Fractured, Vapor-Dominated Geothermal Reservoirs, *J. Geophys. Res.*, Vol 87(B11), p. 9329-9339.

Shook, Mike and D. D. Faulder; 1991; Validation of a Geothermal Simulator, EGG-EP-9851.

Stockton, A. D., R. P. Thomas, R. H. Chapman, and Herman Dykstra; 1983; A Reservoir Assessment of The Geysers Geothermal Field, SPE 11727.

Thompson, Richard C.; 1989; Structural Stratigraphy and Intrusive Rocks at The Geysers Geothermal Field, **Trans.** Geothermal Resources Council, Vol. 13, p. 481-485.

Thompson, Randolph C. and Richard P Gunderson; 1989; The Orientation of Steam-Bearing Fractures at The Geysers Geothermal Field; **Trans.** Geothermal Resources Council, Vol. 13, p. 487-490.

Truesdell, A. H., J. R. Haizlip, W. T. Box, Jr., and F. D'Amore; 1987; Fieldwide Chemical and Isotopic Gradients in Steam from The Geysers; **Proc.** 12th Workshop on Geothermal Reservoir Engineering, Stanford Univ., p. 241-246.

Williamson, K. H.; 1990; Reservoir Simulation of The Geysers Geothermal Field; **Proc.** 15th Workshop on Geothermal Reservoir Engineering, Stanford Univ., p. 113-123.

Table 1

Petrophysical Properties

Porosity

matrix	4.6% - 2.96%	decreasing with depth
fracture	2.0% - 1.45%	decreasing with depth

Permeability

matrix	10 micro Darcy	uniform
fracture	10 to 100 mD	varying

Fracture Spacing

150 feet

Relative Permeability

matrix — Corey type, with Sir = 30%, Sgc = 5%

$$k_{rl} = (S)^4 \qquad k_{rg} = (1 - S)^{2.5} \qquad S = \left(\frac{S_l - S_{ir}}{1 - S_{ir} - S_{gc}}\right)$$

fracture — straight line X curves, no residual saturations

$$k_{rl} = S_l \qquad k_{rg} = \left(1 - S_l\right)$$

Initial Water Saturations

matrix	Sw=82%
fracture	Sw=.04%

Capillary Pressure

matrix $\qquad P_c = \dot{P}_c(1 - S)^2 + P_{entry}$

Heat Flow

500 mW/m^2 top and bottom of model

Rock Thermal Properties

density	170 lbm/ft^3
specific heat	.21 BTU/lbm - F
thermal conductivity	33.3 BTU/ft- F-day

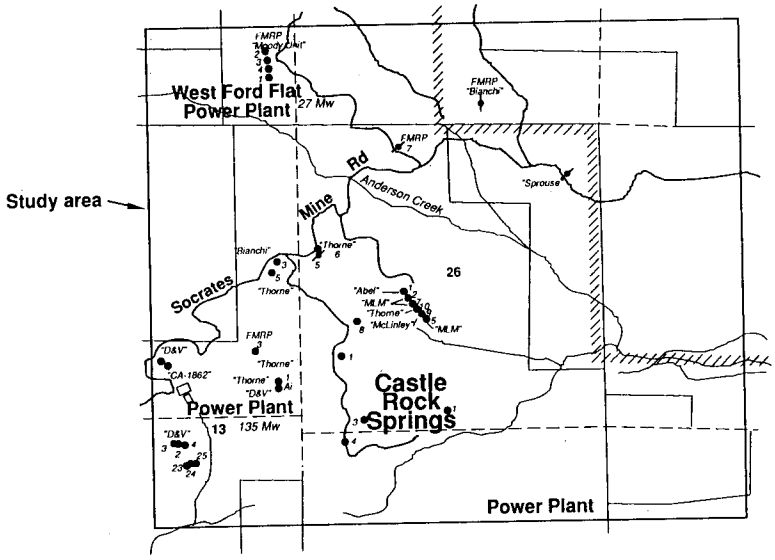

Figure 1 Study Area

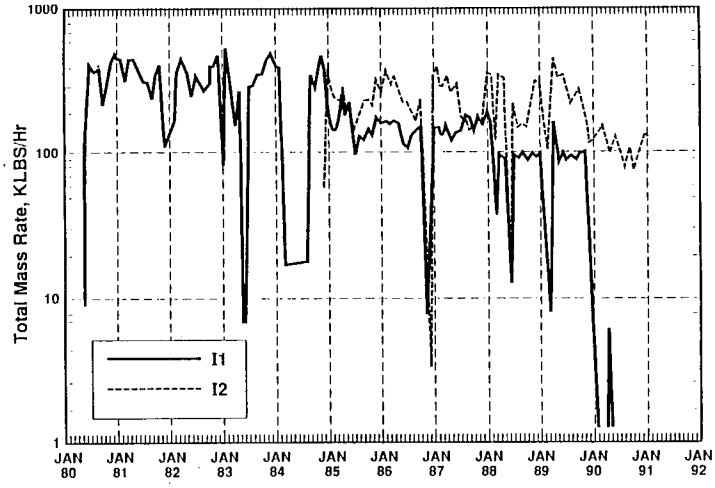

Figure 2 Historical Injection Rates for I1 and I2

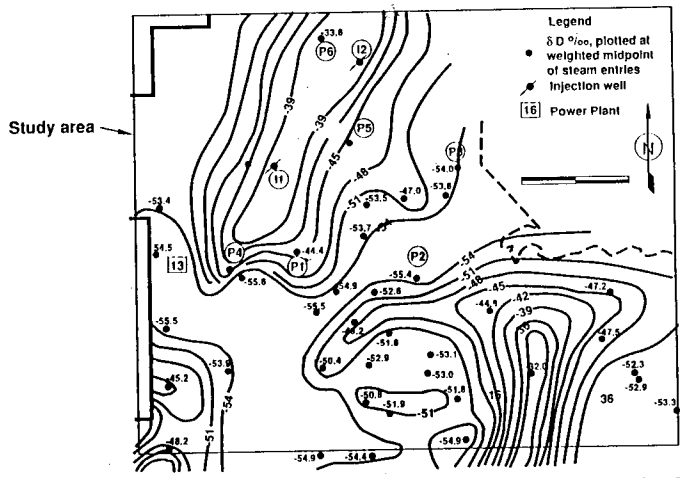

Figure 3 Deuterium Isotopic Shift for Study Area, modified from Beall, Enedy, and Box, 1989.

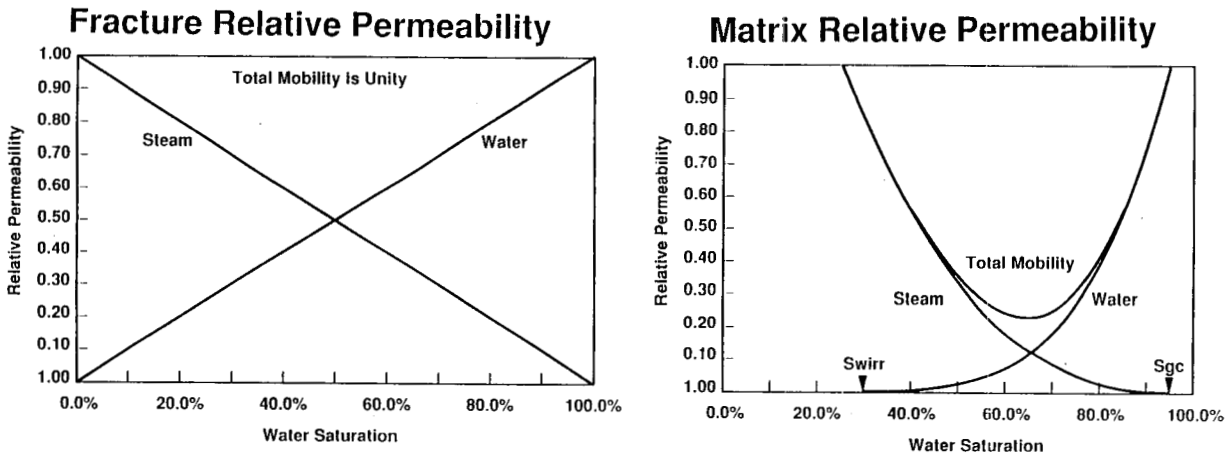

Figure 4 Fracture and Matrix Relative Permeability Curves

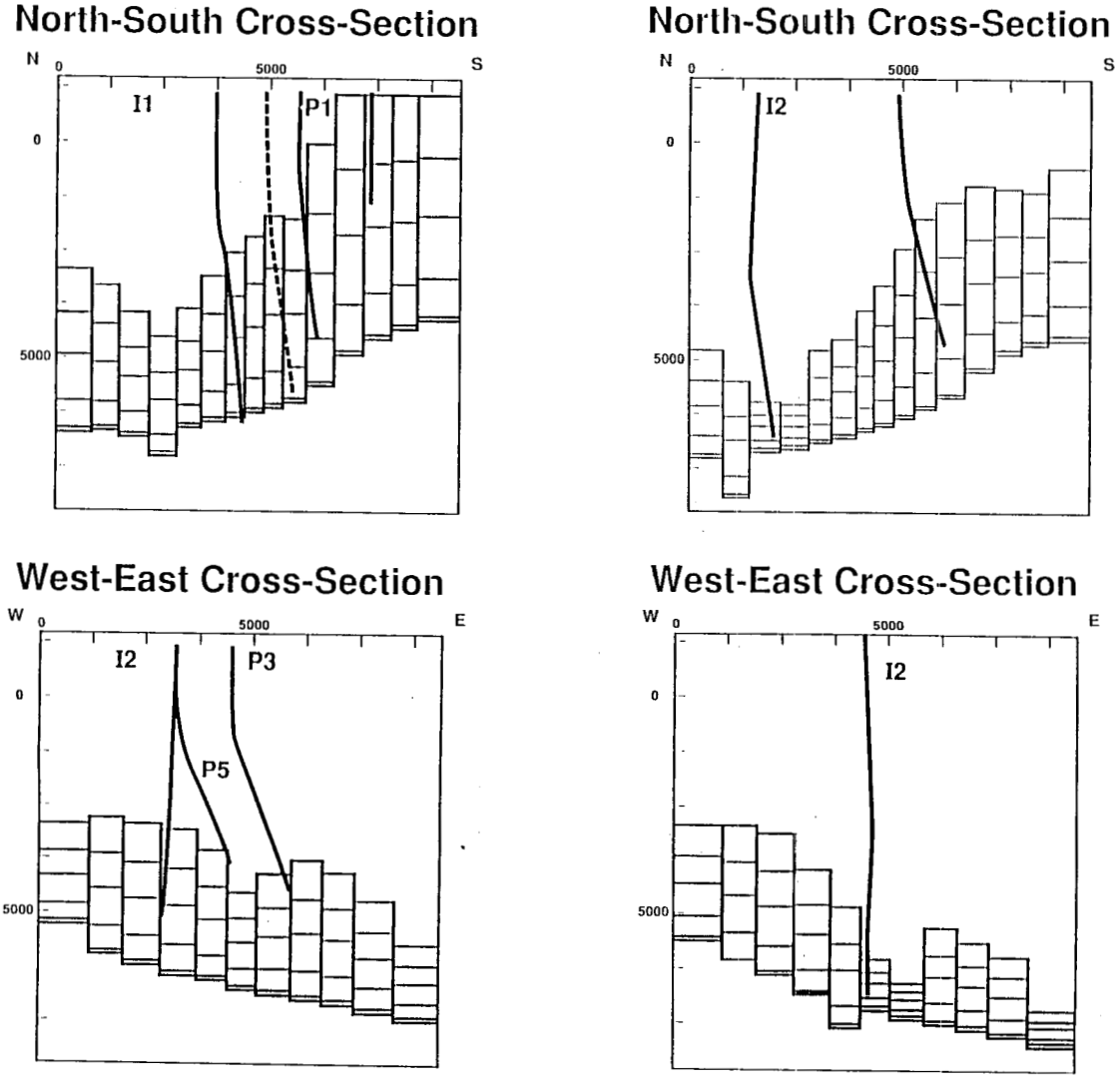

Figure 5 Select Cross-Sections of the Model

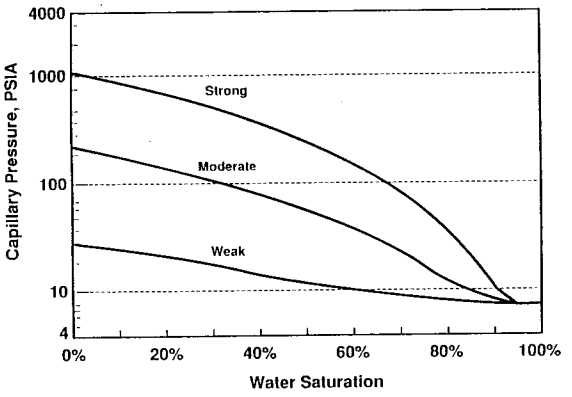

Figure 6 Matrix Capillary Pressure

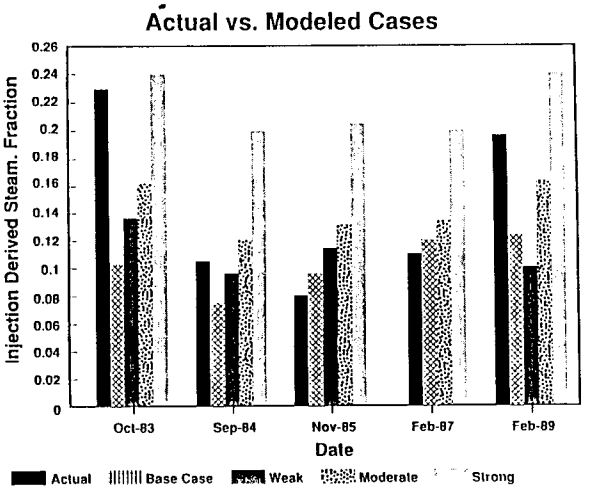

Figure 7 Injection Derived Steam Results for Well P5

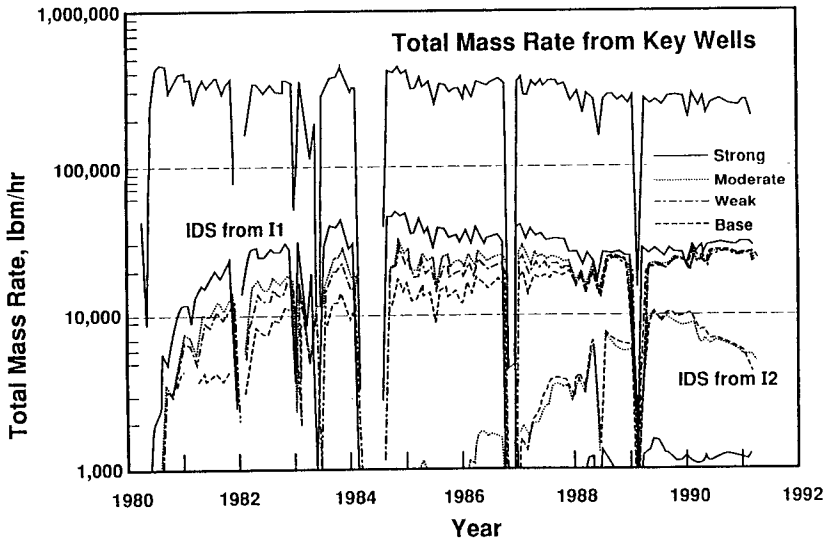

Figure 8 Key Wells Modeled Injection Derived Steam

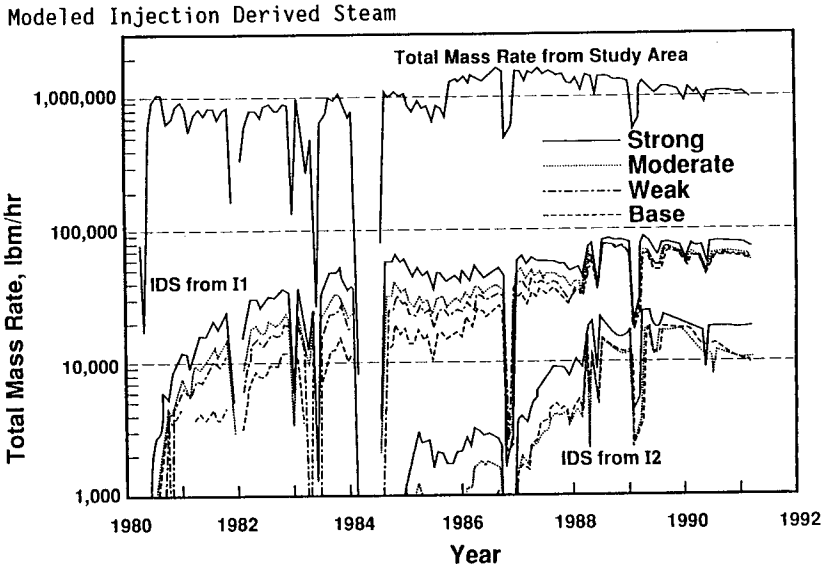

Figure 9 Study Area Modeled Injection Derived Steam

Table 2

Recovery of Injection Derived Steam

Cumulative Injection into I1 1.75E+7 Klbm
Cumulative Injection into I2 1.18E+7 Klbm

Key Wells

Case	% Recovery from I1	% Recovery from I2
Base	7.1	1.9
Weak Capillarity	8.5	1.7
Moderate Capillarity	9.5	1.9
Strong Capillarity	13.2	3.0

Total Study Area

Case	% Recovery from I1	% Recovery from I2
Base	14.5	3.3
Weak Capillarity	16.7	3.1
Moderate Capillarity	18.3	3.3
Strong Capillarity	24.1	5.0

PROCEEDINGS, Seventeenth Workshop on Geothermal Reservoir Engineering
Stanford University, Stanford, California, January 29-31, 1992
SGP-TR-141

Thermal and Chemical Evolution of The Geysers Geothermal System, California

J. N. Moore

University of Utah Research Institute
391 Chipeta Way, Suite C
Salt Lake City, Utah 84109

ABSTRACT

Fluid inclusions and mineral assemblages provide a record of the thermal and chemical changes that occurred during the evolution of The Geysers geothermal system. The data document the presence of an extensive liquid-dominated geothermal system that developed in response to felsite intrusion and its evolution to a vapor-dominated regime. Temperatures within the early liquid-dominated system ranged from 175°C at a distance of 7200 feet from the felsite to more than 350°C near the contact while salinities varied from 5 equivalent weight percent NaCl (at a distance of 5500 feet) to more than 26 weight percent NaCl. As temperatures around the felsite declined, the liquid-dominated system collapsed upon itself. Downward migration of the low salinity waters resulted in dilution of the fluids present in regions now occupied by the caprock and normal vapor-dominated reservoir. In contrast, dilution was minor in rocks now hosting the high-temperature vapor-dominated reservoir. This suggests that low permeabilities are the primary reason for the development of the high-temperature reservoir.

Boiling within the caprock produced late-stage veins of calcite and quartz. As the fluid boiled off, condensate was trapped as low salinity fluid inclusions. Within the main body of the reservoir, a liquid phase with salinities of up to 7 equivalent weight percent NaCl persisted to temperatures between 250° and 270°C. However, except for the presence of vapor-rich inclusions, little evidence of boiling within the reservoir rocks was preserved.

INTRODUCTION

Although the pioneering work of White and others (1971) provided the basic framework needed for understanding the origin of The Geysers steam field, many of their hypotheses have remained untested and new questions have been raised as a result of recent field developments. For example, little direct information is available on the composition of the early fluids, the nature of the reservoir boundaries, and the differences between the normal 240°C vapor-dominated reservoir (NVDR) and the underlying high-temperature vapor-dominated reservoir (HTVDR).

Answers to these and other questions require information on the compositional and thermal evolution of the system. Sternfeld (1981) and Moore and others (1989) used fluid inclusions in cuttings to characterize the early hydrothermal system that developed above the present steam reservoir. These studies demonstrated that temperatures had been significantly higher in the past and that the salinities of the fluids were on the order of several weight percent. In this paper we expand significantly on the earlier fluid inclusion investigations. More than a thousand new measurements have been made on core and cuttings samples from 8 Calpine Corp. and 10 Unocal Geothermal Division wells (Fig. 1; Table 1). These new data are combined with the existing information to characterize the conditions within the caprock, the NVDR, and the HTVDR during the evolution of The Geysers geothermal system.

MINERALOGIC RELATIONSHIPS

The rocks at the Geysers show evidence of two distinct periods of alteration (Lambert, 1976; Sternfeld and Elders, 1982; Walters and others, 1988; Moore and others, 1989; Hulen and others, 1991). The oldest event is the result of high-pressure, low-temperature regional metamorphism during Franciscan time (Late Mesozoic). This metamorphism produced, in addition to phases such as lawsonite and pumpellyite, widespread veins of calcite and quartz. The second period of alteration is related to the intrusion of a felsic, composite Plio-Pleistocene pluton beneath The Geysers (Schriener and Suemnicht, 1980; Thompson, 1989). This pluton, which is commonly referred to as the felsite, produced calc-silicate and boron-bearing mineral assemblages. In this investigation, five major vein assemblages were studied. With increasing distance from the pluton, the key vein assemblages are:

1: tourmaline-biotite-actinolite-clinopyroxene-epidote-quartz-potassium feldspar;

2: biotite-actinolite-clinopyroxene-epidote-quartz-potassium feldspar;

3: actinolite-ferroaxinite-epidote-quartz-prehnite-potassium feldspar;

4: epidote-chlorite-quartz-potassium feldspar;

5: quartz-potassium feldspar-calcite.

In addition to these minerals, Hulen and others (1991) have identified prehnite in assemblage 4 and late-stage wairakite that postdates assemblage 5.

As the system cooled, the early veins were crosscut by veins typical of greater distances from the felsite. The extent of this cooling is documented in the fluid inclusion data discussed below. Assemblages 1 through 4 occur within highly contorted metamorphosed quartz-calcite veins of Franciscan age and in younger crosscutting fractures. Within the Franciscan veins, the calc-silicate minerals form small, commonly porous aggregates that replace preexisting calcite (Hulen and others, 1991).

Calcite is much more abundant in the caprock than it is in the NVDR (Sternfeld and Elders, 1982; Thompson and Gunderson, 1989; Sternfeld, 1989; Gunderson, 1990; Hulen and others, 1991). Within the caprock, calcite occurs as both a late-stage mineral

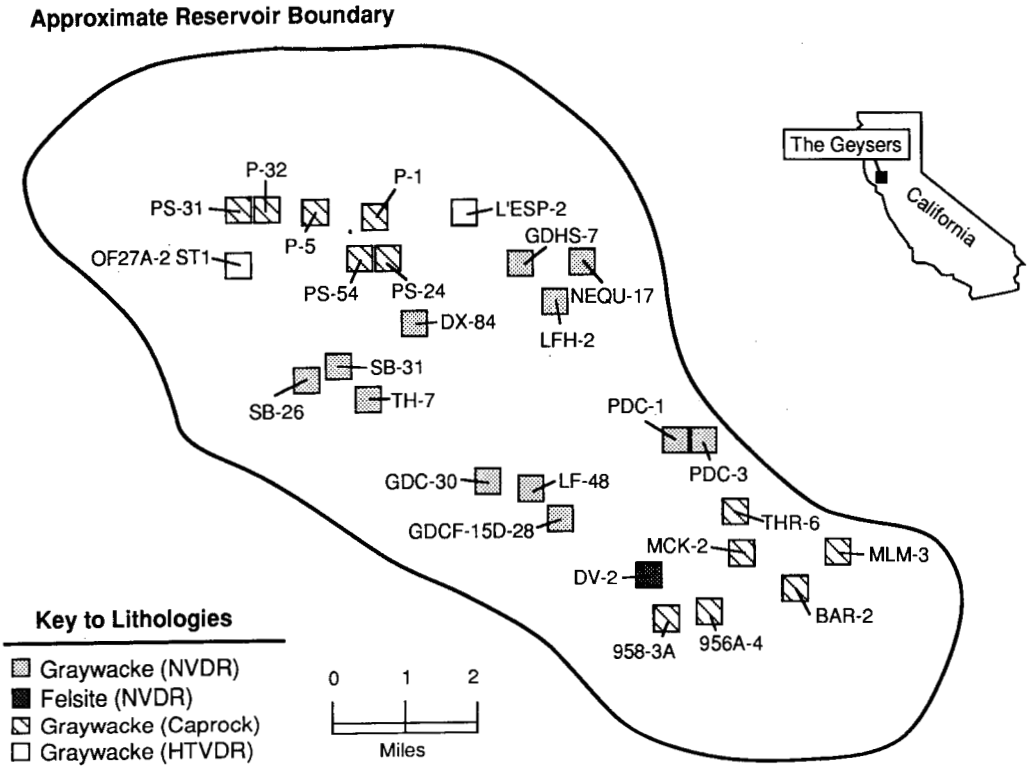

Fig. 1. Locations and lithologies of the samples studied. Data from LFH-2 and SB-26 are from Sternfeld (1981). Abbreviations: NVDR = normal vapor-dominated reservoir; HTVDR = high-temperature vapor dominated reservoir.

Name	Sample from	Drilled Depth	Elev. MSL	Distance from Felsite
956A-4	Caprock	2070	1233	4733
958-3A	Caprock	2440	536	3036
BAR-2	Caprock	2500	-273	5227
DV-2	NVDR	3713	-665	-365
DX-84	NVDR	7736	-4180	2020
GDC-30	NVDR	5022	-2920	1080
GDCF-15D-28	NVDR	5032	-2015	485
GDHS-7	NVDR	8075	-4825	3175
L'ESP-2	HTVDR	11059	-8075	925
LFH-2	Caprock	3100	495	7995
LFH-2	Caprock	3800	-205	7295
LFH-2	Caprock	4800	-1198	6302
LFH-2	Caprock	5200	-1592	5908
LFH-2	Caprock	5600	-1985	5515
LFH-2	Caprock	5800	-2182	5318
LFH-2	Caprock	6000	-2379	5121
MCK-2	Caprock	2170	312	5512
MLM-3	Caprock	4330	-2216	4284
NEGU-17	NVDR	8531	-5245	3755
OF27A-2 ST1	HTVDR	10377	-7225	775
PDC-1	NVDR	5140	-2326	4174
PDC-3	NVDR	5990	-3140	3360
P-1	Caprock	5160	-2032	4968
P-1	Caprock	5170	-2042	4958
P-1	Caprock	5190	-2062	4938
P-5	Caprock	4170	-1572	5428
P-32	Caprock	5960	-3793	3207

Name	Sample from	Drilled Depth	Elev. MSL	Distance from Felsite
PS-24	Caprock	4080	-1426	5574
PS-31	Caprock	4650	-2480	4520
PS-31	Caprock	5090	-2904	4096
PS-54	Caprock	4140	-1477	5523
SB-26	Caprock	360	1752	6752
SB-26	Caprock	820	1292	6292
SB-26	Caprock	1100	1012	6012
SB-26	Caprock	1360	753	5753
SB-26	Caprock	1400	713	5713
SB-26	Caprock	1700	418	5418
SB-26	Caprock	2000	130	5130
SB-26	Caprock	2340	-192	4808
SB-26	Caprock	2500	-345	4655
SB-26	Caprock	2540	-384	4616
SB-26	Caprock	2700	-537	4463
SB-26	Caprock	2740	-575	4425
SB31	NVDR	3740	-1565	3135
TH-7	NVDR	1000	740	5240
THR-6	Caprock	3490	-1121	5379
THR-6	Caprock	4020	-1601	4834
THR-6	Caprock	4110	-1692	4808
THR-6	Caprock	5430	-2902	3598

Table 1. Depths and distance from the felsite of the samples studied. All depths are in feet. Elev. MSL = elevation relative to mean sea level. Other abbreviations as in Fig 1. LHF-2 and SB-26 data are from Sternfeld (1981).

intergrown with quartz or as bladed crystals (assemblage 5), and as a relict phase in the Franciscan veins associated with actinolite and epidote. These late-stage textures indicate deposition from boiling fluids. Except for the shallow reservoir represented by TH-7 (Gunderson, 1989), calcite is not common as a late-stage mineral in the NVDR and little carbonate remains in the Franciscan veins. The loss of calcite has been ascribed to the formation of the calc-silicate minerals and to dissolution (Gunderson, 1989; Hulen and others, 1991).

Most of the quartz within the Franciscan veins contains abundant small fluid inclusions that gives it a turbid appearance. In contrast, quartz that is intergrown with the calc-silicate aggregates is often clear. This quartz appears to have formed during the metamorphism that accompanied emplacement of the felsite. Most of the fluid inclusion data described in the following sections was obtained on grains of this clear quartz.

FLUID-INCLUSION SYSTEMATICS

Fluid inclusions are common in the veins. They can be classified into several types on the basis of their compositions and phase relationships. These include: two-phase liquid-rich inclusions whose final phase to melt is ice; two-phase vapor-rich inclusions; two-phase liquid-rich inclusions whose final phase to melt is CO_2 clathrate; three-phase liquid-rich inclusions containing daughter crystals of halite; and four-phase liquid-rich inclusions containing daughter crystals of halite and sylvite.

Most of the fluid inclusions occurring in the samples are vapor-rich. These inclusions are found randomly distributed throughout the grains and as planar arrays that define healed fractures. The presence of secondary planes that lack liquid-rich inclusions provides evidence of boiling throughout the system.

The majority of the fluid inclusions examined in this study were of secondary or undefined origin. Primary fluid inclusions are uncommon, occurring primarily within the caprock.

Heating and freezing measurements were made on liquid-rich fluid inclusions using a Fluid Inc. adapted U.S.G.S.-type heating/freezing stage calibrated with synthetic fluid inclusions. The accuracy of the microthermometric measurements, based on repeated measurements of the synthetic fluid inclusion samples, is estimated to be ± 0.1°C at temperatures below 0.0°C and ± 3°C at 374°C.

The fluid-inclusion measurements define strong gradients in the compositions and temperatures of the fluids that have circulated through the geothermal system. Homogenization temperatures (Th) of the inclusions ranged from 120° to 470°C, whereas NaCl contents varied from less than .18 to 42 weight percent. The data are plotted with respect to their vertical distance from the felsite in Figures 2 and 3. These distances were taken from Gunderson (1989) for samples provided by Unocal Geothermal Division or estimated from the data presented by Thompson (1989).

The apparent salinities of the two-phase inclusions were calculated from their ice-melting temperatures using the equation of Potter and others (1978). NaCl contents of halite-bearing inclusions were determined from the dissolution temperature of the salt using data summarized by Sourirajan and Kennedy (1962). If the dissolution temperature could not be measured, a minimum value of 26 weight percent NaCl was assigned to the inclusions. No quantitative compositional data was obtained on inclusions containing halite and sylvite was because of their small size.

A few of the fluid inclusions from the caprock and NVDR contained enough CO_2 to produce CO_2 clathrate on cooling below 0°C. Low CO_2 clathrate dissociation temperatures of up to 1.7°C indicate that their CO_2 contents were on the order of 5 weight percent.

DISCUSSION

The Caprock and Normal Vapor-Dominated Reservoir

Fluid inclusions from the caprock were studied in samples from the northwest and southeast parts of The Geysers while those from the NVDR come primarily from the central portions of the field (Fig. 1). Despite the spatial separation of the samples, comparison of the data shows that similar temperature and salinity relationships existed throughout the field.

Fluid-inclusion data were obtained on calcite and quartz from the caprock and on quartz, epidote, actinolite, and ferroaxinite from the NVDR (Figs. 2 and 3). Figure 2 shows that the maximum homogenization temperatures of the samples increase with decreasing distance to the felsite. The minimum homogenization temperatures of the NVDR samples range from 250° at distances of less than 4000 feet from the felsite to 240°C at greater distances.

The maximum salinities of the inclusion fluids also increase as the felsite is approached (Fig. 3). The highest values are found in tourmaline-bearing veins. Fluid inclusions in these veins frequently contain halite, indicating NaCl contents of at least 26 weight percent, and less commonly halite and sylvite.

As the geothermal system evolved, both fluid temperatures and salinities decreased. A good example of this relationship is provided by data from DV-2, which was taken from the felsite. This sample is characterized by early tourmaline-bearing veins. High-salinity fluid inclusions in the tourmaline-bearing veins contain halite or halite and sylvite and have average homogenization temperatures of 328°C. The younger quartz veins are characterized by inclusion fluids with salinities of 3 to 6 equivalent weight percent NaCl and average homogenization temperatures of 271°C. Similar, moderate salinity fluids are found throughout the caprock and NVDR (Fig. 3).

Fluid inclusions with very low salinities, between 0.0 and 0.4 equivalent weight percent NaCl, are common within the caprock but only occur sporadically within the NVDR. The combination of high homogenization temperatures (>200°C) and low salinities suggests that the fluids consist of condensate or mixtures of condensate and saline fluid.

The High-Temperature Vapor-Dominated Reservoir

Two samples from the HTVDR were studied. OF27A-2 ST1 is characterized by tourmaline-bearing veins (assemblage 1) that show little evidence of retrograde metamorphism or secondary alteration. Veins in L'ESP-2 contain assemblage 2 in which biotite has been chloritized or chlorite and pyrite (assemblage 4).

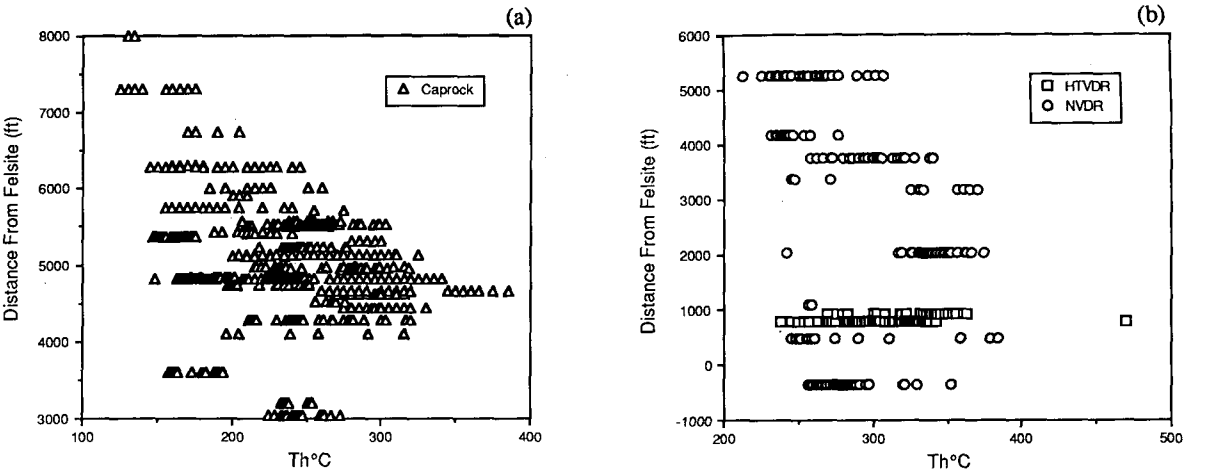

Fig. 2. Homogenization temperatures (Th) of fluid inclusions from the (a) caprock and (b) NVDR and HTVDR. The data are plotted with respect to their vertical distance from the felsite. Abbreviations as in Fig. 1.

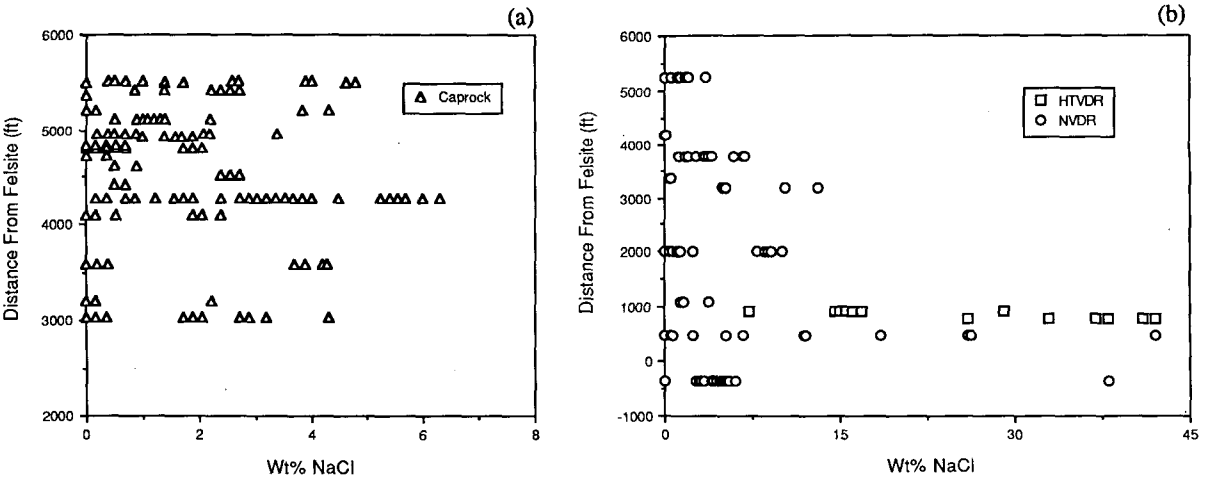

Fig. 3. NaCl contents in weight % (Wt%) of fluid inclusions from the (a) caprock and (b) NVDR and HTVDR. Abbreviations as in Fig. 1. The data are plotted with respect to their vertical distance from the felsite. See text for determination of NaCl contents.

Both samples of the HTVDR contained secondary inclusions in quartz that were suitable for study. With the exception of a single allanite(?)-bearing inclusion from OF27A-2 ST1 (Th≈470°C), the samples had generally similar homogenization temperatures. These temperatures ranged from 237° to 342°C in OF27A-2 ST1 and from 269° to 363°C in L'ESP-2. The highest temperatures are comparable to those samples from the NVDR that contain assemblage 1.

It was more difficult to estimate the salinities of these inclusions because of their small size. In OF27A-2 ST1, only inclusions containing halite could be accurately measured. The NaCl contents of these inclusions ranged up to 42 weight percent. The salinities of the fluid inclusions in LESP-2 were lower, ranging generally from 7 to 17 equivalent weight percent NaCl. Although the number of salinity measurements on samples from the high-temperature reservoir is small, it is significant that no evidence was found for the low salinity fluids that were preserved in vein assemblage 1 in the reservoir rocks (0 to 5 equivalent weight percent NaCl).

Origin of the Temperature and Salinity Variations

The data discussed above demonstrate that the gradients in the temperatures and salinities of the inclusion fluids can be related to both time and distance from the felsite. Figure 4 illustrates the salinities and homogenization temperatures for individual inclusions. The overall trend of fluid inclusions from the caprock and NVDR is one of decreasing salinity with decreasing temperature. This relationship suggests that dilution was the primary cause of the variations in fluid chemistry and temperature. However, the vein relationships discussed above indicate that temperatures and salinities also declined as the system evolved. These changes could have resulted from the collapse of

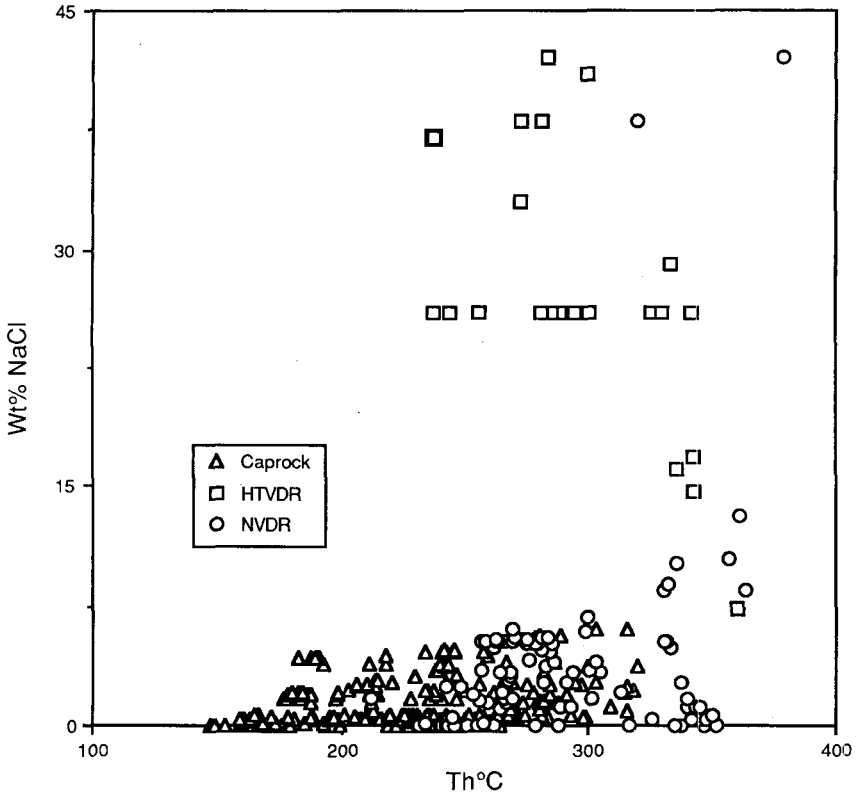

Fig. 4. Crossplot of homogenization temperatures (Th) and NaCl contents of individual fluid inclusions. Abbreviations as in Fig. 1.

the early liquid-dominated hydrothermal system as the felsite cooled, allowing the shallow, dilute fluids to migrate downward into the region now occupied by the NVDR.

Highly saline fluids, some of which were saturated with respect to halite, characterize the HTVDR and the tourmaline-bearing assemblages from the reservoir. Although the halite saturated fluids from the HTVDR display a broad range of homogenization temperatures from 235° to 350°C, they display no obvious dilution trends (refer to Fig. 4). Thus, cooling may have largely conductive.

The compositions of fluid inclusions with homogenization temperatures near 350°C and salinities between 0 and 17 equivalent weight percent NaCl may reflect the effects of boiling. The high-temperatures of the lowest salinity fluids suggest that they represent steam condensate. Thus, the salinity variations of these inclusion fluids may be due to mixing between condensate and paleoreservoir fluids as well as to salinity increases due to boiling. Similar processes may have contributed to the salinity variations observed in the caprock and upper part of the reservoir.

CONCLUSIONS

Fluid inclusion and mineralogic data show, as was proposed by Sternfeld and Elders (1982), that a large scale liquid-dominated geothermal system developed in response to the intrusion of the felsite. During the initial development of this hydrothermal system, temperatures and salinities appear to varied continuously between what is now the caprock, the normal vapor-dominated reservoir (NVDR) and the high-temperature vapor-dominated reservoir (HTVDR). Fluids in the vicinity of the felsite locally reached temperatures exceeding 350°C and NaCl contents in excess of 26 weight percent. The initial salinities and temperatures decreased with increasing distance from the felsite. As the felsite cooled, the hydrothermal system within the caprock and NVDR collapsed downward, progressively diluting the initial high-salinity fluids.

Two samples of the HTVDR were studied. Although fluid inclusions in samples from the HTVDR have homogenization temperatures similar to those in the NVDR, inclusions from the HTVDR typically record much higher salinities. In one sample of the HTVDR containing abundant fresh biotite, fluid inclusions saturated with halite (>26 weight percent NaCl) displayed homogenization temperatures ranging from 237° to 305°C. This suggests that the incursion of low salinity fluids was severely limited by low permeabilities and that temperature changes may have been due largely to conductive cooling. The conclusion that permeabilities were low in the HTVDR is further supported by the lack of retrograde alteration of biotite to chlorite in one of the samples.

The caprock is distinguished from the reservoir rocks by the abundance of calcite. Within the caprock, late-stage calcite was deposited by boiling fluids. As boiling proceeded, acidic condensates, preserved as low salinity fluid inclusions, formed and reacted with the host rocks to produce illite, mixed-layer clays and locally kaolin (Moore and others, 1989; Hulen and others, 1991). These minerals further reduced the permeabilities of the caprock.

Homogenization temperatures indicate that saline water persisted to temperatures between 250° and 270°C within the main part of the reservoir and to slightly lower temperatures in its upper part where calcite locally remained stable. Low CO_2 contents of the late-stage boiling fluids, caused by the upward migration of gas and steam, may have been the primary reason for the absence of late-stage calcite in the developing vapor-dominated reservoir.

ACKNOWLEDGEMENTS

This project would not have been possible without the support of the management and staff of Calpine Corp. and Unocal Geothermal Division. I particularly want to thank T. Box, J. Beall, R. Gunderson, P. Molling and M. Stoh-Twichell who painstakingly hand- picked samples of the cuttings for future studies. An early version of this paper was reviewed by M. Adams, R. Gunderson, and J. Hulen. Their suggestions are greatly appreciated.

This work was supported by the U.S. Department of Energy, Contract No. DE-AC07-85ID12489. Such support does not constitute an endorsement by the U.S. Department of Energy of the views expressed in this publication.

REFERENCES

Gunderson, R. P., 1990, Reservoir matrix porosity at The Geysers from core measurements: Geothermal Resources Council Trans., v. 14, p. 1661-1665

Hulen, J. B., Walters, M. A., and Nielson, D. L., 1991, Comparison of reservoir and caprock core from the Northwest Geysers steam field, California: Geothermal Resources Council Trans., v. 15, p. 11-18.

Lambert, S. J., 1976, Stable isotope studies of some active hydrothermal systems: Ph.D thesis, California Institute of Technology, Pasadena CA, 362 p.

Moore, J. N., Hulen, J. B., Lemieux, M. M., Sternfeld, J. N., and Walters, M. A., 1989, Petrographic and fluid inclusion evidence for past boiling, brecciation, and associated hydrothermal alteration above the Northwest Geysers steam field, California: Geothermal Resources Council Trans., v. 13, p. 467-472.

Potter R. W., II, Clynne M. A., and Brown D. L., 1978, Freezing point depression of aqueous sodium chloride solutions. Economic Geology, v. 73, 284-285.

Schriener, A. Jr., and Suemnicht, G. A., 1980, Subsurface intrusive rocks at The Geysers geothermal area: In Silberman, M. C., and others (eds.), Proceedings of the Symposium on Mineral Deposition in the Pacific NW, U.S.G.S. Open File Report, 81-355, p. 294-303

Sourirajan, S. and Kennedy, G. C., 1962, The system H_2O-NaCl at elevated temperatures and pressures: American Journal of Science, 60, p. 115-141.

Sternfeld, J. N., 1981, The hydrothermal petrology and stable isotope geochemistry of two wells in The Geysers geothermal field, Sonoma County, California: M. S. Thesis, University of California, Riverside, 202 p.

Sternfeld, J. N., 1989, Lithologic influences on fracture permeability and the distribution of steam in the Northwest Geysers steam field, Sonoma County, California: Geothermal Resources Council Trans., v. 13, p. 473-479.

Sternfeld, J. N., and Elders, W. A., 1982, Mineral zonation and stable isotope geochemistry of a production well in The Geysers geothermal field, California. Geothermal Resources Council Trans., v. 6, p. 51-54.

Thompson, R. C., Structural stratigraphy and intrusive rocks at The Geysers geothermal field: Geothermal Resources Council Trans., v. 13, p. 481-485.

Thompson, R. C., and Gunderson, R. P., The orientation of steam-bearing fractures at The Geysers geothermal field: Geothermal Resources Council Trans., v. 13, p. 487-490.

White, D. E., Muffler, L. J. P., and Truesdell, A. H., 1971, Vapor-dominated hydrothermal systems compared with hot water systems: Economic Geology, v. 66, p. 73-81.

PROCEEDINGS, Seventeenth Workshop on Geothermal Reservoir Engineering
Stanford University, Stanford, California, January 29-31, 1992
SGP-TR-141

PRELIMINARY RESERVOIR ENGINEERING STUDIES OF THE MIRAVALLES GEOTHERMAL FIELD, COSTA RICA

C. Haukwa,[1] G. S. Bodvarsson,[1] M. J. Lippmann[1] and A. Mainieri[2]

[1]Earth Sciences Division
Lawrence Berkeley Laboratory
Berkeley, CA 94720

[2]Instituto Costarricense de Electricidad
San Jose, Costa Rica

ABSTRACT

The Earth Sciences Division of Lawrence Berkeley Laboratory in cooperation with the Instituto Costarricense de Electricidad is conducting a reservoir engineering study of the Miravalles geothermal field, Costa Rica. Using data from eight exploration wells, a two-dimensional areal, natural-state model of Miravalles has been developed. The model was calibrated by fitting the observed temperature and pressure distributions and requires a geothermal upflow zone in the northern part of the field, associated with the Miravalles volcano and an outflow towards the south. The total hot (about 260°C) water recharge is 130 kg/s, corresponding to a thermal input of about 150 MWt.

On the basis of the natural-state model a two-dimensional exploitation model was developed. The field has a production area of about 10 km^2, with temperatures exceeding 220°C. The model indicated that power generation of 55 MWe can be maintained for 30 years, with or without injection of the separated geothermal brine. Generation of 110 MWe could be problematic. Until more information becomes available on the areal extent of the field and the properties of the reservoir rocks, especially their relative permeability characteristics, it is difficult to ascertain if 110 MWe can be sustained during a 30-year period.

INTRODUCTION

Eight deep wells, with depths varying between 1162 and 2270 m, have been drilled at the Miravalles geothermal field (Figures 1 and 2) and the construction of a 55 MWe power plant is underway (Alvarado, 1987; Mainieri and Vaca, 1990). The field is located within a Pleistocene volcanic caldera. The Miravalles volcano itself, northeast of the wellfield, is a post-caldera feature that developed on the caldera rim.

The successful wells have been completed at the intersection of west-east and north-south trending faults (Mainieri et al., 1985). The lithology of the area consists of a series of volcanic flows and pyroclastic units. Geothermal fluids are produced from fractures, mainly in the so-called "basement" which is comprised of crystal-lithic tuffs, andesitic lavas and welded tuffs (Mainieri et al., 1985). Details on the geologic characterists of the area can be found in ICE-ELC (1988) and Mora (1988, 1989).

Analysis of the available well log and well test data was carried out in order to characterize the physical and thermodynamic properties of the reservoir, as well as to develop a conceptual model of the field. Then, following a general approach to evaluate such systems (Bodvarsson and Witherspoon, 1989), natural state and exploitation models of the Miravalles system were developed and used to study the power generation potential of the field.

RESERVOIR ENGINEERING STUDIES

Initial Temperature Distribution

Figure 3 (ICE-ELC, 1988) presents E-W and NNE/SSW geologic sections, as well as the temperature

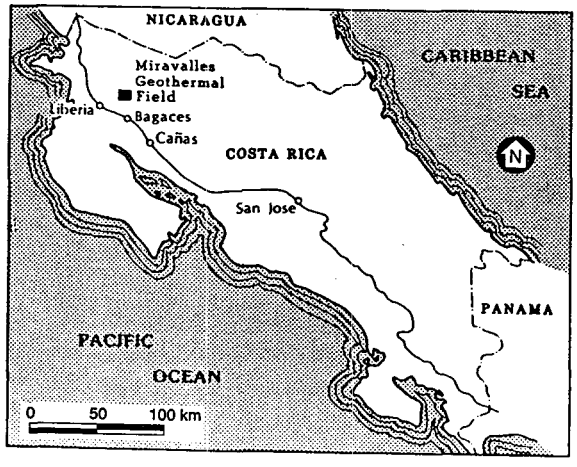

Figure 1. Location of the Miravalles geothermal field.

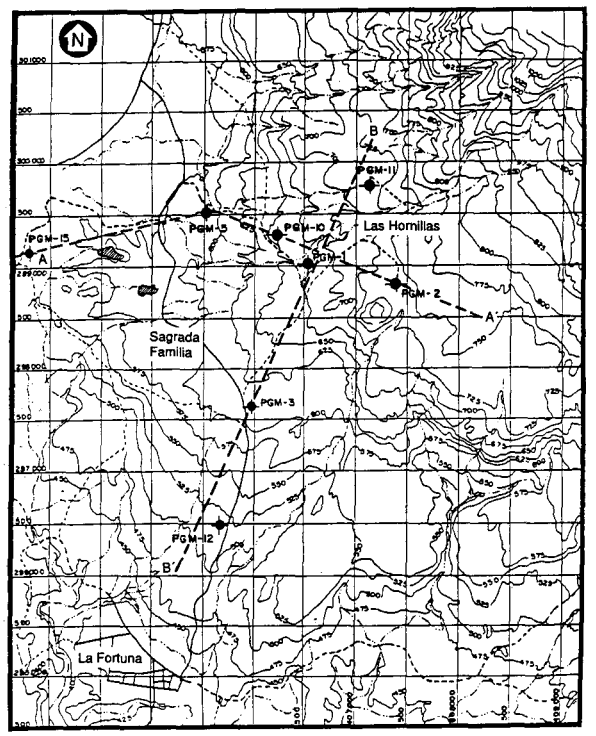

XBL 9112-6887

Figure 2. Location of Miravalles wells and cross-sections shown in Figure 3.

distribution in Miravalles; the location of the sections is given in Figure 2. On the basis of the isotherms shown in the E-W section (Figure 3a), the center of the convective plume is considered to be around wells PGM-1 and 10, with temperatures decreasing towards the west, and then falling steeply about 1 km west of PGM-5. The eastern limit of the field is indicated by the strong thermal inversion observed in PGM-2.

The NNE-SSW section (Figure 3b) shows higher temperatures to the north with the highest (exceeding 255°C) near PGM-11 at approximately −250 to −450 masl. Below that elevation downhole logs in PGM-11 indicate a reversal with temperature decreasing to 245°C at −550 masl. The inferred sharp temperature drop west of PGM-3 is likely distorted by the strong internal wellbore flow that masks the true temperatures. Therefore, the actual 235 and 245°C isotherms are probably more gradual than depicted in Figure 3b.

Fluid-inclusion studies suggest that temperatures in parts of the field were significantly warmer in the past. Homogenization temperatures for liquid-rich fluid inclusions were up to about 70°C hotter than those measured at some sampled depths (Bargar and Fournier, 1988).

Temperature logs for Miravalles wells PGM-1, 2, 3, 5, 10, 11, 12 and 15 were analyzed to obtain the initial (pre-exploitation) state temperature distribution at the reference elevation of −200 masl. The logs show a nearly uniform reservoir top at an elevation of 200-250 masl over the central part of the field, but dropping steeply to the west (towards PGM-15) and gradually to the south. The measurements show that at an elevation of −200 masl the temperature is highest around well PGM-11 (above 240°C), with isotherms elongated in a SSW direction (Figure 4). This temperature distribution corresponds approximately with the heat flow maps developed by Koenig (1980) and indicates an upflow region in the area of PGM-11, 10 and 1, and outflow south of PGM-12; this agrees with the model of Grigsby et al. (1989). The sharp drop of temperature towards PGM-15 suggests a hydrological barrier or cold water encroachment from the west.

Initial Pressure Distribution

Downhole pressure logs data obtained in the Miravalles wells were analyzed to obtain pressures at −200 masl, an elevation where all the wells except PGM-15 show permeability. The pressure logs taken in 1988-1989 following long periods of recovery, are believed to best represent the undisturbed reservoir pressure. However, many of the wells have internal flow which masks true reservoir pressures.

The measured pressure distribution at −200 masl (Table 1, Figure 5) shows the highest pressure in PGM-11 (51 bar), fairly uniform pressure around PGM-1, 2 and 10, and a general gradient toward the SSW over the wellfield. To the west, beyond PGM-5, the pressure distribution is not well defined due to lack of subsurface data. Southward the pressure drops gradually at about 1 bar/km. This pressure distribution combined with the corresponding temperature distribution indicates that the outflow zone for the geothermal system is towards the south, perhaps associated with the Bagaces hot springs (see Figure 6) and other surface manifestations to the south.

Well Tests

A number of injection and production tests were performed to obtain the hydraulic and production characteristics of the wells and reservoir. Transient injection and fall-off tests were carried out in wells PGM-2, 10, 11, 12 and 15. The results are summarized in Table 1. All were short-duration tests (typically less than 1-1/2 hour) and pressures did not stabilize. In PGM-15, even long injection steps of up to 6 hours did not result in stable pressure due to low formation permeabilities.

Pressure profiles measured in PGM-1, 2, 3, 5, 10 and 12 during flow were used to obtain well productivity indices (Table 1). No measurable drawdown was observed in PGM-1 and 3, indicating very high reservoir permeability.

Variable flow discharge tests were performed in PGM-1, 3, 5, 10 and 11. These tests referred to as Reservoir Characterization Curves (RCC), were used to obtain

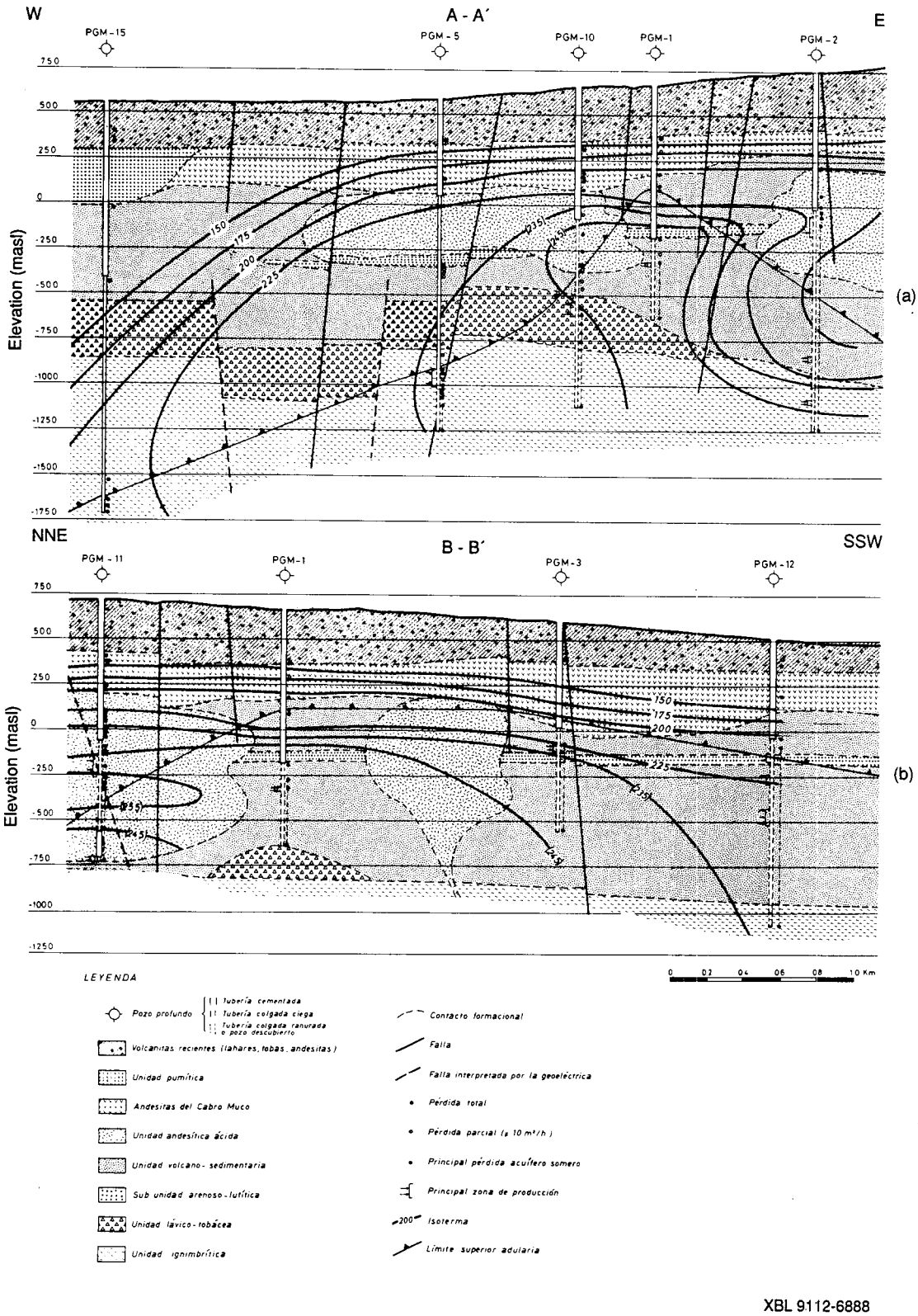

Figure 3. Geologic sections and temperature distribution in the Miravalles field (from ICE-ELC, 1988).

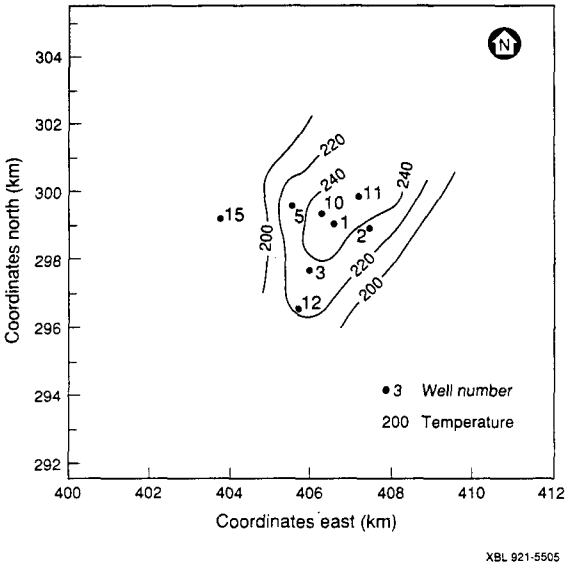

Figure 4. Measured temperature distribution at −200 masl (in °C)

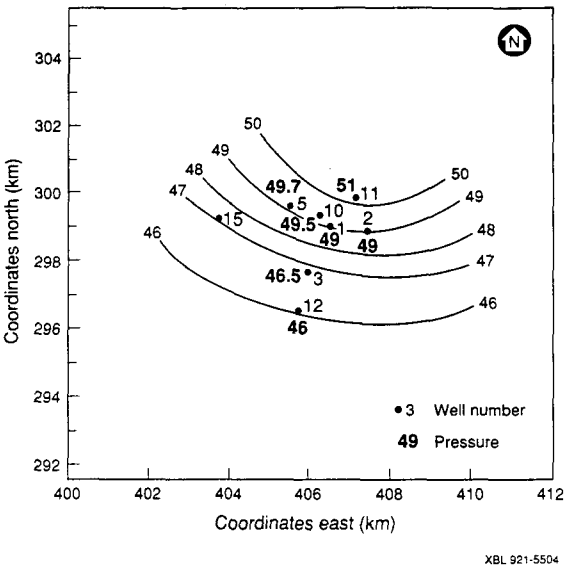

Figure. 5. Measured pressure distribution at −200 masl (in bar)

Table 1. Characteristics of Miravalles Wells

Well No.	Injectivity Index (kg/s/bar)	Productivity Index (kg/s/bar)	Flow Rate[a] (kg/s)	Enthalpy[a] (kJ/kg)	Power[a] (MWe)	Temperature at -200 masl (°C)	Pressure at -200 masl (bar)
1.	-	-	70.0	1050	5.5	250	49.0
2.[b]	2.4	0.3(10.0[c])	60.8	1040	4.6	235	49.0
3.	-	-	90.0	1040	6.9	240	46.5
5.	-	6.0(3.0[d])	65.0	1030	4.8	230	49.7
5.	-	0.7–3.5[e]					
10.[f]	1.0	1.5(0.6)	28.0	1030	2.1	250	49.5
11.	3.3-4.2	-	65.0	1100	5.7	255	51.0
12.	10.0	11.2	135.0	1030	10.0	235	46.0
15.	0.6	-	-	-	-	102	-
		TOTAL	513.8		39.6		

Notes
a. Flow rate, enthalpy and power correspond to 10 bar WHP.
b. After deepening, it produced acid fluid (pH 2.2).
c. After the well was deepened.
d. Repeat test after 50 days of production tests, from flowing pressure profiles. Reduced permeability possibly due to scaling.
e. Increase of productivity index with flow rate, from variable flow test.
f. Transient pressure tests indicate skin damage.

well production characteristics as well as the productivity indices, by monitoring pressure at a single downhole location while the flow rate was changed. No reliable results were obtained for PGM-1, 3, and 11 because the tools were not placed at depths near productive zones. PGM-5 showed an increase in the productivity index with flow rate, from 0.7 to 3.5 kg/s/bar. The well also showed a 50% drop in productivity index following 50 days of discharge. This drop is probably attributable to calcite scaling. PGM-10 indicated skin damage from the pressure recovery following discharge, suggesting the low measured productivity index does not represent the average productivity of the reservoir tapped by this well (Table 1).

The results of the transient and production tests therefore suggest very high permeabilities for wells PGM-1, 2, 3 and 12, and moderate ones for wells PGM-5 and 10. However, due to a high potential for calcite scaling (Granados and Gudmundsson, 1985; Vaca et al., 1989), results of transient pressure tests conducted after prolonged periods of production may not give good indication of undisturbed reservoir permeabilities.

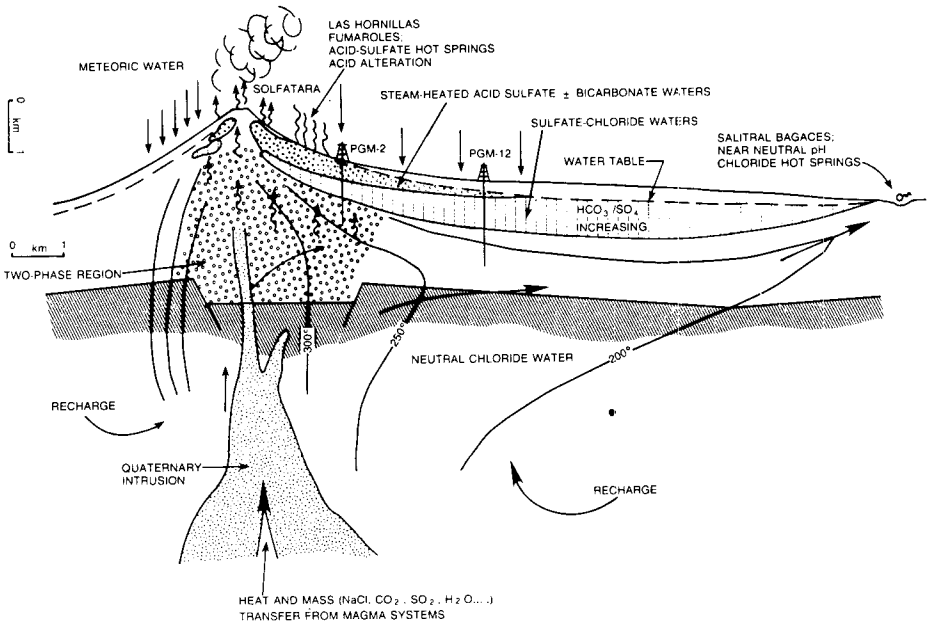

Figure 6. Conceptual model of Miravalles geothermal field (from Grigsby et al., 1989; adapted from Henley and Ellis, 1983).

The production tests show that the wells produce single phase liquid with an average enthalpy of 1045 kJ/kg and that they have capacities that range from 2.1 to 10.0 MWe, at 10 bar wellhead pressure (WHP; Table 1). In PGM-2, when deepened from 1210 to 2000 m, the tests indicated acid fluid production (pH 2.2; Truesdell, 1991). This fluid is produced from feed zones below 1500 m depth (below −760 masl), making the deep zones near PGM-2 unsuitable for production.

In June 1990 began a 92-day interference and tracer test. Well PGM-11 was produced at 36 kg/s, and 32 kg/s of 845 kJ/kg separated brine was injected into well PGM-2. The pressure drawdown was measured in wells PGM-1 and 5. During this test 63 kg of Iodine-131 tracer was injected into PGM-2 and tracer returns sampled in PGM-3, 10, 11 and 12. From the tests the maximum pressure drawdown in PGM-1 and 5 was only 0.2 bar and the pressure showed large fluctuations attributable to instrument errors or unstable reservoir pressures. The measured tracer velocities were 350 m/day at PGM-3, 150 m/day at PGM-12 and 100 m/day at PGM-10. No tracer return was measured at PGM-11, indicating either a hydraulic barrier between PGM-11 and 2 or a level of production/injection insufficient to reverse the general north-south pressure gradient.

Conceptual Model

The observed temperature and pressure distributions (Figures 3-5) suggest that the heat source for the geothermal system is related to the Miravalles volcano, which is centered about 4.5 km northeast of PGM-11. As deep circulating meteoric waters are heated and rise, they form a two-phase boiling zone (≥ 250 °C) centered in the reservoir in the area of wells PGM-1, 2, 10 and 11. Some geothermal fluid is discharged at the surface through fumaroles and acid sulfate hot springs located in the northern part of the field. The majority of the fluid however, flows to the south and manifests itself as near neutral-pH chloride hot springs. A schematic representation of this hydrogeological model is shown in Figure 6 (from Grigsby et al., 1989).

Natural-State Model

As a first step in constructing a detailed three-dimensional exploitation model for Miravalles, a two-dimensional areal, natural-state model was developed. A natural-state model of a geothermal area, gives quantitative estimates of the heat and mass throughput in the system. It should ideally reproduce the observed temperature and pressure distributions and give global estimate of reservoir permeability. Most geothermal reservoirs exhibit a high degree of fracture control of permeability in which thin, highly conductive channels (i.e faults and fractures) transmit most of the fluid.

Based on the observed temperature and pressure distributions the two-dimensional horizontal natural state model was centered at an elevation of −200 masl, with a uniform thickness of 1000 m (i.e., top of the model at 300 masl; bottom at −700 masl). The model is about 96 km wide in the E-W direction and about 112 km long in the N-S direction. This large areal extent was used so that no boundary effects would be felt when simulating the exploitation of the field. For the 12 km × 14 km central part of the field (Figure 7), conductive heat loss

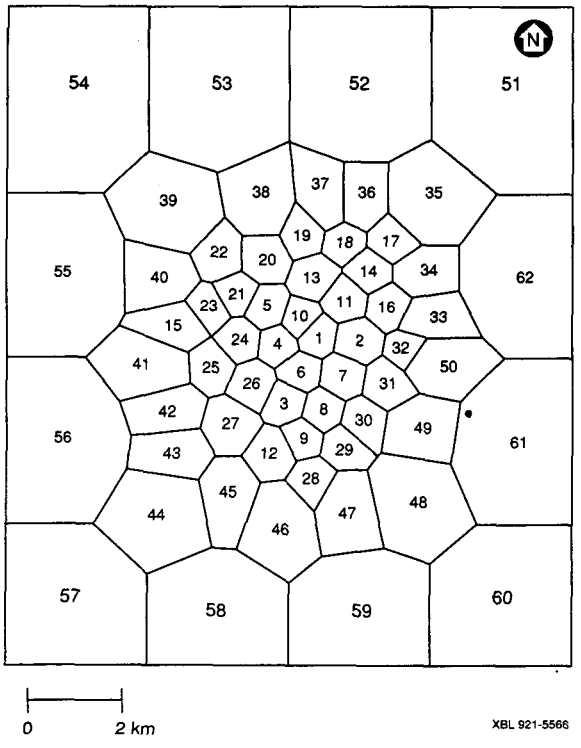

Figure 7. Two-dimensional mesh used for the natural and exploitation state models. (mesh elements 1, 2, 3, 5, 10, 11, 12 and 15 are centered on the deep exploration wells)

to a constant 20°C surface was allowed in the model. The vertical distances between the model nodes and the surface were based on the estimated depth to the reservoir top.

The formation properties used were: density 2600 kg/m^3, porosity 6%, thermal conductivity 3 W/m/°C and specific heat capacity 1000 J/kg/°C. The permeability was initially selected based on the values used in the modeling studies by ICE-ELC (1988). These permeabilities were then adjusted in order to match the natural state temperature and pressure distributions. An anisotropic porous medium was assumed. Permeability increases of up to two orders of magnitude were required in the direction of the high-permeability faults, to match the observed natural-state temperature distribution. The boundary blocks were modeled simply as low permeability areas. Hot fluid at variable temperatures and rates was injected into elements 11, 13, 14, 16, 17, 18, 34 and 35 (Figure 7). Fluid losses of 0.5 kg/s were allowed through elements 2, 5 and 45 to represent surface manifestation discharge. Element 58 to the south was selected as the natural fluid sink, with fluid extracted at a rate q proportional to a specified productivity index PI and against a specified downhole pressure P_{wb} according to the following formula,

$$q_\beta = \frac{k_{r\beta}}{\mu_\beta} \rho_\beta \, PI \, (P_\beta - P_{wb})$$

Where $k_{r\beta}$ is the relative permeability, μ_β is the viscosity and ρ_β is the density of each phase β. Linear relative permeability curves were used with residual liquid and vapor saturations of 25% and 1%, respectively.

The numerical simulation was carried out using the multiphase, multidimensional code TOUGH2 (Pruess, 1990), and run through a simulation time of about 2 million years. The calculated steady-state temperature and pressure distributions were compared to measured values (Figures 4 and 5, respectively). The permeabilities and the flow rates were then adjusted until a reasonable match was obtained with the observed natural-state pressure and temperature distributions. The permeabilities needed to match these distributions are shown in Figure 8. The highest permeability are in the element corresponding to PGM-12 and a general N-S high-permeability zone exists across the field indicating that the north-south fault system controls the fluid flow in the system.

Using the 200 and 240°C isotherms as references, the best match to the measured temperature distribution (Figure 9) is obtained using a total recharge of 130 kg/s of 1140 kJ/kg fluid (at about 260°C), representing a thermal through-flow of about 150 MWt. Figure 10 shows the computed natural-state pressure distribution for this model. The calculated N-S pressure gradient matches well the measured pressures in the northern part of the field. The match in the south and on the east-west section is rather poor. However, considering the uncertainties in the measured pressure caused by internal borehole flow, this match was considered to be adequate.

Exploitation model

In order to estimate the generating capacity of the Miravalles field and evaluate its response to different production-injection scenarios, a lumped-wellfield exploitation model (Bodvarsson and Witherspoon,

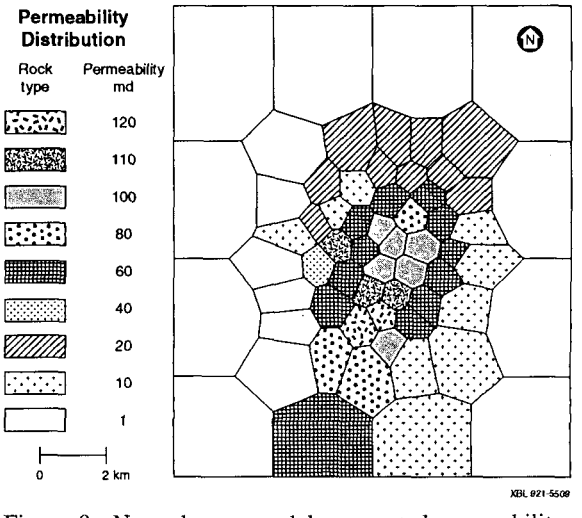

Figure 8. Natural-state model, computed permeability distribution.

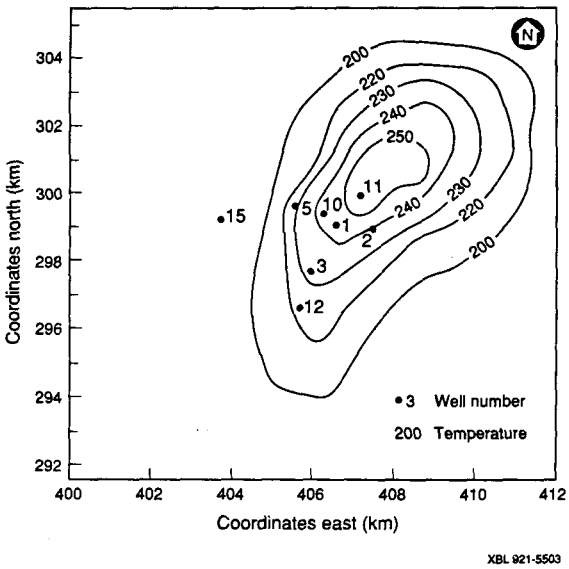

Figure 9. Best model. Computed natural-state temperature distribution at –200 masl (in °C).

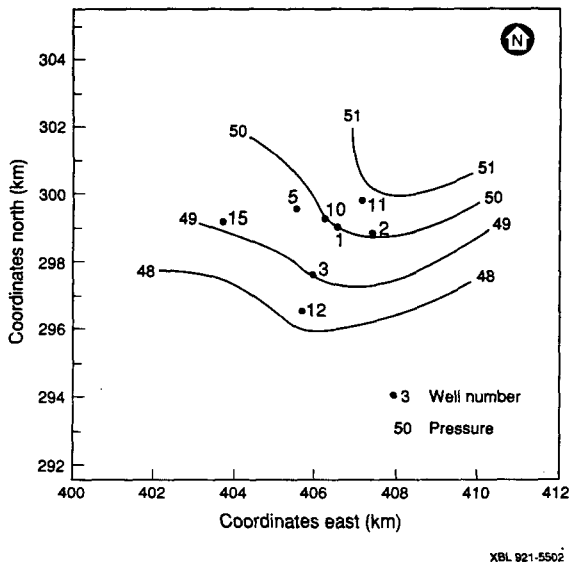

Figure 10. Best model. Computed natural-state pressure distribution at –200 masl (in bar).

1989) was developed. The computational mesh, formation properties, boundary and initial conditions used in the exploitation model were based on those of the natural-state model. The production area was assumed to be within the region enclosed by the 220°C isotherm (Figures 4 and 9). This 10 km^2 area includes seven of the deep exploration wells drilled in the field (not PGM-15) and is represented roughly in the model by elements 1 to 14 and 16 (Figure 11). In PGM-2 only the shallow (normal) production zone was included in the simulation since the bottom of the mesh is at –700 masl.

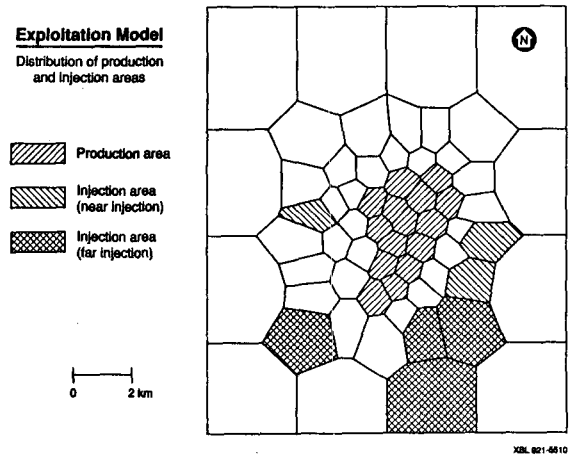

Figure 11. Distribution of production and injection areas in the model (element numbers are given in Figure 7).

As an initial calibration of the exploitation model, the drawdown observed during the June 1990 interference test was matched. The test was modeled by extracting 36 kg/s from element 11 and injecting 32 kg/s into element 2 and computing the pressure changes in elements 1 and 5. To match both the natural-state temperature and pressure distributions and the pressure drop observed in PGM-1 and 5 during the test, required to center of the upflow in element 17, (1.5 km north-east of element 11; Figure 7).

PRELIMINARY RESERVOIR PERFORMANCE STUDIES

Based on projected power development options for Miravalles, the model was used to simulate power production of 55 MWe and 110 MWe for 30 years, with and without injection (a power plant conversion of 2.5 kg/s of steam per MWe was assumed in the calculations). To achieve these levels of electricity generation over that period of time, up to a total of 75 production and make-up wells were placed in elements 1 to 16 (excluding element 15; Figure 7). At the end of the 30 years, most of these elements had an average well density of 8 wells/km^2.

Because at Miravalles the separated fluid must be injected, we examined two injection options: near injection for pressure support and far injection for fluid disposal. Based on the natural-state pressure gradients, injection in the northern part of the field was not considered because of the potential for rapid return of the injected fluid into the production wellfield. Therefore, a main injection area to the east and southeast of PGM-2 was selected (Figure 11). In the model, this area corresponds to elements 47, 48, 49, 50 and 59. Elements 28 to 33 separate the production field from the main injection area. In addition, because of the low permeability in PGM-15 above –700 masl, only small

injection rates were allocated to elements 15 and 44 to the west and south-west of the production field.

The effect of injection for pressure support was investigated by assuming high injection rates into elements 47, 48, 49 and 50; for fluid disposal the high-rate injection was into elements 44, 47, 48 and 59, which are closer to the natural outflow area in the system. In all cases the total injection rate was calculated as a percentage of the total mass produced. The percentages used were 90%, 80%, 50% and 0%. A constant injection enthalpy of 676 kJ/kg, corresponding to hot separated water at about 160°C was assumed.

Production/Injection Simulation

A slightly modified version of TOUGH2 (Pruess, 1990) was used in the study of different production and injection scenarios. For production, a constant productivity index was assigned to each well. The indices used were derived based on data from flowing pressure profiles and calculated or assigned permeability in the elements. The productivity indices ranged between 4.5×10^{-12} and 9.0×10^{-12} m^3, and were conservatively assigned based on the low measured values and on observed well production data.

The computed production rates under the above conditions will depend on the specified flowing bottomhole pressure (PWB) in the well. This pressure as observed from flowing pressure profiles, depends on the flow rate, well geometry and the produced fluid density (which is a function of enthalpy). When production causes pressure drawdown and boiling, it results in decreased flow and increased enthalpy. Therefore, keeping a high fixed PWB will unnecessarily throttle well flow. On the other hand, assuming a low fixed PWB and thus underestimating the hydrostatic component, results in excessively high early-time production rates.

To account for wellbore pressure variations, a wellbore simulator (Aunzo et al., 1991), was used to obtain curves for flowing bottom hole pressure as a function of enthalpy and flow rate, assuming a fixed well geometry. In this model the Armand (1945) correlations were used for prediction of the two-phase pressure drop, because it gives monotonically varying pressures at all flows and enthalpies in contrast to the Orkiszewski (1967) correlations. To correct for PWB variations, the flow rate and enthalpy at a given time step was used to calculate PWB, which was then used to compute the flow rate at the next time step.

In all cases the reservoir performance calculations assumed constant (20 or 30 bar) or variable PWB and examined injection near or far away from the production area. In the former case, because of thermal breakthrough (i.e., lower average enthalpies and steam rates per well) a large number of producers are needed to supply the total required steam rate. The variable PWB cases were found to give more realistic wellbore flow conditions over the 30-year period and are presented below. The effects the relative permeability functions on the results were also examined.

RESULTS OF PERFORMANCE PREDICTION STUDIES

55 MWe Generation

With near injection. The results for this case are shown in Figures 12 and 13. Sufficient steam for 55 MWe is available for 30 years with and without injection. For the 0% injection case the initial average enthalpy of 1100 kJ/kg increases to 1600 kJ/kg after 30 years (Figure 12). For 80% and 90% near injection, the production enthalpy initially rises to 1250 kJ/kg and then declines to 1150-1200 kJ/kg between 10 and 30 years Figure 12). The total number of production wells required over the 30-year period varies from 24 for no injection to 27 for 90% injection (Figure 13).

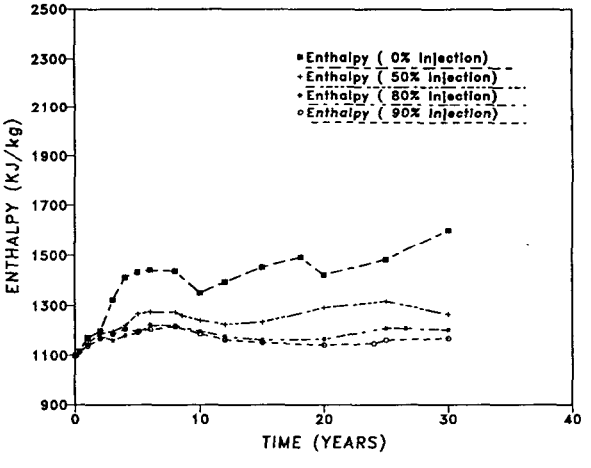

Figure 12. 55 MWe, near injection case. Enthalpy history.

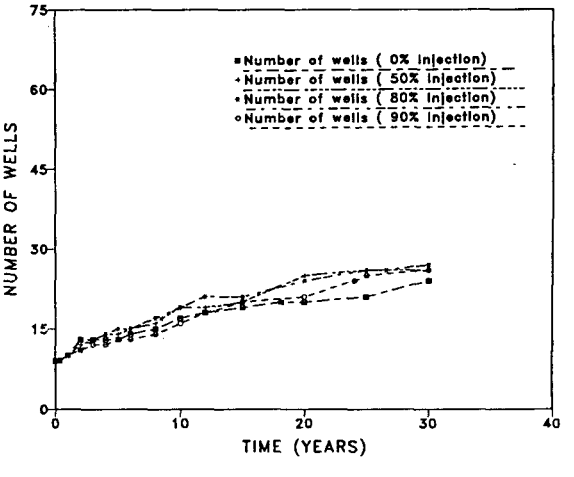

Figure 13. 55 MWe, near injection. Number of required production wells.

With far injection. Figures 14 and 15 show the results for this case. As in the previous case of 55 MWe with near injection, sufficient steam is produced to generate 55 MWe for 30 years with or without injection. However, because there is only a limited thermal impact on the production area, the 80% and 90% injection cases give nearly identical results, with an average produced fluid enthalpy of 1160-1250 kJ/kg, compared to about 1450-1600 kJ/kg for the case of no injection (Figure 14). The number of production wells required over the 30-year period is 27 for both 80% and 90% injection (Figure 15), similar to the near injection case, indicating limited sensitivity to the location of injection wells within the selected injection area.

110 MWe Generation

With near injection. In all cases sufficient steam can be produced to generate 110 MWe during the 30-year period. With 50% injection, the maximum average enthalpy drops to about 1400 kJ/kg (Figure 16) and the total number of production wells reaches 66 at the end of the 30-year period (Figure 17). For the cases of 80% and 90% injection the number production wells rises to 69 and the maximum average enthalpy declines to 1250 kJ/kg for 80% injection and 1200 kJ/kg for 90% injection due to increased return of injected fluid and earlier thermal breakthrough. For the case without injection, rapid pressure drawdown is experienced and production enthalpy rises to 2380 kJ/kg due to boiling within the reservoir (Figure 16). This case requires a total of 53 production wells during the 30-year period (Figure 17).

Therefore, although 110 MWe can be supported over the entire period, a high percentage of injection can be detrimental due to reservoir temperature decline, especially in the areas nearest to the injectors.

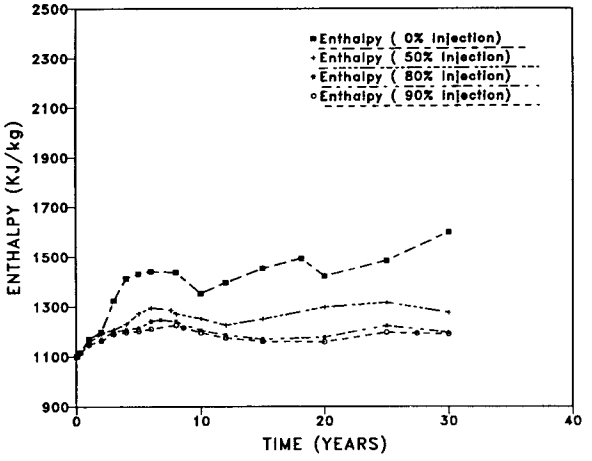

Figure 14. 55 MWe, far injection. Enthalpy history.

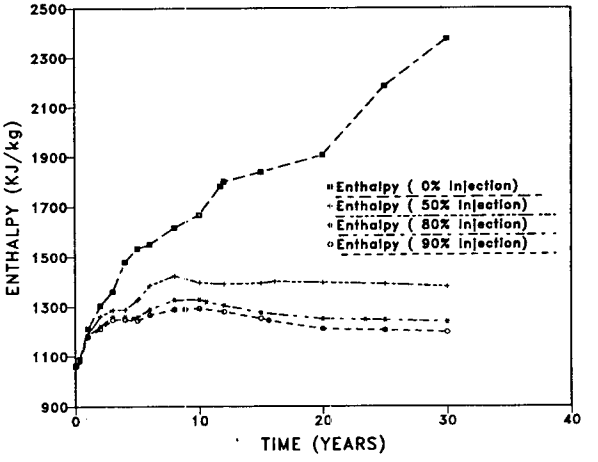

Figure 16. 110 MWe, near injection. Enthalpy history.

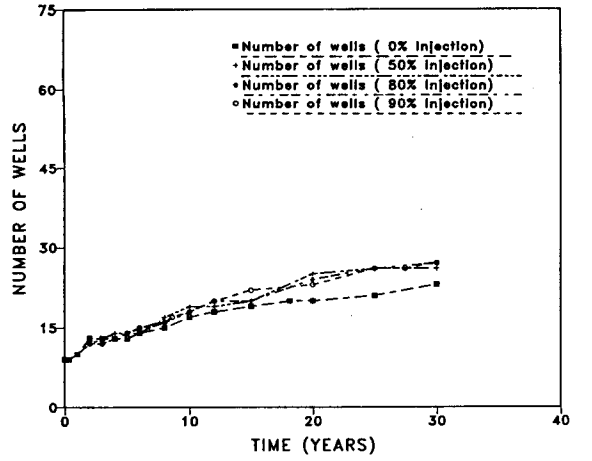

Figure 15. 55 MWe, far injection. Number of required production wells.

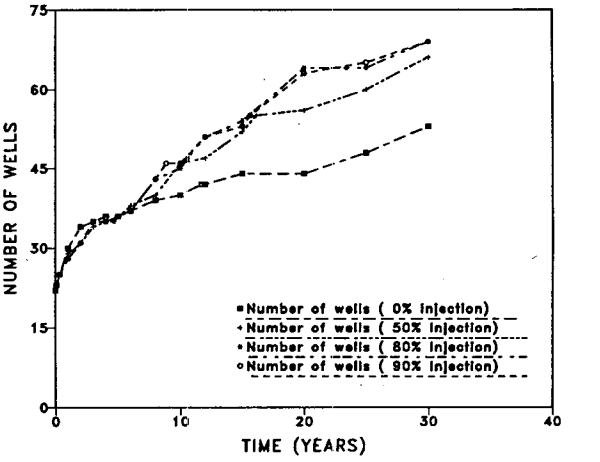

Figure 17. 110 MWe, near injection. Number of required production wells.

With far injection. In all cases with and without injection sufficient steam is produced to generate 110 MWe for 30 years. Injection rates of 80% and 90% have nearly identical effects. The production enthalpy rises to a maximum of 1350 kJ/kg at 12 years, after which the cooling effect of the injected fluid causes the produced enthalpy to drop to an average of 1255 kJ/kg between 20 and 30 years (Figure 18). The total number of required production wells is 67 for 80% injection and 69 for 90% injection (Figure 19).

Thus, even with far injection mainly in the south, there is sufficient pressure support to prevent large-scale reservoir boiling, although individual wells in the north show localized boiling (e.g., enthalpies of up to 1800 kJ/kg for wells located in mesh element 11). Since large-scale boiling may lead to formation scaling due to calcite precipitation, 110 MWe with far injection does not seem to be a feasible alternative for Miravalles. Thermal breakthrough and reservoir boiling with associated scaling, could reduce the total steam production below the required levels.

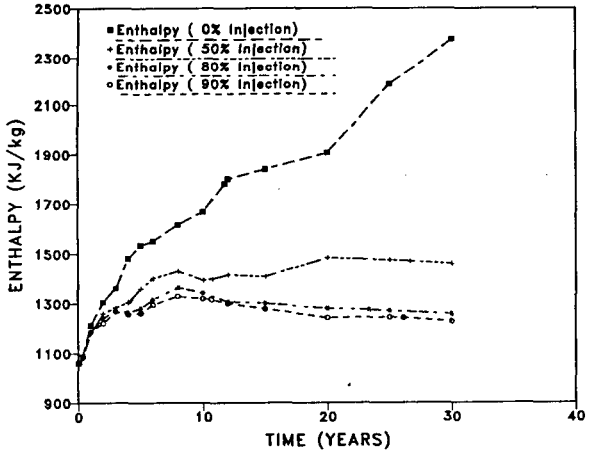

Figure 18. 110 MWe, far injection. Enthalpy history.

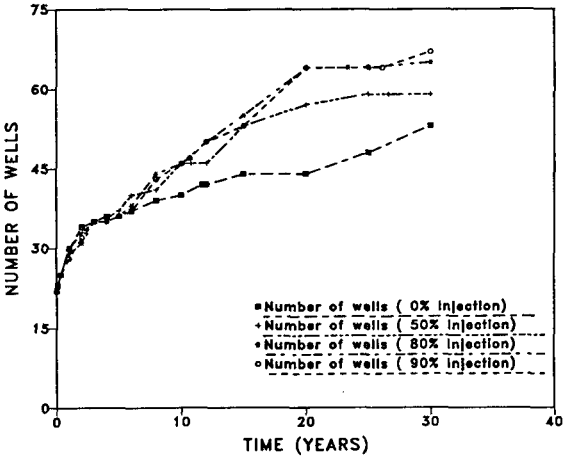

Figure 19. 110 MWe, far injection. Number of required production wells.

Effect of Relative Permeability Functions

In all the cases discussed above linear relative permeability curves were used, with residual saturations of 25% for the liquid and 1% for the vapor. The choice of given relative permeability functions should ideally be based on the observed produced vapor-liquid ratio and the relative saturation of the phases in the reservoir.

Since no such data exist for Miravalles, there is no definite criteria for selecting particular relative permeability curves. Until such data are available it is only possible to perform a sensitivity analysis by evaluating the impact of the relative permeability function on the performance predictions. For example, when Corey relative permeability curves were used with residual saturations of 25% for the liquid and 5% for the vapor, the results showed that generation of 110 MWe could only be supported assuming far injection, with injection rates less than 50%. For the 50% case, a total of 75 wells were required compared to 57 when using the linear relative permeability curves, indicating that the results are very sensitive to the assumed relative permeability functions. It should also be pointed out here that the effects of production/injection cannot be fully analyzed using a two-dimensional areal model. Development of a 3-D model that will take into account the effects of vertical permeability, gravity and depth of injection/production, will give a more realistic prediction of the evolution of the reservoir during exploitation.

CONCLUSIONS AND RECOMMENDATIONS

Eight deep exploration wells at Miravalles have confirmed the presence of a 10 km^2 liquid-dominated geothermal reservoir with temperatures between 220 and 260 °C; the highest temperatures and pressures found in the northern part of the field.

The upflow zone for this system, with a recharge estimated at 150 MWt, is north of PGM-11 and is related to the Miravalles volcano. The main outflow is found to the south, perhaps associated with the Bagaces hot springs (Figure 6). Permeability within the field is controlled by the north-south and the east-west fault systems, with the former dominating. Individual wells produce enough steam to generate 2.1 to 10 MWe, at 10 bar WHP.

The study indicates that at Miravalles the known system can reliably support a power generation of 55 MWe over a period of 30 years, and that a total of 24 to 28 production wells may be required contingent on the type of injection operation that is implemented.

Generation of 110 MWe for 30 years appears possible; 53 to 70 producers may be needed depending on the location of the injection wells and the rate of injection. However, there might be potential problems related to thermal breakthrough and formation scaling. Since these predictions strongly depend on assumed relative

permeability functions, information on an initial 55 MWe development should be used to re-evaluate the response of the field to 110 MWe production.

A high rate of injection for pressure support is required to prevent boiling and minimize calcite scaling within the formation. Based on our model, injection will have to be sited E and SE of PGM-2. A three-dimensional model will give a better indication of the location of injection wells by studying deep and shallow injection.

To prove the existence of high temperatures and pressures to the north and northeast of PGM-11, further wells should be sited in that area.

Since PGM-2 encountered acid fluids after it was deepened, the extent of the acid reservoir should be ascertained by drilling a deep well at about one km east of PGM-2. This proposed well could also be used for injection during the exploitation of the field. The connection between the acid reservoir and the main, shallow reservoir should be ascertained by planning long-term injection tests or by high-rate injection tests in PGM-2.

ACKNOWLEDGEMENTS

We appreciate the technical review by Emilio Antúnez and Norman Goldstein and the production of the paper by Judith Peterson and Ellen Klahn. This work was sponsored by the Los Alamos National Laboratory through a contract from the United States Agency for International Development and was also supported by the U. S. Department of Energy, under contract No. DE-AC03-76SF00098.

REFERENCES

Alvarado J., J. A. 1987. Perforación y mediciones en el proyecto geotérmico Miravalles. Proceedings International Symposium on Development and Exploitation of Geothermal Resources, October 5-9, Cuernavaca, Morelos, Mexico, 159-165.

Armand, A. A., 1945. Resistance to two-phase flow in horizontal tubes (in Russian). Izv. VTI, 1946, 15(1), 16-23.

Aunzo, Z. P., Bjornsson, G. and Bodvarsson, G. S., 1991. Wellbore models GWELL, GWNACL, and HOLA. Lawrence Berkeley Laboratory report LBL-31428.

Bargar, K. E. and Fournier, R. O., 1988. Fluid-inclusion evidence for previous higher temperatures in the Miravalles geothermal field, Costa Rica, *Geothermics, 17* (5/6), 681-693.

Bodvarsson, G. S. and Witherspoon, P. A., 1989. Geothermal reservoir engineering, Part I. *Geothermal Science and Technology, 2*(1), 1-68.

Granados, E. G. and Gudmundsson, J. S., 1985. Production testing in Miravalles geothermal field, Costa Rica. *Geothermics, 14*(4), 525-538.

Grigsby, C. O., Goff, F., Trujillo Jr., P. E., Counce, D. A., Dennis, B., Kolar, J. and Corrales, R., 1989. Results of investigation at the Miravalles geothermal field, Costa Rica, Part 2: Downhole fluid sampling. Los Alamos National Laboratory report LA-11510-MS, Part 2.

Henley, R. W. and Ellis, A. J., 1983. Geothermal systems ancient and modern: A geochemical review. *Earth-Sci. Rev., 19,* 1-50.

ICE-ELC, 1988. Programa de obras de generación; perïodo 1990-1993. Informe de factibilidad. Planta geotérmica de Miravalles, 2da. Unidad. ICE internal report.

Koenig, J. B., 1980. Exploration and discovery of the Miravalles geothermal field, Costa Rica: A case study. Geothermal Resources Council Special Report 9, 59-70.

Mainieri P., A. and Vaca C., L., 1990. Costa Rica: Country update report, *Geothermal Resources Council Trans., 14*(I), 23-29.

Mainieri, A., Granados, E., Corrales, R. and Vaca, L., 1985. Miravalles geothermal field, Costa Rica. Technical report. *Geothermal Resources Council Trans., 9*(I), 279-283.

Mora P., O., 1988. Geologïa de las piroclastitas en los alrededores de Bagaces, Provincia de Guanacaste, Costa Rica. Tesis de licenciatura, Escuela Centroamericana de Geologïa, Universidad de Costa Rica, San José, Costa Rica.

Mora P., O., 1989. Borehole geology and alteration mineralogy of well PGM-5, Miravalles, Guanacaste, Costa Rica. UNU Geothermal Training Programme, Reykjavik, Iceland, Report 5-1989.

Orkiszewski J., 1967. Predicting two-phase pressure drop in vertical pipe. Journal of Petroleum Technology, June 1967, 829-838.

Pruess K., 1990. TOUGH2- A general purpose numerical simulator for multiphase fluid and heat flow. Lawrence Berkeley Laboratory report LBL-29400.

Truesdell, A. H., 1991. Origin of acid fluids in geothermal reservoirs. *Geothermal Resources Council Trans., 15,* 289-296.

Vaca, L., Alvarado, A. and Corrales, R., 1989. Calcite deposition at Miravalles geothermal field, Costa Rica. *Geothermics, 18*(1/2), 305-312.

PROCEEDINGS, Seventeenth Workshop on Geothermal Reservoir Engineering
Stanford University, Stanford, California, January 29-31, 1992
SGP-TR-141

APPLICATION OF A MATRIX-FRACTURE TRANSFER PSEUDOFUNCTION IN GEOTHERMAL RESERVOIR SIMULATION

K.T. Lim*, K.L. Enedy†, K.K. Bloomfield†, and K. Aziz*

*Stanford University
Stanford, CA 94305

†Pacific Gas and Electric
111 Stony Circle
Santa Rosa, CA 95401

ABSTRACT

A fine-grid, single porosity model of a matrix-fracture system was used to visualize the pressure response and mass transfer mechanisms in a vapor-dominated geothermal reservoir. The observed pressure response and saturation distributions were used to generate a pseudofunction representing the product of vapor phase relative permeability and matrix-fracture transfer shape factor for a dual-porosity model. The pseudofunction was found to be a function of vapor saturation. It was used in place of the gas relative permeability curve. With the application of the pseudofunction, the dual-porosity model produced pressure decline trends similar to those observed in the fine-grid models. The pseudofunction approach was successfully applied in the history matching of a single Geysers producing well. The TETRAD simulation code was used in this study.

INTRODUCTION

Simulation of The Geysers reservoir requires the application of a dual-porosity model. In this reservoir, the matrix contains most of the mass in-place while the fractures provide the flow channels to production wells. The conventional approach uses a matrix-fracture transfer function to calculate the mass flow rate between the matrix and the fracture (Kazemi et al., 1976). Currently, available transfer functions are based on flow in oil reservoirs where mass transfer mechanisms are different from those in geothermal reservoirs. An alternate approach for considering matrix-fracture interaction was investigated in this study. Fluid movements in geothermal reservoirs are often accompanied by phase changes as a result of vaporization and condensation of water. Our objective was to incorporate the phase changes associated with matrix-fracture transfer in geothermal reservoirs in the transfer function.

In the dual-porosity simulation model used for this study, the rate of mass transfer, q, (in barrels/day) between the matrix and the fracture is calculated using the following function (Kazemi et al., 1976, and SERVIPETROL LTD., 1991):

$$q = 0.001127 \cdot V_b \cdot \sigma \cdot k_m \cdot \frac{k_r}{\mu} \cdot \Delta\phi \qquad (1)$$

where,

V_b = bulk volume of gridblock, cu-ft
σ = shape factor, 1/sq-ft
k_r = relative permeability
μ = viscosity, cp
k_m = matrix permeability, md
$\Delta\Phi$ = potential difference between matrix and fracture, psi.

The underlying assumption in the derivation of an expression for σ in Equation (1) is that pseudosteady state exists in the matrix at all times (Warren and Root, 1963). This assumption may not be valid if the transient period is long.

This study used the TETRAD numerical simulator (SERVIPETROL LTD., 1991) to investigate the following: 1) representative models of a matrix-fracture system at a very fine scale, 2) how the fluid movement mechanisms in a geothermal reservoir will affect the matrix-fracture transfer calculations at a larger scale, and 3) a model of a segment of The Geysers containing one producer using a psuedofunction based on fine-grid simulations.

FINE-GRID MODEL APPROACH

A fine-grid model simulates mass transfer between the matrix and the fracture without the application of the dual-porosity concept. This eliminated the uncertainties associated with using

a transfer function used in Equation 1 to describe the matrix-fracture transfer. The fine grids enabled the visualization of the mechanisms by which mass is transported from the matrix to the fracture.

A linear, one-dimensional (1-D) model was selected as illustrated in Figure 1. The model had one gridblock representing the fracture, with the remaining 24 gridblocks representing the matrix. The model dimensions were 100 feet by 1 foot by 1 foot. The fracture gridblock dimension was 0.01 foot in width. The matrix gridblock width ranged from 0.01 foot to 29.405 feet and increased in width with distance from the fracture. It modeled an element of the matrix-fracture system with a matrix block length of 200 feet. Because of the symmetry of the system, only a 100 feet length was modeled. A closed outer boundary was assumed. Assuming a homogeneous system with uniform withdrawal from the fracture, the assumption of no-flow boundaries in the fine-grid model was a reasonable approximation for understanding the mechanisms of matrix-fracture fluid transfer. This simple, one-dimensional model was effective in illustrating the mechanisms of mass transfer.

Another model was constructed to investigate the effect of changing flow area along the flow path. It was a one-dimensional radial model, also shown in Figure 1. It was scaled to have an area equivalent to that of a single matrix-fracture sub-block in a dual-porosity model. The model size was 66.67 feet in radius and 2.865 feet thick. A total of 100 gridblocks were used. The gridblock sizes in the radial direction ranged from 0.9425 foot to 0.01 foot, with the outermost block representing the fracture (see Figure 1).

A single-gridblock dual-porosity model was also constructed. It required the use of a shape factor to model the matrix-fracture transfer. A 200 feet fracture spacing was used. The objective was to investigate how the results obtained with different shape factors in the dual-porosity model compared with those of the fine-grid model. Four different shape factors were studied. They ranged from $12/L^2$ to $100/L^2$ (where L is the matrix block length). A shape factor of $12/L^2$ is most commonly used in the petroleum engineering literature (Kazemi et al., 1976).

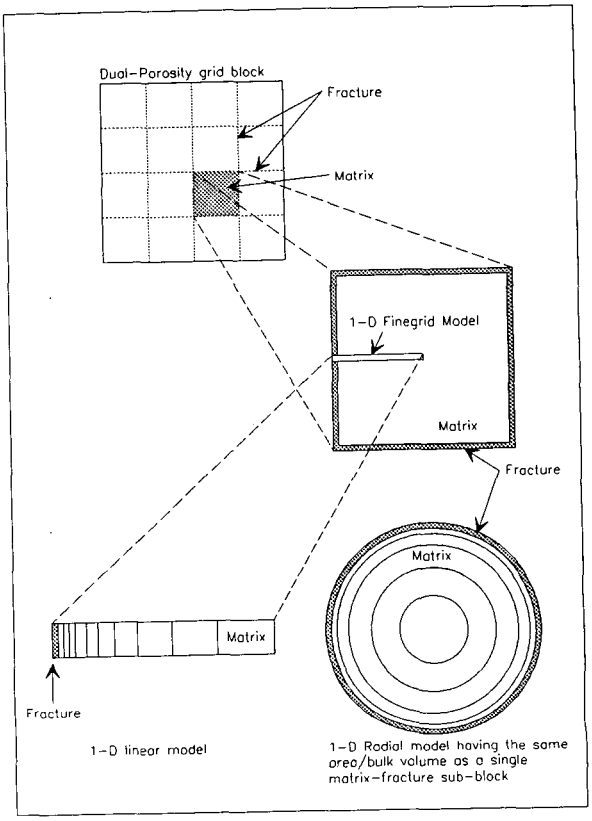

Figure 1: Schematic of Fine-grid Model Selection

Both the 1-D radial model and the single block dual-porosity model had similar fracture surface area to matrix bulk volume ratio of 0.03 sq-ft/cu-ft. This was necessary in order to compare the two models.

Matrix porosity and permeability were 0.04 and 0.01 md, respectively. A linear relative permeability versus water saturation curve was assumed. Connate water saturation was 25 percent.

A constant rate of withdrawal, equivalent to 11.5% per year of the mass in-place, was applied to all models. Mass was withdrawn from the fracture only.

RESULTS OF FINE-GRID MODELS

Figures 2 and 3 show the pressure, temperature and vapor saturation profiles of the 1-D linear model at 50 and 400 days, respectively. Pressure gradient in the matrix even at 400 days was still transient.

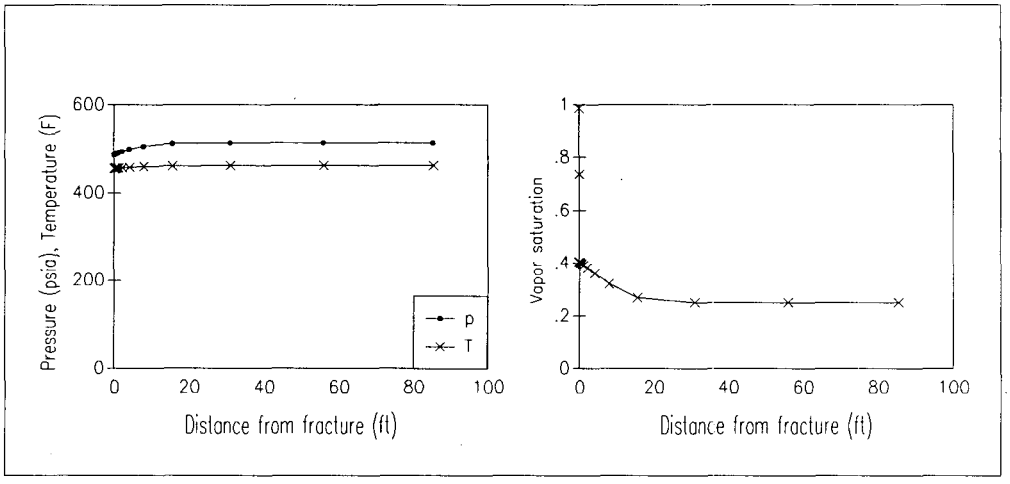

Figure 2: 1-D Linear Model - Pressure, Temperature and Saturation Profiles at 50 days

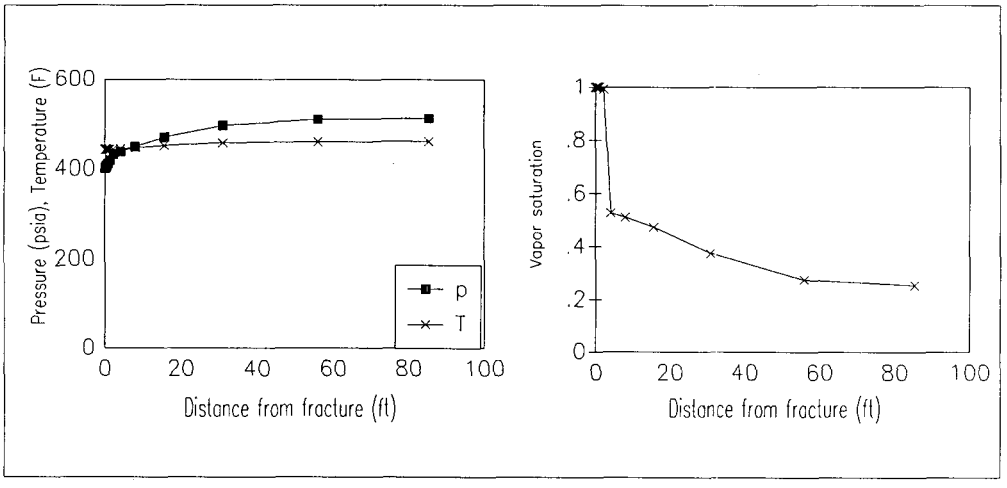

Figure 3: 1-D Linear Model - Pressure, Temperature and Saturation Profiles at 400 days

The temperature remained fairly constant throughout. The pressure profiles showed depletion with time and were dependent on the distance the pressure transient had travelled from the fracture. The vapor saturation profiles were indicative of the mass transfer mechanisms. The vapor saturation at the matrix-fracture interface were near unity or at unity at all times. The TETRAD simulator uses flat-surface boiling calculations and does not include effects of adsorption/desorption (Hsieh and Ramey, 1983). At these vapor saturations, the relative permeability to water was zero. In other words, only the vapor phase was mobile at the matrix-fracture interface. The mechanism by which mass was transferred from the matrix to the fracture was first by vaporization in the matrix. The mass was subsequently transferred through the matrix to the fracture as a single-phase vapor.

The σ in Equation (1) was back-calculated using the observed fracture and average matrix pressures, matrix temperature and vapor saturation of the 1-D radial model. Note that it no longer represents the shape factor. The computations assumed mass transfer as a single-phase vapor and that the gas viscosity was constant, since the temperature was fairly constant. The results (Figure 4) indicated that if a dual-porosity model is to be used to reproduce the fine-grid model results, this factor would have to change, especially during the early times of production.

COMPARISON OF RESULTS OF 1-D RADIAL AND DUAL-POROSITY MODELS

Figure 5 summarizes the calculated fracture pressure responses. The matrix pressures were almost identical for all

cases. The fracture pressure decline rate increased with time in the fine-grid model, while those of the dual-porosity model showed a slower decline rate after about 1200 days. The expanding vapor saturated zone in the 1-D radial model, which increased the distance mass (water) had to travel from the matrix to the fracture, probably caused the increased pressure decline. On the other hand, the 'distance' between the matrix and the fracture in a dual-porosity model was fixed. As a result, the trend of pressure decline in the dual-porosity model was strongly influenced by the relative permeabilities to gas and water.

The major difference between the two types of models was the mechanism of mass transfer from the matrix to the fracture. The fine-grid models indicated that mass was transferred from the matrix to the fracture as a single-phase vapor. On the other hand, the dual-porosity model assumed a two-phase (water and steam) mass transfer. The dual-porosity model assumed that one matrix block (or a group of matrix blocks as an entity) was connected to one fracture (or a group of fractures as an entity) in a given direction. Assuming the capillary pressure between vapor and water is negligible, the total mass transfer from the matrix to the fracture becomes:

$$q=0.001127 \cdot v_b \cdot k_m \cdot \sigma \cdot [\frac{k_{rw}}{\mu_w}+\frac{k_{rg}}{\mu_g}] \cdot \Delta\phi \qquad (2)$$

where the subscript w and g denote water and vapor phase, respectively.

Since the average water saturation of the matrix did not reduce to zero or to a value below the residual saturation, the mobility of water resulted in liquid phase mass transfer being computed. Therefore, it was not surprising that a dual-porosity model could not reproduce the results observed in the fine-grid model, regardless of the shape factor used.

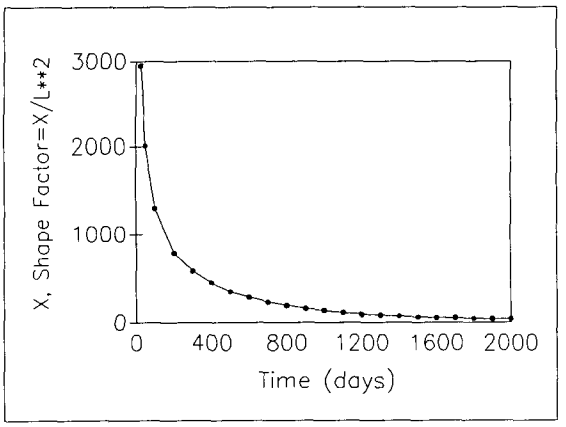

Figure 4: Calculated Shape Factor from Fine-grid 1-D Radial Model

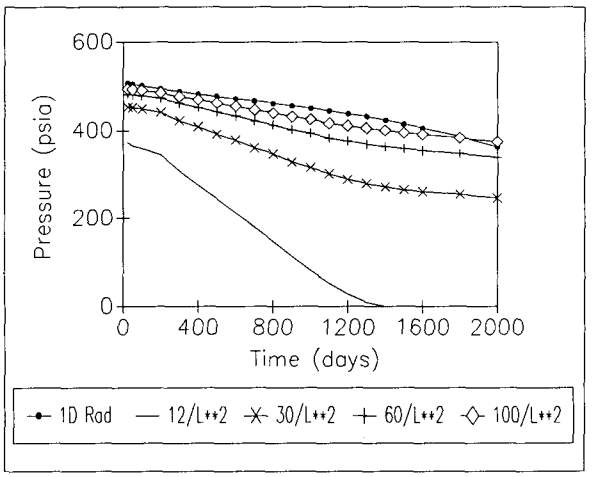

Figure 5: Calculated Fracture Pressure
Fracture surface area - matrix bulk volume ratio = 0.03 sq-ft/cu-ft

PSEUDOFUNCTION

One way of ensuring that mass transfer from the matrix is always in the form of vapor is to set the relative permeability to water in the matrix to zero and modify the relative permeability to gas. One convenient way to accomplish this is to rewrite Equation (1) as:

$$q=0.001127 \cdot V_b \cdot \sigma^* \cdot F \cdot k_m \cdot (\frac{1}{\mu}) \cdot \Delta\phi \qquad (3)$$

where,

σ^* = any appropriate fixed shape factor, 1/sq-ft

F = a dimensionless pseudofunction dependent on vapor saturation

The pseudofunction, F, accounts for the combined effects of phase changes and resistance to flow. It can be determined from the results of a fine-grid model representing the matrix-fracture system of interest. In this study the 1-D radial model described earlier was used. The calculated pseudofunction for a ratio of fracture surface area to matrix block volume of 0.03 sq-ft/cu-ft and $\sigma^*=12/L^2$ is shown in Figure 6. The results obtained by the application of the pseudofunction in

the dual-porosity model are shown in Figure 7. The results of the corresponding fine-grid 1-D radial model is also shown for comparison. A reasonable agreement between the calculated fracture pressures was obtained. Some refinements to the pseudofunction, especially at high vapor saturations, may be necessary to obtain a better match.

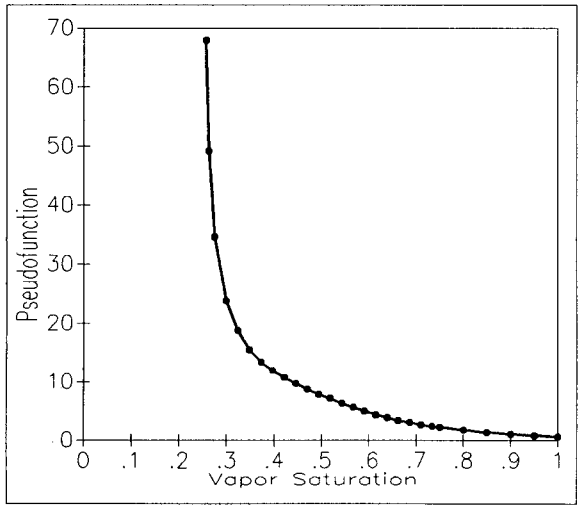

Figure 6: Pseudofunction vs Vapor Saturation

Fracture area / matrix bulk volume = 0.03 sq-ft/cu-ft
Equivalent matrix block length in dual-porosity model = 200 ft

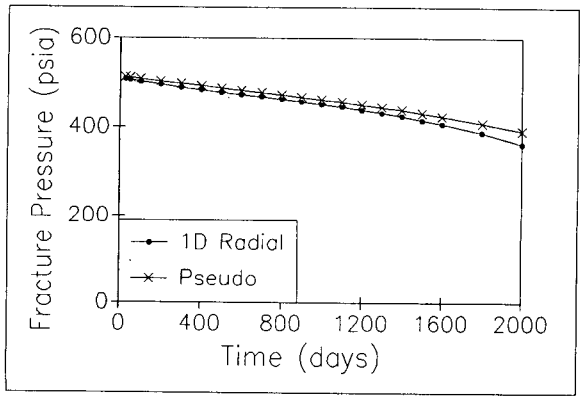

Figure 7: Results of 1-D Block Dual-Porosity Model with the Application of a Pseudofunction

1. Radius of 1-D model = 66.67 ft
2. Matrix block length in D-P model = 200 ft
3. Fracture area / matrix BV = 0.03 sq-ft/cu-ft.

MODELING A SINGLE GEYSERS WELL

McKinley-3 was selected for the purpose of applying the pseudofunction approach to model a producer at The Geysers. Sufficient data were available from McKinley-3 to enable the construction and verification of the model by history matching (Box, 1991 and California Department of Oil and Gas, 1991). McKinley-3 was drilled and completed in October 1969. Production started in early 1980. By the end of May 1991, cumulative production was 7.5 G-lb (10^9 lb).

The observed decline trend of P/Z against cumulative production is shown in Figure 8. Two distinct trends were observed: 1) an initial trend pointing to a mass in-place of 31 G-lb and 2) a current trend indicating a mass in-place of 9.1 G-lb. The apparent timing of the change in the P/Z decline trend is at a cumulative production of 4 G-lb, or the end of July 1985. The increase in pressure decline can be attributed to the increased offset steam production. The history matching process would either require flow across boundaries to allow for the withdrawal from nearby producers or a method to take into account the shrinking drainage area. The latter appeared to be the simpler approach. The approach of reinitializing a history match has been reported by Enedy (1989). In applying the Fetkovich type curve matching of McKinley-3 production history, reinitialization was made in October 1985. This compares favorably to a reinitialization of August 1985 used in this study.

A model containing 31 G-lb of mass initially in-place was constructed. A 100 year pre-exploitation run was made to allow the model to come into equilibrium. The model was subject to rate specified production from March 1980 until the end of July 1985, when the cumulative production was 4 G-lb. The gridblock parameters at the end of this run were used to reinitialize the model, but with a smaller drainage area and mass in-place. The smaller model was used for matching the current decline trend.

A dual-porosity (matrix-fracture) model with 5x5x5 gridblocks was selected. Five vertical layers of 2000 feet each were used. With a fracture permeability of 10 md, the permeability-thickness product is 100,000 md-ft which is comparable to that obtained from well tests. The well was located at the center of the topmost layer. The size of the uniform areal gridblocks was varied when adjusting the amount of mass in-place. Typical Geysers reservoir data from published literature were used (Barker et al., 1989). Appropriate modifications were made where applicable.

A pseudofunction for the field case (Figure 9) was derived by the procedure outlined earlier. The gridblock dimensions are similar to the 1-D radial model. Relative permeabilities consistent with Geysers reservoirs were used in the fine-grid model (Dykstra, 1991). The application of the pseudofunction was achieved by setting the relative permeability to water in the matrix to zero and replacing the relative permeability to gas with the pseudofunction.

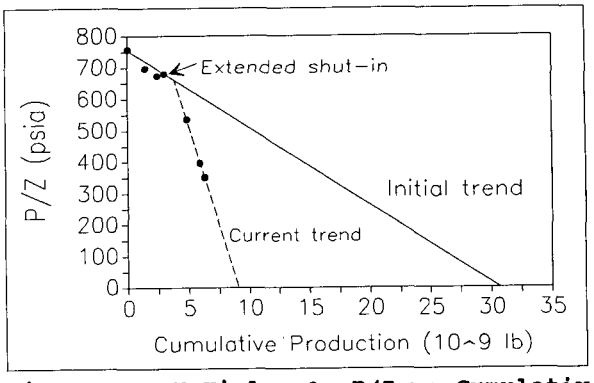

Figure 8: McKinley-3: P/Z vs Cumulative Production

RESULTS OF HISTORY MATCHING

The initial model contained 31 G-lb mass in-place. The model drainage area is approximately 2090 square feet. Rate specified production was imposed until the cumulative production became 4 G-lb. Excellent pressure matches were obtained, verifying that the mass in-place is reasonable. The results at the end of this run were used to reinitialize the model, but with a smaller mass in-place.

A reinitialized mass in-place of 11 G-lb was found to give the closest match with the observed decline trend. (Figure 10). It corresponds to a model with a drainage area of 1300 square feet. This area compares reasonably with the approximate drainage area of McKinley-3. The match was obtained without further adjustment of the input data. Results obtained using a fixed shape factor (Kazemi et al.,1976) of $12/L'$ showed a different decline trend (Figure 10).

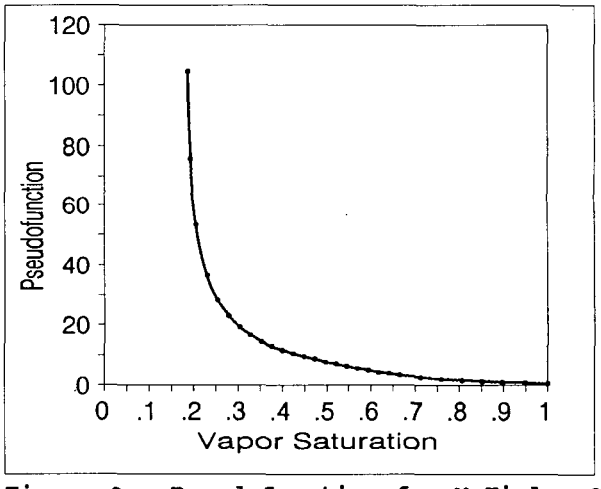

Figure 9: Pseudofunction for McKinley-3 Model

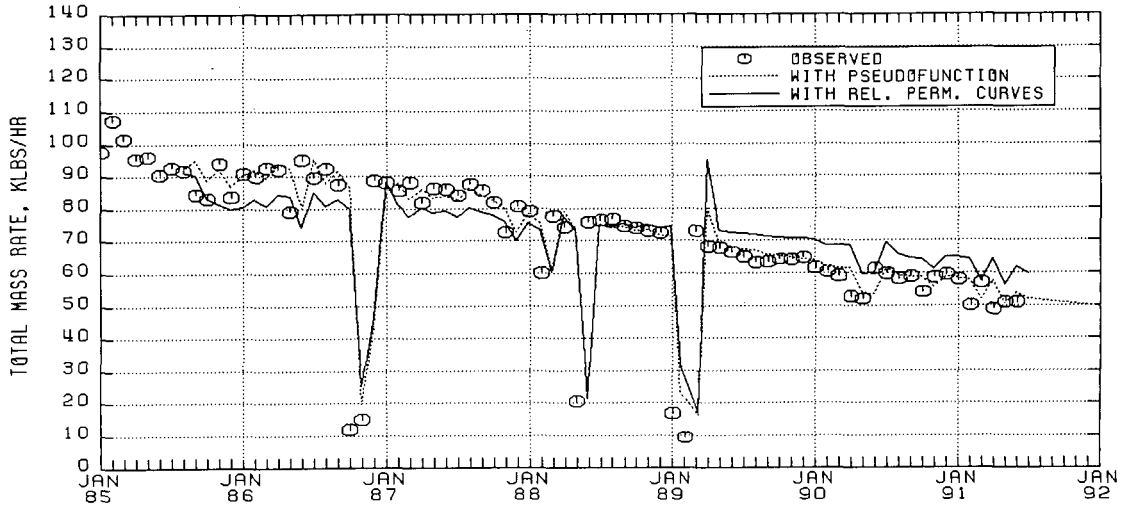

Figure 10: McKinley-3 Model History Matching

CONCLUSIONS

Based on preceeding discussions, the following may be concluded:

1. The fine-grid models indicate that mass transfer from the matrix to the fracture occurred as a single-phase vapor.

2. Mass transfer calculated using a constant shape factor in a dual-porosity model may be inconsistent with the observed transport mechanisms in a vapor-dominated geothermal reservoir.

3. A method to develop a psuedofunction which accounts for the combined effect of matrix pressure transient and single-phase mass transfer was proposed.

4. The psuedofunction has been successfully applied in the history matching of a single-well Geysers model.

ACKNOWLEDGEMENTS

The authors gratefully acknowledge Pacific Gas and Electric Company for financial support of this work and permission to publish. Special thanks are due to Tom Box of Calpine Corporation for providing additional field data on McKinley-3 used in this study.

REFERENCES

Barker, B.J., Gulati, M.S., Bryan, M.A. and Riedel, K.L., (1989), "Geysers Reservoir Performance", Geothermal Resources Council Transactions, Vol. 13, pp. 349.

Box, W.T., Jr., (1991), Personal communication, July.

Dykstra, H., (1991), Personal communication, July.

California Department of Oil and Gas, (1991), public information.

Enedy, K.L., (1989), "The Role of Decline Curve Analysis At The Geysers", Geothermal Resources Council Transactions, Vol. 13, pp. 383-391.

Hsieh, C. and Ramey, H.J., Jr., (1983) "Vapor-Pressure Lowering in Geothermal Systems", SPEJ, February, pp. 157-167.

Kazemi, H., Merrill, L.S., Jr., Porterfield, K.L. and Zeman, P.R., (1976), "Numerical Simulation of Water-Oil Flow in Naturally Fractured Reservoirs", SPEJ, December, pp. 317-326.

SERVIPETROL LTD., (1991), "TETRAD User Manual", Version 9.2.

Warren, J.E. and Root, P.J., (1963), "The Behavior of Naturally Fractured Reservoirs", SPEJ, September, pp. 245-255.

PROCEEDINGS, Seventeenth Workshop on Geothermal Reservoir Engineering
Stanford University, Stanford, California, January 29-31, 1992
SGP-TR-141

DEVELOPMENT OF EXPERT SYSTEM FOR LOST CIRCULATION PROBLEMS

Masami Hyodo, Shinji Takasugi, and Shigeki Muramatsu

Department of Research and Development, Geothermal Energy Research and Development Co., Ltd., Tokyo 103, Japan

ABSTRACT

Lost circulation (LC) is the phenomenon where circulating drilling fluid is lost to fracture or porous in the rock formation rather than returning to the surface. For drilling geothermal well, LC can be serious problem that contributes greatly to the cost of the average geothermal well and completion of the well.

We studied "The research and development of lost circulation techniques in geothermal wells" to permit systematical lost circulation treatment undertaking committed by the New Energy and Industrial Technology Development Organization (NEDO) from 1986 to 1990, whose program consists of detection of LC analysis techniques, plugging materials, and treatment techniques.

In this project, the expert system for lost circulation problems, so-called LC expert, was developed to support determination of LC treatment method for drilling engineers. The LC expert suggests drilling engineers to design the optimum LC treatment. We believe these suggestions would reduce uncertainty and mistake in decision process of field personnel.

Developed LC expert designs the optimal solutions for LC treatment according to the information obtained from the LC detection tool and its data processing, knowledge base including experiences of drilling experts, properties of each plugging materials, knowledge obtained from simulation test, and knowledge from field test.

It was evaluated by drilling experts and actual field tests that the LC expert inferred the LC treatment method quite adequately.

1. BACKGROUND OF DEVELOPMENT

Drilling cost is approximately 50% in geothermal energy development, so it is very important for geothermal developers to reduce the drilling cost.

Lost circulation is one of the most difficult obstacle for treatment which we encounter during drilling or completion of wells. We have a large size of LC quite frequently in geothermal drilling rather than oil/gas well. And further LC also would be the cause of formation collapse and/or stuck of drill strings, and cause of failure of casing cementing which is very important when geothermal fluid is produced.

To solve the lost circulation problem, we develop the LC expert system which is systematical and effective system to suggest optimum treatment using AI (artificial intelligence) technology.

LC expert system can exclude the method of trial and error owing to development of LC zone detection and analysis techniques as well as optimum plugging materials and treatment processes.

2. POSITION OF LC EXPERT SYSTEM IN LC R&D PROJECT

Whole subjects of "The research and development of lost circulation techniques in geothermal wells" are shown in Fig. 1. In this figure, LC expert is not main subject in the project. However, we consider this is very important for the project, because this system manages all information and data obtained at the field.

3. OUTLINE OF THE LC EXPERT

3.1 Object

The object of LC expert system development is to select optimum LC treatment method corresponding to the lost circulation characterization. To develop the LC expert system, we represent following items on the computer to support determination of LC treatment method.

(a) Effective experienced rules of drilling engineers
(b) LC zone detecting system (developed item)
(c) Analysis programs of LC characterization (developed item)
(d) Plugging materials and treatment method (developed item)
(e) Simulation test of plugging process (developed item)
(f) Well test (developed item)

Then the expert system includes all developed items in the LC R&D project. And the system can support drilling engineer according to the situation of each LC condition at the field.

The general advantages of expert system are as follows.

(a) It is possible to judge from a lot of data, rather than limited experience of engineers as usual now.
(b) It is possible to judge correctly, even in case judgment is required in hurry, because the system judges from knowledge base.
(c) We can use more clever LC expert if the knowledge base is refined.

3.2 Structure and Function of the LC Expert

LC expert is the computer system which infers the result from rules based on the knowledge base. Based upon the characterization of LC zone, knowledge from experiences

of drilling engineers, properties of plugging materials, and results of simulation test, LC expert infers the treatment method according to information. If the treatment is succeed, the result is recorded in the hard disk of LC expert system. When, however, the treatment is failed, the system diagnoses the reason of failure and determines retrial method.

LC expert is composed of following three essential components.

(1) Tool for knowledge engineering

The first component is tool for knowledge engineering which is composed of knowledgebase, inference engine, knowledge control system, and user interface. Knowledge base includes rules from experiences of drilling experts, data from detection test, and simulation test of the plugging materials. The rule composes rules for presumption of LC characterization which infers LC geometry (severity, zone, depth, and type), rules for determination of treatment method which infers the definite treatment method/procedure (plugging material and injection method) according to information of treatment object etc., evaluation (treatment result), rules for diagnosis of failure which diagnoses according to the treatment result, rules for determination of retrial treatment method which depends on the result of diagnosis of failure, and rules for system control including communication with user-interface.

The expert system infers LC treatment method using the input data in each step and conducts the result. The LC expert can be used for "general inference" which infers all steps of rules and "individual inference" which can infer specific step is available, then users can select the system depending on their purpose. Flowchart of "general inference" of LC expert system is shown in Fig. 2.

The LC expert system can conduct some recommendations rather than one if the results have some possibility or effectiveness. So that operator has the final decision, because the purpose of this system is to support of determination of drilling engineer and it is difficult to decide the only one LC treatment from present LC technology.

(2) User-interface program

The second component is user-interface program which is composed of following nine screens.

(a) Data input screen
(b) Output of inference result screen
(c) Help screen
(d) LC detection/pressure analysis/temperature analysis screen
(e) List of LC records screen
(f) Material stock screen
(g) Well graphics screen
(h) System flowchart screen
(i) Fortran program (calculation) screen

Screen of data input has seven screens which are presumption of LC characterization, determination of plugging material, determination of injection method, determination of treatment method, evaluation, determination of retrial treatment, and record screens. All these screens have function of output of inference result, help, list of LC record, stock of materials, well graphics, system flowchart and calculation programs, and users can refer to one of these function in any time. User-interface displays Japanese characters for Japanese.

(3) Application programs

The third component is application programs which are composed of calculation programs, mud properties, properties of materials, reference from LC records, etc. We can select these applications in the input screen at any time.

3.3 Computer System for Development

(1) Hardware

Model: HP9000/375
CPU: Motorola 68030 (33MHz)
Memory: 32MB
Hard disk: 132MB (OS)
571MB (programs and knowledge base)

(2) Software

OS: HP-UNIX Version 7.0
Language: C
Fortran
Tools for knowledge engineering
Window system: X WINDOW X-II

4. KNOWLEDGE BASE

Knowledge base is one of the most important element in expert system and it dominates quality of the system. Improvement method of knowledge base for LC expert is shown in Fig. 3.

For knowledge acquisition of experiences of drilling experts, we tried many approaches such as discussion with drillers on LC treatment to drilling experts and field test. And we included the rules obtained from LC detection system and simulation test results of plugging materials.

It is difficult, in general, to evaluate system only from number of rules, however as one of indexes, progress of rule numbers is shown in Fig. 4. Total rule number of knowledge base is 338 rules.

5. EXAMPLE OF INFERENCE

Item of input and output in each inference step is shown in Table 1.

We show some input/output examples of LC expert in Figs. 5 to 13. The mouse is basically used for system operation to allow easier and quicker.

6. EVALUATION OF LC EXPERT

For the evaluation of the developed LC expert, we conduct user's test twice by drilling engineers who are related to geothermal energy development, in 1990. Through improvement of the problems which were pointed out about knowledge-base and user-interface, we developed better operability and high performance system.

We tested the developed expert system for the lost circulation which occurred 16 times in the LC-1 well

drilled as a test well for the LC R&D project. In these tests, drillers used the same materials six times as the expert system inferred in six times lost circulation. And they succeeded to plug the lost circulation three times.

It was concluded that the system generally inferred the treatment method quite adequately and no error was caused during the operation.

7. CONCLUSIONS

We drew following conclusions and future research from the work in this report.

(a) The LC expert could suggest support optimum LC treatment method according to the LC characterization obtained from the LC detection tool and analysis, knowledge base including experiences of drilling experts, and properties of plugging materials obtained from simulation tests.
(b) The LC expert was evaluated by drilling experts and field tests that the LC expert inferred the treatment method quite adequately and good performance of operation.
(c) Using this system, it is possible to get procedure of optimum LC treatment quickly.

If we have an opportunity in future, we would like to polish up and expand rules and knowledge base, and make system working with portable computer. Then this expert system will become more practical tool, we believe.

ACKNOWLEDGMENTS

We gratefully acknowledge the New Energy and Industrial Technology Development Organization (NEDO) for allowing us to present "The research and development of lost circulation techniques in geothermal wells", which was conducted from the Fiscal Year 1986 to the Fiscal Year 1990 in the Sunshine Project of MITI.

REFERENCES

Messenger, J.U. (1981), "Lost Circulation," PennWell Publishing Company, Oklahoma.

Hayes-Roth, F., Waterman, D.A., and Lenat, D.B. (1983), "Building Expert Systems," Addison Weley Publishing, Massachusetts.

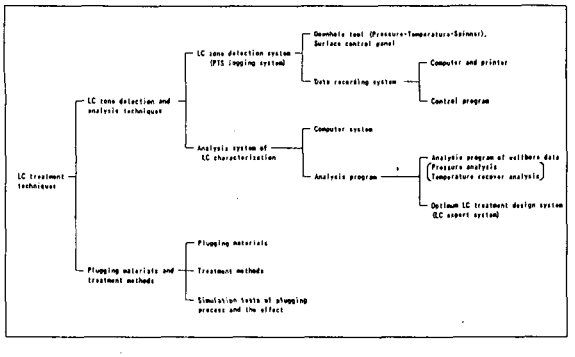

Figure 1 Research subjects of LC R&D

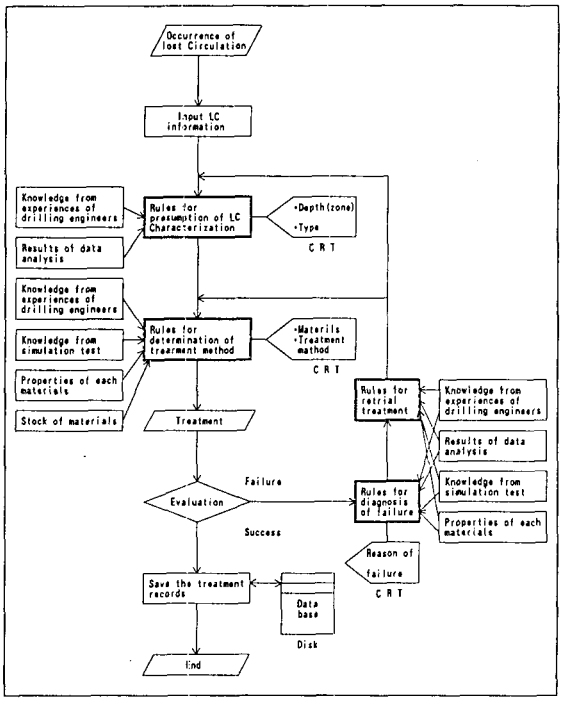

Figure 2 Flowchart of LC expert

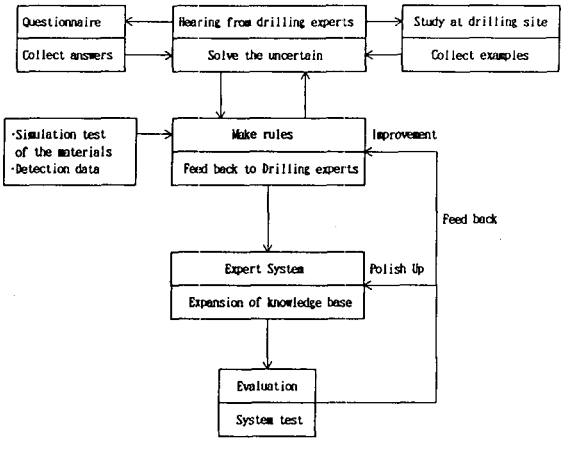

Figure 3 Improvement of knowledge base for LC expert

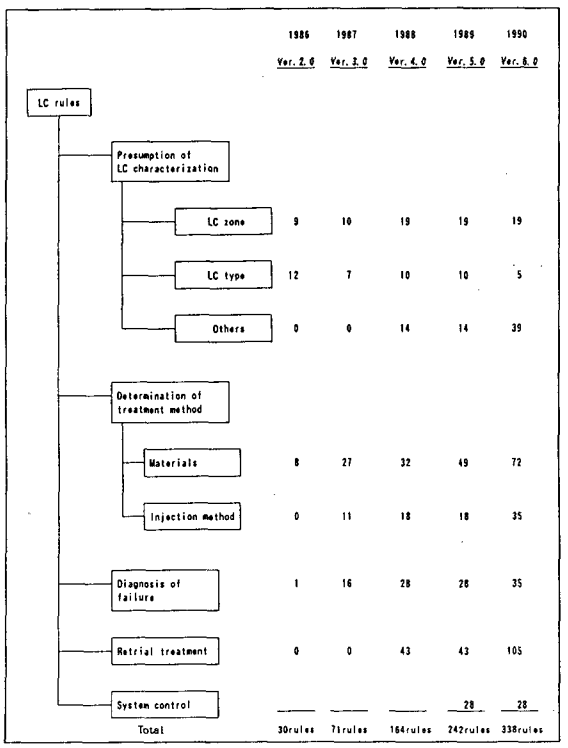

Figure 4 Rule structure and progress of rule numbers

Table 1 Input/output in each inference step

Step	LC characterization	Materials	Injection method	Result/Retrial	Record
Input	Well name well diameter Well depth Casing shoe depth Depth when LC occurred Loss rate Pump rate Fluid level Operation when LC occurred Bottom fill Collapse formation Rock type Bit weight	Purpose/ Completion Mud density Estimated temperature LC zone LC depth LC severity LC type	Material Cement density Cement volume Density of LCM slurry LCM slurry volume Bit nozzle size LC severity LC zone LC depth Mud density Estimated temp. Pump rate Loss rate	Result Pump rate Loss rate Fluid level Lost cement volume Lost LCM volume TOC Relapse depth	No Well Area Date Depth Loss/Pump rate material method result
Output	·LC depth ·LC severity ·LC type	·Plugging materials	·Injection method	·Reason of failure ·Retrial method	

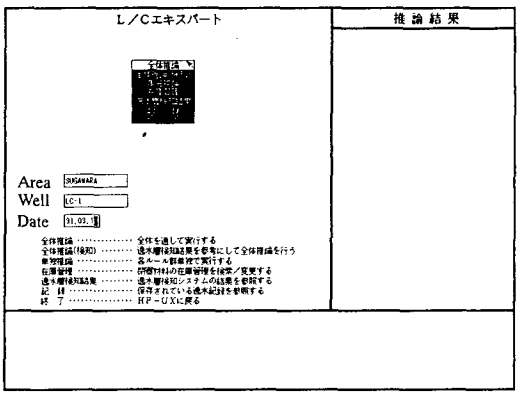

Select from 1) General inference, 2) General inference with detection system, 3) Individual inference, 4) Stock information of materials, 5) LC detection (PTS) analysis, and 6) LC data base (records).

Figure 5 Initial menu

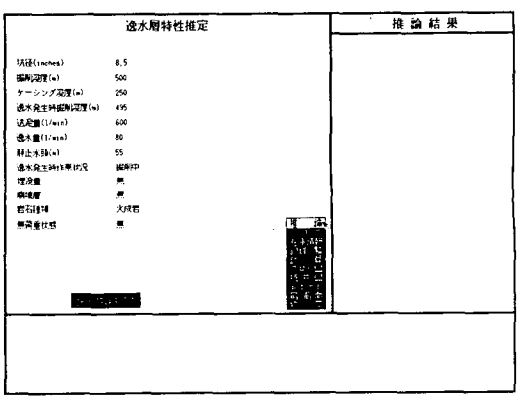

Input 1) Well diameter, 2) Well depth, 3) Casing depth, 4) Drilling depth when LC occurred, 5) Pump rate, 6) Loss rate, 7) Fluid level, 8) Operation when LC occurred, 9) Bottom fill, 10) Collapse formation, 11) Rock type, and 12) No load condition.

Figure 6 Input LC information for presumption of LC properties

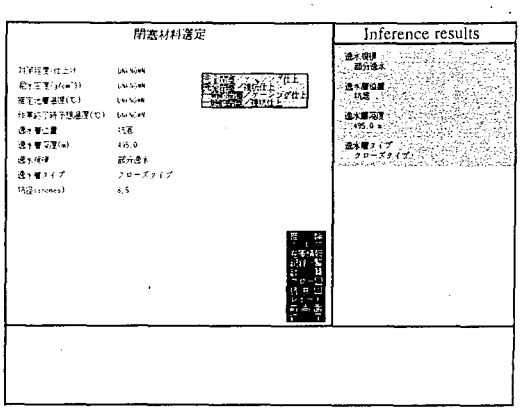

Input 1) Purpose/completion, 2) Mud density, 3) Estimated formation temperature, and 4) Estimated temperature after treatment operation.

Inference results: 1) Severity of lost circulation, 2) LC zone, 3) LC depth, and 4) LC type.

Figure 7 Determination of treatment material

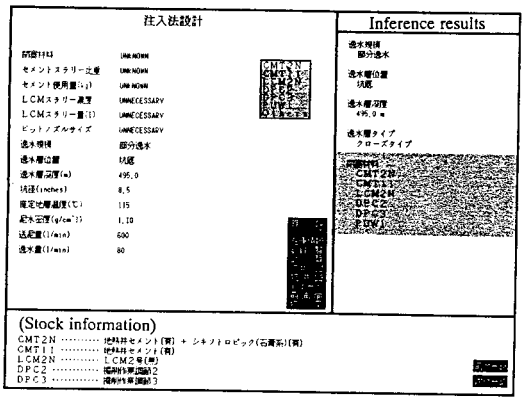

Input 1) Plugging material, 2) Density of cement slurry, 3) Cement volume, 4) Density of LCM slurry, 5) LCM slurry volume, and 6) Bit nozzle size.

Inference results: Recommended materials.

Figure 8 Determination of injection method

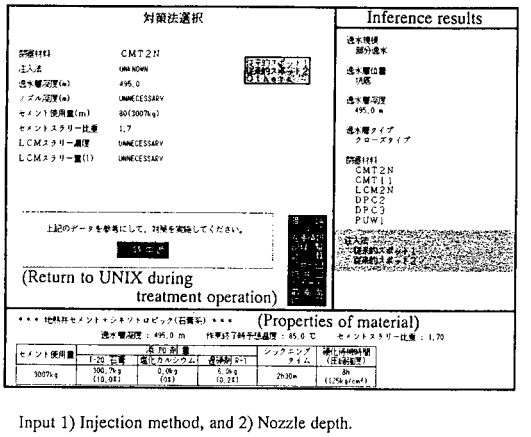

Input 1) Injection method, and 2) Nozzle depth.

Inference results: Recommended injection method.

Figure 9 Determination of treatment method

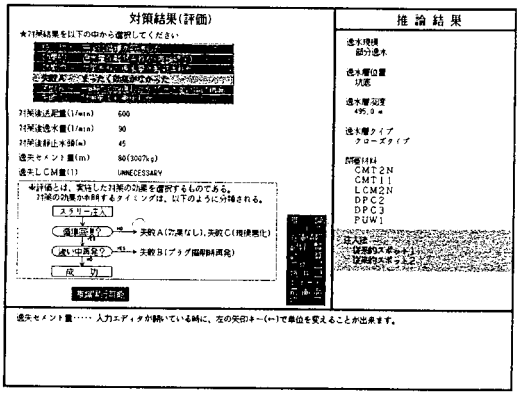

Select from 1) Circulation recover completely, 2) Effective, reduce loss rate (finish), 3) Effective, reduce loss rate (continuance), 4) No effect at all, 5) Relapse when drilling out LC zone, and 6) Become worse.

Figure 10 Input of treatment result

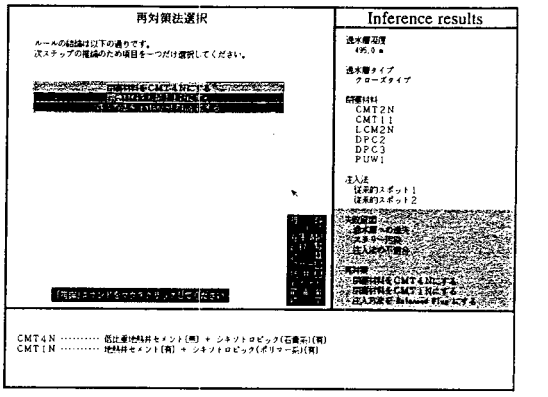

Input Retrial treatment method.

Inference results: 1) Reason of failure, and 2) Recommended retrial treatment method.

Figure 11 Determination of retrial treatment

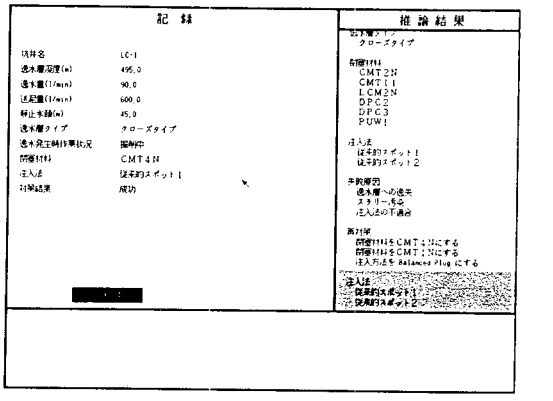

Figure 12 Recording

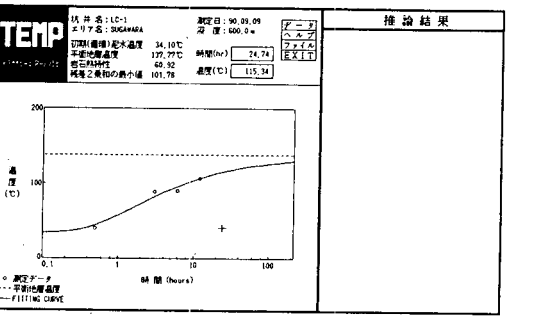

Figure 13 Example of temperature recovery analysis

PROCEEDINGS, Seventeenth Workshop on Geothermal Reservoir Engineering
Stanford University, Stanford, California, January 29-31, 1992
SGP-TR-141

Modelling of Terrain-Induced Advective Flow in Tibet: Implications for Assessment of Crustal Heat Flow

M.P. HOCHSTEIN and YANG ZHONGKE

Geothermal Institute and Department of Engineering Science,
University of Auckland, NZ

Abstract

In steep terrain the effect of advective flow can be significant, as it can distort the temperature field in the upper brittle crust. The effect was studied by modelling advective flow across a large valley system in Tibet which is associated with several geothermal hot spring systems, the Yanbajing Valley. It was found that, in this setting, all near-surface temperature gradients are significantly disturbed, attaining values differing by up to half an order of magnitude from those resulting from conductive heat transfer. Allowing for advective effects, it was found that the crustal heat flux within the Himalayan Geothermal Belt lies within the range of 60 to 90 mW/m^2 in the Lhasa-Yanbajing area.

Introduction

Over 1000 hot and warm springs occur in Tibet. They are manifestations of numerous low and high temperature systems associated with deep-reaching fracture zones. High temperature systems (as indicated by cation geothermometers) discharging significant heat (say, >3 MW) at the surface are rare. Using the inventory of Zhang Zhifei and Zhang Mingtao (1985) and our own field observations, it was found that heat losses of some Tibetan systems have been over-estimated (Hochstein, 1988). There are probably only 5 high temperature systems with a natural heat discharge in the range of 30 to 100 MW; the majority of high temperature systems are associated with moderate discharges of the order of 3 to 30 MW. If one plots on a map (see Fig. 1) all prospects that discharge fluids close to boiling point temperatures, they fall within a 150 to 200 km wide belt which, in the framework of Plate Tectonics, lies in front of the indenting Indian Plate. Chinese scientists have called this belt the 'Himalayan Geothermal Belt (HGB)' (Tong W. and Zhang M., 1981).

It has been inferred that the HGB is associated with an anomalously hot upper crust; a high terrestrial heat flux has been postulated to explain the geothermal activity and the anomalous crustal temperature field (Wei S. and Deng X., 1989). Heat flow measurements by Francheteau et al. (1984) in two shallow lakes on a plateau south of the Yarlung Zangpo River (Puma Lake and Yamtso Lake in Fig. 2) provided some evidence for the postulated high crustal heat flow (observed values lie between 90 and 147 mW/m^2).

Efforts to trace the lateral extent of the inferred anomalous heat flow across the belt by measurements in drillholes have been less successful. Most deeper wells in Tibet have been drilled into geothermal reservoirs or associated outflow structures. Data from a few wells in the Lhasa area (Shen, 1989), far away from geothermal activity, point to apparent heat flow values of 60 to 100 mW/m^2. Until recently, the deepest well in Tibet was the 1650 m deep ZK308 well in the Yanbajing prospect (Cappetti and Wu, 1985), drilled through a shallow thermal outflow. The well stands almost entirely in Tertiary granites; the temperature profile at the bottom of the well is linear. If this gradient (36E-3°C/m) were controlled by conductive heat transfer, it is unlikely that the deeper heat flux would be greater than 90 mW/m^2.

Most of the heat flow data for Tibet previously published have been reduced for terrain effects assuming purely conductive heat transfer. However, it is known that, in steeper terrain, advective fluid flow can distort the temperature field of the brittle crust (Beck et al., 1989). A modelling study of the Zhangzhou low temperature system in South China (Yang Zhongke et al., 1990) has shown, for example, that even in moderate terrain a low temperature system can be set up by advective flow. At Zhangzhou, this flow sweeps heat from thick crustal granites into a fracture zone system within a large basin where deep fluids are discharged at boiling point temperature at the surface; neither high crustal heat flow nor crustal intrusions are required to maintain the Zhangzhou system. A gross permeability structure could be obtained by matching observed temperature gradients in wells of intermediate depths in the recharge and discharge areas. The gradients were lower in the mountains and significantly higher in the basin than those given by a 'normal' heat flow (Yang Zhongke et al., 1990).

If terrain-induced advective flow were significant in the steep valleys of Tibet, one could postulate that such flow would also produce a disturbed temperature field similar to that beneath the Zhangzhou prospect. In this case, most of the temperature gradients in wells standing in valleys should be disturbed (i.e., too high apparent heat flow values), and the widespread occurrence of thermal systems in the Himalayan Geothermal Belt might not necessarily be indicative of an anomalous hot upper crust but could be the result of advective flow.

Advective flow beneath a large valley in Tibet: the model

To assess the effect of advective flow we set up a model of an idealized large valley system in Tibet - which we call the 'Yanbajing Valley'. This large valley trends about NW-SW (see Fig. 2) for a distance of almost 200 km; geothermal systems are concentrated here. Figure 2 shows that there are three different systems in the valley which discharge fluids at boiling point temperature. The Yanbajing system is the largest of these (natural discharge of the order of 90 MW, according to Hochstein, 1988). It is probably the

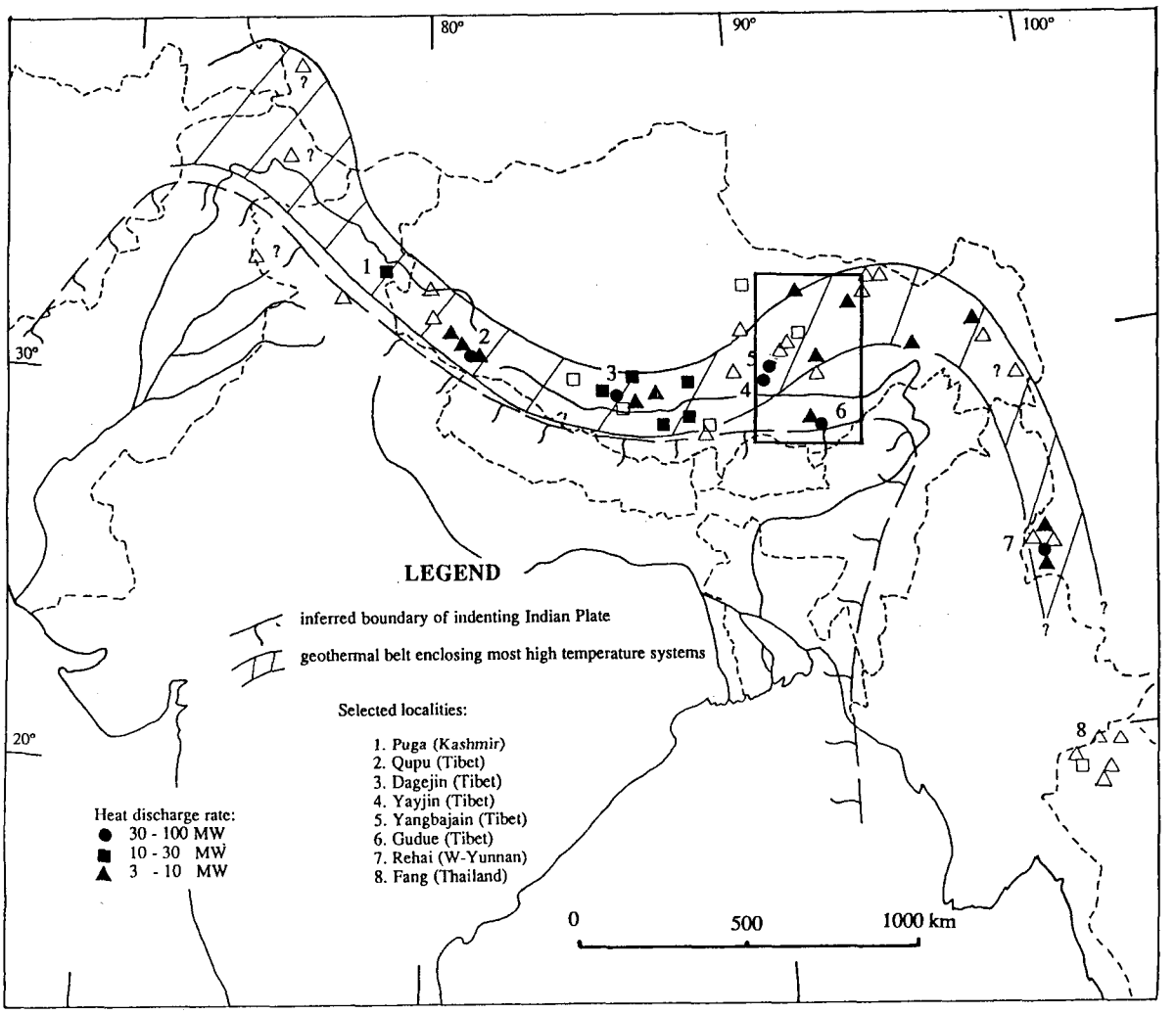

Fig. 1 Map showing the locality of geothermal systems in the Himalayan Geothermal Belt which discharge fluids close to boiling point temperature at the surface and which discharge heat at a rate greater than 3 MW. Solid symbols refer to high temperature systems (cation equilibrium temperatures greater than 200°C); open symbols refer to intermediate temperature systems (equilibria temperatures between 150 and 200°C). Low temperature systems are not shown. The approximate area covered by the map shown in Fig. 2 is framed.

largest geothermal system in Tibet. The valley is bounded in the NW by the Nyanchen Thanglha mountain range, with summit heights typically between 6500 and 7000 m; in the SE lies the Tang mountain range, with summit heights between 5500 and 6300 m elevation. The valley floor is at 4250 m elevation at Yanbajing and up to 4400 m elsewhere.

A smoothed two-dimensional topographic section was constructed for profile A-A' shown in the lower part of Fig. 3. From our own field observations in 1986 we constructed an inferred groundwater level for the whole section. The level was constrained by that of mountain creeks with continuous annual flow and high level springs. The configuration of saturated rocks was approximated by a sequence of slightly permeable, horizontal layers. The effect of a glacial cover in the valley was neglected. All rocks above the inferred piezometric level were assumed to be dry.

Since the temperature of the high springs is close to the mean annual temperature at Yanbajing (about 3°C), the piezometric level is the upper constant pressure and constant temperature boundary of the model. It was assumed that this boundary did not change significantly during the Quaternary (i.e. last 2 M yrs). Infiltration is maintained by melting of the snow pack.

Most rocks along the section are Lower Tertiary granites and volcanics; the metamorphic basement rocks (gneiss) of the Nyanchen Thanglha range are also intruded by Tertiary granites. It was assumed that the physical constants of all rocks exposed along the section are similar to those of the granites exposed in the valley. These have a mean (saturated) density of about 2650 kg/m^3, an average porosity of only 0.03, a mean (saturated) thermal conductivity of about 2.5 W/mK, and a thermal capacity of 1000 kJ/kg K.

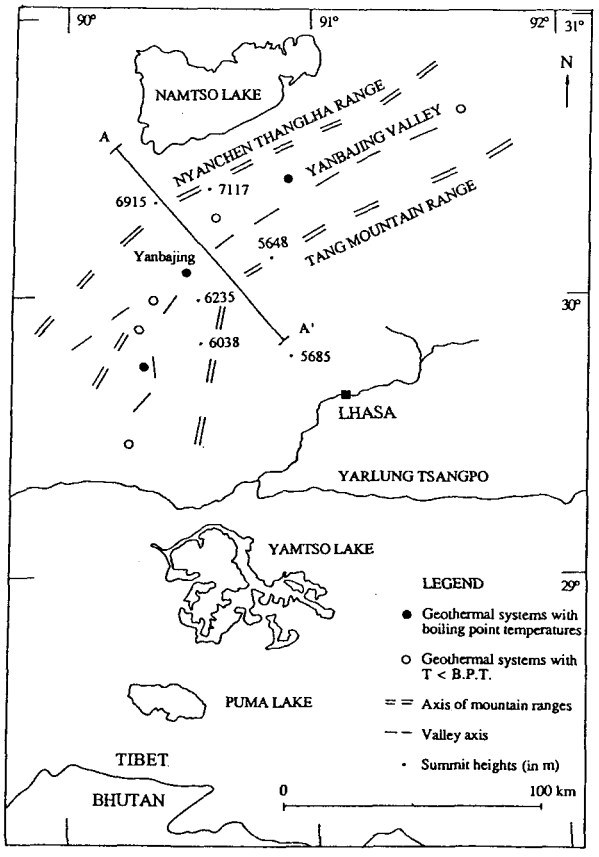

Fig. 2 Map showing the location of the extended Yanbajing Valley system; the locality of geothermal prospects is indicated by solid and open circles. The location of the section in Fig. 3 is shown by profile A-A'. Shown also are the locality of the two large lakes south of the Yarlung Zangpo Valley where heat flow studies have been conducted.

In an earlier, unpublished, modelling study of the outflow structure of the Yanbajing system (UNDP project CPR/81/011), which modelled natural state condition, an average isotropic permeability of 1 millidarcy (1 mD = 10^{-15} m^2) had been used for the granite basement (G. Cappetti, pers. comm. 1986).

Since the physical parameters of the granites in the Yanbajing Valley are similar to those of the Mesozoic granodiorites in the Zhangzhou prospect (Yang Zhongke et al., 1990), we adopted the crustal permeability structure of the Zhangzhou catchment to model the advective flow for the section shown in Fig. 3. Initially, we therefore used a structure with a permeability k_z = 0.5 mD and $k_{x,y}$ = 1 mD for all rocks lying above the level of 3000 m, and k_z = 0.2 mD, $k_{x,y}$ = 0.5 mD for all rocks between 3000 m and sea level. Since we were mainly interested in assessing the advective effects in shallow levels, the permeability structure of rocks below sea level was neglected (i.e. k_z = $k_{x,y}$ = 0 below sea level). The model therefore extends for another 2 km below the bottom level of the section shown in Fig. 3. The advective flow was simulated by using a modified MULKOM program (Pruess, 1983). The initial temperature field was that given by conductive heat transfer, assuming a deep crustal heat flux of 90 (60) mW/m^2 at sea level. By using increasing time steps, the effects of advection were monitored until almost steady-state temperatures were obtained (≥2 M yr). The modelling procedure was the same as that described by Yang Zhongke et al. (1990).

Results

Results of the simulation are shown in Figs. 3 and 4. The resulting temperature field, assuming a deep crustal flux of 90 mW/m^2, is shown in the lower part of Fig. 3. Advection has caused a temperature 'plume' beneath the valley; the shaded area in the model outlines the temperature field where temperatures are significantly greater than those produced by conductive transfer. Crustal temperatures beneath the mountain ranges are depressed. The anomaly extends down to sea level.

Temperature gradients at a depth of 250 m beneath the inferred water table, [G_{90} (-0.25)] curve in upper part of Fig. 3, vary from 10E–3 °C/m) (mountain range) to 95E–3 °C/m (valley), and correspond to an apparent heat flux of 25 and 240 mW/m^2 respectively. The effect of advective convection is more than half an order of magnitude greater than the terrain effect for a conductive setting. The advective effects decrease if the magnitude of deeper heat flux is less. For a flux of 60 mW/m^2, the gradients [G_{60} (–0.25) in Fig. 3] attain values of 8E–3 °C/m beneath the mountain ranges, and about 55E–3 °C/m beneath the valley. The resulting gradients are therefore not linearly proportional to the magnitude of crustal heat flux, even for rocks with such a low permeability.

If the convective 'plume' beneath the valley were intersected by a deep-reaching fracture zone, similar to that which we modelled for the Fuzhou system (Hochstein et al., 1990), low temperature systems would develop, leading to a further distortion of the temperature field in the upper crust. Using the analogy of the Zhangzhou study, one can infer that most of the systems in the Yanbajing Valley developed as fracture zone systems within a temperature plume beneath the valley.

The problem of obtaining representative heat flow values from temperature profiles in wells in the valley is indicated by the profiles shown in Fig. 4. It can be seen that the temperature gradients (G_{90} and G_{60} in Fig. 4) decrease continuously with depth without reaching constant values. For depths greater than 1.7 km, these gradients show an 'overshoot' pattern, attaining even lower than 'normal' values, where 'normal' refers to the undisturbed conductive gradient (i.e. 36E–3 °C/m for G_{90} and 24E–3 °C/m for G_{60}).

Since the permeability of the outcropping rocks could be lower than that assumed for the initial model, we also assessed the effects of advective flow for surface rocks of low permeability (k_z = 0.2 mD, $k_{x,y}$ = 0.5 mD down to 3000 m). The resulting temperature changes in all blocks are small and are only a few centigrade lower at 2 km depth than those shown in Fig. 4, thus indicating that most of the advective flow occurs below the 3000 m level. This finding is similar to that of a sensitivity analysis of the permeability structure beneath the Zhangzhou prospect (Yang Zhongke et al., 1990).

It is obviously a difficult task to obtain a representative value for the deeper flux from temperature measurements even in very deep wells if advection is significant. Curves

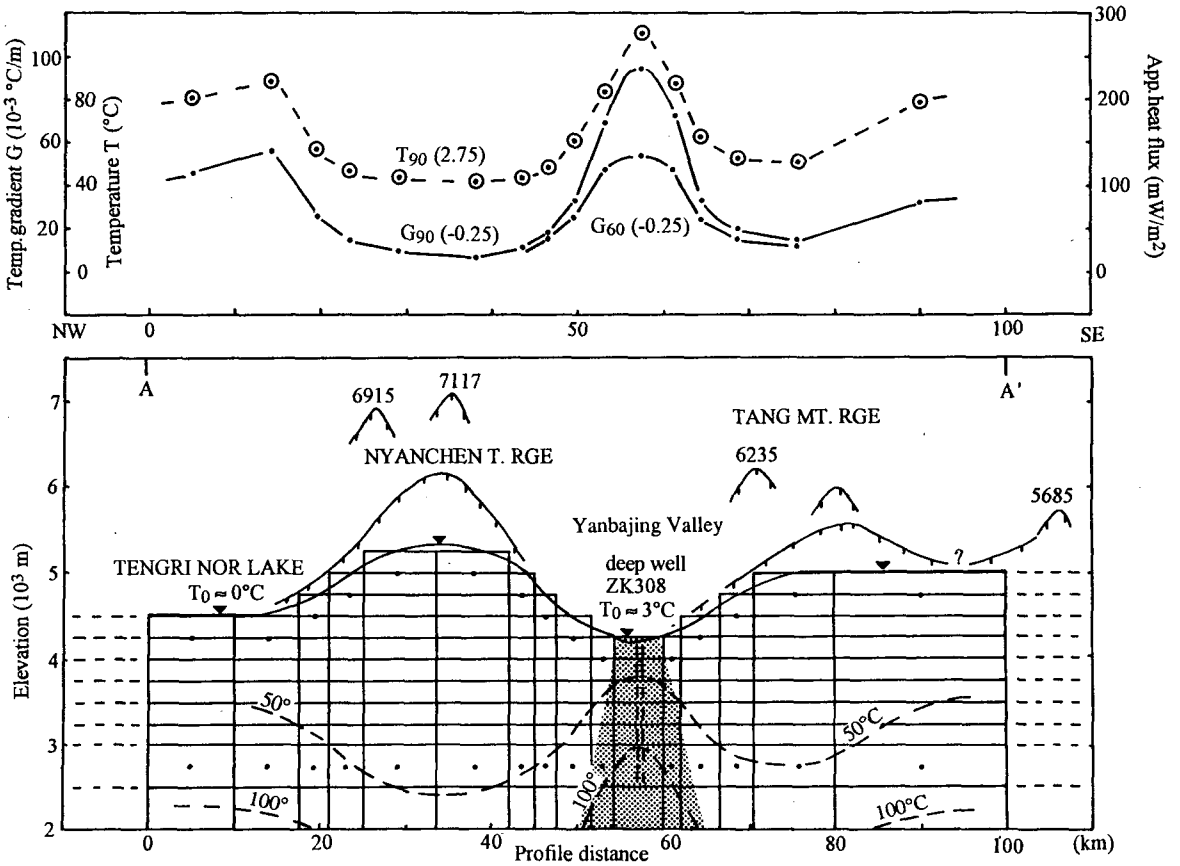

Fig. 3 Advective flow beneath the greater Yanbajing Valley. The section in the lower half shows the two-dimensional topographic model and the block structure of the saturated rocks. The lower part of the model which extends to sea level is not shown. The temperature contours (50°C, 100°C) in the block model refer to computed temperatures using a deeper crustal heat flux of 90 mW/m^2; the temperatures in the shaded plume are all greater than those produced by conductive heat transfer. The curve G_{90} (–0.25) in the upper half refers to the stable temperature gradient at a depth of 0.25 km beneath the water table based on a model with a deep crustal flux of 90 mW/m^2; the curve G_{60}(–0.25) refers to similar data but for 60 mW/m^2. The upper curve T_{90} (2.75) denotes the temperature at a level of 2.75 km (flux 90 mW/m^2).

similar to those shown in Fig. 4, however, can be used to obtain an estimate of the deeper flux. The temperature profile for the bottom 500 m section of the deep ZK308 well at Yangbajing is linear, indicating a gradient of about 36E–3 °C/m at a mean depth of 1375 m. Assuming that this gradient is not significantly disturbed, and that the advective flow beneath the valley is similar to that of the model shown in Fig. 3, the deep gradient in well ZK308 indicates a value for the crustal flux within the range of 60 to 90 mW/m^2 (see Fig. 4).

Since the Lhasa Valley has a morphology similar to that of the valley shown in Fig. 3, one can also use the data in Fig. 4 to assess an approximate value for the deep heat flow in the Lhasa Valley. Shen (1989) observed a gradient of 36E-3° C/m near the bottom of the 500 m deep GEOTH. No. 2 well in the Lhasa Valley. Rocks in the Lhasa section are also (early) Tertiary granites. The position of this data point in Fig. 4 indicates that the deeper heat flux at Lhasa is either less than 60 mW/m^2 or that it is disturbed by significant local infiltration of permeable fractures.

Discussion

Modelling the effects of advective flow beneath a large valley in Tibet has shown that this flow can disturb the crustal temperature field. Advective flow results in a redistribution of crustal heat, causing the development of thermal 'plumes' beneath valleys and other depressions. Surface temperature gradients in valleys can attain values more than half an order of magnitude greater than those resulting from conductive transfer. Since, in the past, most heat flow measurements in Tibet have been made in wells standing in valleys, it is likely that the published data contain a systematic error. The effect of advective flow is difficult to reduce since one has to use an inferred crustal crustal permeability structure.

With respect to the questions raised in the Introduction, we believe now that there is no conclusive evidence for the assumption of an anomalously hot brittle crust beneath the Himalayan Geothermal Belt, or that the accumulation of geothermal systems in this belt supports the inference of (upper) crustal magma chambers. There is indeed no

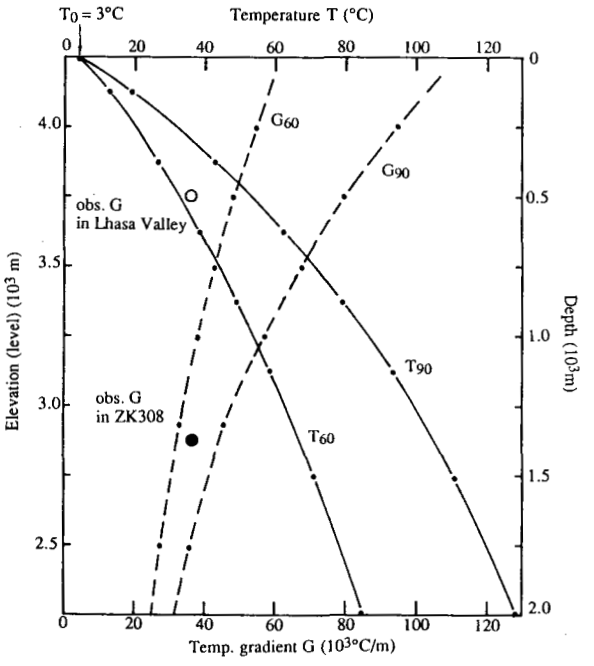

Fig. 4 Temperatures and temperature gradients within the central block lying beneath the Yanbajing Valley shown in Fig. 3. The temperature profiles T_{90} and T_{60} refer to temperatures produced by advection for a deeper crustal flux of 90 and 60 mW/m^2 respectively. The same applies for the temperature gradient profiles G_{90} and G_{60}. "Obs. G" refers to observed temperature gradients of selected wells in the Yanbajing and Lhasa valleys.

evidence for any volcanic activity in Tibet which is younger than 25 M yrs.

However, it is likely that the deeper, ductile crust is anomalously hot, as indicated by crustal seismic studies (i.e. lower shear wave velocities, anomalous attenuation, updomed level of the Curie point temperature). One can reconcile these findings with the results of this study by assuming that the brittle crust has been cooled by deep-reaching advective flow, probably reaching deeper than the flow pattern modelled in this study.

References

Beck, A.E.; Garven, G.; Stegena, L. (1989), "Hydrogeological regimes and their subsurface thermal effects." Geophysical Monograph 47, IUGG Volume 2, Am. Geophysical Union, 158 pp.

Cappetti, G.; Wu Fangzhi (1985), "Present status and prospects of Yangbajain Geothermal Field." Proc. Geothermal Resources Council, 1985 Int. Symposium on Geothermal Energy (Int. Volume), 563-568.

Francheteau, J.; Jaupart, C.; Shen Xian Jie; Kang Wen-Hua; Lee De-Lu; Bai Jia-Chi; Wei Hung-Pin; Deng Hsia-Yeu (1984), "High heat flow in southern Tibet." Nature 307, 32-36.

Hochstein, M.P. (1988), "Assessment of natural heat loss by the balance method." Proc. 10th NZ Geothermal Workshop, Univ. of Auckland, pp. 291-294.

Hochstein, M.P.; Yang Zhongke; Ehara, S. (1990), "The Fuzhou Geothermal System (P.R. China): modelling study of a low temperature fracture zone system." Geothermics 19, 43-60.

Pruess, K. (1983), "Development of the general purpose simulator MULKOM." Annual Report 1982, Earth Sciences Division, Lawrence Berkeley Laboratory, report LBL-15500.

Shen Xian Jie; Zhang Wen-ren; Yang Shu-zen; Shen Ji-ying; Zhang Rong-Yan; Yang Zhongke; Xia Si-Gao (1989), "Updated report on heat flow data in Xizang." Chinese Science Bull. 34(20), 1728-1732.

Tong Wei and Zhang Mingtao (1981), "Characteristics of geothermal activities in Xizang Plateau and their controlling influence on Plateau's tectonic model." In: Geological and Ecological Studies of Qinghai-Xizang Plateau, vol. 1, Gordon and Breach, New York, 841-846.

Wei Si-Yu and Deng Xiao-Yue (1989), "Geothermal activity, geophysical anomalies and the geothermal state of the crust and upper mantle in the Yarlung Zangpo river zone." Tectonophysics 159, 247-254.

Yang Zhongke; Hu Shengbiao; Hochstein, M.P. (1990), "Conceptual model of the Zhangzhou low temperature system and its surrounding catchment (Fujian Province, P.R. China)." Proc. 15th Workshop on Geothermal Reservoir Engineering, Stanford University, 97-102.

Zhang Zhifei and Zhang Mingtao (1985), "Assessment of geothermal reservoir within hydrothermal systems in Xizang (Tibet)". In: Liu Dian Gun (Ed.): "Research on Yangbajing geothermal power station." Publishing House (Chongqing Branch), Beijing, 160-176 (in Chinese).

PROCEEDINGS, Seventeenth Workshop on Geothermal Reservoir Engineering
Stanford University, Stanford, California, January 29-31, 1992
SGP-TR-141

A DUAL-POROSITY RESERVOIR MODEL WITH AN IMPROVED COUPLING TERM

Robert W. Zimmerman, Gang Chen, and Gudmundur S. Bodvarsson

Earth Sciences Division
Lawrence Berkeley Laboratory
University of California
Berkeley, CA 94720

Abstract

A new dual-porosity model is developed for single-phase flow in fractured/porous media. As in the commonly-used approach, flow is assumed to take place through the fracture network, and between the fractures and matrix blocks. The matrix blocks are treated in a lumped-parameter manner, with a single average pressure used for each matrix block. However, instead of assuming that fracture/matrix flux is proportional to the difference between the fracture pressure and matrix pressure at each point, as in the Warren-Root model, a nonlinear equation is used which accurately models the flux at both early and late times. This flux equation is verified against analytical solutions for spherical blocks with prescribed pressure variations on their boundaries. This equation is then used as a source/sink term in the numerical simulator TOUGH. The modified code allows more accurate simulations than the conventional Warren-Root method, and with a large savings in computational time compared to methods which explicitly discretize the matrix blocks.

Introduction

Numerical simulation of flow processes in fractured rocks is a formidable task, due to the often complex geological and hydrological characteristics of such formations. The specific specific geometry and other characteristics of the fracture system is generally not known, so it is not possible to explicitly model individual fractures or individual matrix blocks. To circumvent this difficulty, so-called "double-porosity" models are often used. In double(or dual)-porosity models, knowledge of the actual geometric and hydrological features of the fracture network are not required, but instead only "average" properties, such as a typical fracture spacing, are needed. In a numerical simulation of a flow process in a dual-porosity system, the individual computational cells are assumed to be sufficiently large so that it is meaningful to assign suitably-averaged "effective" properties to them. Despite this simplification, numerical modeling of dual-porosity reservoirs is still a complicated and costly process. In general, fairly fine spatial discretization is needed in the matrix blocks - typically five to ten "matrix" cells are required for each "fracture" cell. Hence modeling of a fractured reservoir will require five-to-ten times as many computational cells as would be needed for a porous medium simulation of a reservoir of the same overall size.

Although most geothermal reservoirs reside in fractured rocks, most models that have been developed to analyze their behavior have been based on porous medium approximations. It is well-known, however, that porous medium models are poorly suited for predicting certain aspects of the behavior of geothermal wells, especially enthalpy transients, thermal front migration due to injection, or chemical tracer movement. Nevertheless, in many cases the porous medium approximation must be invoked, due to constraints of time or cost. There is consequently a great need for improved numerical capabilities for the modeling of fractured geothermal reservoirs, using accurate and appropriate models.

In this paper we present a new method for modeling fractured reservoirs that can simulate reservoir behavior more efficiently and economically. The method involves analytical treatment of fracture/matrix interflow, eliminating the need for discretization of the matrix blocks. This allows accurate dual-porosity simulations, using a substantially smaller number of cells than would be needed in a fully-discretized simulation. Although at this time we can simulate only single-phase, isothermal processes with our semi-analytical approach, our intention is to extend the basic approach to the treatment of two-phase, non-isothermal processes.

Dual-Porosity Models

When a single-phase, slightly compressible fluid flows through a macroscopically-homogeneous fractured medium, the fluid pressure in the fractures is governed by the usual diffusion equation used in reservoir engineering (Matthews and Russell, 1967):

$$\phi_f c_f \frac{\partial P_f(x_f,t)}{\partial t} = \frac{k_f}{\mu}\nabla^2 P_f(x_f,t) + Q(x_f,t). \qquad (1)$$

In this equation, t is the time, x_f is the position vector of a point in the fracture continuum, k_f is the absolute permeability of the fracture continuum, ϕ_f is the total fracture porosity, and c_f is the total compressibility of the fractures and the fluid within them. Q is a source term that represents the net addition of fluid to the fracture system from the matrix blocks, per unit of total volume. The pressure P_f represents the fluid pressure in the fractures, averaged over some suitably large representative elementary volume (REV; see Chen, 1989). The Laplacian operator ∇^2 represents the divergence of the gradient, and takes on different specific

forms for each type of coordinate system (*i.e.*, Cartesian, cylindrical, or spherical). The fracture continuum is assumed to occupy all of the physical space spanned by the variable x_f, with the actual pore volume of the fractures accounted for by the porosity factor.

A dual-porosity model can be formulated by first imagining that, at each point x_f, there is located a matrix block of some specified shape. Inside each block the fluid pressure P_m will, in general, vary from point to point. Two position variables are needed to identify a point inside a matrix block; x_m will locate the point within the block, relative to, say, the block's center of gravity, while x_f is needed as a label to fix the location of that particular block within the fracture continuum. Fluid flow *within* each matrix block is governed by an equation of a similar form as (1), which can be written as

$$\phi_m c_m \frac{\partial P_m(x_m, t; x_f)}{\partial t} = \frac{k_m}{\mu} \nabla^2 P_m(x_m, t; x_f) . \qquad (2)$$

In this equation, the parameters have meanings analogous to those in eq. (1). The derivatives implicit in the operator ∇^2 are taken with respect to the local variable x_m, while the variable x_f is merely used as a label. The fracture/matrix interflow term Q does not appear explicitly in eq. (2) since, whereas the interflow is assumed to be *distributed* throughout the fracture continuum as a source/sink term, the interflow enters the matrix blocks only at their *boundaries*. The pressures at the outer boundary of a given matrix block located at point x_f in the fracture continuum are always assumed to be equal to the fracture pressure at that point - *i.e.*, if x_m is on the boundary of the matrix block, then $P_m(x_m, t; x_f) = P_f(x_f, t)$.

The system of equations (1) and (2) actually represent a single equation for the fracture continuum, along with a family of equations for the matrix blocks that are located at each point x_f. These equations are coupled through the term Q, which can be found by integrating the flux out of the boundary of each matrix block, using Darcy's law (see Duguid and Lee, 1977):

$$Q(x_f, t) = \frac{-1}{V_m} \int_{\partial V_m} \frac{k_m}{\mu} \frac{\partial P_m}{\partial n} dA , \qquad (3)$$

where the derivative of P_m is taken in the direction of the outward unit normal vector to the boundary ∂V_m of the block, and the integral is taken over the entire boundary. A well-posed boundary-value problem for the system of equations (1-3) would typically require initial conditions for P_m and P_f, as well as boundary conditions for the pressures at the outer boundary of the macroscopic region under investigation, *i.e.*, at the outer boundary of the x_f domain. If the initial state were one of local equilibrium, as would often be the case, we would have $P_f(x_f, t=0) = P_m(x_m, t=0; x_f)$ at each point x_f.

Dual-porosity models of the type discussed above, in which diffusion equations are solved in both the fracture and the matrix systems, are sometimes used in numerical simulations. An example is the MINC method (Pruess and Narasimhan, 1985), in which the matrix blocks are discretized into nested shell-like cells. In order to achieve high accuracy over all time scales, however, we have found that about ten computational cells are needed in each matrix block. In some cases, only one cell is used to model each matrix block; this approach is then basically a numerical implementation of the Warren-Root model, which is discussed below. As is well known, when solving problems in dual-porosity media, the Warren-Root model is inaccurate during a certain intermediate time regime. The MINC method approaches the exact response as the number of nested matrix shells increases. The method we have developed, which treats fracture/matrix flow with a nonlinear ordinary differential equation, is reasonably accurate over all time scales.

Warren-Root Lumped-Parameter Models

The Warren and Root (1963) model is a simplified form of dual-porosity model in which no attempt is made to solve the diffusion equation within each block, but the blocks are instead treated in a "lumped parameter" fashion. The pressure in the matrix blocks is then governed by an ordinary, rather than partial, differential equation. If implemented into numerical simulators in the form of a source/sink term for the fracture elements, the amount of computational time spent on solving for the matrix block pressure, and the fluid-interaction term Q, becomes negligible compared to the time spent solving the diffusion equation (1) in the fracture continuum. This model can be derived by first replacing the pressure distribution in each block, $P_m(x_m, t; x_f)$, by the average pressure within the block,

$$\bar{P}_m(x_f, t) = \frac{1}{V_m} \int_{V_m} P_m(x_m, t; x_f) \, dV . \qquad (4)$$

A more rigorous definition of $\bar{P}_m$ would involve some sort of weighted average over the block, to account for the fact that the fluid compressibility varies with the thermodynamic state of the fluid. However, for isothermal single-phase flow, with moderate pressure variations, the fluid compressibility is nearly constant, and definition (4) suffices. Eq. (1) can still be used for the pressure within the fracture network, but eq. (2) governing the pressure distribution within the matrix blocks is no longer meaningful, since the pressure P_m is no longer defined at each point x_m within the matrix block. Instead, we integrate eq. (2) over an entire matrix block centered at point x_f, use the divergence theorem to convert the volume integral of $\nabla^2 P_m$ into a surface integral of $\partial P_m / \partial n$, and divide the resulting equation by V_m, to arrive at

$$\phi_m c_m \frac{\partial \bar{P}_m(x_f, t)}{\partial t} = \frac{1}{V_m} \int_{\partial V_m} \frac{k_m}{\mu} \frac{\partial P_m}{\partial n} dA . \qquad (5)$$

By comparison of eq. (5) with eq. (3), we see that the mean pressure in the matrix block is governed by the following ordinary differential equation:

$$\phi_m c_m \frac{d\bar{P}_m(x_f, t)}{dt} = -Q(x_f, t) . \qquad (6)$$

Equations (1) and (6) now govern the behavior of a lumped-parameter type dual-porosity model. Note that

since the local variable x_m within each matrix block has been integrated out, Q cannot be evaluated as in eq. (3), but must somehow be related to the two pressures P_f and $\bar{P}_m$.

In order to maintain the linearity and relative simplicity of the system of differential equations, Warren and Root (1963) chose to model the flux term Q by assuming that it is directly proportional to the difference between P_f and $\bar{P}_m$:

$$Q(x_f,t) = \frac{-\alpha k_m}{\mu}(P_f - \bar{P}_m) , \tag{7}$$

where α is a parameter that depends on block shape, and has dimensions of 1/Area. The governing equation (6) for $\bar{P}_m$ then takes the form

$$\phi_m c_m \frac{d\bar{P}_m(x_f,t)}{dt} = \frac{\alpha k_m}{\mu}(P_f - \bar{P}_m) . \tag{8}$$

Expressions (7) and (8) for the flux and the matrix pressure are often referred to as the "quasi-steady-state" approximation (Chen, 1989). This terminology reflects the fact that, under conditions of a step-function increase in pressure at the outer boundary of the block, the mean pressure in the block is governed by an equation of the form (8). For simple geometries, such as spheres or cubes, the parameter α can be related to the relaxation time of the most-slowly decaying Fourier component of the step-function response. For spherical blocks of radius a_m, for example, we find (Crank, 1975) that $\alpha = \pi^2/a_m^2$.

Potential difficulties with equations of the form (8) can be anticipated from the fact that this equation only strictly holds for large times, and even then only for step-function boundary conditions. The errors incurred by using eq. (8) will generally be quite large at "small" times, for any type of boundary condition. The aim of our work is to incorporate a modification of eq. (8) into a dual-porosity simulator, which will be accurate over all ranges of time scales, and for more general boundary conditions.

Fully-Transient Coupling Term

Our intention is to maintain the computational simplicity inherent in a lumped-parameter formulation of a dual-porosity model, but with equations (7) and (8) replaced by equations that more accurately account for fracture/matrix flow interactions. This approach requires the derivation of an equation for Q, which depends on P_f and $\bar{P}_m$, as well as the various physical parameters of the problem, but which does not necessarily have the same exact form as eqs. (7) and (8). Since the Warren-Root interaction equation can be derived by differentiating the large-time approximation to the step-function pressure response, it might be thought that a more general interaction equation could be derived by differentiating the exact step-function pressure response, which is (Crank, 1975)

$$\frac{\bar{P}_m - P_i}{P_o - P_i} = 1 - \frac{6}{\pi^2}\sum_{n=1}^{\infty}\frac{1}{n^2}\exp(-n^2\pi^2 k_m t/\phi_m \mu c_m a_m^2), \tag{9}$$

where P_i is the initial pressure in the block, and P_o is the pressure imposed at the outer boundary of the block at $t = 0$. Unfortunately, if we attempt this procedure, it is not possible to eliminate t from explicitly appearing in the resulting differential equation. A related approach is to first find an algebraically simple approximation to the step-function response, and then find the first-order differential equation that it satisfies. To do this, we start with the observation by Vermeulen (1953) that the step-function pressure response (9) can be approximated, over all time scales, by

$$\frac{\bar{P}_m - P_i}{P_o - P_i} = \left[1 - \exp(-\pi^2 k_m t/\phi_m \mu c_m a_m^2)\right]^{1/2} . \tag{10}$$

Differentiating eq. (10) with respect to t, and then eliminating t from the result, leads to

$$\frac{d\bar{P}_m}{dt} = \frac{\pi^2 k_m[(P_o - P_i)^2 - (\bar{P}_m - P_i)^2]}{2\phi_m \mu c_m a_m^2(\bar{P}_m - P_i)} . \tag{11}$$

We now generalize eq. (11) by assuming that P_o represents the fracture pressure P_f, even if P_f varies with time:

$$\frac{d\bar{P}_m}{dt} = \frac{\pi^2 k_m[(P_f - P_i)^2 - (\bar{P}_m - P_i)^2]}{2\phi_m \mu c_m a_m^2(\bar{P}_m - P_i)} . \tag{12}$$

For the step-function boundary conditions, eq. (12) integrates to eq. (10), which is a very close approximation to the exact step-function response, eq. (9). Using the value $\alpha = \pi^2/a_m^2$ that is appropriate for a spherical block, the Warren-Root equation (8) can be integrated to yield the following step-function response:

$$\frac{\bar{P}_m - P_i}{P_o - P_i} = 1 - \exp(-\pi^2 k_m t/\phi_m \mu c_m a_m^2) . \tag{13}$$

The Warren-Root step-function response is compared in Fig. 1 to the exact response, and to the response predicted by the Vermeulen equation. While both the Warren-Root and Vermeulen approximations are valid as $t \to \infty$, the Warren-Root step-function response is very inaccurate at small times, whereas the Vermeulen equation is accurate for all values of t. Note that various authors have used slightly different values for the parameter α, particularly for the case of cubical matrix blocks (cf., deSwaan, 1990). Such choices cannot remedy the fact that a Warren-Root-type equation will predict the incorrect exponent for the time-dependence of the pressure in the small-time limit.

The superiority of the Vermeulen differential equation (12) over the Warren-Root differential equation (8), for step-function boundary conditions, is to be expected, since eq. (12) was derived for those conditions. However, we have (fortuitously) found that the Vermeulen equation is also more accurate than Warren-Root under very general types of boundary conditions. For example, consider a ramp-function increase in P_f, which can be specified by

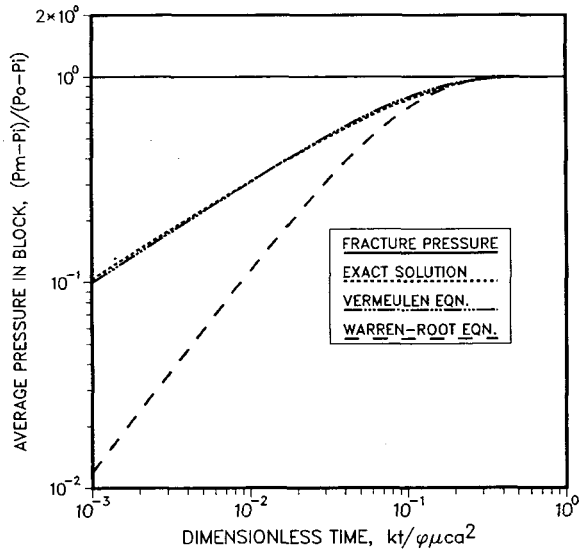

Fig. 1. Normalized average matrix pressure for a spherical block subjected to a step-function increase in the pressure at its boundary, as given by the exact solution (9), the Vermeulen prediction (10), and the Warren-Root prediction (13). For comparison, the pressure at the boundary (*i.e.*, in the fractures) is also shown.

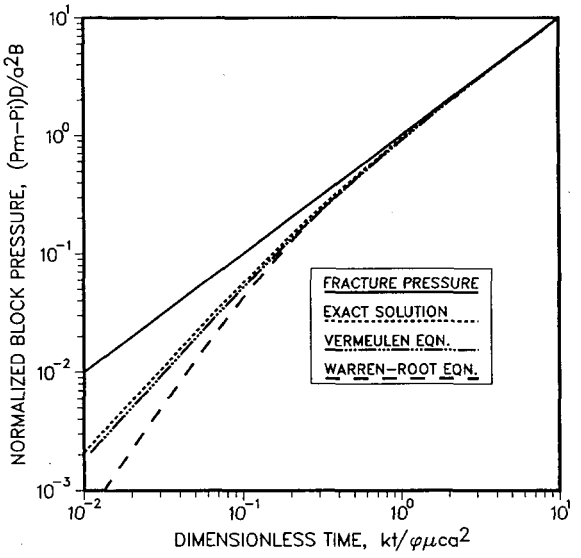

Fig. 2. Same as Fig. 1, for a ramp-function increase in the boundary pressure. The diffusion coefficient D is defined as $k_m/\phi_m \mu c_m$.

$$\bar{P}_m(t=0) = P_i \ , \tag{14}$$

$$P_f(t>0) = P_i + Bt \ , \tag{15}$$

where B is some constant with dimensions of pressure/time. The exact solution for $\bar{P}_m$ in this case is (Crank, 1975)

$$\frac{k_m(\bar{P}_m - P_i)}{\phi_m \mu c_m a_m^2 B} = \frac{k_m t}{\phi_m \mu c_m a_m^2} - \frac{1}{15}$$

$$+ \frac{6}{\pi^4} \sum_{n=1}^{\infty} \frac{1}{n^4} \exp(-n^2 \pi^2 k_m t / \phi_m \mu c_m a_m^2) \ . \tag{16}$$

The ramp-function response predicted by the Warren-Root equation can be found by solving eq. (8) subject to conditions (14) and (15), to yield

$$\frac{k_m(\bar{P}_m - P_i)}{\phi_m \mu c_m a_m^2 B} = \frac{k_m t}{\phi_m \mu c_m a_m^2} - \frac{1}{\pi^2}$$

$$+ \frac{1}{\pi^2} \exp(-\pi^2 k_m t / \phi_m \mu c_m a_m^2) \ . \tag{17}$$

The Vermeulen equation cannot be solved in closed-form for the ramp-function boundary condition, but can be integrated numerically to yield the results plotted in Fig. 2. As was the case for the step-function boundary condition, the Vermeulen equation is considerably more accurate than the Warren-Root equation in predicting the matrix block pressures. Furthermore, it can also be shown that the Vermeulen differential equation *always* predicts the correct exponent in the time-dependence for the pressure in the small-time limit, whereas the Warren-Root equation always predicts an *incorrect* exponent, for arbitrary variations in P_f. Hence, it seems that eq. (12) can be used to model the mean matrix block pressure, in cases where the pressure at the boundary of the block is specified as a function of time. With this in mind, we have modified an existing numerical simulator so as to use eq. (12) to compute fracture/matrix flow. This modified simulator can be used to solve large-scale reservoir problems in which, in general, the fracture pressures are not known in advance, and must be found, in a coupled manner along with the matrix block pressures, as part of the solution.

Coupled Dual-Porosity Simulator

Numerical reservoir simulators used for single-continuum systems typically solve eq. (1) by discretizing the reservoir into a number of computational cells, and use some numerical scheme such as finite-differences (Huyakorn and Pinder, 1983), finite elements (Pinder and Gray, 1977), or integral finite-differences (Edwards, 1972; Narasimhan and Witherspoon, 1976), to reduce the partial differential equation to a set of algebraic equations. These algebraic equations are solved at each time-step, t_n, in order to yield the pressures in each cell at the next time-step, $t_{n+1} = t_n + \Delta t$. Our approach is to assign to the computational cells those properties that correspond to the fractured continuum, averaged over a suitably-large REV. Fluid that enters or leaves the fracture system from the matrix blocks is then treated as a source/sink term. This approach requires minimal modifications to existing simulators, which typically allow for sources/sinks of various kinds. A certain number of matrix blocks will

be associated with each computational cell, with physical properties $\{k_m, \phi_m, a_m, \text{and } c_m\}$ that must be entered as input for each cell. Each computational cell will have associated with it a new variable, $\bar{P}_m$, which represent the average matrix pressure in those matrix blocks that are contained in that cell.

We have implemented this approach using the TOUGH simulator (Pruess, 1987), an integral-finite-difference code that has been shown to accurately simulate three-dimensional, single-phase, isothermal flow processes such as those discussed in this paper (as well as non-isothermal and two-phase processes). The fracture/matrix interaction equation has been incorporated as an option in a subroutine which is normally used for sources/sinks that represent injection or withdrawal of fluid from a well, etc. As a test of the use of our modified dual-porosity code, consider the problem of linear one-dimensional flow from a boundary that is maintained at some pressure P_o, into a semi-infinite formation that is initially at pressure P_i. We have also tested the modified version of TOUGH on problems involving radial flow to a well, and under constant-flux boundary conditions. However, the problem discussed here seems to most clearly illustrate the different time regimes, and the effects of fracture/matrix flow. The boundary and initial conditions for this problem are

$$P_f(x_f, t=0) = \bar{P}_m(x_f, t=0) = P_i \ , \tag{18}$$

$$P_f(x_f = 0, t > 0) = P_o \ , \tag{19}$$

$$\lim_{x_f \to \infty} P_f(x_f, t) = P_i \ . \tag{20}$$

The results of the simulation using the new semi-analytical dual-porosity version of TOUGH, incorporating eq. (12) as the fluid coupling term, are presented in Fig. 3. The figure shows the flowrate from the inlet feeding the fractures, as a function of time. In the simulation, the permeabilities were taken as $k_f = 10^{-15}\,\text{m}^2$ and $k_m = 10^{-18}\,\text{m}^2$, the porosities were taken as $\phi_f = 0.001$ and $\phi_m = 0.1$, and the matrix block radii were taken to be $a_m = 1\,\text{m}$. The temperature was set at 20 °C, and the boundary and initial pressures were taken to be $P_i = 10\,\text{MPa}$ and $P_o = 11\,\text{MPa}$. Under these conditions, the viscosity of water is roughly $0.001\,\text{Pa·s}$, and the compressibility is roughly $4.5 \times 10^{-10}\,/\,\text{Pa}$, although the TOUGH code actually uses more accurate values that are computed at each temperature and pressure from empirically-derived equations of state. For simplicity, we assume that the rock is rigid, so that the compressibility term reflects only the compressibility of the water.

At small times, flow takes place primarily in the fractures, and the flux varies as $t^{-1/2}$, as is typical in a one-dimensional diffusion problem. However, as time progresses, the leakage of fluid into the matrix blocks has the effect of temporarily halting the decline of the flux into the system, as is seen in Fig. 3. According to the Warren-Root method, this leads to an intermediate-time regime in which the overall flux is essentially constant. However, Nitao and Buscheck (1991) have shown that in this intermediate regime, the flux actually decreases as $t^{-1/4}$, which is in agreement with the results of our semi-analytical dual-porosity calculation. Also

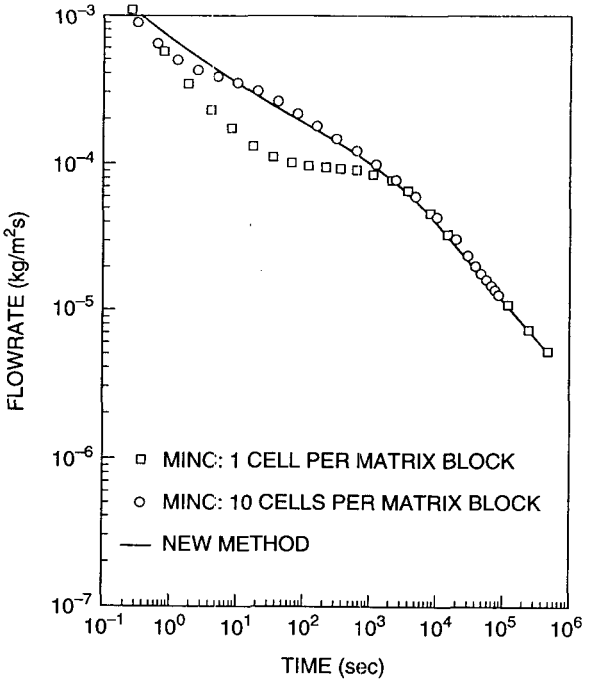

Fig. 3. Total instantaneous flux for one-dimensional flow into a dual-porosity formation with constant boundary pressure. The meaning of the parameters, and their values, are discussed in the text. MINC simulations were carried out using TOUGH code; "new method" simulation was carried out using modified TOUGH.

shown are the results calculated using a fully discretized MINC-type approach, in which each spherical matrix block is broken up into ten nested shells; the MINC simulation with one cell per matrix block corresponds to the Warren-Root model. Note that as the number of shells in the MINC simulation increases, the fluxes approach those calculated with our new semi-analytical approach. As expected, the Warren-Root method overestimates the time needed for flow into the matrix blocks to begin to appreciably influence the overall flowrate into the formation, and gives an inaccurate flowrate variation for intermediate times. At large times, the matrix blocks near the $x = 0$ inlet have been filled, and the overall response is similar to that of a single-porosity medium with an effective porosity of $\phi_m + \phi_f \simeq \phi_m$, and an effective permeability of $k_m + k_f \simeq k_f$. Hence at large times the flowrate again drops off as $t^{-1/2}$, but with a multiplicative constant that is larger by a factor of about $\sqrt{(\phi_m + \phi_f)/(k_m + k_f)}/\sqrt{\phi_f / k_f} \simeq \sqrt{\phi_m / \phi_f}$.

Conclusions

We have developed a new dual-porosity model for single-phase flow in porous/fractured media. Instead of using a Warren-Root-type equation for fracture/matrix flow, in which the flux is proportional to the difference between the fracture pressure and the mean matrix pressure, we use a nonlinear differential equation. This equation is more accurate than the Warren-Root equation, for a wide variety of matrix block boundary conditions. This differential equation has been incorporated

into the numerical simulator TOUGH, to serve as a source/sink term for the discretized fracture continuum. For the test problems we have simulated, the modified TOUGH code is more accurate than the Warren-Root model, and is more computationally efficient than models which require discretization of the matrix blocks.

Acknowledgments

This work was supported by the Assistant Secretary for Conservation and Renewable Energy, Geothermal Division, U.S. Department of Energy, under Contract No. DE-AC03-76SF00098, with the Lawrence Berkeley Laboratory. The authors thank Marcelo Lippmann and Lea Cox of LBL for reviewing this paper.

References

Chen, Z.-X. (1989), "Transient flow of slightly compressible fluids through double-porosity, double-permeability systems - A state-of-the-art review," *Transp. Porous Media, 4,* 147-184.

Crank, J. (1975), *The Mathematics of Diffusion,* Clarendon Press, Oxford.

deSwaan, A. (1990), "Influence of shape and skin of matrix-rock blocks on pressure transients in fractured reservoirs," *Soc. Petrol. Eng. Format. Eval., 5,* 344-352.

Duguid, J. O., and Lee, P. C. Y. (1977), "Flow in fractured porous media," *Water Resour. Res., 13,* 558-566.

Edwards, A. L. (1972), TRUMP: A computer program for transient and steady state temperature distribution in multidimensional systems, *Rep. UCRL-14754, Rev. 3,* Lawrence Livermore National Laboratory, Livermore, Calif.

Huyakorn, P. S., and Pinder, G. F. (1983), *Computational Methods in Subsurface Flow,* Academic Press, San Diego, Calif.

Matthews, C. S., and Russell, D. G. (1967), *Pressure Buildup and Flow Tests in Wells,* Society of Petroleum Engineers, Dallas.

Narasimhan, T. N., and Witherspoon, P. A. (1976), "An integrated finite-difference method for analyzing fluid flow in porous media," *Water Resour. Res., 12,* 57-64.

Nitao, J. J., and Buscheck, T. A. (1991), "Infiltration of a liquid front in an unsaturated, fractured porous medium," *Water Resour. Res., 27,* 2099-2112.

Pinder, G. F., and Gray, W. G. (1977), *Finite Element Simulation in Surface and Subsurface Hydrology,* Academic Press, San Diego, Calif.

Pruess, K. (1987), TOUGH User's Guide, *Rep. LBL-20700,* Lawrence Berkeley Laboratory, Berkeley, Calif.

Pruess, K., and Narasimhan, T. N. (1985), "A practical method for modeling heat and fluid flow in fractured porous media," *Soc. Petrol. Eng. J., 25,* 14-26.

Vermeulen, T. (1953), "Theory of irreversible and constant-pattern solid diffusion," *Ind. Eng. Chem., 45,* 1664-1670.

Warren, J. E., and Root, P. J. (1963), "The behavior of naturally fractured reservoirs," *Soc. Petrol. Eng. J., 3,* 245-255.

PROCEEDINGS, Seventeenth Workshop on Geothermal Reservoir Engineering
Stanford University, Stanford, California, January 29-31, 1992
SGP-TR-141

EFFECTS OF CAPILLARITY AND VAPOR ADSORPTION IN THE DEPLETION OF VAPOR-DOMINATED GEOTHERMAL RESERVOIRS

Karsten Pruess* and Michael O'Sullivan†

*Earth Sciences Division
Lawrence Berkeley Laboratory
Berkeley, CA 94720

†Department of Engineering Science
University of Auckland
Auckland, New Zealand

INTRODUCTION

Vapor-dominated geothermal reservoirs in natural (undisturbed) conditions contain water as both vapor and liquid phases. The most compelling evidence for the presence of distributed liquid water is the observation that vapor pressures in these systems are close to saturated vapor pressure for measured reservoir temperatures (White et al., 1971; Truesdell and White, 1973). Analysis of natural heat flow conditions provides additional, indirect evidence for the ubiquitous presence of liquid. From an analysis of the heat pipe process (vapor-liquid counterflow) Pruess (1985) inferred that effective vertical permeability to liquid phase in vapor-dominated reservoirs is approximately 10^{-17} m^2, for a heat flux of 1 W/m^2. This value appears to be at the high end of matrix permeabilities of unfractured rocks at The Geysers, suggesting that at least the smaller fractures contribute to liquid permeability. For liquid to be mobile in fractures, the rock matrix must be essentially completely liquid-saturated, because otherwise liquid phase would be sucked from the fractures into the matrix by capillary force. Large water saturation in the matrix, well above the irreducible saturation of perhaps 30%, has been shown to be compatible with production of superheated steam (Pruess and Narasimhan, 1982).

In response to fluid production the liquid phase will boil, with heat of vaporization supplied by the reservoir rocks. As reservoir temperatures decline reservoir pressures will decline also. For depletion of "bulk" liquid, the pressure would decline along the saturated vapor pressure curve, while for liquid held by capillary and adsorptive forces inside porous media, an additional decline will arise from "vapor pressure lowering."

Capillary pressure and vapor adsorption effects, and associated vapor pressure lowering phenomena, have received considerable attention in the geothermal literature, and also in studies related to geologic disposal of heat generating nuclear wastes, and in the drying of porous materials. Geothermally oriented studies were presented by Chicoine et al. (1977), Hsieh and Ramey (1978, 1981), Herkelrath et al. (1983), and Nghiem and Ramey (1991). Nuclear waste-related work includes papers by Herkelrath and O'Neal (1985), Pollock (1986), Eaton and Bixler (1987), Pruess et al. (1990), Nitao (1990), and Doughty and Pruess (1991). Applications to industrial drying of porous materials have been discussed by Harmathy (1969) and Whitaker (1977).

This paper is primarily concerned with evaluating the impact of vapor pressure lowering (VPL) effects on the depletion behavior of vapor-dominated reservoirs. We have examined experimental data on vapor adsorption and capillary pressures in an effort to identify constitutive relationships that would be applicable to the tight matrix rocks of vapor-dominated systems. Numerical simulations have been performed to evaluate the impact of these effects on the depletion of vapor-dominated reservoirs.

CAPILLARY SUCTION, VAPOR ADSORPTION, AND VAPOR PRESSURE LOWERING

Thermodynamic analysis shows that for pure single-component fluids such as water, coexistence of liquid and vapor phases at any given temperature T is possible only for a certain unique pressure, which is termed the saturated vapor pressure, or saturation pressure, $P_{sat}(T)$. The thermodynamic properties of liquid and vapor, and the conditions under which these phases can coexist, are altered inside porous media by interfacial forces between rock minerals and fluids (Edlefsen and Anderson, 1943; Calhoun et al., 1949; Philip, 1978; Udell, 1982). Liquid water wets rocks preferentially compared to vapor and is held by adsorptive forces as a thin layer of a few molecular thicknesses on the rock surfaces (He, Cushman, and Diestler, 1987). In addition, liquid water is held by capillary forces in the smaller pores. Both liquid adsorption and capillarity cause liquid phase pressure P_l to be lower than vapor phase pressure P_v; the difference

$$P_l - P_v = P_{suc} < 0 \qquad (1)$$

is termed the suction pressure, P_{suc}. In most of the literature, the difference in phase pressures is referred to as "capillary pressure" P_{cap} which is given by

$$P_{cap} = -\frac{2\sigma\cos(\alpha)}{r} \quad . \qquad (2)$$

Here σ is the surface tension of the wetting phase, α is the contact angle, and r is the mean radius of curvature of the capillary meniscus. We prefer the more general term suction pressure because this is not limited to a specific mechanism, such as capillarity. Experimentally one measures a suction pressure that results from the combined effects of capillarity and adsorption. The suction exerted on the liquid phase diminishes its tendency for vaporization. Vapor pressure above a liquid held by capillary or adsorptive forces is therefore reduced in comparison to vapor pressure above the flat surface of a bulk liquid. The reduction is expressed in terms of a vapor pressure lowering factor, or relative vapor pressure, β, defined by

$$\beta = P_v/P_{sat}(T) \quad . \qquad (3)$$

The relationship between β and P_{suc} is given by the Kelvin equation

$$\beta = \exp\left[\frac{M_{H_2O}\, P_{suc}}{\rho_l R(T+273.15)}\right] \quad , \qquad (4)$$

where M_{H_2O} is the molecular weight of water, ρ_l is liquid phase density, R is the universal gas constant, and temperature T is measured in °C. β depends chiefly on suction pressure, which in turn is primarily a function of liquid saturation, S_l. At typical vapor-dominated conditions of T = 240°C, the suction pressures required for 1%, 10%, and 20% vapor pressure lowering (i.e., β equal to 0.99, 0.90, and 0.80) are, respectively, −19.4 bars, −203 bars, and −430 bars. Thus, significant reduction in vapor pressure will occur only for very large suction pressures.

The Kelvin equation establishes a connection between adsorption of vapor on porous materials, and the suction pressure experienced by the adsorbed liquid phase: When vapor at a pressure $P_v < P_{sat}$ is brought in contact with a porous medium, adsorption and capillary condensation will take place until a liquid saturation S_l is established such that the corresponding suction pressure P_{suc} satisfies Equations (3) and (4). The results of vapor adsorption experiments are usually given in terms of mass of adsorbed vapor X_v per mass of porous material, as function of relative vapor pressure β. (Some authors measure adsorbed mass in molar rather than mass units.) Assuming that the density of the adsorbed phase is close to that of liquid water, the corresponding saturation of adsorbed liquid phase can be calculated as

$$S_l = \frac{X_v\,(1-\phi)\,\rho_R}{\phi\rho_l} \quad . \qquad (5)$$

Here ϕ is the porosity of the medium, and ρ_R is rock grain density. Equations (4) and (5) can be used to convert adsorption data of X_v versus β to an equivalent suction pressure relationship, S_l versus P_{suc}.

EXPERIMENTAL DATA

Several different experimental techniques are available for measuring suction pressure and vapor adsorption characteristics of porous materials (summarized by Evans, 1983). Suction pressures can be obtained through direct measurement or control of the pressure difference between wetting and non-wetting phases, or through mercury intrusion experiments with subsequent scaling for surface tension and contact angle. Vapor pressure lowering effects can be measured through thermocouple psychrometry, or through vapor pressure measurements for known amounts of adsorbed vapor. Where different techniques could be employed to measure suction pressures and/or vapor pressure lowering in overlapping regimes, consistent results have been obtained (Melrose, 1988). Illustrative data from the literature are given in Figures 1 and 2 in the form of mass fraction of water adsorbed (or held by capillarity) vs. relative vapor pressure $\beta = P_v/P_{sat}$; the data sources are summarized in Table 1. Some of the same data are replotted in Figure 3 in the form of liquid saturation vs. suction pressure (see Equations 4 and 5).

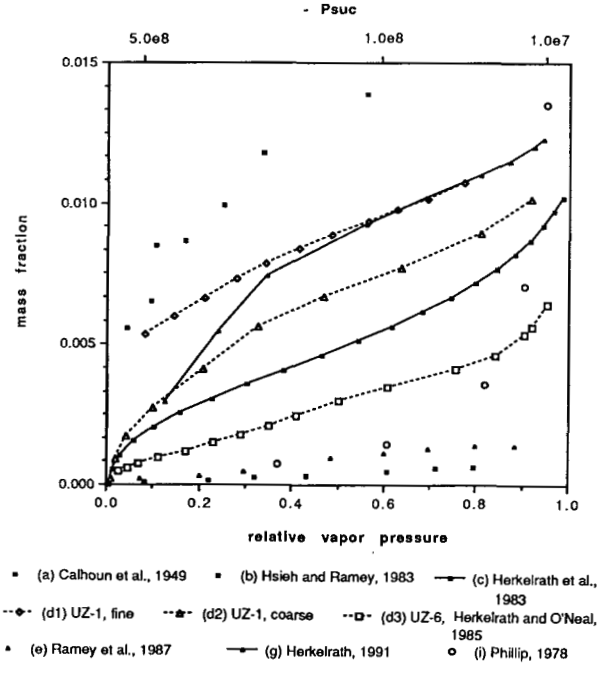

Figure 1. Data on vapor adsorption from different literature sources.

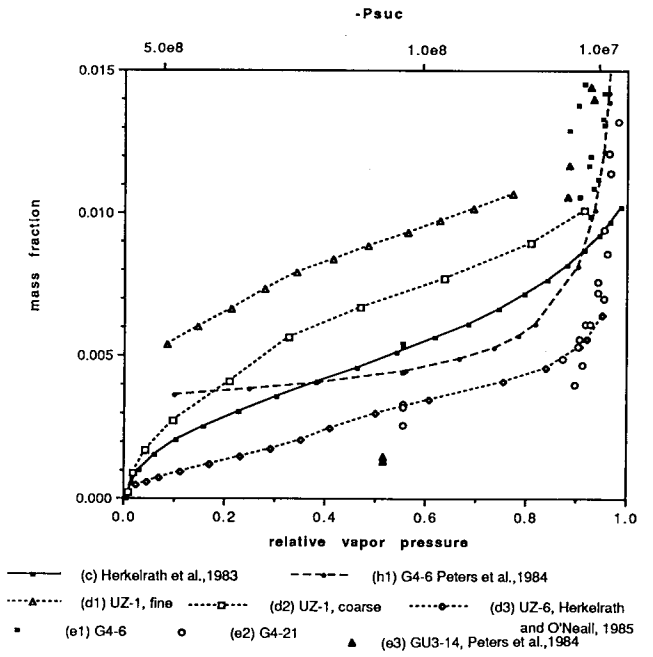

Figure 2. Another collection of literature data on vapor adsorption.

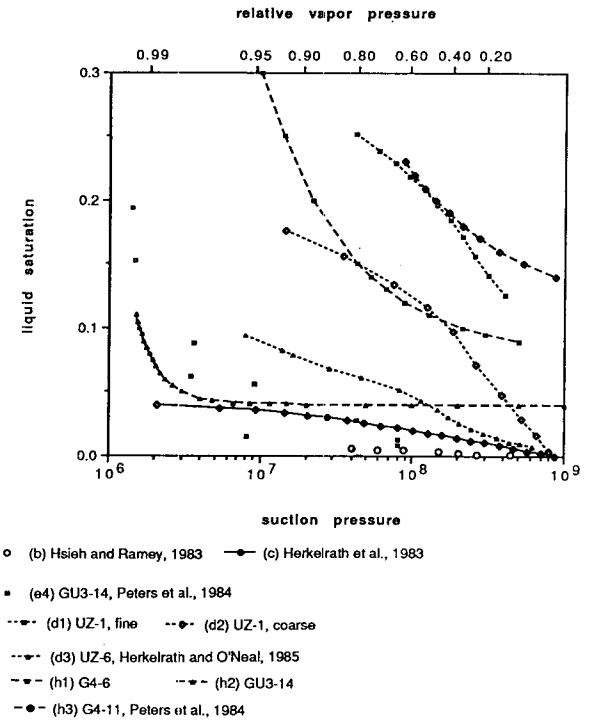

Figure 3. Liquid suction pressure characteristics for different geologic materials.

Table 1. Literature data on vapor adsorption and liquid suction

Reference	Experimental Sample	Measurement
Calhoun et al., 1949	manufactured consolidated quartz	(a,c) 36°C
Hsieh and Ramey, 1983	Berea sandstone	(c) 146°C
Herkelrath et al., 1983	unconsolidated natural sand	(c) 100, 125, 146°C
Peters et al., 1984	welded and nonwelded tuffs from Yucca Mountain	(b,d) ambient T
Herkelrath and O'Neal, 1985	Topopah Spring welded tuff	(c) 100°C
Ramey et al., 1987	cores from The Geysers	(c) 180, 200°C
Herkelrath, 1991	graywacke from The Geysers	(c) 100°C

(a) direct measurement of water suction pressure
(b) mercury intrusion
(c) vapor adsorption measurement
(d) vapor pressure lowering by thermocouple psychrometry

From Figures 1-3 it is apparent that geologic media display a great diversity of vapor pressure lowering and suction pressure relationships, which reflects the tremendous diversity in the distribution of pore sizes, and in the composition and activity of mineral surfaces. Suction pressures are generally stronger for tight media with small pores.

A number of theoretical formulae have been suggested for calculating the quantity of water adsorbed on solid surfaces. The simplest, credited to Langmuir (1916), is

$$X_v = \frac{\beta}{a+b\beta}. \qquad (6)$$

Here a and b are fitting parameters. Nghiem and Ramey (1991) used (6) to obtain a good match to the Topopah Spring welded tuff data of Herkelrath and O'Neal (1985), and to unpublished vapor adsorption measurements by Herkelrath on graywacke samples from The Geysers (also made available for the present study).

The BET formula (Brunauer, Emmett and Teller, 1938) has also been used to match adsorption data. This formula can be written in the form

$$X_v = \frac{c\beta x_m}{(1-\beta)[1+(c-1)\beta]}, \qquad (7)$$

with fitting parameters c and x_m. Hsieh and Ramey (1978) used Equation (7) to obtain an excellent fit to the data of Calhoun et al. (1949). Herkelrath and O'Neal (1985) obtained a good fit to Topopah Spring welded tuff data using a BET curve in the range $0<\beta<0.35$.

Herkelrath et al. (1983) obtained a good fit to data for unconsolidated material, containing sand, silt and clay, using the empirical formula

$$\beta = A(10^{[-10^{[B-S_l]/C}]}) \qquad (8)$$

Here A, B, and C are fitting parameters.

In an extensive study Peters et al. (1984) measured suction pressure vs. mass fraction of water adsorbed for a number of samples of tuffaceous materials from Yucca Mountain, Nevada. They converted each measurement of mass fraction of water adsorbed into an equivalent liquid saturation and were then able to obtain reasonable fits to their data with van Genuchten's expression (1980), which we write in the form

$$P_{suc} = -P_o\left[S_{ef}^{-1/\lambda}-1\right]^{1-\lambda}, \qquad (9)$$

where

$$S_{ef} = \frac{S_l - S_{lr}}{1 - S_{lr}}. \qquad (10)$$

Here P_o and λ are fitting parameters and S_{lr} is the residual liquid saturation. While providing a good fit to the data of Peters et al. (1984) over most of the suction pressure range, the van Genuchten expression Equation (9) tends to overpredict liquid saturation at large suction pressures. The Langmuir and BET formulae (Equations (6) and (7)) also cannot fit the data over the complete range. They do not have the correct shape to give the rapid decline in adsorbed mass as the relative vapor pressure decreases below 1.0. It appears that the van Genuchten expression is most applicable to the capillary regime of weaker suction pressures, while the Langmuir or BET equations describe the adsorptive regime of strong suction.

There is considerable variation in the shape of the curves and the values of the fitting parameters for samples from similar materials. This seems to be related mainly to the variation of porosity and therefore perhaps to the balance between capillary and surface adsorption effects. The data given by Peters et al. (1984) cover a much wider range than most of the data shown in Figures 1 and 2. In particular some large porosity samples gave much larger values for adsorbed mass. However, few of the samples gave values of adsorbed mass lower than those depicted by the points labeled e1, e2 and e3 in Figure 2. The data given by Hsieh and Ramey (1983) and Ramey et al. (1987) stand out as very low, with adsorbed mass well below all the other experiments.

Figure 3 shows some of the same data as in Figures 1 and 2 converted, using Equations (4) and (5), to give S_l as a function of P_{suc}. Also best fit van Genuchten curves for some of the data from Peters et al. (1984) are plotted. These plots clearly show the problem with the van Genuchten curves. They approach a finite liquid saturation as suction pressure tends to infinity. To fit the data well a two stage function would be required which drops rapidly near $-P_{suc} = 10^6$ Pa and then declines more slowly towards zero at large $-P_{suc}$. Possibly the rapid initial drop is associated with capillary effects and the subsequent drop is associated with surface adsorption. In the numerical simulations, below, we have avoided the infinity in P_{suc} by employing a cutoff of $-P_{suc} \le 5000$ bars.

Although the range of different suction behavior is large, it is seen that significant reduction of vapor pressure, 10% say, will occur only for rather small liquid saturations of the order of 20% or less. Vapor pressure lowering effects will be unimportant for reservoir processes at higher liquid saturations.

NUMERICAL SIMULATIONS

From a phenomenological viewpoint, capillarity and adsorption can be viewed as mechanisms that tend to retain fluid in the reservoir, making it less accessible to extraction. In practical circumstances, other fluid retention mechanisms will be present as well. For example,

fluid reserves may be stored in matrix rocks of low permeability, from which they can only slowly discharge to the fracture system to become available for production. Fluid retention will cause a more rapid pressure decline when producing at prescribed rates, and a more rapid rate decline when producing at prescribed pressures.

We have performed numerical simulations to examine and evaluate the nature and strength of fluid retention from capillarity and adsorption. The calculations were performed with LBL's general-purpose simulator TOUGH2, which implements the general MULKOM architecture for coupled multiphase fluid and heat flows (Pruess, 1983, 1991). TOUGH2 models vapor pressure lowering effects by means of the Kelvin equation (4). Our first simulation examines constant-rate production from a zero-dimensional "lumped-parameter" reservoir model (single grid block). In this case there is no flow in the reservoir; all of the fluid reserves are equally accessible to production, and differences in depletion behavior for cases with and without vapor pressure lowering are solely due to differences in the thermodynamic properties (vapor pressure, enthalpy of vaporization) between "free" water (no VPL) and water held by capillary or adsorptive forces (VPL). Subsequently we simulate distributed-parameter models to examine VPL effects on flow processes.

For the illustrative calculations in this paper we have used the suction pressure relationship obtained by Peters et al. (1984) for their sample G4-6, employing a cutoff of $-P_{suc} \leq 5000$ bars. This is a tight welded tuff with a permeability of 1.9×10^{-18} m^2(1.9 microdarcies), which may be representative of the tight reservoir rocks of The Geysers. Apart from providing a reasonable fit to suction pressure characteristics over a wide range, the van Genuchten curves have the advantage that they permit a consistent evaluation of liquid relative permeability from Mualem's model (1976) in closed form:

$$k_{rl} = \sqrt{S_{ef}}\left[1 - (1 - S_{ef}^{1/\lambda})^{\lambda}\right]^2 \qquad (11)$$

S_{ef} is defined in Equation (10). Gas (vapor) phase relative permeability was assumed as $k_{rg} = 1 - k_{rl}$. Other parameters used in the simulations are summarized in Table 2. Additional parameter specifications are given in the presentation of the different cases, below. Initial reservoir temperature in all cases was near 240°C.

Thermodynamic Effects

We consider a zero-dimensional reservoir of 1 km^3 volume, with an initial liquid saturation of 80% and a pressure of 33.44 bars, corresponding to a saturation temperature of 239.93°C. No permeability specifications are needed in this problem because the reservoir is modeled as a single grid block. Production occurs at a constant rate of 34.37 kg/s, which at initial fluid reserves of 32.716×10^9 kg (without VPL effects; when VPL is included, initial reserves are 32.691×10^9 kg) can be sustained for 30.16 years. The system is taken through 20 depletion steps of 1.5 years each, and simulated pressures, temperatures, and liquid saturations with and without VPL are given in Table 3.

The reservoir with VPL effects starts off with a temperature that is slightly higher (0.44°C) than the reservoir without VPL, in order to attain the same vapor pressure as in the no VPL system. Temperatures and liquid saturations for depletion with and without VPL are seen to remain very close at all times. Differences in reservoir pressures are small at early times, reaching 0.7 bars at 50% depletion (15 years), 2.7 bars at 75% depletion (22.5 years), and becoming very large as ultimate dry-up with extremely strong suction pressures and VPL effects is approached. Thus, VPL effects are insignificant for most of the productive life of the system.

Table 2. Formation parameters for simulation problems

rock grain density	2600	kg/m^3
rock specific heat	920	J/kg.°C
formation thermal conductivity	2.51	W/m°C
matrix porosity	5%	
matrix permeability (*)	10^{-18},	5×10^{-18} m^2
formation permeability (&)	5×10^{-14} m^2	
formation compressibility	0	bar^{-1}
suction pressure data: van Genuchten fit of Peters et al. (1984) for welded tuff sample G4-6, with parameters		
λ = 0.4438		
S_{lr} = 0.0801		
P_o = 1.727×10^6 Pa		

(*) Block depletion problem. (&) Radial flow to a well.

Table 3. Depletion of zero-dimensional reservoir

Time Step	Time (yrs)	Pressure (bars) VPL	Pressure (bars) No VPL	Temperature (°C) VPL	Temperature (°C) No VPL	Liquid Saturation (%) VPL	Liquid Saturation (%) No VPL
	0	33.44	33.44	240.37	239.93	80	80
1	1.5	32.69	32.73	239.15	238.72	75.76	75.77
2	3	31.95	32.04	237.94	237.15	71.55	71.56
3	4.5	31.21	31.34	236.71	236.28	67.36	67.37
4	6	30.48	30.66	235.48	235.05	63.19	63.20
5	7.5	29.74	29.98	234.24	233.81	59.04	59.05
6	9	29.01	29.32	233.00	232.57	54.91	54.92
7	10.5	28.28	28.66	231.74	231.31	50.80	50.81
8	12	27.54	28.00	230.48	230.05	46.72	46.73
9	13.5	26.80	27.36	229.21	228.78	42.65	42.66
10	15	26.03	26.72	227.94	227.51	38.61	38.61
11	16.5	25.24	26.09	226.66	226.23	34.59	34.58
12	18	24.40	25.47	225.37	224.94	30.59	30.58
13	19.5	23.47	24.86	224.07	223.64	26.62	26.59
14	21	22.36	24.25	222.77	222.34	22.68	22.62
15	22.5	20.90	23.66	221.46	221.03	18.77	18.66
16	24	18.49	23.07	220.15	219.71	14.95	14.73
17	25.5	12.71	22.49	218.87	218.38	11.33	10.81
18	27	1.62	21.92	217.64	217.05	8.00	6.92
19	28.5	1.57	21.35	216.23	215.71	4.13	3.04
20	30.0	1.53	7.66	214.82	214.56	0.28	0

Depletion of Tight Matrix Blocks

Most of the fluid reserves in vapor-dominated systems are stored in tight matrix blocks with permeability of order 1 microdarcy (10^{-18} m^2). The fracture system is believed to contribute little to fluid storage, but provides large-scale permeability. We have simulated fluid production from tight matrix blocks under conditions considered representative for the depletion of vapor-dominated systems such as The Geysers and Larderello.

The model system (see Figure 4) consists of a single block of rock matrix in the shape of a cube with side length D = 50 m, which is to be viewed as a subdomain of a large reservoir volume. Matrix permeability is of order 10^{-18} m^2, and matrix porosity is 5%. The block is surrounded by fractures which are assigned an arbitrary (small) fractional volume of 10^{-4}. Initial conditions are a pressure of 33.44 bar throughout, and liquid saturation of 80% in the matrix block, 1% in the fractures, respectively. Liquid relative permeability is taken as the van Genuchten form (Equation (11)) with parameters identical to those obtained by Peters et al. (1984) for the suction pressure relationship of sample G4-6. Gas relative permeability is assumed as $k_{rg} = 1 - k_{rl}$.

Depletion is initiated by placing a "well" on deliverability in the fractures. Well specifications are a bottomhole pressure of 10 bars, and a productivity index of 1.788×10^{-13} m^3. For the depletion simulation the matrix block is discretized according to the MINC method (Pruess and Narasimhan, 1982, 1985) with 9 nested cubes, using the following volume fractions (from outside to inside): 2%, 4%, 6%, 8%, 10%, 13%, 16%, 20%, and 21%. For matrix permeabilities of 1 and 5×10^{-18} m^2, three different cases were simulated: (Case 1) including both suction pressure and VPL effects, (Case 2) including suction pressures but no VPL effects, and (Case 3) "conventional" approach, neglecting capillary- and adsorption-induced suction pressures (and consequently neglecting VPL effects as well).

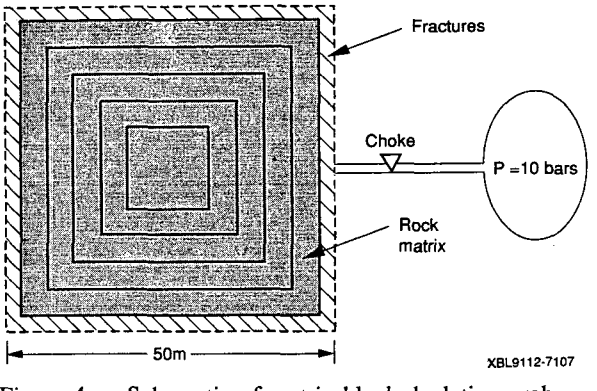

Figure 4. Schematic of matrix block depletion problem, with MINC discretization.

Depletion proceeds at high rates of mass discharge initially, and then slows down as discharge rates from the block decline in response to declining pressures and fluid mobilities (Figure 5). Relative to Case 3 (no suction pressures), introduction of suction pressures (Case 2) introduces an additional force for driving liquid towards the matrix block surface, where suction pressures are strongest because of diminishing liquid saturation from vaporization. Therefore, Case 2 yields generally higher flow rates and a more rapid depletion than Case 3 (Figures 5 - 7).

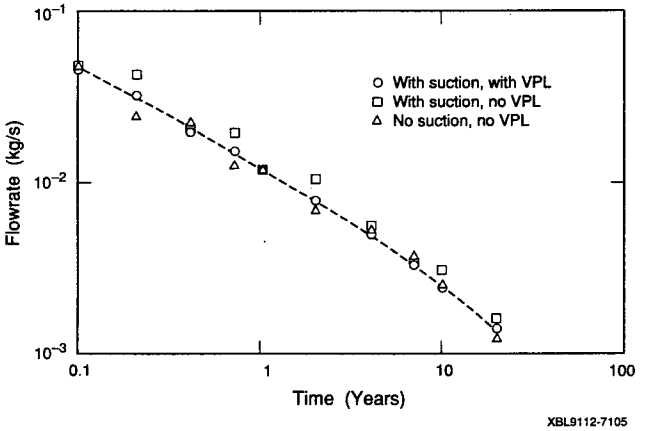

Figure 5. Simulated time dependence of flow rates in block depletion problem for matrix permeability of 10^{-18} m^2.

The effect of vapor pressure lowering (Case 1) is to accelerate pressure decline as fluid discharge proceeds from the block, diminishing the driving force for vapor outflow from the block, and consequently slowing depletion of fluid reserves. For the parameters used here, this effect tends to approximately cancel the increase in depletion rate from suction pressure effects, so that the depletion behavior in Case 1 is very similar to that in Case 3. The effects from suction pressures and vapor pressure lowering are rather modest. Total produced mass in Case 2 is approximately 20% larger at all times than cumulative production in Case 3 (Figure 6). For a matrix permeability of 10^{-18} m^2, cumulative production in Case 1 exceeds that of Case 3 by typically 5% or less. Produced enthalpies are virtually identical in all cases, being 2.88 MJ/kg (± 0.5%) for times greater than 0.1 years. For the larger matrix permeability of 5×10^{-18} m^2 fluid recovery is more rapid (Figure 7), but the differences between the Cases 1, 2, and 3 are again modest and very similar to those for the tighter matrix block.

From Figure 5 it is seen that in Case 1 (with VPL) there is a very smooth dependence of flow rate on time, while in the no VPL and no P_{suc} cases periodic excursions are superimposed on the overall trend of declining flow rates. The excursions reflect discretization effects: flow rates are controlled by the pressure of the outermost grid block that is still in two-phase (boiling) conditions, and pressures there are constrained to be equal to

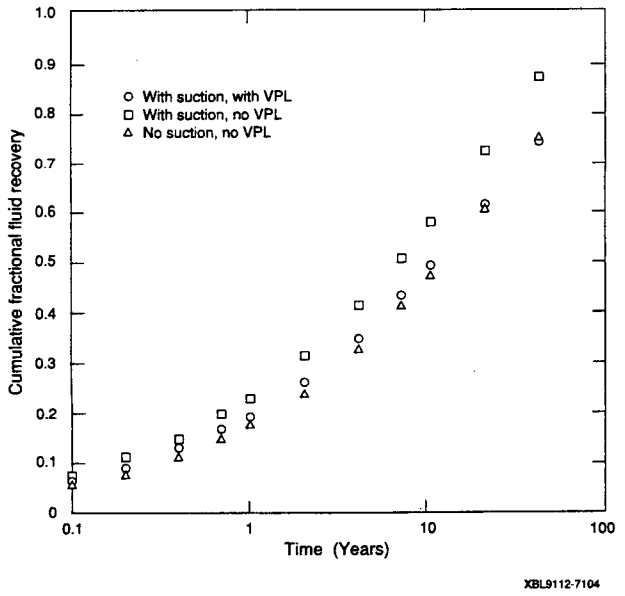

Figure 6. Cumulative fluid recovery in block depletion problem for matrix permeability of 10^{-18} m^2.

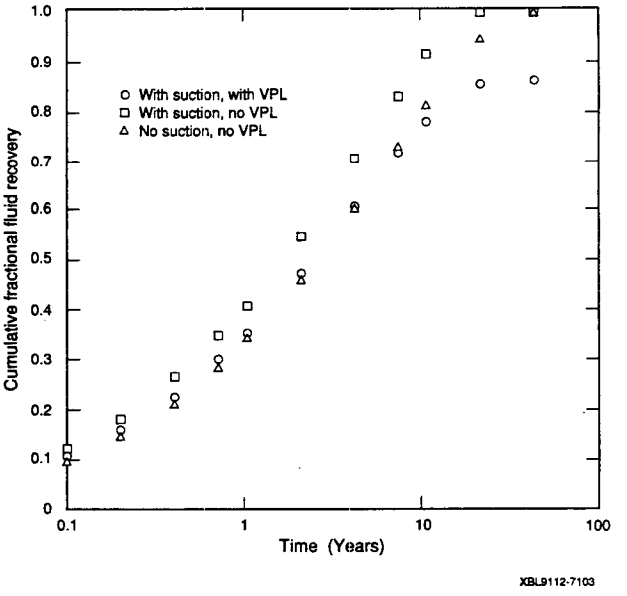

Figure 7. Cumulative fluid recovery in block depletion problem for matrix permeability of 5×10^{-18} m^2.

saturation pressure at prevailing temperature. Every time a grid block dries out pressure control "jumps" to the next block towards the interior of the matrix, with a discrete jump in path length for vapor flow and associated drop in flow rate. Inclusion of VPL effects removes the strict correspondence between temperature and pressure in two-phase conditions. Vapor pressure decreases gradually as liquid saturation declines. Thus, from a numerical simulation viewpoint, vapor pressure lowering has the beneficial effect of broadening what otherwise would be a sharp phase front between single-phase vapor and two-phase conditions.

Radial Flow to a Well

To evaluate the possible impact of VPL effects on well testing in superheated vapor zones we model flow to a production well in one-dimensional radial geometry. We consider a cylindrical reservoir with a large radius of 10 km, a thickness of H = 1000 m, and permeability of 50×10^{-15} m^2, for a total permeability-thickness product of 50×10^{-12} m^3 (50 darcy-meters). Effective well radius is assumed as r_w = 10 m which, for a well of 0.2 m diameter (8 inches), corresponds to a skin factor of s = −4.605, typical for fractured wells. Initial reservoir conditions are a temperature of 240°C and a pressure of 10 bars, corresponding to highly superheated steam. According to the Kelvin equation, this vapor pressure corresponds to a liquid suction pressure of −2328.2 bars, for which the G4-6 characteristic curve of Peters et al. (1984) gives a liquid saturation of 9.848%. A comparison case without VPL effects was also simulated; this has zero liquid saturation (single-phase vapor) because $P_v < P_{sat}$. The reservoir is discretized into 100 grid blocks with radial increments logarithmically increasing from Δr_1 = 1 m. Production occurs at a constant rate of 5 kg/s. Relative permeabilities are assumed equal to 1 for gas, 0 for liquid, regardless of saturation.

Figure 8 shows results for calculations with and without VPL effects, plotted as pressure-squared versus the logarithm of the similarity variable t/r^2 (O'Sullivan, 1981). In each case results for two different times fall on the same curve, confirming the similarity variable t/r^2. With the exception of small values of t/r^2, the data fall very accurately on semilog straight lines. Both straight lines have the same slope of 14.7 bar^2 per log-cycle in t/r^2. Using the asymptotic solution for radial gas flow (Matthews and Russel, 1967)

$$P_i^2 - P(r,t)^2 = \frac{q_m \mu}{2\pi kH} \frac{zR(T+273.15)}{M_{H_2O}} \times \left[\ln \frac{t}{r^2} + \ln \frac{k}{\phi \mu c} + 0.80907 \right] \qquad (12)$$

this slope translates into a permeability-thickness product of $kH = 49.93 \times 10^{-12}$ m^3, in excellent agreement with the value of 50×10^{-12} m^3 used in the simulation. In Equation (12) P_i is initial pressure, q_m is mass flow rate, μ is viscosity, z the real gas compressibility factor, and c is total (fluid plus formation) compressibility. From the t/r^2 values at which the extrapolated straight lines reach the initial pressure $P_i^2 = 100$ bar^2 we obtain from Equation (12) values for fluid compressibility of $c = 3.95 \times 10^{-6}$ Pa^{-1} with VPL and $c = 1.30 \times 10^{-6}$ Pa^{-1} without VPL. Thus it is seen that VPL effects increase effective fluid compressibility relative to single-phase vapor. However, fluid compressibility with VPL is smaller than typical two-phase compressibility without VPL (Grant and Sorey, 1979).

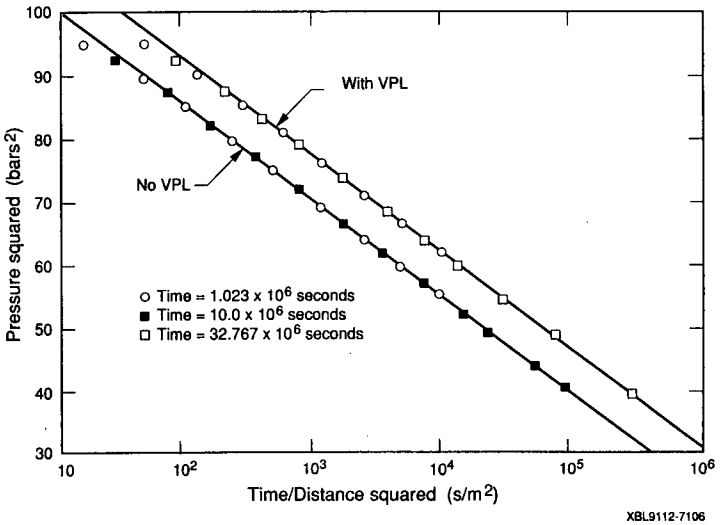

Figure 8. Semilog plot of pressure-squared in radial flow problem.

DISCUSSION AND CONCLUSIONS

Capillarity, vapor adsorption on rock surfaces, and vapor pressure lowering are interrelated and strongly coupled effects. Different geologic media show a tremendous variety of capillary and adsorptive behavior. Although existing data are insufficient for a detailed quantitative description of vapor pressure lowering effects in vapor-dominated reservoirs such as The Geysers and Larderello, a survey of literature data indicates that VPL effects will become significant (reducing vapor pressure by 10% or more) only at low liquid saturations of 20% or less. Initial liquid saturations in vapor-dominated systems are believed to be large, in excess of 80% and most likely close to 100% (Pruess and Narasimhan, 1982; Pruess, 1985), so that VPL effects on production rates and pressures will be negligible for most of the productive life of vapor-dominated systems, playing a role only in the final stages of reservoir dry-out.

Depending on the relative permeability behavior of vapor-dominated systems, which has not yet been well characterized, it is possible that the suction effects from capillarity and vapor adsorption may significantly affect liquid flow in the matrix blocks. While of minor importance for pressure and flow-rate behavior of vapor-dominated systems, the presence of adsorbed and capillary water at pressures below saturated values may play a crucial role in rock-fluid reactions, and in the release and transport of non-condensible gases.

ACKNOWLEDGEMENT

The authors would like to thank Dr. W. Herkelrath of the U.S.G.S., Menlo Park, for kindly providing us his unpublished measurements of vapor adsorption on graywacke samples from The Geysers. Drs. M. Lippmann and G. Moridis reviewed the manuscript and suggested improvements. This work was supported by the Geothermal Technology Division, U. S. Department of Energy, under Contract No. DE-AC03-76SF00098.

REFERENCES

Brunauer, S., Emmett, P. H., and Teller, E. "Adsorption of Gases in Multimolecular Layers," *J. Amer. Chem. Soc., 60,* 1938, 309-319.

Calhoun, J. C., Jr., Lewis, M., Jr. and Newman, R. C. "Experiments on the Capillary Properties of Porous Solids," *Petroleum Trans. AIME,* 1949, 189-196.

Chicoine, S. D., Strobel, C. J., and Ramey, H. J., Jr. "Vapor Pressure Lowering in Two-Phase Geothermal Systems," paper SPE-6767, presented at Society of Petroleum Engineers 52nd Annual Fall Technical Conference and Exhibition, Denver, CO, October 1977.

Doughty, C. and Pruess, K. "A Similarity Solution for Two-Phase Water, Air, and Heat Flow near a Linear Heat Source in a Porous Medium," to appear in *J. of Geophys. Res., 1991.*

Eaton, R. R. and Bixler, N. E. "Analysis of a Multiphase Porous Flow Imbibition Experiment in Fractured Volcanic Tuff," in: D. D. Evans and T. J. Nicholson (eds.), *Flow and Transport through Unsaturated Fractured Rock,* Geophysical Monograph 42, American Geophysical Union, Washington, D. C., 1987.

Edlefsen, N. E. and Anderson, A. B. C. "Thermodynamics of Soil Moisture," *Hilgardia, 15,* (2) 1943, 31-298.

Evans, D. D. "Unsaturated Flow and Transport through Fractured Rock - Related to High-Level Waste Repositories," Final Report – Phase I, Department of Hydrology and Water Resources, University of Arizona, prepared for U. S. Nuclear Regulatory Commission, Report NUREG/CR-3206, March 1983.

Grant, M. A. and Sorey, M. L. "The Compressibility and Hydraulic Diffusivity of Water-Steam Flow," *Water Resources Res., 15,* 1979, 684-686.

Harmathy, T. Z. "Simultaneous Moisture and Heat Transfer in Porous Systems with Particular Reference to Drying," *I&EC Fundamentals, 8,* (1) 1969, 92-103.

He, H. X., Cushman, J. H. and Diestler, D. J. "Molecular Dynamics of Water near an Uncharged Silicate Surface: Anisotropic Diffusion," in: D. D. Evans and T. J. Nicholson (eds.) *Flow and Transport through Unsaturated Fractured Rock,* Geophysical Monograph 42, American Geophysical Union, Washington, D. C. 1987.

Herkelrath, W. N., Moench, A. F. and O'Neal II, C. F. "Laboratory Investigations of Steam Flow in a Porous Medium," *Water Resources Res., 19,* (4) August 1983, 931-937.

Herkelrath, W. N. and O'Neal II, C. F. "Water Vapor Adsorption in Low-Permeability Rocks," International Association of Hydrogeologists (ed.), Memoires, Vol. XVII, Part 1, 1985, 248-253.

Hsieh, C. H. and Ramey, H. J., Jr. "An Inspection of Experimental Data on Vapor Pressure Lowering in Porous Media," *Geothermal Resources Council, Transactions, 2,* July 1978, 295-296.

Hsieh, C. H. and Ramey, H. J., Jr. "Vapor Pressure Lowering in Geothermal Systems," Society of Petroleum Engineers, paper SPE-9926, presented at the 1981 California Regional Meeting, Bakersfield, March 1981.

Langmuir, I. "The Constitution and Fundamental Properties of Solids and Liquids, Part I. Solids," *J. Amer. Chem. Soc., 38,* 1916, 2221-2295.

Matthews, C. S. and Russel, D. G. "Pressure Buildup and Flow Tests in Wells," Society of Petroleum Engineers, Monograph, Vol. 1, New York, 1967.

Melrose, J. C. "Use of Water-Vapor Desorption Data in the Determination of Capillary Pressures at Low Water Saturations," SPE Reservoir Engineering, August 1988, 913-918.

Mualem, Y. "A New Model for Predicting the Hydraulic Conductivity of Unsaturated Porous Media," *Water Resources Res., 12,* 1976, 513-522.

Nghiem, C. P. and Ramey, H. J., Jr. "One-Dimensional Steam Flow in Porous Media under Desorption," paper presented at Sixteenth Workshop Geothermal Reservoir Engineering, Stanford University, January 1991.

Nitao, J. J. "Increasing the Efficiency of the TOUGH Code for Running Large-Scale Problems in Nuclear Waste Isolation, in: K. Pruess (ed.), Proceedings of the TOUGH Workshop, Lawrence Berkeley Laboratory Report LBL-29710, September 1990, 143-148.

O'Sullivan, M. J. "A Similarity Method for Geothermal Well Test Analysis," *Water Resources Res., 17,* (2) April 1981, 390-398,

Peters, R. R., Klavetter, E. A., Hall, I. J., Blair, S. C., Heller, P. R. and Gee, G. W. "Fracture and Matrix Hydrologic Characteristics of Tuffaceous Materials from Yucca Mountain, Nye County, Nevada," Sandia National Laboratories, Report SAND84-1471, Albuquerque, NM, December 1984.

Philip, J. R. "Adsorption and Capillary Condensation on Rough Surfaces," *J. of Phys. Chem., 82,* (12) 1978, 1379-1385.

Pollock, D. W. "Simulation of Fluid Flow and Energy Transport Processes Associated with High-Level Radioactive Waste Disposal in Unsaturated Alluvium," *Water Resources Res., 22,* (5) 1986, 765-775.

Pruess, K. "Development of the General Purpose Simulator MULKOM," Annual Report 1982, Earth Sciences Division, Lawrence Berkeley Laboratory Report LBL-15500, 1983.

Pruess, K., "A Quantitative Model of Vapor Dominated Geothermal Reservoirs as Heat Pipes in Fractured Porous Rock," *Geothermal Resources Council, Transactions, 9,* Part II, August 1985, 353-361.

Pruess, K. "TOUGH2 – A General-Purpose Numerical Simulator for Multiphase Fluid and Heat Flow," Lawrence Berkeley Laboratory Report LBL-29400, May 1991.

Pruess, K., and Narasimhan, T. N. "On Fluid Reserves and the Production of Superheated Steam from Fractured, Vapor-Dominated Geothermal Reservoirs," *J. of Geophys. Res., 87,* (B11) 1982, 9329-9339.

Pruess, K., and Narasimhan, T. N. "A Practical Method for Modeling Fluid and Heat Flow in Fractured Porous Media," *Society of Petroleum Engineers Journal, 25,* (1) February 1985, 14-26.

Pruess, K., Wang, J. S. Y. and Tsang, Y. W. "On Thermohydrological Conditions near High-Level Nuclear Wastes Emplaced in Partially Saturated Fractured Tuff. Part 1: Simulation Studies with Explicit Consideration of Fracture Effects," *Water Resources Res., 26,* (6) 1990, 1235-1248.

Ramey, H. J., Jr., et al. "Stanford Geothermal Program, Quarterly Report, January – March 1987," Stanford University, 1987.

Truesdell, A. H. and White, D. E. "Production of Superheated Steam from Vapor-Dominated Geothermal Reservoirs," *Geothermics, 2,* (3-4) September-December 1973, 154-173.

Udell, K. S. "The Thermodynamics of Evaporation and Condensation in a Porous Media," paper SPE-10779, presented at the Society of Petroleum Engineers California Regional Meeting, San Francisco, CA, March 1982.

van Genuchten, M. Th. "A Closed-Form Equation for Predicting the Hydraulic Conductivity of Unsaturated Soils," *Soil Sci. Soc. Am., J., 44,* 1980, 892-898.

Whitaker, S. "Simultaneous Heat, Mass, and Momentum Transfer in Porous Media: A Theory of Drying," *Adv. in Heat Transfer, 14,* 1977, 119-203.

White, D. E., Muffler, L. J. P. and Truesdell, A. H. "Vapor-Dominated Hydrothermal Systems Compared with Hot-Water Systems," *Economic Geology, 66,* (1) 1971, 75-97.

PROCEEDINGS, Seventeenth Workshop on Geothermal Reservoir Engineering
Stanford University, Stanford, California, January 29-31, 1992
SGP-TR-141

Adding Adsorption to a Geothermal Simulator

R. Holt
Stanford University

A. Pingol
Unocal

Abstract

Physical adsorption of steam has increasingly become recognized as an important storage mechanism in vapor dominated geothermal reservoirs. A method has been developed which allows the effects of adsorption to be modeled using TETRAD, a commercially available geothermal simulator. The method consists of replacing the standard steam table with a new steam table which has been derived to include adsorptive effects. The TETRAD simulator, when run with the pseudo steam table, approximately matches the pressure, production, and saturation behavior of a desorbing geothermal system.

Adsorption can be described as the existence of an immobile layer of liquid on the surfaces within a porous medium. The presence of an adsorbed liquid water layer in rocks has been shown experimentally to cause the vapor pressure of steam to be lower than its flat surface vapor pressure for a particular temperature[1],[2]. The pseudo steam table accounts for this vapor pressure lowering effect.

A test run was made with TETRAD using the pseudo steam table and a low porosity, low permeability reservoir matrix. This test run was compared to an equivalent run made with Stanford Geothermal Program's simulator, ADSORB. The program ADSORB is a one dimensional simulator which has adsorption effects built into its difference equations. The comparison of these runs shows that the pseudo steam table allows TETRAD to match the behavior of the ADSORB simulator. Injection was not investigated in this study.

A convenient method of modeling adsorption with TETRAD is to use standard steam tables while allowing for the vapor pressure lowering effect of adsorption. This will require modifications of the equations in the code that describe the partial pressure of the steam phase.

Introduction

The ability to include adsorption in numerical simulation has become important to operators who use simulators to make reservoir predictions. It is, however, largely impractical to write and test completely new simulator codes which have been written specifically to include adsorptive effects. If possible, it is more useful to include adsorptive effects in existing simulators. This will allow adsorption to be included only in situations or reservoirs where it is believed to occur. The objective of this study is to develop a practical means of modeling a desorbing geothermal system using the TETRAD simulator. This is accomplished through a new input card, 'DESORB'. The implementation of the DESORB card requires changes in the partial pressure calculation code in TETRAD.

Adsorption has been shown experimentally to cause a vapor pressure lowering effect. Conventional simulators, such as TETRAD, use a standard steam table to predict the reservoir pressure-temperature relationship. If adsorption is taking place, this standard steam table approach is inadequate. Adsorption has been shown experimentally and numerically to cause a substantial effect on the flow of steam through porous medium[1],[4],[5].The Stanford Geothermal Program has written a one dimensional simulator program called ADSORB[5]. The ADSORB simulator has adsorptive effects built into its difference equations in a rigorous manner. Runs made with ADSORB were therefore used to represent the behavior of a system producing under desorption. Using concepts explained later, a special steam table was derived. This pseudo steam table, when placed in TETRAD's input deck, causes TETRAD to duplicate the results of the runs made with ADSORB.

The pseudo steam table, although successful in modeling adsorptive effects, is cumbersome to use.

A new pseudo steam table must be generated when any input parameters are changed. To allow convenient adsorption modeling, a new input card, DESORB, is proposed. The DESORB card will invoke a steam partial pressure lowering algorithm. The pseudo steam table run serves, however, as a test of the validity of the overall technique.

Macroscopic Effects of Adsorption

Physical adsorption of steam is caused by attractive forces between water molecules and rock surfaces. A finite layer of adsorbed liquid water forms on the rock surfaces. This layer of water has a thermodynamic behavior which is quite different from what is described by standard steam tables. The way in which the microscopic physics of adsorption affects macroscopic reservoir performance is studied here.

Ignoring capillary effects, vapor pressure is represented in steam tables as a function of temperature only. Therefore, in the absence of adsorption, the functional form of Equation 1 applies for vapor pressure.

(1) $$P_{sat}=f(T)$$

If adsorption is occurring, however, vapor pressure is a function of both temperature and liquid saturation. Thus if adsorption is occurring, the functional form of Equation 2 applies for vapor pressure.

(2) $$P_{sat}=f(T)*g(S_w)$$

The fact that adsorption causes vapor pressure to be a function of both temperature and liquid saturation is key to understanding how to model the process.

A classic model for vapor pressure lowering due to adsorption is presented by Langmuir[3]. Equation 3 is referred to as the Langmuir isotherm, and applies at a fixed temperature.

(3) $$X=\frac{(P/P_{sat})}{A+B(P/P_{sat})}$$

In Equation 3, X is mass fraction of adsorbed liquid in gram/gram rock, P is vapor pressure, Psat is steam table vapor pressure. The ratio (P/Psat) is called the steam partial pressure. The constants A and B are rock properties. In observations of experimental data, Nghiem and Ramey suggest that A=31 and B=53 may be suitable values for many reservoir rocks[5]. Equation 3 can be expressed in terms of water saturation, porosity, and densities as shown in Equation 4.

(4) $$S_w=\frac{(1-\phi)}{\phi}\frac{\rho_r}{\rho_w}X$$

The entire Langmuir isotherm behavior can be expressed using Equations 5, 6, and 7. Equations 3 and 4 are combined to produce Equation 5. Note that there is a critical water saturation, Swcrit, above which steam partial pressure is equal to 1.0. The critical water saturation is determined by Equation 7. Equations 5, 6, and 7 apply at a fixed temperature.

(5) $$(P/P_{sat})=\frac{S_wA\frac{\phi}{(1-\phi)}\frac{\rho_w}{\rho_r}}{1-S_wB\frac{\phi}{(1-\phi)}\frac{\rho_w}{\rho_r}} \qquad 0<Sw<Swcrit$$

(6) $$(P/P_{sat})=1.0 \qquad S_{wcrit}<S_w<1$$

(7) $$S_{wcrit}=\frac{(1-\phi)}{\phi}\frac{\rho_r}{\rho_w}\frac{1}{(A+B)}$$

Equations 5, 6 ,and 7 are presented in graphical form in Figure 1. Note that the steam partial pressure, P/Psat, varies from 0.0 to 1.0 as water saturation varies from 0% to about 96% for this particular system.

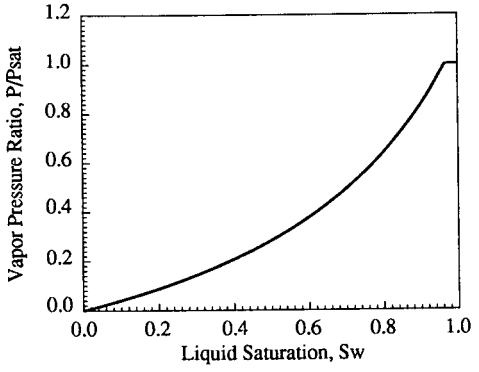

Figure 1 - The Langmuir Isotherm for A=31, B=53 and porosity= 4%. Equations 5, 6, and 7.

The ADSORB Program

A test run was made with the ADSORB program for use as a comparison to later TETRAD runs. The sample case used throughout this study is shown in Figure 2.

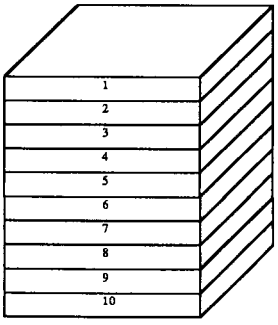

ϕ	=	0.04
L	=	200 ft.
X	=	200 ft.
Y	=	200 ft.
k	=	0.05 mD
q	=	45 lbs/hr
Pmin	=	115 psia
Pi	=	514 psi
Ti	=	470 F
Swi	=	0.9656
N	=	10 blocks

Figure 2 - Simulation test case for all runs in study.

A desorbing geothermal system is modeled as a porous rock with an immobile water saturation which vaporizes into the gas phase and flows to a well. Therefore, at all saturations, Krg=1.0 and Krw=0.0. Initial water saturation is set to Swcrit, which for this system is Swi=96%. A 200 foot cube of reservoir rock is used to resemble a unit of reservoir matrix located between fractures. This cube is split into 10 blocks of 20 feet each. Block #1 contains the production well. Initial production rate is set to 45 lbs steam/hour. This rate is maintained until block #1 reaches a pressure of 115 psia. At this point, block #1 produces at a constant pressure while production rate declines. The results of this ADSORB test run are shown below in Figures 3, 4, and 5.

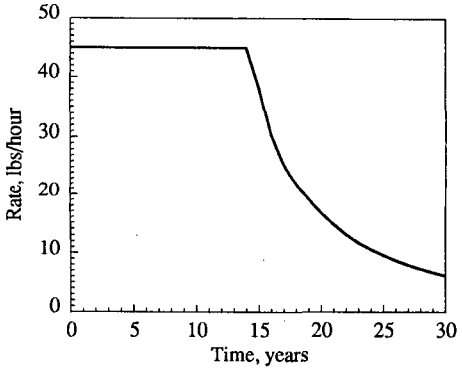

Figure 3 - Rate vs. time for ADSORB run.

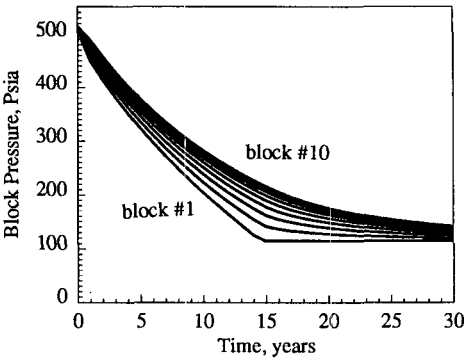

Figure 4 - Pressure vs. time for each of ten blocks in ADSORB run.

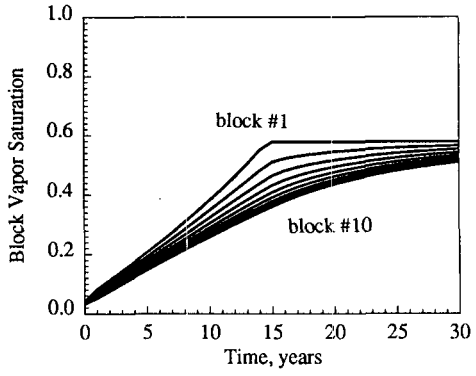

Figure 5 - Steam saturation vs. time for each of ten blocks in ADSORB run.

A Standard TETRAD Run Without Adsorption

As a starting point an initial TETRAD run was made with no provision for the inclusion of adsorption. The standard steam table was used. The input parameters and geometry exactly match those described in Figure 2. Therefore a direct comparison of the ADSORB run and this TETRAD run will show the effects that adsorption has on reservoir performance. The results of this TETRAD run are shown in Figures 6, 7, and 8.

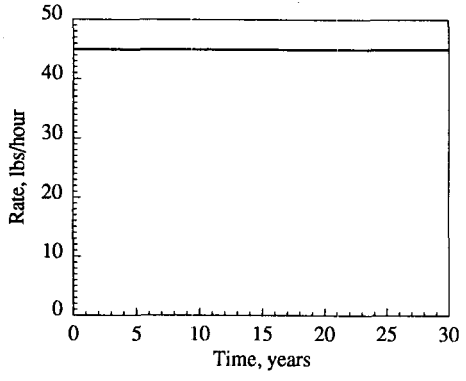

Figure 6 - Rate vs time for standard TETRAD run with no adsorption.

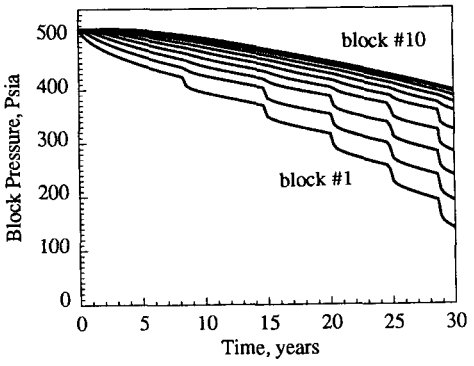

Figure 7 - Pressure vs. time for each of ten blocks the standard TETRAD run with no adsorption.

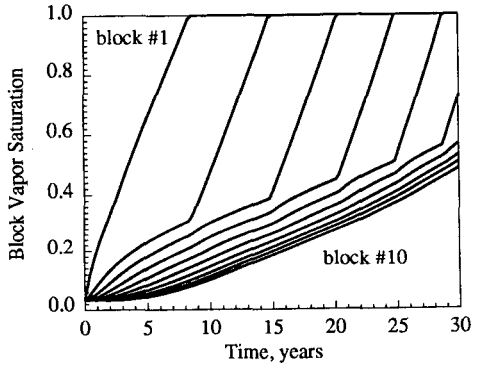

Figure 8 - Steam saturation vs. time for each of ten blocks in the standard TETRAD run with no adsorption.

In Figure 7, discontinuities in the pressure response are a numerical artifact. This is caused when a block reaches 100% gas saturation. On the comparison of the standard TETRAD run with the ADSORB run, the following observations are made:

1. The presence of adsorption reduces the length of time that the production plateau of 45 lbs/hour can be maintained. This is shown by a comparison of Figure 6 and Figure 3.

2. The presence of adsorption causes block pressures to decline more rapidly. This is shown by a comparison of Figure 7 and Figure 4.

3. The presence of adsorption prevents gas saturation from reaching 100%. This is shown by a comparison of Figure 8 and Figure 5. In the presence of adsorption, gas saturation becomes 100% only if pressure is 0 psia. Therefore, significant liquid saturations may be present at low pressures, if adsorption is taking place.

The Pseudo Steam Table

In order to incorporate adsorption into TETRAD, a technique is needed which will allow vapor pressure to be a function of both temperature and liquid saturation. In the existing version of TETRAD, steam vapor pressure is calculated by entering a standard steam table with a known block temperature and reading vapor pressure. Initial attempts to model adsorption were thus directed at the steam table.

It is desired to make the vapor pressure in the steam table such that it can approximately match the sum behavior of Equations 5, 6, and 7. A complication arises, however, because Equations 5, 6, and 7 are functions of liquid saturation, and the steam table (flat surface vapor pressure) is a function of temperature. A relationship between temperature and saturation is needed. Such a relationship will allow saturation and temperature to be used interchangeably in Equations 5, 6, and 7.

Consider a geothermal system with some finite immobile liquid saturation. As the system is produced, liquid is continuously vaporizing and flowing toward the well as steam. As this liquid vaporizes, the rock matrix cools as energy goes into vaporizing the liquid. If there is no injection, and the thermal conductivity of the system is low, then temperature can be related directly to saturation. This is done by using an energy balance.

The system of interest is a porous rock with a vaporizing immobile liquid saturation. An energy balance applied to this system produces Equation 8.

$$(8) \qquad (S_{wi}-S_w) = \frac{(1-\phi)}{\phi}\frac{C_{prock}}{h_{fg}}\frac{\rho_r}{\rho_w}(T_i-T)$$

In Equation 8, two assumptions have been made. First, it is assumed that all thermal properties are independent of temperature. Second, it is assumed that the thermal capacities of the liquid water and steam saturations are negligible when compared to the rock thermal capacity. Table 1 lists the thermal properties used throughout this study.

Table 1

ϕ	=	0.04
C_{prock}	=	0.232 *btu/lbm F*
ρ_{rock}	=	2.65 *g/cc*
ρ_{H2O}	=	0.7841 *g/cc*
h_{fg}	=	770 *btu/lbm*
S_{wi}	=	0.9656
T_i	=	470 *F*

The values in Table 1 are inserted into Equation 8 and the numerical result is Equation 9.

(9) $S_w = 0.9656 - 0.024 * (470 - T)$

Equation 9 is a simple linear equation which can convert temperature values into saturation values. Using Equation 9, Sw can be substituted out of Equation 5. The result is an equation which expresses adsorption vapor pressure lowering as a function of temperature. A new steam table can now be produced. The technique involves using Equation 7 to calculate Swcrit. Equation 9 is then used to convert Swcrit to a temperature Tcrit. P/Psat is then calculated for each temperature in the steam table below Tcrit. Note that P/Psat has a minimum value of zero. Finally, the calculated values of P/Psat are multiplied by the corresponding steam table vapor pressure values to produce an adsorption pseudo steam table. Figure 9 is a plot of the standard steam table and the pseudo steam table.

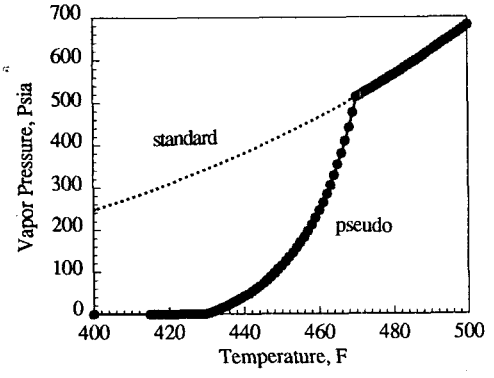

Figure 9 - The standard steam table and the pseudo steam table. Vapor pressure as a function of temperature.

Note that the vapor pressure values in the pseudo steam table are drastically lower than those in the standard steam table. This lowering of vapor pressure approximately accounts for the effect of adsorption.

TETRAD Run with the Pseudo Steam Table

The pseudo steam table shown in Figure 9 was used in place of the standard steam table for a TETRAD test run. This test run is identical to the first TETRAD with the following exception. The pseudo steam table was used in place of the standard steam table in the input deck.

The results of this run are shown in Figures 10, 11, and 12.

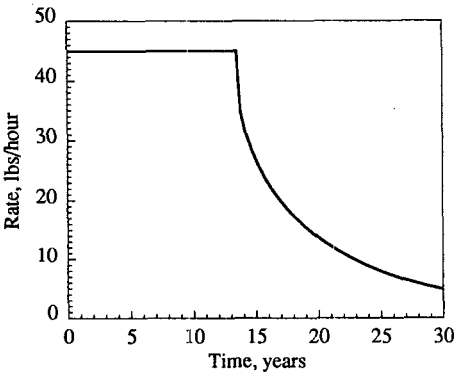

Figure 10 - Rate vs. time for TETRAD with adsorption run.

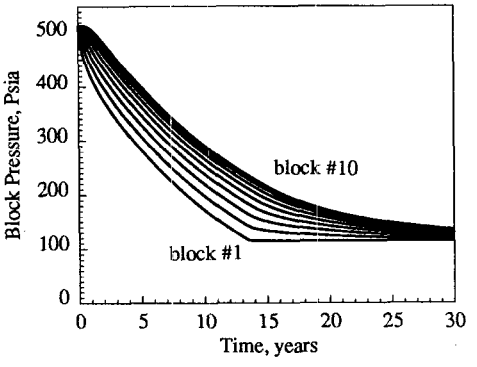

Figure 11 - Pressure vs. time for each of ten blocks in TETRAD with adsorption run.

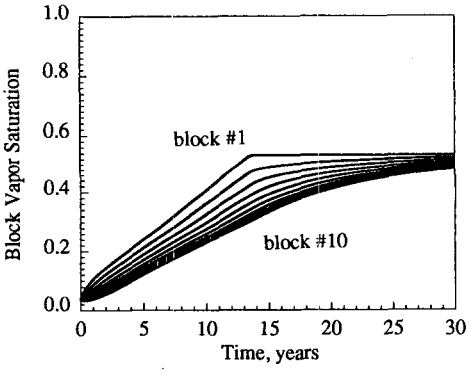

Figure 12 - Steam saturation vs. time for each of ten blocks in TETRAD with adsorption run.

The TETRAD run with the psuedo steam table shows good agreement with the results from the ADSORB run. This can be seen by comparing Figures 10, 11, and 12 with Figures 3, 4, and 5 respectively. The good agreement between these two runs shows that TETRAD can be used to model the effects of adsorption if the steam vapor pressure is reduced judiciously. This pseudo steam table technique although successful, is cumbersome to

employ. This exercise proves, however, that the concept of lowering vapor pressure to model adsorption does indeed produce desired results.

The 'DESORB' Input Card

A new input card, DESORB, has been proposed. Its accompanying algorithm will lower the steam phase partial pressure as a direct function of saturation. The concept of partial pressure classically applies to a multicomponent system. Specifically, if a gas phase consisted of several components, then each component's partial pressure would depend on its relative mole fraction. Typical simulators have a built in framework which allows this type of partial pressure manipulation. Therefore, the proposed modeling technique will use this existing framework.

In geothermal simulation, the partial pressure of steam equals unity because a one component model is usually assumed. To model a desorbing system, the partial pressure of steam will be allowed to vary from 0.0 to 1.0.

When the DESORB card is invoked, the partial pressure of steam will be calculated as a function of liquid saturation using Equations 5, 6, and 7. Depending on liquid saturation, Equations 5, 6, and 7 will return a steam partial pressure between 0.0 and 1.0. This partial pressure will then be multiplied by the standard steam table vapor pressure. This will produce a lowered, adsorption vapor pressure.

The Effect of Thermal Conductivity

In the Tetrad run with the pseudo steam table, all thermal conductivities were set to zero. This was required to allow direct coupling of temperature and saturation. Real systems, however, do have finite thermal conductivities. To investigate the importance of thermal conductivity to the present study, the TETRAD with pseudo steam table run was repeated with normal thermal conductivities. It was found that the inclusion of thermal conductivity had a minor effect on the results. In summary, block number 1, which contained the production well, behaved differently from the previous run. Blocks 2 through 10, however, showed similar behavior to the run which had zero thermal conductivity. This suggests that for this case, the omission or inclusion of thermal conductivity has a stronger effect on the near wellbore vicinity where temperature gradients were largest. It can therefore be said that the inclusion of thermal conductivity does affect the behavoir of the simulation, but it does not nullify the effects of adsorption. It is expected that the thermal conductivity effect will be reduced further when the DESORB partial pressure algorithm is employed.

Conclusions

The TETRAD geothermal simulator, with minor modifications, can be used to model a reservoir producing under desorbing conditions. This can be accomplised by correctly adjusting the steam partial pressure. This process can be performed by a proposed new input card and its accompanying algorithm. A successful test of this method was performed by accordingly lowering the vapor pressure in a steam table used for a test run. This test run matched the behavior expected from a purely desorbing system. A comparison of simulation runs which contained adsorption to ones that did not contain adsorption was made. This comparison showed that adsorption can be expected to affect the production, pressure, and saturation behavior of a desorbing geothermal system. With the DESORB option, adsorption can be included in full scale simulation to explore adsorption's effect on a producing reservoir's overall preformance.

Acknowledgements

The authors gratefully thank Unocal for permission to publish this work. The authors also acknowledge Cuong Phu Nghiem and Henry J. Ramey Jr. of the Stanford Geothermal Program for providing and supporting the ADSORB simulator.

References

(1) Herkelrath, W.N. and A.F.Moench, "Laboratory Investigations of the Physics of Steam Flow in a Porous Medium," USGS Open-File Report 82-95, 1982.

(2) Hsieh, C.H. and H.J.Ramey Jr, "Vapor-Pressure Lowering in Geothermal Systems," SPEJ, February 1983, 157-167.

(3) Langmuir, I.,"The Constitution and Fundamental Properties of Solids and Liquids," Part I. Solids. J. Amer. Chem. Soc., 38,2221-2295, 1916.

(4) Moench, A.F. and P.G. Atkinson, "Transient-Pressure Analysis in Geothermal Steam Reservoirs with an Immobile Vaporizing Liquid Phase," Geothermics, vol. 7, No. 2-4, 1978, 253-264.

(5) Nghiem, C.P. and H.J.Ramey Jr.,"One-Dimensional Steam Flow Under Desorption," Sixteenth Workshop of Geothermal Reservoir Engineering, Stanford University, January, 1991

PROCEEDINGS, Seventeenth Workshop on Geothermal Reservoir Engineering
Stanford University, Stanford, California, January 29-31, 1992
SGP-TR-141

ANALYSIS OF PRESSURE TRANSIENT DATA FROM THE SUMIKAWA GEOTHERMAL FIELD

T. Ishido, T. Kikuchi, Y. Yano, Y. Miyazaki and S. Nakao
Geological Survey of Japan
Tsukuba, Ibaraki 305, Japan

K. Hatakeyama
Mitsubishi Materials Corporation
Kazuno, Akita 018-51, Japan

ABSTRACT

The permeability structure of the Sumikawa geothermal field in northern Japan has been the subject of an extensive pressure-transient testing investigation since 1986. In this paper, various pertinent data sets are presented and analyzed, including results showing reservoir heterogeneity (i.e. boundary) effects and apparent double porosity behavior. Interference tests between wells SB-3 and SD-2 (both of which have feedpoints in dacitic layers in the "marine-volcanic complex" formation) were carried out during 1990. The results have been interpreted to indicate the presence of a moderately high permeability (~ 4 darcy-meters) layer with two impermeable boundaries intersecting at a right angle. The 1988 pressure buildup data for well SN-7D are also explained by assuming two impermeable boundaries in a high transmissivity reservoir within the deep "granodiorite" formation. Interference tests between wells S-4 and KY-1 have suggested that a very permeable north-south channel is present in the "altered andesite" layer. Although the response was successfully interpreted using an "anisotropic line-source model" by Garg et al.(1991), a "double porosity channel model" seems to be particularly applicable for explaining both the short-term and long-term behavior observed in this series of tests.

INTRODUCTION

The Sumikawa geothermal field is located in the Hachimantai volcanic zone of the Sengan thermal area in northern Honshu, Japan. Exploratory studies have been in progress at Sumikawa since 1981 by Mitsubishi Materials Corporation (MMC) and Mitsubishi Gas Chemical Corporation (MGC); this comprehensive program incorporates a variety of geochemical and geophysical surveys and an extensive drilling investigation. The drilling program has revealed a complex geological structure and has made possible a very thorough pressure-transient testing program involving both short-term single-well and long-term multi-well pressure interference tests. These studies were first carried out jointly by MMC and NEDO (the New Energy and Industrial Technology Development Organization) from 1985 to 1989, and then by MMC and GSJ (Geological Survey of Japan) in 1990 and 1991.

The area depicted in Figure 1 is about 42 square kilometers; the Sumikawa field lies in the western part of the area, which may be regarded as centered in the neighborhood of the S-series wells (S-1, S-2, S-3, and S-4). To the east, the Ohnuma geothermal power station has been producing about 10 MW of electricity for several years. Within the area, the ground surface averages about 1000 meters above sea level (ASL), but slopes sharply down from south (> 1300 m ASL near Mt. Yake) to north (< 700 m ASL near the Akagawa hot spring area). The major geological formations in the area are as follows, in order of increasing depth:

"ST" Formation: Surface andesitic tuffs, lavas and pyroclastics of Recent origin.

"LS" Formation: Lake sediments; Pleistocene tuffs, sandstones, siltstones and mudstones.

"DA" Formation: Pliocene dacites, dacitic tuffs and breccias.

"MV" Formation: "Marine/Volcanic Complex"; interbedded Miocene dacitic volcanic rocks and "black shale" marine sediments.

"AA" Formation: Altered andesitic rocks which are apparently extensively fractured.

"GR" Formation: Crystalline intrusive rocks, mainly granodiorite and diorite.

The various pressure transient tests performed so far have helped to clarify the permeability structure of the Sumikawa reservoir (see e.g. Garg et al., 1991). Three of the above formations ("DA", "AA" and "GR") appear to be fairly permeable; the "LS" layer is an impermeable aquitard, and the "MV" formation, while permeable to horizontal fluid motion, acts as a barrier to vertical flow.

In this paper, we discuss pressure transient measurements indicative of reservoir heterogeneity (i.e. impermeable boundary) effects; first, the 1990 interference test between wells SB-3 and SD-2 (both of which have feedpoints in the "MV" formation), and then the 1988 buildup test of well SN-7D (which penetrates the "GR" formation).

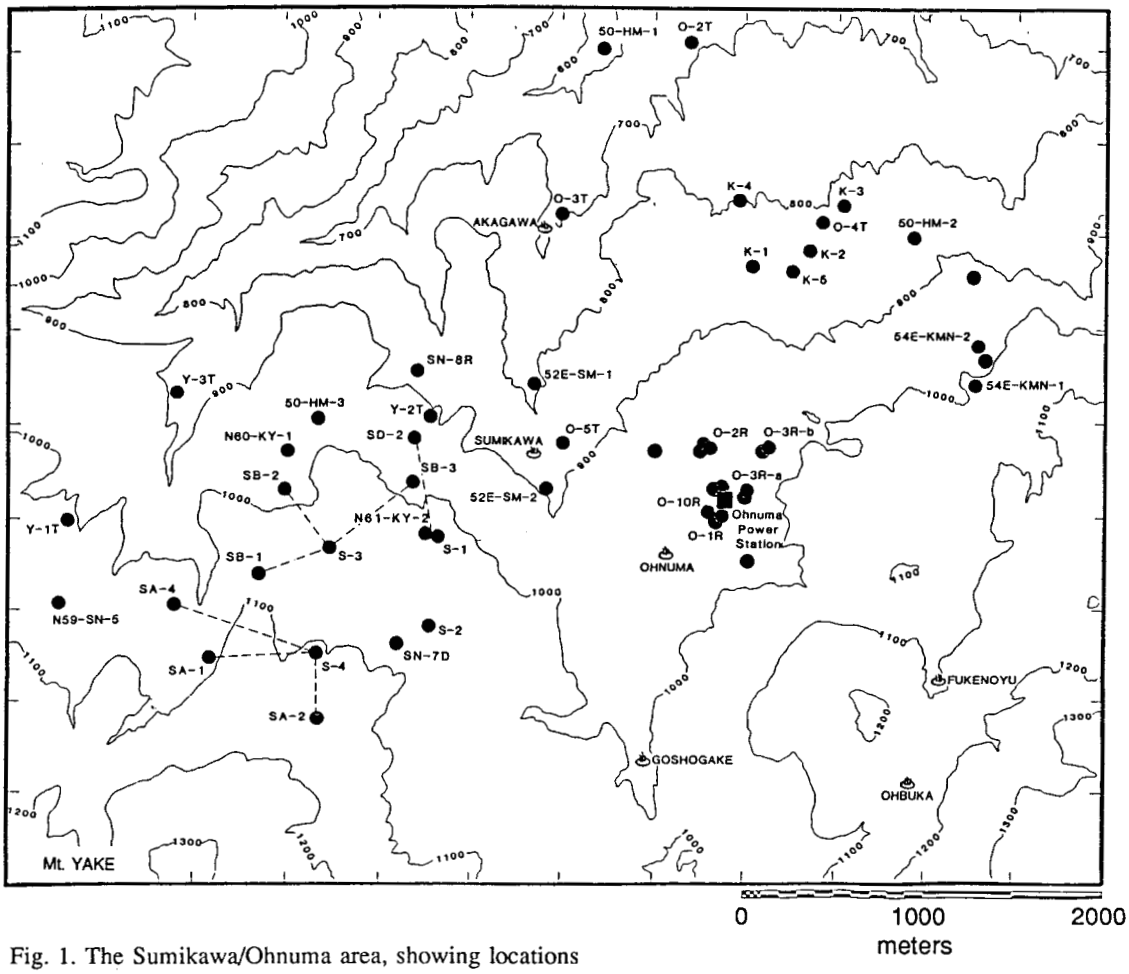

Fig. 1. The Sumikawa/Ohnuma area, showing locations of wells.

Finally, we present a new model for the very permeable north-south channel in the "AA" layer (which has been revealed by several pressure interference experiments involving flowing of well S-4 and the observation of pressure in well KY-1).

RESERVOIR BOUNDARIES

The pressure signal recorded in well SD-2 using a downhole gauge of the capillary tube type clearly shows a response to a four-hour injection of cold water into nearby well SB-3 which started at 09:00 on June 6, 1990 (see Figure 2). The pressure signal appears to propagate through a dacite aquifer embedded within the "MV" formation which is intercepted by both wells. The spatial separation between the SB-3 feedpoint and the upper SD-2 feedpoint (in the "MV" formation) is 354 meters. The reported injection rate history for well SB-3 is as follows:

Time Interval 06/06/90	Injection Rate
prior to 09:00	0 kg/s
09:00 to 09:30	51.7 kg/s
09:30 to 10:00	61.4 kg/s
10:00 to 10:30	77.8 kg/s
10:30 to 11:00	77.9 kg/s
11:00 to 11:30	79.4 kg/s
11:30 to 12:00	83.9 kg/s
12:00 to 12:30	84.9 kg/s
12:30 to 13:00	76.2 kg/s
after 13:00	0 kg/s

We used the classical line-source solution throughout to analyze this test. Initial estimates of transmissivity and diffusivity were obtained (assuming an unbounded aquifer) by type-curve matching, considering only the buildup (flowing) portion of the pressure record. Then, repetitive forward calculations were carried out to refine these estimates (still assuming an infinite aquifer and considering buildup only). The following values were finally obtained in this way:

$T=kh/\mu=3.0\times10^{-8}$ m^3/Pa-s

$\eta=k/\phi C_t\mu=5.7$ m^2/s

Next, to improve the match for the falloff (shutin) portion of the pressure record, we introduced linear impermeable boundaries and performed additional repetitive calculations, this time varying the distances to the boundaries from case to case. The best match was obtained by assuming that the aquifer was constrained by two impermeable boundaries intersecting at a right angle - this match is shown as the line in Figure 2. This aquifer boundary geometry may be treated as equivalent to the total effect (at the observation well location) of the actual flowing well together with three fictitious "image" wells in an unbounded aquifer, which in turn may be represented using superposition of line-source solutions. This final representation yields the following values for the distances between observation well SD-2 and the two primary "image" wells (the first reflections of the flowing well SB-3 across each boundary):

R1 = R2 = 1000 m

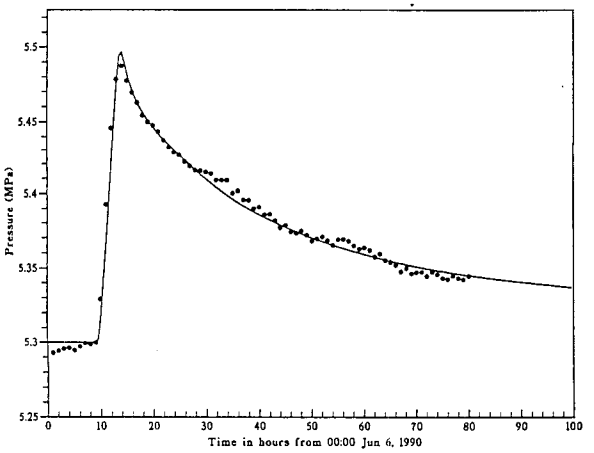

Fig. 2. Comparison of pressure measurements in well SD-2 with computed response due to cold water injection into well SB-3 on June 6, 1990 (t=9 to 13 hours). Measured pressures are corrected for a linear background trend (150 Pa/hour) observed over a five-day period prior to the test.

The distance between the third image well and observation well SD-2 is given by:

$$\sqrt{R1^2 + R2^2 - L^2}$$

where L (354 m) is the distance between wells SB-3 and SD-2.

SN-7D BUILDUP DATA

Well SN-7D is the deepest well (total depth about 2486 m) at Sumikawa. The major feedpoint for well SN-7D is located in the granodiorite/granite/diorite rocks ("GR" formation) at about 2320 m depth. Well SN-7D is one of the best producers we have ever had in Japan; total (water plus steam) flow rates up to 500 tons/hour were recorded during various discharge tests carried out between 1988 and 1991.

Downhole pressures were monitored using a downhole capillary tube gauge in three separate discharge tests (two in 1988 and one in 1989). The pressure buildup data obtained after the first 1988 test are shown in Figure 3, a multi-rate Horner plot in which buildup pressures are plotted against "reduced time":

$$\text{reduced time} = \Sigma_{i=1}^{N}(q_i/q_N)\log[(t_N+\Delta t-t_i)/(t_N+\Delta t-t_{i-1})]$$

The permeability-thickness product is about 37 darcy-meters based upon the slope of the Horner plot for early times (prior to ~10 hours of shutin time, or ~1.2 "reduced time").

At later times, the effects of boundaries appear to make themselves manifest. Another straight-line segment (of greater slope) may be perceived between ~ 20 and ~ 50 hours of shutin, and a third segment (of even greater slope) appears to prevail after ~ 50 hours. The solid curve shown in Figure 3 was computed from a mathematical model which assumes the following properties (Ishido et al., 1989):

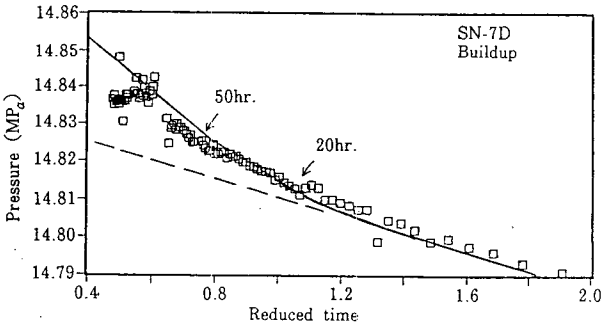

Fig. 3. Comparison of measured and computed (solid curve) pressure buildup histories after first 1988 SN-7D discharge test.

ϕ(rock porosity)=0.02
μ(fluid viscosity)=10^{-4} Pa-s
C_t(total compressibility)=1.5×10^{-9} Pa^{-1}
ρ(in-situ fluid density)=800 kg/m^3
k(permeability)=74 md
h(formation thickness)=500 meters
p_i(initial pressure)=14.89 MPa

L1(distance to the first impermeable boundary)
=990 meters
L2(distance to the second impermeable boundary)
=1650 meters

The radius of investigation corresponding to the producing interval (9 days) is:

Ri = ~ 8.7 kilometers = 8.8L1 = 5.3L2

which implies that the test was of sufficient duration to unambiguously identify these boundaries.

It appears that the volume of the deep permeable zone within the "GR" formation tapped by well SN-7D is at least a few cubic kilometers. During the SN-7D discharge tests, five other wells were equipped with downhole pressure gauges. No signal attributable to the discharge of SN- 7D was observed in any of these wells; this implies that the deep reservoir penetrated by well SN-7D is probably isolated from the shallower reservoir in the "altered andesites". Further pressure transient testing of well SN-7D is needed. The best way to characterize this deep reservoir (confirm and locate reservoir boundaries, appraise volume, etc.) is to drill new wells into the "GR" formation and then to perform long-term interference tests involving these wells and SN-7D.

DOUBLE POROSITY BEHAVIOR

Interference tests between wells S-4 and KY-1

The first large-scale pressure-interference experiment at Sumikawa was carried out in 1986. Deep well S-4 was discharged starting on September 2 and was subsequently shut in on November 3; the liquid fraction of the discharge was simultaneously reinjected into nearby shallow well S-2. A clear pressure response was immediately observed in well KY-1 (see Figure 4), located 1.1 km north of S-4 (see e.g. Kawano et al., 1989). The principal feedpoints for wells KY-1 and S-4 both lie within the "altered andesite" (AA) layer, below the "MV" formation explored by wells SD-2 and SB-3, and above the crystalline "GR" layer penetrated by well SN-7D.

To explain the pressure response observed in well KY-1 due to the 1986 S-4 discharge, Pritchett et. al. (1989) proposed the following one-dimensional "channel-flow" model. It is assumed that a permeable horizontal "channel" of constant cross-section area and constant permeability is present, oriented north-south, which contains the feedpoints of both wells (S-4 and KY-1). The east, west, upper and lower boundaries of the channel are impermeable. To the north, the channel terminates at an impermeable northern barrier; to the south, it ends at a constant-pressure boundary (representing the influence of a two-phase region). Minimization of the deviations between measurements and computed pressures yielded the following parameter values:

Cross-section =0.51 square kilometers
Permeability =195 millidarcies
Impermeable boundary
position: 1.44 km north of well KY-1
Constant-pressure
boundary position: 9.86 km south of S-4

The above parameter values are consistent with the geological structure of the area, to the extent that it is known from drilling logs (see e.g. Pritchett et.al., 1989). The "altered andesite" formation is very permeable, and the cross-section area of the channel is substantial. This permeability is presumably due to the presence of a system of fractures (probably oriented approximately north-south); although well S-4 intersected only one of these fractures at its primary feedpoint, the frequent intersections of the individual fractures within the channel served to distribute the pressure signal from S-4 throughout the entire fracture network in the formation such that the apparent cross-section area and aquifer volume were large.

Subsequently, between 1 May and 4 May 1989, cold water was intermittently injected into well S-4 (each injection episode lasted a few hours). Pressures measured downhole in well KY-1 responded quickly to each change in the S-4 injection rate (see Figure 5). These 1989 tests involved short-term response (time scales of hours) as compared to the long-term response characterized by the 1986 test discussed above (weeks). If the mathematical "channel flow" model outlined above is used to forecast the pressure disturbance in KY-1 due to these short term injection tests, the resulting computed pressure history is not in good agreement with the high-frequency features of the observed pressure signal. Consequently, Garg, et al. (1991) presented an alternative "anisotropic line-source model", which assumes that the east-west permeability is much smaller than the north-south permeability. (The earlier "channel model", on the other hand, assumes that the east-west permeability is sufficiently large that the reservoir behaves in an essentially one-dimensional manner.) This "anisotropic line-source model" (which is not too different from the "channel model" as regards the reservoir cross-section and the distances to the northern and southern boundaries) was successfully used to explain both the 1986 and 1989 test data.

Double porosity channel model

As an alternative, we herein present a "double porosity channel model", which has the same geometry, boundary conditions and global properties (transmissivity and

storativity) as those of the "channel model" originally developed by Pritchett, et al. (1989). In the present model, a MINC representation (Pruess and Narasimhan, 1982) is used to represent the influence of fractured reservoir behavior. The essential hypothesis is that the lack of good high-frequency agreement between short-term pressure test results and the original "channel" model arises from the latter's "porous medium" assumption that pressures equilibrate instantaneously between the relatively high-permeability "fracture zone" and the relatively low-permeability "country rock".

These calculations were performed using the STAR general-purpose geothermal reservoir simulator (Pritchett, 1989). In the "double porosity (MINC) medium" representation, on the sub-grid scale the STAR simulator idealizes a "typical" block of country rock (matrix) as a sphere, surrounded by a concentric spherical shell of high-permeability material representing the fracture zone. In the present calculations, the matrix region was subdivided into 10 concentric spherical shells for numerical purposes (for explanation of the MINC representation employed in the STAR code, see e.g. Pritchett and Garg, 1990).

In the "porous medium" limit, the present model gives results identical to the analytical solutions for the "channel model" originally proposed by Pritchett, et al. (1989). As shown in Figure 4, pressure values computed using the present model with a "porous medium" representation are in good agreement with the measured 1986 pressure history. On the other hand, the computed response does not reproduce the measured 1989 data very well (see Figure 5). The overall pressure rise is approximately reproduced, but high-frequency fluctuations are not adequately represented.

To try to improve agreement with the 1989 data, we next carried out a series of calculations using the "double porosity channel model", varying the fracture-to-total storage ratio (ω) and the permeability of the matrix (k_m) within the following range:

$$0.01 < \omega = \psi\phi_f/\phi < 0.3$$

$$10^{-18} < k_m < 10^{-16} \quad (m^2)$$

where ψ is the fracture zone volume fraction, ϕ_f is the porosity of fracture zone, and ϕ $(=\psi\phi_f+(1-\psi)\phi_m)$ is the total porosity, fixed at 0.05 (ϕ_m: the porosity of representative matrix block). The upper limit on k_m was set such that the time required for pressure equilibrium to be reached between the fracture zone and the matrix block would exceed 10 hours, the representative time-scale of individual injection events in the 1989 test. This time (see e.g. Pritchett and Garg, 1990) may be expressed as:

$$\tau = \phi_m C_t \rho \nu \lambda^2 / 10 k_m$$

where λ is the fracture spacing (the diameter of the representative spherical matrix block). On the basis of drilling experience in the "AA" formation, λ was assumed

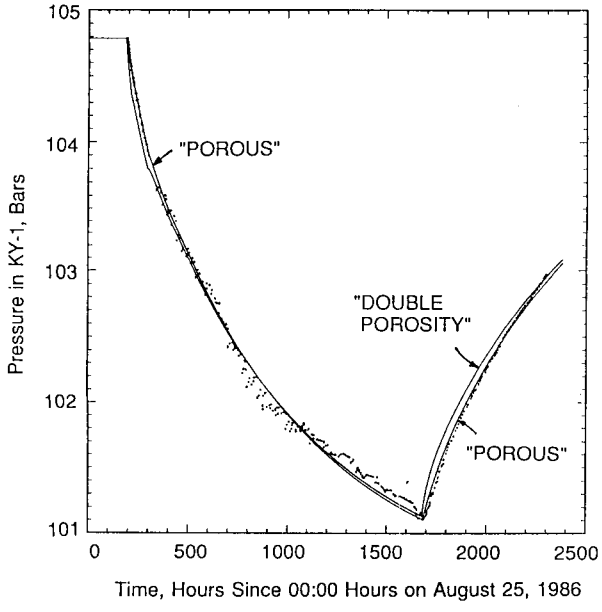

Fig. 4. Comparison of computed 1986 pressure disturbances in well KY-1 with measurements.

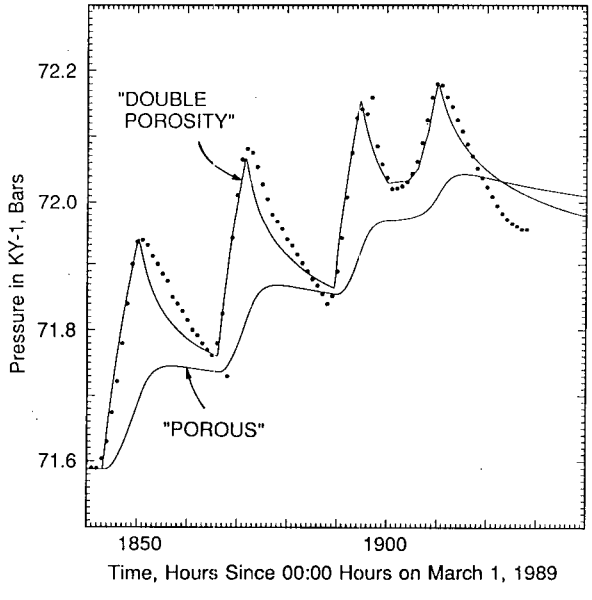

Fig. 5. Comparison of computed pressure response of KY-1 with measurements due to 1989 cold water injection into well S-4.

to be 100 meters and was not changed during the series of calculations.

The 1989 test data was best explained by the present model using the following parameter values:

$\omega = 0.2$

$k_m = 10^{-17}$ m^2

As shown in Figure 5, the agreement between the measured and computed response is reasonably good. The falloff after each injection in the measured data is slower than the computed response; this is probably explained by the fact that observation well KY-1 does not itself intersect any large permeable fractures (responsible for the observed pressure response); although KY-1 reacts quickly to pressure changes in the "AA" aquifer, the injectivity measured for well KY-1 is very low.

The 1986 pressure response computed using the present "double porosity channel model" with the above parameter values is shown in Figure 4. In view of the uncertainty associated with the 1986 well S-4 flow rate data (see e.g. Garg et al., 1991), the agreement between the measured and computed response, while not as good as that for "porous medium" case, is certainly adequate.

An extensive two-phase (water/steam) flow zone is present in the southern part of the Sumikawa reservoir under natural state conditions (see e.g. Pritchett et al., 1991). When fluid production begins, the volume of the two-phase zone is expected to increase substantially and to invade the north-south channel in the "AA" layer due to production-induced pressure decline. This "AA" aquifer represents the main production horizon for the Sumikawa field. Under two-phase conditions the effective total compressibility (C_t) can be quite large, so that for the present "double porosity channel model" the time required for pressure equilibrium between fracture and matrix zones to be attained can reach as much as 30 years (as compared to 10 days for the single-phase liquid case), which is comparable to the economic lifetime of the reservoir. Under these conditions, as discussed by Pritchett and Garg (1990) some treatment other than the traditional "equivalent porous medium" representation will be required to predict reservoir behavior under exploitation.

REFERENCES

Garg, S.K., J.W. Pritchett, K. Ariki and Y. Kawano (1991) "Pressure-Interference testing of the Sumikawa Geothermal Field", Proc. Sixteenth Workshop on Geothermal Reservoir Engineering, Stanford University.

Ishido, T., T. Kikuchi and T. Noda (1989) "Analysis of Pressure Transient Test Data from Well SN-7D", presented at the Annual Meeting of the Geothermal Research Society of Japan, Tokyo, Oct. 23 - 25.

Kawano, Y., H. Maki, T. Ishido and Y. Kubota (1989) "NEDO's Project on Geothermal Reservoir Engineering: A Reservoir Engineering Study of the Sumikawa Geothermal Field, Japan", Proc. Fourteenth Workshop on Geothermal Reservoir Engineering, Stanford University, pp. 55 - 59.

Pritchett, J.W. (1989) "STAR User's Manual", S-Cubed Report SSS-TR-89-10242.

Pritchett, J.W. and S.K. Garg (1990) "On Similitude, Heat Conduction, and Two-Phase Flow in Fractured Porous Media", Proc. Fifteenth Workshop on Geothermal Reservoir Engineering, Stanford University.

Pritchett, J.W., S.K. Garg, K. Ariki and Y. Kawano (1991) "Numerical Simulation of the Sumikawa Geothermal Field in the Natural State", Proc. Sixteenth Workshop on Geothermal Reservoir Engineering, Stanford University.

Pritchett, J.W., S.K. Garg, H. Maki and Y. Kubota (1989) "Hydrology of the Sumikawa Geothermal Prospect, Japan", Proc. Fourteenth Workshop on Geothermal Reservoir Engineering, Stanford University, pp. 61 - 66.

Pruess, K. and T.N. Narasimhan (1982) "A Practical Method for Modeling Fluid and Heat Flow in Fractured Porous Media", presented at the Reservoir Simulation Symposium of the Society of Petroleum Engineers, New Orleans, Louisiana, Jan. 31 - Feb. 3. (Also see SPE Journal, Feb. 1985, pp. 14 - 26.)

PROCEEDINGS, Seventeenth Workshop on Geothermal Reservoir Engineering
Stanford University, Stanford, California, January 29-31, 1992
SGP-TR-141

PRODUCTION DIAGNOSTICS OF GEOTHERMAL WELLS BY MEANS OF A COMPUTERIZED EXPERT SYSTEM

Victor M. Arellano, Eduardo R. Iglesias,
Gregorio San Román and David Nieva

Instituto de Investigaciones Eléctricas
Departamento de Geotermia
Apartado Postal 475, Cuernavaca 62000, Mor., México

ABSTRACT

Diagnostic of production problems in geothermal wells is a complex inferential task, which requires considerable knowledge of its possible causes, careful assessment of (sometimes bewildering) multidisciplinary evidence, and, of course, enough experience. These characteristics make this task a good candidate for a computerized expert system. On this conviction, we have developed the first version of WELL_DR, an expert system for geothermal-well production diagnostics. Though still in a rapid stage of evolution, this expert system already provides a convenient and useful tool for geothermal field development, operation and management.

INTRODUCTION

Energy production is the ultimate goal of any geothermal development. Energy production is accomplished through wells. Wells act as conduits for production of fluid and heat, and provide crucial information about the reservoir (or reservoirs) they intersect. For these reasons, wells are critical components of exploited geothermal fields.

Production of geothermal wells varies with time. This may be due to "normal" or to "pathological" causes. Normally, well production diminishes with time due, mainly, to exploitation-induced reservoir pressure drawdown. Figures 1-5 show an example of this type of behavior. They also demonstrate the type of information often available about the production history of a geothermal well.

On the "pathological" side, several causes may impair the capacity of a well as a conduit. For example, mechanical damage of its internal casing (piping), scaling by minerals precipitated from the produced fluid, partial occlusion by measuring or drilling equipment accidentally left in the well, etc. Production

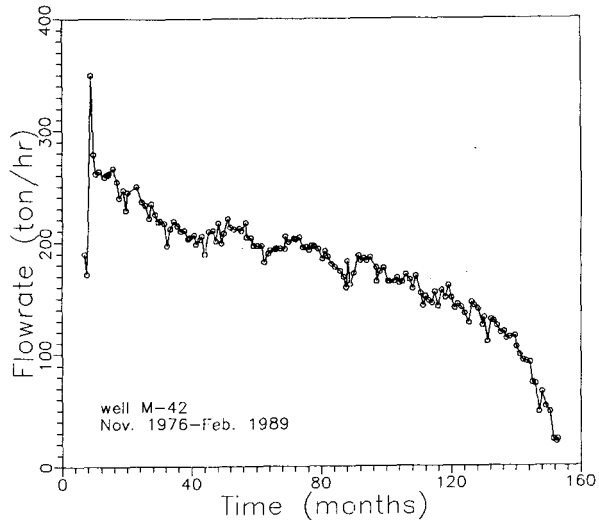

Fig. 1 Flowrate history of Cerro Prieto well M-42.

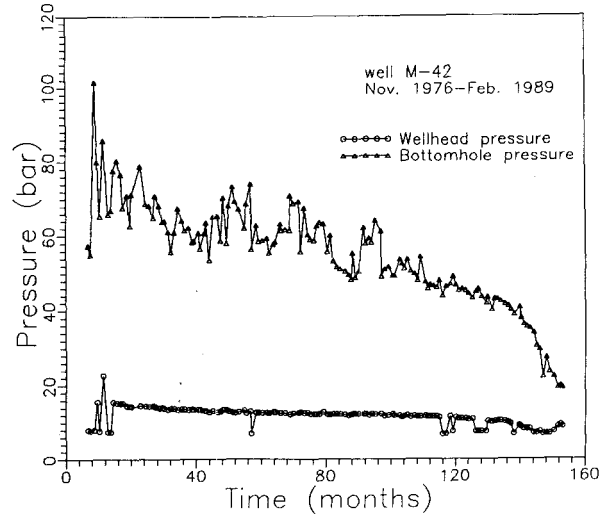

Fig. 2 Pressure history of Cerro Prieto well M-42.

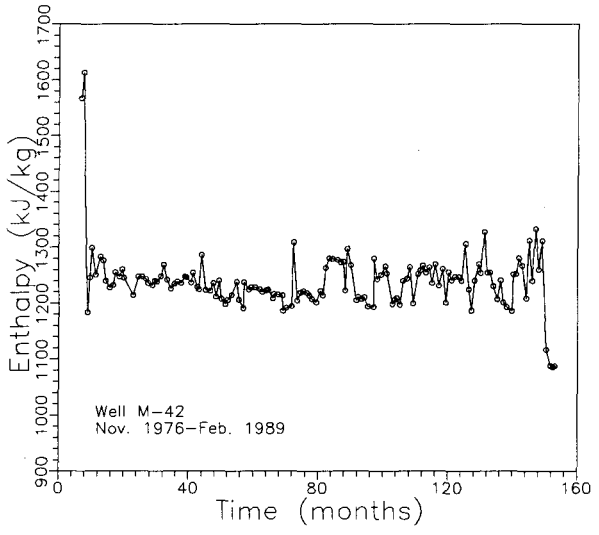

Fig. 3 Enthalpy history of Cerro Priero well M-42.

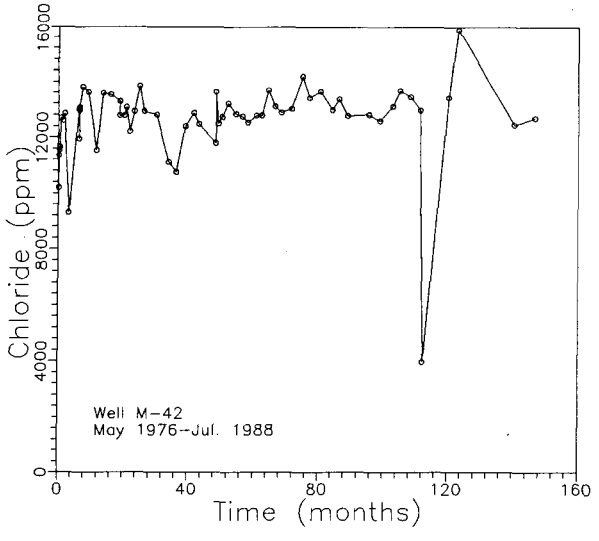

Fig. 4 Chloride history of Cerro Prieto well M-42.

may also be influenced by many "pathological" causes affecting the reservoir (or reservoirs) intersected by the well. These include invasion by colder waters from neighboring aquifers or from injection of spent brines, permeability reduction near the well by mineral deposition triggered by boiling or by mixing of different fluids, production from two or more reservoirs having fluids with different enthalpies or chemical compositions, etc., and combinations of these. Often

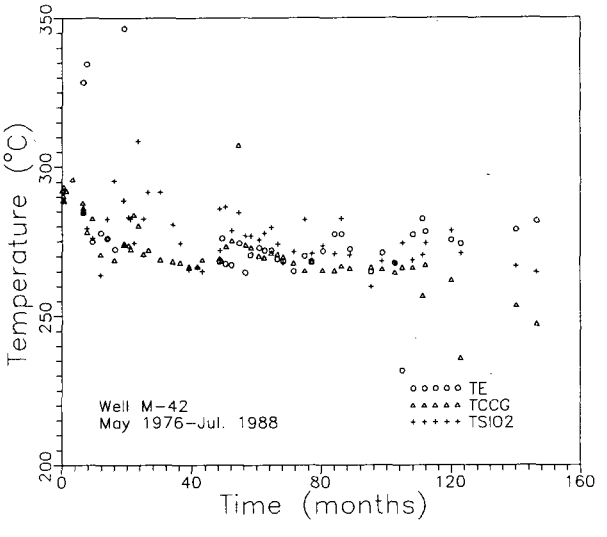

Fig. 5 Geothermometric temperature histories of Cerro Prieto well M-42.

some of these causes affect production not only at the reservoir level, but also by impairing the capacity of the well as a conduit (e.g., scaling of the well piping induced by the arrival of a cold front).

From a practical point of view, production problems can be classified into those that affect only one well, and those that affect some or all the wells in a certain area. In economic terms, the latter are obviously more important. In general, production problems with the capacity to affect a significant area, or even a whole field, can be detected early in one or a few wells, before much damage is done. Early detection allows, in many cases, implementation of remedial actions to correct the causes of the problem, or to delay as much as possible their effects on production. Though usually less important, diagnostic of individual well production problems is also economically significant. For these reasons, diagnostic of production problems in wells is a crucial capability to have, for successfully managing geothermal fields.

Diagnostic of production problems in geothermal wells is a complex inferential task, which requires considerable knowledge of its possible causes, careful assessment of (sometimes bewildering) multidisciplinary evidence, and, of course, enough experience. These characteristics make this task a good candidate for a computerized expert system. On this conviction, we have developed the first version of WELL_DR, an expert system for geothermal-well production diagnostics.

We are unaware of any previous similar work.

The next section describes the architecture of WELL_DR, the following section presents application examples and the last section presents the conclusions.

ARCHITECTURE OF WELL_DR

For prototyping and developing WELL_DR we chose a commercial, generalized expert system development package (a shell, in the parlance of the trade). For practical reasons (cost, hardware availability, installed base, portability), we adopted a shell that runs on personal computers under the DOS operative system. Should WELL_DR grow beyond reasonable response time running in DOS platforms, it could be easily ported to platforms with greater computational resources, because there are versions of the adopted shell that run in workstations and minicomputers under the UNIX and VMS operative systems.

Like most other expert system implementations, this shell offers three main components: an inference engine, a user interfase and a knowledge base.

Inference engine

The inference engine drives the diagnostic process. It may operate either in forward or backward chaining mode. Normally, the inference engine test rules by looking for the first rule with the first final (as oposite to intermediate) conclusion (final conclusions = diagnostics are assigned an order by the developer) in its THEN or ELSE part, and tests the IF condition of that rule. If any information on the IF conditions can be derived from other rules, those rules are invoked through backward chaining. The program then looks for the next rule relevant to the first final conclusion, etc., until it has gone through all of the rules. The process is then repeated for those rules relevant to the second final conclusion, third final conclusion, etc., until the list of final conclusions is completely tested. If a rule is not relevant to any final conclusion, or does not assign values to a variable whose value is displayed at the end of a run, it will not be used.

User interfase

The user interfase implements dialogue boxes, in which WELL_DR asks for the necessary information. Some dialogue boxes include technical graphs to help the user decide what type of trend is present in his data. Figures (6-7) illustrate some technical graphs already in use. At any stage of the process, the user can ask why a particular conclusion was reached, and get the corresponding explanation. If more than one diagnostic is possible, the program will provide a list of the possible diagnostics arranged in order of probability.

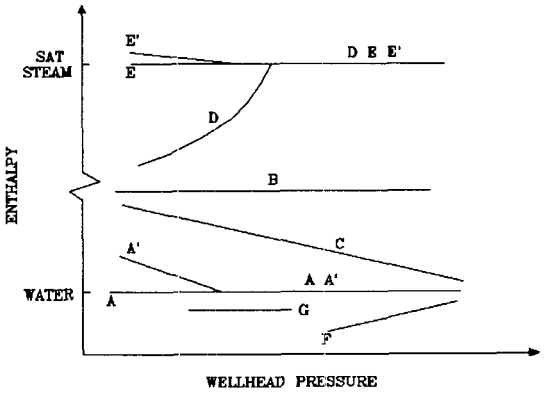

Fig. 6 Output curves: form of the variation of enthalpy with wellhead pressure (After Grant et al., 1982).

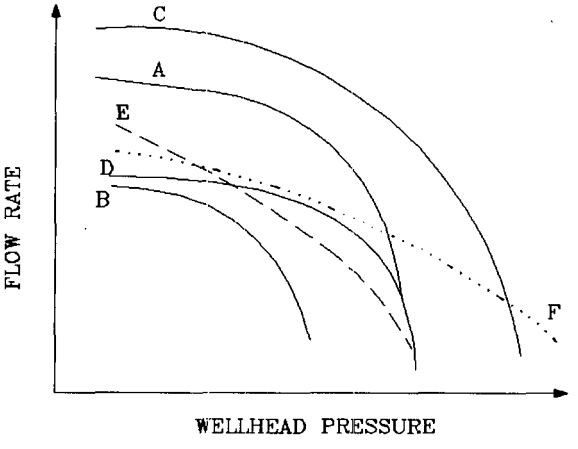

Fig. 7 Output curves: form of the variation of mass flow with wellhead pressure (After Grant et al., 1982).

Knowledge base

The knowledge base uses a knowledge representation scheme based on production rules. These rules are of the well-known IF-THE-ELSE form. They include heuristic probabilities assigned by the developers. There are three choices to assign probabilities. One of them allows computation of dependent and of independent probabilities, at will. This is the choice adopted for WELL_DR.

Currently, our knowledge base includes more than 65 rules. The number of final conclusions (diagnostics) that can be reached is 24.

Our knowledge base was compiled from our own and other people's experience. Main contributions came from Arellano et al. (1990), Arellano et al. (1991), Grant et al. (1981), Grant et al. (1982), Nathenson (1975), Truesdell et al. (1979), Truesdell et al. (1989).

Whenever possible, we tried to test the final conclusions (diagnostics) by more than one independent line of evidence. To that end, the knowledge base includes three main topics:

Initial state of the well

Production tests

Production history

In the cases where the diagnostic is backed by more than one independent line of evidence, the probability of the diagnostic is computed correspondingly.

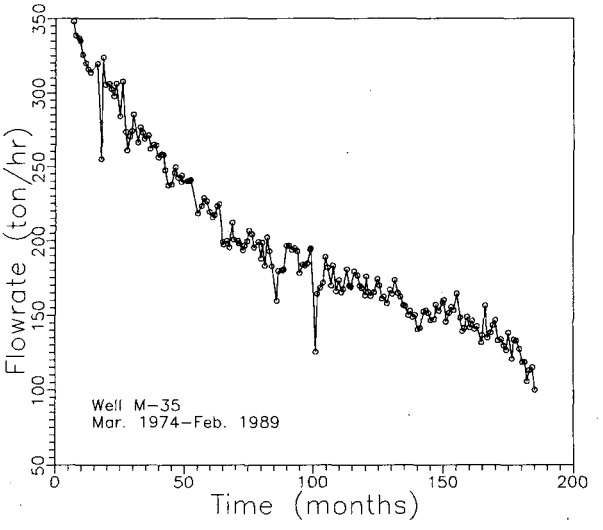

Fig. 8 Flowrate history of Cerro Prieto well M-35.

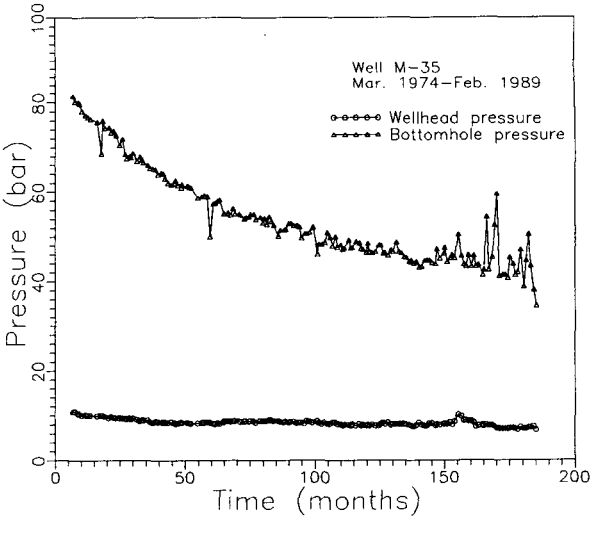

Fig. 9 Pressure history of Cerro Prieto well M-35.

APPLICATION EXAMPLES

This example deals with well M-35 from the Cerro Prieto, Mexico, geothermal field. Figures (8-12) illustrate production histories of this well.

This case was correctly diagnosed as "chemical breaktrough of cooler water", with a confidence of 9.4/10, from two independent rules:

RULE 22

IF [CHLORIDE DECREASES WITH TIME AND DISCHARGE ENTHALPY DECREASES WITH TIME]

THEN

[CHEMICAL BREAKTHROUGH OF COOLER WATER]

CONFIDENCE = 7/10

RULE 23

IF [TE = TSIO2 > TCCG]

THEN

[CHEMICAL BREAKTHROUGH OF COOLER WATER]

CONFIDENCE = 7/10

Figures 10-11 indicate that the conditions of Rule 22 are met by this well, and Fig. 12 shows that the conditions of Rule 23 are also satisfied. Data plots like (8-12) must be available to the user running the diagnostic analysis, in order to answer the questions posed by WELL_DR.

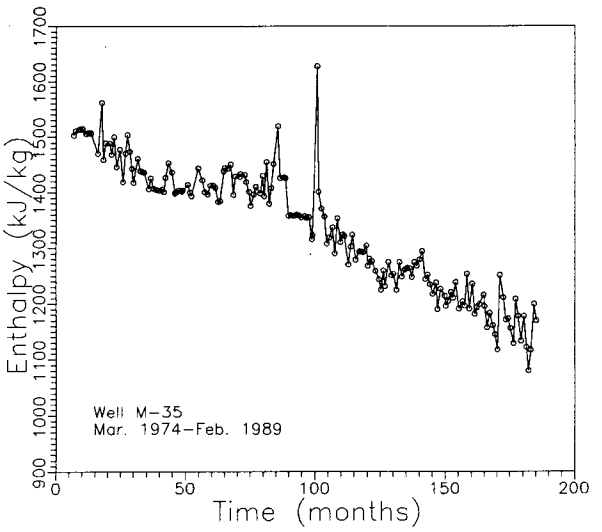

Fig. 10 Enthalpy history of Cerro Priero well M-35.

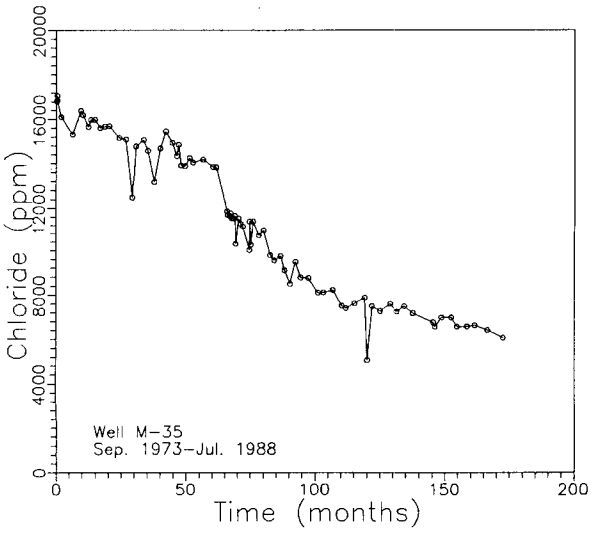

Fig. 11 Chloride history of Cerro Prieto well M-35.

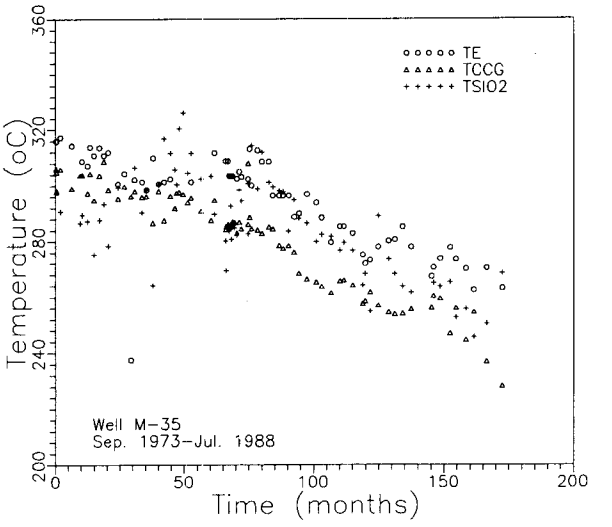

Fig. 12 Geothermometric temperature histories of Cerro Prieto well M-35.

The next example demonstrates the usefulness of the technical graphs presented by WELL_DR to the user, when trying to prove certain groups of rules. The user is asked to compare his data plots to those shown in the screen, and choose the option that best resembles his data. Thus, the user would compare Fig. 13 with Fig. 7, and choose A and D. WELL_DR would then conclude that there is scaling in the wellbore with confidence equal to 6/10. This conclusion would be correct: in June 1986 well M-109 from Cerro Prieto had to be reworked due to scaling.

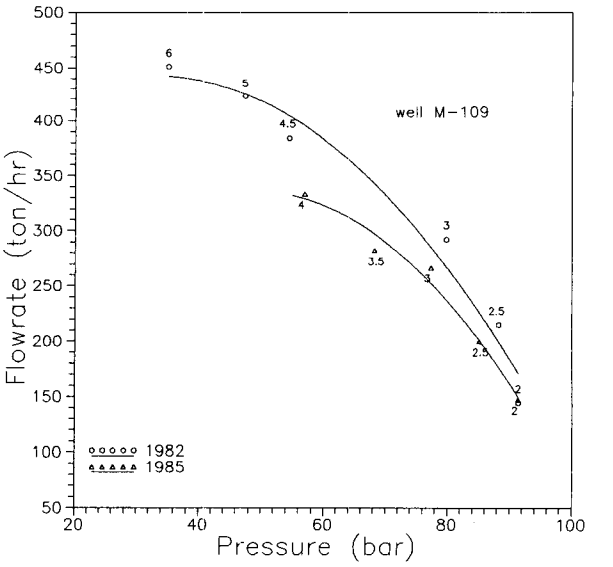

Fig. 13 Output curves of Cerro Prieto well M-109.

SUMMARY AND CONCLUSIONS

We have developed the first version of WELL_DR, an expert system for geothermal-well production diagnostics.

WELL_DR was implemented with a commercial, generalized expert system development package. It runs on personal computers under the MS-DOS operative system. Its knowledge base consists of IF-THE-ELSE type rules that include heuristic probabilities.

Interaction with the user is implemented via dialogue boxes, in which WELL_DR asks for the necessary information. Some dialogue boxes include technical graphs to help the user decide what type of trend is present in his data. The user can ask why a particular conclusion was reached, and get the corresponding explanation. If more than one diagnostic is possible, the program will provide a list of the possible diagnostics arranged in order of probability.

Though still in a rapid stage of evolution, this expert system already provides a convenient and useful tool for geothermal field development, operation and management.

REFERENCES

Arellano, V.M., Barragan, R.M., and Nieva, D., (1990), "Desarrollo de criterios de operación para minimizar problemas de obturación de la zona de alimentación de pozos de Cerro Prieto", Informe IIE/11/2730/I 02/F, Cuernavaca, Mor.

Arellano, V.M., Nieva, D., Barragan, R.M., and De Leon J., (1991), "Developments in geothermal energy in Mexico-Part thirty-seven. Procedure to diagnose production abatement problems in geothermal wells", Heat Recovery Systems & CHP, Vol. 11, No. 6, pp. 471-481.

Grant, M., Truesdell, A.H., and Mañon, A., (1981) "Production induced boiling and cold water entry in the Cerro Prieto geothermal reservoir indicated by chemical and physical measurements", Proceedings Third Symposium on the Cerro Prieto Geothermal Field, Baja California, México, San Francisco Ca., March 24-26, pp. 221-237.

Grant, M., Donaldson, I., and Bixley P., (1982), "Geothermal reservoir engineering", Academic Press, New York, pp. 137-144

Nathenson, M. (1975), "Physical factors determining the fraction of stored energy recoverable from hydrothermal convection systems and conduction dominated areas", U.S. Geological Survey Open-file Report 75-525, 51 p.

Truesdell, A.H., Mañon, A., Jimenez, E., Sanchez, A., and Fausto, J., (1979), "Geochemical evidence of drawdown in the Cerro Prieto geothermal field", Geothermics, Vol. 8, pp. 257-265.

Truesdell, A.H., Aunzo, Z., Bodvarsson, Alonso, J., and Campos, A., (1989), "The use of Ahuachapan fluid chemistry to indicate natural state conditions and reservoir processes during exploitation", Proceedings, Fourteenth Workshop on Geothermal Reservoir Engineering, Stanford University, Stanford Ca., January 24-26, pp. 273-278.

PROCEEDINGS, Seventeenth Workshop on Geothermal Reservoir Engineering
Stanford University, Stanford, California, January 29-31, 1992
SGP-TR-141

FRACTURE OPENING/ PROPAGATION BEHAVIOR AND THEIR SIGNIFICANCE ON PRESSURE-TIME RECORDS DURING HYDRAULIC FRACTURING

Takashi Kojima, Yasuhiko Nakagawa*
Koji Matsuki and Toshiyuki Hashida

Faculty of Eng., Tohoku Univ., Sendai 980
* Hitachi Tohoku Software,LTD.,Sendai 980

ABSTRACT

Hydraulic fracturing with constant fluid injection rate was numerically modelled for a pair of rectangular longitudinal fractures intersecting a wellbore in an impermeable rock mass, and numerical calculations have been performed to investigate the relations among the form of pressure-time curves, fracture opening/propagation behavior and permeability of the mechanically closed fractures. The results have shown that both permeability of the fractures and fluid injection rate significantly influence the form of the pressure-time relations on the early stage of fracture opening. Furthermore it has been shown that wellbore pressure during fracture propagation is affected by the pre-existing fracture length.

INTRODUCTION

Hydraulic fracturing is widely used for stimulating low permeability reservoirs in geothermal, oil and gas fields. In order to accomplish the fracturing job efficiently, it is desirable to know the fracture opening/propagation behavior and the permeability of the fracture during the job. In this study, in order to extract these information from pressure-time records during the hydraulic fracturing, the fracturing process was numerically simulated. Recent years, a number of mumerical studies for hydraulic fracturing were reported, for example, Lam et al.(1988), Vandamme et al.(1989) and Boone et al.(1990). However mostly the purposes were to design hydraulic fracturing and to estimate the fracture dimensions. Accordingly they assumed incompressible fluid flow, which is valid for the purposes, and didn't pay enough attention to pressure-time curves. For simulating a complete pressure-time curve, we must consider the compressibility of fluid. Numerical simulations, in which the compressibility of fluid was taken into account, were carried out by Hardy et al.(1989) and Ito et al.(1990), whose purpose was to investigate fracture reopening pressure for techtonic stress measurement with hydraulic fracturing. However these studies were restricted to the simulations of small scale fracturing.

In our numerical study, by taking the compressibility of fluid into account, the relations between fracture opening/propagation behavior and pressure-time curves were investigated. We numerically modelled the hydraulic fracturing conducted on a pair of pre-existing fractures intersecting a wellbore. This is the case often experienced in actual geothermal fields. In addition, permeability of the mechanically closed fractures were taken into account as one of parameters in the numerical calculations.

MATHEMATICAL FORMULATION OF THE PROBLEM

Consider a pair of pre-existing rectangular fractures intersecting a vertical wellbore in a rock mass which is assumed to be homogeneous, isotropic, linear elastic, infinite and impermeable. By injecting fluid with constant rate through the wellbore, the fractures open and propagate. The geometry of the hydraulic fracturing model is shown in Fig.1 with

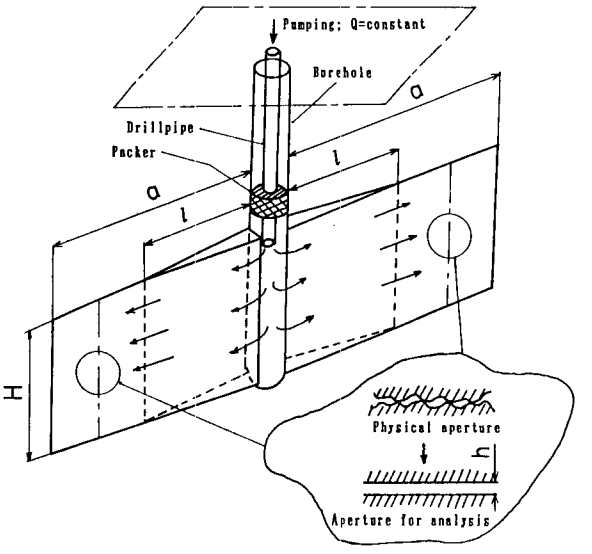

Fig.1. The model of hydraulic fracturing for numerical analysys.

symbols of dimensions we used. We made the following additional assumptions:

(1) The hight of the fractures is constant.

(2) Slippage at the top and the bottom of the fracture is allowed in the direction perpendicular to the fracture plane. Therefore the cross sectional area perpendicular to the direction of fracture propagation is rectangular in shape.

(3) There is no leak-off of the injection fluid. All the fluid is used for pressurization of the system (a drillpipe and a packed section of the wellbore) and the fractures.

(4) The fluid flow in the fractures are 1-D laminar flow parallel to the direction of fracture propagation.

(5) The flow rate at the tips of the fractures is zero.

(6) Although the fractures are mechanically closed, there are pore spaces available for fluid flow because of asperities at the surfaces. We substituted the physical aperture by the aperture h between smooth paralell walls (Fig.1). This aperture is equivalent to the physical aperture in permeability, and, here, is named hydromecanical aperture of a closed fracture.

From the above assumptions, the problem of fracture opening/propagation was reduced to a plane strain problem concerning with 2-D surface cracks emanating from a cylindrical cavity in an infinite elastic medium (Fig.2). Let (x,y) be the Cartesian

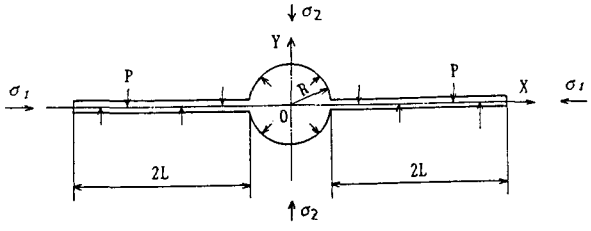

Fig.2. Two-dimensional modelling of fractures for stress / displacement analysis.

coordinate system with the origin at the center of the cavity, as shown in Fig.2. The cavity and the cracks are subjected to a fluid pressure $P(x)$ and the elastic medium is subjected to a biaxial compressive stress field (σ_1 and σ_2, $\sigma_1 > \sigma_2$) at infinity. R and $2L$ denote the radius of the cavity and the length of the cracks, respectively. In the analysis of fracture opening, $2L$ corresponds to fracture opening length l (Fig.1), and in the analysis of fracture propagation, it corresponds to fracture length a (Fig.1). Here, by using complex stress functions and the method of continuous distribution of edge dislocations, this problem comes to solving a singular integral equation of the Cauchy type (Hayashi et al., 1989), where the unknown function is the gradient of the crack opening displacement $b(x)$ along the crack line. The basic integral equation is:

$$\gamma \int_R^{R+2L} \{\frac{1}{x-\tau} + \frac{1}{R}K(x,\tau)\}b(\tau) = f(x), \qquad (R < x < R+2L), \tag{1}$$

where

$$K(x,\tau) = R\{-\frac{1}{x+\tau} + 2\frac{\tau^2-R^2}{\tau x^2} - \frac{\tau}{\tau x - R^2} + \frac{\tau}{\tau x + R^2} - \frac{\tau(\tau^2-R^2)}{(\tau x - R^2)^2} - \frac{\tau(\tau^2-R^2)}{(\tau x+R^2)^2} + \frac{R^2(\tau^2-R^2)^2}{\tau(\tau x - R^2)^3} - \frac{R^2(\tau^2-R^2)^2}{\tau(\tau x+R^2)^3}\}, \tag{2}$$

$$f(x) = \frac{1}{4}(\sigma_1+\sigma_2)(1+\frac{R^2}{x^2}) - \frac{1}{4}(\sigma_1-\sigma_2)(1+\frac{3R^4}{x^4}) - \frac{1}{2}(P(x)+\frac{R^2}{x^2}P(R)), \tag{3}$$

$$\gamma = \frac{G}{4\pi(1-\nu)}, \tag{4}$$

Here G and ν are shear modulus and Poisson's ratio, respectively. Crack opening displacement $w(x)$ and stress intensity factor K_I are given by:

$$w(x) = -\int_{R+2L}^{x} b(\tau)d\tau, \tag{5}$$

$$K_I = \lim_{x \to (R+2L)^+} \sqrt{2\pi(x-(R+2L))}\,\sigma_y = 4\sqrt{\pi L}\,\sigma_2 \phi(1), \tag{6}$$

where ϕ is a bounded function on the crack such that:

$$\frac{G}{4(1-\nu)\sigma_2} b(x) = \phi\left(\frac{x-L-R}{L}\right)\sqrt{\frac{x-R}{2L+R-x}}, \tag{7}$$

Let $W(x)$ denote the fracture width, which is given by adding the hydromechanical aperture h of the closed fractures to the crack opening displacement $w(x)$, as:

$$W(x) = h + w(x), \tag{8}$$

For the fluid flow in the fracture, the equation of continuity is:

$$\frac{\partial}{\partial t}(\rho W) + \frac{\partial}{\partial x}(\rho u W) = 0, \tag{9}$$

where ρ is the density of the fluid and u denotes the flow rate that is given by:

$$u = -\frac{W^2}{12\mu}\frac{\partial P}{\partial x}, \tag{10}$$

where μ is the fluid viscosity. For a fluid whose compressibility is β,

$$\frac{\partial \rho}{\partial t} = \rho\beta\frac{\partial P}{\partial t}, \qquad \frac{\partial \rho}{\partial x} = \rho\beta\frac{\partial P}{\partial x}, \tag{11}$$

Equations (9)-(11) lead to the following differential equation governing $W(x)$ and $P(x)$:

$$W\beta\frac{\partial P}{\partial t}+\frac{\partial W}{\partial t}=\frac{\partial}{\partial x}\left(\frac{W^3}{12\mu}\frac{\partial P}{\partial x}\right), \tag{12}$$

The initial and boundary conditions are:

$$P=P_0, \qquad W=h, \tag{13}$$

$$\left.\begin{aligned} &Q=Q_D+Q_C, && Q_D=\beta V_D\frac{\partial P}{\partial x}\Big|_{x=R}, \\ &Q_C=-\frac{HW^3}{6\mu}\frac{\partial P}{\partial x}\Big|_{x=R}, && \frac{\partial P}{\partial x}\Big|_{x=a}=0, \end{aligned}\right\} \tag{14}$$

where P_0 is the initial value of $P(x)$ and Q is the volumetric flow rate of the injected fluid, which is divided into Q_D used for pressurization of the system and Q_C for the fracture, and V denotes the volume of the system. From equations (12)-(14), the changes of the wellbore pressure $P(R)$ with time are obtained.

NUMERICAL PROCEDURE

The fracture opening/propagation and the fluid flow in the fractures were coupled numerically by an iteration loop for each fracture opening/propagation step t, as illustrated in Fig.3. First we estimate both the fracture width distribution W^t at the fracture opening(or propagation) length $2L^{t-1}+\Delta L$ and the time Δt required to an extention of opening(or propagation) length ΔL. Secondly using these estimated values and the implicit method, equation (12) is solved numerically to give the pressure distiribution P^t. Thirdly from P^t and equations (1)-(8), a stress intensity factor K_I and a temporary fracture width distribution W^* are obtained. Equation (1) was solved numerically using Causs-Jacobi integration formular (Erdogan, 1978). Finally comparing K_I with the fracture toughness of rock K_{IC}($K_{IC}=0$ for fracture opening) and comparing W^* with W^t, thier differences was checked. The maximum error allowed was 10^{-5} MPa m for $|K_{IC}-K_I|$and 0.01 for $|W^*-W^t|/W^t$. At the (j+1)th iteration the fracture width W_{j+1} is estimated by:

$$W_{j+1}=W_j+\lambda(W_j^*-W_j), \tag{15}$$

where λ is the relaxation parameter, which ranged from 0.5 to 0.7 in this study.

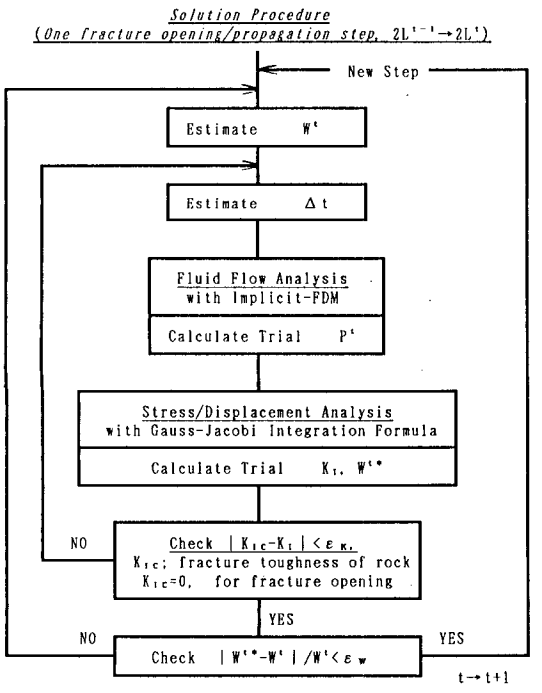

Fig.3. A flow chart of calculation procedure.

RESULTS AND DISCUSSION

Numerical calculations were performed to know the relations between fracture opening/propagation behavior and pressure changes with time by using the following values:
$\sigma_1=30$MPa, $\sigma_2=20$MPa, $P_0=10$MPa,
$G=3.5\text{X}10^4$MPa, $\beta=4.1\text{X}10^{-4}$MPa^{-1},
$\mu=5.5\text{X}10^{-10}$MPa·s
$R=0.682$m, $H=10$m, $V=3.0$m^3
The values associated with rocks were for hard rocks. In order to investigate the influences of both the fluid injection rate and the hydromechanical aperture of the closed fracture, Q and h were changed as $Q=10$, 100, 1000l/min and $h=10$, 500μm.

Opening Process of the Pre-exisiting Fractures

Fig.4 shows both the pressure-time curves and the change of fracture opening length with time for different hydromechanical aperture. In these calculations, the pre-existing fracture length a is long enough to be 1000m and Q is 100l/min. The pressure-time curves before the wellbore pressure reaches 17MPa aren't shown in the figures since the pressure-time curves are linear up to around 20MPa. The pressure at which the fractures begin to open is 15MPa in these cases. Therefore, it can be seen that the beginning of the fracture opening has no effect on the pressure-time curves, which is consistent with the result reported by Ito et al.(1990). When h is 10μm (Fig.4(a)), the wellbore pressure exhibits nonlinear increase with time from 20MPa to the maximum, 20.8MPa, and decreases gradually after the peak. On the other hand, when h is greater ($h=500\mu$m, Fig.4(b)), the wellbore pressure has no peak and becomes almost constant after it reaches about 20MPa which is equal to σ_2. Thus, the permeability of the closed fractures significantly affects the form of

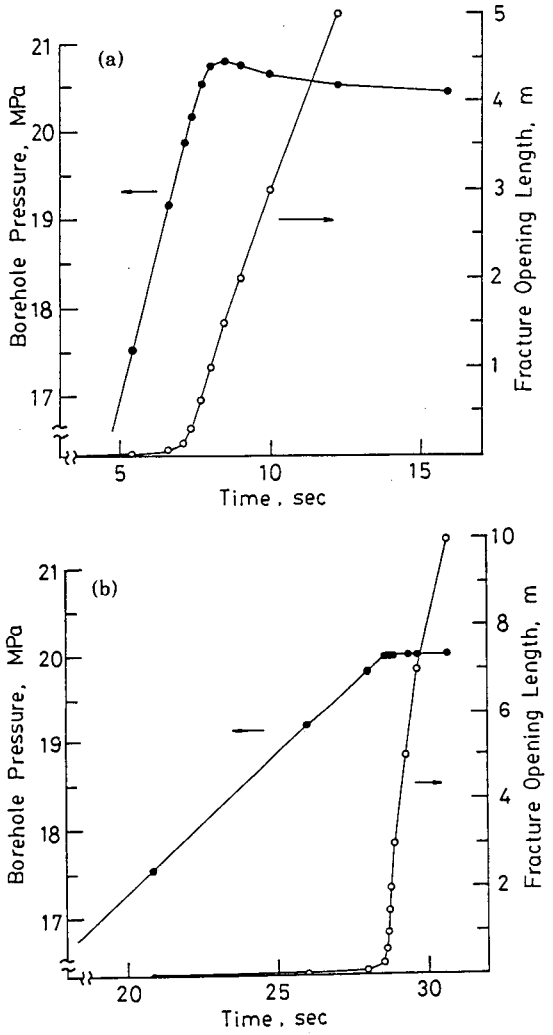

Fig.4. The change of borehole pressure and fracture opening length with time ((a) hydromechanical aperture $h=10\mu$m, (b) $h=500\mu$m).

pressure-time curves. Furthermore, from the change of fracture opening length with time, we can see that the fracture opening rate increases abruptly at the pressure, about 20MPa which is equal to σ_2.

As the peak in the pressure-time curves appear before the fracture opening length reaches 2m, let us look into the pressure distributions in the fracture within 2m from the wellbore surface (Fig.5). In the case of $h=10\mu$m, the pressure gradient in the opened portion is rather high owing to the low permeability of the closed portion, and the gradient begins to decrease from the wellbore side as the fractures open. In the case of $h=500\mu$m, on the other hand, the pressure gradient is fairly low due to the sufficiently high permeability. Figs.6(a) and 6(b) show the distributions of the fracture opening width, corresponding to Figs.5(a) and 5(b), respectively. The

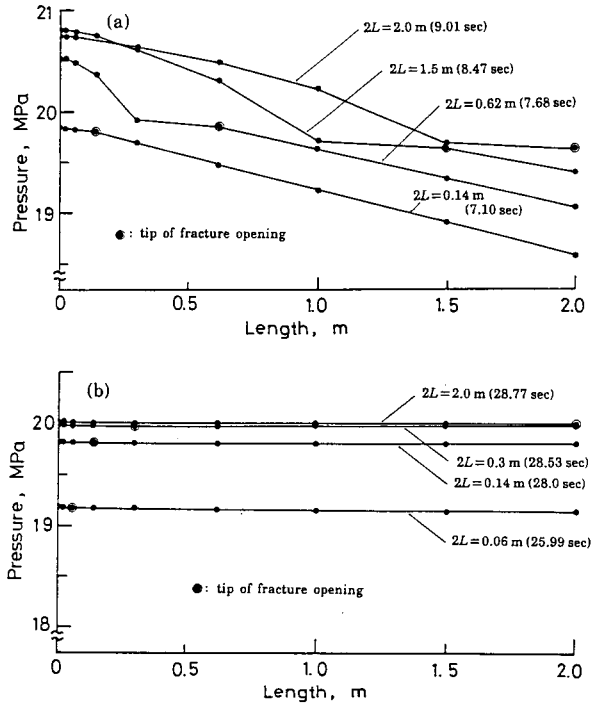

Fig.5. Pressure distribution in the pre-existing fracture during hydraulic fracturing ((a)hydromechanical aperture $h=10\mu$m, (b) $h=500\mu$m).

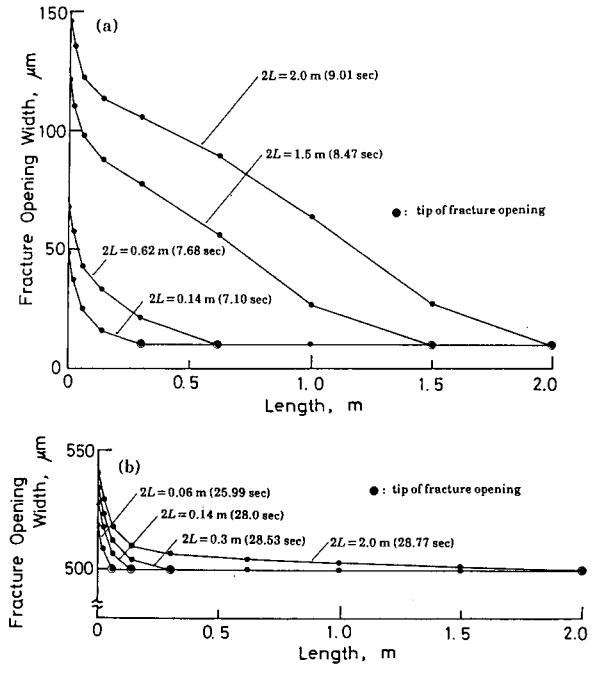

Fig.6. The distribution of fracture opening displacement during hudraulic fracturing ((a) hydromechanical aperture $h=10\mu$m, (b) $h=500\mu$m).

fracture opening displacements are greater in the case of $h=10\mu$m than those in the case of $h=500\mu$m because the pressure is much higher in the case of $h=10\mu$m. We can also see that in the case of $h=500\mu$m, the fracture opening displacement is considerably smaller than the hydromechanical aperture.

From Figs.5 and 6, we can now understand the reason for the differences in the form of the pressure-time curves shown Fig.4. When h is large, 500μm, because of the fairly low pressure gradient, the maximum pressure can not become significantly higher than 20MPa which is balanced with the normal stress acting across the fractures. On the other hand, when h is small, 10μm, the fluid pressure exceeds 20MPa at the wellbore in the early stage of fracture opening because of the higher pressure gradient. After that, by the further progression of fracture opening, the permeability and the volume of the aperture at the opened portion increase abruptly, and consequently the wellbore pressure begins to decrease. Thus, a clear peak appears in the pressure-time curves.

Fig.7 shows the influence of the hydromechanical aperture of the closed fractures on the pressure-time curves for various fluid injection rate, $Q=10$l/min, 100l/min and 1000l/min. In this figure, at the termination of each curves, the fracture opening length reaches 50m. As can be seen from the figure, both the permeability of the closed fractures and fluid injection rate have significant influence upon the form of pressure-time curves. The pressure-time curves have a peak only when the permeability is low enough, and the peak pressure becomes higher with the fluid injection rate. In adition, it is worthwhile to note here that in the case of $h=10\mu$m and $Q=1000$l/min, the pressure-time curve has a higher and sharper peak, whose form is similar to that of breakdown pressure which is observed at fracture initiation from a intact wellbore surface.

Fracture Propagation

Fracture propagations were simulated for the cases of pre-existing fracture length $a=1$m and $a=5$m, and the results are shown in Figs. 8(a) and 8(b), respectively. In these calculations, h, Q and K_{IC} were 10μm, 100l/min and 2.0MPa $\sqrt{\text{m}}$, respectively. In the case of $a=1$m, the pressure increases even after the fractures fully open and the pressure decreases soon after the fracture propagation. Accordingly the fracture propagation can be distinguished from the pressure-time curve. On the other hand, in the case of $a=5$m, the peak is induced only in the fracture opening process. As a consequence, it is difficult to distinguish the fracture propagation. By fracture mechanics consideration, it is obvious that the longer the pre-existing fracture length is, the lower the wellbore pressure which makes K_I of the fracture tip to be K_{IC}. Hence, it can be also concluded that for the pre-existing fracture whose length is greater than 5m, we can not know its propagation on the pressure-time cuve any longer.

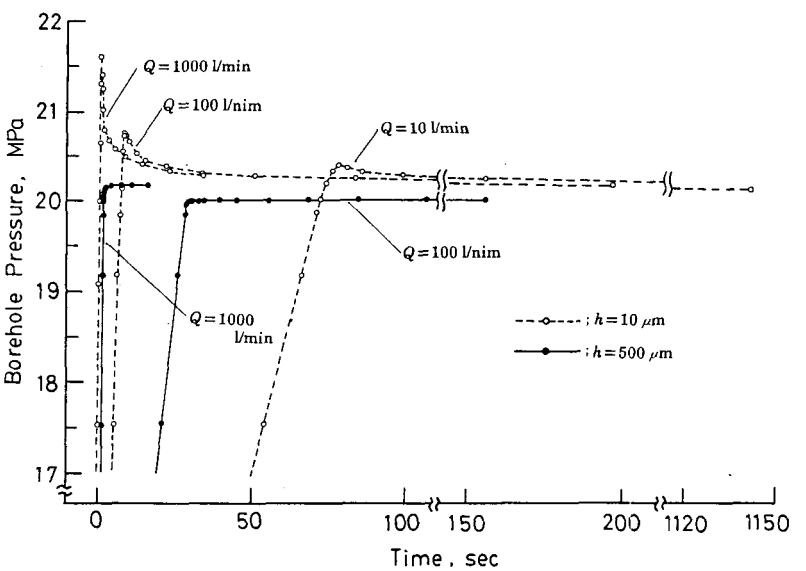

Fig.7. Influence of both permeability of fracture and fluid injection rate on pressure-time records during hydraulic fractureing.

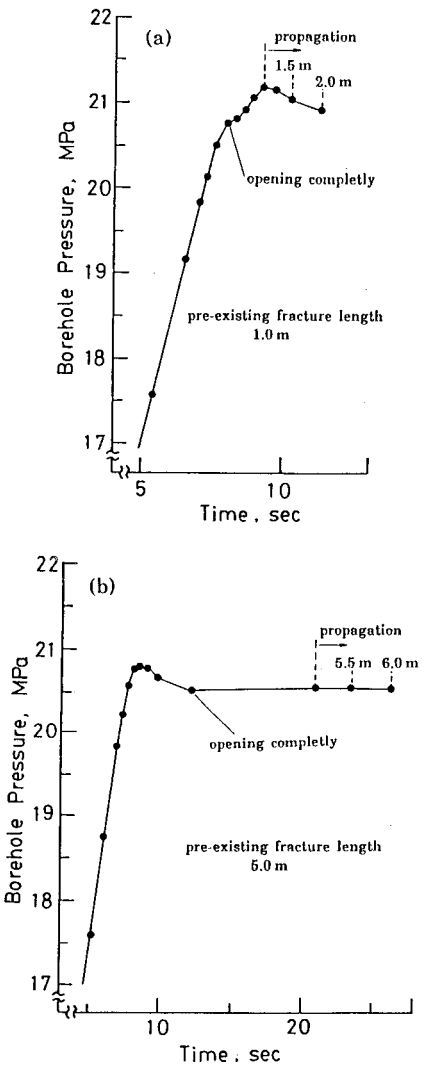

Fig.8. Influence of fracture propagation on pressure-time records during hydraulic fracturing ((a) pre-existing fracture length $a = 1$m, (b) $a = 5$m).

CONCLUDING REMARKS

In order to investigate the relations among fracture opening/propagation behavior, permeability of mechanically closed fracture and the form of pressure-time curves, hydraulic fracturing conducted on a pair of pre-existing fractures in a impermeable rock was numerically simulated and following results were obtained:

(1) Permeability of closed fracture affects significantly on the form of the pressure-time curves. When the permeability is sufficiently high, there is no peak in the pressure-time curves. On the other hand, when the permeability is low, the pressure-time curves have a peak, whose pressure becomes higher with the fluid injection rate.

(2) In the case of fracture propagation, wellbore pressure is influenced by the pre-existing fracture length. When the length is short enough, the pressure-time curves have the peak induced by the fracture propagation. On the other hand, when the length is long, the fracture propagation hardly influences the form of the pressure-time curves.

(3) In a series of hydraulic fracturing treatment, propping material injection for the sake of improving the fracture permeability is one of the important job. The dependence of the form of pressure-time curves on the permeability, which is shown in our results, shows that it is possible to judge the success of the job from the pressure-time records.

ACKOWLEDGMENT

The authors wish to thank Professors H.Abé, H.Takahashi and S.Suzuki, Faculty of Engineering, Tohoku University, for their encouragements throughout the course of the investigation. The authors also would like to acknowledge Pro. K.Hayashi, the Institute of Fluid Sience, Tohoku University, for his helpful advice.

REFERENCES

Boone,T.J. et al.(1990),"A Numerical Procedure for Simulation of Hydraulically-Driven Fracture Propagation in Porelastic Media," Int.J.Num.Anal.Methods Geomech., 14, 27-47

Erdogan,F.(1978),"Mixed Boundary-Value Problems in Mechanics," Mechnics Today, 4, 1-84

Hardy,M.P. et al.(1989),"Fracture Reopening during Hydrauric Fracuring Stress Determinations," Int.J.Rock Mech.Min.Sci.& Geomech.Abstr., 26, 489-497

Hayashi,K. et al.(1989),"Interpretation of Hydrauric Fracture Sut-in Curves for Tectonic Stress Measurement," Int.J.Rock Mech.Min.Sci.& Geomech.Abstr., 26, 477-482

Ito t. et al.(1991),"Theoretical Analysis of Crack Reopening Behavior in Hydraulic Fracturing Tectonic Stress Measurements," Transactions of the JSME, 57, 1715-1719

Lam,K.Y. et al.(1988),"Three-Dimensional Fracture Propagation under Specified Well-Bore Pressure," Int.J.Num.Anal.Methods Geomech., 12, 583-598

Vandamme,L. et al.(1989),"A Three-Dimentional Hydraulic Fracturing Simulator," Int.J.Num.Methods Eng., s28, 909-927

PROCEEDINGS, Seventeenth Workshop on Geothermal Reservoir Engineering
Stanford University, Stanford, California, January 29-31, 1992
SGP-TR-141

PREDICTION OF EFFECTS OF HYDRAULIC FRACTURING USING RESERVOIR AND WELL FLOW SIMULATION

Mineyuki Hanano and Tayuki Kondo

Geothermal Energy Research and Development Co., Ltd.
72-2 Sasamori, Ukai, Takizawa-mura, Iwate 020-01, JAPAN
(original affiliation : Japan Metals and Chemicals Co., Ltd.)

ABSTRACT

This paper presents a method to predict and evaluate effects of hydraulic fracturing jobs by using reservoir and well flow numerical simulation. The concept of the method is that steam production rate at the operating well head pressure is predicted with different fracture conditions which would be attained by the hydraulic fracturing jobs. Then, the effects of the hydraulic fracturing is evaluated by comparing the predicted steam production rate and that before the hydraulic fracturing. This course of analysis will suggest how large fracture should be created by the fracturing job to attain large enough increase in steam production at the operating condition and the best scheme of the hydraulic fracturing job.

INTRODUCTION

This study was carried out in the project Technology for Increasing Geothermal Energy Recovery (TIGER) (Yokoi et al., 1989) assigned to Geothermal Energy Research and Development Co., Ltd. by New Energy and Industrial Technology Development Organization.

To increase steam production of geothermal wells, hydraulic fracturing jobs are commonly applied (e.g., Katagiri et al., 1980; Katagiri and Ott, 1983). However, it was sometimes not possible to attain large enough increase in steam production by the hydraulic fracturing. This suggests that plans and procedures of hydraulic fracturing jobs are very important to attain good results. This also suggests that it is important to quantitatively predict effects of the fracturing job and to evaluate how large fracture should be created in advance of the fracturing job to establish the best fracturing scheme. This study is motivated by this reason. The purpose of this study is as follows:

1) To develop a method to quantitatively predict effects of hydraulic fracturing jobs.

2) To develop a method to quantitatively compare hydraulic fracturing schemes each other from an economical point of view.

3) To develop a method to establish a quantitative target for hydraulic fracturing jobs to attain.

In this study, we employed reservoir and well flow numerical simulation to predict effects of different fracture conditions which would be attained by different fracturing jobs, and quantitatively studied how steam production of wells of different fractures differ at operating condition. In this paper, we describe the method and some results of the simulation study.

CONCEPT OF THE METHOD

A flow chart of the method is shown in Fig. 1. This method consists of a numerical simulation of fracture propagation under various hydraulic fracturing conditions, a conversion of fracture parameters into permeability and other parameters for numerical simulation grids, and prediction and evaluation of steam production at operating well head pressure using a reservoir and well flow simulator. This course of study would be continued by modifying fracturing parameters until feasible fracturing scheme is found. In this paper, we concentrate on the second and the third items. The first item, the numerical simulation of fracture propagation, is in progress as another part of the TIGER project.

CONVERSION OF FRACTURE WIDTH INTO GRID BLOCK PERMEABILITY

The Cubic Law is commonly applied to convert fracture width into fracture permeability (e.g., Snow, 1968;

Witherspoon et al., 1979). The Cubic Law assumes laminar flow in the fracture. Ignoring the effects of turbulent flow, we employed this Cubic Law in this study, which is written in the following form:

$$k = w^2/12 \qquad (1)$$

where, k is the fracture permeability (m^2), w is the fracture width (m). To convert this fracture permeability into grid block permeability, we adopted the concept of Equivalent Porous Media (e.g., Gale, 1982). It is written in the following form:

$$k_1 \cdot w_1 = k_2 \cdot w_2 \qquad (2)$$

where, k_1 is the fracture permeability (m^2), w_1 is the fracture width (m), k_2 is the grid block permeability (m^2), w_2 is the grid block width (m).

EVALUATION OF WELL PRODUCTIVITY

In most geothermal power plants, wells are operated to maintain its well head pressure to feed the turbine with steam of the specified pressure. Therefore the evaluation of steam production rate at the operating well head pressure is important from an industrial point of view (Hanano et al., 1990).

Behavior of geothermal reservoir/well system in production consists of reservoir draw down, in-flow performance and ascending flow in the well (e.g., Gudmundsson and Marcou, 1986). Thus, it is necessary to analyze these three behaviors to evaluate steam production rate at the operating well head pressure (Hanano et al., 1990). Therefore, the reservoir simulator is used to analyze reservoir draw down and in-flow draw down, and the well flow simulator is used for ascending flow and two-phase flow in the well.

A flow chart of this evaluation is shown in Fig. 2. To evaluate the change of well productivity at the operating condition, reservoir simulation is carried out to estimate temperature and pressure distribution. Then the steam production rate is evaluated by the well flow simulation using the temperature and pressure at the feed zone. And then, the reservoir simulation is carried out again using the production rate evaluated by the well flow simulation. Through this course of analysis, change of steam production rate at the operating condition is obtained.

DESCRIPTION OF SOME EXAMPLE RUNS

To improve the understanding of the method described above and to investigate the relation between the well productivity and fracture parameters, some example simulations were conducted. In these example runs, two porous reservoir models, a horizontal fracture model and a vertical fracture model, were employed. Porous models were chosen because it was possible to account for fracture domain by reducing the grid block size around the fracture. Also finely grided porous models can provide better understanding of the flow around the fracture.

Grid geometries of the models are shown in Figs 3 and 4. The horizontal fracture model is the vertical cross sectional model of two-dimensional radial flow (Fig. 3), and the vertical fracture model is a quarter of the three dimensional Cartesian model (Fig. 4). These reservoir models account for both reservoir draw down and in-flow draw down, with fine grids around well blocks and with relatively coarse grids away from the well blocks. Using these models, effects of various fracture length, fracture width and fracture height on steam production at the operating condition were investigated.

Simulation parameters are shown in Table 1. Matrix permeability, porosity, rock heat capacity were referred from typical values used in our field analysis. Also fracture widths estimated from our field data were used. The reservoir simulator is a fully implicit finite difference model which is equivalent to that of Coats (1977). The well flow simulator is the one described by Takahashi (1988).

RESULTS AND DISCUSSION

Change of steam production rate at constant well head pressure of 0.65MPa of the horizontal fracture model is shown in Fig. 5. This result implies that:

1) As soon as the production started, reservoir pressure starts to draw down quickly. This cause the quick decrease in steam production rate shown in Fig. 5. But the draw down of reservoir pressure slows down after a while , resulting from a pressure gradient created in the reservoir. Thus the decrease in steam production rate slows down and approaches to quasi-steady state (Fig. 5).

2) Longer fracture length gives larger steam production (Fig. 5). This is because longer fracture length gives

the larger fracture surface area resulting in smaller flow resistance between fracture and matrix.

Since the steam production at the well head approaches quasi-steady state after approximately 1000 days of production (Fig. 5), we use these values for further discussion.

Differences in steam production with different fracture length and fracture block width are shown in Fig. 6. This result implies that:

1) Longer fracture length gives larger steam production, however its increase becomes saturated with longer fracture length. This is because larger flow rates in the fracture accelerates the flow resistance around the well bore resulting in larger pressure draw down around the well.

2) Wider fracture block width gives larger steam production, however their maximum steam production rates are different. This is because wider fracture block gives smaller flow resistance, but its effect also saturates as the block width becomes wider.

These results imply that the steam productivity of wells is controlled by combination of fracture length and fracture width. Thus, fracture block volume was chosen to investigate relationship between fracture dimension and steam productivity of wells. The fracture block volume is mostly proportional to amount of fluid injected for the hydraulic fracturing. Steam productivity of various fracture block volume of both the horizontal fracture model and vertical fracture model is shown in Fig. 7. This result implies that:

1) Larger fracture block volume gives larger steam production, because of larger fracture surface area and/or thick fracture block width.

2) Steam productions are different at the same fracture block volume if the fracture width or fracture height is different. There is a combination of fracture length and fracture width (height) to give the maximum steam production. This relation is shown as thick solid lines in Fig. 7. The best combination is the case of larger fracture width when the fracture length is long, and that of narrower fracture width when the fracture length is short. This indicates that fracture length and width have different effect on steam production and they affect each other independently as discussed above.

3) The vertical fracture gives larger steam production than the horizontal fracture does even if the fracture block volumes are the same, because of the difference in flow resistance; the flow in the vertical fracture is linear but the flow in the horizontal fracture is radial; the vertical fracture has larger contact area to the well bore than that of the horizontal fracture, resulting in lower flow resistance in the vertical fracture than that of the horizontal fracture.

CONCLUSIONS

1) Longer and wider fracture can give larger steam production. Thus, it is desirable to enlarge its size by the hydraulic fracturing, to increase well productivity at the operating condition.

2) There is the best combination of fracture length and the fracture width to maximize the well productivity at the operating condition for the same fracture volume. Thus, the balance of the fracture length and fracture width is important in creating fractures by the hydraulic fracturing.

3) The method described in this paper enables us to quantitatively predict the effects of the hydraulic fracturing and evaluate the best combination of the fracture geometry, for planning the best hydraulic fracturing job.

ACKNOWLEDGEMENTS

This study was carried out in the project Technology for Increasing Geothermal Energy Recovery assigned to Geothermal Energy Research & Development Co., Ltd. (GERD) by New Energy and Industrial Technology Development Organization (NEDO). We are grateful to NEDO and GERD for their permission to publish this paper.

REFERENCES

Coats, K.H. (1977) Geothermal Reservoir Modeling, SPE-6892.

Gale, J.E. (1982) Assessing the Permeability Characteristics of Fractured Rock. Geological Society of America, Special Paper 189, pp. 163-181.

Gudmundsson, J.S. and Marcou, J.A. (1986) Deliverability and its Effects on Geothermal Power Costs. Proc., 11th Workshop on Geothermal Reservoir Engineering, Stanford University, pp. 217-222.

Hanano, M., Takahashi, M., Hirako, Y., Nakamura, H., Fuwa, S., Nose, J. and Itoi, R. (1990) Longevity Evaluation for Optimum Development in a Liquid-Dominated Geothermal Field: Effects of Interaction of Reservoir Pressure and Fluid Temperature on Steam Production at Operating Conditions, Geothermics 19, pp. 199-211.

Katagiri, K. and Ott, W.K. (1983) Frac Treatment Boosts Geothermal Well Production. World Oil 194(Sept.), pp. 64-67.

Katagiri, K., Ott, W.K. and Nutley, B.G. (1980) Hydraulic Fracturing Aids Geothermal Field Development. World Oil 191(Dec.), pp. 75-88.

Snow, D.T. (1968) Rock Fracture Spacing, Openings, and Porosities. Soil Mech. Found. Div., Proc. Am. Soc. Civ. Eng. 94, pp. 73-91.

Takahashi, M. (1988) A Wellbore Flow Model in the Presence of CO_2 Gas, Proc., 13th Workshop on Geothermal Reservoir Engineering, Stanford University, pp. 151-157.

Witherspoon, P.A., Wang, J.C.Y., Iwai, K. and Gale, J.E. (1979) Validity of the Cubic Law for Fluid Flow in a Deformable Rock Fracture, Water Resour. Res. 16, pp. 1016-1024.

Yokoi, H., Kobayashi, H. and Inoue, K. (1989) Technology for Increasing Geothermal Energy Recovery, Proc., 11th New Zealand Geothermal Workshop, pp. 123-125.

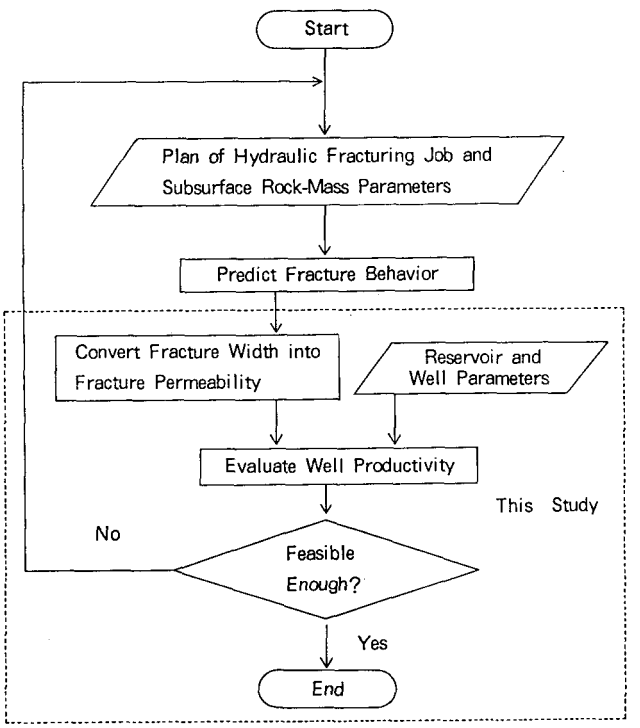

Fig. 1 A Flow Chart to Predict and Evaluate Effects of Hydraulic Fracturing Jobs. Items in a Dotted Box are Treated in this Study.

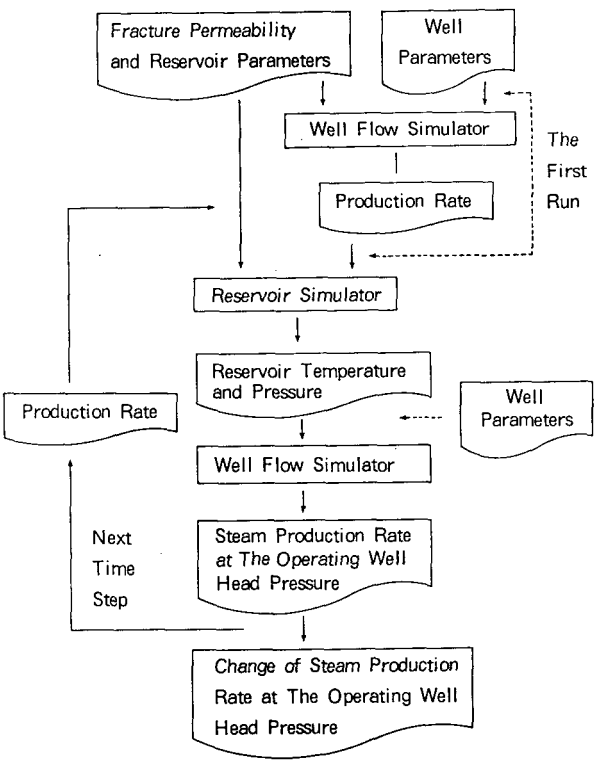

Fig. 2 A Flow Chart to Evaluate Well Productivity.

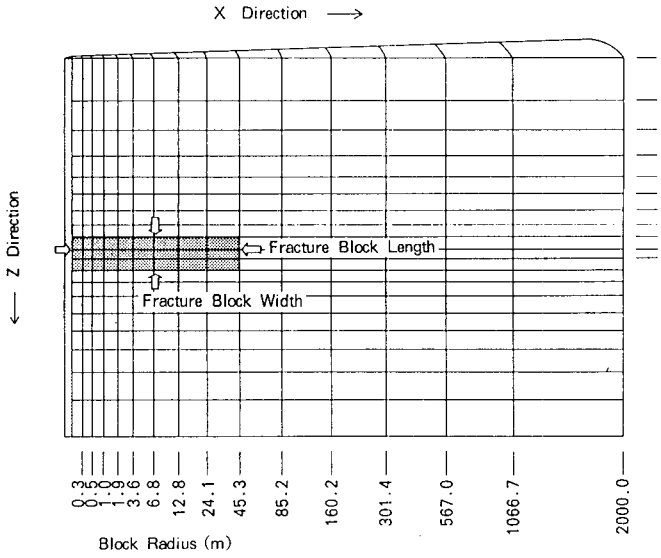

Fig. 3 Grid Geometry of the Horizontal Fracture Model.

Table 1 Simulation Parameters of Horizontal Fracture Model (Fig. 3), Vertical Fracture Model (Fig. 4), and Well Flow Model.

* : Boundary Conditions of One Side of X and Y Direction of the Vertical Fracture Model are Closed.

	Parameter (Symbol)	Value
Horizontal and Vertical Fracture Model	Center Depth of Fracture Layer	2000 m
	Reservoir Pressure at 2000m	20 MPa
	Other Depths	Hydrostatic Pressure
	Reservoir Temperature	230 ℃
	Boundary Condition	Open on All Direction * (Constant Temp./Press.)
	Porosity	
	Fracture Block	0.8
	Matrix Block	0.1
	Well Block	0.999
	Rock Heat Capacity	2MJ/m³·K
	Rock Termal Conductivity	2W/m·K
	Permeability	
	Fracuture Block	100×10^{-12} m²
	Matrix Block	25×10^{-15} m²
	Well Block	1000×10^{-12} m²
Horizontal Fracture Model	Fracture Block Length (Lf)	45.3, 85.2, 160.2 301.4, 567.0 m
	Fracture Block Width (Wf)	0.05, 0.25, 0.55 m
Vertical Fracture Model	Fracture Block Length (Lf)	50, 150, 450 m
	Fracture Block Height (Hf)	20, 40 m
	Fracture Block Width	0.3 m
Well Flow Model	Well Head Pressure	0.65 MPa
	Depth of Feed Point	2000 m
	Diameter of Well	0.30 m

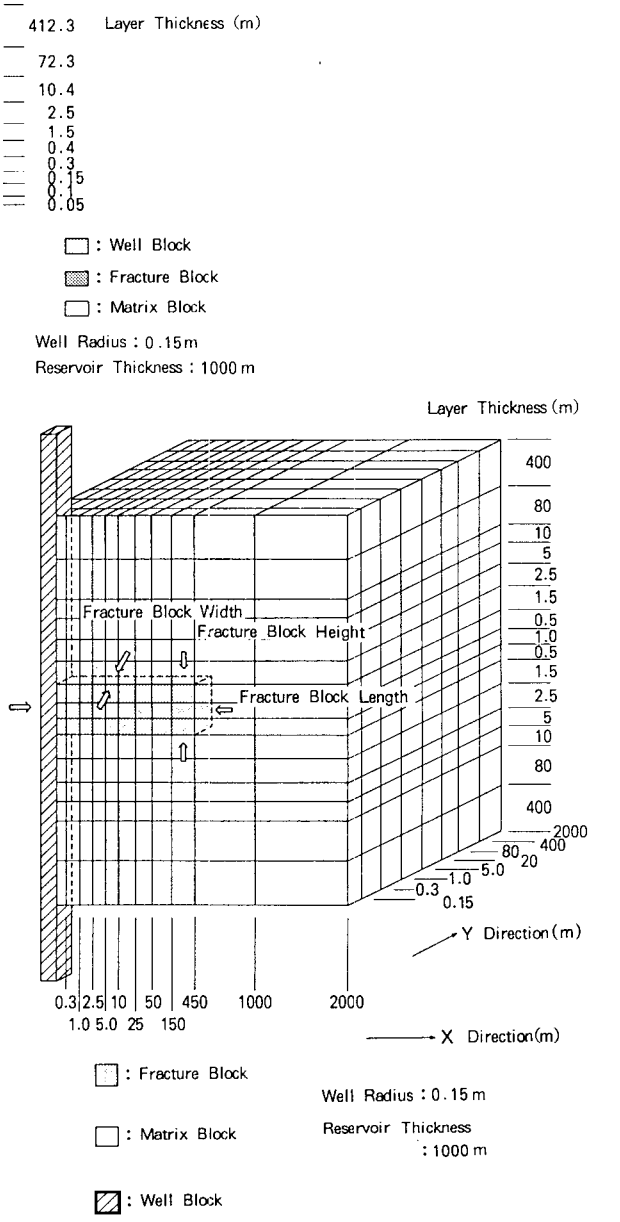

Fig. 4 Grid Geometry of the Vertical Fracture Model.

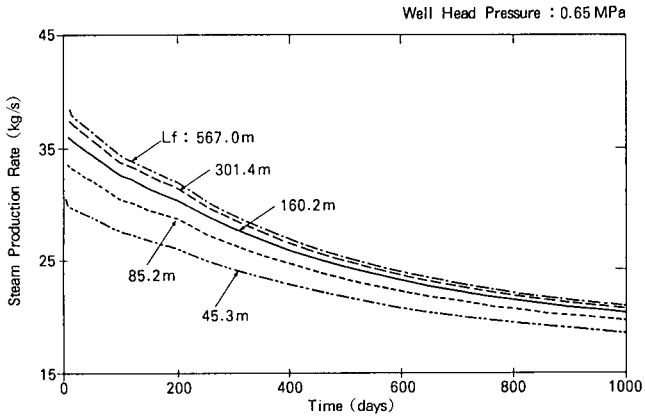

Fig. 5 Change of Steam Production Rate at Constant Well Head Pressure of 0.65MPa (Horizontal Fracture Model, Wf=0.25m).

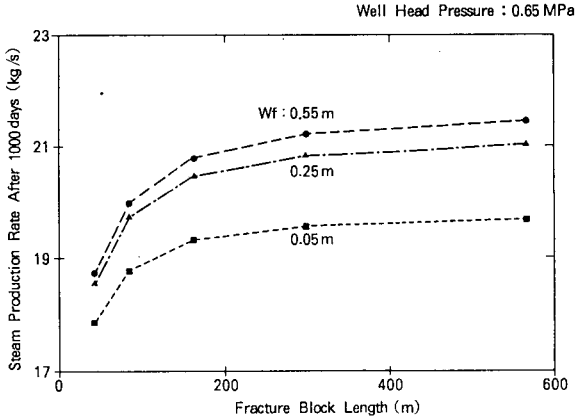

Fig. 6 Differences in Steam Production With Different Fracture Length and Fracture Block Width (Horizontal Fracture Model).

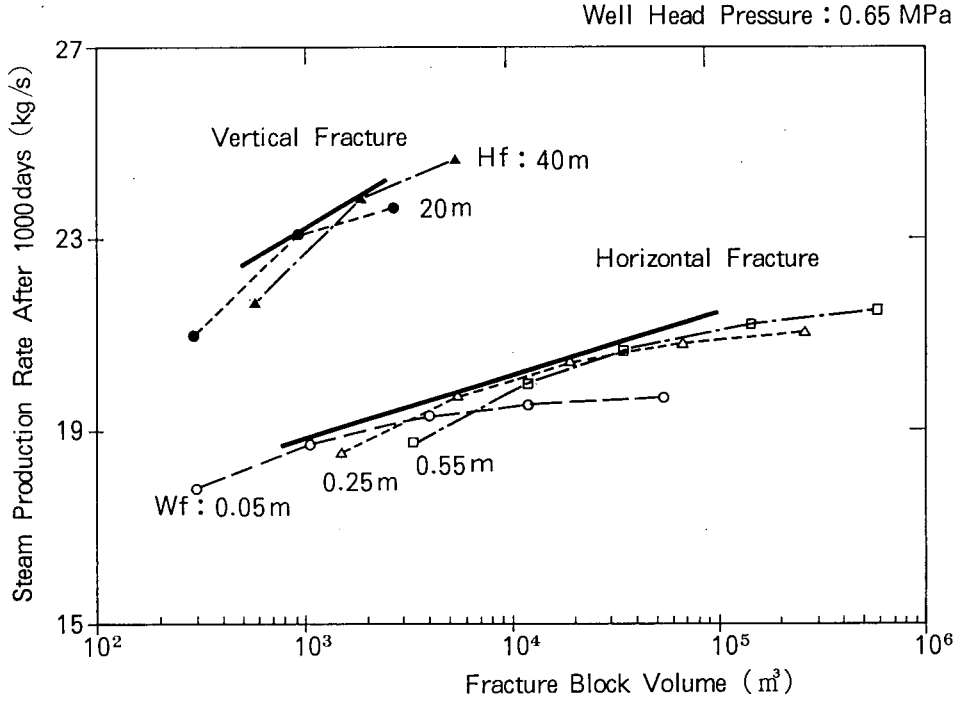

Fig. 7 Steam Productivity of Various Fracture Block Volume of Both the Horizontal Fracture Model and Vertical Fracture Model.

PROCEEDINGS, Seventeenth Workshop on Geothermal Reservoir Engineering
Stanford University, Stanford, California, January 29-31, 1992
SGP-TR-141

BOILING AND CONDENSATION PROCESSES IN THE CERRO PRIETO BETA RESERVOIR UNDER EXPLOITATION

Alfred Truesdell[1], Alfredo Mañón[2], Luís Quijano[2],
Tyler Coplen[3] and Marcelo Lippmann[4]

[1]Consultant, Menlo Park, California
[2]Comisión Federal de Electricidad, Morelia, Mexico
[3]U.S. Geological Survey, Reston, Virginia.
[4]Lawrence Berkeley Laboratory, Berkeley, California.

ABSTRACT

The deep Cerro Prieto (Baja California, Mexico) beta reservoir is offset vertically by the southwest-northeast trending, normal H fault. Under exploitation pressures in the upthrown block have decreased strongly resulting in boiling and high-enthalpy production fluids. Significant differences in fluid chemical and isotopic compositions are observed in the two parts of the reservoir and particularly in an anomalous zone associated with the H fault. These differences result from intense boiling and adiabatic steam condensation, as well as from leakage of overlying cooler water along the fault.

Introduction

The Cerro Prieto geothermal field has three reservoirs developed in sandstones and sandy shales of the Colorado River delta. The shallow (1000 to 1500 m depth) alpha reservoir in the west of the field was developed first and has been partly abandoned because of decreasing fluid temperatures. Most production is now from the deeper (1500 to 2700 m depth) beta reservoir which underlies the whole field. There are a few wells that produce from the yet deeper gamma reservoir. The beta reservoir is offset by the "H" fault of Halfman *et al.* (1986) with the downthrown block mainly exploited by the CP-II power plant and the upthrown block by the CP-III plant. The position of the H fault (top of the upthrown block to the top of the downthrown block) from these authors is shown in Figure 1. After these plants went on line in 1986-7, large quantities of fluids were withdrawn and reservoir pressures decreased more or less strongly depending on initial pressure and degree of isolation from other aquifers. The response to pressure decrease in the alpha reservoir, exploited since 1973 by the CP-I power plant, has been an influx of cooler waters from the sides and above with limited local boiling (Grant *et al.*, 1984; Truesdell *et al.*, 1989). The response to pressure decrease in the beta reservoir is not as well known because a much shorter production record is available.

The beta reservoir is not well connected to cooler water aquifers except on the western margin (in the CP-I area) and possibly in the south. The upthrown block (CP-III) shows strong boiling (de León Vivar, 1988) apparently because it is closed to the north by an undefined barrier and has only limited connections with cooler aquifers in the west at a distance of 2-3 kilometers. Boiling in the CP-III area appears to occur generally throughout the reservoir with a gravity segregation of steam and water resulting in separate entries of steam and water in producing wells (Truesdell *et al.*, 1989; Truesdell and Lippmann, 1990). Simulation studies (Lippmann and Truesdell, 1990) show that the general CP-III boiling results from closed reservoir boundaries or restricted recharge while localized near-well boiling observed in the shallow reservoir of the CP-I area is related to constant pressure boundaries.

Anomalous fluids related to boiling in the CP-III area were described by Stallard *et al.* (1987), who showed that some high-enthalpy, high-deuterium, low-chloride fluids did not fall on the chloride-deuterium (or chloride-oxygen 18) mixing line that characterized most of the field. All of these observations are consistent with boiling, phase segregation and preferential steam flow to the wells. In some fluids a small increase of oxygen-18 (up to 0.5 permil) was observed which is not consistent with increased steam entry. At the time of the 1987 study, this anomaly could not be examined in detail because most CP-III wells had been in production for only one year . With two or three years more of production and geochemical data available we have reexamined processes in the beta reservoir related to continued production.

Data collection and analysis

Water samples were collected by the staff of the Comisión Federal de Electricidad (CFE) and by members of the U.S. Geological Survey (USGS) from production separators after one or two stages of steam separation and cooled or flashed to atmospheric pressure. Chemical analyses of flashed water samples were made in the laboratories of CFE at Cerro Prieto. Isotope analyses were made at the USGS Laboratories in Reston, Virginia, on samples of steam and separated water cooled without flashing. In most cases total fluid enthalpy (H_{total}) measurements were made within less than 15 days of the time of sample collection. Aquifer liquid temperatures and enthalpies were calculated by the use of geothermometers and steam tables based on pure water. Near-well aquifer chloride concentrations ($Cl_{aquifer}$) were calculated from analysis of flashed samples using aquifer liquid enthalpy (H_{total})

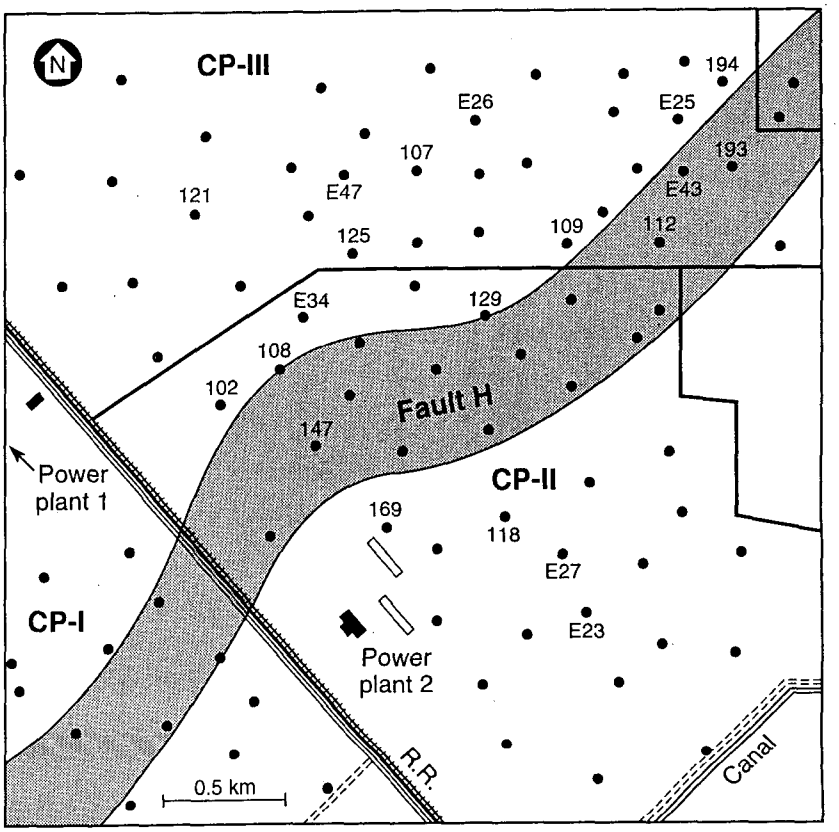

Figure 1. Map of the Cerro Prieto geothermal field showing the boundaries of the CP-I, CP-II and CP-III areas, the position of the H fault at reservoir level and the locations of wells mentioned in the text.

calculated from Na/K temperatures (Fournier, 1979). The equation used is

$$Cl_{aquifer} = Cl_{water}(sep) \times \frac{H_{steam}(sep) - H_{total}}{H_{steam}(sep) - H_{water}(sep)}$$

for a single separation and repeated for each additional stage of separation including flashing during collection. Data at separation conditions are denoted by (sep); enthalpy values for separator conditions are from steam tables. These calculated aquifer chloride concentrations (rather than analytical concentrations) are used throughout the paper.

The fraction of "excess" steam entering the well from reservoir two-phase fluid (the inlet vapor fraction or IVF) was calculated from the equation (Truesdell *et al.*, 1989),

$$IVF = \frac{H_{total} - H_{water}(inlet)}{H_{steam}(inlet) - H_{water}(inlet)}$$

with inlet temperatures based on Na/K rather than silica because some waters may become diluted near to or in the well (discussed below).

Results

Maps of 1990 excess steam fractions (IVF), chloride concentrations in the aquifer liquid, Na/K geochemical temperatures and total-discharge isotope compositions (for 1989) show similarities and differences between fluids from the CP-II and CP-III parts of the beta reservoir (Figures 2-6). The northeast-striking, southeast-dipping, normal H fault divides the beta reservoir into two blocks. The fault at reservoir level approximately follows the boundary between CP-II and CP-III (Figure 1). Compared with fluids of the southeast block, those of the northwest upthrown block show higher excess steam, generally lower and variable reservoir chloride, higher oxygen-18 concentrations but similar deuterium concentrations and chemical (Na/K) temperatures. There is a more or less well-defined anomalous zone of low temperatures, low aquifer chloride concentrations and somewhat lighter isotope compositions approximately along the trace of the H fault at reservoir level (Figures 3-6). The general character of fluids from the southeast and northwest parts of the reservoir are considered first and the anomalous area later.

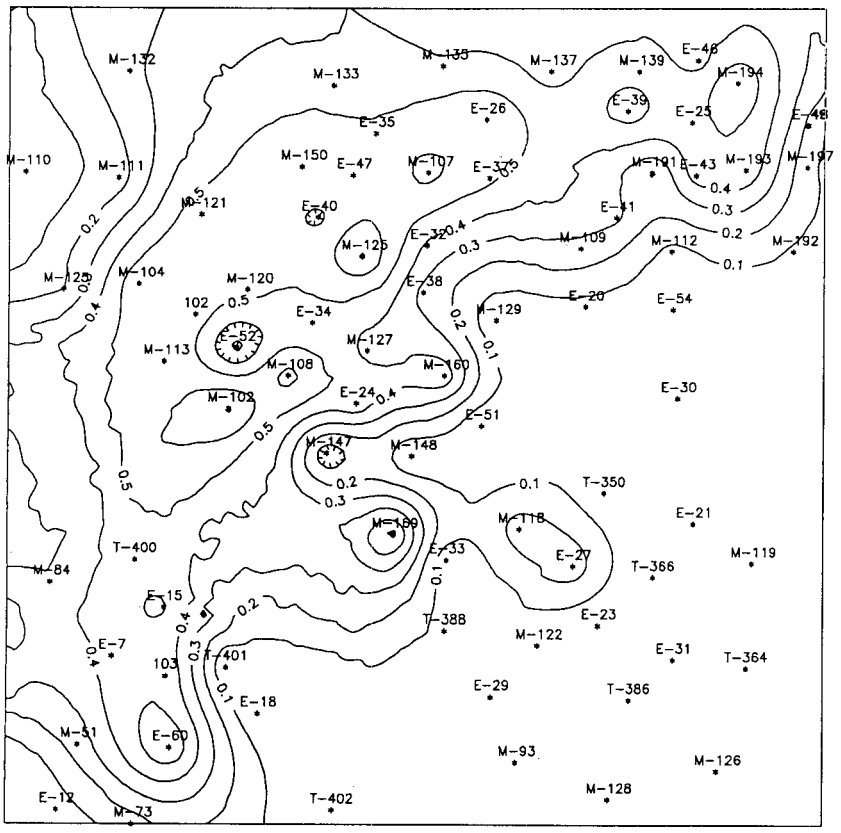

Figure 2. Inlet vapor fraction (excess steam) for Cerro Prieto wells producing in 1990. Measured enthalpy values and chemical analyses are from CFE. The area and scale of this and following maps are the same as Figure 1.

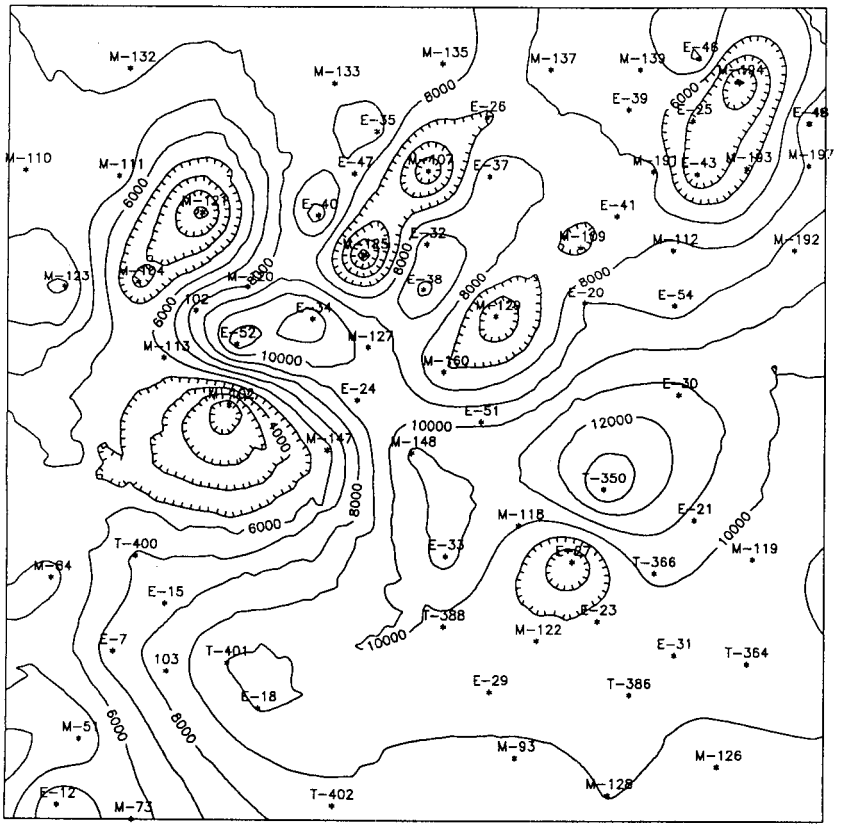

Figure 3. Aquifer liquid chloride concentrations (in mg/kg) for Cerro Prieto wells producing in 1990. In equation 1 (text), aquifer liquid enthalpy values have been calculated from silica temperatures. Analyses are from CFE.

Figure 4. Na/K geothermometer temperatures (in °C) for 1990 Cerro Prieto fluids, calculated using the equation of Fournier (1979). Water analyses are from CFE. The locations of the eastern and western lines of anomalous wells are indicated.

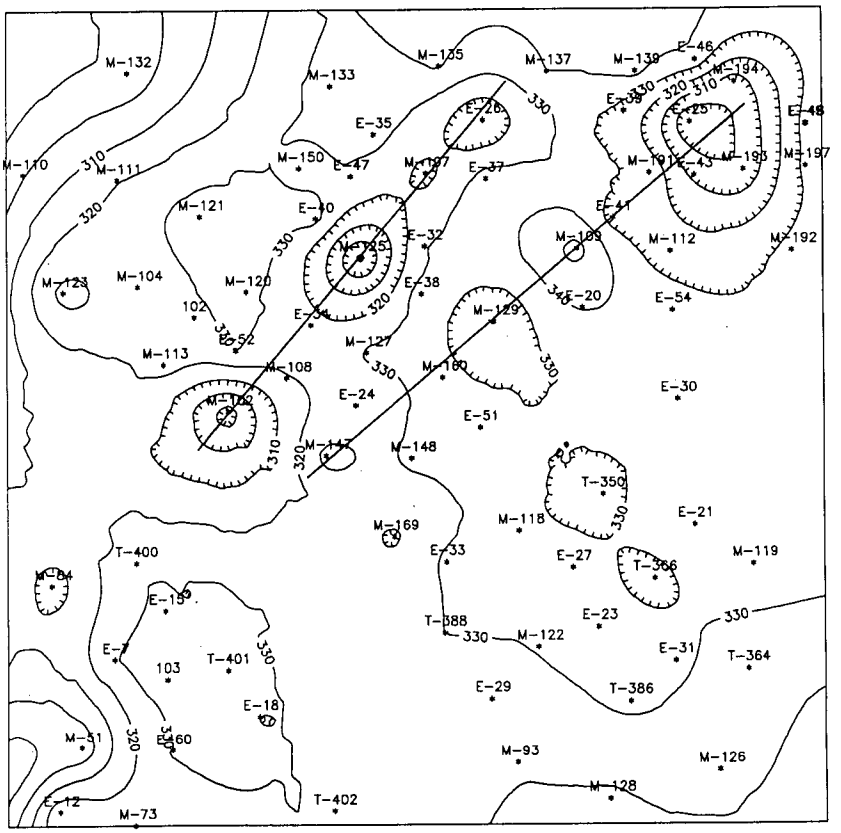

Figure 5. Total discharge oxygen-18 compositions of Cerro Prieto well fluids collected in 1989. Calculated values are from steam and water analyses by the USGS. Units are permil SMOW.

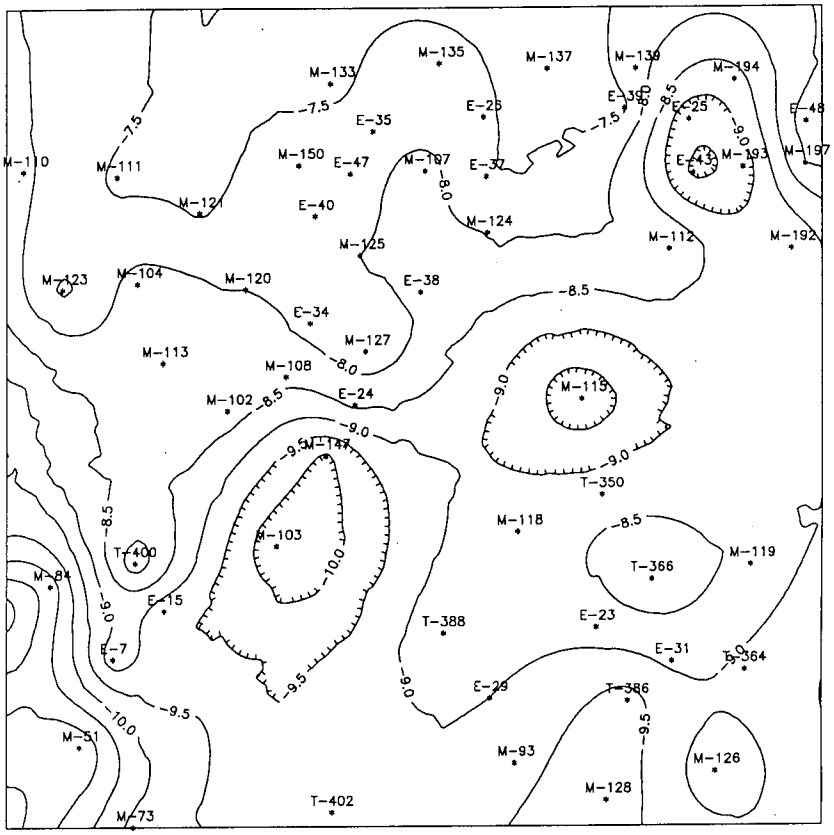

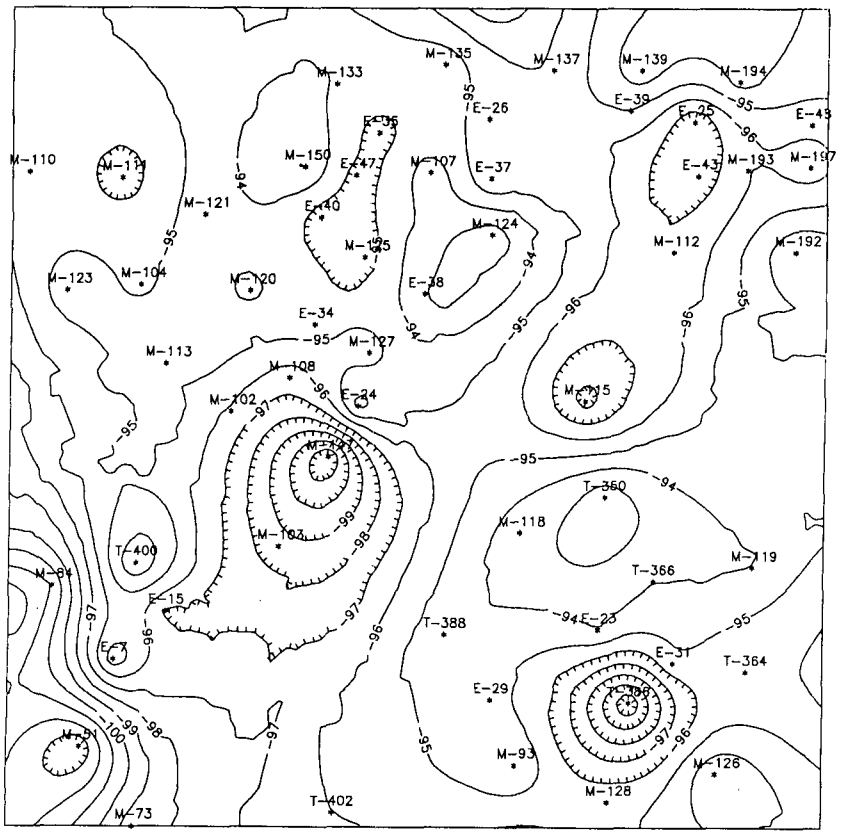

Figure 6. Total discharge deuterium compositions of Cerro Prieto well fluids collected in 1989. Calculated values are from steam and water analyses by the USGS. Units are permil SMOW.

Cerro Prieto II fluids

As was described earlier (e.g. Truesdell *et al.*, 1989; Lippmann *et al.*, 1991), the downthrown block of the beta reservoir shows only limited boiling because of its great depth and possibly because of connections with cooler fluids to the south. The lack of reservoir boiling is seen in the excess steam (IVF) map (Figure 2) in which almost all fluids southeast of a line between wells M-129 and M-169 show inlet vapor fractions less than 0.1. The exceptions are wells M-118 and E-27 which showed IVF values greater than 0.2 in 1990. The low values of IVF are confirmed by detailed enthalpy and chloride histories of typical well fluids (Figure 7) which show neither near-well boiling (which would lower silica enthalpy) nor general boiling and steam-water phase segregation (which would increase measured enthalpy). The O-18 isotope map (Figure 5) shows decreases to the southwest and (less strongly) to the south. These trends in O-18 and excess steam together with the decrease toward the south of aquifer chloride from greater than 10,000 ppm to less than 9000 ppm (Figure 3) suggest mixing with somewhat less saline water. The temperature effect of this mixing is less well defined (Figure 4) with 1990 Na/K temperatures near 320°C along the boundary, only 10-15°C cooler than elsewhere. The location of the H fault at the boundary with the northwest block is clearly shown in the excess steam (Figure 2) with near zero IVF values changing to greater than 0.4 IVF within a distance of 250-500 m.

The oxygen-18 compositions show almost exactly the same location for the H fault (Figure 5). The southeastern part of CP-II is characterized by fluids with oxygen-18 compositions between -8.5 and -10 permil SMOW which changes to values between -7.5 to -8.5 in the area with high excess steam. This is something of a paradox because at equilibrium steam is 0.7 to 1.0 permil lower in O-18 than liquid water at the temperature of the Cerro Prieto reservoirs (320-340°C), thus light isotopes (i.e. lower O-18/O-16 ratios) should accompany higher-enthalpy discharge.

Deuterium shows little experimental liquid-vapor fractionation at 320 to 340°C (steam is less than 2 permil enriched in deuterium) and there are few large changes throughout the CP-II reservoir (Figure 6) with southern fluids about 1 permil lighter than central CP-II fluids (-96 permil compared with -95 permil SMOW). The relatively small liquid-vapor fractionation factors for deuterium above 200°C and the lack of a "deuterium shift" from exchange with rock minerals make deuterium a less sensitive indicator of boiling and mixing processes in geothermal systems than oxygen-18. Although oxygen-18 isotopes are more sensitive to boiling processes at high temperatures, the "oxygen isotope shift" resulting from oxygen-18 exchange between water and rock, depends on temperature, rock type and duration of contact and may also produce variation in isotope compositions. Fluids with lower deuterium (to -97 permil) are found in part of the zone of anomalous fluids along the excess enthalpy boundary (the H fault). These are discussed below.

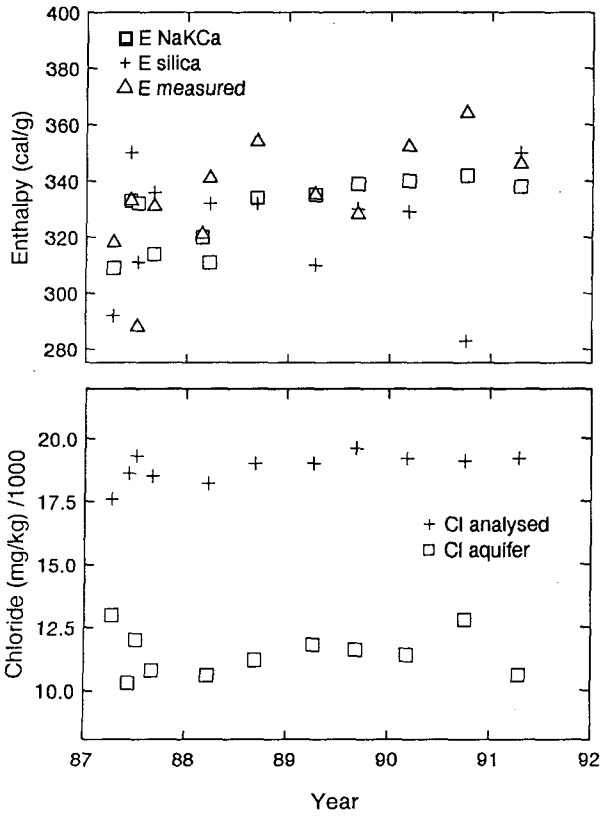

Figure 7. Geochemical history of E-23, a typical CP-II well. This includes measured total fluid enthalpy and calculated aquifer liquid enthalpy from silica and NaKCa geothermometers, along with measured and calculated aquifer liquid chloride based on silica temperatures. Enthalpy measurements and water analyses are from CFE.

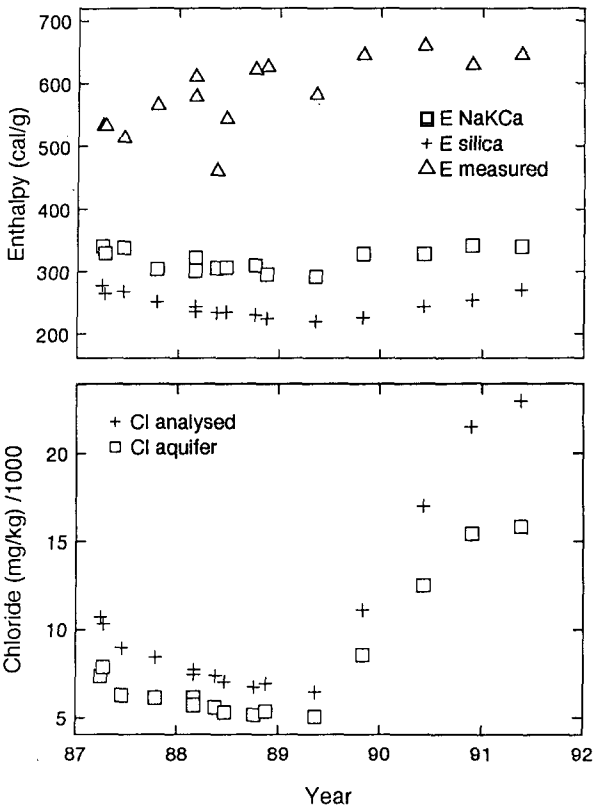

Figure 8. Geochemical history of M-121, a typical CP-III well. Quantities are as in Figure 7.

Cerro Prieto III fluids

The CP-III area (Figure 1) is very interesting geochemically. As mentioned earlier, fluids from this part of the field have high excess steam resulting from widespread boiling and phase segregation with steam entering wells separately from the liquid. This steam-rich fluid should show depletion of oxygen-18 on a total fluid basis and increase of chloride in the liquid (but not in the total fluid) as a result of boiling. CP-III fluids have, however, enriched total discharge oxygen-18 (Figure 5) and low (but highly variable) aquifer liquid chloride concentrations (Figure 3) compared with CP-II fluids. High oxygen-18 in CP-III fluids may be unrelated to boiling and result instead from oxygen isotope shift enhanced by limited fluid circulation. Although Na/K temperatures (Figure 4) show no significant differences between CP-III and CP-II, CP-III silica temperatures are typically lower by 25-50°C (Figure 8). This could result from near-well boiling and quartz deposition, but in the absence of the exponential decline of excess steam characteristic of near-well boiling (Lippmann and Truesdell, 1990), another explanation is suggested (see below). The fluids produced from wells at the boundary between CP-II and CP-III are anomalous in one or more of these quantities compared to either part of the reservoir.

Anomalous fluids

A number of wells along two northeast-southwest trends near the CP-II/CP-III boundary have shown anomalous behavior in 1988-1990. The map of Na/K temperatures for 1990 (Figure 4) shows that fluids from the anomalous wells (marked by lines) have temperatures 10 to 40°C lower than adjacent wells. The anomalous wells form two lines and include M-102, M-125, M-107 and E-26 in the western line and M-194, E-25, E-43, M-193, M-109, M-129 and M-147 in the eastern line. A few wells (M-147, M-109) did not have anomalous temperatures but were abnormal in other ways. Other wells along the same lines show no anomalies (for example M-108 and E-34) and some of the abnormal wells show only small temperature deficits in 1990 but showed large ones in previous years (e.g. M-129 in 1988). Some other wells off the trend had anomalous fluid temperatures for short periods (e.g. E-47 in 1988, M-169 in 1989). Some (but not all) wells with low 1990 temperatures show low aquifer chloride (M-102, M-194 and adjacent wells, and M-129). Some of the wells (E-25, E-43, M-193 and M-147) had low oxygen-18 (Figure 5) and deuterium (Figure

6). Finally, most of the anomalous wells (but not E-26, M-109 and M-129) showed high excess steam in 1990 (Figure 2) with IVF values greater than 0.5 in the western line (usually more than 0.1 higher than adjacent wells). Wells in the eastern line have lower but still elevated IVF values (>0.4).

Interpretation of anomalous fluid compositions

The wells with the most consistently anomalous fluids are M-102 and the group including M-194, E-25, E-43 and M-193. A map of the top of the producing interval (Figure 9) shows that this group of wells (except M-102 and M-194) have unusually shallow production intervals, as much as 250 m above adjacent wells (E-43 at 1900 m depth has the shallowest production in the western half of CP-III). Wells M-129 and M-147 also have shallow production and anomalous fluids, but in M-127 shallow production did not lead to anomalous fluids. This partial correlation of fluid anomalies and shallow production suggests that part of these fluids may have been produced in or migrated to the upper parts of the reservoir. Note that a band of steep gradient in production depth runs from northeast to southwest almost coincident with the position of the H fault determined by Halfman *et al.* (1986) from well logs.

Two possible causes of anomalous fluids at the top of the reservoir are gravity-induced steam segregation after extensive boiling, and recharge of cooler water from above. Some observations (high excess enthalpy, low total chloride) suggest steam segregation while others (low geothermometer temperatures, low liquid chloride) imply cool recharge. It is important to note that in 1989 light isotopes were associated only with the eastern line of anomalous fluids (wells in the M-194 group, and M-147; data for M-109 and M-129 are not available for that year).

The inconsistent nature of the anomalies suggests that more than one factor may apply. In general wells in the western anomaly (M-102, M-125, M-107 and E-26) have very high excess steam and no evidence of light isotopes, while those in the eastern anomaly have light isotopes with low (M-147, M-112, M-109) or moderate (wells near M-194) excess steam. Of these factors, low total discharge deuterium values are clearly related to cooler, less-saline waters (which have a larger fraction of Colorado river water, low in salts and deuterium; Stallard *et al.*, 1987). High excess steam is probably related to segregation of steam and its preferential flow to wells. The M-194 group has both low deuterium and moderately high excess steam, with shallow feed zones. Thus these wells may have both influences. The addition of cooler water to the western wells is strongly indicated by their low Na/K temperatures and aquifer chloride concentrations, but they show no anomalies in total-fluid isotope compositions. It seems likely that because these wells have such high excess steam, the composition of the liquid fraction has little influence on the total-discharge isotope compositions. Thus it is possible that cooler recharge could cause low geothermometer temperatures and aquifer chloride concentrations, because these quantites are related to liquid compositions, but isotope compositions remain strongly influenced by high excess steam. The high excess steam could also contribute to lower aquifer chloride and silica-geothermometer temperatures in the manner discussed next.

High excess steam and low chloride in CP-III fluids

As mentioned above, the CP-III area generally has high excess steam (Figure 2) and low variable aquifer chloride concentrations (Figures 3 and 8). Intuitively, since boiling and steam separation should leave residual water enriched in chloride, high rather than low aquifer chloride would be expected. In addition the extreme range in chloride (e.g. 5000 to 15,000 mg/kg in M-121; Figure 8) is not consistent with these waters starting with 11,000-12,000 mg/kg chloride as found in CP-II, and becoming more concentrated by boiling off steam. A possible explanation of the low and variable chloride found, lies in the boiling and condensation processes that may be expected for very high-temperature waters. This sort of argument was used by James (1968) to explain the preference of vapor-dominated reservoirs for 240°C, the temperature corresponding to the enthalpy maximum of steam.

The processes suggested can be understood by considering the enthalpy-pressure diagram for water constructed from steam table data (White *et al.*, 1971). This diagram is for pure water, but can be applied to Cerro Prieto waters which all have less than 2% NaCl equivalent concentration. Figure 10 shows an outline of the two-phase region, and isotherms for 150, 200 (partial) and 300°C along with the hypothesized boiling and condensation processes.

The generalized initial state of Cerro Prieto III water before exploitation is shown at point A. This fluid is compressed liquid at supercritical pressure but subcritical temperature. At the start of exploitation the liquid undergoes decompression along the 350°C isotherm with temperature buffered by heat in the rock, to reach the two-phase region at point B. From B to C the liquid boils at constant enthalpy with phase separation at C to form residual liquid of composition L1 and vapor, V1. The fraction of vapor formed is about 0.14 and if the initial chloride concentration is about 10,000 mg/kg (as in CP-II), then the concentration in residual liquid would be 11,600 mg/kg. This process is similar to boiling in a separator except that heat may be transfered from the rock as the fluid decreases in pressure and temperature from B to C. Initially this heat transfer must increase the fluid enthalpy so that the steam fraction is higher than 0.14 and the residual chloride, greater than 11,600 mg/kg. With time, rock temperatures equilibrate with boiling fluid temperatures and the process becomes isoenthalpic.

The CP-III reservoir has very low recharge (i.e. is nearly closed) and the pressure drop from exploitation would have propagated widely causing widespread boiling. Since boiling is not limited to the near-well region,

Figure 9. Map of the top of the producing intervals (depths in meters) of Cerro Prieto wells in the beta reservoir (Ricardo Márquez, CFE Cerro Prieto; personal commun., 1991).

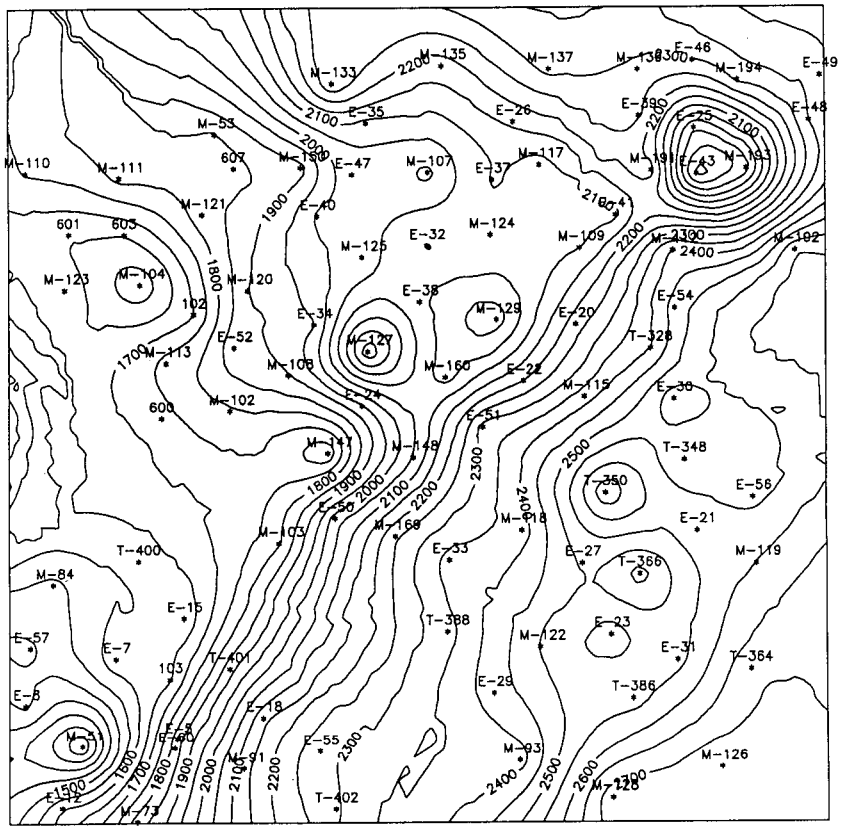

Figure 10. Part of the enthalpy - pressure diagram for pure water from White *et al.*(1971) showing hypothetical boiling and condensation processes.

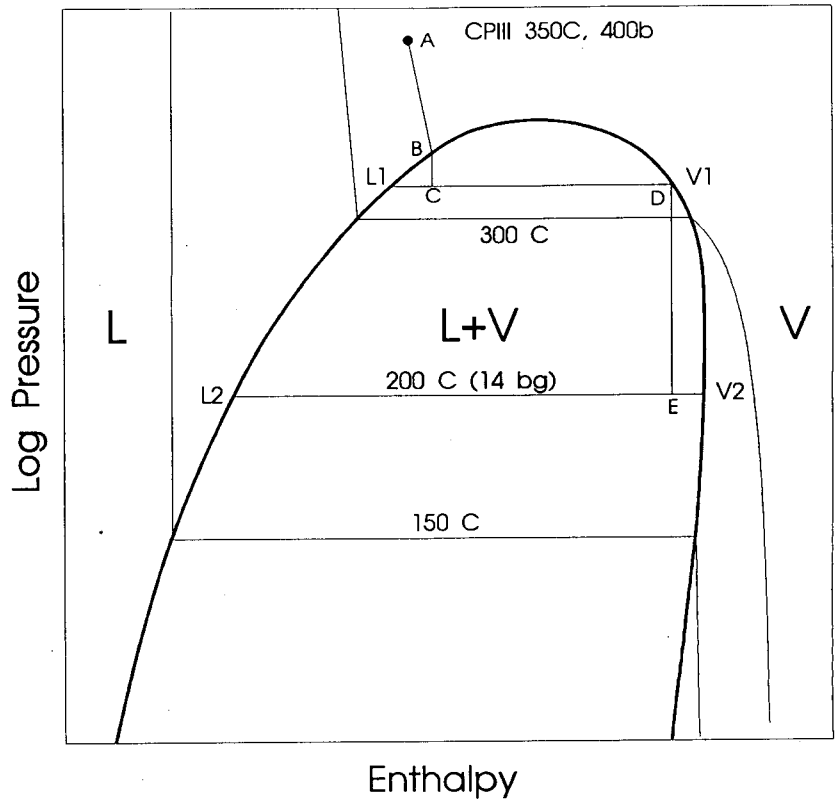

gravity segregation could occur and it is likely that before or during flow to the wells, the residual liquid would flow to lower zones and steam would flow toward upper zones. Steam at point D (composition V1) would continue to decrease in pressure and temperature as it flowed toward the wells and, because it has a temperature well above 240°C (and therefore less than maximum enthalpy), it can condense at constant enthalpy to form a low-enthalpy liquid (L2) and higher-enthalpy steam (V2). The condensation process shown in Figure 10 is for final separation at 200°C and 14 bars gage, typical of the high pressure separators at CP-III. The decompression process shown from D to E occurs at least partly in the wellbore and separator (at constant enthalpy), but is likely to also occur partly in the reservoir.

The liquid L2 is steam condensate which contains negligible chloride and represents about 0.06 of the total fluid separating from L1. If all of this condensate is carried into the well (or formed in the well) and the excess vapor fraction (IVF) of the well is high (as for most CP-III wells), then this condensate could significantly dilute brine from the lower reservoir zones. If the condensation ocurred partly in the reservoir as the steam flows toward the well, then a smaller fraction might enter the well and the remainder might mix with and partially dilute the brine outside the well.

These processes allow for a great variety in apparent aquifer liquid chloride with all or nearly all fluids showing some dilution. The degree of dilution depends on conditions that would not be consistent from well to well or with time in a single well. This agrees with the observed variation in aquifer chloride concentrations of CP-III reservoir fluids (Figures 3 and 8). Dilution with condensate would also affect calculated silica temperatures and produce the greatly depressed silica temperatures observed in CP-III fluids. Low chloride and silica concentrations associated with the CP-III fluids also characterize anomalous well fluids along the western line. These fluids have extremely high excess steam and must also show the effects of these boiling and condensation effects. However the low Na/K temperatures of these fluids could not be produced by condensation and near-well dilution, but must result from the entry of cooler waters.

Summary

The beta reservoir at Cerro Prieto shows several types of production mechanisms. Fault-H divides the reservoir into a deeper block in the southeast and a shallower block in the northwest. The southeast part, producing steam mainly for powerplant CP-II, shows limited boiling due to its greater depth and higher initial pressure, and probably because pressures are maintained by its connections to cooler aquifers. The northwest part supplying steam mainly to powerplant CP-III shows intense boiling with phase segregation and preferential steam flow to wells resulting in high excess steam. The fluids from the CP-III area have aquifer chloride concentrations about 20% lower than those from the central CP-II area and are relatively enriched in oxygen-18.

Near the trace of the H fault at reservoir level, there are two lines of wells with anomalous fluids. The western line shows high excess steam with low aquifer liquid chloride, low Na/K temperatures and total-discharge deuterium concentrations similar to most other fluids from the beta reservoir. The eastern line shows lower excess steam, low chloride, low Na/K temperatures and low deuterium values. These anomalous fluids appear to result in part from cool water recharge from above and in part from exceptionally large amounts of excess steam (high IVF values). The generally lower aquifer chloride in CP-III fluids may be due to isoenthalpic condensation of very high-temperature steam with resulting dilution of reservoir liquids with condensate. This process also may contribute to the low chloride of the western anomalous fluids. The high oxygen-18 in CP-III fluid probably results from oxygen isotope shift.

If cooler water is entering the beta reservoir along the line of anomalous wells, then it is probably moving down the H fault. Not only is the fault zone a possible conduit, but because of the offset of the shale layer overlying the beta reservoir, the distance from the hot reservoir to overlying cooler groundwater is the least along the fault trace. Inflow of cooler water into the greatly decompressed northwest block of the beta reservoir would be beneficial providing it is dispersed through the reservoir and not concentrated in a limited area.

Acknowledgements

We wish to thank our colleagues at the Comisión Federal de Electricidad (CFE), in particular Ricardo Márquez at Cerro Prieto, for useful discussions, and for providing data and ideas. We appreciate technical reviews by Emilio Antúnez and Mack Kennedy and the production of the paper by Judith Peterson at LBL. This work was supported in part by the geothermal programs of CFE, the Lawrence Berkeley Laboratory and the U.S. Geological Survey and in part by the Geothermal Division of the Department of Energy through a contract to LBL.

Bibliography

de León Vivar, J., 1988, Presencia de dos fases en el yacimiento del campo geotérmico de Cerro Prieto, Geotermia, Rev. Mex. de Geoenergía, v.4, p.203-211.

Fournier, R.O., 1979, A revised equation for the Na/K geothermometer, Geothermal Resources Council Trans., v.3, p.221-224.

Grant, M.A., Truesdell, A.H. and Mañón A., 1984, Production induced boiling and cold water entry in the Cerro Prieto geothermal reservoir indicated by chemical and physical measurements, Geothermics, v.13, p.117-140.

Halfman, S.E., Mañón, A. and Lippmann, M.J., 1986, Update of the hydrogeologic model of the Cerro Prieto field based on recent well log data, Geothermal Resources Council Trans., v.10, p.369-375.

James, R., 1968, Wairakei and Larderello: Geothermal power systems compared, New Zealand Journal of Science, v.11, p.706-719.

Lippmann, M.J. and Truesdell, A.H., 1990, Reservoir simulation and geochemical study of Cerro Prieto I wells, Proc. Fifteenth Workshop on Geothermal Reservoir Engineering, Jan. 23-25, Stanford, CA, p.211-220.

Lippmann, M.J., Truesdell, A.H., Halfman-Dooley, S.E., and Mañón, A., 1991, A review of the hydrogeologic-geochemical model for Cerro Prieto, Geothermics, v.20, p.39-52.

Stallard, M.L., Winnett, T.L., Truesdell, A.H., Coplen, T.B., Kendall, C., White, L.D., Janik, C.J. and Thompson, J.M., 1987, Patterns of change in water isotopes from the Cerro Prieto geothermal field, Baja California, Mexico: 1977-1986, Geothermal Resources Council Trans., v.11, p.203-210.

Truesdell, A.H. and Lippmann, M.J., 1990, Interaction of cold-water aquifers with exploited reservoirs of the Cerro Prieto geothermal system, Geothermal Resources Council Trans., v.14, p.735-741.

Truesdell, A.H., Terrazas, B., Hernández, L., Janik, C.J., Quijano, L. and Tovar, R., 1989, The response of the Cerro Prieto reservoir to exploitation as indicated by fluid geochemistry, Proc. CFE-DOE Symposium in Geothermal Energy, DOE Report CONF 8904129, p.123-132.

White, D.E., Muffler, L.J.P. and Truesdell, A.H., 1971, Vapor-dominated hydrothermal systems compared with hot-water systems, Economic Geology, v.66, p.75-97.

PROCEEDINGS, Seventeenth Workshop on Geothermal Reservoir Engineering
Stanford University, Stanford, California, January 29-31, 1992
SGP-TR-141

EXPERIMENTAL STUDY OF TWO-PHASE FLOW IN ROUGH FRACTURES

M. Fourar, S. Bories, and R. Lenormand *

Institut de Mécanique des Fluides, 31400, Toulouse, France

* Institut Français du Pétrole, 92506, Rueil Malmaison, France

ABSTRACT

Two-phase (air-water) flow experiments were conducted in horizontal artificial fractures. The fractures were between glass plates (1 x 0.5 m) artificially roughened by gluing a layer of glass beads of Imm diameter. Three rough fractures were studied: one with the two surfaces in contact, and two without contact. Videotape observations revealed flow structures similar to those observed in two-phase flow in pipes, with structures depending upon the gas and liquid flow rates. The data of flow rates, pressure gradients and saturations were interpreted using the generalized Darcy's law. Relative permeabilities curves were found to be similar to classical curves in porous medium, but not unique functions of saturations. The sum of gas and liquid relative permeabilities were found to be less than one at all saturations.

INTRODUCTION

Two-phase flow in fractured rocks occurs in recovery of petroleum or natural gas, recovery of coalbed methane, exploitation of geothermal energy, and isolation of radioactive waste. Models to predict two-phase flow in fractures are therefore of practical interest, but little is known of the laws governing such flow.

The approach most commonly taken to model two-phase flow in a single fracture is to treat the fracture as a 2-dimensional porous medium, and write Darcy's law for each phase. For horizontal flow:

$$V_{LS} = -\frac{K_0 K_{rL}}{\mu_L} \nabla P_L \qquad (1)$$

$$V_{GS} = -\frac{K_0 K_{rG}}{\mu_G} \nabla P_G \qquad (2)$$

where V is velocity, μ is viscosity, P is pressure, K_0 is the intrinsic permeability and K_r the relative permeability. Subscripts L and G represent liquid and gas respectively, and subscript S represents superficial velocity (also called Darcy velocity). The relative permeability factors account for the fact that each phase interferes with the flow of the other, and (at least in porous media) the K_{rL} and K_{rG} functions are strongly dependent upon phase saturation.

For lack of data, it is generally assumed for modeling purposes that in fractures the relative permeability to each phase is equal to its saturation; that is, each phase does not interfere with the flow of the other, and $K_{rL} + K_{rG} = 1$. This assumption is based upon the experimental work of Romm (1966), in which oil and water were confined to different regions of a smooth fracture by controlling the wettability of the fracture surfaces; and upon analysis of field data from geothermal reservoirs (Pruess et al 1983, 1984). But theoretical analysis and numerical simulations by Pruess and Tsang (1990) showed that in a rough fracture, significant phase interference would occur, and this was confirmed by the experimental work of Persoff et al. (1991) and Fourar et al. (1991,1992).

Roughness of the fracture walls is important in single phase flow because it increases friction and causes streamlines to be crooked even in laminar flow. In two- (or multi-) phase flow, wall roughness causes the aperture to vary from point to point in the fracture. Regions of smaller aperture (like smaller pores in porous medium) are more attractive to the wetting phase, and generally constitute the flow path for that phase. In this work we conducted two-phase flow experiments in rough fractures with openings of order of 1 mm. The data are interpreted using Darcy's model.

APPARATUS

A schematic view of the apparatus is shown in Fig. 1. The fracture consisted of two horizontal glass plates, 1 m long and 0.5 m wide. The plates were artificially roughened by gluing a single layer of 1 mm glass beads to each plate. Three sets of experiments were done: one with the rough surfaces in contact (h1) and two with the surfaces spaced apart (h2 and h3). For all the fractures, steel bars were tightened in place to prevent the glass from bulging at high flow rates.

The flow injector consisted of 500 stainless steel tubes of 1 mm o.d. and 0.66 mm i.d. Air and water were injected through alternating tubes to achieve uniform distribution of flow at the inlet. Air was injected at constant pressure, and its volumetric flow rate, corrected to standard pressure, was measured by an inline rotameter. Water was injected by a calibrated pump. At the outlet of the fracture, gas escaped to the atmosphere and water was collected in a decanter and recycled.

Nine liquid-filled pressure taps were cemented into holes drilled along the center line of the lower plate. Any pair of taps could be connected by valves to a differential transducer. This arrangement allowed measurement of non-uniform pressure gradients, but in the experiments the pressure gradient was always found to be uniform along the length of the fracture. The measured pressure gradient varied rapidly as the two taps were contacted by air or water, and only the time-averaged values were recorded.

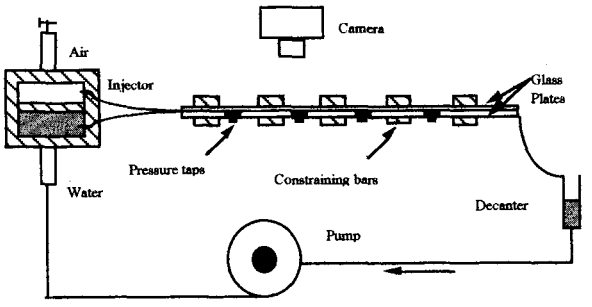

Fig. 1. Experimental apparatus

For each experiment, the fracture was initially saturated with water, and water was injected at a constant rate through the fracture. Air injection was started and increased stepwise through a range of flow rates. When steady state was reached for each flow rate, the pressure gradient and liquid saturation were measured. The fracture was Then resaturated with water and the experiment was repeated several times at different liquid flow rates.

Liquid saturation was measured by a volume-balance method. The water volume in the decanter was measured at the start of the experiment, with the fracture completely saturated with flowing water, and again when steady state had been reached at each air flow rate. Changes in the water volume in the decanter were then used to calculate a water balance, from which the liquid saturation in the fracture was determined.

RESULTS

Calculation of hydraulic aperture

The hydraulic aperture of each fracture was calculated from the single-phase liquid-flow data shown in Fig. 2. In this figure the data for the rough fractures plot as parabolas. Deviation from linearity indicates deviation from Darcy's law but does not necessarily indicate turbulent flow.

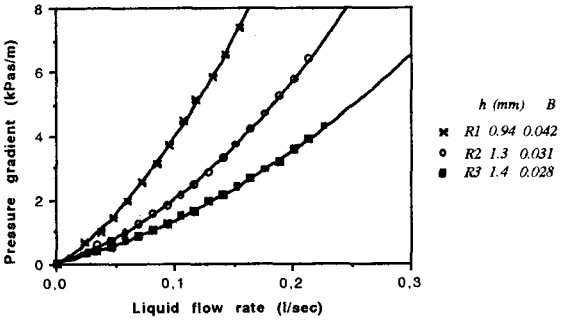

Fig. 2. Single-phase liquid flow

Such deviation has been observed in porous media (see reviews by Houper, 1974 and Temeng and Horne, 1988) and in rough fractures (Schrauf and Evans, 1986). The deviation from Darcy's law is attributed to inertial forces, which, at small Reynolds numbers, are negligible in comparison to viscosity forces. The relationship between pressure gradient and flow rate is then written (Schrauf and Evans, 1986):

$$VP = -\frac{12\mu}{h^2}Q - B\frac{\rho}{h^3}Q^2 \qquad (3)$$

Where Q is the volumetric flow rate per unit width of the fracture, B is a dimensionless number, a measure of the roughness, and h is the hydraulic aperture. Values of h and B determined from the parabolas are shown in Fig. 2.

Two-phase flow structures

The flow structures observed in our experiments are similar to those observed in pipe flow. By varying gas flow rate at a given liquid flow rate, we have identified several structures: bubbles, fingering bubbles, complex, films, and drops. Their maps are presented in Figure 3. In these figures, the volumetric flow rate of liquid and gas have been converted to superficial velocities.

INTERPRETATION

To correlate our data of flow rates, pressure drop, and saturation, we have used the generalized Darcy law.

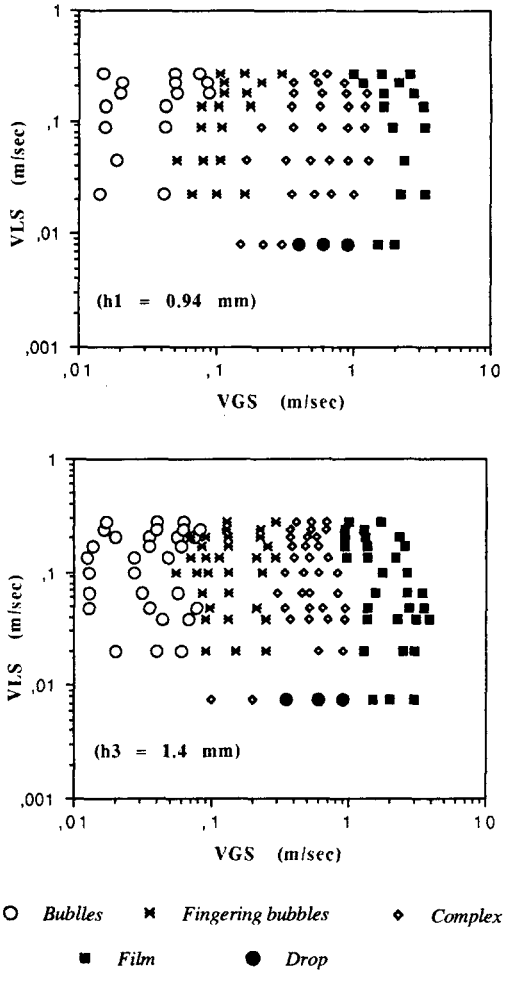

Fig. 3. Flow structure map

Model of Darcy

We suppose that the two-phase flow in fractures is governed by the generalized Darcy's law (1) and (2). In these equations, the relative permeability expresses the degree to which each phase impedes the flow of the other. In our experiments, the capillary pressure is uniform, then $\nabla P_G = \nabla P_L = \nabla P$, where ∇P is the observed pressure gradient under two-phase flow conditions. Then:

$$K_{rL} = -\frac{12\mu_L V_{LS}}{h^2 \nabla P} \quad (4)$$

$$K_{rG} = -\frac{12\mu_G V_{GS}}{h^2 \nabla P} \quad (5)$$

The calculated K_{rL} and K_{rG} are plotted against the measured saturation in Fig. 4. The curves are qualitatively similar to classical K_r curves obtained in porous media.

However, a family of curves are found (instead of one single curve as in porous media) depending on V_{LS} and V_{GS}. Relative permeabilities are therefore not unique functions of saturation under these conditions. In Fig. 5, the data are replotted as K_{rL} vs K_{rG}. These figures show that there is no unique relationship between K_{rL} and K_{rG} and the sum of K_{rL} and K_{rG} is less than one at all saturations.

The generalized Darcy's law cannot be used to correlate our relative permeabilities and saturations data because it does not take into account inertial forces or phase interference (coupling). Actually, the data in Fig. 2. show that in rough fractures even in single-phase liquid flow, the effect of inertial forces is not negligible.

CONCLUSIONS

Two-phase (air-water) flow experiments have been conducted in artificially roughened fractures of hydraulic aperture approximately 1 mm. The fracture consisted of

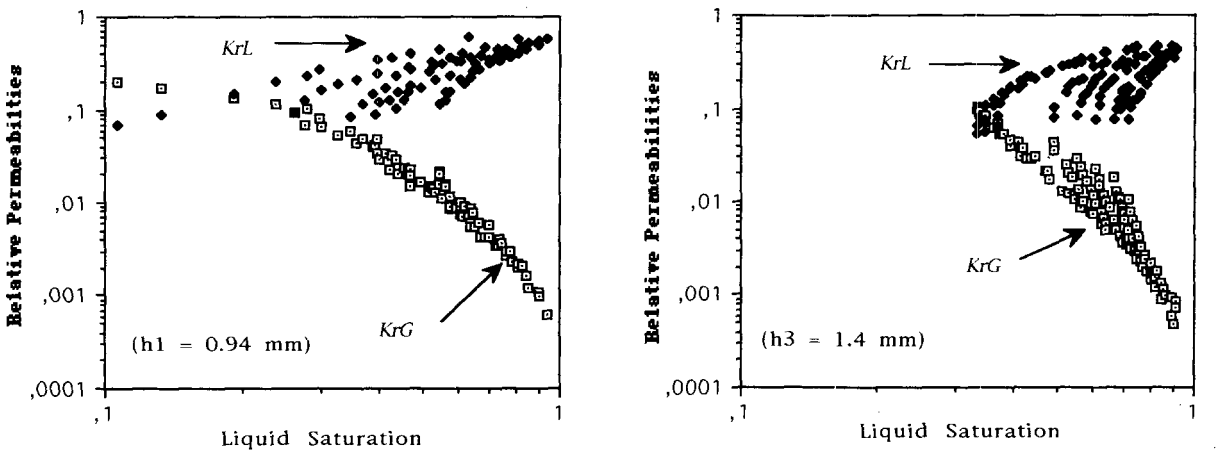

Fig. 4 Model of Darcy

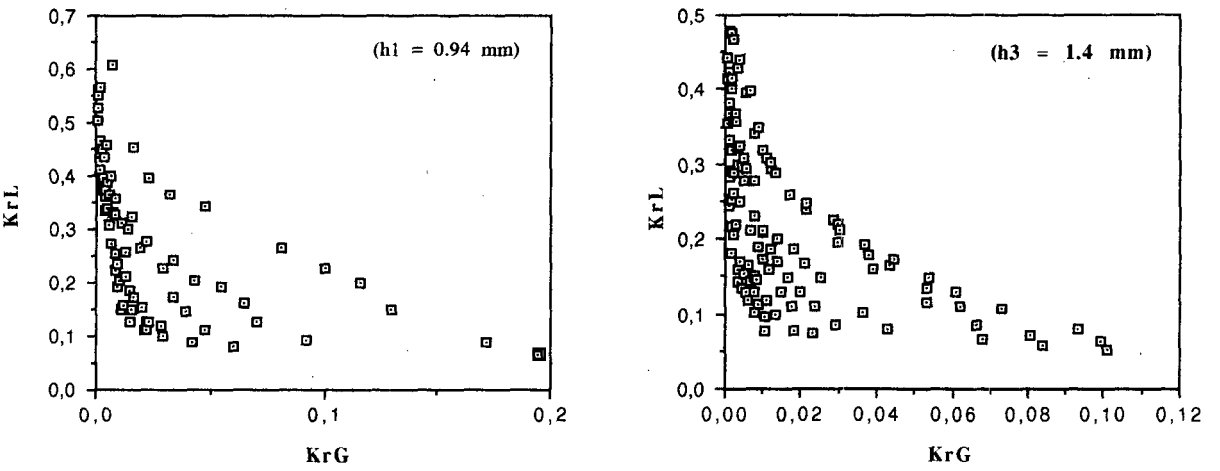

Fig. 5. Relative permeability factors

two horizontal glass plates, Im long and 0.5 m wide. The plates were artificially roughened by gluing a single layer of 1 mm glass beads to each plate.

Hydraulic aperture was calculated from the single-phase liquid flow taking into account the inertial forces due to roughness of the fracture walls.

By varying liquid and gas flow rates, we have identified several flow structures: bubbles, fingering bubbles, complex, films, and drops. These structures are similar to those observed in two-phase flow in pipes.

To interpret our data of flow rates, pressure drops, and saturations, we have used the generalized Darcy's law. The data showed that, contrary to what is commonly assumed, the relative permeability factors are not linearly dependent on saturations. Thus, K_{rL} is not a unique function of K_{rG}, and the sum of K_{rL} and K_{rG} is less than one at all saturations.

Because the flow structures observed present similarity to the structures observed in pipe flow, models for two-phase flow in pipes were examined (Fourar et al. 1992) in order to fit the data.

ACKNOWLEDGMENTS

The authors thank Peter Persoff for great help in translating the manuscript, and appreciate helpful discussions with Karsten Pruess and Cézar Zarcone.

REFERENCES

Fourar M. Piquemal J. and Bories S., (1991). Ecoulement diphasique bidimensionel plan liquide-gaz. II. Gradients de pression et fractions volumiques des phases d'un écoulement horizontal, Comptes Rendus Acad. Sci. Paris, 313 (II), 477-480.

Fourar, M., Bories S., Lenormand R. and Persoff P. (1992). Two-Phase Flow in Smooth and Rough Fractures: Measurement and correlation by Porous-Media and Pipe-Flow Models. (To be published)

Houper, A. (1974) Mécanique des Fluides dans les Milieux Poreux: Critiques et Recherches. Editions Technip, Paris.

Persoff, P. Pruess K., and Myer L. (1991). Two-Phase Flow Visualization and Relative Permeability Measurement in Transparent Replicas of Rough-Walled Rock Fractures, presented at Sixteenth Stanford Geothermal Workshop, Stanford University, Jan. 25-27.

Pruess, K. Bodvarsson G.S. and Stefansson V. (1983) Analysis of Production Data from The Krafla Geothermal Field, Iceland in Proceeding, Ninth Workshop on Geothermal Reservoir Engineering, Stanford University, pp. 345-350.

Pruess, K., Bodvarsson G.S., Stefansson V. and Eliasson E.T. (1984) The Krafla Geothermal Field,

Pruess, K. and Tsang Y.V. (1990). On Two-Phase Relative Permeability and Capillary in Rough-Walled Rock Fractures. Water Res. Res., 26 (9), 1915-1926.

Romm, E.S. (1966). Fluid Flow in Fractured Rocks (in Russian), Nedra Publishing House, Moscow. (English translation, W.R. Blake, Bartlesville, OK, 1972.)

Schrauf T.W. and Evans D.D. (1986). Laboratory Studies of Gas Flow Through a Single Natural Fracture. Water Res. Res., 22 (9), 1038-1050.

Temeng, K.O. and Home R.N. (1988). The Effect of High Pressure Gradients on Gas Flow. Paper SPE-18269 presented at 63rd Annual Technical Conference and Exhibition of SPE, Houston, TX.

PROCEEDINGS, Seventeenth Workshop on Geothermal Reservoir Engineering
Stanford University, Stanford, California, January 29-31, 1992
SGP-TR-141

EVALUATION OF SMALL DIAMETER COREHOLES FOR RESERVOIR INFORMATION

Susan Petty and Richard G. Adair
Susan Petty Consulting
and
Bill Livesay
Livesay Consultants

1.0 Introduction

Geothermal exploration has been highly successful to date in locating targets for drilling. However, the requirements for an economically successful geothermal well are both high flow rate and high temperature. Most geophysical and geochemical exploration methods have not been highly accurate in predicting the depth and actual temperature of a reservoir, nor have they been able to locate high permeability zones. The result is that most geothermal exploration is conducted by drilling core holes to better understand the heat flow in an area followed by drilling of production diameter exploration wells which can be flow tested to ascertain the permeability.

The goal of any exploration program is to determine reservoir economics. The cost of wells makes up between one quarter and one half the total cost of producing geothermal power. The number, design, depth of wells and placement of injectors are important to the optimal exploitation of the reservoir. Although early efforts at development have focused on rapid plant construction to begin cash flow, the history of producing fields emphasizes that understanding reservoirs can reduce the risk of rapid temperature or pressure declines and increase the success of step out drilling following initial exploitation. The high cost of large diameter production wells makes the collecting of exploration data on the reservoir through some less expensive method desirable.

Geothermal developers are still drilling resources with surface expression, hot springs and surface mappable fractures and faults. As these obvious resources are developed and as the obvious targets in productive fields are exhausted, new exploration tools are needed. One possibility is the use of deep core holes drilled for temperature gradient data to provide more reservoir information. Two methods not previously applied to geothermal reservoir assessment are suggested to augment other data obtained from coreholes.

2.0 Reservoir Information

To date only a part of the information needed for assessing reservoir economics has been obtainable from narrow diameter core holes. Even deep core holes yielded at most information about lithology, temperature and occasionally if a fluid sample was possible, fluid chemistry.

The information we need most about the reservoir, such as well productivity, reservoir size and storage, hydraulic conductivity and fluid chemistry is obtained by flow testing production diameters wells. Small diameter core holes or stratigraphic wells generally would not flow due to large frictional pressure drops. If slim holes did flow the rates were often to low to stress the reservoir as at Mt. McKushin on Unalaska Island in the Aleutions. Injection yielded some information, but in fractured formations, injectivity can be twice to five times the productivity of the same well due to increased fracture aperture due to thermal contraction of the rock and pressure propping, and due to density related changes in head.

3.0 Retrieving Reservoir Information from Slim Holes

Since coreholes have always been drilled for exploration purposes to obtain temperature logs, heat flow data and lithology, it seems appropriate to obtain as much information as possible from them. The idea of obtaining reservoir information from narrow diameter holes has been neglected due to the lack of success at flowing the wells and the lack of correlation between injection tests and later production. A suite of testing methods is suggested for improving the quantity and quality of reservoir data

obtained from coreholes.

4.0 Earthtide and Barometric Induced Pressure Changes in Reservoirs

Earthtides have frequently been suggested as a means of obtaining useful reservoir information through relatively inexpensive passive pressure measurements. Jacob first described the effect of barometric pressure changes on water levels in confined aquifers and developed the mathematics for calculating the storage coefficient from such measurements. Several other researchers have used tidal methods for reservoir analysis over a long period including Bredehoeft (1967), Van der Kamp and Gale (1983), Arditty (1978), Kanehiro (1979) and Axelsson (1980). Hanson describes the collection and analysis of earthtide data from the Raft River geothermal field in his 1984 report for Lawrence Livermore. More recently, Evans, et. al. (1991) used earth tides and barometric fluctuation methods to evaluate permeability and storage coefficients of sands near the Asswan dam in Egypt.

4.1 Parameters

There is some discussion about the parameters which can be evaluated using earth tide and barometric responses in aquifers. The total compressibility thickness product, ϕch or specific storage, S_s can often be calculated more accurately than through flow testing using such methods, particularly if flow test data from a single well test is considered. This can be of some significance in the long term prediction of reservoir behavior since many geothermal reservoirs are in fractured igneous or metamorphic rock with large variation in storage coefficient and which differ to a high degree from the typical sedimentary rocks of petroleum reservoirs or groundwater aquifers. If barometric effects are also considered, the average porosity of the reservoir can also be determined in combination with earth tide analysis (Bredehoeft, 1967).

The gravitational forces acting on the solid earth stress the formation, deforming the pore spaces containing the fluids. The ratio between the predicted tidal stress and the observed fluid level or pressure changes in a borehole is related to the elastic properties of the fluid, the rock and to the porosity of the rock as well as the permeability. Since the tidal stress acts over a very large area, the properties affecting the tidal response in the wellbore are averaged over a broad area.

Hanson (1984) uses the earth tide response of a well in a fractured reservoir with very low permeability in the formation to estimate the fracture direction. The high contrast between the fracture permeability and the formation permeability allows the phase shift and the admittance to vary sufficiently for different tidal periods to calculate the permeability under some circumstances. However, Hanson uses the correlation between the directional predicted stress and the observed phase lag and admittance at different frequencies to calculate fracture direction and dip. Figure 1 shows an example of one step in this method applied to data from a fractured well in the Imperial Valley. Earth tidal stresses normal to planes at various orientations were predicted using tidal software developed by Duncan Agnew (1984, personal communication). The cross correlations between the predicted tides and the observed tides were then calculated until a good match was found. This was then assumed to be the fracture dip and direction. The best match for Britz 3 was found at a strike of N42°E and a dip of 80°. The problem can be computationally reduced by generating a set of equations to be solved by a non-linear least-squares method. Hanson (1984).

4.2 Borehole Diameter Effect

Small borehole diameters, all other factors remaining constant, have the effect of increasing the tidal amplification of the borehole at tidal frequencies. The very small amounts of fluid squeezed from the formation during tidal dilatation result in large water level fluctuations for a small diameter well with a free liquid surface. In a well with a positive shut-in wellhead pressure, the well bore radius has the same effect; however, the effect of the well depth, which is to reduce the amplification, may overwhelm the affect of well radius.

Bredehoeft (1967) shows that the tidal amplification factor (which is comparable to the tidal admittance used by others) for the large permeabilities and borehole diameters less than 10 cm. (4 in.) and depths encountered in geothermal coreholes is always 1 at tidal periods. This makes it impossible to calculate permeability using earth tide analysis, since the permeability (and the transmissivity) are related to the admittance at

different tidal periods. However, under special circumstances where either the permeability is low, less than 0.929 cm^2/sec for the very large well bore radius of 30.5 cm. (12 in.) or greater, the tidal admittance or amplification factor varies sufficiently to be useful for calculating the permeability at tidal periods of 12 hours to 24 hours. Hanson's more detailed analysis yields similar results.

4.3 Tool Requirements

Although pressure sensors are available which in heat shields can be left in high temperature wells (500°F) for up to 12 hours, the earth tide and barometric pressure methods require that data be collected over a period of at least two weeks, preferably longer. The pressure responses in deep bore holes are commonly of the order of 0.01 to 0.1 psid. The fact that the difference in pressure or water level is the quantity to be measured makes the resolution and repeatability of the measurement more important than the absolute accuracy of the pressure measured. For this reason it is acceptable to use a system of capillary tubing with an expansion chamber of size at least twice the tubing volume set at depths of 25 m. or greater below the water level in the well. The pressure measurement should be made with a high resolution transducer such as the Paroscientific quartz transducer. Since the absolute pressures are not high, the resolution can be improved by using a transducer with a low pressure range. The system is purged with an inert gas such as nitrogen to reduce corrosion. Helium is not recommended due the difficulty of sealing leaks in helium systems. The system is purged periodically to remove condensed liquid and ensure pressure transmission to the transducer.

Leaks in the tubing and valves and fittings at the surface will cause pressure drops with time which recover dramatically after purging. Although the pressure transducer itself is not very sensitive to diurnal temperature fluctuations, heating and cooling of the tubing, valves and fittings at the surface can result in 24 hour period noise in the measured signal. If diurnal temperature changes are measured, this noise can be filtered mathematically from the signal, but ever effort should be made to reduce this noise by burying the transducer, excess tubing and associated valving in insulated boxes. Other sources of noise include high frequency atmospheric pressure fluctuations and heating and cooling cycling in the wellbore due to internal well circulation. These effects can often be removed by post processing. Radio interference can cause sharp spikes in the signal and any surface wiring should be shielded. High energy radio or other airwave transmissions such as LORAN can cause serious interference with pressure measurements of this type. Signal amplification and isolation can help to reduce these effects.

Monitoring of barometric pressure fluctuations using a transducer open to atmosphere allows for the most accurate analysis of barometric efficiency values and can be used to remove barometric effects from the data. Software for this purpose has been developed by the authors and used on data from the Philippines and Steamboat, NV. The best results are obtained when barometric pressure and water level changes are measured at the same sampling interval.

Sampling interval can be calculated from the Nyquist frequency:

$$f = n/2$$

where n is the sampling rate in $time^{-1}$ and f is the highest frequency which this sampling rate will accurately measure. However, if there is considerable energy in higher frequencies, aliasing of the data can occur. For example if a tidal period of 3 hours or 1×10^{-4} sec^{-1} is the highest frequency of interest then the sampling interval is 1.5 hours or 90 minutes. However, if barometric pressure changes are occurring at shorter than 3 hour periods or there is considerable noise from thermal cycling at periods of less than this then the data can be aliased. Most time series data is filtered during collection by building an instrument that doesn't respond to signals at higher frequencies than the Nyquist frequency. Since this isn't possible with pressure transducers, the only way to avoid these problems is to over sample and check the amplitude spectrum for high frequency noise. This might mean that ten minute sample intervals would be warranted for a few days to determine if there is significant energy at high frequencies.

4.4 Borehole Design Requirements

Since no flow of the well is needed for earth tide and barometric

pressure measurements, the requirements for well construction are only that the formation of interest is isolated by casing or intervening impermeable material and that the borehole is open to the formation or fracture. Significant skin effects can affect earth tide and barometric pressure measurements, so that an open, undamaged borehole is the best completion for this type of analysis. Most temperature gradient wells are completed with sealed 1.25 in. diameter tubing for running temperature probes. The effect of the tubing on the earth tide response is complex, but it can be analyzed. (See Evans, et al, 1991) However, these methods are best in open bore holes. Decreasing borehole diameter does not affect the ability to collect the measurements since the expansion chamber on the capillary tubing system can be as small as 1 cm od. as long as the length of the chamber allows for twice the volume of the tubing.

5.0 Borehole Seismics

A promising area for more detailed investigation of fractured reservoir properties is the use of borehole seismic techniques to evaluate fracture permeability, combined fracture and matrix permeability, fracture aperture and fracture height. Under the optimal circumstances this assessment can be not only qualitative, but also quantitative.

The techniques described here are currently being used experimentally by the oil and gas industry and for evaluation of nuclear waste disposal sites in Canada. They hold promise for evaluation of fractured geothermal reservoirs if the instrumentation required can be adapted for high temperature use.

5.1 Description of Method

The original work done in the development of borehole seismic fracture characterization methods was conducted by Atomic Energy of Canada Limited for the purpose of better characterizing fractures in potential nuclear waste repositories. A seismic source either in the borehole or on the surface causes fractures to expand and contract, stimulating a seismic wave in the borehole as well as an accompanying P wave. (Figure 2) The borehole acts as a waveguide for a trapped mode called a Stoneley wave, tube wave or in some sources, a water hammer wave. The volume of fluid ejected from the fracture is the same as the tube wave volumetric strain. Beydoun, et al (1985) showed that fracture permeability could be determined from tube waves generated in a tilted borehole intersecting a dipping fracture with parallel walls. His experiments used an array of sensors in the well and a source at varying distances from the well. The fracture permeability can be evaluated from the tube wave amplitude normalized to the direct P wave amplitude in the fluid, the pressure ratio shown in Figure 3.In addition to determining fracture permeability, the fracture length could also be observed under some circumstances. However, the technique required a costly vertical array and Vibroseis (TM Conoco) truck and it has never become popular.

Further information on the formation and fracture such as the fracture aperture and the bulk rock permeability can be obtained using the full waveform obtained during acoustic logging. (Tang, Cheng and Toksöz, 1991) In this method the source and multiple receivers are in the same borehole and can be on the some tool. Energy from a broad band source is absorbed by the fracture or permeable formation. Tube waves generated by the vibrating fracture are used to calculate fracture aperture.

More recently, Schlumberger has used full waveform sonic logging to evaluate permeability in a sandstone reservoir in the North Sea (Hornby, et al, 1991). Theoretical work by Chang, et al (1988) showed that velocity and attenuation of borehole Stoneley waves or tubewaves is dependant on the frequency, borehole radius, and the impedance in the permeable borehole wall. This impedance is inversely proportional to the formation permeability, but is also affected by the fluid viscosity. The largest difference in Stoneley wave velocity and attenuation occurs at low frequencies, below 10 kHz, making it necessary to use a source with energy in these frequencies and receivers which can respond to them.

Laboratory experiments currently being conducted at MIT, (Tang, et al, 1991) have applied similar methods to determination of fracture permeability in vertical and horizontal fractures. Energy absorbed by the fracture opens and closes it, moving a fluid volume in and out of the borehole which is seen as a Stoneley wave on the full wave form acoustic log. The fracture aperture is proportional to the velocity and attenuation of the

Stoneley wave. At low frequencies there is significant difference in the predicted Stoneley wave velocities and attenuation at different frequencies.

5.2 Borehole Diameter Effect

The generation of tube waves is integrally dependent on the borehole diameter. The smaller the diameter the larger the amplitude of the generated wave, since in a large diameter well more water is moved around and energy dissipated in its motion. However, petroleum well diameters are generally around 4-5 in., so this size is not considered a slim hole for them. Figure 4 shows plots of Stoneley wave response in three borehole sizes ranging from 1.5 to 4 in. Note that not only the wave amplitude, but the arrival time for the borehole stonely wave is altered by the diameter. This requires that analysis of data be modified by the borehole diameter information.

5.3 Tool Requirements

The experimental tool being using by Schlumberger has 11 receivers and a single transmitter 4.8 m. from the first receiver. The receivers are spaced at 15 cm. intervals. The source is fired every 7.5 cm as it is run with data recorded on magnetic tape. The tools are designed to run in holes as small as 3.5 in. diameter. However, the added thickness of heat shielding for operation in high temperatures, and the need for redesign of the tool to accommodate source and receiver pass through preclude the use of such tools in high temperature, narrow diameter holes without further development. The receivers and source are fairly robust for use in high temperature environments if appropriate materials are selected. Only the data collection and preprocessing electronics would be likely to require heat shielding. Such development from the private sector is unlikely in the present economic climate. However, an increase in demand for such services could stimulate development.

5.4 Borehole Design Requirements

Since flow is not required for borehole seismic methods, and the method itself determines the depth of fractures or permeable zones and their separate permeability, the completion requirements for seismic methods are even less difficult than for earth tide methods. Since the tool is long, 10 to 60 ft depending on the number of receivers and their separation, lubricators suitable for the tool length are required.

6.0 Recommended Slim Hole Exploration Program

Figure 5 shows a core hole which is suitable for use with shielded borehole seismic logging tools which can be envisioned for the immediate future. This well is also designed to accommodate flow without jeopardizing fresh water aquifers or risking subsurface blowout should very high temperature fluids be encountered at shallow depths. The well could also be used for injection testing. The design depth for cost estimation is 1640 m. (5000 feet). Lost circulation problems which can be severe in very large diameter production wells are somewhat reduced by the smaller hole size.

Many geothermal areas have attractive thermal features such as hot springs, geysers or fumaroles. It is often of interest to the community to protect such features. In order to do this the effect of geothermal production on these features needs to be predicted. Interference testing while monitoring thermal features and wells penetrating thermal aquifers can provide useful data for determining long term effects of production on thermal features. Coreholes drilled as part of an exploration program often are used for long term monitoring of the field. It becomes increasingly important to plan their construction for such uses. The design well has a sufficiently long mechanical life to be suitable for long term monitoring of the field.

Although temperature gradient wells are frequently left uncased, they are generally abandoned after less than a year and are for the most part of shallow depth. The well design presented here is intended to penetrate reservoirs with high temperature fluids and can accommodate accidental flows of high temperature fluids with reduced danger of subsurface blowout if the flow is contained.

6.1 Estimated Cost

The design well should cost about $600,000 in a typical metamorphic or igneous geothermal field with lost circulation problems in the first 2500 ft. For comparison, a production diameter well would cost between $1,200,000 and $1,400,000. The upper portion of the well is drilled with conventional rotary technology using a

rig capable of both rotary drilling and coring. Rig costs are about $3000/day with $10/foot for coring.

Significant cost savings can be realized by designing holes for short lifetimes before abandonment and not using the holes for flow or injection. The hole can be cased to a shallower depth, smaller diameter surface casing and smaller core diameters can be used. This further reduces the risk of lost circulation. This type of well can not be flowed, and may not be suitable for long term monitoring.

7.0 Conclusions

A suite of test methods run on coreholes drilled for temperature and lithology information into geothermal reservoirs can yield reservoir data useful for prediction of future well behavior. Cores yield lithology for understanding reservoir geology and as input for elastic parameters in seismic methods. Temperature with depth and heat flow data can be collected by repeated temperature logging of the well. Fluid sampling can yield information about reservoir chemistry. Long term collection of small scale pressure variation with time in the static well bore coupled with surface measurement of barometric pressure fluctuations can be used to calculated average reservoir storage, porosity, fracture direction and under some circumstances permeability.

Development of seismic logging tools for high temperature environments could further improve reservoir information from coreholes. Seismic methods allow the measurement of bulk formation permeability as well as the depth, permeability and fracture aperture of individual fractures. These reservoir parameters can be used to predict reservoir behavior with time under production conditions. Combining this information with well bore flow models can predict well productivity. The coreholes can be used for long term monitoring of reservoir drawdown during production, interference effects and injection/production well interference. Further development work is needed before the current experimental tools can be run in high temperature wells. However, if a market for such tools existed, the development needed is not extensive and could be rapidly accomplished.

References:

Arditty, Patricia, The Earth Tide Effects on Petroleum Reservoirs: Preliminary Study, Thesis, Stanford University, 1978.

Axelsson, Gudni, Tidal Tilt Observation in the Krafla Geothermal Area in North Iceland, Masters Thesis, Oregon State University, 1978.

Beydoun, W. B., Cheng, C. H. and Toksöz, M. N., "Detection of Subsurface Fractures and Permeable Zones by the Analysis of Tube Waves,"

Bredehoeft, John D., "Response of Well-Aquifer Systems to Earth Tides", Journal of Geophysical Research, Vol. 72, No. 12, June, 1967.

Chang, S. K., Liu, H. L. and Johnson, D. L., "Low-frequency tube waves in permeable rocks," Geophysics, Vol. 53, No 4, April, 1988.

Evans, Keith, Beavan, J., and Simpson, D., "Estimating Aquifer Parameters from Analysis of Forced Fluctuation in Well Level: An Example From the Nubian Formation Near Aswan, Egypt. 1. Hydrogeological Background and Large-Scale Permeability Estimates," Journal of Geophysical Research, Vol. 96, No. B7, July 10, 1991.

Hanson, Jonathan M., Evaluation of Subsurface Fracture Geometry Using Fluid Pressure Response to Solid Earth Tidal Strain, Lawrence Livermore National Laboratory, UCID-20156, September, 1984.

Hornby, Brian E., Murphy III, W. F., Liu, H.L., and Hsu, K., "Reservoir sonics: A North Sea case study," Geophysics, Vol. 57, No. 1, January, 1992.

Kanehiro, Brian, The Response of Aquifers to the Earth Tides, Masters Thesis, University of California at Berkeley, 1979.

Tang, X. M., Cheng, C. H., and Toksöz, M. N., "Stoneley-wave Propagation in a Fluid-Filled Borehole with a Vertical Fracture," Geophysics, Vol. 56, No. 4, April, 1991.

Toksöz, M. N., Cheng, C. H., and Willis, M. E., "Seismic Waves in a Borehole - A Review,"

van der Kamp, G. and Gale, J. E., "Theory of Earthtide and Barometric Effects in Porous Formations With Compressible Grains," Water Resources Research, Vol. 19, No. 2, April, 1983.

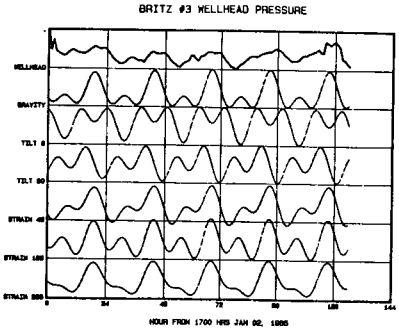

Figure 1 Britz 3 earth tide response and predicted directional tidal strain. Tilt 0° - Stress on horizontal plane, Tilt 90° - Stress on vertical plane. Strains are shown for vertical planes with orientation in degrees from north.

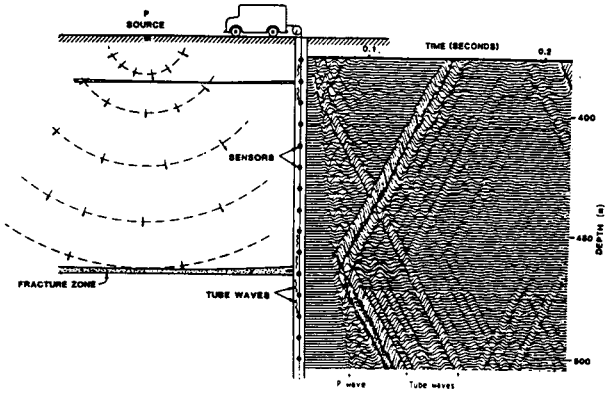

Figure 2 Schematic diagram of the mechanism of generation of tube waves (left) and an actual hydrophone VSP section. Beydoun, 1985.

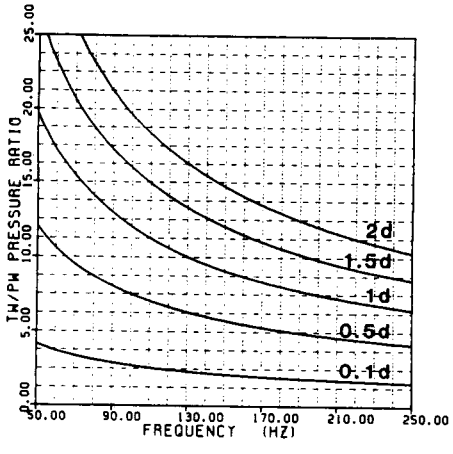

Figure 3 Tube wave to P wave pressure ratios as a function of frequency and permeability in granite. Beydoun, 1985.

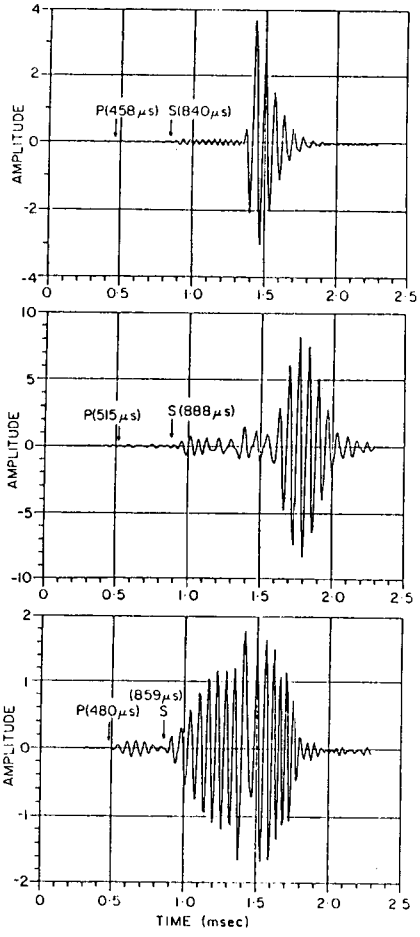

Figure 4 Synthetic microseismograms generated using identical formation and borehole parameters, but with different borehole radii. The top diagram is for a radius of 4.5 cm. (1.8 in.), The middle is for 10 cm. (4 in.), and the bottom for an intermediate size of 6.7 cm. (2.64 in.) Toksöz(1988)

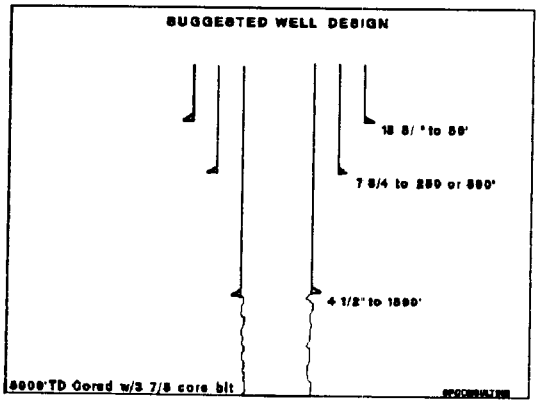

Figure 5 Wellbore diagram for typical corehole designed to maximize reservoir data, minimize cost and reduce safty risks.

PROCEEDINGS, Seventeenth Workshop on Geothermal Reservoir Engineering
Stanford University, Stanford, California, January 29-31, 1992
SGP-TR-141

Laboratory Measurement of Sorption in Porous Media

M. S. Harr, P. Pettit and H. J. Ramey Jr.

Stanford Geothermal Program
Department of Petroleum Engineering
Stanford University, Stanford, CA 94305

ABSTRACT

A new apparatus for measuring steam adsorption-desorption isothermally on rock samples has been installed and initial runs made for rock samples from geothermal reservoirs. The amounts adsorbed measured in these experiments are the same order of magnitude as previous experiments.

INTRODUCTION

Adsorption occurs on rock surfaces and in micropores, which are pores less than 20 A in diameter. Micropore adsorption is larger than surface adsorption, thus the distribution and abundance of micropores plays a key role in the amount of adsorbate. Formations with large amounts of space available in the micropores are typically low permeability formations.

Normally in petroleum engineering, gas is believed to be stored as a compressed gas in the pore space and as solution gas in liquids. In coal beds and Devonian shales, methane adsorption is believed to be a major factor in the storage and release of gas. In these systems, adsorption is believed to be the dominant reservoir storage mechanism.

Not long after the tax trial for the Geysers steam producers in 1968, it became evident that steam was stored in the reservoir as a liquid. However, the reservoir pressure was too low for a liquid to exist at the reservoir temperature. Ramey (1990) called this the "Geysers paradox". Adsorption is a mechanism which permits existence of liquid at pressures below the saturation vapor pressure. In this study, reservoir engineering for geothermal systems under adsorption will be considered.

APPARATUS AND PROCEDURE

The most popular method for measuring the equilibrium mass of fluid adsorbed is the BET method named for Brunauer, Emmit and Teller (1938). In this method, porous material is exposed to a known volume of gas. The pressure is allowed to equilibrate. The amount of gas adsorbed can derived from the difference between the amount of gas injected and the amount of gas at the equilibrium pressure. This type of instrument is available commercially for the measurement of adsorption of gas on a solid.

Equilibrium measurements of adsorption were made using a Porous Materials, Inc. (PMI) Sorptometer. The PMI Sorptometer is a fully automated BET type apparatus. This equipment was modified by Porous Materials, Inc. for the Stanford Geothermal Program.

The instrument requires weighing, loading and removing samples. Prior to a run, samples were packed into the sample holder, and were then weighed. The sample was placed in the apparatus and adsorption and desorption was measured. Upon completion of the measurements, the sample was reweighed. This weight was entered into the computer for data reduction.

Sorption isotherms were measured at 100 C for all samples. Most of the runs were measured at pressures from 1 psia to pressures close to 14 psia. Desorption data were measured from the maximum pressure to 0.5 psia. Measurements at 140 C were made from 5 psia to pressures close to 40 psia and back to 5 psia. Attempts were made to reach the flat surface saturation vapor pressure, but the instrument was unable to build enough pressure.

The equilibrium pressures and volumes of steam adsorbed are recorded in a data file. The Sorptometer processes the data by using the ideal gas law to convert steam adsorbed to standard cubic centimeters of water vapor

at atmospheric pressure and 0 C per gram of rock. This output was converted to grams of gas adsorbed per gram of rock and pressure was converted to relative pressure (pressure divided by saturation pressure).

RESULTS

Adsorption and desorption isotherms for samples from different geothermal fields were measured using the PMI Sorptometer. The first sample was a piece of graywacke core material from an unknown well in the Geysers shallow reservoir in the southwestern part of the field. The sample was ground into pieces small enough to fit into the sample holder. Figure 1 is the adsorption and desorption isotherms at 100 C for particles larger than 2.362 millimeters.

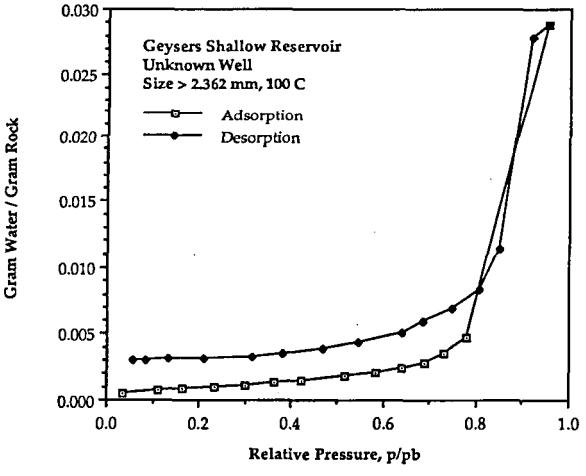

Figure 1: Sorption isotherms at 100 C for an unknown well in the Geysers Shallow Reservoir; particle sizes greater than 2.361 mm.

The second sample was well cuttings from the Geysers Field well OF52-11 from a depth of between 5000 to 5200 feet. The cuttings were cleaned and sieved. A sample of particles greater than a No. 270, 0.0533 millimeters, sieve was used. Adsorption and desorption isotherms measured at 100 C are shown in Figure 2 and results at 140 C are shown in 3.

The maximum amount adsorbed ranged from 0.029 to 0.053 grams of water per gram of rock at 100 C. At relative pressures close to 0.8 the amount adsorbed ranged from 0.0046 to 0.0062 grams of water per gram of rock. Herkelrath measured an adsorption amount of 0.011 gram of water per gram of

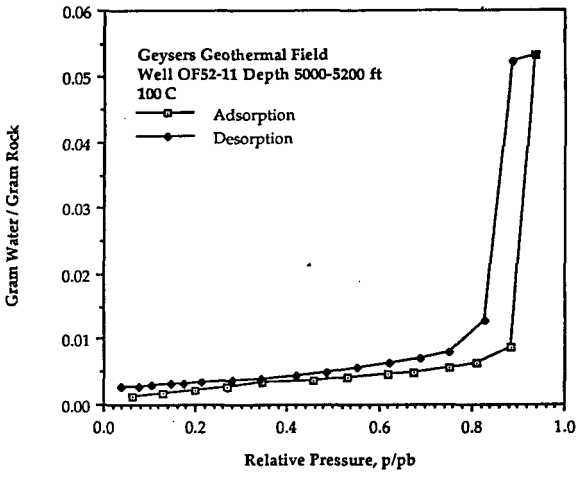

Figure 2: Sorption isotherms at 100 C for the Geysers Well OF52-11 5000-5200 ft. depth

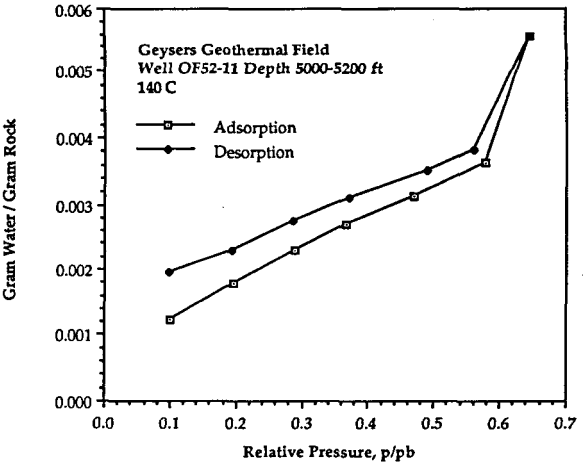

Figure 3: Sorption isotherms at 140 C for the Geysers Well OF52-11 5000-5200 ft. depth

rock at a relative pressure of 0.8 and a maximum of 0.012 grams of water per gram of rock. At a relative pressure of 0.8, the values from this study are approximately one half of those measured by Herkelrath, but the maximum amounts were more than twice of those of Herkelrath.

CONCLUSIONS

A new apparatus has been installed to measure steam adsorption in porous media. Compared to the work of previous researchers, results are of the same order of magnitude. Detail on results are presented by Harr (1991).

Although the equipment appears to be working well and meets most objectives, there are problems which will be checked during the coming year. There appears to be an unusual amount of hysteresis between adsorption and desorption for some runs. We believe rock samples were ground too fine for the initial runs and this may have affected the high adsorption at high relative pressures.

Runs have been made for some limestone geothermal samples from several geothermal fields other than The Geysers. Results require checking. It is intended to run many samples from The Geysers and other fields to explore the range of results to be expected in any geothermal field.

BIBLIOGRAPHY

Brunauer, S., Emmit, P.H. and Teller, E.: "Adsorption of Gases in Multimolecular Layers,"J. Amer. Chem. Soc. (February, 1938) Vol. 60, pp 309-319.

Harr, M.: Sorption of Steam in Geothermal Rocks, M.S. Thesis, Stanford University,(August, 1991).

Herkelrath, W. N. and Moench, A. F.: "Laboratory Investigations of the Physics of Steam Flow in a Porous Medium," Open File Report No. 82-95, U.S. Geological Survey (1982).

Hsieh, C. H.: Vapor Pressure Lowering in Porous Media, PhD dissertation, Stanford University (August, 1980).

Luetkehans, J.: A Laboratory Investigation of Steam Adsorption in Geothermal Reservoir Rocks, M. S. Thesis, Stanford University (March, 1988).

PMI Automated BET Sorptometer, Porous Materials, Inc., 83 Brown Road, Ithaca, NY 14850.

Properties of Saturated and Superheated Steam, American Society of Mechanical Engineers (1967).

Ramey, H. J. Jr.: "Adsorption in Vapor Dominated Systems," USDOE Geothermal Program Review VII[I (April, 1990), pp 63-67.

PROCEEDINGS, Seventeenth Workshop on Geothermal Reservoir Engineering
Stanford University, Stanford, California, January 29-31, 1992
SGP-TR-141

AN ACCURATE FORMULATION OF THE SOLUBILITY OF CO_2 IN WATER, FOR GEOTHERMAL APPLICATIONS

Eduardo R. Iglesias and Sara L. Moya

Instituto de Investigaciones Eléctricas
Departamento de Geotermia
Apartado Postal 475, Cuernavaca 62000, Mor., México

ABSTRACT

The solubility correlations for the H_2O-CO_2 system applied so far for numerical simulation of geothermal reservoir and well flows are crude. This is due, at least partly, to the significant disagreement existing between the solubility models and results published in the specialized literature. In this work we analyze the reasons underlying this disagreement. On this basis, we propose a thermodynamically correct, and numerically accurate model for the solubility of carbon dioxide in water. Its range of validity is up to 350 °C and 500 bar. Our main contributions are: (a) the adoption of an equation of state for the gas phase that reallistically acounts for the non-ideal behavior of both components and that of the mixture, within the P-T range considered; and (b) to accurately include the effects of temperature and pressure on the solubility of carbon dioxide in the liquid phase. The proposed model fits the available phase equilibrium data for the H_2O-CO_2 system nicely. In particular, it does not present the severe conflict between the linearity of the model and the lack of linearity of the data, evident in earlier models. The tight fit obtained with our model indicates that the complexities of H_2O-CO_2 phase equlibrium are well represented by it.

INTRODUCTION

Numerical simulation of geothermal flows in reservoirs and wellbores requires knowledge of thermophysical properties of the fluids involved. In some cases the pure-water approximation is satisfactory. In others, the presence of noncondensible gases makes it inaccurate. Usually, carbon dioxide is, by far, the predominant gas in geothermal fluids. Thus, several models of the thermophysical properties of H_2O-CO_2 mixtures (e.g., Sutton 1976; O'Sullivan et al., 19; Pritchett et al., 1981) have been applied in the geothermal literature (e.g., Sutton 1976; Sutton and McNabb, 1977; Straus and Schubert, 1979; Iglesias and Schroeder, 1979; Pritchett et al., 1981; O'Sullivan et al., 1985; Mc Kibbin and Pruess, 1988).

The approximations to the solubility of CO_2 in water implemented in these models are not very accurate, as recognized by their authors. This is hardly surprising, because the solubilities inferred by specialists (e.g., Ellis, 1959; Ellis and Golding, 1963; Takenouchi and Kennedy, 1964; Malinin, 1974; Zawisza and Malesiñska, 1981; Nighswander et al., 1989), for temperature and pressure conditions of geothermal interest, disagree significantly (Fig.1). In this work we discuss the reasons underlying this disagreement, and propose an accurate formulation, suitable for geothermal applications.

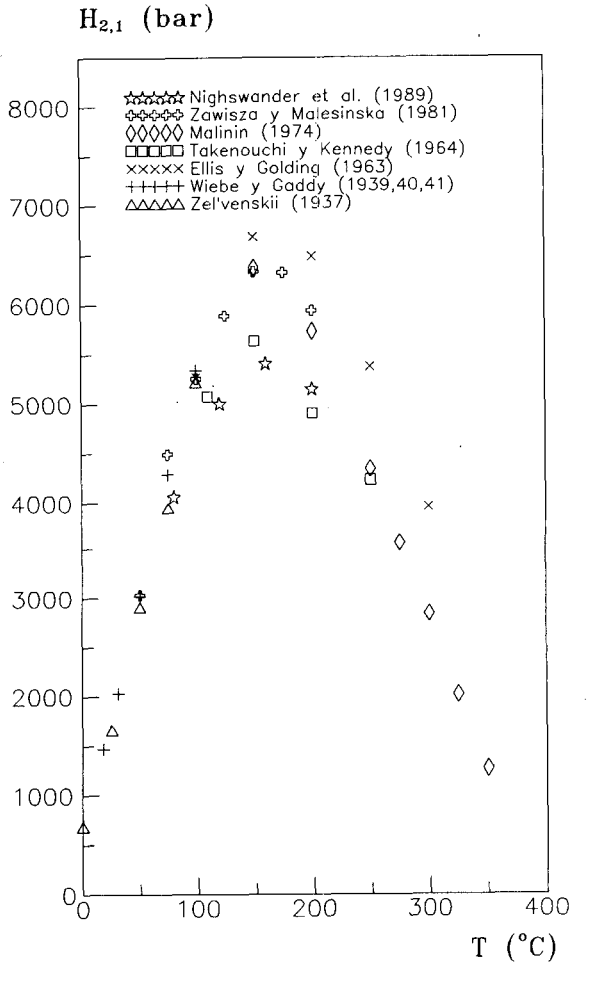

Fig. 1. Values of Henry's law constant by different authors.

THERMODYNAMICS OF CO_2 SOLUBILITY

The solubility of a gas in a liquid is determined by the thermodynamic equations of phase equilibrium. If a gaseous phase (G) and a liquid phase (L) are in equilibrium, then for any component i the fugacities in both phases must be the same (e.g., Prausnitz, 1969):

$$f^G_i = f^L_i \quad (1)$$

For the CO_2 component ($i = 2$), equation (1) may be conveniently rewritten as (e.g., Prausnitz, 1969):

$$\phi_2 y_2 P = \gamma_2 x_2 H_{2,1}(P_1^s) \exp \int_{P_1^s}^{P} \frac{v_2^\infty}{RT} dP \quad (2)$$

where ϕ is the fugacity coefficient, P total pressure, x and y liquid- and gaseous-phase mole fractions respectively, γ the activity coefficient, $H_{2,1}$ the thermodynamic equivalent of Henry's law constant, P_1^s the saturation pressure of water, v_2^∞ the partial molar volume of CO_2 in the liquid phase, T absolute temperature and R the gas constant. Note that, in general,

$$\phi_2 = \phi_2(T, P, y_1, y_2) \quad (3)$$

$$\gamma_2 = \gamma_2(T, P, y_1, y_2) \quad (4)$$

$$v_2^\infty = v_2^\infty(T, P) \quad (5)$$

DISCUSSION OF PREVIOUS WORK

As shown in Fig. 1, there is good agreement on the values of $H_{2,1}$ for t≤100 °C. Thus, we shall concentrate our discussion on the temperature range 100<t≤350 °C. The determinations of CO_2 solubility published in the specialized literature are based on different approximations to eq. (2). From this equation follows that the dispersion shown in Fig. 1 must arise from incompatibility of solubility data and/or from differences in the approximations adopted for variables appearing in (2).

The available experimental data cover a wide range of solubility. The experimental setups also differ, sometimes considerably. Some authors measured the compositions of both phases along isotherms, for different pressures (e.g., Malinin, 1959; Todheide and Franck, 1963; Takenouchi y Kennedy, 1964). Others simply measured the total pressure of the system and the liquid phase composition along isotherms and somehow estimated y_2 (e.g., Ellis, 1959; Ellis and Golding, 1963; Nighswander et al., 1989). Thus, there are several sets of (x_2, y_2, T, P) and (x_2, T, P) data available. Furthermore, the ranges of pressures and temperatures covered by different authors vary widely. Due to the experimental difficulties involved, some serious disagreements exist betwen some of these data sets. For example, Ellis and Golding (1963) found significant disagreement with Ellis' (1959) results, in the range 100 °C<t<300 °C; and Takenouchi and Kennedy (1964) showed that their solubility data agree reasonably with that of Malinin (1959) but are differ significantly from those of Todheide and Franck (1963) for some isotherms.

As to the approximations used in (2) by different workers to infer the thermodynamic equivalent of Henry's law constant, four parameters must be examined: P_2 the partial pressure of CO_2, ϕ_2, γ_2, and the integral in eq. (2), which is called the Poynting correction.

Ellis (1959) and Ellis and Golding (1963) approximated P_2 as $(P-P_1^s)$; Nighswander et al. (1989) seem to have done the same (they do not state explicitly how they computed the partial pressure of CO_2). This is a good approximation when $y_1 << y_2$. However, for the H_2O-CO_2 system, y_1 varies in a complex way, from about 0.04 to about 0.92, for 110≤t≤350 °C and 100≤P≤500 bar (e.g., Takenouchi and Kennedy, 1964). Most other workers cited in Fig. 1 adopted the correct thermodynamic definition: $P_2 = y_2 P$.

For the CO_2 fugacity coefficient, several authors (Ellis, 1959; Ellis and Golding, 1963; Takenouchi and Kennedy, 1964; Malinin, 1974) adopted the Lewis fugacity rule that estimates the fugacity coefficient of a component in a gas mixture as the fugacity coefficient of the pure component at the same temperature and presure of the mixture. Although this is a good approximation for any gas mixture at any pressure when the component is present in large excess (say y_2>0.9, e.g., Prausnitz, 1969), the range of compositions found at the temperatures and pressures of geothermal interest (see preceding paragraph) preclude its utilization for H_2O-CO_2 mixtures. Moreover, for components of significantly different molecular properties, such as H_2O and CO_2, the error introduced by the Lewis rule is often extremely large (Prauznitz, 1969). Zawisza and Malesiñska (1981) computed ϕ_2 from a virial equation of state truncated after the second term, and their own measurements of the molar volume of the gas mixture. Nighswander et al. derived their fugacity coefficients from a Peng-Robinson equation of state for the gaseous mixture.

The activity coefficient γ_2 was taken equal to unity by all the authors cited in Fig. 1, with the exception of Malinin (1974). This last author adopted $\gamma_2 = \exp[A(1-x_1^2)/RT]$, a standard approximation first derived by Krichevsky and Illinskaya (1945), where A is an empirical constant determined by the intermolecular forces in the solution. Whether or not γ_2 can be taken equal to unity is a matter best resolved by comparing the model with the data. More discussion on this below.

The Poynting correction was assumed negligible by Ellis (1959) and Ellis and Golding (1963); Takenouchi and Kennedy (1964) adopted the Krichevsky-Kasarnovsky (1935) formulation, which implies that ν_2^∞ does not depend on pressure; Zawisza and Malesiñska (1981) assumed ν_2^∞ to be independent of pressure and temperature. Malinin (1974) showed that ν_2^∞ varies significantly with temperature and pressure, and used a (different) mean value of ν_2^∞ for each isotherm to approximate the Poynting correction. Nighswander et al. (1989) assumed ν_2^∞ inversely proportional to their measured liquid density, which resulted a function of T but independent of P (i.e., $\nu_2^\infty(T)$) and adopted the Krichevsky-Kasarnovsky approximation. Within the P-t range considered in this work (up to 350 °C and 500 bar), Malinin's data for ν_2^∞ result in values of the Poynting correction varying from negligible to more than 0.7. Thus, the value of the exponential factor in eq. (2) may be as high as about 2, and cannot be ignored. Moreover, the variability of ν_2^∞ with T and P is not accurately represented by Malinin's approach to compute the Poynting correction.

PROPOSED MODEL

The preceding discussion indicates that a main source of error for the earlier solubility models is the choice of the Lewis fugacity rule to estimate ϕ_2. Fortunately, Spycher and Reed (1988) recently provided a way to compute reliable fugacity coefficients for H_2O-CO_2 mixtures, at temperatures and pressures of geothermal interest. We adopted their method, which is based on a virial equation of state for gas mixtures, that includes up to the third virial coefficient. The virial equation of state is the only one known to have a thoroughly sound theoretical foundation for pure and mixed gases (Mason and Spurling, 1969). Unlike empirical or semi-empirical equations of state, it does not require the introduction of hard-to-justify mixing rules. The inclusion of the third virial coefficient was required to accurately fit the experimental data (Spycher and Reed, 1988).

To preserve accuracy, Spycher and Reed considered two P-t ranges: one up to 350 °C and 500 bar, and the other fron 450 °C to 1000 °C and up to 1000 bar. As our present goal relates to subcritical geothermal systems, this work incorporates only the lower range.

Appendix 1 presents the formulae and the necessary coefficients to compute ϕ_2 whith this model.

Another significant source of error indicated by the discussion of the preceding section is the Poynting correction. As mentioned, Malinin (1974) demonstrated the dependence of ν_2^∞ on temperature and pressure (Fig. 2). The 300 kg cm^{-2} isobar represents also the behavior of ν_2^∞ at lower pressures. To facilitate accurate computation of the Poynting correction, we correlated Malinin's results as described in Appendix 2. The lines of Fig. 2 demonstrate the resulting fit. This fit is applied to compute the Poynting correction in our solubility model.

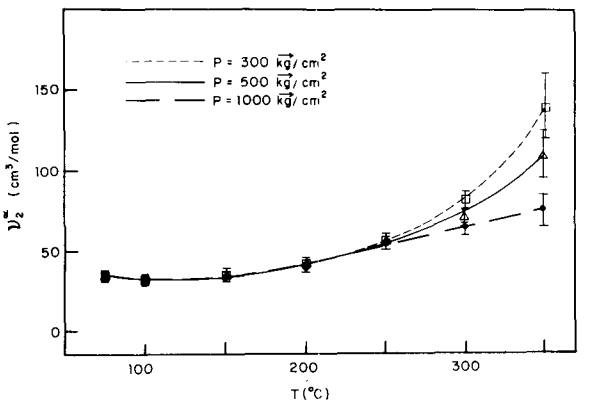

Fig. 2. Partial molar volume of CO_2 in liquid water, after Malinin (1974). The lines represent our fit.

The last important parameter in eq. (2) to be defined for our model is the activity coefficient. Our choice of more realistic fugacity coefficients and a more accurate way to account for the Poynting correction, promised significant improvements on earlier models of CO_2 solubility in water. Thus, we decided to first adopt the simplest approximation for the activity coefficient, i.e. $\gamma_2=1$, verify the consistency between the model and the data, and then decide whether a more involved approximation was necessary.

To complete the model, self-consistent values of $H_{2,1}(T)$ were needed. Replacing our fit for ν_2^∞ in eq. (2), integrating, taking logaritms and rearranging we obtained

$$\left[\log\left(\frac{\phi_2 y_2 P}{x_2}\right) - AP^2\right] - BP + C \qquad (6)$$

where

$$A = \left[\frac{v_{300}('T')}{2 \cdot 2 \cdot 303 \cdot RT}\right]\left[\alpha T + \sigma\right] \qquad (7)$$

$$B = \left[\frac{v_{300}('T')}{2 \cdot 303 \cdot RT'}\right]\left[\alpha T + \sigma\right] \qquad (8)$$

$$C = \log H_{2,1} - \left[AP_1^s + B(P_1^s)^2\right] \qquad (9)$$

Note that A, B and C depend only on temperature. Equation (6) is similar to that used by most authors to compute values of $H_{2,1}(T)$ from phase equilibrium data measured along isotherms. The left term is computable from experimental data and, in our case, Spycher and Reed's fugacity coefficients (Appendix 1). The right term is a linear function of pressure along isotherms. B, the slope, is a known quantity in our model. From C, the intercept, one infers the values of $H_{2,1}(T)$ for the available experimental isotherms.

We procesed 11 isotherms from Malinin (1959), Todheide and Franck (1963) and Takenouchi and Kennedy (1964), that span the ranges $110 \leq t \leq 350$ °C and $P \leq 500$ bar. We selected isotherms for which there were at least 3 (x_2, y_2, P, T) data points. The intercepts were obtained fron least square fits, constrained by our knowledge of B (eq. (8)). Our fits (Fig. 3) are satisfactory. In particular, they do not present the severe lack of linearity evidenced by Malinin's (1974) and Takenouchi and Kennedy's (1964) results in the lower pressure range. Moreover, the agreement between model and data indicates that the assumption of ideal solution (i.e., $\gamma_2=1$) was warranted. In all, the tight fit obtained with our model indicates that the complexities of H_2O-CO_2 phase equlibrium are well represented by it.

Figure 4 compares our results for $H_{2,1}(T)$ with those of previous work. Clearly, our values are significantly lower than the rest, for $110 < t \leq 325$ °C. Two main factors are responsible for this behavior. First, our fugacity coefficients differ significantly from the pure-gas coefficients of Majumdar and Roy (1956) adopted by Takenouchi and Kennedy and by Malinin (Figs. 5-6). Second, our values of the Poynting correction are significantly greater than those of Malinin (1974), for $t > 250$ °C and $P > 300$ bar, due to Malinin's averaging of the partial molar volumen to approximate the integral. The interplay between these two factors explains why our $H_{2,1}(T)$ results are lower. According to eq. (2), $H_{2,1}(T)$ is proportional to ϕ_2 and inverserly proportional to the exponential of the Poynting integral. Thus, for $t < 250$ °C, our smaller values of ϕ_2 tend to result in lower values of $H_{2,1}$, while for $t > 250$ °C happens the opposite. On the other hand, our grteater values of the Poynting correction have the effect of decreasing the values of $\log(f_2^G/x_2)$-AP^2 within the ranges of t and P just mentioned, which, in turn, tends to drag the values of the intercept C (and therefore, those of $H_{2,1}$) downwards in our model, due to the constraint imposed by the known values of the slope B. Thus, our results tend to be significantly smaller than Malinin's for $t \leq 250$ °C and grow closer to them for higher temperatures (Fig. 4).

To complete our formulation we wanted to fit our $H_{2,1}$ results with a convenient expression. As shown in Fig. 4, there is good agreement on the values of $H_{2,1}$ for $t \leq 100$ °C. Thus we fitted the low-temperature results of other workers and our own results for $t > 100$ °C by

$$H_{2,1}(t) = H_0 + H_1 t + H_2 t^2 + H_3 t^3 + H_4 t^4 + H_5 t^5 \quad (10)$$

where

H_0=666.128, H_1=37.084, H_2=0.325222
H_3=-4.27297 10^{-3}, H_4=1.34383 10^{-5}, H_5=-1.3431 10^{-8}

The resulting fit is presented in Fig. 7.

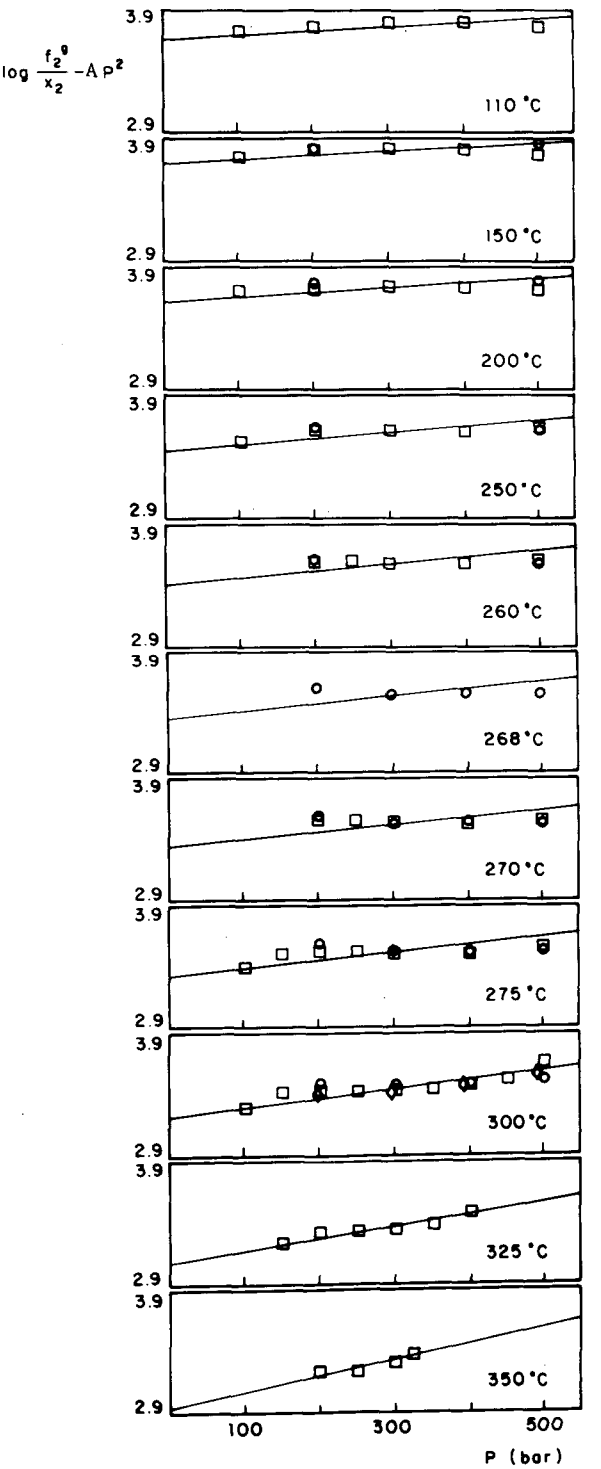

Fig. 3. Our fits to phase equilibrium data for the H_2O-CO_2 system.

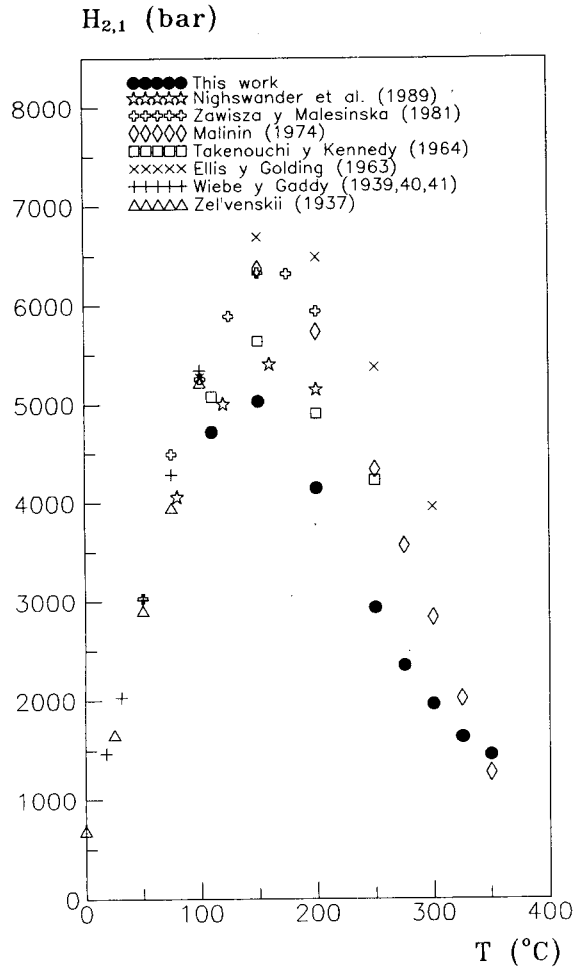

Fig. 4. Comparison of our results with previous ones.

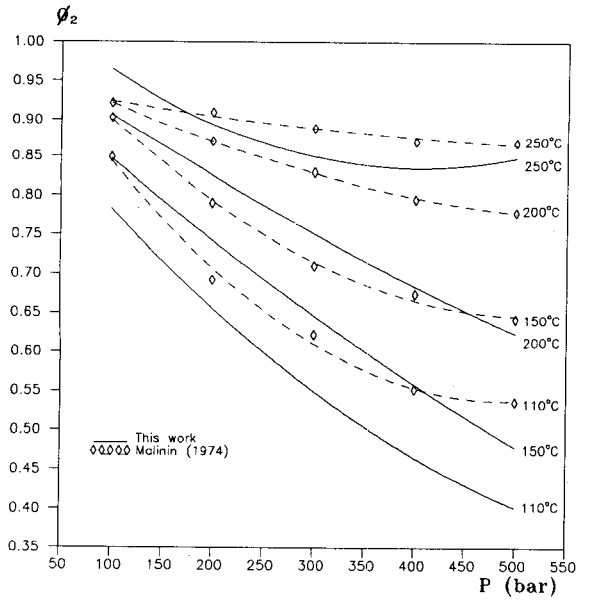

Fig. 5. Comparison of our fugacity coefficients with Majumdar and Roy's (1956) for pure CO_2, used in most previous work.

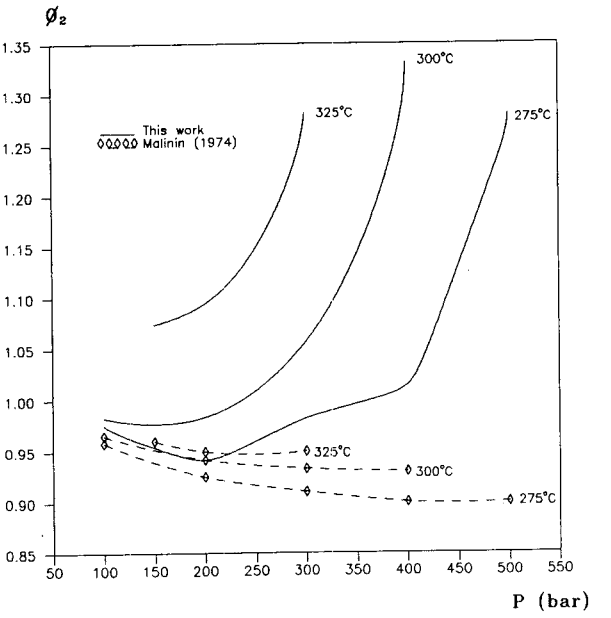

Fig. 6. Comparison of our fugacity coefficients with Majumdar and Roy's (1956) for pure CO_2, used in most previous work.

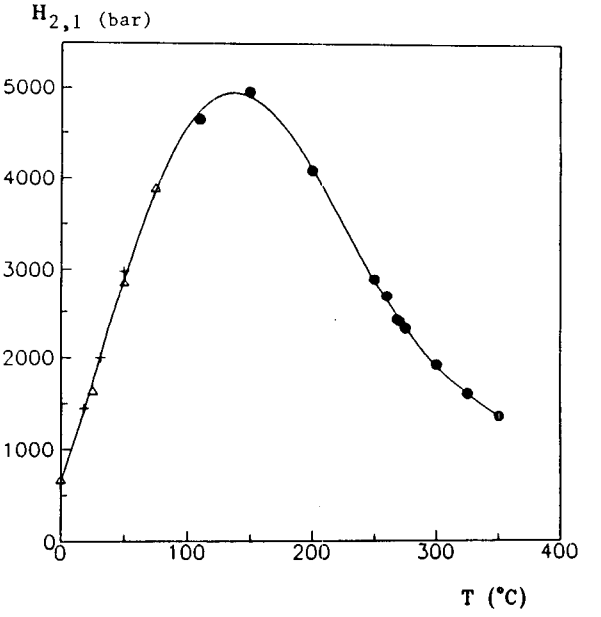

Fig. 7. Fit of expression (10) to our results for $H_{2,1}$.

SUMMARY AND CONCLUSIONS

We present a thermodynamically correct model for the solubility of carbon dioxide in water. Previous models rely on more-or-less crude approximations to represent the fugacity coefficient of CO_2 in the gas phase. Unlike them, we adopted a formulation that reallistically acounts for the non-ideal behavior of both components and that of the mixture, within the P-T range considered. Furthermore, our model accounts accurately for the effects of temperature and pressure, in integral form, in the Poynting correction.

The proposed model fits the available phase equilibrium data for the H_2O-CO_2 system nicely. In particular, it does not present the severe conflict between the linearity of the model and the lack of linearity of the data, evident in earlier models. The tight fit obtained with our model indicates that the complexities of H_2O-CO_2 phase equlibrium are well represented by it.

Our model provides a thermodynamically correct, accurate and straightforward way to compute the effects of CO_2 in geothermal flows, for numerical reservoir and wellbore simulators.

REFERENCES

Ellis, A.J., 1959 "The solubility of carbon dioxide in water at high temperatures", Am. J. Science, vol. 257, pp. 217-234.

Ellis, A.J. and Golding, R.M., 1963 "The solubility of carbon dioxide above 100 °C in water and in sodium chloride solutions", Am. J. Science, vol. 261, pp. 47-60.

Iglesias, E.R. y Schroeder, R.C., 1980 "Properties of H_2O-CO_2 mixtures for geothermal reservoir and wellbore simulators", en Earth Sciences Division, Annual Report 1979, Lawrence Berkeley Laboratory Report LBL-10686, pp. 95-98.

Iglesias, E.R., 1981, "Thermodynamic models for geothermal and geopressured fluids", en Earth Sciences Division, Annual Report 1980, Lawrence Berkeley Laboratory Report LBL-12100, pp. 105-108.

Krichevsky, I.R. and Kasarnovsky, J.S., 1935, J. Am. Chem. Soc., vol. 57, pp. 2168-.

Krichevsky, I.R. and Ilinskaya, A.A., 1945, Zh. fiz. khim. USSR, vol. 19, pp. 621-.

McKibbin, R. and Pruess K., 1988 "Some effects of non-condensible gas in geothermal reservoirs with steam-water counterflow", Proc. 13th Work. Geothermal Res. Eng., Stanford, Calif., pp. 165-171.

Malinin, S.D., 1959 "The H_2O-CO_2 system at high temperatures and presures", Geokhimiya, no. 3, pp. 235-245.

Malinin, S.D., 1974 "Thermodynamics of the H_2O-CO_2 system", Geochemistry International, vol. 11, pp. 1060-1085.

Nighswander, J.A., Kalogerakis, N. and Mehrotra, A.K., 1989 "Solubilities of carbon dioxide in water an 1 wt% NaCl solution at pressures up to 10 MPa and temperatures from 80 to 200 °C", J. Chem. Eng. Data, vol. 34, pp. 355-360.

O'Sullivan, M.J., Bodvarsson, G.S., Pruess, K. and Blakely, M.R., 1985 "Fluid and heat flow in gas-rich geothermal reservoirs", Soc. Pet. Eng. Journal, (April), pp. 215-226.

Prausnitz, J.M., 1969 "Molecular thermodynamics of fluid-phase equilibria", Prentice Hall Inc.

Pritchett, J.W., Rice, M.H. and Riney, T.D., 1981 "EOS for water-carbon dioxide mixtures: implications for Baca reservoir", DOE/ET/27163-8.

Spycher, N.F. and Reed, M.H, 1988 "Fugacity coefficients of H_2, CO_2, CH_4, H_2O and of H_2O-CO_2-CH_4 mixtures: A virial equation treatment for moderate pressures and temperatures applicable to calculations of hydrothermal boiling", Geochim. Cosmochim. Acta, vol. 52, pp. 739-749.

Strauss, J.M. and Schubert, G., 1979 "Effect of CO_2 on the buoyancy of geothermal fluids", Geophysical Research Letters, vol. 6, pp. 5-8.

Sutton, F.M., 1976 "Pressure temperature curves for a two-phase mixture of water and carbon dioxide", New Zealand J. of Science, vol. 19, pp. 297-301.

Sutton, F.M. and McNabb, A., 1977 "Boiling curves at Broadlands geothermal field, New Zealand", New Zealand J. of Science, vol. 20, pp. 333-337.

Takenouchi, S. and Kennedy, G.C., 1964 "The binary system H_2O-CO_2 at high temperatures and presures", Am. J. Science, vol. 262, pp. 1055-1074.

Todheide, K. and Frack, E.U., 1963 "Das Zweiphasengebiet und die kritische Kurve im System Kohlendioxid-Wasser bis zu Drucken von 3500 bar", Z. Physikalische Chemie Neue Folge, vol. 37, pp. 387-401.

Zawisza, A. and Malesiñska, B., 1981 "Solubility of carbon dioxide in liquid water and of water in gaseous carbon dioxide in the range 0.2-5 MPa and at temperatutes up to 473 K", J. Chem. Eng. Data, vol. 26, pp. 388-391.

APPENDIX 1

Equations (11)-(18) allow accurate computation of the fugacity coefficient for carbon dioxide in H_2O-CO_2 gaseous mixtures, up to 350 °C and 500 bar (Spycher and Reed, 1988). T is in °K and P is in bar.

$$\ln \phi_2 = (2y_1B_{21} + 2y_2B_{22} - B_{mez})P + (3y_1^2C_{211} + 6y_1y_2C_{221} + 3y_2^2C_{222} - 2C_{mez})\frac{P^2}{2} \quad (11)$$

$$B_{11} = B_{22} = a/T^2 + b/T + c \quad (12)$$

$$C_{111} = C_{222} = d/T^2 + e/T + f \quad (13)$$

$$B_{12} = B_{21} = a_{12}/T^2 + B_{12}/T + c_{12} \quad (14)$$

$$C_{112} = C_{211} = C_{121} = d_{112}/T^2 + e_{112}/T + f_{112} \quad (15)$$

$$C_{122} = C_{221} = C_{212} = d_{122}/T^2 + e_{122}/T + f_{122} \quad (16)$$

$$B_{mez} = y_1^2B_{11} + 2y_1y_2B_{12} + y_2^2B_{22} \quad (17)$$

$$C_{mez} = y_1^3C_{111} + 3y_1^2y_2C_{112} + 3y_1y_2^2C_{122} + y_2^3C_{222} \quad (18)$$

Table 1 provides the values of the coefficients a through f required to compute B_{ii} and C_{iii}. Table 2 presents the values of the remaining coefficients.

Table 1. Constants for pure components (after Spycher and Reed, 1988)

Gas	Range of T (°C)	P_{max} (bar)	a	b	10^5c	10^2d	10^5e	10^8f
H_2O	0-340	saturation	-6191.41	14.8528	-914.267	-6633.26	18277.00	-13274.00
CO_2	50-350	500	-1430.87	3.5980	-227.376	347.64	-1042.47	846.27

Table 2. Constants for cross virial coefficients (after Spycher and Reed, 1988).

a_{12}	b_{12}	10^2c_{12}	d_{112}	10^2e_{112}	10^5f_{112}	d_{122}	10^2e_{122}	10^5f_{122}
-1954.7	7.74805	-1.02901	104.453	-38.4283	36.5858	-8.28426	1.19097	0.808886

APPENDIX 2

We fitted Malinin's (1974) partial molar volume results as follows:

$$v_{300}(T) = \exp(154.7881 - 3582.4521\,T^{-1} - 26.775773\,\ln T + 0.045234908\,T) \quad \textbf{(19)}$$

where T is absolute temperature,

$$v_2^{\infty}(P,T) = v_{300}(T) \quad \textbf{(20)}$$

for $P \leq 300$ Kg/cm^2 and $T \leq 523.15$ K, and

$$v_2^{\infty}(P,T) = v_{300}(T)(a_P T + b_P) \quad \textbf{(21)}$$

for $P > 300$ kg/cm^2 and $T > 523.15$ K, with

$$a_P = \alpha P + \beta \qquad y \qquad b_P = \sigma P + \delta \quad \textbf{(22)}$$

where
$\alpha = -6.387005 \times 10^{-6}$, $\beta = 1.638605 \times 10^{-3}$
$\sigma = 3.387074 \times 10^{-3}$, $\delta = 1.239184 \times 10^{-1}$

PROCEEDINGS, Seventeenth Workshop on Geothermal Reservoir Engineering
Stanford University, Stanford, California, January 29-31, 1992
SGP-TR-141

AN ACCURATE PVT MODEL FOR GEOTHERMAL FLUIDS AS REPRESENTED BY H_2O-CO_2-NaCl MIXTURES

G. Andersen, A. Probst, L. Murray, S. Butler

Unocal Science & Technology
376 S. Valencia
Brea, CA 92621

ABSTRACT

Estimates for the pressure decline in high TDS geothermal fluids containing dissolved gases are extremely sensitive to the PVT representation of the reservoir fluid. Significant errors in predicted pressures will occur if the geothermal fluid is represented by one or two pseudo components with modified water properties. As a result, we have developed a PVT model to predict the thermodynamic properties of a prototype geothermal fluid as represented by three-component H_2O-CO_2-NaCl mixtures. The range of applicability of the model is: Temperatures from 75 to 700+°F, pressures from 14.7 to 5000 psi, carbon dioxide content from 0 - 5 wt%, and salt concentrations to 30 wt%.

The model has been implemented into Unocal's version of a commercially available reservoir simulator and is currently being used to study one of Unocal's high salinity reservoirs located in the Imperial Valley of California.

INTRODUCTION

The first geothermal fields to be commercially exploited contained essentially hot water and steam. As a result, lumped and distributed parameter reservoir simulation models have provided reasonable performance predictions using steam table thermodynamic data.

More recently, a number of reservoirs have come under development in which the reservoir fluid can not be adequately represented by pure water with the most obvious examples being the Salton Sea and Broadlands fields in the United States and New Zealand respectively. These fields contains large quantities of either dissolved solids or non-condensable gases, components which substantially alter the thermodynamic behavior of the reservoir fluid. Preliminary modeling by our engineers and others have indicated that the presence of both components can drastically alter the pressure decline of a reservoir through their impact on the saturation pressure of the fluid. However, these previous studies have used models of the liquid-vapor equilibria that are severely limited in the range of pressures, temperatures and compositions that can be considered. Additionally, no systematic effort has been undertaken to test the accuracy of these models against the large quantity of known experimental data on these systems.

Unocal recognizes that accurate reservoir modeling of their geothermal resources has to explicitly take into account the multicomponent nature of the reservoir fluid. As a result we have developed a thermodynamic model which can represent the thermodynamic behavior of a prototype geothermal fluid as represented by mixtures of water, carbon dioxide and sodium chloride. The model has been tested against a wide class of literature data on H_2O-NaCl, H_2O-CO_2, and H_2O-CO_2-NaCl mixtures and accurately reproduces the known saturation pressures, densities and enthalpies at conditions appropriate to most known geothermal fields. This model has been implemented into a commercially available geothermal reservoir simulator and is currently being used to model the Salton Sea reservoir located in California's Imperial Valley.

PHASE EQUILIBRIUM CALCULATIONS

The presence of two coexisting phases in the reservoir has a dramatic effect on the reservoir pressure decline and the production well enthalpies. Thus, in reservoir modeling it is essential to accurately determine the quantity and composition of the liquid and vapor phases. This is performed through a combination of heat, material balance and phase equilibrium conditions.

The Condition for Phase Equilibria:

A requirement of phase equilibrium in any two-component liquid-vapor system is the equality of the chemical potential, or fugacity, of the components in the two phases:

$$f_i^l = f_i^g \qquad (1)$$

where i indicates a given component and l and g refers to the liquid and vapor phases respectively. The individual fugacities can be written as follows:

$$f^{v}_{co2} = P \cdot y_{CO2} \cdot \phi_{CO2} \quad (2a)$$

$$f^{l}_{co2} = H_{sat} \cdot x_{CO2} \cdot \gamma_{CO2} \cdot Pc_{CO2} \quad (2b)$$

$$f^{l}_{h2o} = P_{sat} \cdot \phi_{sat} \cdot a_{H2O} \cdot Pc_{H2O} \quad (2c)$$

$$f^{v}_{h2o} = P \cdot y_{H2O} \cdot \phi_{H2O} \quad (2d)$$

where

P = System pressure

y_{CO2} = CO_2 mole fraction in the vapor phase

ϕ_{CO2} = Vapor phase fugacity coefficient for CO_2

H_{sat} = Henry's law constant along the water saturation line

x_{CO2} = CO_2 mole fraction in the liquid phase

γ_{CO2} = Liquid phase activity coefficient for CO_2

Pc_{CO2} = Poynting correction for CO_2

P_{sat} = Saturation pressure of H_2O

ϕ_{sat} = Fugacity coefficient of H_2O at P_{sat}

ϕ_{H2O} = Vapor phase fugacity coefficient for H_2O

a_{H2O} = Liquid phase activity for H_2O

Pc_{H2O} = Poynting correction for H_2O

The APPENDIX lists the functional forms for most of the above listed variables.

The approach summarized in EQUATIONS 2a-d has been quite successful in correlating gas solubilities in a wide class of systems(Prausnitz, 1986). The model assumes a reference condition that is centered on the pure solvent with most of the terms in EQUATION 1 being correction factors calculated from this point. It is these correction factors that have been generally ignored in previous studies. Additionally, previous works have used correlations for the temperature dependence of the Henry's law constant that have questionable accuracy above 600°F. In the present model we describe a method for linearizing the temperature dependence of H_{sat} which allows the function to be accurately extended up to the critical point of water.

The above thermodynamic model does have limitations with respect to geothermal applications. Quantities such as the saturation pressure and Henry's law constant in EQUATION 2 are formally defined only for temperatures below the critical point of the solvent which, for H_2O, is approximately 700°F. For geothermal systems containing high levels of dissolved solids the reservoir temperature can exceed this value. Our experience has shown that our correlations for those previously mentioned properties appear to be extrapolatable and give reasonable results for many thermodynamic properties up to approximately 750°F.

We also recognize that the above approach is probably not appropriate for describing near critical mixtures. For these situations we feel that equations of states which assume a continuity between liquid and vapor phases will provide a better description. As of this time, this has not been a limitation in our reservoir modeling.

H_2O-NaCl SYSTEM

Bubble Point Pressures

For the two-component H_2O-NaCl system the change in the vapor pressure from its pure water value is accounted for in the composition dependence of the activity of water. The activity was fit to the saturation pressures reported by Haas(1976), Pitzer(1984), and Bischoff(1989). In FIGURE 1 we compare model predictions for the saturation pressure at a series of sodium chloride concentrations with that reported by Haas for temperatures up to 575°F. The maximum deviation is less than 1%. For more extreme conditions comparisons are with the data from Bischoff and Pitzer. At the highest temperature and salt concentration the error is around 2%. These results indicate that the model can accurately reproduce the experimental saturation pressures up to 750°F.

CO_2-H_2O SYSTEM

Experimental Data:

The data used to construct and test the model was obtained from six different sources and spans temperatures from 60 to 660°F and pressures from 20 to 50,000 psi. These data contain measurements of carbon dioxide solubility at conditions that cover

most known geothermal reservoir conditions of pressure, temperature and CO_2 concentration. All of the available data at pressures less than 5000 psi has been used to test the model.

Henry's Law Constant

The calculation of the solubility of CO_2 in water is primarily determined by the Henry's Law constant H_{sat}. The experimental data available on H_{sat} are not entirely consistent, particularly at higher temperatures. FIGURE 2 presents the reported Henry's law constants, and those calculated by ourselves for the data of Takenouchi(1964) and Toedheide(1963), as a function of temperature. The maximum in the Henry's Law constant at approximately 300°F is a feature common to slightly soluble gases. It presents difficulties in developing a simple empirical correlation that can be accurately extrapolated to higher temperatures. As a result we have used an approach recently developed by Harvey & Levelt-Sengers(1990) which expresses the Henry's constant as a function of the density of the solvent. The exact form of the correlation is given in the Appendix. In FIGURE 3 we compare calculated versus observed Henry's law constants for CO_2 along the saturation line of pure water.

Vapor-Phase Fugacity Coefficients, Poynting Corrections and Activity Coefficients

Fugacity coefficients were initially calculated using the Peng-Robinson(Peng, 1980) equation-of-state. In order to minimize the computational overhead in the reservoir simulator we also evaluated using a composition independent correlation for the fugacity coefficient. The correlation provided minimal degradation in accuracy from the equation-of-state solution and as a result, all phase equilibrium calculations were performed using the latter. Apparent molar volumes of CO_2 for the Poynting correction and activity coefficient parameters for CO_2 in pure water were obtained from the literature.

Saturation and Bubble Point Pressures

We also compared model predictions for the equilibrium saturation pressures with the reported values. Model results were generated from the reported liquid-phase compositions. This is shown in FIGURE 4 where the deviation between model predictions and the data is less than 5% for the majority of the measurements. At higher temperatures the data is less certain and the error can be as large as 15%.

Zawisza(1981) provided information on the bubble point pressure in the carbon dioxide-water system over the temperature range of 120-400°F and the pressure range of 20-800 psi. Experimental versus predicted results are shown in FIGURE 5 and the agreement has a standard deviation of 5%.

Dew Point Pressures

Zawisza also determined the dew point pressures for a number of different H_2O-CO_2 mixtures. In TABLE 1 we show that model predictions are in good agreement with the data at two compositions, at three different temperatures.

TABLE 1

T °F	y_{CO2}	P_{exp}(psi)	P_{model}(psi)	Error (%)
392	0.065	239.5	241.8	1.0
347	0.065	135.3	138.5	2.3
392	0.297	328.4	331.1	0.8
347	0.297	189.6	187.6	1.1
302	0.297	96.9	99.0	2.2

H_2O-CO_2-NaCl SYSTEM

Extending the model from the two-component systems to three components involves including the effect of NaCl on the activity coefficient of CO_2. The actual form of the activity coefficient is given in the Appendix and is derived from the data of Ellis et. al. as reported by Mason and Kao(1980).

Bubble Point Pressures

FIGURE 6 compares the predicted equilibrium pressure of two-phase solutions to the experimental data of Ellis @ Golding(1963) which spans concentrations from 0 to 10.5 wt % NaCl and 0 to 5 wt % CO2. The standard deviation between the model's predictions and the experimental data is approximately 5%. The predicted pressures are somewhat lower than those reported by Ellis. This was expected since Ellis's Henry's Law constant was consistently lower than those predicted by the model.

In FIGURE 7 we compare model predictions for the bubble point pressures in the three-component system with the data of Gehrig(1980) for a 6 wt % NaCl solution with 0.42 and 8.4 wt % CO_2. At the lower CO_2 concentrations there is good agreement between model and experimental data at all temperatures. At the higher CO_2 concentrations the agreement degrades. However, this pressure and concentration of CO_2 is well above what is normally seen in two-phase geothermal reservoirs but was included to show that, even in extreme cases, the model

gives good qualitative predictions of the experimental data.

Gehrig also measured a few data points at higher salt concentrations. Model predictions versus experimental results for those conditions are given in TABLE 2 where compositions are expressed in weight percent.

TABLE 2

T(°F)	x_{NaCl}	x_{CO2}	P_{model}(psi)	P_{exp}(psi)	Error(%)
619	9.5	4.7	4200	4400	-4.8
536	19.9	0.6	1800	1700	5.5
701	19.9	0.6	3300	3400	-3.0

These results indicate that the model provides reasonable predictions for the saturation pressure at NaCl concentrations significantly greater than those covered in the Ellis experiments. The latter were used to determine the NaCl dependence of the activity coefficient of CO_2 in the model.

VAPOR-PHASE DENSITY

The density of the two-component vapor-phase composed of CO_2 and H_2O is calculated using a four parameter cubic equation-of-state developed by P. K. Vinsome(1991). FIGURE 8 compares the predicted vapor densities for pure water vapor at the saturation pressure to steam table data (Burnham, 1969). Predicted densities for pure carbon dioxide at the saturation pressure of water are also compared to the experimental data of Chen(1959). Predicted densities for carbon dioxide are in good agreement with the experimental data over the entire range of temperatures considered. Predicted steam densities agree with the steam table data to approximately 675°F. However, as the temperature approaches the critical point the density estimate is less accurate.

LIQUID-PHASE DENSITY

A variety of approaches were evaluated for modeling the liquid density. The first method considered was that used by our reservoir simulator which expresses the volume of the solution as a sum of partial molar volumes of the individual components

$$V = \Sigma\, x_i \cdot \nu_i^\circ \cdot (1.0 + C_i \cdot (P - P_{sat})) \qquad (3)$$

where, V is the liquid volume and x_i, ν_i° and C_i are the mole fraction, saturated partial molar volume and compressibility factor for each component. The term $(P-P_{sat})$ is the deviation of the pressure from its saturation value. Notice that the pressure dependence is represented by linearized compressibility factors of the individual components.

H_2O-CO_2

The effect of CO_2 on the liquid phase density was calculated using EQUATION 3. Essentially no information is available on the effect of CO_2 on the compressibility of the liquid phase. We neglect this effect by assuming that the fluid compresses as if the CO_2 were not present.

NaCl-H_2O

While EQUATION 3 works well over a broad range of temperatures for the above two-component system, problems were encountered with the method for small salt concentrations near the critical temperature of water. In that region of the phase diagram the system is extremely compressible and the partial molar volume of NaCl approaches negative infinity. An alternative approach that gave good results for all concentrations and temperatures was a corresponding states-like expression in which the molar volume of the salt solution along the saturation line is expressed in terms of a function of the reduced temperature ($T/T_{critical}$) of the mixture. The expression used was similar to that of Torquato and Stell(1982) and accurately reproduces the experimental density of water up to its critical point. A correlation for the critical temperature of sodium chloride solutions was derived from the data of Marshall and Jones(1974). The experimental density data of Potter(1978) was then used to fit the one remaining adjustable parameter in the correlation. The compressibility factor for the NaCl solution was also correlated to the reduced temperature of the mixture using the Potter data at 4350 psi. The derivation of these correlations is detailed in the APPENDIX.

FIGURE 9 compares the model predicted densities to experimental data for the pure water and two-component system at various NaCl concentrations. The density correlation accurately reproduces the water data to the critical point, 705°F. and is within 1% of the experimental data of sodium chloride brines to 800°F. Errors are slightly higher for low salinity solutions at higher temperatures.

NaCl-H_2O-CO_2

The effect of CO_2 on a NaCl-H_2O liquid phase density was calculated using EQUATION 3 assuming that the partial molar volume of CO_2 was equal to its pure water value. This is a reasonable assumption except near the critical temperature of

water. Due to its low solubility, carbon dioxide has only a marginal impact on the brine density. At 200°F, the addition of 1.0 weight percent carbon dioxide increases the density of a 30 wt% NaCl solution by 0.3%.

LIQUID-PHASE ENTHALPY

$NaCl-H_2O$

For both the liquid and vapor phases we assume the enthalpy is given by

$$H = \Sigma\, x_i \cdot H_i \qquad (4)$$

where, x_i and H_i are the mole fraction and partial molar enthalpy of each component. As for the densities, we assume the enthalpy of the water-NaCl component is given by a corresponding states-like expression. The actual functional form is given in the appendix and the adjustable parameters were fit to the data of Haas(1976). The partial molar enthalpy of CO_2 in the liquid is obtained from the appropriate temperature derivative of its K value combined with the CO_2 vapor phase enthalpy.

FIGURE 10 shows the comparison of the experimental and predicted enthalpies for the $NaCl-H_2O$ system. Pure water enthalpies are accurately reproduced to the critical point of water. Model generated brine enthalpies are within 1% of the experimental data from 250 to 600°F. At lower temperatures, the discrepancy between the predicted and experimental values is somewhat larger. At higher temperatures model predictions agree with those of the recently developed Tanger(1989) equation-of-state for $NaCl-H_2O$ mixtures.

VAPOR-PHASE ENTHALPY

We assume that NaCl does not partition into the vapor phase and the remaining two partial molar enthalpies are approximated by their pure component vapor-phase values. The detailed correlations for each component are given in the APPENDIX. Experimental and predicted enthalpies for CO_2 in the vapor phase are compared in FIGURE 11. All enthalpy predictions are well within 1% of the experimental values. Experimental and predicted enthalpies for steam and water are compared in FIGURE 12. The agreement with the experimental data is excellent over the temperature range 25-700°F.

CONCLUSIONS

The model described above provides accurate predictions of the thermodynamic of mixtures containing H_2O, CO_2 and NaCl for temperatures in excess of 600°F and NaCl concentrations up to 20 wt %. Model predictions at higher temperatures and salt concentrations in the three-component system have not been verified due to the lack of experimental data. We are currently starting an experimental program that will obtain such data. The model is sufficiently general that it can be specifically tuned to match the properties of real geothermal fluids comprised of multiple chloride salts and noncondensable gases given the appropriate measured data. We are currently pursuing such a program for the Salton Sea reservoir in California.

ACKNOWLEDGEMENT

We thank the management of Unocal for permission to publish this paper.

APPENDIX

HENRY'S LAW CONSTANT

$$H_{sat} = P_{sat} \cdot \phi_{sat} \cdot \exp(\, HLSC / T)$$

$$HLSC = -491 + 3863 \cdot \rho_{H2O} - 150 \cdot \rho_{H2O} \cdot \exp[(273.15-T)/50]$$

where

H_{sat} = Henry's law constant for CO_2 along pure water saturation line

ρ_{H2O} = Density of liquid H_2O at saturation (g/cc)

T = Temperature (°K)

ACTIVITY OF WATER

$$a_{H2O} = 1 + A \cdot m_{NaCl} + B \cdot m^2_{NaCl}$$

$$A = 0.13635 - 1.3885e\text{-}3 \cdot T + 4.1784e\text{-}6 \cdot T^2 - 5.5362e\text{-}9 \cdot T^3 + 2.8178e\text{-}12 \cdot T^4$$

$$B = -0.01113 + 6.875e\text{-}5 \cdot T + 1.8375e\text{-}7 \cdot T^2 + 2.4087e\text{-}10 \cdot T^3 - 1.23545e\text{-}13 \cdot T^4$$

ACTIVITY COEFFICIENT OF CO_2

$$\ln(\gamma_{CO2*}) = B_{CO2} \cdot m_{CO2} + B_{NaCl} \cdot m^2_{NaCl}$$

$$B_{CO2} = -0.143 + 34.56/T$$

$$B_{NaCl} = 0.30912 - 2.04898e\text{-}3 \cdot T + 7.8867e\text{-}6 \cdot T^2$$

Here, m_{CO2} and m_{NaCl} are the molalities of carbon dioxide and sodium chloride in the solution. T is the temperature in °K.

H_2O-NaCl MOLAR VOLUME

$$\ln(V_{sat}) = V0 + V1\cdot\tau^{0.325} + V2\cdot\tau^{0.8915} + V3\cdot\tau^{0.825} + V4\cdot\tau + V5\cdot\tau^2 + V6\tau^3 + V7\cdot\tau^4 + V8\cdot\tau^5$$

$$\tau = 1.0 - T/T_c$$

$$V0 = 4.0208 + 3.30\cdot x_{NaCl}$$
$$V1 = -1.9286$$
$$V2 = -34.214$$
$$V3 = +20.1$$
$$V4 = +15.45 - 4.7\cdot x_{NaCl}$$
$$V5 = -1.2059$$
$$V6 = +0.63339$$
$$V7 = +0.0$$
$$V8 = +0.47437$$

The volume of compressed fluids is determined relative to the volume of the saturated fluid as follows:

$$V = V_{sat}\cdot(1.0 + C\cdot(P-P_{sat}))$$

$$C = -1.14e\text{-}6 / [\tau^{1.25} - 5.6\cdot x_{NaCl}{}^{1.5} + 0.005]$$

V and V_{sat} are in cc/gm-mole, T and T_c are in °K, P and P_{sat} are in psi, and x_{NaCl} is the mole fraction of sodium chloride in the solution.

PARTIAL MOLAR VOLUME OF CO_2

$$v_{CO2}^{\circ} = 37.36 - 7.109e\text{-}2\cdot T - 3.812e\text{-}5\cdot T^2 + 3.296e\text{-}6\cdot T^3 - 3.702e\text{-}9\cdot T^4$$

T = ° C, V = cc/g-mole

H_2O-NaCl MOLAR ENTHALPY

$$H_{NaCl} = V0 + V1\cdot\tau^{0.325} + V2\cdot\tau^{0.825} + V3\cdot\tau^{1.2165} + V4\cdot\tau + V5\cdot\tau^2$$

$$\tau = 1.0 - T/T_c$$

$$V1 = -1.9286$$
$$V2 = -34.214$$
$$V3 = +20.1$$
$$V5 = -1.2059$$

x_{NaCl} < 0.0089 ml pct

$$V0 = +17036 + 161850.\cdot x_{NaCl}$$
$$V4 = -138743. - 221842.\cdot x_{NaCl}$$

x_{NaCl} > 0.0089 ml pct

$$V0 = +17036. + 80511.\cdot x_{NaCl}$$
$$V4 = -140011. - 79426.\cdot x_{NaCl}$$

H_{NaCl} is in BTU/lb-mole, T and T_c are in °K, and x_{NaCl} is the mole fraction of sodium chloride in the solution.

CO_2(vapor) ENTHALPY

$$H_{CO2,v} = 298.833 + .2055\cdot T + (.03821\text{-}9.35e\text{-}5\cdot T + 6.875e\text{-}8\cdot T^2)\cdot(P-P_{sat})$$

Here, T is the temperature in °F and P is the pressure of carbon dioxide gas in psi. The resulting enthalpy is in BTU/lb.

STEAM ENTHALPY

The steam enthalpy is expressed as follows:

$$H_{steam} = H_{sat} + H_{superheat}$$

$$H_{sat} = 2083.81 + 1113.4\cdot\tau^{.325} + 7485.9\cdot\tau^{.825} + 7408.2\cdot\tau^{1.2165} - 14125.\cdot\tau - 4031.\cdot\tau^2 + 1832.7\cdot\tau^3 + 1184.8\cdot\tau^4 - 832.1\cdot\tau^5$$

$$\Delta H_{superheat} = (1.9976 + .04177\cdot P - 4.2979e\text{-}5\cdot P^2 + 7.9985e\text{-}7\cdot P^3)\cdot\Delta T - (5.3805e\text{-}7 + 7.1562e\text{-}5\cdot P + 2.575e\text{-}6\cdot P^2)\cdot\Delta T^2$$

$$\ln(T_r) = .13611\cdot\ln(P_r) + 7.4972e\text{-}3\cdot(\ln(P_r))^2 + 2.2713e\text{-}4\cdot(\ln(P_r))^3$$

$$\Delta T = T - T_{sat}$$
$$\tau = 1.0 - T_r$$
$$T_r = T_{sat}/647.067$$
$$P_r = P/220.52$$

Here, temperature is °K, the pressure is bar and enthalpy is cal/g.

CARBON DIOXIDE HEAT OF SOLUTION

The heat of solution for CO_2 is derived from the derivative(Denbigh, 1971) of our equilibrium expression for the K-value for carbon dioxide as follows:

$$H_{CO2,sol} = -R\cdot T^2\cdot\ln(K_{CO2}/P))dT$$

$$H_{CO2,sol} = -119.94 + 1.3324e\text{-}2\cdot T - 1.298e\text{-}2\cdot T^2 - 3.267e\text{-}5\cdot T^3 + 2.810e\text{-}8\cdot T^4$$

At temperatures greater than 650°F, the heat of solution changes rapidly and we add an additional term to the above relationship as follows:

$$H_{CO2,sol} = H_{CO2,sol\ @\ 650°F} + 44.86\cdot(T-650)$$

In these equations the temperature is °F and the heat of solution is BTU/lb. Our predicted values are close to those derived by Ellis and Golding(1963).

REFERENCES

1) Burnham, C. W., Holloway, R. J. and Davis, N. F., "Thermodynamic Properties of Water to 1000°C and 10,000 Bars", Geological Society of America, Special Paper Number 132, 1969

2) Chen, L. H., "Thermodynamic and Transport Properties of Gaseous Carbon Dioxide", Thermodynamic & Transport Properties of Gases, Liquids & Solids, Am. Soc. Mech. Eng., 1959, pp. 358-369

3) Denbigh, K., The Principles of Chemical Equilibrium, Cambridge University Press, 1971

4) Ellis, A. J. and Golding, R. M., "The Solubility of Carbon Dioxide above 100 C in Water and in Sodium Chloride Solutions", Amer. J. Sci., 1963, Vol. 261, pp. 47-60

5) Gehrig, M., "Phasenleichgewichte und PVT-Daten Ternarer Mishungen asu H_2O-CO_2-NaCl bis 3 Kbar und 550 C', Diss. Rer. Nat. Karlsruhe, 1980

6) Gillespie, P. C. and Wilson, G. M., "Vapor-Liquid and Liquid-Liquid Equilibria: Water-Methane, Water-Carbon Dioxide, Water-Hydrogen Sulfide, Water-n-Pentane, Water-Methane-n-Pentane", GPA RR-48, 1982

7) Haas, J. L., "Physical Properties of the Coexisting Phases and Thermochemical Properties of the H_2O Component in Boil in NaCl Solutions", Geological Survey Bull. 1421-A (1976)

8) Harvey, A. H. and Levelt-Sengers, J. M. H., "Correlation of Aqueous Henry's Constants from 0 degrees Centigrade to the Critical Point", AIChE Journal, 1990, Vol. 36, No.4, pp. 539-545

9) Marshall, W. M. and Jones, E. V., J. of Inorg. and Nucl. Chem., (1974) vol. 36, pp. 2313-2318

10) Mason, D. M. and Kao, R., "Correlation of Vapor-liquid Equilibria of Aqueous Condensates from Coal Processing" Thermodynamics of Aqueous Systems with Industrial Applications, ACS Symposium Series 133, 1980 pp. 107-138

11) Peng, D. Y. and Robinson, "Two- and Three-Phase Equilibrium Calculations for Coal Gasification and Related Processes", Thermodynamics of Aqueous Systems with Industrial Applications, ACS Symposium Series 133, 1980 pp. 393-413

12) Pitzer, K. S., Peiper, J. C. and Busey, R. H., "Thermodynamic Properties of Aqueous Sodium Chloride Solutions", J. Phys. Chem. Ref. Data, Vol. 13, No. 1 (1984), pp. 1-104

13) Pitzer, K. S. and Bischoff, J. L., "Liquid-Vapor Relations for the System NaCl-H_2O: Summary of the P-T-x Surface from 300 to 500 C", Amer. J. Sci. V 289 p. 217 (1989)

14) Potter, R. W., and Haas, J. L., J. Res. U.S. Geol. Survey, V 6, No 2 (1978)

15) Prausnitz, J. M., Lichtenthaler, R. N and Azevedo, E. G., "Molecular Thermodynamics of Fluid-Phase Equilibria", Prentice-Hall, N.J. (1986)

16) Takenouchi, S. and Kennedy, G. C., "The Binary System H2O-CO2 at High Temperatures and Pressures", Am. J. Sci., 1964, Vol. 262, pp. 1055-1074

17) Tanger, J. C. and Pitzer, K. S., Geochimica et Cosmochimica Acta, V 53 (1989)

18) Toedheide, K., Franck, E. U., "Das Zweiphasengebiet die Kritishe Kurve im System Kohlendioxid-Wasser bis au Drucken von 3500 bar", Z. Phys. Chem., 1963, Vol 37., pp. 387-401

19) Torquato, S. and Stell, G. R., "An Equation for the Latent Heat of Vaporization" Ind. Eng. Chem. Fundam., 1982, vol. 21, pp. 202-205

20) Vinsome, P. K., private communication.

21) Weibe, R. and Gaddy, V. L., "The Solubility in Water of Carbon Dioxide at 50, 75 and 100 degrees, at Pressures to 700 Atmospheres", Amer. Chem. Soc. J., 1939, Vol 61, pp. 315-318

22) Zawisza, A. and Malesinska, B., "Solubility of Carbon Dioxide in Liquid Water and of Water in Gaseous Carbon Dioxide in the Range 0.2-5 MPa and at Temperatures up to 473 K", J Chem. Eng. Data, 1981 Vol. 26, pp. 391-395

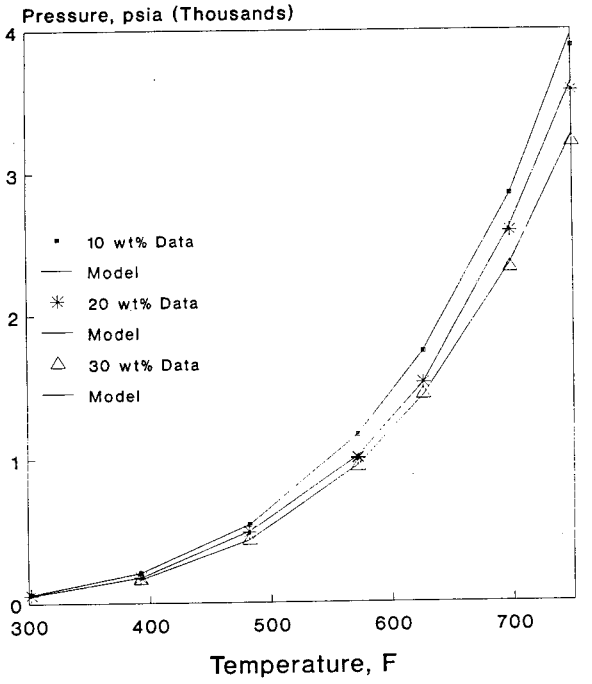

Fig. 1. Vapor pressure of NaCl solutions

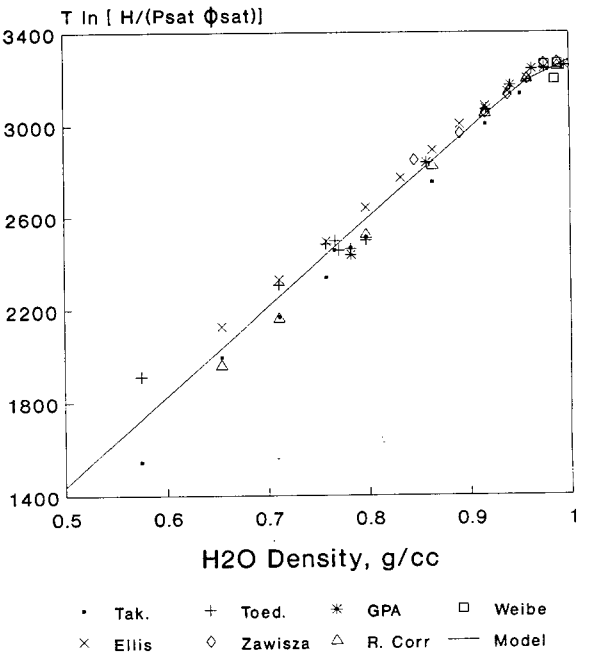

Fig. 3. Linear correlation for Henry's constant

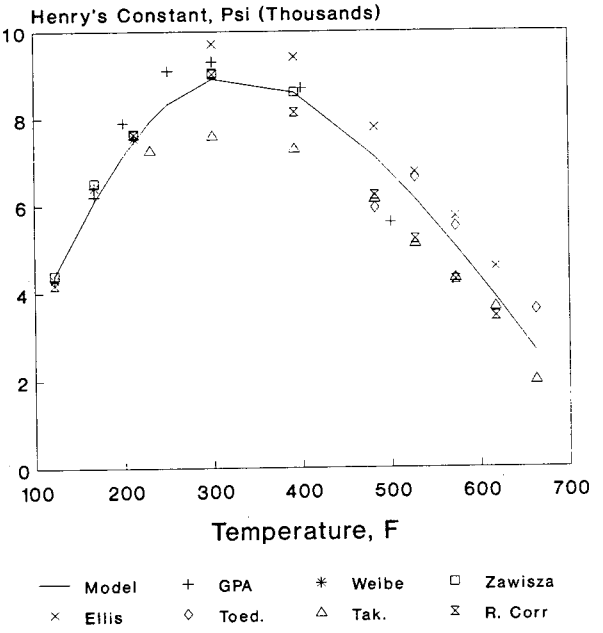

Fig. 2. Henry's constant vs. temperature (model and experimental data)

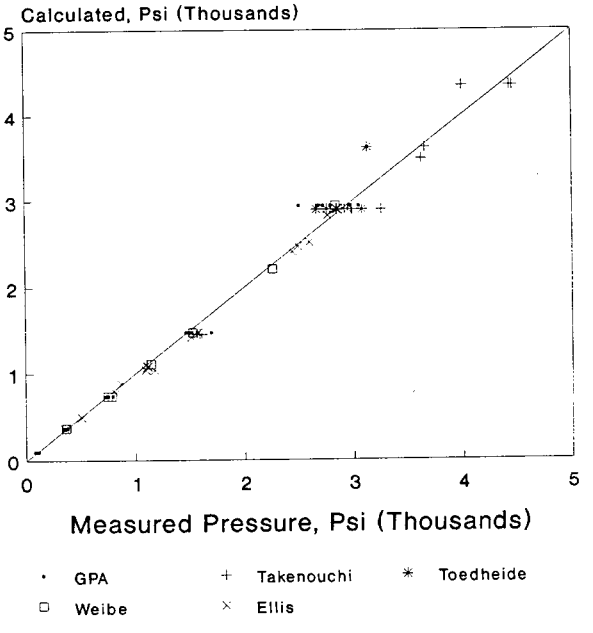

Fig. 4. Pressures for H_2O-CO_2 system (experimental vs. calculated)

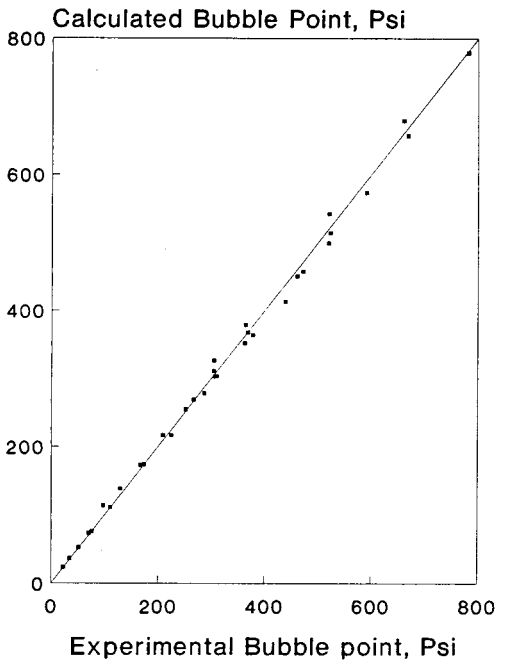

Fig. 5. Bubble point pressure for CO_2-H_2O system (calculated vs. Zawisza experimental data)

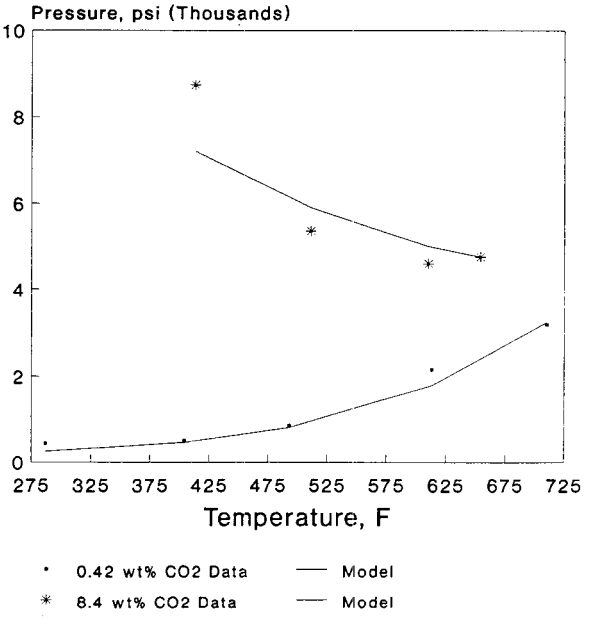

Fig. 7. Gehrig bubble point data (6.0 wt% NaCl-CO_2-H_2O system)

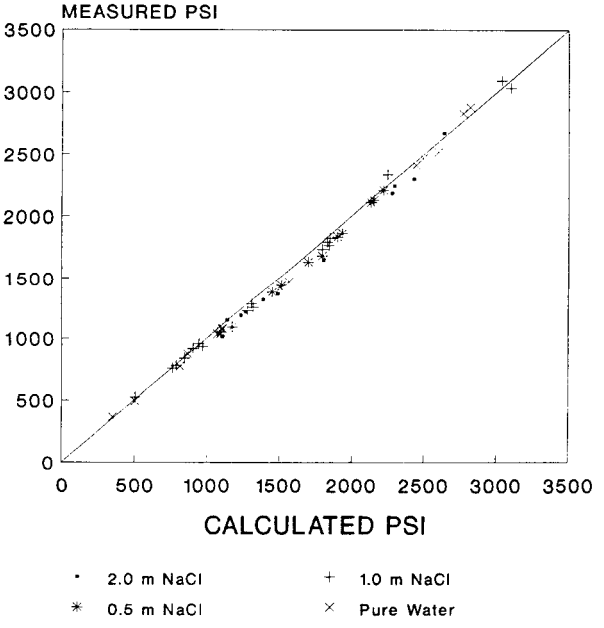

Fig. 6. Pressures for NaCl-H_2O-CO_2 system (Ellis data vs. calculated values)

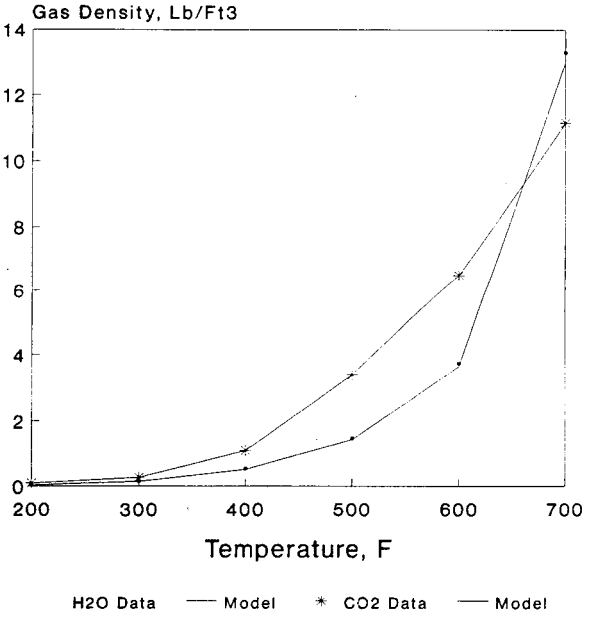

Fig. 8. Gas density from EOS (at home saturation pressure)

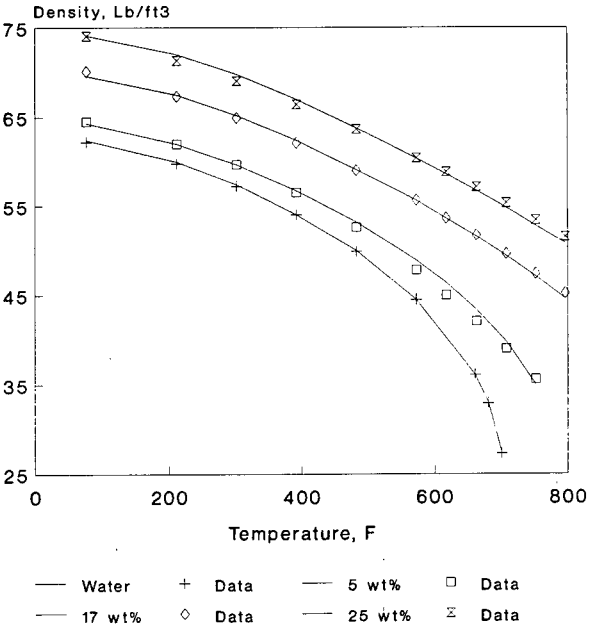

Fig. 9. Density of NaCl solutions (at water saturation pressure)

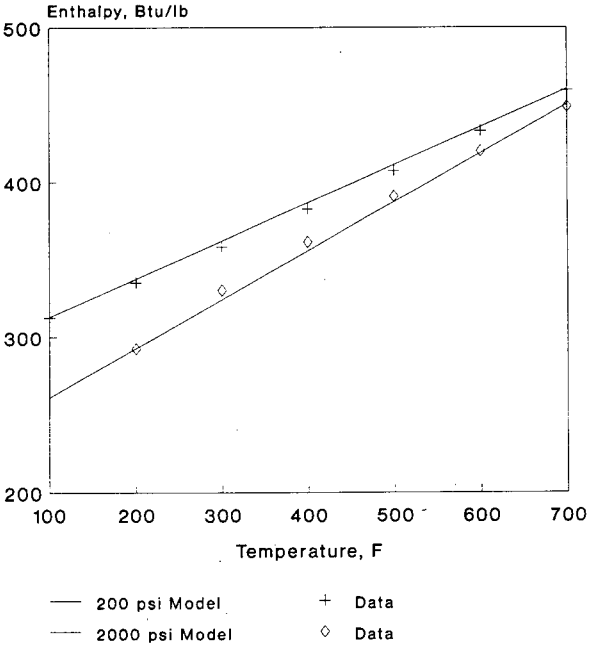

Fig. 11. Enthalpy of vapor-phase CO2

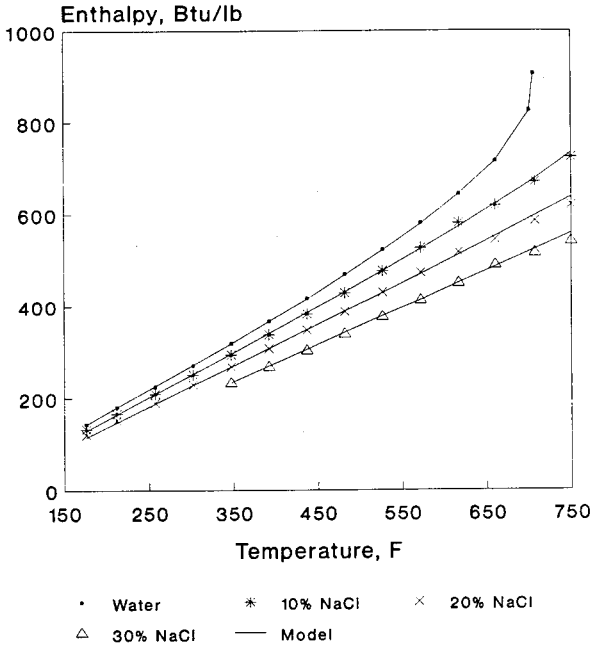

Fig. 10. Enthalpy of NaCl solutions

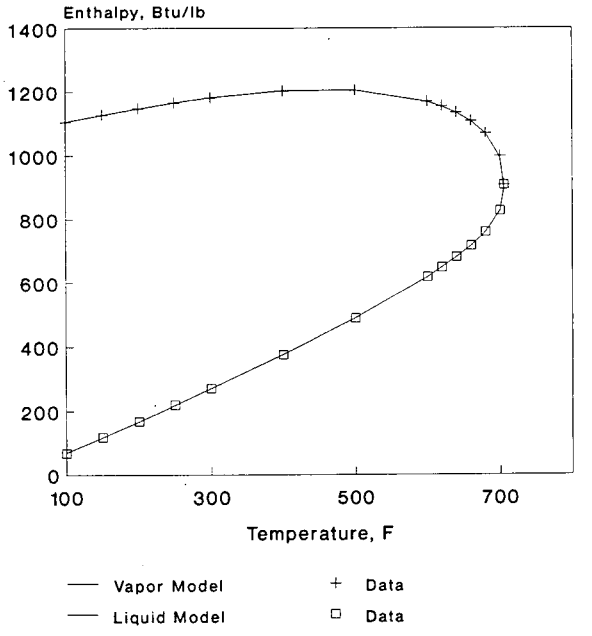

Fig. 12. Vapor and liquid enthalpy for water (at water saturation pressure)

PROCEEDINGS, Seventeenth Workshop on Geothermal Reservoir Engineering
Stanford University, Stanford, California, January 29-31, 1992
SGP-TR-141

ACCOUNTING FOR THE EFFECT OF TDS AND NCG ON SALTON SEA RESERVOIR RESPONSE

Steven J. Butler

Unocal Geothermal Division
81-711 Highway 111
Indio, California 92201

ABSTRACT

The Salton Sea reservoir, located in Imperial County, Ca., is unique in several ways from most liquid-dominated geothermal reservoirs that have been developed to date. One of these differences is the presence of hyper-saline brines containing up to 28% TDS (Total Dissolved Solids) and up to 0.2% NCG (Non-Condensible Gas).

A simple material and energy balance model has been developed to study the effect of TDS and NCG on Salton Sea reservoir response. This study demonstrated that during the development of a two-phase system the partitioning of the NCG into the vapor phase and the consequential concentration of the TDS in the brine drastically alters the reservoir fluid properties. In modeling pressure depletion of hyper-saline reservoirs, such as the Salton Sea, these changes in reservoir fluid composition were shown to seriously affect the simulation results.

As a result of these findings, a compositional fluid property package was developed using published data on H_2O-CO_2-NaCl mixtures. This fluid property package was then incorporated into the simulation program used by Unocal. Validation of the fluid property package in this simulation program was made using measured reservoir temperature, surface enthalpy, and surface flash data.

The development of a compositional simulation program for geothermal applications has advanced our ability to study depletion mechanisms that are sensitive to compositional changes. This program is currently being used to study the effect of injection and steam cap development on long term operations and to develop a field model of the Salton Sea reservoir.

INTRODUCTION

The fluid contained in geothermal reservoirs is a mixture of a multitude of chemicals. Components present in reservoir brine other than water are normally grouped into two categories, namely non-condensable gas (NCG) and total dissolved solids (TDS). For hyper-saline brines, such as the Salton Sea reservoir brine, the total dissolved solids group is comprised mainly of salts with NaCl being the most abundant species. Non-Condensible gas contained in the Salton Sea brine is primarily CO_2.

Early modeling of geothermal reservoirs was based on simulation programs using pure water properties. The level of inaccuracy in modeling geothermal reservoirs containing hyper-saline brines using pure water fluid properties has been a topic of discussion for some time. To our knowledge no one has determined magnitude of error on calculating reservoir response if TDS and NCG levels observed at the Salton Sea are not included in the simulation program.

To determine the magnitude of error on reservoir response calculations introduced by use of pure water fluid properties a simple material and energy balance model was developed. In this model the fluid properties are calculated using a PVT package capable of handling pure water and H_2O-CO_2-NaCl mixtures. The non-condensible gas and salts present in the reservoir fluid at the Salton Sea are believed to behave in a similar manner as the CO_2 and NaCl present in this model.

SINGLE BLOCK MODEL

Many methods have been developed over the years to estimate the recovery from oil & gas reservoirs. Material balance type methods, such as those developed by Muskat and by Tarner (Craft and Hawkins, 1959), can be powerful tools in predicting overall performance of volumetric (*i.e.*, solution gas drive) oil reservoirs. Since the production mechanism of liquid dominated geothermal reservoirs is similar to a solution gas drive, these material balance type of methods should also be applicable to geothermal reservoirs. An important addition to these types of calculations required for geothermal reservoir performance predictions is the addition of energy balance terms to the overall mass balance equations.

To study the effect of brine composition on overall recovery from a geothermal reservoir, a single block material & energy balance model was developed using FORTRAN coding. In this model, TDS is modeled as pure NaCl and NCG is modeled as pure CO_2. Fluids are produced from this block in a step wise manner similar to Muskat's method.

This step wise integration of the depletion process can be best explained by referring to a physical model shown in *Figure 1* below:

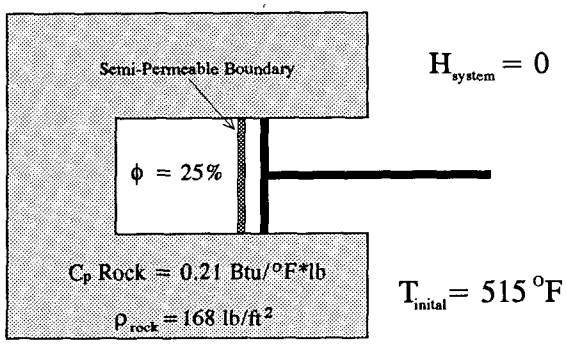

Figure 1. Single block geothermal reservoir model

On each integration step the pressure in the block is reduced by pulling the piston shown in *Figure 1* back. The fluid is then allowed to expand into the space between the semi-permeable boundary and the piston. The ratio of liquid to vapor that flows into this space is based on relative permeability data that was assigned to this semi-permeable boundary, as shown in *Figure 2* below:

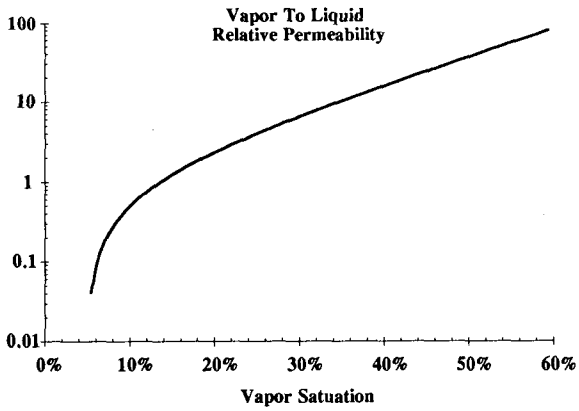

Figure 2. Relative permeability data assigned to the semi-permeable boundary used in the model.

After the system has come to thermal and pressure equilibrium, the volume of fluid between the piston and the semi-permeable boundary is produced by slowly moving the piston back to its original position while the fluid is bled off at a constant pressure.

The produced liquid is then flashed down to 100 psig. The resulting steam from these flash calculations is added to the steam contained in the produced vapor. The total steam produced is then divided by the original mass in place to yield a recovery factor. These step wise depletion steps are carried out until a desired recovery or lower reservoir pressure limit is reached.

MODEL RESULTS

Reservoir simulation runs, using the model discussed above, where made for a reservoir containing pure water, containing brine of a composition typical of the Salton Sea Field, and containing brine with a trace of NCG. A plot of reservoir pressure *v.s.* recovery factor for these three reservoir fluids is shown in *Figure 3* below:

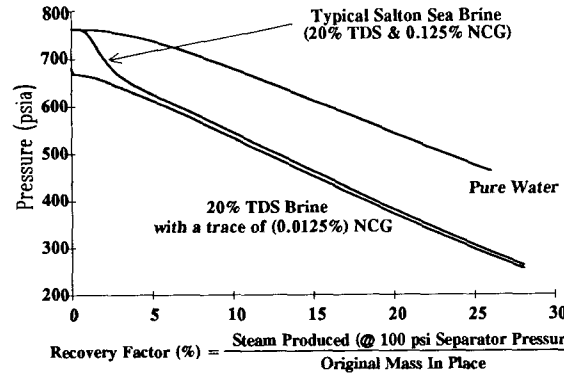

Figure 3. Reservoir Pressure v.s. Recovery Factor

The effects on the bubble point pressure resulting from the NCG and TDS contained in the brine found at the Salton Sea Field tend to cancel each other out and thereby result in a bubble point pressure that is close to that of pure water. With essentially the same bubble point pressure the recovery curves for pure water and for Salton Sea brine are similar to each other at recoveries below 1%.

As the reservoir is depleted, and the vapor saturation increases, most of the CO_2 in the Salton Sea brine partitions into the vapor phase. This loss of CO_2 from the liquid phase results in a rapid pressure depletion as shown in *Figure 3* above. By the time 4% recovery is

reached, the pressure depletion levels off and begins to follow the curve for brine containing only a trace of CO_2.

As depletion continues, partitioning of the CO_2 from the liquid phase into the vapor phase results in high levels of CO_2 in the vapor phase. Above the critical vapor saturation, this vapor phase becomes mobile and the concentration of CO_2 in the produced 100 psi steam quickly rises as shown in *Figure 4* below:

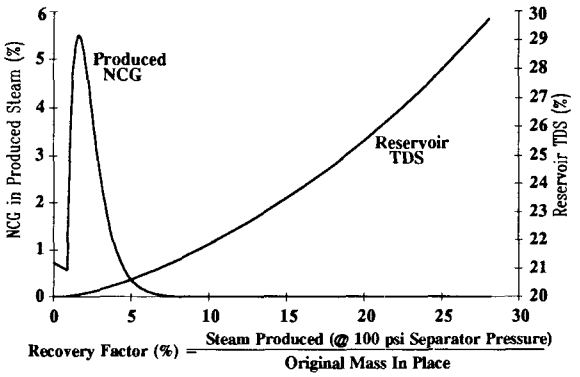

Figure 4. Produced NCG & Reservoir TDS as a function of Recovery Factor.

As depletion progresses, the CO_2 is swept out of the reservoir and the concentration the CO_2 in the steam drops. Later in the production life of a geothermal field flashing of the less mobile liquid phase results in concentration of the brine. This brine concentration process could result in high reservoir TDS values as shown in *Figure 4* above .

PVT MODEL FOR GEOTHERMAL FLUIDS

As a result of these findings a compositional fluid properties package (*i.e.*, PVT model) for geothermal fluids was developed using literature data on H_2O-CO_2-NaCl mixtures (Anderson and Probst, 1992). This package is similar to the package used in the single block model discussed previously but is capable of estimating properties over a much wider range of pressure, temperature and compositions required in reservoir simulations. This fluid property package was then incorporated into the simulation program used by Unocal.

The assumption that the fluid properties package in this simulation program, which models the reservoir brine as a mixture of H_2O-CO_2-NaCl, accurately matches the complex brine mixture at the Salton Sea was then tested. Using this program, production enthalpy and surface flash predictions were made for an average brine composition and average production interval temperature observed at the Salton Sea. These results agreed closely with observed separator enthalpy and flash data.

An experimental program is currently underway to obtain fluid property data on actual geothermal brines. Results from this program will then be used to fine tune the fluid properties package for the Salton Sea.

CONCLUSIONS

The presence of TDS & NCG in hyper-saline geothermal reservoirs exerts a strong influence on the recovery performance. For the same recovery factor, a reservoir containing brine of a composition typical of the Salton Sea reservoir will experience about twice the pressure depletion as compared to a reservoir containing pure water. Partitioning of the NCG into the vapor phase and brine concentration effects are important to consider.

Development of a compositional reservoir simulation program, which models hyper-saline geothermal reservoir brine properties as H_2O-CO_2-NaCl, has advanced our ability to study reservoir depletion mechanisms that are sensitive to compositional changes. From these studies improved reservoir performance predictions and reserves estimations can be made.

ACKNOWLEDGMENTS

The author would like to express his appreciation to those individuals who provided important comments on the work presented in this paper. Although it would be impossible to name them all, G.R. Anderson, P.G. Mogen, and L.E. Murray were especially helpful. The author also express his appreciation to the management of Unocal Geothermal Division for their permission to publish this paper.

REFERENCES

Anderson, G.R. and Probst, A., 1992, "AN ACCURATE PVT MODEL FOR GEOTHERMAL FLUIDS AS REPRESENTED BY H_20-CO_2-NaCl MIXTURES", Proc., Seventeenth Workshop on Geothermal Reservoir Enginerring, Stanford University.

Craft, B.C. and Hawkins, M.F., 1959, APPLIED PETROLEUM RESERVOIR ENGINEERING, (Prentice-Hall Inc), pages 376-390.

PROCEEDINGS, Seventeenth Workshop on Geothermal Reservoir Engineering
Stanford University, Stanford, California, January 29-31, 1992
SGP-TR-141

MICROSEISMIC MONITORING OF HYDRAULIC EXPERIMENTS UNDERTAKEN DURING PHASE IIA OF THE SOULTZ HDR PROJECT (ALSACE, FRANCE)

A. Beauce, R. Jones**, H. Fabriol*, C. Twose**, C. Hulot**

*BRGM/IMRG, BP. 6009, 45060 Orléans Cedex 2, France
**CSMA, Rosemanowes Quarry, Herniss, Penryn, Cornwall, UK

ABSTRACT

In the framework of the European HDR Project of SOULTZ, co-sponsored by European Community, two 50 hour-hydraulic injections were carried out in the main borehole GPK1. This borehole reached a depth of 2000 m (600 m of granite under a 1400-m-thick sedimentary cover) and a bottom hole temperature of 140°C. Both injections tests were made between a packer sited at 1968 m and bottom hole, with injection flow-rates of 7 l/s and 15 l/s.

3-axis accelerometer probes designed to withstand high temperatures up to at least 135°C were installed at the bottom of three boreholes which reached the granite. This network was supplemented by high temperature hydrophone sensors deployed in a fourth borehole (EPS1) at depth of about 2000 m. Data were transmitted to an on-line computer to perform preliminary interpretations.

During the tests, 135 and 239 induced microseismic events respectively were recorded. Present results show that seismicity starts off very close to the injection point and spreads out to form a cloud with a North-West to South-East elongation.

According to previous interpretations, the direction of the maximum horizontal stress component deduced by BHTV data analysis and hydrofracture in-situ stress measurements led to values of respectively 175°N and 155°N. During the second injection experiment a concentration of seismicity was revealed to the N-W of GPK1. This cloud also shows a trend to grow downwards and no seismicity extends more than 300 m away from the injection interval.

INTRODUCTION

Within the frame of the validation of a new power generation concept, research into the development of "Hot Dry Rock" geothermal energy began in the early 1970's in the US (Los Alamos) and later on, in Europe - Camborne (UK), Urach (Germany), Mayet de Montagne (France) - and in Japan. In all these projects, the monitoring of the microseismicity induced during hydraulic injection tests has proved to be fundamental in the understanding of the growth and size of the stimulated regions (Baria,R. & al.,1989; Matsunaga, I., 1990; Mock, J., 1989).

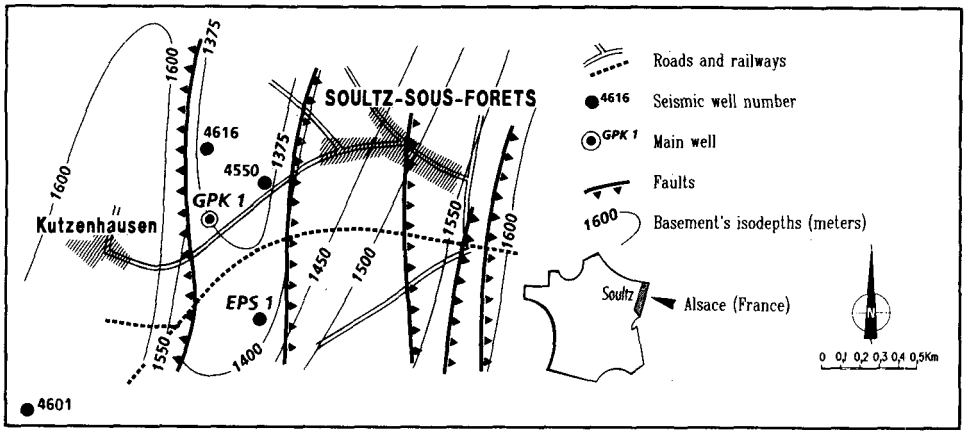

Fig. 1 - Location map of the project

The HDR site of Soultz, situated in the northeastern part of France in Alsace, was chosen in 1986 on top of a very large thermal anomaly which extend over about 4000 km^2 in the Rhine graben (Figure 1).

Prefeasability studies (Phase I) began in 1987 after the drilling of the main well GPK1 down to 2000 m (Kappelmeyer & al. , 1991). This borehole reached temperatures of 125°C at the top of the granite and 140°C at bottom-hole. A first small scale hydraulic stimulation (at a flowrate of 3 l/s for 3 days) took place in GPK1 at the end of 1988, and the associated seismicity was monitored (Beauce,A. & al., 1991).

In 1990, Phase IIa of the project started with the drilling of a second exploratory borehole (EPS1), sited at about 500 m S-E of GPK1 and planned to reach 3500 m; but, due to technical reasons and a very significant deviation of more than 15°, this well was stopped at about 2000 m. At total depth, final temperature of this borehole was 150°C.

During this phase, two 50-hour hydraulic stimulation experiments were undertaken in GPK1 between a packer set at 1968 m and bottom-hole: one of 7 l/s and one of 15 l/s.

MICROSEISMIC MONITORING NETWORK

To monitor the site during these experiments, three old oil wells (4616, 4550, 4601, see Figure 1) were successfully recovered in the surroundings of GPK1. As deduced from Phase I, and in order to avoid the attenuation effects observed on the seismic signals during their propagation in the sedimentary layers, these boreholes were deepened inside the granite. The coordinates of the sensors are given in Table 1, where the origin of the coordinate system is the wellhead of GPK1.

TABLE 1

SENSOR	X (m)	Y (m)	Z (m)	MD (m)	Depth in granite (m)
4516	-45.03	353.61	1382.81	1387.2	7
4550	285.23	205.12	1492.63	1492.0	87
4601	-1118.05	-864.35	1580.76	1599.0	26
Hydro 1	197.45	-363.95	1917.24	1945.0	~500
Hydro 2	210.45	-353.95	1974.82	2004.5	~500

Three 3-axis accelerometer probes were especially designed by CSM Associates Ltd to withstand the rough temperature and corrosion conditions, and deployed at the bottom of each of these wells. Various technical problems connected with borehole completion, prevented the correct cementation of these units before the hydraulic stimulations.

Data delivered by the accelerometer and hydrophone units were lowpass filtered downhole at 1500 Hz and analog transmitted using wires to the computer room in order to be continously monitored and pre-processed on a micro-VAX. Sampling rate was 5000 cps/channel and a window of 1.6 s (including pre-trigger) of data was stored on disk when an event was detected.

During the hydraulic stimulations either a single hydrophone (during the 7 l/s test), either a pair of hydrophones (during the 15 l/s test) were used. When only the single unit was deployed, then it was placed at the same position as the lower of the pair when that was used.

All the trajectories of these boreholes were measured using a gyroscopic tool.

An additionnal analog telemetry link seismic network composed of 8 mobile stations was also deployed on surface at about 1 km from the GPK1 wellhead by Institut de Physique du Globe de Strasbourg (IPGS); but no seismicity was recorded during the injection experiments.

VELOCITY MODEL

In order to obtain a velocity field around GPK1, and thus to allow reliable locations, a calibration shot of 300 g of explosives was fired at a depth of 1992 m in GPK1. Clear P-wave onsets were produced on all the sensors of the network; only one S-wave arrival was observed (on probe 4616).

The P-wave calculated velocities are given in Table 2:

TABLE 2

SENSOR	P-wave velocity (km/s)
4616	5.715
4550	5.745
4601	5.465
Hydrophone 1	5.940
Hydrophone 2	5.930

The deduced velocities between borehole pairs GPK1-4616 and GPK1-4550 are similar and in agreement with the results obtained in Phase I, i.e. an average velocity of 5.680 km/s.

However, an important discrepency is observed for the path GPK1-EPS1 that could be due to well survey errors, as borehole EPS1 was highly deviated.

More problematic is the low velocity measured between GPK1 and 4601 and the preceeding reason seems to be unlikely as both boreholes are almost vertical. At present, the problem of velocity anisotropy is not completely resolved but it could be

due to the conjonction of two factors: its relative long distance of this probe from the injection interval (around 1470 m) and the presence of an important NE-SW fault affecting the sedimentary layers and the granite which was revealed by a past reflection seismic survey. In order to not perturbate the location results of the microseismic events and to preserve a relative homogeneity in the results, it has been decided not to use the data from this probe at this stage of interpretation.

Bearing in mind these factors, it has been decided to adopt for locations an isotropic average P-wave velocity model of 5.85 km/s and to apply respective calculated time delays to the monitoring stations. As it was not really possible to deduced a good S-wave velocity model from the calibration shot data, no station delays were considered for these waves and a Vp/Vs ratio of 1.73 has been chosen.

INDUCED MICROSEISMICITY DURING THE 7 l/s HYDRAULIC INJECTION TEST

The 7 l/s hydraulic stimulation started on July 11th at 1 p.m., over a 30-m-long vertical section of GPK1 well, between a packer sited at 1968 m and bottom-hole. After eight and a half hours, and an injected volume of about 160 m^3, the experiment was stopped as the pressure in the annulus began to increase. The injection restarted at 1:15 p.m. on 12th and carried on from the next 50 hours.

Figure 2 shows a plot of the seismic event rate and down-hole pressure recorded during this period. A total of 135 microseismic events were induced during this test and seismic rate decreased immediatly when the injection stopped.

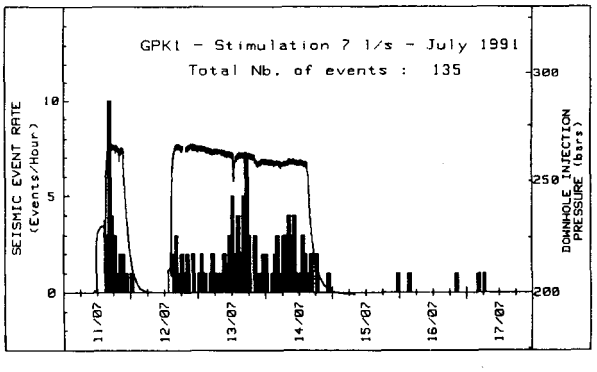

Fig. 2 - Hydraulic and seismic event rate data recorded during the 7 l/s stimulation in GPK1

These events have shown clear P and S wave onsets on the different probes of the network (see figure 3). It must be noted that the probe deployed in the borehole 4601 recorded only about 20% of the whole recorded seismic activity.

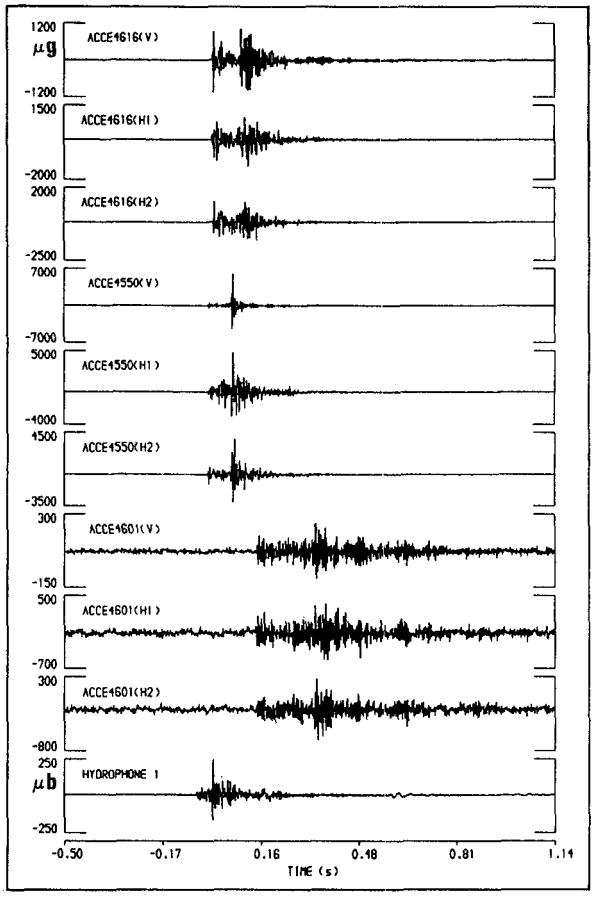

Fig. 3 - Signatures from down-hole accelerometers and hydrophone recorded during the 7 l/s hydraulic injection in GPK1 Event 26 - 11/07/1991 - 17:27:54

Microseismic location results

Of all the seismicity recorded during this test, 60% of the events have been interpreted and located (see figure 4) using the isotropic velocity model presented above. During this test only one hydrophone was deployed in the borehole EPS1. In consequence, as data from 4601 probe was not used for the locations, we only have a coplanar network. So, location results gave dual solutions images which form a mirror image in the plane defined by these sensors: the decision to choose the deepest solutions was based on the results obtained when we have more sensors and a non-coplanar network, i.e. during the 15 l/s injection test.

The plan view of figure 4 shows how the seismicity develops during this test to form an overall cloud with a N-W to S-E elongation, while the vertical plan view from 150°N shows a trend to grow downward.

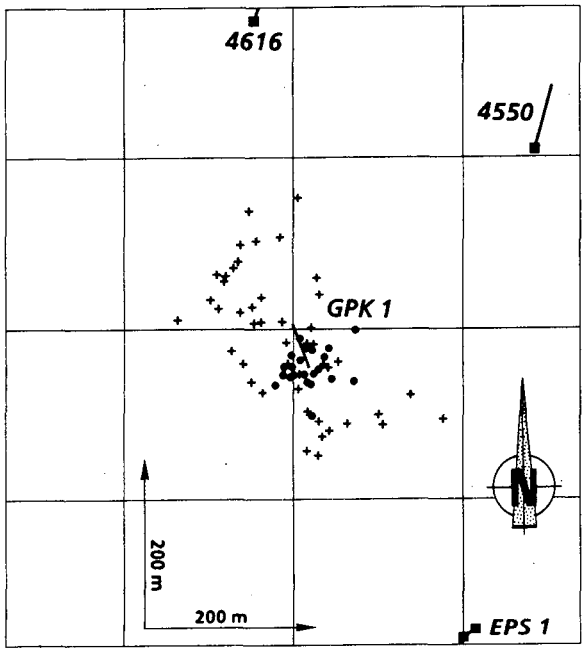

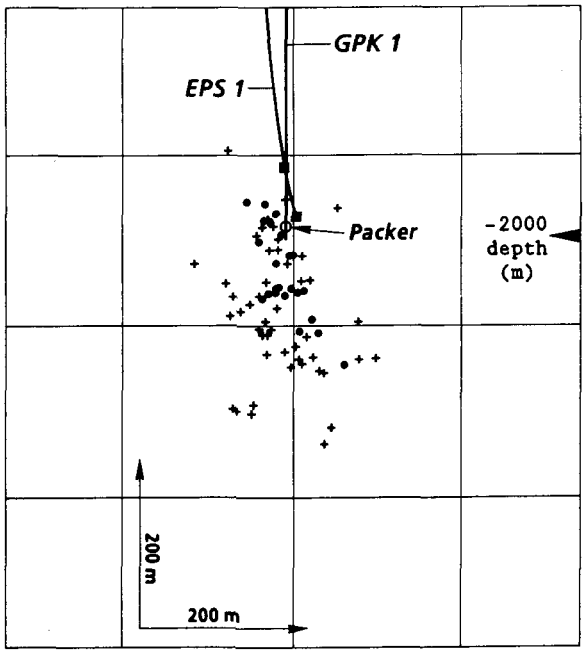

Fig. 4 - Microseismicity during the 7 l/s hydraulic injection in GPK1
Plan view and vertical section view (azimuth 150°N)
● first phase, + second phase
■ seismic probe

More precisely, on the first phase (full circles) the seismicity mainly concentrates near GPK1 and only on the south-southeastern side at depths between 1950 m and 2100 m. These results are in agreement with what was found during Phase I of the project with an hydraulic test with a flowrate of 3 l/s.

During the second phase, the seismicity extends away from GPK1 and at depths down to 2150 m, but in addition and corresponding to the second peak of seismicity observed on figure 2, a new seismic active zone appears on the north-northeastern side of GPK1 during the third day of the injection.

INDUCED MICROSEISMICITY DURING THE 15 L/S HYDRAULIC INJECTION TEST

The 15 l/s injection in GPK1 started on 18th of July at 9 a.m. and lasted about 50 hours in similar conditions to the previous experiment. A total volume of 2300 m^3 of fresh water was injected. Figure 5 shows the downhole injection pressure recorded during this test and the associated seismic event rate. The first event occured after an injected volume of 35 m^3 and a total of 239 induced events were recorded. In comparaison with the previous test, the average seismic rate (4 events/hour) was double. Moreover, the seismicity still persisted after the end of the stimulation, suggesting the existence of a remanent pressurized zone sited away from the borehole injection interval.

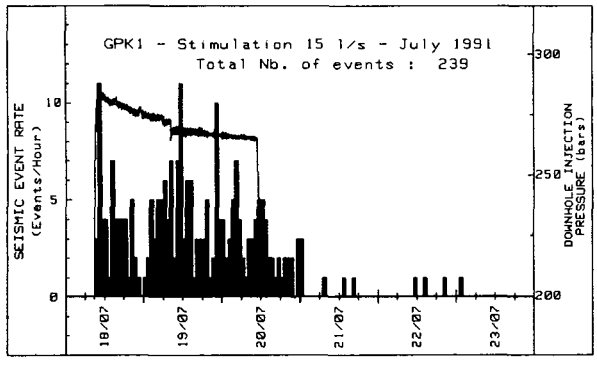

Fig. 5 - Hydraulic and seismic event rate data recorded during the 15 l/s stimulation in GPK1

Microseismic location results

During this injection the string of 2 hydrophones was deployed in EPS1, and again data recorded by the probe sited in borehole 4601 were not used for the locations of the events.

Figure 6 illustrates the chronological migration of the induced microseismicity as a function of days of injection in plan view and associated vertical plane viewed from the azimuth 150°N. During the first day, the seismicity grows downward to a maximum depth of 2150 m but only on the S-SE sector from GPK1 wellhead as it was observed during the beginning of preceeding test. On the second day, this seismic zone ceases to be active and a migration of the seismicity towards the N-W of GPK1 clearly appears; this new cloud concentrates at depths between 2150 m and 2250 m and still remains the principal active zone during the last day. When the injection stopped, this zone still also remained active for a few hours.

Once more, the general trend of seismicity is the same as observed during the 7 l/s injection test, that is along a NW-SE axis.

CONCLUSIONS

These preliminary results, both for the 7 l/s and 15 l/s hydraulic stimulations, have shown that the respective seismic clouds seem to organize along a NW-SE axis, and to grow downward from the injection interval. This trend must be associated with the present knowledge of the stress field which indicates an extension regime typical of a graben system with a maximum horizontal stress component of the tensor oriented 155°N to 175°N (Rummel F. & al., 1991).

However, the seismicity did not grow symmetrically along this axis in reference to GPK1 wellhead; in a first stage, the events appeared in the SE sector around the injection interval and deepened as the injection went on. Afterwards, this volume ceased to be seismically active - that was clear in a more obvious way during the second test after an injected volume of about 1000 m^3 - and a new zone sited on the NE sector and at depths between 2150 m and 2250 m began to activate.

At this stage of interpretation, it is therefore also necessary to point out that the network configuration will cause difficulties in the forthcoming detailed interpretations of fault plane solutions and source mechanisms.

ACKNOWLEDGEMENTS

This work was financially supported by the Commission of the European Communities, the Bureau de Recherches Géologiques et Minières and the Agence Française pour la Maîtrise de l'Energie.

The work described in this research note was also carried out under contract to the UK Department of Energy's Renewable Energy Research and Development programme, managed by the Energy Technology Support Unit (ETSU) at Harwell. The views and judgements expressed in this research note are those of the authors and do not necessarily reflect those of ETSU or the Department of Energy.

REFERENCES

Baria, R., Green, A.S.P, (1989), "Microseismics: a key to understanding reservoir growth", International HDR Geothermal Energy Conference, Camborne(UK), 27-30 June 1989, pp 363-377.

Beauce, A., Fabriol, H., Le Masne, D., Cavoit, C., Mechler, P., Chen, XK., (1991), "Seismic studies on the HDR site of Soultz-sous-Forêts (Alsace-France)", Geotherm. Sci. & Tech., Vol. 3 (1-4), pp. 239-266.

Kappelmeyer, O., Gérard, A., Schloemer, W., Ferrandes, R., Rummel, F., Benderitter, Y., (1991), "European HDR project at Soultz-sous-Forêts: general presentation", Geotherm. Sci. & Tech., Vol. 2 (4), pp. 263-289.

Matsunaga, I., (1990), "Development of hydrothermal power generation plants: development of technologies for a power generation system in HDR", 10th annual NEDO conference on Geothermal Energy Technologies, Oct. 1990, pp. 69-86.

Mock, J., 1989, "The U.S. Hot Dry Rock program", International HDR Geothermal Energy Conference, Camborne (U.K.), 27-30 June 1989, pp 149-158.

Rummel ,F., and Baumgartner, J., (1991) "Hydraulic fracturing stress measurements in the GPK1 borehole, Soultz-sous-Forêts", Geotherm. Sci. & Tech., Vol. 3 (1-4), pp. 119-148.

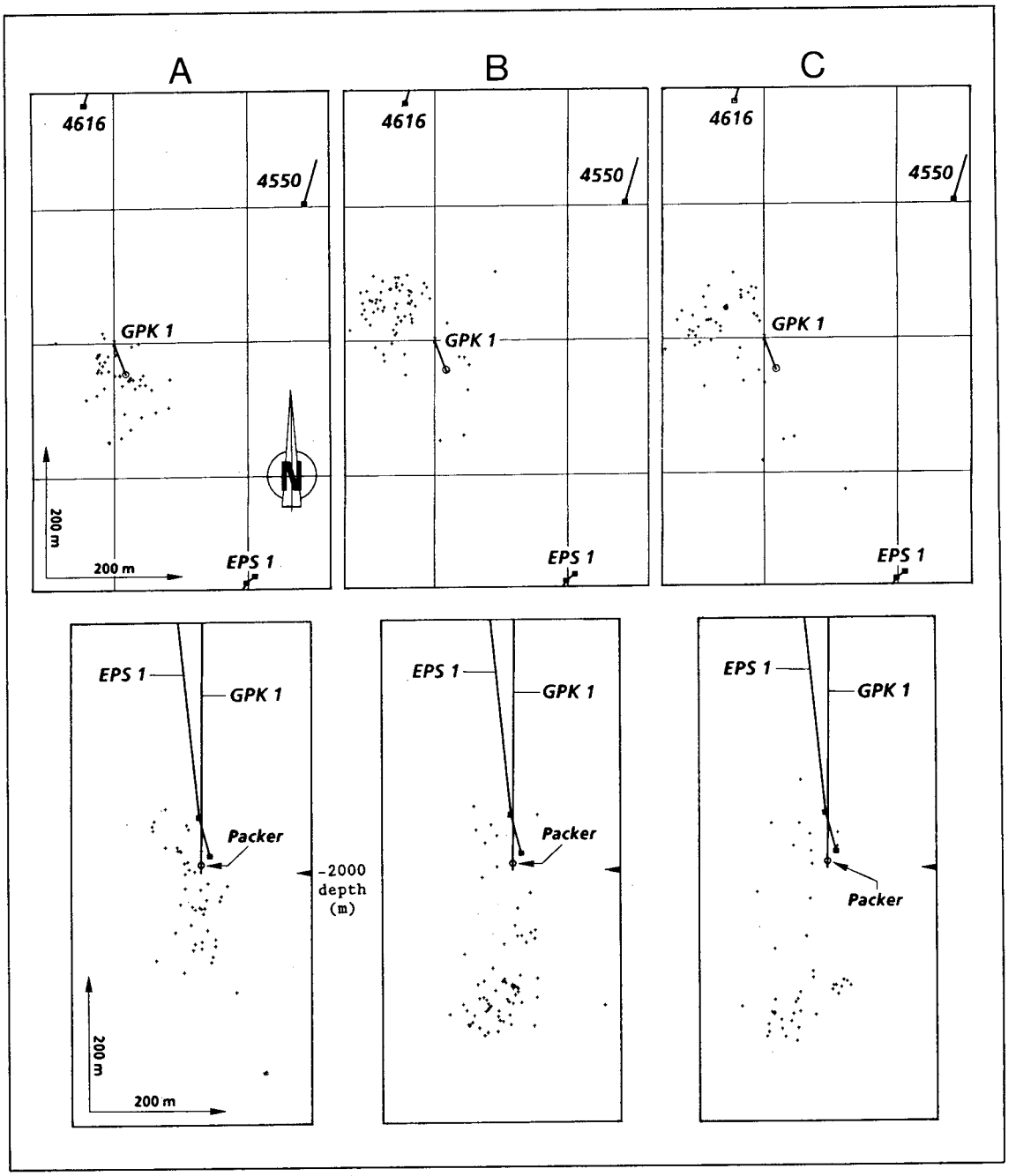

Fig. 6 - Microseismicity during the 15 l/s injection in GPK1
Plan view and vertical section view (azimuth 150°N)
A = first day, B = second day, C = third day
■ : seismic probe

PROCEEDINGS, Seventeenth Workshop on Geothermal Reservoir Engineering
Stanford University, Stanford, California, January 29-31, 1992
SGP-TR-141

A Fast Method for Evaluating A Simplified Hot Dry Rock Heat Flow Problem

R.G. Adair
Susan Petty Consulting
703 Santa Paula
Solana Beach, CA 92075

ABSTRACT

I present optimizations to the computation of Elsworth's single zone, hot dry rock thermal recovery model. These enhancements lead to as much as a 6-fold increase in computational speed. The greatest time savings derive from an efficient evaluation of the model's thermal response due to a step in heat flux, which is required for solution of the more general problem via Duhamel's Principle. Further enhancements come from taking advantage of the special structure of the model's finite difference equation.

Reductions in execution speed were sought in order to facilitate the model's implementation on AT-class microcomputers. The PC-based application requires multiple evaluations of the model. Typical execution times on a 33 MHz 80386 microcomputer for 128 time steps were 7 seconds, as compared with 25-42 seconds for the non-optimized approach, and for 512 time steps were 28 and 100-168 seconds, respectively; the timing of the non-optimized method depended upon particulars of the dimensionless variables.

INTRODUCTION

DOE is sponsoring the development of software tools which estimate the impact of research and development on the cost of geothermal power generation [*Petty et al.*, 1988]. Although a mature tool for hydrothermal resources exists, work on geopressured and hot dry rock resources continues. A goal for this software is that it execute in a reasonable amount of time on AT-class microcomputers. To this end, computational enhancements were sought for the single zone, hot dry rock thermal recovery model of *Elsworth* [1989a], which was adopted for the hot dry rock software tool. Figure (1) shows a typical prediction of Elsworth's model for parameters assumed to be appropriate for the Fenton Hill Hot Dry Rock Project [*Robinson and Kruger*, 1988], which Table (1) lists. The results illustrate the difference in magnitude of temperature change with time for a large (800 m) single reservoir compared to a small (200 m) reservoir. Note that in all of the cases the temperature has dropped below a 150° C temperature by the end of a typical 30 year project life.

This paper describes the enhancements to the methods of *Elsworth* [1989a]. The greatest savings in time come from the efficient evaluation of the step response of the spherical reservoir, including its analytic evaluation, which Elsworth computes numerically. Further savings come from exploiting the special structure of the finite difference equations which approximate the pertinent differential equation. The resulting matrix equation was amenable to a fast inversion method which also has extremely modest memory requirements. In addition, given one solution, a solution correct to first order in small perturbations to the dimensionless variables can be computed with substantially less effort that the exact solution.

Elsworth [1989b] has since expanded his model to include multiple porous zones. The methods presented here can be applied with minor modification to *Elsworth* [1989b].

ELSWORTH'S MODEL

Statement of the Problem

The theory which *Elsworth* [1989a] presents will only be summarized here. Conceptually, heat is extracted from a porous, spherical inclusion in an otherwise uniform, infinite half space. Water of a given initial temperature circulates through the sphere and returns at a time varying temperature which the flow rate and the reservoir porosity dictate. The inclusion and half space are in thermal equilibrium with each other prior to the circulation of water.

Elsworth assumes that the circulating water immediately attains equilibrium with the reservoir upon entry, a reasonable assumption given the low thermal con-

ductivity of most host rocks. To render the problem tractable, Elsworth further considers only the temperature averaged over the surface of the sphere.

Given this model and its assumptions, Elsworth shows how to compute the time variation of the average temperature from the step heat flow response of a sphere in an infinite space. The solution in an infinite half space follows from the method of images to satisfy either zero heat flux or constant temperature at the surface of the infinite half space. Application of Duhamel's Principle then defines the heat flux variation into the half space at the sphere's surface in terms of the temperature rate. The following differential equation describes the energy balance between the semi-infinite heat reservoir and the spherical inclusion:

$$\begin{aligned} \langle q_T \rangle &= q_F \rho_F c_F \langle T_o(t) - T_i \rangle + \frac{4\pi a^3 \rho_S c_S}{3} \frac{\partial}{\partial t} \langle T_o \rangle \\ &= 4\pi a \int_0^t C(t-\tau) \frac{\partial}{\partial \tau} \langle T_R - T_o(\tau) \rangle \, d\tau \qquad (1) \\ \langle T_o(t=0) \rangle &= T_R \end{aligned}$$

or in terms of dimensionless variables, assuming that the inlet and initial half space temperatures T_i and T_R are constant, and after some rearrangement,

$$\frac{Q_D}{4\pi} T_D + \frac{\Phi_D}{3} \frac{\partial T_D}{\partial t_D} + \left(\frac{\partial T_D}{\partial t_D} \right) \star_D C = 0, \quad t_D > 0 \qquad (2)$$

$$T_D = 1, \quad t_D = 0. \qquad (3)$$

Table 2 defines the dimensionless parameters in terms of physical parameters, which are themselves defined in Table 1. The function C above is the reciprocal of the sphere's step heat flux response, which depends on dimensionless sphere radius $\hat{a} = a/z$ and dimensionless time $t_D = K_R t / \rho_R c_R a^2$. The notation $\star_D$ denotes convolution performed in dimensionless time. The notation $< \cdot >$ denotes an average of the bracketed quantity over the spherical surface.

The density and thermal capacity of the spherical reservoir here are defined in terms of the corresponding properties of the fluid and rock and its porosity ϕ:

$$\rho_S \, c_S = (1-\phi) \rho_R \, c_R + \phi \, \rho_F \, c_F. \qquad (4)$$

The convolutional integral in these equation builds the general heat flux solution in terms of the temperature variation on the boundary using the basic building block provided by the function C.

Finite Difference Approximation to the Differential Equation

If time is discretized in Equation (2) over N time steps $k \, \Delta t_D$, $k = 1, ..., N$, and the discrete versions of derivatives and integrals are employed, then the following matrix equation in terms of dimensionless parameters results:

$$\left[\Delta t_D \frac{Q_D}{4\pi} \mathbf{I} + \frac{\Phi_D}{3} \boldsymbol{\partial} + \boldsymbol{\partial} \mathbf{L}(\vec{C}) \right] \vec{\mathrm{T}}_D = \left(\vec{C} + \frac{\Phi_D}{3} \hat{\mathbf{e}}_1 \right) T_0 \qquad (5)$$

Here, $\mathbf{I}$ is the order N identity matrix; $\boldsymbol{\partial}$ is a matrix which is all ones along the main diagonal and all -1's along the first sub-diagonal; $\mathbf{L}(\vec{C})$ is a lower triangular matrix, which has the vector $\vec{C}$ as it first column, constant entries along the main and sub-diagonals, and all zeros above the main diagonal; $\vec{C}$ is a column vector with k'th element which is the integral of the reciprocal step response C evaluated between dimensionless times $(k-1)\Delta t_D$ and $k \Delta t_D$; $\vec{\mathrm{T}}_D$ is a column vector of the dimensionless temperature values, so that element k is the dimensionless temperature at time step k; and $\hat{\mathbf{e}}_1$ is a unit column vector of all zeros except for the first element, which is one. T_0 is the initial value of the dimensionless temperature, which by definition is just 1. In the following, this value is inserted, and T_0 is dropped.

SOLUTION OF ELSWORTH'S PROBLEM

Computing the Step Response

The step response C describes the simplest heat flux response of Elsworth's model. Its reciprocal is the temperature variation, averaged over the sphere's surface, due to a step in heat flux over that surface. This reciprocal is the sum of the self-heat C_1 due to the sphere, and the heat C_2 due to the image source, which maintains boundary conditions of either constant flux or temperature at the surface of the earth. The image source heat is expressible in polar spherical coordinates as an integral over co-latitude angle. Elsworth computes this integral numerically. However, as I show in Appendix A, it may be expressed in closed form, and therefore need not be numerically evaluated.

While the closed form evaluation of the integral C_2 provides a savings in numerical effort, as well as an assurance of accuracy, there still remains the need to integrate $1/(C_1 \pm C_2)$ over the intervals of discrete time in the finite difference equation. Consideration of the behavior of the step response at small and large times suggests approximations, described in Appendix A, which require only 10%-20% of the computational effort as the exact expression, depending upon the boundary condition. These approximations, which are sums of exponentials in $\log t_D$, provide excellent fits over the entire allowable ranges of dimensionless time and radius.

Inverting the Finite Difference Matrix

The matrices of Equation (5), I, $\boldsymbol{\partial}$, and C, have special structures. First note that the entries along any diagonal are constant, which is the defining feature of a *Toeplitz* matrix. Second, all diagonals above the main diagonal are zeros, making them *lower triangular* matrices. Thus, the first column, or last row, completely specify a lower triangular Toeplitz matrix. As I show in Appendix B, such a matrix can be inverted with an effort proportional to $N \log_2 N$ floating point operations, or `flops`, where N is the number of time steps and where one `flop` may be roughly defined as a computational effort which requires one multiplication or division of two floating point numbers, plus the effort to add or subtract two floating point numbers. The time required to finish a software task is generally proportional to the number of `flops` expended. The next best method, back substitution, requires $N(N+1)/2$ `flops`. The fast method derives its speed from the fact that the matrix multiplications can be computed from convolutions of the first columns of the matrices, which in turn can be done quickly with Fast Fourier Transforms. The fastest implementation of this method requires that N be an integer power of 2.

In principal this algorithm is both fast and concise. In practice, the overhead associated with the partitioning and the various FFT-aided convolutions keeps this algorithm from surpassing back substitution for $N \leq 128$ time steps. Table 3 shows a comparison of the back substitution and FFT-based methods, averaged over 4 trials, applied to random Toeplitz matrices of various sizes to solve the matrix equation $\mathsf{A}\vec{x} = \vec{y}$ for vector $\vec{x}$. These numbers were computed with The MathWorks' matrix manipulation software AT-MATLAB^{TM} on a 33 mHz 80386-based PC using a math coprocessor. The table gives the required execution time and the computational effort, which MATLAB provides. For a length of 1024 points, the FFT-based method took 6 seconds, as compared with 40 seconds for the back substitution method, a factor of nearly 7 faster. Note also, in this particular case, that the results for $N = 256$ and 512 show that the number of `flops` required do not necessarily dictate the execution time. The FFT-based method requires 1.5 to 3 times more `flops` than the back substitution method, yet executed faster. This is because MATLAB provides optimized code for power-of-2 length FFT's.

Solution for Small Perturbations

Suppose that the reservoir parameters Q_D, Φ_D and $\vec{C}$ are subjected to a small perturbation δQ_D, $\delta\Phi_D$ and $\delta\vec{C}$. Denote the lower triangular Toeplitz matrix generated by the unperturbed values as $\mathsf{H}(Q_D, \Phi_D, \vec{C})$. Then the resulting temperature perturbation $\delta\vec{T}_D(\delta Q_D, \delta\Phi_D, \delta\vec{C})$, correct to first order in the perturbations, can be found from the solution $\vec{T}_D(Q_D, \Phi_D, \vec{C})$ and the inverse matrix $\mathsf{H}^{-1}(Q_D, \Phi_D, \vec{C})$ with much less effort than the exact solution. This perturbation can be found from the Taylor series of $\vec{T}_D(x + \delta x)$, where x is a scalar:

$$\vec{T}_D(x + \delta x) = \vec{T}_D(x) + \delta x \frac{\partial}{\partial x}\vec{T}_D(x) + \mathcal{O}((\delta x)^2)\,, \quad (6)$$

so that to first order in δx,

$$\delta\vec{T}_D \;=\; \delta x \frac{\partial}{\partial x}\vec{T}_D(x)\,. \quad (7)$$

Recalling that $\vec{T}_D = \mathsf{H}^{-1}\vec{y}$, where $\vec{y} = \vec{C} + \hat{\mathbf{e}}_1\Phi_D/3$, and using the result

$$\frac{\partial}{\partial x}\mathsf{H}^{-1}(x) = -\mathsf{H}^{-1}\,\frac{\partial}{\partial x}\mathsf{H}(x)\,\mathsf{H}^{-1}\,, \quad (8)$$

(see, for example, *Gradshteyn and Ryzhik* [1980, p 1107]) the perturbation to the temperature is, after some rearrangement,

$$\delta\vec{T}_D = \delta x\left[\mathsf{H}^{-1}\frac{\partial}{\partial x}\vec{y} - \mathsf{H}^{-1}\left(\frac{\partial}{\partial x}\mathsf{H}\right)\vec{T}_D\right]\,. \quad (9)$$

Consider first a perturbation δQ_D to the dimensionless flow rate. From the last equation,

$$\delta\vec{T}_D(\delta Q_D) = -\Delta t_D \frac{\delta Q_D}{4\pi}\mathsf{H}^{-1}\vec{T}_D\,, \quad (10)$$

where the parameter dependence is on the unperturbed values unless otherwise explicitly stated. This matrix multiplication requires only one convolution to compute.

Consider next a perturbation $\delta\Phi_D$ to the dimensionless porosity. Proceeding as above,

$$\delta\vec{T}_D(\delta\Phi_D) = \frac{\delta\Phi_D}{3}\left[\mathsf{H}^{-1}\hat{\mathbf{e}}_1 - \boldsymbol{\partial}\mathsf{H}^{-1}\vec{T}_D\right]\,, \quad (11)$$

where the result $\mathsf{H}^{-1}\boldsymbol{\partial} = \boldsymbol{\partial}\mathsf{H}^{-1}$ was used. This perturbation can also be performed with a single convolution, as follows. First, note that $\mathsf{H}^{-1}\hat{\mathbf{e}}_1$ is just the first column of H^{-1}, $\vec{x}$, say, so that no computations at all are required for this operation. Next, note that the matrix $\boldsymbol{\partial}\mathsf{H}^{-1}$ can be computed from the first differences of H^{-1}. No recourse to convolution is needed to compute this. Thus, only the convolution of $\vec{T}_D$ with this vector difference is required.

Finally, suppose a perturbation $\delta\vec{C}$ to the step response. Considering the individual perturbations due

to each element of $\delta\vec{C}$ in Equation (8), the aggregate first order perturbation to $\vec{T}_D$ is

$$\delta\vec{T}_D(\delta\vec{C}) = \mathbf{H}^{-1}\delta\vec{C} - \boldsymbol{\partial}\,\mathbf{H}^{-1}\,\mathbf{L}(\delta\vec{C})\,\vec{T}_D\,, \qquad (12)$$

where the commutability of the matrices were applied. This operation requires two convolutions. The first convolution yields the vector $\mathbf{H}^{-1}\delta\vec{C}$. Then, the matrix product $\boldsymbol{\partial}\,\mathbf{H}^{-1}\,\mathbf{L}(\delta\vec{C})$ is found from first differences of the vector $\mathbf{H}^{-1}\delta\vec{C}$, without recourse to convolution. A second convolution yields the product of this difference operation with $\vec{T}_D$.

If sufficiently small perturbations occur to all quantities, the net result is just the sum of these three individual results.

DISCUSSION

The ideas of this paper were implemented with Microsoft's QUICKBASIC 4.5. Recursive calls were not used to invert the Toeplitz matrix. To facilitate comparison, Elsworth's original FORTRAN code was translated to QUICKBASIC 4.5. The execution time of the original code was sensitive to the particulars of the problem, while that of the optimized code was not. Several runs of 128 time steps on a 33 MHz 80386 clone without benefit of a math coprocessor yielded average execution times of 6.7 seconds for the enhanced code. On the other hand, the original code times ranged between 24.1 and 41.8 seconds, with time increasing as with the product $Q_D t_D$. Runs of 512 points required 27 seconds for the optimized code and 107—168 seconds for the original code. These results attest the success of the streamlining efforts. Furthermore, use of the perturbation scheme yielded new solutions in less than one second, typically.

Application to Multiple Zones

Elsworth [1989b] extends the single zone problem to describe a multiple zone hot dry rock resource. The discrete problem can be cast as a lower triangular *block* Toeplitz matrix equation, where the fixed diagonal entries are matrices rather than scalars. Each of the matrix entries are square matrices of order M which describe the mutual effects of the M subzones on one another at a given time step, while the temperature vector comprises subvectors of length M which give the average temperature of the M source zones at a given time step. The mutual effects of each zone play the role of the image source in the single source model. The Toeplitz matrices in Equation (5) carry over in a straightforward manner to the multiple zone problem. For example, the 1's in the matrix $\boldsymbol{\partial}$ become identity matrices of order M. It may be shown that each of the special properties of the scalar problem carry over into the matrix problem (see *Bitmead and Anderson* [1980]). In particular, the inverse matrix is also lower triangular block Toeplitz, so that its first column of matrices entries completely describe it.

Although in general these matrix entries need have no special structure, the assumptions of *Elsworth* [1989b] result in each being a symmetric Toeplitz matrix. To render this problem tractable, Elsworth assumes that the resource comprises several proximate single zones in an infinite whole space, and that the size and thermal properties of each zone are identical. This special structure means that matrix multiplications can be performed with convolutions, either directly for small M or by FFT's for larger M.

ACKNOWLEDGEMENTS

This work described in this paper was funded in part by Sandia National Laboratory Contract 66-8860 Derek Elsworth generously provided the advice, software and articles on which this paper is based. This paper would not have been possible without the comments and encouragement of S. Petty.

REFERENCES

Bitmead, Robert R., and Anderson, Brian D.O. Asymptotically fast solution of Toeplitz and related systems of linear equations. *Linear Algebra and its Applications, 34*(1), 103—116, 1980.

Elsworth, Derek. Theory of thermal recovery from a spherically stimulated hot dry rock reservoir. *J. Geophys. Res., 94*(B2), 1927—1934, 1989a.

——— Thermal recovery from a multiple stimulated HDR reservoir. *Geothermics, 18*(5/6), 761—774, 1989b.

Gradshteyn, I.S., and Ryzhik, I.M. Tables of Integrals, Series, and Products. 1160 pp. (New York: Academic Press) 1980.

Petty, S., Entingh, D., Livesay, B. Impact Of R&D On Cost of Geothermal Power. Documentation of Model Version 2.09. Sandia Report SAND87-7018, February, 1988.

Press, W.H., Flannery, B.P., Teukolsky, S.A., and Vetterling, W.T. Numerical Recipes. The Art of Scientific Computing. 818 pp. 3rd ed. (Cambridge: Cambridge University Press) 1986.

Robinson, B.A., and Kruger, P. A comparison of two heat transfer models for estimating thermal drawdown in hot dry rock reservoirs. Proceedings, 13th Workshop on Geothermal Reservoir Engineering, Stanford University, January 19—21, 1988.

APPENDIX A
COMPUTING THE STEP RESPONSE

Analytic Solution

Elsworth [1989a] characterizes the thermal recovery of the hot dry rock resource by the average temperature variation $\langle T_R - T_o \rangle$ over the spherical reservoir surface:

$$\langle T_R - T_o \rangle = \frac{1}{4\pi a K_R} (C_1 \pm C_2), \qquad \text{(A1)}$$

where

$$C_1(t_D) = 1 - e^{t_D} \operatorname{erfc}(\sqrt{t_D}), \qquad \text{(A2)}$$

and

$$C_2 = \frac{1}{2} \int_0^\pi \frac{\sin\theta d\theta}{\hat{r}(\theta)} \left\{ \operatorname{erfc}\left(\frac{\hat{r}-1}{2\sqrt{t_D}}\right) - e^{(\hat{r}-1+t_D)} \operatorname{erfc}\left(\frac{\hat{r}-1}{2\sqrt{t_D}} + \sqrt{t_D}\right) \right\} \qquad \text{(A3)}$$

C_1 describes the thermal flux due to the sphere, while C_2 describes that due to a fictitious image source at distance $2z$ from the sphere, where z is the depth of the sphere in the half space. The image source maintains either constant flux (C_2 is added) or constant temperature (C_2 is subtracted) at the surface of the infinite half space. In these equations, t_D is dimensionless time, and $\hat{r} = r/a$, where r is the distance from the image source to a particular spot on the sphere's surface. The colatitude angle θ completely specifies r in a spherical coordinate system centered on the sphere with the vertical axis along the line to the image source,

$$r(\theta) = a\sqrt{1 + 4/\hat{a}^2 - (4\cos\theta)/\hat{a}}, \qquad \text{(A4)}$$

where $\hat{a} = a/z$.

Elsworth evaluates C_2 numerically; however, it has a closed form evaluation. Note that, from the above equation, $d\theta = d\hat{r}\ \hat{a}\hat{r}/2\sin\theta$, so that for any function $f(\hat{r}(\theta))$,

$$\int_0^\pi f(\hat{r}(\theta)) \frac{\sin\theta d\theta}{\hat{r}(\theta)} = \frac{\hat{a}}{2} \int_{\hat{r}(0)}^{\hat{r}(\pi)} f(\hat{r})\, d\hat{r}. \qquad \text{(A5)}$$

Thus, the angular integral for C_2 is equivalent to one in $\hat{r}$,

$$C_2 = \frac{\hat{a}}{4} \int_{\hat{r}(0)}^{\hat{r}(\pi)} \left[\operatorname{erfc}\left(\frac{\hat{r}-1}{2\sqrt{t_D}}\right) - e^{(\hat{r}-1+t_D)} \left(\operatorname{erfc}\frac{\hat{r}-1}{2\sqrt{t_D}} + \sqrt{t_D} \right) \right] d\hat{r}. \qquad \text{(A6)}$$

The solution of this integral is now straightforward, e.g. using integration by parts:

$$C_2 = \frac{1}{4} \left\{ (\hat{a}+2)\operatorname{erfc}\left(\frac{1}{\hat{a}\sqrt{t_D}}\right) + (\hat{a}-2)\operatorname{erfc}\left(\frac{1-\hat{a}}{\hat{a}\sqrt{t_D}}\right) + \frac{2\hat{a}\sqrt{t_D}}{\sqrt{\pi}} \left(e^{-(1-\hat{a})^2/\hat{a}^2 t_D} - e^{-1/\hat{a}^2 t_D} \right) + \hat{a} \left[e^{(2(1-\hat{a})/\hat{a}+t_D)} \operatorname{erfc}\left(\frac{1-\hat{a}}{\hat{a}\sqrt{t_D}} + \sqrt{t_D}\right) - e^{(2/\hat{a}+t_D)} \operatorname{erfc}\left(\frac{1}{\hat{a}\sqrt{t_D}} + \sqrt{t_D}\right) \right] \right\}. \qquad \text{(A7)}$$

Approximating the Analytic Solution

Approximations to the reciprocal step response C are presented here which facilitate the rapid evaluation of both C and its integral over intervals of discrete time. At small dimensionless times $t_D \leq 10^{-3}$, the self heat term dominates with a value of approximately $2\sqrt{t_D/\pi}$, so that the integral of the reciprocal presents an integrable singularity. At larger dimensionless times $1/(C_1 \pm C_2)$ is well approximated by sums of exponential terms with exponents which are quadratic in the logarithm of time. The forms of the curve fits are constrained by the values of the step responses at large times. The integral of such a fit can generally be expressed as the sum of a linear term and erfc functions, but simple trapezoidal rule integration of the erfc terms was found to be sufficiently accurate for typical values of $\Delta t_D \leq 1$.

In the case of a constant flux boundary condition, where the step response is $C_+ = C_1 + C_2$, the functional fit for $t_D > 10^{-3}$ is

$$\begin{aligned} Q_+(x) &= ax^2 + bx + c \\ &= \log\left(\frac{\alpha_+}{C_+} - 1\right), \end{aligned} \qquad \text{(A8)}$$

where $x = \log t_D$ and $\alpha_+ = 1 + \hat{a}/2$, so that

$$\int_{(k-1)\Delta t_D}^{k\Delta t_D} \frac{dt_D}{C_+} \approx \frac{\Delta t_D}{\alpha_+} + \frac{1}{2\alpha_+} \left(e^{Q_+(x_{k-1})} + e^{Q_+(x_k)} \right). \qquad \text{(A9)}$$

The situation for the constant temperature boundary condition, with step response $C_- = C_1 - C_2$, is more complicated. In this case, the fit is to

$$Q_-(x) = \log\left[1 - \left(\frac{1}{C_-} - \frac{1}{C_+} \right) \frac{1}{\beta} \right], \qquad \text{(A10)}$$

where $\beta = 1/\alpha_- - 1/\alpha_+$, with $\alpha_- = 1 - \hat{a}/2$. Then,

$$\int_{(k-1)\Delta t_D}^{k\Delta t_D} \frac{dt_D}{C_-} \approx \frac{\Delta t_D}{\alpha_-} + \frac{1}{2\alpha_+} \left(e^{Q_+(x_{k-1})} + e^{Q_+(x_k)} \right) - \frac{\beta}{2} \left(e^{Q_-(x_{k-1})} + e^{Q_-(x_k)} \right). \qquad \text{(A11)}$$

Thus, a strategy would be to sample the exact step response over, say, half decade intervals in dimensionless

time (12 functional evaluations in the 6 decades spanning $10^{-3} \leq t_D \leq 10^3$, for example), and to curve fit according to the proposed models.

APPENDIX B
INVERTING A LOWER TRIANGULAR TOEPLITZ MATRIX

The bracketed matrix expression in Equation (5) is a lower triangular Toeplitz. The general solution of any lower triangular matrix system, say $\mathbf{A}\ \vec{x} = \vec{y}$, can be computed with *back substitution*, in which element k is

$$x_k = \frac{1}{A_{kk}}(y_k - \sum_{j=1}^{k-1} A_{kj}\, x_j)\,, \qquad \text{(B1)}$$

where A_{kj} is the element of $\mathbf{A}$ in the k'th row and j'th column. Back substitution uses previously computed values of the vector $\vec{x}$ to define the next value. Thus, evaluation of this equation must proceed from $k = 1$ to N in order, where N is the number of time steps. This scheme requires $\sum_{k=1}^{N} k = N(N+1)/2$ `flops`.

While this strategy is a vast improvement over general matrix inversion, which requires on the order of N^3 `flops` to evaluate, even greater improvement is possible by exploiting the Toeplitz structure of the matrix and its equivalence to convolution. Below, I develop an algorithm which requires order $N \log_2 N$ `flops` following the work of *Bitmead and Anderson* [1980], who show how to find the inverse of a general, full Toeplitz matrix.

The basis of the algorithm is the structure of inverse matrix. This inverse is itself lower triangular Toeplitz. If $\mathbf{L}(\vec{x})$ denotes a lower triangular Toeplitz matrix with first column $\vec{x}$, the inverse $\mathbf{L}^{-1}(\vec{x})$ of an order N, lower triangular Toeplitz matrix $\mathbf{L}(\vec{x})$ has the partitioned structure

$$\mathbf{S} \equiv \mathbf{L}^{-1}(\vec{x}) = \begin{pmatrix} \mathbf{S}_{11} & \mathbf{S}_{12} \\ \mathbf{S}_{21} & \mathbf{S}_{22} \end{pmatrix} \qquad \text{(B2)}$$

where $\mathbf{S}_{11} = \mathbf{L}^{-1}(\vec{x}[1\!:\!k])$ is a lower triangular, square Toeplitz matrix of order k; $\mathbf{S}_{12}$ is a $k \times j$ matrix of all zeros, with $j = N - k$; $\mathbf{S}_{22} = \mathbf{L}^{-1}(\vec{x}[1\!:\!j])$ is a lower triangular, square Toeplitz matrix of order j; and $\mathbf{S}_{21} = -\mathbf{S}_{22}\, \mathbf{L}(\vec{x})_{21}\, \mathbf{S}_{11}$ is a rectangular Toeplitz matrix of size $j \times k$, where $\mathbf{L}(\vec{x})_{21}$ is the corresponding $j \times k$ partitioning of the original matrix. The notation $\vec{x}[j\!:\!k]$ denotes a column vector formed from elements j through k of $\vec{x}$.

The algorithm proceeds by recognizing that the inverse matrix is completely defined by its first column; that the various matrix multiplications involved in defining the $\mathbf{S}$ partitions are essentially convolutions, which can be rapidly computed using FFT's *Press et al.* [1986, Ch. 12]; and that the solution can be found by recursively calling the algorithm to solve successively smaller partitions of the original matrix. Note, however, that the algorithm need not be formulated recursively. In general, the algorithm must call itself twice per recursion: once to find $\mathbf{S}_{11}$, and again to find $\mathbf{S}_{22}$. Only the first column of $\mathbf{S}_{21}$ is required to complete the computation of the inverse of the lower triangular Toeplitz matrix which was passed to the routine. Moreover, the memory requirements are of order N since only single column vectors are needed to specify the matrices, in contrast to the N^2 values needed for a full matrix.

In particular, if the lower triangular Toeplitz matrix has order N which is a power of 2, and the partitioning is done by halving the matrix size, so that the partition matrices are all the same size, the algorithm is at its fastest. This is because, first, $\mathbf{S}_{11} = \mathbf{S}_{22}$, which obviates the need for computing one matrix inversion per recursion, and, second, power-of-two FFT's are computed most quickly.

Once the inverse of the Toeplitz equation is found, the solution to the finite difference equation, Equation (5), is given by the convolution of the vector on the right hand side of this equation with the vector which defines the inverse matrix, again a task which can be done quickly with FFT's. Explicitly, if $\mathbf{L}(\vec{x})$ defines the inverse matrix, then the solution is given by the first half of

$$\vec{x} \star \left(\vec{C} + \frac{\Phi_D}{3}\hat{\mathbf{e}}_1\right) \qquad \text{(B3)}$$

Implementing the Inversion Algorithm

Figure 2 describes the implementation of the inversion algorithm. Only the recursive implementation is outlined, but the extension to non-recursive inversion is straightforward. Various notations are adopted to facilitate concise pseudo-code. $\vec{x}[j\!:\!k]$ denotes a vector comprising elements j through k of vector $\vec{x}$. $\mathbf{L}(\vec{x})$ denotes a lower triangular Toeplitz matrix which has $\vec{x}$ as its first column. $[\vec{x};\ \vec{y}]$ denotes an augmented column vector comprising $\vec{x}$ atop $\vec{y}$. Also, in performing FFT-aided convolutions, vectors of length N must be augmented, or padded, by N zeros. Unless otherwise stated, this augmentation occurs at the end of the vector. The latter half of this convolution is generally discarded, while the other half represents the operation of the matrix multiplication.

Table 1. Physical Parameter Definition

Parameter	Units	Definition	Fig. 1 Values
t	s	Time	$\leq$ 30 years
$q_T(r,t)$	W	Thermal flux	
q_F	m^3/s	Fluid flow rate	150 & 300 gal/min
c_F	J/kg-deg C	Fluid heat capacity	2095
ρ_F	kg/m^3	Fluid density	895
T_i	deg C	Fluid inlet temperature	50
$T_o(t)$	deg C	Fluid outlet temperature	
K_R	W/m-deg C	Rock thermal conductivity	2.5
c_R	J/kg-deg C	Rock heat capacity	1020
ρ_R	kg/m^3	Rock density	2600
T_R	deg C	Rock initial temperature	275
a	m	Sphere radius	200 & 800
z	m	Depth of sphere's center	4000
c_S	J/kg-deg C	Sphere heat capacity	
ρ_S	kg/m^3	Sphere density	
ϕ	(fraction)	Sphere porosity	0.05
$C(t)$	(none)	Heat flux step response	

PREDICTED TEMPERATURE DRAWDOWN FOR FENTON HILL

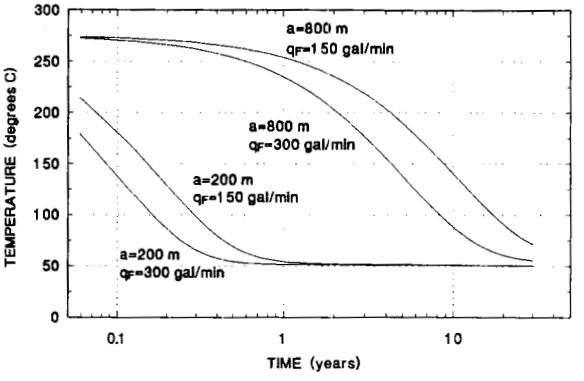

Figure 1

Table 2. Dimensionless Parameter Definition

Parameter	Definition	Name
$\hat{a}$	$\frac{a}{z}$	Radius
Φ_D	$\frac{\rho_S c_S}{\rho_R c_R}$	Porosity or heat capacity
Q_D	$\frac{q_F \rho_F c_F}{K_R a}$	Flow rate
T_D	$\frac{< T_o - T_i >}{T_R - T_i}$	Temperature
t_D	$\frac{K_R t}{\rho_R c_R a^2}$	Time

Table 3. Comparison of Toeplitz Inversion Methods

	FFT-Based		Back Substitution	
Time Steps	Compute Time (s)	Effort (flops)	Compute Time (s)	Effort (flops)
4	0.11	907	0.03	22
8	0.29	2,713	0.06	78
16	0.49	6,992	0.08	286
32	0.74	16,499	0.18	1,086
64	1.10	37,401	0.41	4,222
128	1.61	83,089	1.13	16,638
256	2.43	182,522	3.34	66,046
512	3.91	390,208	11.08	263,166
1024	5.78	824,717	39.64	1,050,622

Recursive Inversion of Lower Triangular Toeplitz Matrix

1. Given: First column $\vec{x}$ of order N lower triangular Toeplitz matrix. N must be a power of 2.
2. If length of vector $N = 1$
   (a) Return first column of inverse $= 1/x[1]$.
3. Else
   (a) Use algorithm (recurse) to compute first column $\vec{L}_{11}$ of $\mathbf{L}^{-1}(\vec{x}[1{:}N/2])$.
   (b) Compute convolution $\vec{L}_{11} \star \vec{x}[N/2{+}1{:}N]$ using FFTs. Save first half as $\vec{L}_{21}$.
   (c) Compute convolution $\vec{L}_{11} \star [\vec{0}; \vec{x}[2{:}N/2]]$ using FFTs. Add first half to $\vec{L}_{21}$. Note that $\vec{x}[2{:}N/2]$ is pre-padded with $N/2+1$ zeros.
   (d) Compute convolution $\vec{L}_{11} \star \vec{L}_{21}$ using FFTs. Save first half as $\vec{L}_{21}$
   (e) Return first column of inverse of $\mathbf{L}(\vec{x})$ as augmented vector $[\vec{L}_{11}; -\vec{L}_{21}]$.

Figure 2

SEVENTEENTH ANNUAL WORKSHOP ON GEOTHERMAL RESERVOIR ENGINEERING STANFORD UNIVERSITY

Participants List

Jorge Acuna
Univ. of Southern California
Pet. Eng. Dept., Univ. Park
Los Angeles, CA 90089-1211
(213) 740-0322

Jeff W. Adams
State Lands Commission
245 W. Broadway, Suite 425
Long Beach, CA 90802
(310) 590-5201, FAX (310) 590-5295

Greg Andersen
Unocal Science & Technology
376 S. Valencia
Brea, CA 92621
(714) 577-2279

Emilio U. Antunez
Lawrence Berkeley Laboratory
1 Cyclotron Road, Bldg. 50E-146
Berkeley, CA 94720
(510) 486-5866, FAX (510) 486-5686

Paul Atkinson
Unocal
3576 Unocal Place
Santa Rosa, CA 95403
(707) 545-7600, FAX (707) 545-8746

Russell Bainbridge
INVOIL, Inc.
6640 Melrose Lane
Oklahoma City, OK 73127

Benjamin Barker
Unocal Geothermal
3576 Unocal Place
Santa Rosa, CA 95403
(707) 545-7600, FAX (707) 545-8746

Terrance G. Barker
S-Cubed
P.O.Box 1620
La Jolla, CA 92038-1620
(619) 453-0060, FAX (619) 755-0474

K. Kit Bloomfield
Pacific Gas & Electric
P.O.Box 456
Healdsburg, CA 95448
(707) 431-3810, FAX (707) 431-4066

P. Gordon Bloomquist,
Washington State Energy Office
809 Legion Way SE
Olympia, WA 98504-3165
FAX (206) 956-2016

Timothy S. Boardman
Calif Division of Oil & Gas
485 Broadway, Suite B
El Centro, CA 92243
(619) 353-9900, FAX (619) 353-9594

Gudmundur Bodvarsson
Earth Sci Division, LBL
1 Cyclotron Road
Berkeley, CA 94720
(510) 486-4789, FAX (510) 486-5686

Steve Butler
Unocal/Philippine Geo. Inc.
81-711,Hwy 111
Indio, CA 92201
(619) 342-4723, FAX (619) 347-4224

Claudio Calore
Int Inst. Geothermal Res-CNR
Piazza Solferino 2
Pisa, Italy 56126
39-50-46069, FAX 39-50-47055

Don A. Campbell
Mesquite Group, Inc.
P.O. Box 1283
Fullerton, CA 92632
(714) 738-8224, FAX (714) 525-2852

Guido Cappetti
ENEL
Via A. Pisano, 120
Pisa, Italy 56122
39-50-535781, FAX 39-50-533290

Raffaele Cataldi
E.N.E.L. International
Via Cesare Battisti, M47
Pisa, Italy 56125
39-50-53-57-71, FAX 39-50-53-58-76

Jim Combs
Geo Hills Associates
27790 Edgerton Road
Los Altos Hills, CA 94022
(415)941-5480, FAX (415) 941-5480

Jean W. Cook
SGP, Petroleum Engineering Dept.
Stanford University
Stanford, CA 94305
(415) 723-4745, FAX (415) 725-2099

John F. Copp
Califonia Energy Co., Inc.
P.O. Box 185/900 N Heritage
Ridgecrest, CA 93555
(619) 499-2336, FAX (619) 499-2308

John Counsil
Consultant
1148 Shadyoak Place
Santa Rosa, CA 95404
(707) 538-7251

Bob Creed
DOE Idaho
785 DOE Place, MS 1220
Idaho Falls, Idaho 83401-1562
(208) 526-9063, FAX (208) 526-1184

Nobuhiro Demboya
New Energy & Ind. Tech. Dev. Org.
SUNSHINE 60,1-1,3-Chome
Higashi-Ikebukuro,Toshim-ku
Tokyo, 170, Japan
03-3987-9451, FAX 03-3986-8197

David Duchane
Los Alamos Nat'l Lab.
P.O. Box 12663, MS D443
Los Alamos, NM 87545
(505) 667-9893, FAX (505) 667-8487

Herman Dykstra
Consultant
4180 Treat Blvd, Suite I
Concord, CA 94518
(510) 676-7464

Kathleen Enedy
Pacific Gas & Electric
111 Stony Circle
Santa Rosa, Ca 95401
(707) 577-7061, FAX (707) 577-7067

Steve Enedy
NCPA
P.O. Box 663
Middletown, CA 95461
(707) 987-3101, FAX (707) 987-2088

Iraj Ershaghi
USC/Pet. Eng. Progam
University Park- HED 316
Los Angeles, CA 90089-1211
(213) 740-0320

David Faulder
INEL
P.O. Box 1625
Idaho Falls, ID 83414-2107
(208) 526-0674, FAX (208) 526-0875

Shaun D. Fitzgerald
University of Cambridge
Earth Sciences, Downing St.
Cambridge, CG1 BEQ U.K.
44-223-333419, FAX 44-223-333450

Mostafa Fourar
Inst de Mecaniqe Des Fluides
Ave. Prof. Camille Soula
31400 Toulouse, France
61-28-58-70, FAX 61-28-58-99

Robert O. Fournier
USGS, MS 910
345 Middlefield Road
Menlo Park, CA 94025
(415) 329-5205, FAX (415) 329-5203

Sabodh K. Garg
S-Cubed
P.O. Box 1620
La Jolla, CA 92038-1620
(619) 453-0060, FAX (619) 755-0474

John Garnish
Comm. of the European
Communities
SDME3/4, Rue de la Loi 200
B-1049 Brussels Belgium
(322) 235-8518, FAX (322) 236-3024

Albert Genter
Bureau Recherches Geologiques
Ave. de Concyr- BP6009
45060 Orleans, Cedex 2 France
33-38-64-39-38, FAX 33-38-64-31-72

Keshav Goyal
Calpine Corporation
P.O.Box 11279
Santa Rosa, CA 95406-1279
(707) 527-6700, FAX (707) 544-2422

Francois Groff
SGP, Petroleum Engineering Dept.
Stanford University, Stanford, CA 94305
(415) 723-4744, FAX (415) 725-2099

Mohinder Gulati
Unocal
Room M-36, P.O. Box 7600
Los Angeles, Ca 90051
(213) 977-7486, FAX (213) 977-6333

Richard Gunderson
Unocal
P.O. Box 6854
Santa Rosa, CA 95406
(707) 545-7600, FAX (707) 544-6855

Hector Gutieriez
CFE, Mexico
Alejandro Volta 655
Morelia 58260, Mich., Mexico
(451) 5-6-7-82

Toshiyuki Hashida
R.I.F.T., Tohoku University
Aramaki, Aobaku,
Sendai 980, Japan
022-222-1800

Charles B. Haukwa
LBL, Bldg 50E
I Cyclotron Road
Berkeley, CA 94720
(510) 486-4160, FAX (510) 486-5401

Manfred P. Hockstein
Geothermal Institute, Univ. of Auckland
Private Bag, New Zealand
(9) 373 7999, FAX (9) 373 7436

Roland N. Horne
SGP, Petroleum Engineering Dept.
Stanford University
Stanford, CA 93405-2220
(415) 723-9595, FAX (415) 725-2099

Glenn D. Horton
Pacific Gas & Electric
111 Stony Circle
Santa Rosa, CA 95401
(707) 577-7062, FAX (707) 577-7067

Masami Hyodo
Geothermal Energy R. & D. Co., Ltd.
Kyodo Bldg, 11-7, Kabuto-cho
Nihonbashi, Chuo-ku
Tokyo 103, Japan
(03) 3666-5822, FAX (03) 3666-5289

Eduardo R. Iglesias
Instituto de Invest'nes Electricas
Apartado Postal 475
2000 Cuernavaca, Mor. Mexico
(73) 18-38-11, FAX (73) 18-25-26

Steve Ingebritsen
U.S. Geological Survey
345 Middlefield Rd, MS 439
Menlo Park, CA 94025
(415) 329-4422, FAX (415) 329-4463

Joe Iovenitti
Weiss Associates
5500 Shellmound Street
Emeryville, CA 94608
(510) 547-5420, (510) 543-5043

T. Ishido
Geological Survey of Japan
10103 Higashi, Tsukuba
Ibaraki 305, Japan
298-54-3736, FAX 298-54-3533

Jun-ichi Ishikawa
New Energy & Ind. Tech. Dev. Org.
SUNSHINE 60, 1-1,3-chome,
Higashi-Ikebukuro, Toshima-ku,
Tokyo, 170 Japan
03-3987-9451, FAX 03-3986-8197

Steve Jones
NCPA
P.O. Box 663
Middletown, CA 95461
(707) 987-3101, FAX (707) 987-2088

Dennis Kaspereit
California Energy Company Inc.
P.O.Box 185
Ridgecrest, California 93556
(619) 499-2300, FAX (619) 499-2308

Tayuki Kondo
JMC Geothermal Res. Dev. Co.
72-2 Sasamori, Ukai, Takazawa-Mura
Iwate 020-01, Japan
81-196-84-4114, FAX 81-196-84-6231

Paul Kruger
Civil Engineering Department
Stanford University
Stanford, CA 94305
(415) 725-2382

Mark Kumataka
Santa Fe Geothermal, Inc.
P.O. Box 1009
Middletown, CA 95461
(707) 987-2335, FAX (707) 987-2353

Pete Ledingham
Geoscience Ltd
Falmouth Bus. Park, Bickland W R
Falmouth,Cornwall TR11 4SZ
United Kingdom
44-326-211070, FAX 44-326-211073

An Lin-Ji
University of Southern Calif.
Pet. Eng. Prog., Univ. Park-HED 316
Los Angeles, CA 90089-1211
(213) 740-0322

Marcelo J. Lippmann
Lawrence Berkeley Laboratory
Bldg 50E
Berkeley, CA 94720
(510) 486-5035

David B. Lombard
U.S. Dept. of Energy
Geothermal Division, CE-122
Washington, D.C. 20585
(202) 586-4952, FAX (202) 586-8134

James Lovekin
California Energy Company, Inc.
900 N. Heritage, Bldg D
Ridgecrest, CA 93555
(619) 499-2322, FAX (619) 499-2308

Paul Macdonald
AEA Technology
Energy Technology Support Unit
Harwell, Oxford, OX11 ORA
United Kingdom
0235-432251, FAX 0235-432817

E. James Macias
Pacific Gas & Electric
111 Stony Circle
Santa Rosa, CA 95401
(707) 577-7061, FAX (707) 577-7067

Harada Madoka
Electric Power Dev. Co., Ltd.
15-1, Ginza 6-chome,Chuo-ku
Tokyo 103, Japan
03-3546-2211, FAX 03-3546-1685

Celso C. Maligalig
Unocal Geothermal Division
81-711 Highway 111,
Indio, CA 92201
(619) 342-4723, FAX (619) 347-4224

H.K. 'Pete' McCluer
Consultant
P. O. Box 650
Mt. Aukum, CA 95656
(209) 245-4171, (916) 626-0189

James R. McNitt
GeothermEx
5221 Central, Suite 201
Richmond, CA 94804
(510) 527-9876, FAX (510) 527-8163

Dave Meade
U.S.Navy-Geothermal Prog. Office
Naval Air Weapons Station
China Lake, CA 93555
(619) 939-3411, ext. 242,
FAX (619) 939-2449

Tsvi Meidav
Trans-Pacific Geothermal Corp.
1901 Harrison St., Suite 1590
Oakland, CA 94612
(510) 763-7812, FAX (510) 763-2504

Tony Menzies
GeothermEx
5221 Central Ave
Richmond, CA 94804
(510) 527-9876, FAX (510) 527-8163

Donald Michels
Don Michels Associates
PO Box 8652
Missoula, Montana 59807
(406) 728-2576, FAX (406) 721-7671

Frank G. Miller
SGP, Petroleum Engineering Department
Stanford University, Stanford, CA 94305
(415) 723-2938, FAX (415) 725-2099

Leland L. Mink
Idaho Water Resources Res. Inst.
Morrill Hall 106, Univ. Of Idaho
Moscow, Idaho 83843
(208) 885-6429, FAX (208) 885-6431

Dr. John E. Mock
U. S. DOE, Geothermal Division CE 122
1000 Independence Ave
Washington, D.C. 20585
(202) 586-5340, FAX (202) 586-8134

Phil Mogen
Unocal Geothermal
P. 0. Box 1805
Indio, CA 92202
(619) 342-4723, (619) 347-4224

George M. Moore
Kenney, Burd, Knutson & Markowitz
Four Embarcadero Ctr., 25th Floor
San Francisco, CA 94111
(415) 397-3100, FAX (415) 397-3170

Joe Moore
UURI
391 A.Chipeta Way, Research Park
Salt Lake City, UT 84108
(801) 524-3428, FAX (801) 524-3453

Dennis Nielson
UURI
391 C. Chipeta Way, Research Park
Salt Lake City, UT 84108

Gerald Niimi
Thermasource
7825 Farmers Lane, Suite II
Santa Rosa, CA 95402
(707) 523-2960, FAX (707) 523-1029

S. Bwire Ojiambo
KPLC./Univ. Nevada at Reno
1170 The Strand
Reno, NV 89503
(702) 784-6072, FAX (702) 784-1766

Harry J. Olson
University of Hawaii At Manoa
Look Lab, 811 Olomehani Street
Honolulu, Hawaii 96813
(808) 522-5620, FAX (808) 522-5618

Will Osborn
Mission 0 & M, Inc. East Mesa
3300 E. Evans Hewes Highway
Holtville, CA 92250
(619) 356-3020, FAX (619) 356-3035

Carel Otte
Consultant
4261 Commonwealth Ave.
La Cañada, CA 91011
(818) 952-0176

Patricia Patrier
Lab de Pét. des Alt's. Hydrothermales
Bât. GON, 40 Av. du Recteur Pineau
86022 Poitiers Cedex, FRANCE
49-45-37-34, FAX 49-45-36-00

Paul Pettit
Petroleum Engineering Dept.,
Stanford University
Stanford, Ca 94305
(415) 723-0525, FAX (415) 725-2099

Susan Petty
Susan Petty Consulting
704 Santa Paula
Solana Beach, CA 92075
(619) 792-9055, FAX (619) 792-9055

Alfonso S. Pingol
Unocal
3576 Unocal Place
Santa Rosa, CA 95401
(707) 545-7600, FAX (707) 545-8746

Harry Prabowo
Unocal Geothemal of Indonesia
3576 Unocal Place
Santa Rosa, CA 95403
(707) 545-7600, FAX (707) 545-8746

John W. Pritchett
S-Cubed
P.O. Box 1620
La Jolla, CA 92038-1620
(619) 453-0060, FAX (619) 755-0474

Alice Probst
Unocal Science & Technology
376 S. Valencia
Brea, CA 92621
(714) 577-2388, FAX (619) 577-3176

Karsten Pruess
Lawrence Berkeley Laboratory
Mail Stop 50E
Berkeley, CA 94720
(510) 486-6732, FAX (510) 486-5686

Luis Quijano
Comision Federal de Electricidad
Apartado Postal 230-C
Morelia, Mich. 58290 Mexico
(451) 4-49-40, FAX (451) 4-47-35

Henry J. Ramey, Jr.
SGP, Petroleum Engineering Dept.
Stanford University
Stanford, CA 94305
(415) 723-1774, FAX (415) 725-2099

Marshall Reed
US/DOE, Geothermal Division
CE 122
Washington, DC 20585
(202) 586-8076, FAX (510) 586-8134

Joel Renner
Idaho Nat'l Eng. Laboratory
Box 1625
Idaho Falls, ID 83415-3526
(208) 526-9824, (208) 526-0969

Stuart Russell
Russell Associates
2555 Park Blvd, Suite 32
Palo Alto, CA 94306
(415) 321-9545, FAX (415) 321-9550

Muhammad Sahimi
USC
Petr Eng. Prog./University Park
Los Angeles, CA 90089-1211

Fernando Samaniego
UNAM, Div. Estudios de Posgrado
Facultad de Ingenieria 04510
Mexico D.F., Mexico
(525) 550-8712, FAX (525) 548-0950

Charles Sammis
USC, Geol. Sci. Dept.
University Park
Los Angeles, CA 90089
(213) 750-5836

Ron C. Schroeder
Berkeley Group Inc.
1090 Heinz Ave.
Berkeley, CA 94710
(510) 841-9410

Mike Shook
Idaho Nat'l Engineering Lab.
P.O.Box 1625, MS 2107
Idaho Falls, ID 83415
(208) 526-6945, FAX (208) 526-0875

Paul Spielman
California Energy Co., Inc..
900 N. Heritage, Bldg. D
Ridgecrest, CA 93555
(619) 499-2300, FAX (619) 499-2308

Paolo Squarci
Int. Inst. Geothermal Research, CNR
Piazza Solverino - 2
56126 Pisa, Italy
39-50-41503, FAX 39-50-47055

Ken Stelling
State of California
50 'D' Street, Room 300
Santa Rosa, CA 95404
(707) 576-2385, FAX (707) 576-2611

M. Cesar Suarez-Arriaga
Comision Fed. de Electricidad
Apartado Postal 31-G
Morelia, Mich. 58290 Mexico
(451) 56782, FAX (451) 54735

Junji Suyama
Univ. of Nevada, Las Vegas
4-3-15 Yushima, Bunkyo-Ku
Tokyo 113, Japan

Alfred Truesdell
Entropy Inc.
700 Hermosa Way
Menlo Park, CA 94023
(415) 322-6135, FAX (415) 324-4009

Todd Van de Putte
Unocal Geothermal
P.O. Box 1805
Indio, Ca 92202
(619) 342-4723, FAX (619) 342-4224

Mark A. Walters
Russian River Energy Company
1400 No. Dutton Ave., Suite 23
Santa Rosa, CA 95401
(707) 523-4272, FAX (707) 575-8429

Colin F. Williams
U.S. Geological Survey
MS 923, 345 Middlefield Road
Menlo Park, CA 94025
(415) 329-4881, FAX (415) 329-4876

Ken Williamson
Unocal
3576 Unocal Place
Santa Rosa, CA 95406
(707) 545-7600, FAX (707) 545-8760

Phillip Michael Wright
UURI
391 Chipeta Way, Suite C
Salt Lake City, UT 84108
(801) 524-3439, (801) 524-3453

Kasumi Yasukawa
LBL, Earth Sciences Div.
50 E, I Cyclotron Road
Berkeley, CA 94720
(510) 486-4160, FAX (510) 486-5686

Yanis Yortsos
USC, Pet. Engr. Program
Univ. Park HED 316
Los Angeles, CA 90089-1211
(213) 740-0317

Robert W. Zimmerman
Lawrence Berkeley Lab
I Cyclotron Road
Berkeley, CA 94720
(510) 486-7106, FAX (510) 486-5686

SUBJECT INDEX

AUTHOR INDEX